Corrosion Behaviour of AGR Simulated Fuels (SIMFUELs)

Nadya Rauff-Nisthar

B.Sc. (Hons), M.Sc.

Submitted to Lancaster University in partial fulfilment for the

requirements for the degree of

DOCTOR OF PHILOSOPHY

June 2021

In memory of Pat Murphy

Declaration

The work undertaken in this thesis was carried out in the Engineering Department, Lancaster University, and the Institute of Transuranium Elements (ITU), from December 2011 to June 2016. Unless stated otherwise it is the work of the author and has not been submitted in support of any other degree.

Signature: _____

Nadya Rauff-Nisthar

Abstract

The UK radioactive waste inventory includes spent fuels from various reactor types, many of which have compositions and irradiation histories that are unique to the UK. These include uranium oxide fuels from existing Advanced Gas-cooled Reactor (AGR) power stations, of which approximately 4,500 tonnes is forecast not to be reprocessed and thus will require disposal in a Geological Disposal Facility (GDF)(1). The direct disposal of spent nuclear fuel into a geological repository is part of the nuclear waste policy of several mature nuclear states. The vast majority of this fuel is from light-water moderated reactors (LWR) and a significant amount of research has been carried out to support the direct disposal concept in terms of the physical and aqueous durability of the container, the cladding and the irradiated UO_2-based fuel. In the UK, a large proportion of SNF is from indigenous Advanced Gas-cooled Reactors. AGRs, whilst also using UO_2-based fuel, employ CO_2 as coolant and are graphite moderated. Further, the fuel assembly cladding is comprised of 20/25/Nb stainless steel (20% Cr, 20% Ni) rather than zircalloy as is the case in Pressurised Water Reactors (PWRs). Consequently, AGR fuel has unique characteristics that need to be evaluated in order to satisfy safety case requirements before it can be disposed of in a geological repository.

It is expected that, at some point after repository closure, the canisters within which the SNF is sealed will fail, allowing the ingress of groundwater. This groundwater may come into contact with the 20/25/Nb stainless steel cladding and subsequently the UO_2 fuel pellets, initiating corrosion on either one or both elements of the SNF. At this failure point, most β/γ radiation will have decayed away, with just α-radiation remaining, initiating the process of the α-radiolysis of water. Alpha-radiolysis of the invading groundwater contacting the UO_2 fuel pins will generate H_2O_2, which through a conversion mechanism can lead to the formation of studtites. Furthermore, the 20/25/Nb cladding may also show susceptibility to near field corrosion.

The objectives of this work are therefore to examine the mechanisms that occur during the corrosion of annular AGR simulant fuel. This will lead to the establishment of the baseline corrosion behaviour and give a better understanding into the formation of secondary uranyl phases.

A range of AGR SIMFUELs of simulated burn-ups have been fabricated. Using combined Raman and electrochemical studies, the effects of the added dopants on the UO_2 crystal structure have been investigated. The effect of deliberately added H_2O_2 on the surface of simulated AGR fuels has also been studied. Additionally, the electrochemical baseline behaviour of the minor actinide americium in nitric acid media representative of reprocessing within the nuclear fuel cycle and the possible subsequent uptake of americium onto stainless steels representative throughout the nuclear industry have also been investigated.

It was found that SIMFUEL samples prepared in the absence of dopants (pure UO_2 pellets) exhibit the cubic fluorite structure expected of UO_2. This is observed for both 25 and 43 GWd/tU burn-up SIMFUEL, reflecting the introduction of dopant-associated lattice defects into the H_2O_2 matrix. As might be expected, the peak intensity is greater for the 43 GWd/tU sample.

Voltammetry indicates the presence of three oxidation waves in neutral media typical of UK groundwater concepts: the oxidation of UO_{2+x} sites at grain boundaries at -0.6 V vs SCE; the oxidation of UO_2 to UO_{2+x} within the grains at -0.1 V; and the oxidation of UO_{2+x} to U(VI) species at +0.3 V. The currents associated with all three waves increase with simulated burn-up indicating a similarly increasing susceptibility to anodic corrosion reactions with burn-up. The size of the feature at -0.6 V suggests a high concentration of UO_{2+x} sites at grain boundaries. As these may act as preferential and localized corrosion sites, it may be that fission products residing in grain boundaries will be instantly released on contact with groundwater. A literature review exploring the effects of hyperstoichiometric phases on UO_2 dissolution suggest that spent fuel, where grain boundaries can contain non-stoichiometric sites, is able to corrode more quickly in comparison with stoichiometric grains. Therefore the assumption that radionuclides on grain boundaries will be released instantly upon contact with groundwater is a realistic assumption (2)).

An increase in the lattice damage peak in the Raman spectrum is observed when the SIMFUEL is exposed to H_2O_2 representative of a repository near-field, suggesting that the structure at the surface is becoming more distressed. Supported by concurrent E_{OC} measurements, this is consistent with additional point defects being established as the concentration of interstitial oxygen is increased in the lattice via H_2O_2 induced surface oxidation of the SIMFUEL – so increasing the

concentration of UO_{2+x} sites both on and within the grains and thus increasing the susceptibility of the SIMFUEL to corrosion.

Open circuit potential measurements on 43 GWd/tU burn-up AGR SIMFUEL in modified simplified groundwater indicate that the SIMFUEL may corrode in the modified simplified groundwater even in the absence of a peroxide generated oxidative stress. Similar studies of the same SIMFUEL held in contact with samples of the 20/25/Nb steel cladding show that this coupled system exhibits a mixed potential of ~-0.12 V vs SCE. This potential is (i) negative of that adopted by the isolated SIMFUEL and (ii) positive of that adopted by the isolated cladding in electrolytes of the same composition implying that, whilst corrosion at SIMFUEL's grain boundaries may still obtain, the UO_2 matrix is at least in part protected against on-grain corrosion at the expense of the steel cladding.

In the case of americium we found that, by use of cyclic voltammetry, it is possible to indirectly observe the electrochemical oxidation of Am(III) to Am(VI) on glassy carbon electrodes. This oxidation occurs stoichiometrically, yielding a 100% conversion to Am(VI) in the local diffusion layer of the electrode. The electrochemically generated higher oxidation states of Am are stable on the timescale of a typical voltammetric experiment, opening the possibility of an electrochemical route to the reagentless generation of Am(VI) in advanced Am separation schemes that employ the higher oxidation states of americium. It was also confirmed that, under conventional solvent extraction conditions, Am(III) cannot act as a process steel corrosion accelerator via the generation of Am(VI).

References:

(1) **Amec Foster Wheeler.** *Scoping studies of the matrix dissolution rate and instant release fraction of spent AGR fuel.* s.l. : Studsvik Report no. 103583-01, Issue 3, 2016

(2) **H. He, Z. Qin, D.W. Shoesmith.** *Characterizing the relationship between hyperstoichiometry, defect structure and local corrosion kinetics of uranium dioxide.* s.l. : Electrochimica Acta, 2010, Vol. 56. pp. 53-60

Acknowledgements

First and foremost, I would like to express my gratitude to my supervisor Professor Colin Boxall for his patience, guidance and scientific input throughout my PhD journey. I would also like to thank the LRF group, and in particular, my second supervisor Dr Richard Wilbraham for all the help they have given me. It would not have been possible without them.

Secondly, I would like to thank the JRC Karlsruhe for allowing me to carry out experiments at their laboratories, and in particular Dr Detlef Wegen and Dr Rikard Malmbeck for their supervision and experimental support. Especially Detlef, who spent many hours imparting his electrochemical knowledge to me.

I am grateful to the Spent Nuclear Fuel Consortium for their many discussions and contributions towards this project.

I would also like to express my gratitude for the funding received through the Lloyd's Register Foundation as well as the TALISMAN and JRC Traineeship programmes to carry out this work.

Thanks must also be given to Dr Jone Elorrieta for her invaluable assistance with data processing on Origin.

I will always be grateful to my friends at Lancaster who have supported me throughout, and given me fond memories of Lancaster - Becca, Lula, Miriam, Sukhraaj, Pat and Ioannis, thank you.

I would also like to acknowledge my closest friends, in particular Sam & Karmen, as well as my family for their constant support and encouragement.

Last but not least, my deepest gratitude goes to my husband Frédéric, for always keeping me on my toes with his constant teasing and banter – thank you *Doudou*.

Contents

List of Figures

List of Tables

List of Abbreviations

AFM	Atomic Force Microscopy
AGR	Advanced Gas-cooled Reactor
ANDRA	Agence nationale pour la gestion des déchets radioactifs
BSE	Backscattered Electrons
BWR	Boiling Water Reactor
CANDU	CANada Deuterium Uranium
CEA	Commissariat á l'énergie
CE	Counter Electrode
COX	Callovo Oxfordian
CV	Cyclic Voltammetry
DAAP	Diamyl Amylphosphonate
DOS	Density of states
EDF	Électricité de France
EDX	Energy Dispersive X-Ray
EIS	Electrochemical Impedance Spectroscopy
EQCM	Elecrochemical Quartz Crystal Microbalance
fcc	face centred cubic
FISPIN	
GDF	Geological Disposal Facility
GO	Graphene Oxide
GRiN	Graphene Ring Nanoeletrode
HAAR	Highly Active Aqueous Raffinate
HLW	High Level Waste
IAEA	International Atomic Energy Agency
ICDD	International Central Diffraction Data

ILW	Intermediate Level Waste
IR	Infrared
IRF	Instant Release Fraction
LWR	Light Water Reactor
LO	Longitudinal Optical
MAUD	Material Analysis Using Diffraction
MOX	Mixed Oxide Fuel
NDA	Nuclear Decommissioning Authority
NNL	National Nuclear Laboratory
OCP	Open Circuit Potential
PNNL	Pacific Northwest National Laboratory
PTFE	Polytetrafluoroethylene
PUREX	Plutonium Uranium Redox Extraction
PWR	Pressurised Water Reactor
RE	Rare Earth
RE	Reference Electrode
SAM	Scanning Auger Microprobe
SCE	Saturated Calomel Electrode
SDD	Silicon Drift Detector
SECM	Scanning Electrochemical Microscopy
SEM	Scanning Electron Microscopy
SEM-BS	Scanning Electron Microscopy – Back Scattered
SF	Spent Fuel
SHE	Standard Hydrogen Electrode
SIMFUEL	Simulated Fuel
SPM	Scanning Probe Microscopy
SSCE	Silver Silver Chloride Electrode

TBP	TriButyl Phosphate
THORP	THermal Oxide Reprocessing Plant
WE	Working Electrode
WIPP	Waste Isolation Pilot Plant
XPS	X-Ray Photoelectron Spectroscopy
XRD	X-Ray Diffraction

List of Symbols

α	Alpha
ß	Beta
C	Capacitance
CaF_2	Cubic fluorite structure
E_A	Activation energy
E_F	Fermi level
E_{PA}	Anodic peak potential
E_{PC}	Cathodic peak potential
E_{pit}	Critical pitting
E_{pp}	Primary passivation potential
Eg	Band gap of energy
eV	Electron volts
E_{OC}	Open circuit potential
γ	Gamma
GWd/tU	Gigawatt-days per ton of uranium
i	Interstitial site
i_{corr}	Corrosion current density
i_{PA}	Anodic current
i_{PC}	Cathodic current
iR	Current interrupt
I	Current
K	Kelvin
kT	Boltzmann constant x temperature
µ	Micro
mV	Millivolt

Oi	Interstitial oxygen
R	Resistance
T	Temperature
U_{eff}	Coulomb correlation value
V	Volt
Z'	Real impedance
Z"	Imaginary impedance

Contents

Chapter 1 Introduction

1.1 Background

1.1.1 Nuclear Fission

In nuclear chemistry and engineering, nuclear fission is a nuclear reaction in which the nucleus of an atom splits into smaller parts when hit with an incident neutron, releasing energy (1). Nuclear fission can also occur without the bombardment of a neutron, the process of which is known as radioactive decay (1). This type of fission, which is called spontaneous fission, is rare, except for in some cases which involve isotopes from heavy elements. In an engineered nuclear device, such as a nuclear reactor, the former process of a nuclear reaction, where the bombardment of a neutron into an atomic nucleus resulting in the release of energy takes place rather than by the spontaneous radioactive process radioactive decay (1). The schematic below outlines the process of nuclear fission which is described above.

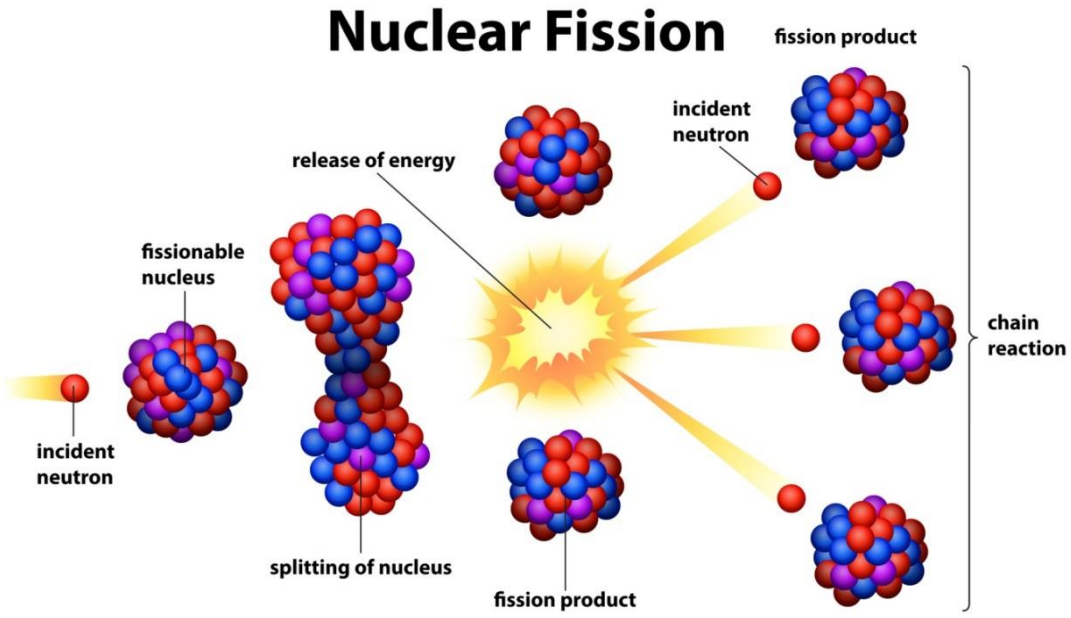

Figure 1-1 showing process of nuclear fission (2)

Nuclear reactors are most commonly thermal reactors, that use slow or thermal neutrons (3). Thermal reactors use a neutron moderator to slow down the neutrons until they have approached the average kinetic energy of the particles that surround the neutron moderator (3). In other words, this process reduces down the speed of the neutron to a low-velocity, thermal neutron (3).

In order for a nuclear reaction to take place in a thermal nuclear reactor, a fissile material must be bred into it. The few fissile nuclei that are found in nature all belong to heavy atoms (4). The most notable of these fissile nuclei from a nuclear power point of view are uranium-233, uranium-235 and plutonium-239 (4). Uranium-233 and plutonium-239 are artificially produced from the fertile materials uranium-238 and thorium-232 respectively, which are the only two naturally occurring fertile materials (5). A fertile material is itself not capable of undergoing fission with low energy neutrons (5). When a fertile material such as thorium-232 is bombarded with a slow neutron, it absorbs the neutron and transmutates to thorium-233. As thorium-233 has a short half-life (22 minutes), it decays into protactinium-233. Protactinium-233, also having a short half-life (27 days), decays into uranium-233 (6). This is how uranium-233 arises in the nuclear fuel cycle, where it is thermally bred from thorium-232 (7). A similar process occurs in uranium breeder reactors where fertile uranium-238 absorbs neutrons to form fissile plutonium-239. When uranium-238 is bombarded with neutrons, it absorbs one neutron and transmutates to uranium-239. This is then followed by two beta-decays, namely uranium-239 to neptunium-239 and finally from neptunium-239 to plutonium-239. Depending on the fuel cycle and the design of the reactor, the uranium-233 that is generated in the first scenario either fissions *in situ* or is chemically separated from the used nuclear fuel and formed into new nuclear fuel (7). The plutonium-239 that is generated as a result of neutron capture by uranium-235 is used as a mixed oxide fuel (MOX) mostly in Belgium, France, Switzerland and Japan. The majority of global nuclear power reactors use uranium-235 based fuels as either the metal or oxide at a range of enrichments. This is especially true for the UK, which is why this chapter will specifically focus on the uranium-235 fuel cycle. The fuel cycle is explained in more detail below.

1.1.2 Nuclear Fuel Cycle

Uanium-235 based fuel pellets contain UO_2 with fissile uranium-235 (U-235), and can therefore be used in the chain reaction that leads to the release of energy (8). Uranium in its natural form is abundant in the earth's crust. The isotope that is predominant in uranium is uranium-238, which is not radioactive and therefore not fissile (9). Natural uranium only contains about 0.7 % of the fissile uranium-235 isotope, which needs to be enriched to a higher concentration in order to be used as nuclear fuel (9). There are currently fourteen Advanced Gas-cooled (AGR) and one Pressurised Water (PWR) reactors in the UK (10). These reactors combined generate approximately 21% of the UK's electricity (9). The UK imports mined uranium which is then milled, enriched and fabricated into fuel. For an AGR reactor, the percentage of enrichment of uranium-235 typically ranges from 3.5-5% (9).

The difference in mass between uranium-235 and uranium-238 will allow for the separation of the isotopes by centrifuging, and therefore enabling the enrichment process of uranium-235 (9). In order for the uranium-235 to be enriched it must be in gaseous form (9). Hence, the nuclear fuel cycle starts with the mining of the uranium ore and the subsequent production of a U_3O_8 concentrate (for enrichment) (8). U_3O_8 in this instance is produced by crushing uranium ore which is then ground into a slurry that is typically leached in sulphuric acid (9). This allows for the separation of waste rocks from the desired uranium (9). The uranium is then recovered from the solution and the final product is precipitated as U_3O_8 concentrate (9). The concentrate is sold in this form for enrichment (9). At a conversion facility, the U_3O_8 will first be converted into uranium hexafluoride (UF_6) and then heated to 57^o C, at which point it is converted into a gas (8). This UF_6 gas is then enriched. Once enriched, the UF_6 gas is converted into UO_2 fuel (8). The route by which the manufacture of UO_2 is achieved is by first undergoing the Integrated Dry Route (IDR), followed by powder conditioning (11).

During the IDR process, the UF_6 is heated up to 250 ^{o}C to produce a flame of the aerosol UO_2F_2. This aerosol is then reduced with hydrogen, along with steam from 550 ^{o}C to 750 ^{o}C to form UO_2 (11). Once the UO_2 has been produced, the powder goes through a conditioning process, which includes sieving, blending to achieve the correct enrichment, the blending in of additives, optimising the pouring properties, and finally the addition of a die lubricant (11). Once the finished fuel has been used for power generation in a reactor, it can either be reprocessed or disposed of.

When the spent fuel from a reactor is reprocessed, the fuel cycle is referred to as a closed fuel cycle, whereas if the spent fuel is not reprocessed, it is referred to as an open fuel cycle (10). Figure 1-2 below shows the complete nuclear fuel cycle.

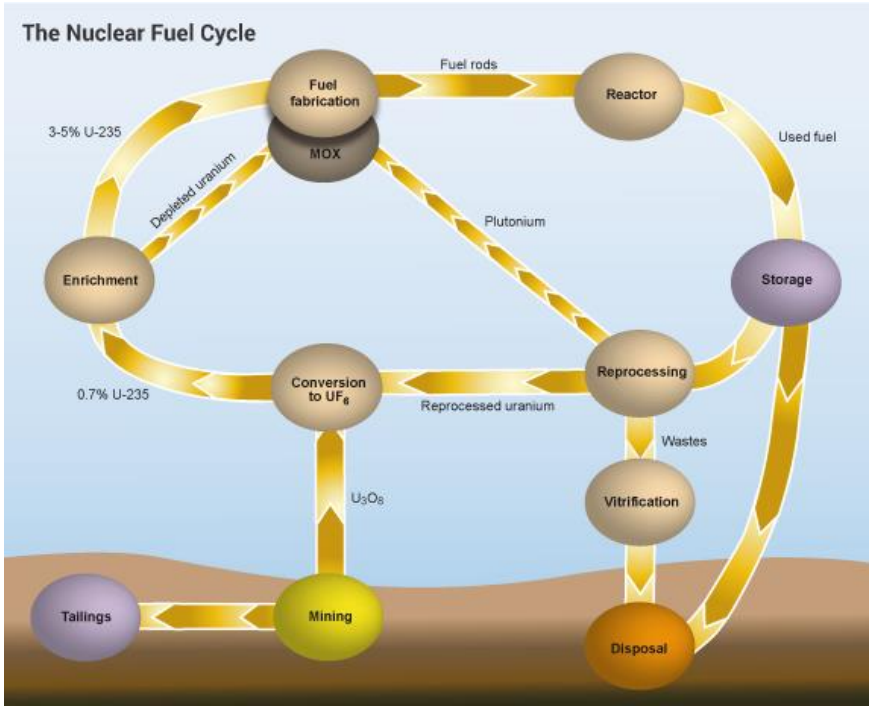

Figure 1-2 showing schematic of uranium-235 in an open and closed fuel cycle (9)

In an open fuel cycle, the spent fuel is sent to interim storage after removal from the reactor. Once stored in interim storage, the spent fuel is destined for final disposal at a Geological Disposal Facility (GDF), which is the end of the open fuel cycle, meaning that the spent fuel will not be reprocessed (10). Up until 2018, which is when the THermal Oxide Reprocessing Plant (THORP) at Sellafield closed, the UK has been operating a closed fuel cycle (12). This will however shift to an open fuel cycle in the future (13), which is why it is important to look into both fuel cycles, in other words, the reprocessing procedure and also the disposal of spent fuel at a GDF.

1.1.3 Reactors in the UK

The first commercial reactors that came into use were the Magnox reactors that are moderated by graphite and cooled by carbon dioxide (14). These Magnox reactors were later superseded by the AGRs between 1960-1970, which function on a slightly enriched oxide in fuel. There are currently 26 Magnox reactors in the UK, all of which have ceased generating power and will be decommissioned over the next 80 years (14). The problems that have been associated with the reactivity of CO_2 at high temperatures, and also the use of low burnup fuel has generally turned attention away from Magnox and towards Light Water Reactors (LWR) (14).

Magnox reactors are named with reference to the magnesium alloy that is used for the cladding that surrounds the natural uranium metal fuel rods. The integrity of the fuel-clad however limits the outlet temperature of the CO_2 to 450 ^oC. The corrosive effects of CO_2 on the mild steel components in the alloy further limits the outlet temperature to 370 ^oC (14). The CO_2 coolant operates at 11 bar and is kept at an inlet temperature of 160 ^oC. The steam generators are operative at two pressures – high and low. Dual pressure steam cycles such as these are rather uncommon in modern reactor designs (14).

The natural uranium that is used in Magnox reactors is susceptible to radiation damage which leads to dimensional changes of the fuel elements. This means that the fuel has to typically be changed after an output of only 3500 MWd/tU. This figure is low when compared to LWR fuel which only has to be changed after 40000 MWd/tU (14). The low output is however partly off-set by the fact that it is possible to refuel on load, meaning the energy production efficiency can be optimised as there is no need to shut down in order to refuel (14). The above-mentioned features stem from the weapons programme when it was possible to easily withdraw fuel during operation, and the build-up of Pu^{240}, which is undesirable for weapons, could be avoided by processing low burnup fuel elements (14). In comparison to modern AGR and LWR reactors, the thermal efficiency and output of a Magnox reactor are low – approximately 25 % and 150 MW electrical power, respectively. Magnox reactors are, however, long-lived, with some operating in excess of 50 years (14). Below is a schematic of a Magnox reactor, as described above.

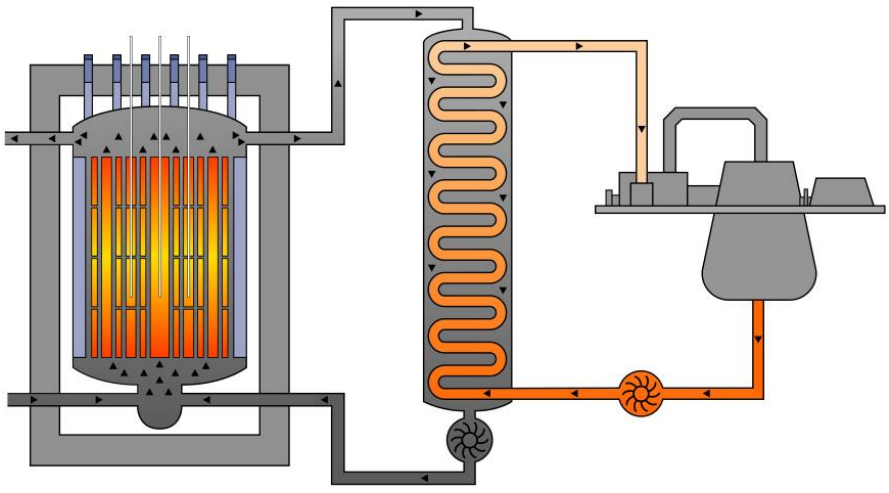

Figure 1-3 schematic of a Magnox reactor (14)

AGRs use a slightly enriched uranium fuel compared to the Magnox reactors which use uranium in its natural form. The UO_2 in AGRs is UO_2 enriched to approximately 2-2.6 %. The core of the AGR fuel is more compact than that of Magnox and also has a lower fuel mass (14). Owing to the improvements in cladding compared to Magnox fuel, the use of an oxide fuel and also improved steel, it has been possible to enable greater pressure and temperature differentials to be maintained, which have subsequently resulted in an increased thermal efficiency of over 40%, when compared to Magnox fuel (14).

Even though the prototype of the AGR had been successful for over the 20 years, the scale –up to commercial operation has proven difficult and costly. A representation of an AGR has been given below.

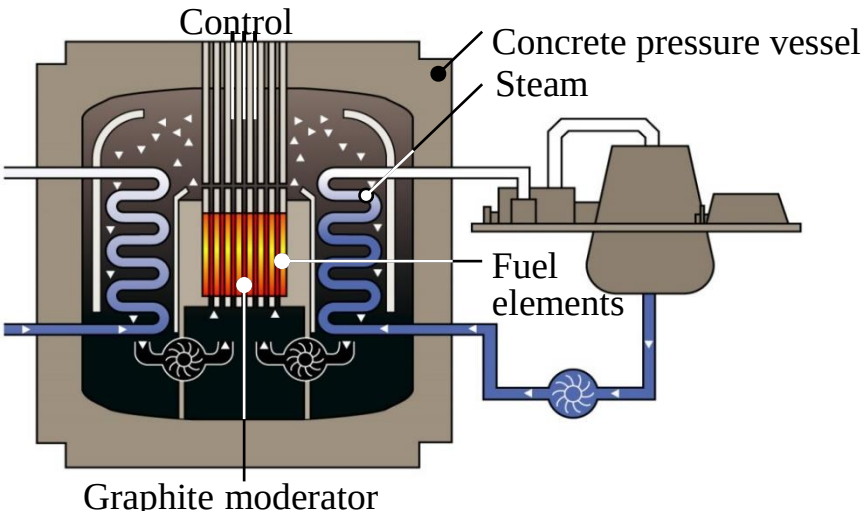

Figure 1-4 schematic of an AGR (14)

There are two types of LWRs, these are Pressurised Water Reactors (PWR), as shown in Figure 1-5 below, and Boiling Water Reactors (BWR). As water is cheap, abundant and has a short-lived diffusion and slowing down lengths, it can be used as both the moderator and the coolant (14). Since the conductivity of water is comparatively high, it is also necessary here to use fuel of slight enrichment. The uranium used in LWRs is enriched to approximately 2.5 – 3% (14).

In PWRs, the water is maintained in the liquid phase, and the primary cooling system is separated during the heat removal stage. In BWRs however, the water exists in both the gas and liquid phase.

The primary cooling system here includes a heat removal phase, which is known as a direct cycle (14). The term 'light' referred to in LWRs is used in order to distinguish the water from heavy water – D_2O.

The first commercial LWR plant was developed in 1957, with building having continued till present day.

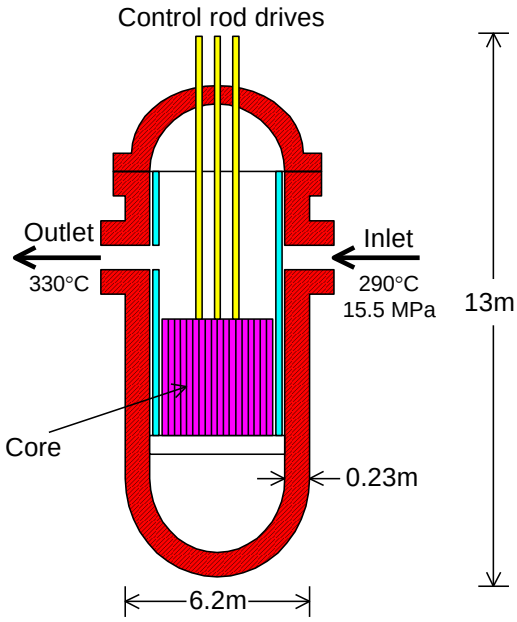

Figure 1-5 schematic of a PWR (14)

The PWR design consists of a primary loop that is in contact with the core, which provides water at a temperature of 330 ^{o}C and a pressure of 15.5 MPa to the secondary loop (14). The secondary loop provides feed water to the steam generators, which give steam at a temperature of 290 ^{o}C and a pressure of 7.2 MPa. The typical thermal power of a PWR is 3800 MW, with an electrical output of 1300 MW, which equals a low thermal efficiency of 34 %. The pressure vessel is made of low-alloy carbon steel, which includes a 33 stainless steel inner liner (14). The assembly of PWR fuel consists of zirconium rods which are transparent to neutrons and are also neutron resistant (14).

There are currently 15 AGRs operational in the UK, with many of them having had their expected life-time extended (9). The focus of this thesis will thus be on AGR, which will be described in more detail below.

1.1.3.1 Advanced Gas-cooled Reactors (AGR)

Like the PWR, the AGR also uses UO_2 as its main fuel material. However, as well as the differences in cladding, moderator and coolant materials used by AGRs compared to PWRs, AGR UO_2 fuel pellets are also different to PWR pellets. The AGR is made up of the following components:

Fuel – UO_2 with a pellet diameter of 14.5 mm

Fuel cladding – Stainless steel cladding consisting of20/25/Nb

Moderator – graphite, CO_2 gas also acts as weak moderator

Coolant – CO_2 gas

The finished AGR fuel is in the form of cylindrical pellets which are annular in shape, i.e. they contain a central hole (15). The annular shape of the pellet reduces the fuel temperature down its centreline, whilst also providing a reservoir for the containment of fission gases released from the fuel during irradiation (16) (17). The shape of the fuel rod has also shown to reduce the amount of stress imposed onto it, resulting in reduced cracking (17).

One fuel element consists of a total of 36 fuel pins (15), each one of which is encased in a 20/25/Nb stainless steel cladding (18), as can be seen in Figure 1-6 below. The composition of this steel is mainly 20 % chromium, 25 % nickel and stabilised with niobium (19).

Figure 1-6 schematic of an AGR fuel assembly cutaway (9)

AGR fuel pellets are encased in a metal cladding. This cladding is made from an austenitic stainless steel alloy consisting of 20Cr/25Ni/Nb (20). Due to the nature of storage of spent AGR fuel clad, there is the possibility of some degree of corrosion of the clad in the cooling ponds (20). The extent of corrosion has been shown to be correlated to the degree of radiation damage to the clad (20). Although the fuel clad encapsulates the fuel pellets in order to prevent fission product release (20), the release, and hence the rate of release of radionuclides from the fuel will be controlled by the rate of dissolution of UO_2 (21).

The main differences between the AGR reactors that are typically found in the UK, compared to light water (LWR) or pressurised water (PWR) reactors are that, the AGRs use graphite as the neutron moderator (22) (graphite is used here to slow down 'fast' neutrons into thermal neutrons which can be used in the fission of uranium-235 (23)), and CO_2 as the coolant (whereas water is used in both LWR and PWR reactors) (22). The annular shape of AGR fuel also differs to that of LWR and PWR fuel – there is no central hole in either LWR or PWR fuel (22). Due to the fact that AGRs operate at higher temperatures compared to LWR and PWR (825° C compared to 300° C), the UO_2 fuel in an AGR needs to be encased in a stainless steel cladding as opposed to a zircalloy cladding (22). The main differences between the reactor types compared here are reproduced in Table 1-1 below.

	Fuel and Cladding	Moderator	Coolant		Spent Fuel Reprocessing	Steam Cycle Efficiency
			Heat extraction	Outlet Temp.		
Magnox	Natural uranium metal (0.7 % U^{235}) Magnesium alloy cladding	Graphite	CO_2 gas heated by fuel raises steam in generator	360° C	Within one year for operational reasons	31 %
AGR	Uranium dioxide enriched to 2.3 % U^{235} Stainless steel cladding	Graphite	CO_2 gas heated by fuel raises steam in generator	650° C	Can be stored under water for tens of years	42 %
PWR	Uranium dioxide enriched to 3.2 % U^{235} Zirconium alloy cladding	Light Water	Pressurised light water pumped to steam generator which raises steam in separate circuit	317° C	Can be stored for long periods under water	32 %
BWR	Uranium dioxide enriched to 2.4 % U^{235} Zirconium alloy cladding	Light Water	Pressurised light water boiling in the pressure vessel produces steam which drives the turbine	286° C	As for PWR	32 %
CANDU	Unenriched uranium dioxide (0.7 % U^{235}) Zirconium alloy cladding	Heavy Water	Light water boiled at pressure – steam used to drive turbine	305° C	As for PWR	30 %

Table 1-1 Summary of the main thermal reactor types (24)

The operation of a reactor is limited by the potential of the fuel, or in other words, its burnup (9). The burnup of a fuel is determined by the level of its enrichment, for example, if the fuel is enriched to 4%, then its subsequent burnup would equal approximately 40 GWd/tU (9). The unit of gigawatt days per tonne of uranium is the conventional measure used for oxide fuels, where for example the amount of burnup, let's say 40 GWd/tU equates to the atomic percent burnup i.e. 4%; which is the amount of uranium atoms that are being burnt or being converted into fissile plutonium (9). The unit gigawatt-days is used at nuclear power plants to approximate the energy produced in one day. The gigawatt-day refers to the thermal power of the reactor, and not the fraction that is converted to electricity. Tonne refers to a metric ton of uranium metal (25).

After continued use, the number of fission products that are produced will amount to such a concentration that it is no longer practical to continue to use the fuel, and thus it is removed from the reactor, even if much of the potential remains within the fuel (9). Due to the radiation and heat that will still be emitted from the fuel, it is stored in ponds for cooling (9). The used fuel taken out of reactor is called spent fuel. Spent AGR fuel in the UK is sent to Sellafield for interim storage in its cooling ponds (26).

At this point, there are two options for the spent fuel; it can either be reprocessed so that the usable potential still contained within the spent fuel can be recycled and reused again in a reactor, or, the spent fuel can be put into long-term storage which is the final disposal route and does not involve any reprocessing (9). If the latter is chosen, it is where the nuclear fuel cycle ends. The complete nuclear fuel cycle is shown in Figure 1-2. In an open fuel cycle the spent fuel is reprocessed, as described below.

1.1.3.2 Nuclear Fuel Reprocessing

Nuclear fuel reprocessing involves the chemical separation of the remaining uranium and plutonium from the fission products and higher actinides contained in the spent fuel (10). Once the uranium has been reprocessed, it can be entered into the fuel cycle once again. All current industrial reprocessing in the UK is based on a liquid-liquid solvent extraction process which is known as the Plutonium Uranium Redox Extraction (PUREX) process (10). Nuclear fuel reprocessing for AGR spent fuel in the UK has been taking place at THORP in Sellafield, Cumbria until 2018. It is foreseen that all remaining spent fuel will be stored at interim storage until a permanent solution for disposal (12).

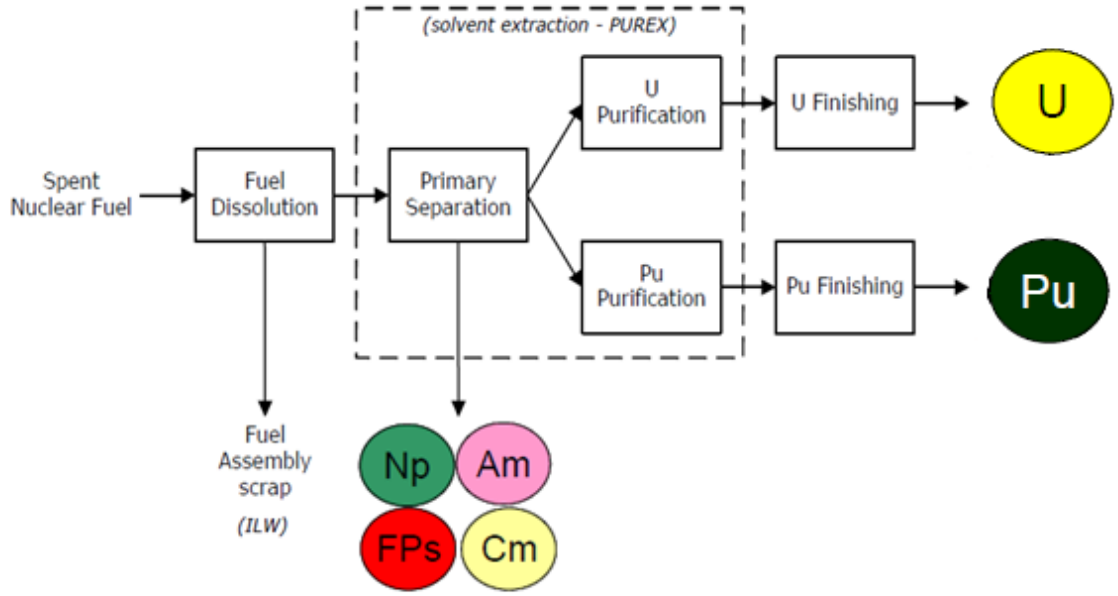

Figure 1-7 showing schematic of reprocessing of AGR spent fuel

In order to reprocess the spent fuel, the cladding must first be removed. In the case of spent AGR fuel, the fuel assembly is taken apart, and the fuel and clad are placed into the dissolver together. The solids from the clad are only separated out after the dissolution has taken place (10). At THORP the AGR fuel assembly is sheared into small pieces of approximately 5 cm in size. These pieces are then allowed to fall into a basket that is partly immersed in approximately 7 mol dm^{-3} nitric acid, at a temperature of 90^{o} C (10). These clad solids, which are often referred to as the hulls, are then removed from the dissolver and discarded as Intermediate Level Waste (ILW). Because the AGR fuel is dissolved in nitric acid, both the uranium and plutonium components of the fuel are oxidised to the +6 valance states. There may also be some nitric oxide or nitrogen dioxide gases that be released according to the following equations (10):

$$3UO_2 + 8HNO_3 \rightarrow 3UO_2(NO_3)_2 + 2NO + 4H_2O$$

Equation 1-1

$$UO_2 + 4HNO_3 \rightarrow UO_2(NO_3)_2 + 2NO_2 + 2H_2O$$

Equation 1-2

During the process of fuel dissolution, some fission products will also be released as gases or as steam. The standard PUREX process cannot be used to separate out long-lived fission products such as Cs and Sr so they end up as high level waste raffinate. Some fission products such as iodine, can however be directed into the off-gases during shearing, and finally removed using a caustic wash (10).

Once the fuel has been dissolved, the nitric acid concentration is adjusted to a lower concentration of 2-3 M. Subsequently, additions of hydrogen peroxide, and either nitrous acid, or, nitrogen tetraoxide are made in order to reduce the plutonium to its most extractable oxidation state, which is +4 (10). The next step in the PUREX process is the chemical separation.

The process of liquid-liquid extraction is how a desired solute is extracted from a feed or inlet stream, containing the substrate to be extracted, by the use of a solvent (10). The solvent in this case is the second immiscible liquid into which the solute is transferred to produce an extract, which is an outlet stream that contains the solute, and a raffinate, which is the feed material minus the solute (10).

During the PUREX process, an aqueous phase that contains all of the dissolved fuel, or feed in other words, is exposed to an organic solvent phase (the solvent in this case), in a series of contactors (10). The two immiscible phases are thoroughly agitated in the contactors, and then allowed to separate out. At each stage the desired products, which in this case are uranium and plutonium, are extracted from the aqueous phase by the organic solvent (10). The solvent phase will subsequently contain the extracted uranium and plutonium, whereas the fission products remain in the aqueous phase, which is the raffinate. The separation process may not be completed in each contactor, which is why several stages are often necessary to achieve the desired separation (10).

During the first of many stages (mentioned above), the uranium and plutonium are separated out from the fission products and minor actinides (such as americium) in the aqueous nitric acid stream using TriButyl Phosphate (TBP) dissolved in odourless kerosene (10). Uranium and plutonium then enter the organic phase as the TBP/nitrate mix complexes as $Pu(NO_3)\cdot TBP$ and $UO_2(NO_3)\cdot$ TBP, whilst the fission products and minor actinides remain in the aqueous phase. During the second stage, the

plutonium is stripped from the solvent phase by reducing the plutonium to Pu(III) using ferrous sulfamate, which allows the plutonium to be back extracted to the aqueous phase (10). Once the uranium and plutonium have been separated out, the uranium is evaporated to $UO_2(NO_3)_2 \cdot 6H_2O$ and thermally de-nitrated to UO_3, while the plutonium is precipitated as PuF_3 and PuO_2. These are then converted into plutonium metal via the reduction with cadmium (10). These high level strategic materials are then either solidified and disposed of, or re-used in fuel manufacture.

Having discussed the processes and chemicals that are involved in the PUREX separation, it is also important to look at the properties of the main material from which reprocessing pipework and associated plants are comprised of; stainless steel. The behaviour of the minor actinides (americium) and their uptake onto commonly used process steels in the nuclear industry will be investigated and discussed in further detail in Chapter 8 'Surface alteration influenced by actinides'. We will now turn our focus back to the disposal route.

1.1.4 Proposed Geological Disposal of Radioactive Waste in the UK

Nuclear waste is categorised into the following three categories: high, intermediate, and low level waste (9). The categorisation of each respective waste helps to determine how the waste should be disposed of. High-level waste requires to be cooled and also to be shielded, whilst low-level waste can easily be handled without shielding (9). Below is a representation showing the different categories of nuclear waste and their disposal routes with respect to their half-lives, as outlined by the International Atomic Energy Agency (IAEA) (27). It should be noted that the term activity content is used due to the generally heterogeneous nature of radioactive waste. In other words, it is a generic term that has been used to cover activity concentration, specific activity, as well as total activity (27).

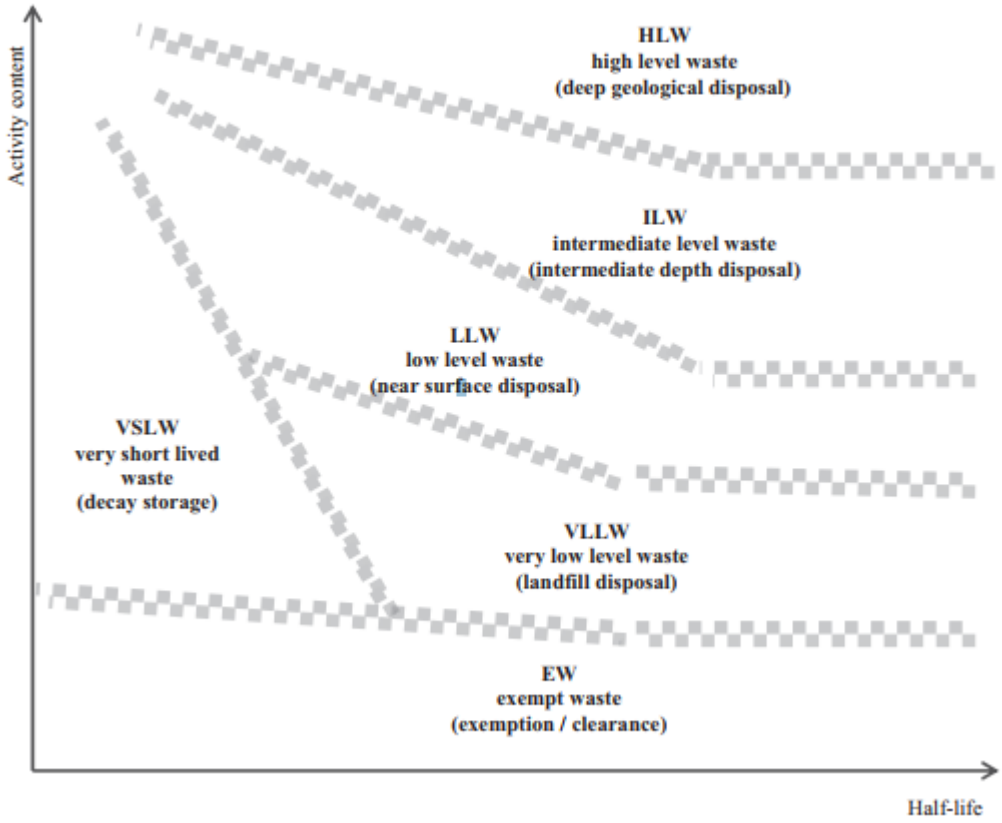

Figure 1-8 schematic showing conceptual illustration of the radioactive waste classification scheme (27)

The x-axis in Figure 1-8 above represents the half-lives of the radionuclides which are contained in the waste. These half-lives can range from short (seconds), to very long (millions of years) time spans (27). According to the IAEA's classification, exempt waste (EW) contains only small concentrations of radionuclides that it can be cleared from regulatory control and does not require provisions for radiation protection. The very short lived waste (VSLW), contains radionuclides of very short half-lives, the activity concentration however being above clearance levels. The waste can therefore be stored until the activity has fallen beneath clearance levels, at which point it is classed as conventional waste (27). Very low level waste (VLLW), may arise from mining or the processing of ores, as well as the operation and decommissioning of nuclear facilities. An adequate level of safety for very low level waste can be achieved by disposing of it in engineered surface landfill facilities, such as the ones which are already in practice for wastes arising from mining practices (27).

Radioactive waste facilities have been designed with various layers of protection, in order to make sure that the environment is protected until the radioactivity from the waste has been reduced down to background levels (9). Low and intermediate level wastes (LLW/ILW) can be buried close to the surface, i.e. low-level waste is not much different from a normal landfill. High-level wastes (HLW) however can remain highly radioactive for thousands of years (9). There is therefore a need to dispose of high-level radioactive waste in engineered facilities which are deep underground and also built in stable geological formations (9).

The UK's proposed disposal of spent nuclear fuel is via underground burial in a geological repository, or in other words, in a Geological Disposal Facility (GDF). Several other nuclear states, such as the USA and Sweden (28) have taken a similar route (29). The nuclear waste from these countries is however, mainly LWR fuel, whereas the UK has a large amount of AGR fuel to dispose of (30)

As aforementioned, where there are significant similarities between LWR and AGR fuel, there are also some important differences between the two fuels. Whilst the disposal of AGR spent fuel will be based on current knowledge of LWR disposal, it is crucial to produce a disposal strategy that is specific to UK AGR fuel. Taking into account the different types of spent fuel that needs to disposed of in the UK, along with the fact that the geology as well as the groundwater compositions in areas of the UK will differ to those of the other nuclear states, it is crucial to develop a safety case that is specific to the UK for the safe underground disposal of spent nuclear fuel. Shown below is a schematic of a typical Geological Disposal Facility (GDF) planned for radioactive waste in the UK.

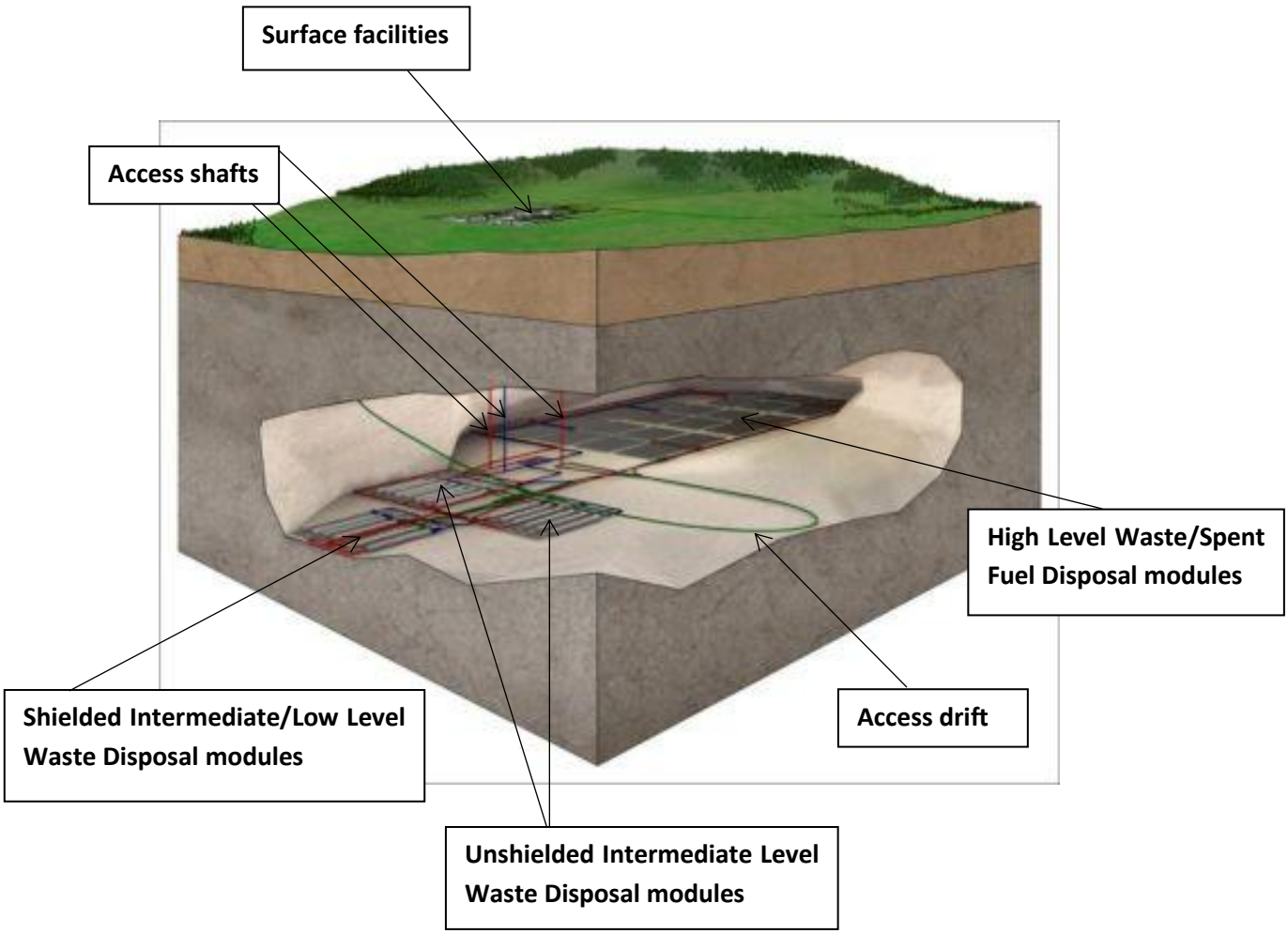

Figure 1-9 showing a schematic representation of a generic geological disposal facility (31)

For a geological disposal facility (GDF) to be built, a suitable site has to first be found which can then be evaluated to see if it meets all the criteria for the safe disposal of spent nuclear waste. Site characterisation is employed to tackle this task.

Site characterisation is made up of detailed surface/subsurface studies which include aspects of the geoscientific, environmental, as well as socio-economic conditions that will be affected throughout the development and implementation of a GDF. However, before detailed site characterisation can be carried out on a site, site selection needs to take place first (30).

The following flowchart is used in the candidate site selection process:

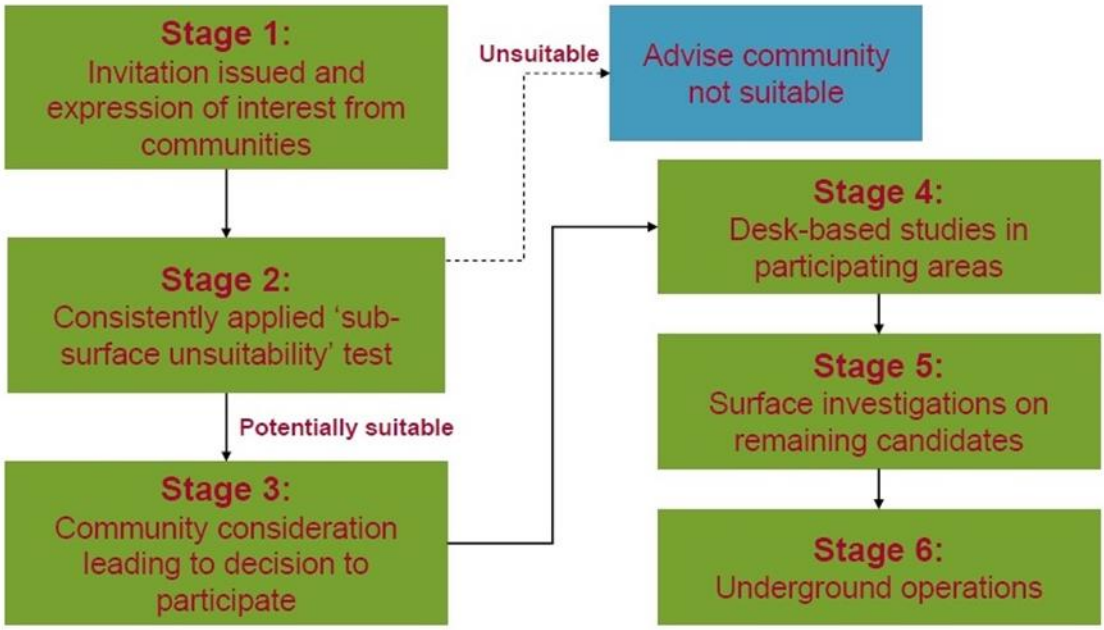

Figure 1-10 showing flowchart used for candidate selection site (32)

Even after candidate sites have been selected, it is still uncertain at this point as to what the geological conditions may be at the candidate site/sites. In order to determine a stable underground setting which would provide long-term safety from radioactive waste, a safety case for the UK has been produced (32). This safety case is, however, a generic one, as it does not relate to any one specific place or disposal site (32). This generic safety case is therefore based on a collaboration of analyses from several nuclear states and various forms of evidence that has been collected (32). It is therefore not possible to generate a complete safety case until the location for geological disposal is known (32). In order to avoid any oversights, the site characterisation studies remain generic at this point and cover the following geological environments (which are all the probable geological environments that could be found within the UK for which site characterisation can be undertaken) (31):

- High strength rocks – these are typically made up of metamorphic and igneous crystalline rock, or sedimentary rock which is geologically older. Any fluid movement found within these types of rocks is predominantly caused by discontinuities

- Low strength rocks (sedimentary) – these are generally made up of sedimentary rocks that are geologically younger (as opposed to high strength rocks). Any fluid movement encountered here is mainly through the matrix of the rock

- Evaporites – these are normally formed through the evaporation of water from water bodies that contain dissolved salts. Typical evaporate rocks include anhydrite; containing anhydrous calcium sulphate, and halite, which is a rock salt (33)

As well as addressing the geological and environmental factors affecting site selection and site characterisation, the physical attributes of a GDF must also be considered. It is proposed that a geological disposal facility would be built at a depth between 200 m and 1000 m underground (32).

Globally there are 25 countries that have decided to use geological disposal as a long-term disposal solution, such as the USA, Sweden, Spain and Finland (32) (34) (35) (36).

Important points that must be taken into consideration for a safety case include the following:

- an understanding of the groundwater system at the proposed site and
- an understanding of how gases that are produced in the geological disposal would migrate through the rock structure or dissolve in groundwater (32)

Both of the above points are determined by the type of rock that the geological disposal will be set in, so the primary focus is on site selection, so that a non-generic safety case may be put forward. The selected site would then have to fulfil the requirements set out by the site-specific safety case.

In 2008, a white paper on nuclear power named 'Meeting the energy challenge' (37) was published by the government. It sets out 6 criteria for the assessment of candidate sites (32). These are:

- to find a suitable geological setting
- to minimise the potential impacts on people – including human health and nuisances/disturbances

- to minimise the potential impact on the environment
- to maximise the beneficial effect on local socio-economic conditions, whilst minimising any adverse effects
- to minimise the requirements for more transport and infrastructure
- to minimise cost and timing whilst maximising ease of implementation (32)

A geological disposal site would mean that effectively, a geological barrier would be in place, which could subsequently help in the safe immobilisation of spent nuclear waste by:

- limiting groundwater flow, in particular into the specific areas where the waste will be disposed of. This can be achieved in the case of low permeability rocks, i.e. the potential for radionuclides to leach from the waste is limited
- allowing enough time for any activity that does come into contact with the groundwater to decay to such low limits that it shall not be harmful when coming into contact with the environment at the surface. This can be achieved by providing a slow and long path for the groundwater to travel from the emplaced waste to the surface environment
- providing rock surfaces that are able to remove radionuclides from the groundwater via chemical-processes that are naturally occurring
- providing fractures or pores that are 'dead-end', so to say areas where the groundwater which contains the radionuclides cannot move any further and will be stagnant
- preventing gases that may be generated by the wastes to directly be released to the surface environment
- protecting the displaced wastes from extreme cases of natural changes or human actions, i.e. ice ages, that may take place at the earth's surface (33)

Thus, a generic plan for a geological disposal facility which addresses the safety points laid out in the White Paper from 2008 exists.

1.1.5 Expected Conditions in Underground Repository

As aforementioned, there are currently, three different host rock types that are being looked at as potential sites for a geological disposal facility.

Host Rock	Illustrative Geological Disposal Concept for High Level Waste/Spent Fuel
Higher strength rocks	Sweden (KBS-3V, Sweden)
Lower strength sedimentary rocks	Switzerland (Opalinus clay, Nagra)
Evaporites	Germany (Salt Dome, DBE Technology)

Table 1-2 showing geological disposal concepts for different host rocks (31)

The groundwater compositions that have been used in recent experimental programmes for High Level Waste (HLW) glass are shown below:

For higher strength rocks:

Composition &pH	Concentration (mol kg^{-1})
Na	3.7×10^{-1}
K	4.4×10^{-3}
Mg	5.7×10^{-3}
Ca	2.9×10^{-2}
Sr	2.0×10^{-3}
Al	1.7×10^{-6}
C	1.0×10^{-3}
Si	2.5×10^{-4}
Cl	4.2×10^{-1}
SO_4^{2-}	1.2×10^{-2}
pH	7.22

Table 1-3 showing composition of saline hard rock groundwater illustrated by Sellafield Borehole RCF3 DET5 (38)

For lower strength sedimentary rocks:

Composition & pH	Concentration (mol kg^{-1})
Na	3.2 x 10-2
K	7.1 x 10-3
Mg	1.4 x 10-2
Ca	1.5 x 10-2
Sr	1.1 x 10-3
Al	6.9 x 10-9
C	3.0 x 10-3
Si	9.4 x 10-5
Cl	3.0 x 10-2
SO42-	3.4 x 10-2
pH	7.0

Table 1-4 showing composition of clay groundwater illustrated by the Callovo-Oxfordian (COX) argillite clay formation groundwater (38)

For evaporite rocks, either:

Composition, temperature & pH	Concentration
Oxygen	< 0.1 mg/L
Na	4870 mmol/L
K	20.3 mmol/L
Mg	82.3 mmol/L
Ca	26.5 mmol/L
HCO_3^-	2.09 mmol/L
SO_4^{2-}	52.9 mmol/L
Cl-	4766 mmol/L
HA	-
FA	0.20 mg C/L
Temperature	16.9 °C
pH	6.3/7.0[b]

Table 1-5 showing composition of the Channel Brine GoHy-514 at 235-238 m depth, Elster. [b] = pH corrected according to Runde (1993) (39)

Or:

Compound	Concentration (g/L)
NaCl	303.22
$NaHCO_3$	0.32
$MgSO_4$	0.62
$NaSO_4$	9.33
$CaCl_2$	0.47

Table 1-6 showing composition of the simulated WIPP-site ground water (40)

Alongside the different water compositions that would be existent with various host rock types, there are other variables that need to be taken into consideration when looking at the expected conditions of an underground repository. Effects that are temperature-related must also be considered regarding the disposal of spent fuel in deep geological repositories (41). The exposure of groundwater to the host rock during the heat pulse (through corrosion of the canister) can lead to

the migration of radionuclides into the environment, so temperature and also pressure related effects need to be investigated (41).

1.1.6 Thermal pulse in GDF

Once the geological disposal facility has been closed shut with the spent nuclear fuel buried within its engineered barriers, there is expected to be a thermal pulse which originates from the heat production of beta/gamma decay from the spent fuel. The thermal pulse is the time frame during which the temperature of the host formation is expected to lie above the range of temperatures within which nominal migration properties can be relied upon by using one or more engineered barriers (42). These engineered barriers are designed to contain the radionuclides and other contaminants during the thermal pulse (42). After the thermal pulse has come to an end, the beta and gamma radiation from the spent nuclear fuel will have subsided, and only alpha radiation is expected to prevail (43). The thermal pulse is expected to last 1000 years (see Figure 1-11 below) (42), after which the alpha radiolysis of water (see Section 1.17) will take place, due to the prevalence of alpha radiation which will come into contact with the groundwater that is expected to enter the fuel canisters once the barriers fail (44). Below is the strategy of the Belgian concept, with the expected timescale of the thermal pulse and system containment (42).

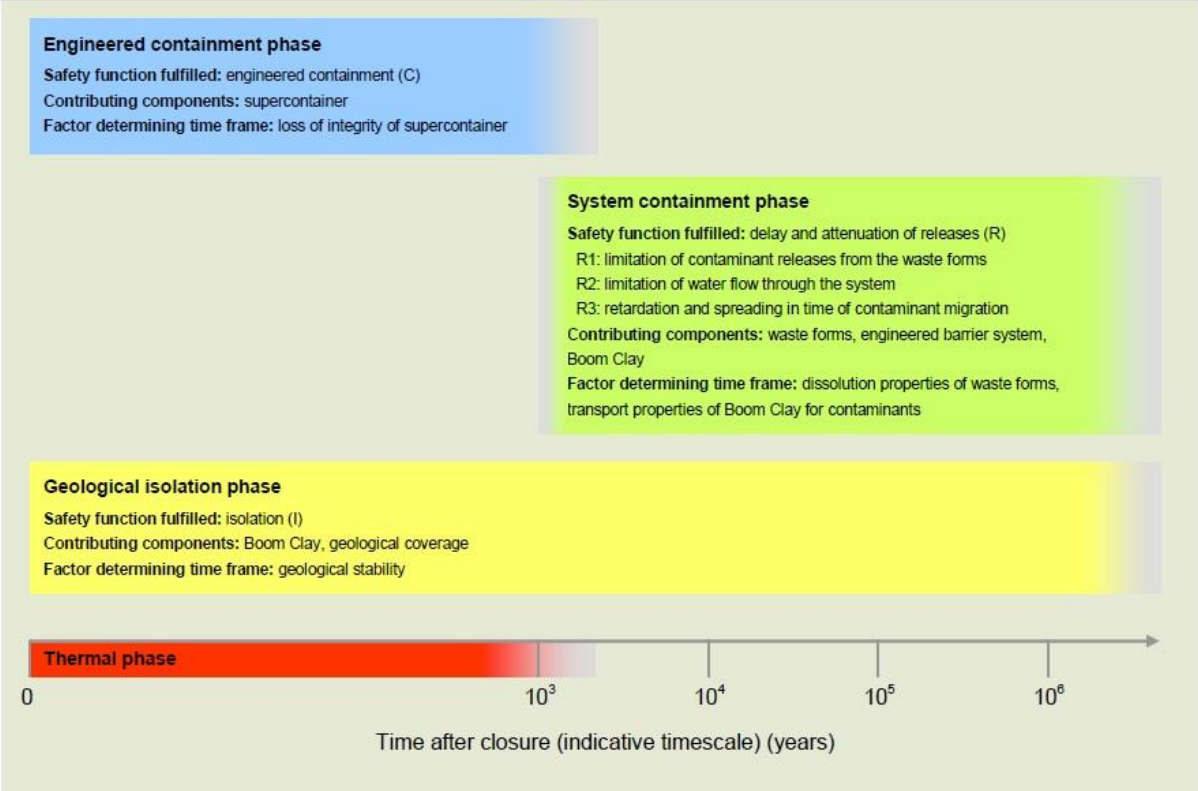

Figure 1-11 showing the safety functions of the Belgian GDF concept and the expected timescale of the thermal pulse of a GDF (42)

A geological disposal facility strategy assessment by the Nuclear Decommissioning Authority (NDA) has considered how spent fuel packages would evolve in the very long term - post-disposal, recognising that radionuclides would be released only following a breach in the disposal canister (45). A limited sensitivity analysis has been carried out for the strategy assessment, examining two different canister materials (copper and steel) and testing the influence of the assumed corrosion properties. Subsequent to any canister failure, the radionuclides associated with the spent fuel would be able to leach into the groundwater (45). The rate at which the radionuclides are leached, in combination with the assumed properties of the host rock, the behaviour of individual radionuclides and also the exposure routes are subsequently used to assess the potential risks to humans (45). The leaching of the radionuclides from the spent nuclear fuel is characterised by an initial Instant Release Fraction (IRF), which is then followed by a more general dissolution rate (45), which is known as matrix dissolution. The IRF is the fraction of the inventory of more mobile radionuclides which is assumed to be readily released upon contact with groundwater and is influenced by the properties of the spent fuel (45). The fraction of fission products from the IRF include the fission gases Iodine-129 and Chlorine-36, as well as caesium isotopes and other volatile radionuclides. These migrate during reactor operations and accumulate at grain boundaries, also known as the grain boundary

inventory, or other accessible parts of the fuel, referred to as the gap inventory - where the gap represents the interconnected volume of the fuel to the cladding gap, fractures in the fuel pellets as well as open fission gas tunnels (46). Following breach of the spent fuel disposal container and of the fuel pin cladding, in safety assessments the IRF is assumed to be readily (instantly) leached into the groundwater. In studies of fractional release rates, the fractional release rates of elements associated with matrix dissolution processes had reached steady state values after about 1 year of leaching (46). After release of the IRF, dissolution of the spent fuel and the radionuclide inventory that is not included in the IRF is controlled by the rate at which the matrix itself dissolves. This process is of great importance, as the vast majority of radioactivity (of the order of 97%) is likely to be present in the fuel matrix (46). Matrix dissolution is influenced by a variety of factors, such as fuel thermal history, the radiation field and the chemistry and redox potential of the water contacting the fuel. Significant dissolution of the spent fuel only occurs under conditions where the relatively stable UO_2 (solid) matrix is oxidised to the more soluble UO_{2+x}, such as occurs under oxic conditions (46). Two examples of repositories currently under oxic conditions are the Waste Isolation Pilot Plant (WIPP) in New Mexico and Yucca Mountain in Nevada, although it should be noted that WIPP will be under anoxic conditions in the near future. The fuel matrix dissolution rate is much slower under reducing conditions because it is likely to be driven by the dissolution of UO_2, which has a much lower solubility and slower dissolution kinetics than UO_{2+x} (46). In the case of higher burnup fuel, the increased irradiation of a third generation pressurised water reactor fuel (EPR) would increase the IRF as compared to that for lower burnup fuel (47). Generally available information on the potential performance of higher burnup fuel has been used to provide a suitable IRF for assessment and the assumptions that have been made above (45).

Below is a schematic of the expected timeline of the Belgian disposal concept.

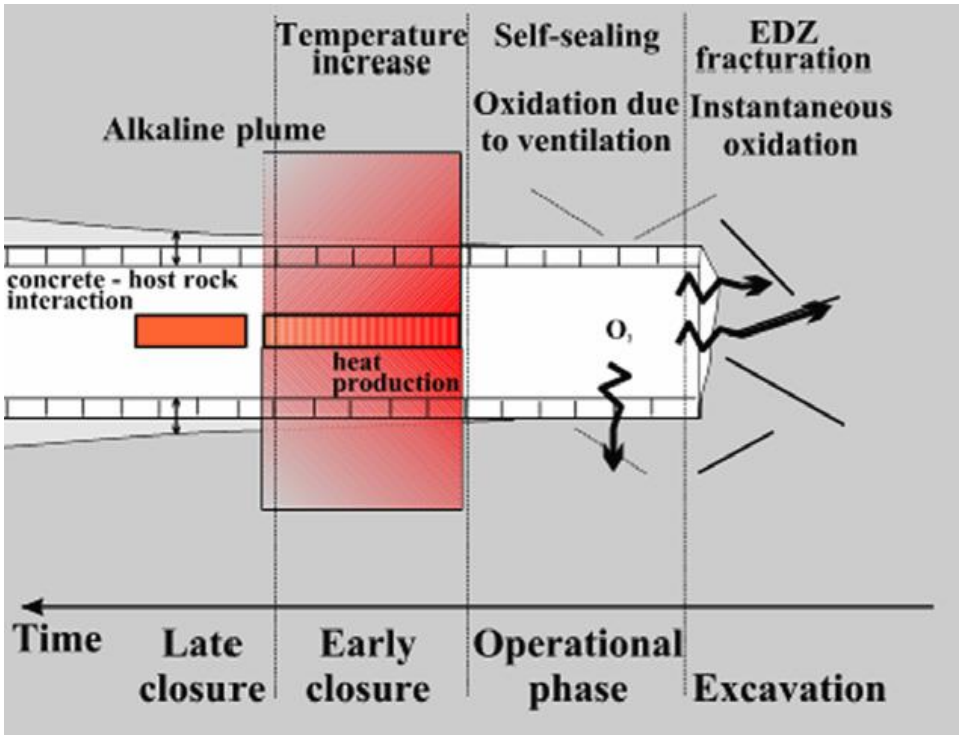

Figure 1-12 schematic showing timeline of Belgian disposal concept (48)

The Belgian concept also outlines the idea of heat production or a 'thermal pulse' during early closure and an interaction between the host rock and the concrete i.e. canister failure and groundwater ingress during late closure, as mentioned above. The Belgian concept should only be taken as an indication of the stages that may occur post-closure in an anoxic GDF, such as the one that is envisaged for the UK.

1.2 Comparison of LWR/PWR Fuel Characteristics to AGR Fuel Characteristics

In the UK, part of the disposal strategy will be based on existing knowledge of LWR fuels under repository conditions. It is however necessary to address the differences between LWR and AGR spent fuel in order to satisfy safety case requirements.

The LWR characteristics that are likely to affect radionuclide release after disposal with regards to high burnup have been assessed and compared to AGR fuel (49). LWR and AGR are

phenomenologically the same in terms of fission gas release during low to intermediate burnup. Despite the similarities, there are two fundamental differences between AGR and LWR fuels:

- The low hydrostatic stress that is imposed onto the AGR fuel pellets (due to the collapsible can concept – the concept refers to the use of collapsible rods in the fuel pellet (50)) leads to the low morphological relaxation of grain face bubbles (49)
- The deposition of carbonaceous material on the outer surface of the AGR pin is likely to increase fuel temperatures by a significant amount, and therefore allowing the release of fission gas (49)

Low morphological relaxation of grain face bubbles are only of concern with a large amount of fission gas release, which is only expected to occur when there are carbonaceous depositions (49). It was found that carbonaceous deposition can lead to an increase of fission gas release, from ca. 0.1 - 5% at an approximate burnup of 20 MWd/kgU. This leads to a significant increase in grain boundary and also pin free volume inventories of long-lived radionuclides such as ^{137}Cs and ^{129}I. If similar depositions occur at higher burnups, then a gas release of higher significance is expected (49).

Due to the similarities between AGR and LWR fuel pellets with regards to maximum fuel centre temperatures and also radial temperature gradients, and given the use of helium gas as a filler for both types of fuel, the average concentrations and chemical forms of fissions products are expected to be similar for a given burnup. There are however expected to be some differences with regards to neutron spectrum, pellet dimensions and chemical interactions between the fuel and the clad or can (49). Below is a table comparing the key parameters between PWR and AGR fuel assemblies.

	17x17 PWR	10x10 BWR	AGR
No. of fuel rods/pins	264	91	288
Rod/pin length (mm)	3863	4081	987
Fuel pellet material	UO_2	UO_2	UO_2
Fuel grain size (µm)	12[a]	12[a]	12[b]
Fuel oxygen to metal ratio[c]	1.995 - 2.005	1.995 - 2.005	2.000 - 2.004
Fuel porosity volume fraction[d]	5%	4%	2%[b]
Fuel pellet length (mm)	13.5	10.5	14.6
Fuel pellet ID (mm)	Zero	Zero	6.4
Fuel pellet OD (mm)	8.19	8.67	14.6
Rod/pin OD (mm)	9.5	10.05	15.3
Clad/can material	Zircaloy-4/M5™	Zircaloy-2[e]	Stainless steel
Clad/can thickness (mm)	0.57	0.605	0.37
Rod/pin fill gas	Helium	Helium	Helium
Rod/pin fill pressure (bar)	25[f]	10[g]	1

Table 1-7 key parameters for PWR, BWR and AGR fuel assemblies (49)

where, a = typical value

b = post 1979 value

c = typical ranges – all three fuel types are effectively stoichiometric

d = calculated from stated fuel densities, assuming a 10960 kg/dm^3 density for fully dense UO_2

e = with Fe enhanced Zr liner

f = typical value

g = typical value for modern BWR fuel (49)

The expectations of LWR fuel with regards to the radioactive fission product inventory in the rod free volume and grain boundaries pre-disposal are to be expected from AGR fuel as well. It is therefore anticipated that:

- the measured rod free volume and also grain boundary inventories of ^{90}Sr and ^{99}Tc are extremely low (between 0.01 – 0.4% of total amounts of radionuclides)

- the rod free volume and grain boundary inventories combined (of ^{129}I and ^{137}Cs) are correlated to fission gas release)
- matrix dissolution is best modelled with a fractional mass-loss of 10^{-7} per annum

The above points all require experimental data on spent AGR fuel (under UK repository conditions) to confirm these expectations. Due to the fact that carbonaceous deposits are expected with AGR pins, and these subsequently have a significantly higher fission gas release, they would also be expected to have a significantly higher grain boundary and pin free volume inventories of ^{129}I and ^{137}Cs (49).

It is also important at this stage to take note of the irradiation conditions of the reactor fuel and the effects that these conditions have on the fuel chemistry. Below is a table outlining the core design parameters and irradiation conditions of LWR and AGR fuels.

	PWR	BWR	AGR
Electrical output (MWe)	1258	1200	660
Active core height (m)	3.66	3.68	8.3
Fuel inventory (tHM)	89	126	110
Number of assemblies	193	700	324
Enrichment: initial core (%)	2.1/2.6/3.1	2.25	1.16/1.54/2.1
Enrichment: reloads (%)	3.1	3.16	2.12-3.42
Cycle length (months)	12[a]	12	4
Core reload fraction per cycle	33	20	7.5
Core average rating (kW/m)	17.8	17.5	16.8
Peak rating (kW/m)	30[b]	30[c]	27.8
Coolant type	Light water	Light water	CO_2
Coolant pressure (MPa)	15.5	7	4.1
Coolant inlet temperature (°C)	292	278	286
Coolant outlet temperature (°C)	323	286	675
Coolant mass flow (t/h)	69000	41040	13700
Average assembly burnup (MWd/kgU)	33	42	24
Peak assembly burnup (MWd/kgU)	45[d]	45	28
Max clad/can temperature (°C)	353	316	825
Max fuel centre temperature (°C)	1400[b]	1300[c]	1500
Max temperature gradient (°C/mm)[e]	210	180	165

Table1- 8 typical LWR and AGR core design parameters and irradiation conditions (49)

where, a = however, Sizewell B is now operating on 18 month cycles, and use of such extended cycles (18 or 24 months) for PWR operation is becoming increasingly common

b = the peak rating and maximum fuel centre temperature for Sizewell B published by NEI are 41.3 kW/m and 1796°C, respectively. These values correspond to operation at maximum local rating limits and are atypical of normal operation. A typical peak rating of 30 kW/m is therefore tabulated, with the maximum fuel centre temperature scaled down from the 1796°C value such that the quoted maximum fuel centreline temperature minus clad temperature to peak rating ratio is maintained

c = the peak rating and maximum fuel centre temperature for Forsmark 3 published by NEI are 44 kW/m and 1800°C, respectively. These values are assumed to correspond to operation at maximum local rating limits and are therefore atypical of normal operation. Hence, a typical peak rating of 30 kW/m is tabulated (core average rating plus ~ 50% of the difference between the NEI peak rating and the core average rating, as per the PWR entry), with the maximum fuel centre temperature scaled down from the 1800°C value such that the quoted maximum fuel centreline temperature minus clad temperature to peak rating ratio is maintained

d = Biblis (Biblis, UK) B value corresponding to an average assembly burnup equal to that for Sizewell B (33 MWd/kgU)

e = maximum pellet average radial temperature gradient calculated from tabulated maximum fuel centre temperature, pellet inner and outer radii from Table 1-8, and an estimated pellet surface temperature. For the PWR and BWR, the pellet surface temperature was assumed to be the maximum clad temperature plus a typical beginning-of-life pellet-clad gap temperature drop at the tabulated peak ratings of 200°C. For the AGR, the pellet surface temperature was taken as the maximum can temperature (since the AGR can is pressurised onto the fuel pellets during manufacture) (49)

The chemical state reached whilst irradiating reactor fuel is influenced by the compositional changes that result from the fission process and also by the redistribution of the fuel and fission product phases (49). The isotopic composition of irradiated fuel can be determined as a function of time from knowledge of fission yield and cross-sectional data, as well as the irradiation conditions (including the fission densities, fuel temperatures and neutron flux spectrum) (49). As a result of the fission process, the average valency of the resulting actinide and fission product mixture will differ from that of the starting material. In oxide fuels, the valency, and hence the oxygen requirements, of the fuel and fission products is controlled by the oxygen potential (partial molar free energy) of the oxidation reactions for the components of the system. Based on the oxygen potential of the various fission product metal/oxide systems, the actinides, namely Np, Pu, and Am, the rare earths elements, namely La, Ce, Pr and Nd, the alkaline earths, namely Sr and Ba and zirconium will exist as the oxide phase in equilibrium with the uranium fuel, either in solution or as separate phases (49). The noble metals, namely Mo, Tc, Ru, Rh and Pd and the fission gases Kr and Xe will remain in the

elemental state (metallic inclusions, and gas atoms/bubbles, respectively) and the volatile elements Cs, Te and I will remain in the elemental state or interact together to form separate phases (49).

In the above section, the properties of AGR fuel and its similarities and differences to PWR/LWR fuel have been discussed. These properties are of relevance to the Instant Release Fraction (IRF), and are not necessarily specific to the behaviour of AGR fuel in a GDF post-thermal pulse. Whilst the above properties point out possible differences in behaviour; such as the IRF and that the compositional and morphological differences may influence long term behaviour in a GDF once the cladding has been compromised post thermal pulse (see Section 1.1.6), the subject of this work is in fact the behaviour of AGR fuel in a GDF, after the thermal pulse has subsided and the containment and cladding have failed. The behaviour of such, in particular the corrosion behaviour of AGR fuel in a GDF, will be discussed hereafter.

1.3 Corrosion in Geological Disposal

In order to be able to assess the matrix dissolution of spent nuclear fuel, it is important to look at the corrosion behaviour of the fuel in question. In other words, the electrochemistry of the material, which in this case is UO_2, must be investigated.

The reason for interest in the redox chemistry of UO_2 is the fact that it has a large change in its aqueous solubility upon oxidation, with changes in redox potential (51). In its fully reduced form, UO_2 is extremely difficult to dissolve, however, under oxidising conditions, the solubility of uranium in its U^{VI} has been determined to be four to ten orders of magnitude higher (51). Subsequently, this means that geological deposits of uranium oxide exist in a composition close to UO_2. The mobilisation of such uranium by transport via dissolved uranium in groundwater requires oxidising conditions. Hence the release of radionuclides from used fuel in a GDF will also be controlled by the redox potential of the groundwater, and will be more rapid under oxidising conditions, as opposed to reducing conditions (51).

The redox conditions which are of importance in relation to a GDF cover a wide range, over which the degree of oxidation of the surface of UO_2, and subsequently its rate of dissolution will change greatly (51). The usefulness of electrochemical techniques in investigating the redox chemistry of UO_2 using UO_2 electrodes has been demonstrated by Nicol et al (52) by showing that dissolution rates of UO_2 that has been exposed to various oxidising agents can be predicted from dissolution currents (51). From the figure below it can be seen that there are similarities in the redox conditions between geochemical and spent fuel disposal environments.

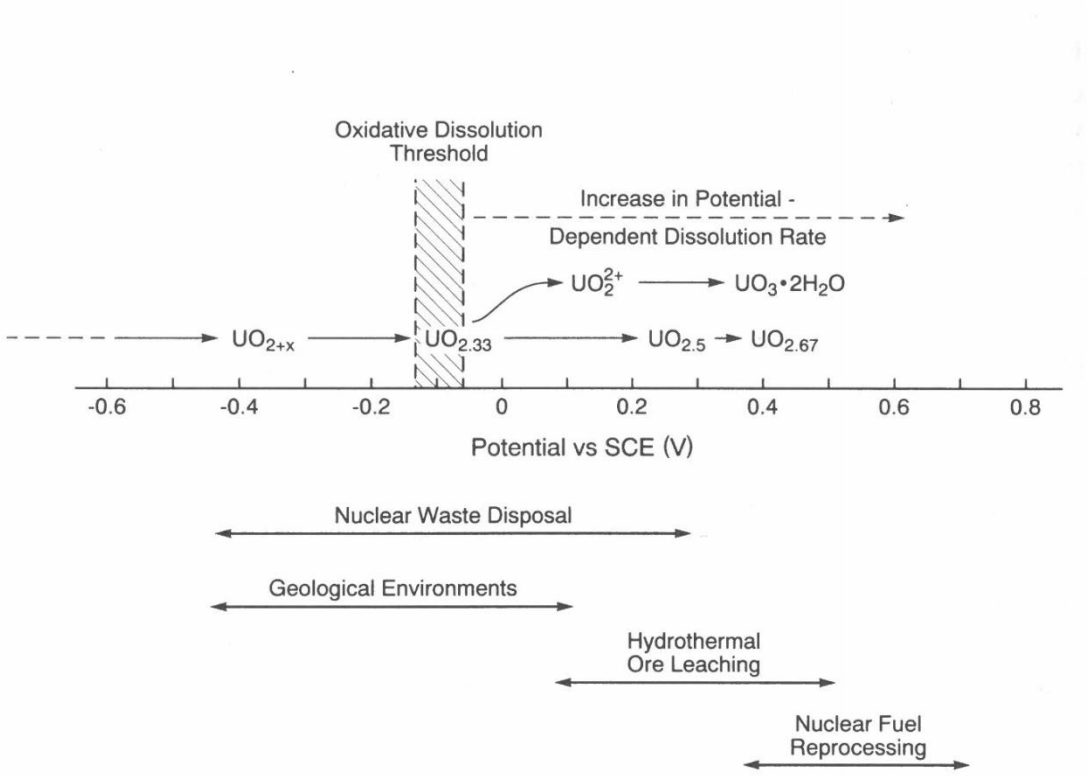

Figure 1-13 showing schematic of change in surface composition of UO_2 and the onset of oxidative dissolution as a function of the potential of a UO_2 electrode (51)

As can be seen from the figure above, although the general chemistry of uranium is similar for geological and spent fuel environments, it should be noted that there are major differences between highly dense sintered uranium pellets, which are altered by in-reactor irradiation and thermal treatments, and natural uraninite deposits which yield distinct differences in the dissolution and corrosion behaviour (51).

The reliable prediction of corrosion damage is a necessity in the evaluation of a repository concept (53). A lot of knowledge has been gained over a period of several thousand years about the

corrosion behaviour of metallic materials (53). There is however, a need to develop this base further. The lifetime of most industrial materials can range from just a few seconds or minutes, for example for rocket engines, to several decades for nuclear power plants, going up to a hundred years for infrastructure such as bridges (53). The approach of many countries in demonstrating the feasibility in predicting the corrosion behaviour of steels over a long period of time is based on the following points (53):

- The comparison of data from experimental studies to that obtained by other international laboratories, which is then used to develop semi-empirical models which are capable of performing initial estimations of service lifetimes. These models include corrosion rate evaluations (53)
- The use of predictive models which are based on corrosion mechanisms. Mechanistically based models can lead to an improved understanding of the evolution of the damage caused (53)
- The use of archaeological artefacts which are used to demonstrate the feasibility of long term storage and to also provide a database which can be used to test and validate models. The investigation of artefacts is showing itself to be a promising approach for validating deterministic models, given that the data of the archaeological data is well understood and also recognised (53)

Given the above points, it can be useful to use computational modelling to predict corrosion behaviour over a longer time-period, thus the next section will focus on feasibility studies carried out by computational modelling.

1.3.1 Modelling to Predict Corrosion over longer Periods

As aforementioned, modelling can be used to predict the corrosion behaviour in an underground repository over long periods of time.

It is important to have a state of knowledge on the kinetics and the corrosion mechanisms of the steels used in the cladding, in the environmental conditions that they will be expected to be in during the various phases of geological disposal (54) (55). These can include dry-hot oxidation,

humid-air atmospheric corrosion, aqueous corrosion (including aerobic and anaerobic corrosion), corrosion in porous argillaceous environments, as well as cementitious environments (54). Semi-empirical laws (which are discussed later on) can be used to describe general and localised corrosion – such as pitting or crevice corrosion. Semi-empirical modelling works by using the longest duration data sets available relating to the corrosion in soils and clay materials (54).

General corrosion, as opposed to pitting or crevice corrosion, is considered to be the prevailing type of corrosion mechanism in the long term (54). Even though there has been some development on mechanistic models for the corrosion of carbon steels in order to make long term predictions on container lifetime, these models do not take into consideration the effect of lowering the corrosion rate brought about by the corrosion products (54). Being modelled through a combination of electrochemical reactions which take place at the carbon steel surface, and the mass transport of oxidants and corrosion products (54). Due to the fact that the build-up of corrosion products inhibits the corrosion, and this fact is neglected in the models, the results obtained by such models do not coincide with experimental results (54). In fact, Gras *et al.* have shown that the modelled corrosion depth after one year of exposure is five times larger than experimental data (54). It is due to this discrepancy, that the French national radioactive waste management agency, along with its partners, have developed a new model which takes into account the possibility of the existence of a layer above the steel surface, which could be susceptible to the pseudo-passivity of the steel (54).

The following is an example of a study carried out in France, which whilst dealing with different conditions to the proposed repository in the UK, can still be used as an indicator when predicting corrosion behaviour over longer time-periods.

The French national radioactive waste management agency (Agence nationale pour la gestion des déchets radioactifs, Andra) has conducted feasibility studies in order to evaluate the long-term evolution of a repository (56). The potential host formation for France is Callovo-Oxfordian clay (56), and Andra's predictions are based on studies of this particular clay formation.

The materials that are used for the containers are generally categorised into these two groups (54):

- Corrosion-allowance materials – the lifetime of these materials is attained adjusting the wall thickness accordingly. These include carbon steels and cast irons (54)
- Corrosion-resistant materials – these materials form a protective/passive film in water making their general corrosion rates extremely low, but are however susceptible to localised corrosion. These materials include austenitic stainless steels and various alloys (54)

Below is a table showing container materials that are used in various countries and their associated problems, outlining that there is not one readily available material that could address all the following problems, hence canister failure at some point is inevitable.

Materials	Countries	Possible modes of attack
Carbon steels	France	General corrosion
Low alloy steels	Germany	Pitting/crevice corrosion
Cast irons	Japan, Spain	Stress corrosion cracking
	Switzerland, UK	Microbial induced corrosion
Copper	Canada	General corrosion
	Finland	Pitting/crevice corrosion
	Sweden	Stress corrosion cracking
Titanium & alloys	Canada	Crevice corrosion
	Japan	Hydrogen embrittlement
Stainless alloys	Belgium	Pitting/crevice corrosion
	France	Stress corrosion cracking
	USA	Microbial induced corrosion

Table 1-9 showing container materials and their associated problems for various countries (54)

As aforementioned, to allow for a realistic prediction of canister lifetime, semi-empirical laws that are based on experimental data can be used which take into account variables such as appropriate wall thickness (of canister), in order to attain realistic mass-balances and so forth (54). Below is a description of semi-empirical modelling.

1.3.2 Semi-Empirical Modelling

The compilation of the results that are collected during certain types of experiments can be used for semi-empirical modelling which in turn can be used for estimating designs and lifetime **(57)**. As

mentioned above for example, in France, where the Callovo-Oxfordian geological formation is the proposed host-rock, the formation has extremely low permeability which significantly reduces the flow of water **(57)**. The semi-empirical model of this system is shown in Figure 1-14 from which it can be seen that 3 mm of metal are corroded in a 1000 years. From this it can be calculated that for example, a flow of 10^{-2} L m^{-2} $year^{-1}$ will limit the rate of corrosion of iron to 3 µm $year^{-1}$, assuming the rate of corrosion to be uniform **(57)**.

Semi-empirical modelling can also be used to calculate the sizing of containers or over-packs of reasonable thicknesses by using the above approaches of over-estimating (54). However the time scales involved can make these predictions less credible and therefore a better understanding of the base mechanism is necessary to prove the lifetime prediction of containers in a more certain way (54).

Experimental work on UO_2 dissolution, as is the focus of this work, can therefore be used, along with other experimental work and semi-empirical modelling to predict the corrosion rates of canisters and canister materials that are envisaged to be used in a GDF in the UK.

As mentioned above, Figure 1-14 below shows an example of where semi-empirical modelling may be used - specifically with respect to the Callovo-Oxfordian geological formation. Semi-empirical modelling uses modelled data as well as 'real' data. For example, in the schematic below, which shows the influence of the flow of water on corrosion rates (57), published data as well as data generated by the French Atomic Energy Commission (Commissariat á l'énergie, CEA) and Électricité de France (EDF) in representative repository conditions, where the corrosion rates of buried archaeological objects made out of iron have been included, has been used to produce the laws to represent rates of generalised corrosion of low and/or non-alloy steels as a function of the temperature expected in a repository, in the absence and presence of oxygen, as shown below (57):

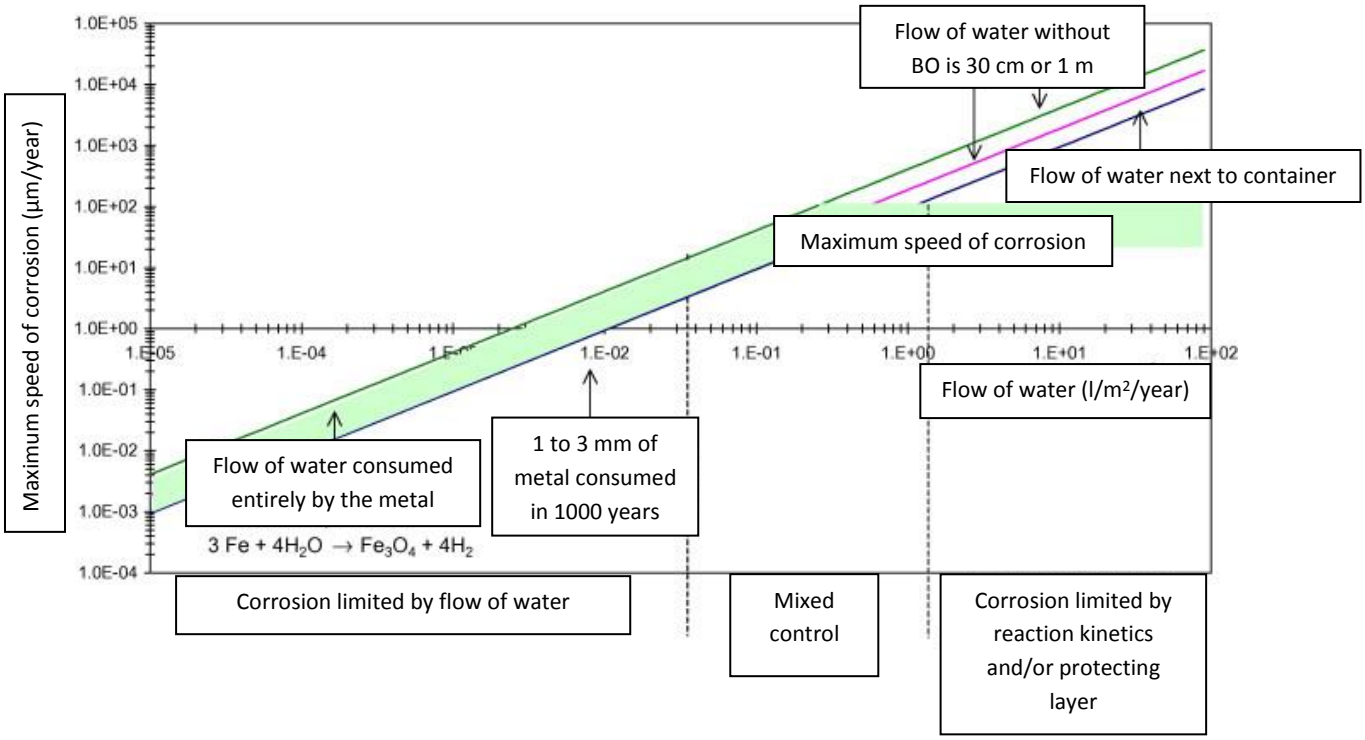

Figure 1-14 showing the influence of the flow of water on the corrosion rates with expected kinetic control domains for a Callovo-Oxfordian rock formation (57)

Even though semi-empirical modelling can be used to predict the life-times of canister and canister material, experimental data is still required to investigate the corrosion of canister material, and more specifically, the corrosion of the spent fuel, once the canister material fails. The next section will focus on the spent fuel matrix, uranium dioxide.

1.4 Structural & Electrical Properties of UO_2

At this point, before going too deeply into the corrosion of UO_2, it is also important to look into the UO_2 fluorite lattice structure and its capacity for accommodating excess oxygen anions, as UO^{2-} ions will be incorporated into the lattice during the initial stages of oxidative corrosion, i.e. during the early transition of $UO_2 \rightarrow UO_{2+x}$. Stoichiometric crystalline UO_2 is isostructural with a cubic fluorite structure (CaF_2). Each unit cell consists of four U ions sitting on a face centered cubic (fcc) sublattice and eight O^{2-} ions forming a cubic sub-lattice embedded in the U^{4+} sublattice. This structure is shown schematically in the figure below.

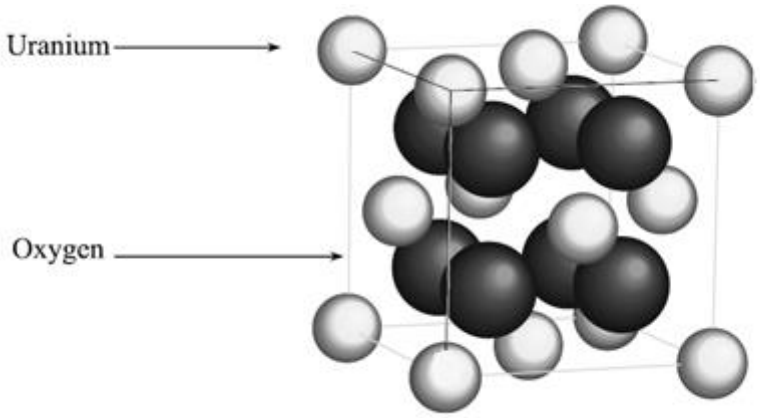

Figure 1-15 showing schematic representation of the cubic fluorite structure of the UO_2 lattice (34)

The fluorite structure of UO_2 is able to generate a number of derivative structures. This flexibility to generate derivative structures exists due the presence of octahedral vacancies at the centre of the unit cell and its capacity to accommodate excess anions. Insertion of O into an interstitial site (*i*) within the UO_2 lattice leads to the formation of point defects within a retained fluorite structure of overall stoichiometry UO_{2+x}. Upon the introduction of further O_i into interstitial sites, the concentration of point defects increases and the fluorite structure becomes more distressed, giving rise to more widespread structural rearrangements and leading to extended defect structures. The generation of these extended defect structures displaces oxygen atoms from the lattice sites that are adjacent to the interstitial sites leading to the creation of additional lattice vacancies. Furthermore, the introduction of hydrogen peroxide (as expected to be found in an underground repository due to the alpha radiolysis of water, see Section 1.4.4) to UO_2 surfaces, complicates the hyperstoichiometric behaviour and thus the corrosion behaviour of UO_2 even more (the effects of

hydrogen peroxide on the undoped UO_2 and SIMFUEL pellets are explored in the Chapter 4). This phenomenon has been recently elucidated and reviewed by He *et al.* (58). As UO_2 moves towards hyperstoichiometry through the peroxide-driven oxidation of U(IV) sites, U(V)/U(IV) donor-acceptor sites may be generated, which in turn catalyse the reduction of H_2O_2 (58). The balance of electrons in this process is provided by coupled chemical/electrochemical oxidation of U(IV) to U(V), catalytically further accelerating the rate of peroxide reduction, and (similarly coupled) U(IV) oxidation to U(VI) with its release to solution as UO_2^{2+}. Generation of UO_2^{2+} in the presence of H_2O_2 may result in the formation of studtite/metastudtite (58). These processes are illustrated in the figure below.

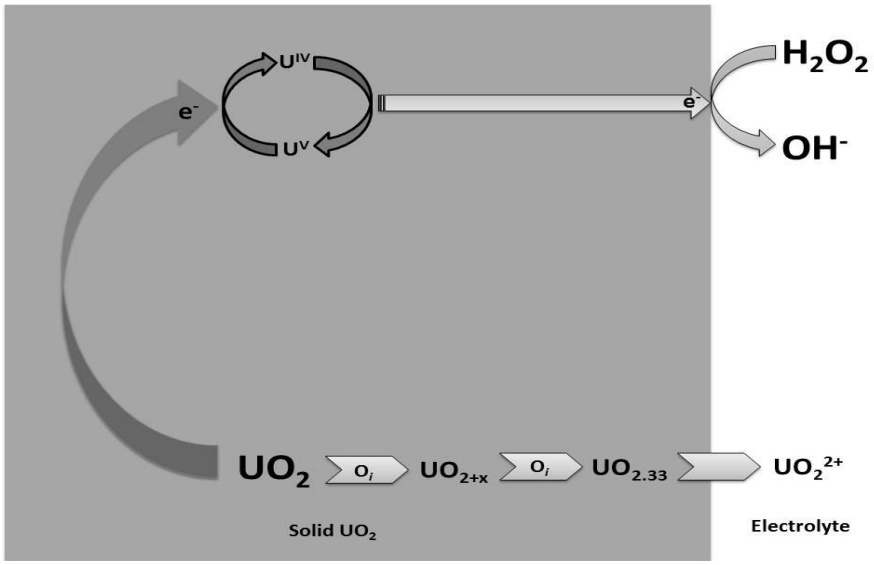

Figure 1-16 schematic representing the mechanism of UO_2 dissolution in the presence of H_2O_2 (34)

Apart from the effect that the addition of hydrogen peroxide has on UO_2 (which is further explored in chapter 4), it is, at this point, essential to once again look into the stoichiometry of UO_2, as undoped UO_2 is only near-stoichiometric (unless it is in single crystal form), as opposed to stoichiometric. It is important to note that the hyperstoichiometry of UO_2 (UO_2 becoming hyperstoichiometric through the addition of interstitial oxygen into vacancies, resulting in UO_{2+x}), will exert a significant influence on the electronic conductivity of UO_2. Hence, the electronic properties of UO_2 will now be explored.

The electronic properties of solids are usually described in terms of the band model. The band model involves the behaviour of electrons moving in the combined field of atomic nuclei and other electrons in an array (59). The formation of a crystalline solid such as TiO can be taken as an

example. As isolated atoms (which are characterised by filled and vacant orbitals), are assembled into a lattice, new molecular orbitals are formed. These orbitals are closely spaced such that they fall into continuous bands. These filled bonding orbitals subsequently form the valence band, and the vacant antibonding orbitals form the conduction band, as seen in Figure 1-17 below (59).

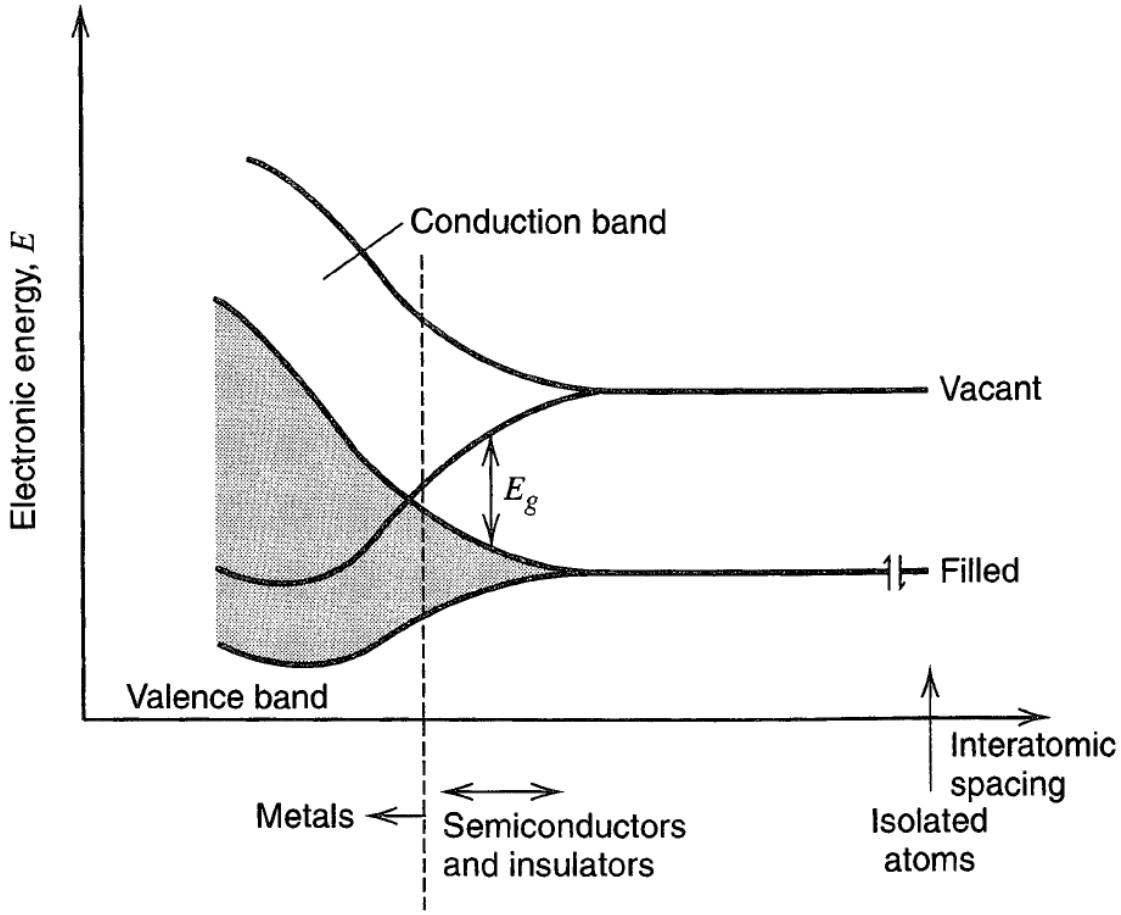

Figure 1-17 showing schematic of filled bonding orbitals and vacant antibonding orbitals (59)

In general, these bands are separated by a forbidden region or a band gap of energy (Eg), which are usually given in units of electron volts (eV). The electrical and optical properties of the solid in question are strongly influenced by the size of the band gap (59).

When the band gap is small, such that the Eg < < kT (Boltzmann constant x temperature), or when the conduction and valence bands overlap, the material is a good conductor of electricity, such as Cu or Ag. Under these circumstances, filled and vacant electronic energy levels exist at virtually the same energy, so that it is possible for an electron to move from one level to another with only a

small E_A (59). This feature provides the electrons with electrical mobility in a solid, and allows them to respond to an electric field. However, electrons in a completely full band, having no empty levels in close proximity, have no means for redistributing themselves spatially in response to an electric field, and therefore they are unable to support electrical conduction (59). For larger values of Eg, such as Si, where Eg = 1.1 eV, the valence band is almost filled, and the conduction band is almost vacant. Here, conduction becomes possible due to the thermal excitation of electrons from the valence band into the conduction band (59). This process generates electrons in the conduction band, that have electrical mobility as they are free to transfer among vacant levels in the conduction band, leaving behind "holes" in the valence band that have mobility. Mobility is enabled due to the fact that the valence band electrons can rearrange themselves to shift the spatial location and energy of the vacancy (59). This type of material is called an intrinsic semiconductor, such as UO_2. In an intrinsic semiconductor, the charge carriers, electrons and holes exist in dynamic equilibrium. They are created by dissociation, and are then eliminated by recombination. In an intrinsic semiconductor, the electron and hole densities are equal (59).

In its stoichiometric form, UO_2 is a Mott-Hubbard insulator, containing a narrow filled 5f band, which contains two electrons per U atom. These are located in the ~5eV gap between the empty conduction band and the filled valence band, as shown in Figure 1-18 (58).

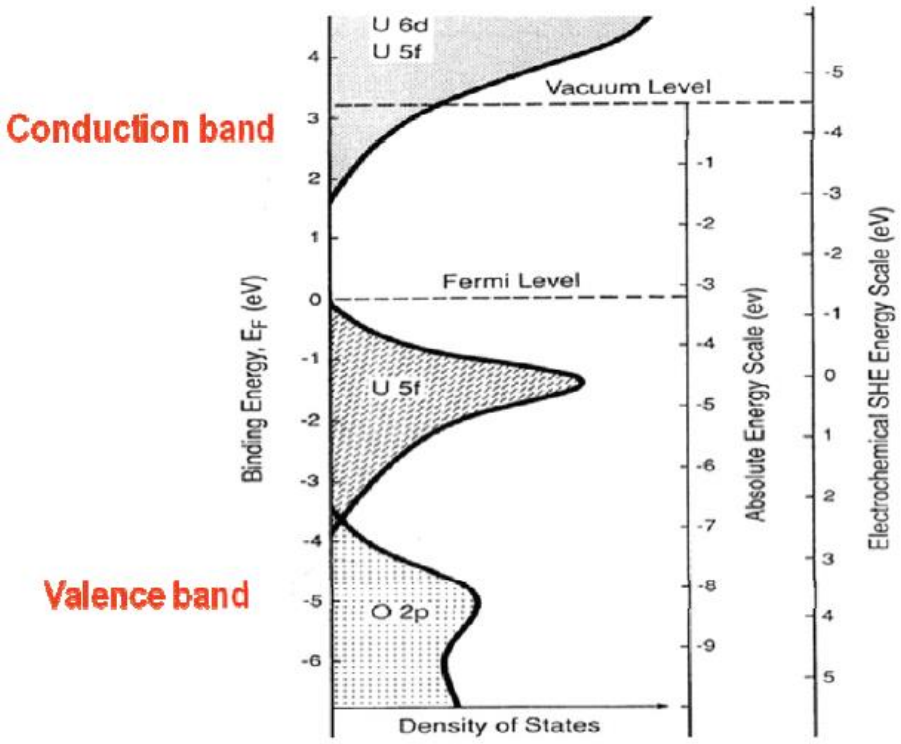

Figure 1-18 schematic energy level diagram for UO_2 expressed on standard hydrogen scale (SHE) (58)

The above diagram represents a schematic energy-level diagram for UO_2 which has been derived from various spectra and theoretical calculations including spectroscopic and electrochemical data, the data being represented against a standard hydrogen electrode (58). The valence band which is fully occupied has a predominance of O 2p character, whilst the empty conduction band consists mainly of U5f, 6d and 7f states. The U5f band contains two electrons per U atom for stoichiometric UO_2. This means that the U5f band falls into the gap between the filled valence band and the empty conduction band as pictured above (58). Although the valence band has a predominant character of O 2p, there is evidence of a small contribution from U 6d and 5f orbitals. The conduction band however consists mainly of various overlaps of U 7s, 6d and 5f states, the energy difference between the empty and occupied and 5f levels being approx. 5 eV (58). This value being the Coulomb correlation energy (U_{eff}). The U 5f subbands in a Mott-Hubbard insulator are much narrower than the U_{eff}, and therefore doped UO_2 produces $5f^1$ or $5f^0$ configurations. In stoichiometric UO_2 however, electrical conductivity would require the promotion of electrons from the occupied U 5f level to the conduction band, with an activation energy (E_A) of approximately 1.1 eV (58). The probability of this taking place at room temperature is extremely low. Since ceramic UO_2 has a slight oxygen excess due to the interstitial oxygen (O^{2-} ions), the overall charge balance is maintained by the ionisation of an

appropriate fraction of U(IV) ions to the U (IV/V) valence states (58). This introduction of non-stoichiometry, in the form of incorporated additional O^{2-} ions, which are accompanied by the creation of U(V) atoms to maintain charge balance, creates holes in the 5f band making the electrical conductivity of UO_{2+x} very sensitive to the degree of non-stoichiometry (58). In addition, non-stoichiometric locations have been shown to provide donor acceptor U(IV)/U(V) sites which catalyse the cathodic reduction of O_2/H_2O_2 (51) (60). If these locations, which appear as grain boundaries (58) also exhibit an enhanced anodic reactivity (i.e. the oxidation and subsequent dissolution outnumbering the stoichiometric locations) then they could be preferential corrosion sites (51). The migration of electrons in this scenario would be enabled via a hopping process with a low E_A of approximately 0.2 eV, due to the narrow occupied U 5f band (58). In the following sections the structural and electronic features that allow for hyperstoichiometry, and its effects on UO_2 corrosion will be discussed.

1.4.1 Conditions affecting Corrosion

As aforementioned, the release of radionuclides from spent fuel under repository conditions will be affected and controlled by radiolytically driven corrosion (61) (62). It is known that prior to irradiation in the reactor, the fuel, uranium dioxide is close to stoichiometric in terms of composition, i.e. $UO_{2.001}$ (61). However during irradiation, the UO_2 fuel will undergo changes with respect to composition and microstructure. The generation of fission and activation products leads to an increase in non-stoichiometry. This increase in non-stoichiometry means that the UO_2 fluorite structure must now accommodate a large number of interstitial oxygen in different lattice sites which lead to the formation of hyperstoichiometric phases (61).

1.4.2 Uranium Dioxide Hyperstoichiometry - Effects of increasing x in UO_{2+x}

As discussed above, uranium dioxide, in its stoichiometric form, is an f-f Mott-Hubbard insulator (63). The 5f orbitals and their respective spatial extents must be taken into consideration here. The early members of the actinide series, including uranium, have a 5f orbital diffuse that is sufficient enough to participate in molecular bonding (63). The 5f orbital diffuse also allows for the formation of metallic bands in the elemental solid (63). In the case of UO_2 and according to theoretical calculations of electronic structure and density of states (DOS), it is evident that a narrow 5f band that is filled with two electrons per uranium atom is found below the Fermi level E_F (61). The unoccupied states which appear at the onset of the conducting band are however, also found to be 5f states (63).

As oxygen is incorporated into the system, an electron from the 5f Hubbard band is removed to create U(V), which in turn removes the Coulomb interaction and thus converts insulating UO_2 to a UO_{2+x} p-type semi-conductor (61). From this it is evident that UO_2 hyperstoichiometry affects electronic conductivity (64); this conditioning can in turn support galvanic coupling between oxidation and reduction reactions on the UO_{2+x} surface and therefore increase the rate of corrosion of UO_2 (61).

Again, as discussed above, it is known that the fluorite structure of UO_2 is able to accommodate additional O as it has empty interstitial spaces in order to do so. According to theoretical calculations, the energies of formation of O interstitials and vacancies are lower when compared to the energy taken to create a U defect (61). This observation is in agreement with neutron capture experimental results which have established that the UO_2 defects originate in the O sub-lattice (61).

The energy of formation for a U vacancy is double the energy of formation of an O vacancy, however the important observation made was that the energy of formation of an O interstitial in the octahedral site is negative (61). This observation explains why the oxidation of uranium dioxide occurs via the addition of O interstitials rather than by the formation of U vacancies, which leads to hyperstoichiometry (61).

The above is in agreement with experimental results obtained by Allen *et al.* in 1986. The study also showed that the interaction between different interstitial defects lead to the production of microscopic substructures or clusters which introduced specific localised properties rather than basing hyperstoichiometric phases on randomly distributed point defects, as they have been in the past (65). This point will be returned to and addressed later on.

1.4.2.1 Effect of Hyperstoichiometric Phases on UO_2 Dissolution

It has recently been established that the local current density (anodic) experienced by a naturally corroding surface can vary by a factor of 5. This factor of 5 depends on the degree of non-stoichiometry present in that location (61).

In accordance with the above, it has also been demonstrated that the locations which are non-stoichiometric are able to provide donor acceptor sites, i.e. U(IV) and U(V), for the reduction (cathodic) of oxidants, including O_2 and H_2O_2. This leads to the acceleration of corrosion at non-stoichiometric locations (61). SECM measurements have shown that the anodic oxidation of UO_{2+x} depends on the degree of hyperstoichiometry. It has also been observed that when point defects that have been randomly distributed had a low degree of non-stoichiometry, that the surface that was originally inert would have its cathodic reactivity enhanced by anodic oxidation of UO_{2+x} (61).

However, if the UO_{2+x} has already been oxidised to a large extent and clusters of a cuboctahedral structure are present, anodic oxidation reduces surface reactivity (61). When intermediate levels of stoichiometry are present and the primary defects are Willis clusters (a Willis cluster is a defect formed by a linear combination of the interstitials O' and O", and the vacancy O_V, and is labelled according to the combination O':O_V:O" (66)) the surface is observed to be reversibly oxidisable (61).

Moreover, a recent study by Elorrieta *et al*. (67) has shown that an addition of *x* up to $UO_{2.05}$ leads to a progressive incorporation of oxygen atoms within its interstitial sites. Starting from $UO_{2.05}$ and up to $UO_{2.11}$, these point defects start to rearrange themselves into ordered defects or Willis clusters (67). At around $UO_{2.11}$ however, part of the Willis clusters start to develop into more densely packed cuboctahedral clusters, at which point a complete rearrangement of the oxygen atoms in the cuboctahedral clusters at around $UO_{2.20}$ leads to a new, fully ordered superstructure containing oxygen vacancies. These are gradually filled until reaching a minimum of $UO_{2.24}$ (67).

As aforementioned, the introduction of non-stoichiometry in the form of O^{2-}, along with the formation of U(V) atoms that maintain the charge balance, increases the electrical conductivity of the oxide whilst simultaneously providing donor/acceptor (U(IV)/U(V)) sites on the surface of the oxide (58). The above have been shown to catalyse oxidant reduction reactions, which introduces the possibility of the overall corrosion process being accelerated (58). Moreover, there is the possibility that the structural changes within the UO_2 lattice caused by the addition of O will influence the anodic kinetics of the corrosion process, i.e. of the dissolution reaction $UO_2 \rightarrow (UO_2)^{2+}$ (58).

It is therefore believed that spent fuel, where grain boundaries can contain non-stoichiometric sites, is able to corrode more quickly in comparison with stoichiometric grains. Therefore the assumption that radionuclides on grain boundaries will be released instantly upon contact with groundwater is realistic (61).

The rate of corrosion of the fuel can be affected by the addition of O, as well as the addition of dopants. Dopants have been added to the SIMFUELs that are studied in this work in order to simulate the amount of fission products that would be present in spent fuel after burnup, i.e. after undergoing fission. The next section will focus on the effects that dopant incorporation has on the dissolution of the fuel matrix.

1.4.3 Effects of dopant incorporation

Some fission products have very limited solubility in the UO_2 lattice which are volatile at reactor operating temperatures (e.g. Kr-85, He-4, A-39r, Tc-99, I-129, C-14, Cs-135, Sn-125, Se-79), and migrate to the fuel/sheath gap during reactor operation, whilst other fission products are non-volatile and migrate to grain boundaries, reside in fission gas bubbles, or separate into solid phases such as perovskites ((Ba, Sr) ZrO_3) and metallic alloy phases (epsilon-particles: Mo, Ru, Rh, Pd, Tc) (68). The majority of fission products and actinides/lanthanides (e.g. Pu-238, Am-241 and Np-239) however, are retained within the UO_2 fuel matrix (68).

The effect of dopants on the air oxidation of UO_2 was found to have a stabilising effect on the cubic fluorite structure (69). An explanation for this was that the dopant cations were stabilised by the formation of dopant-oxygen vacancy clusters known as O_v clusters (68). This effectively leads to a reduction in the availability of the interstitial sites that are required for the fuel oxidation to occur (68).

The phase relationship of the rare-earth oxides and the uranium oxides would suggest that the solubility of the rare-earths decreases with an increase of x in UO_{2+x}, and that these elements are insoluble in the U_3O_8 phase (68). It is however also possible to attain a kinetically metastable state, i.e. a rare-earth doped U_3O_8 phase, by the oxidation of rare-earth doped UO_2 (68). The effects of dopant incorporation in UO_2 fuel will be further discussed in Chapter 3.

The structural and electrical properties, as well as the incorporation of x and dopants into the lattice structure are not the only factors that will affect corrosion of UO_2 in an underground repository. The potential conditions in nuclear waste repositories can vary from being oxidising or reducing to being wet or dry (21). Not all these conditions will apply to UK nuclear waste repositories. However the variables that need to be taken into consideration during the phase of repository life that is the focus of the work presented in this thesis (i.e. during the post-thermal anoxic phase where it is assumed that the cladding has been breached) are as follows:

- the effect of alpha radiation
- the effect of dissolved hydrogen
- the effect of hydrogen peroxide
- the pre-oxidation of the fuel
- the effect of pH
- the effect of temperature and
- the effects of dissolved salts in groundwater compositions (21)

Each of these effects will be discussed in turn, however, prior to their discussion, it is important to have some information of the effects of α, β, and γ radiation and the subsequent radiolysis of water, which will be the focus of discussion below.

1.4.4 Alpha Radiolysis of Water

Emissions of strong α-, β- and γ-radiation fields from spent nuclear fuel can cause the radiolytic decomposition of groundwater (70). Once the thermal pulse has occurred and the beta and gamma radiation has decayed away, only alpha radiation will be prevalent in a GDF (71). Below is a figure demonstrating the radiation fields with their associated time scales in a geological disposal facility.

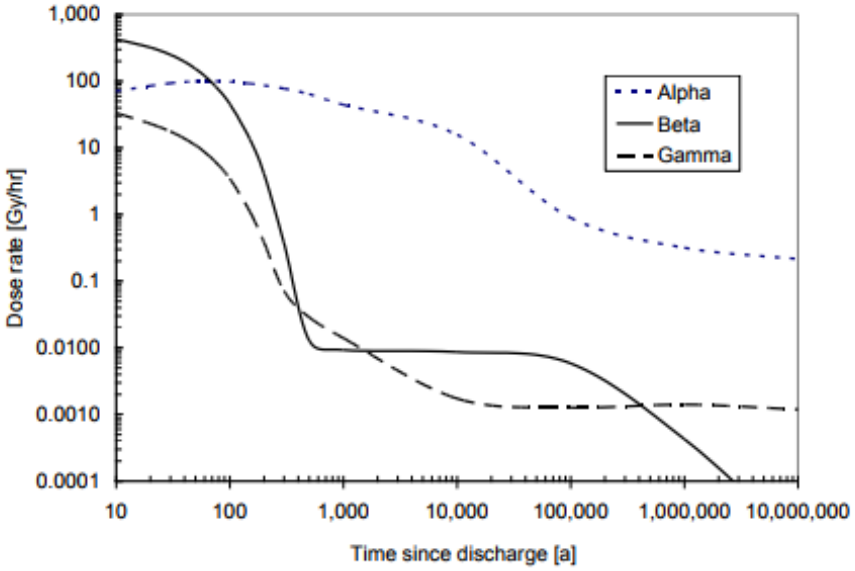

Figure 1-19 showing alpha, beta and gamma radiation dose rates as a function of time from a 220 MWh/kgU of Canadian CANDU fuel sample (72)

Once the canister fails and groundwater comes into contact with the alpha radiation of the spent fuel, the alpha radiolysis of water is expected to take place. Below is a figure representing the mechanisms that occur during the radiolysis of water.

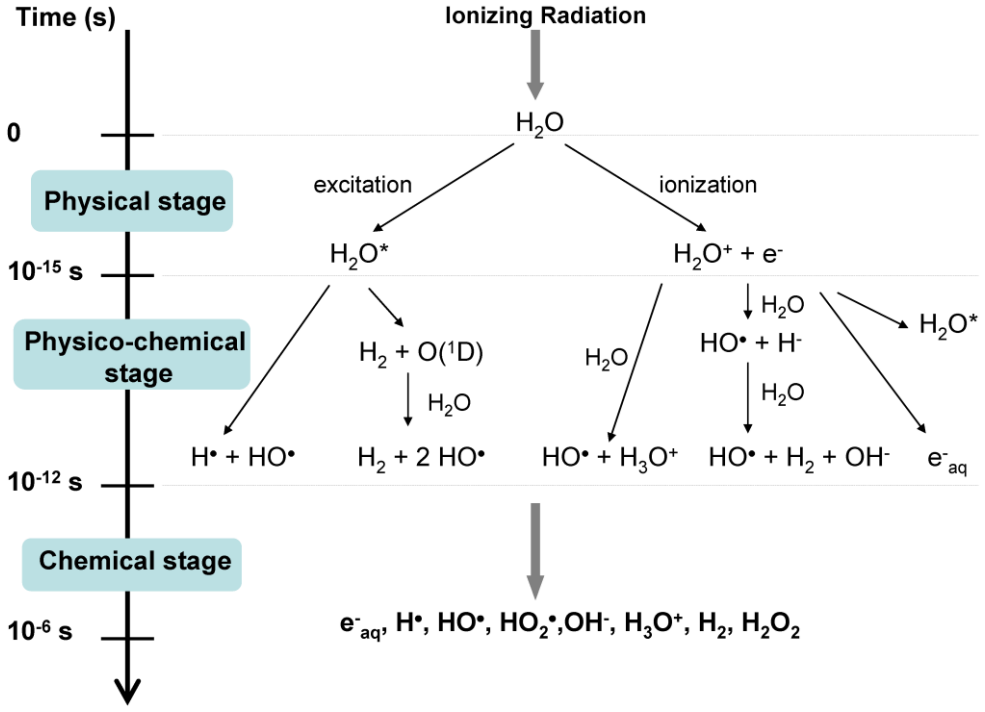

Figure 1-20 showing schematic of species formed during the radiolysis of water (73)

Before the late 1950's, there were two conflicting views about the fate of the electron. One theory was that the electron that was ejected would be thermalised before it would be able to escape from the Coulombic attraction of the parent cation (74), and thus be recaptured to give an excited molecule which would subsequently decompose (74). The second theory was that the electron would, in fact escape the parent ion, but would rapidly react with a neutral water molecule (74). The outcome of either mechanism was however, that the primary products were H· and OH· radicals. Moreover, the initial reaction was also the same in both cases (74).

In 1953, Platzmann *et al.* proposed that the hydrated electrons may exist sufficiently long enough to react with other solutes, and in 1963, Boag *et al.*, Hart *et al*., and Keen *et al.* independently observed the transient (short-lived excited state (75)) spectrum of a hydrated electron in the pulse radiolysis of water (74). Many reactions that had been reported in the past, prior to 1960, for being a H· radical in alkaline or neutral solutions were in fact the reportings of hydrated electrons (74).

Thus, the main products of the radiolysis of water after approximately 10^{-8} s are: $e^-_{(aq)}$, $H^\cdot$, $OH^\cdot$, H_2, H_2O_2, H_3O^+ and OH^- (74). Below is a table showing the amount of each species produced at different pH ranges per 100 eV of energy, given by their G values (74).

pH	0-2	4-11	13-14
$e^-_{(aq)}$	3.65	2.7	3.1
$H^\cdot$	3.65	0.55	0.54
$OH^\cdot$	2.95	2.8	2.9
H_2	0.45	0.45	0.45
H_2O_2	0.8	0.7	0.7
H_3O^+		3.6	
OH^-		~1	

Table 1-10 showing G values of species at different pH ranges (74)

H_2 can escape readily. However if it is in solution then it reacts via the following reaction:

$$H_2 + OH^{\cdot} \rightarrow H_2O + H$$

Equation 1-3

Hydrogen peroxide would also react with the reducing agents $e^-_{(aq)}$ and $H^{\cdot}$ via Equation 1-4 and Equation 1-5:

$$H_2O_2 + e^-_{(aq)} \rightarrow OH^{\cdot} + OH^-$$

Equation 1-4

$$H_2O_2 + H^{\cdot} \rightarrow OH^{\cdot} + H_2O$$

Equation 1-5

During the radiolysis of pure water, H_2 and H_2O_2 are destroyed as fast as they are produced, provided that the H_2 cannot escape (74). In the case that it does escape, O_2 is also produced via the following pathways:

$$H_2O_2 + OH^{\cdot} \rightarrow H_2O + HO_2^{\cdot}$$

Equation 1-6

$$HO_2^{\cdot} + HO_2 \rightarrow H_2O_2 + O_2$$

Equation 1-7

$$HO_2^{\cdot} + OH^{\cdot} \rightarrow H_2O + O_2$$

Equation 1-8

The hydrogen peroxide that is retained in solution may also react with the solutes (74). The hydrated electron that is produced during the radiolysis of water is a powerful reducing agent and reacts via the following mechanisms (74):

$$2e^-_{(aq)} + 2H_20 \longrightarrow H_2 + 2OH^- \text{ (this reaction is fast)}$$

Equation 1-9

$$e^-_{(aq)} + H_2O \rightarrow H^\cdot + OH^\cdot \text{ (this reaction is slow)}$$

Equation 1-10

$$e^-_{(aq)} + S \rightarrow S^\cdot$$

$$e^-_{(aq)} + H^+ \rightarrow H^\cdot$$

with solutes

Equation 1-11

Equation 1-12

It should be noted here that the hydrated electron is a conjugate base with a pKa of approximately 9.7, there are therefore equal amounts of e^-(aq) and $H^\cdot$ at pH 7 (74). The hydrated electron normally reacts by electron attachment, such as:

$$e^-_{(aq)} + {}^\cdot O_2^\cdot \rightarrow O_2^{\cdot -}$$

Equation 1-13

The reaction between the hydrated electron and nitrous oxide is important as the reaction is specific to e^-, and also because the hydrated electron is converted to oxidising radicals (74).

$$N_2O + e^-_{(aq)} \rightarrow [N_2O^{\cdot -}] \rightarrow N_2 + O^{\cdot -}$$

$$\downarrow +H^+ \quad \downarrow +H^+$$

$$N_2OH^\cdot \rightarrow N_2 + OH^\cdot$$

Equation 1-14

$e^-_{(aq)}$ reacts with many uncharged molecules at each encounter, however does not react with alkali metals or alkaline earth metals (74).

The hydrogen radical, $H^{\cdot}$, is not as strong a reducing agent as is $e^-_{(aq)}$. In an acidic solution, $e^-_{(aq)}$ is converted to an $H^{\cdot}$ radical via the following reaction (74):

$$e^-_{(aq)} + H^+ \rightarrow H^{\cdot}$$

Equation 1-15

In an alkaline solution, the following takes place:

$$H^{\cdot} + OH^- \rightarrow e^-_{(aq)} + H_2O$$

Equation 1-16

The $H^{\cdot}$ radicals main reaction is with O_2, to give a hydroperoxyl radical (74):

$$^{\cdot}O_2^{\cdot} + H^{\cdot} \rightarrow HO_2^{\cdot}$$

Equation 1-17

The hydroxyl radical is a powerful, uncharged oxidising species. It forms the following in an alkaline solution:

$$OH^- + OH^{\cdot} \leftrightarrow H_2O + O^{\cdot -}$$

Equation 1-18

The conjugate base that is formed here can react with O_2 in aerated solutions (74). In the absence of a solute, the following takes place and hydrogen peroxide is formed:

$OH^{\cdot} + OH^{\cdot} \leftrightarrow H_2O_2$

Equation 1-19

The hydroperoxyl radical formed via Equation 1- is a weak radical and is found in tracks of heavy particles in de-aerated water (74). It can also be formed by the hydroxyl radical reaction with hydrogen peroxide:

$OH^{\cdot} + H_2O_2 \rightarrow H_2O + HO_2^{\cdot}$

Equation 1-20

An ionised form of the hydroperoxyl radical can also be formed by reaction with light particles in water:

$^{\cdot}O2^{\cdot} + e^{-}_{(aq)} \rightarrow O2^{\cdot -}$ (ionised form of $HO_2^{\cdot}$)

Equation 1-21

The hydroperoxyl radical is also formed in a non- ionised form:

$^{\cdot}O_2^{\cdot} + H^{\cdot} \rightarrow HO_2^{\cdot}$

Equation 1-22

However the hydroperoxyl radical usually disappears in reaction with itself:

$HO_2^{\cdot} + HO_2^{\cdot} \rightarrow H_2O_2 + O_2$

Equation 1-23

Most radiolysis models that take the formation of the above species into account have concentrated on the water radiolysis in the presence of gamma radiation, and not alpha radiation (76). In the event of canister failure, groundwater is expected to come into contact with the spent fuel. The water that reaches the fuel will be subjected to alpha radiation as beta/gamma radiation would have decayed by the time that canister failure is expected to take place. It is therefore important to model the generation of the species that are expected to be formed during the alpha radiolysis of water.

Researchers at Pacific Northwest National Laboratory (PNNL) have created models to perform radiolysis predictions for fuel corrosion in an anoxic atmosphere, and within a thin layer of water, driven by the alpha radiolysis of water (76). The figure below shows a plot of the species that are expected to be generated during the alpha-radiolysis of water in a geological disposal facility. The plot is divided into a time-dependant portion, where the second half of the plot shows the concentrations of the species, varying with distance, once the system has reached steady-state conditions (76).

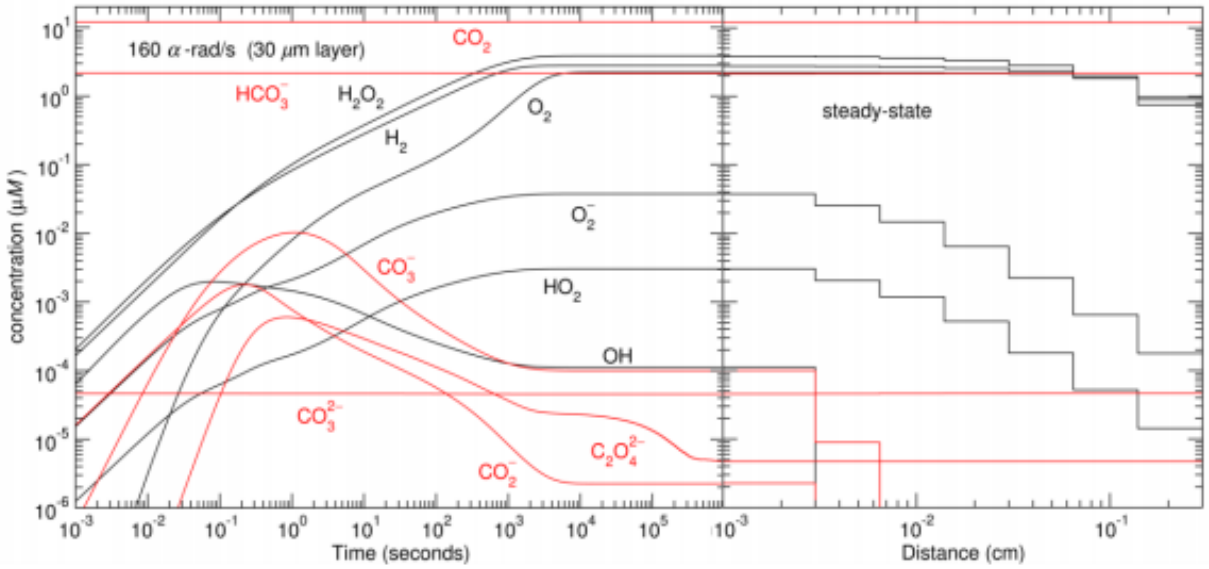

Figure 1-21 showing the calculated environment within 30 mm of a 160 rad/s alpha field in an anoxic environment illustrating the time dependence of dominant species (76)

From the figure above it can be seen that the species most likely to be generated via the alpha-radiolysis of water in a geological disposal facility are hydrogen and hydrogen peroxide. Hence we

will focus on the effects that these two species have on the corrosion of spent fuel in a GDF in the following sections.

1.4.5 Effects of alpha radiation on UO_2

As discussed above, should a nuclear waste container in an underground repository fail, then the dissolution of the spent fuel will occur (72). The main factors that control the dissolution of spent fuel are the redox conditions that are generated by the radiolysis of water (see Section 1.4.4) at the fuel surface (72). Before going into detail of the effects that hydrogen and hydrogen peroxide have on the corrosion of nuclear waste, we will discuss below the effects that an external source of alpha radiation could have on the corrosion of UO_2 and in effect spent nuclear fuel.

The prevalent ionising radiation from spent fuel, which is alpha radiation as shown in the figure above, would generate species such as hydrogen peroxide, O_2 and $OH^{\cdot}$ radicals (of which H_2 and H_2O_2 are discussed further in the next section) (77). The effects of alpha radiolysis of water on the oxidation and dissolution of uranium dioxide have previously been studied using two different techniques, which are discussed below. In conclusion to these experiments, it was found that a significant amount of dissolution of UO_2 is expected to occur when the surface has reached a composition of $UO_{2.33}$ (77) (see Section 1.4.2 for uranium dioxide hyperstoichiometry).

In order to investigate the effects of alpha radiolysis of water on UO_2 corrosion, in 2005 Lucchini *et al.* looked at the uranium dioxide/water interface under irradiation as a function of alpha flux (77). The alpha flux was provided by a particle beam from a cyclotron (77). The irradiation method used by Lucchini *et al*. involved the use of an alpha-source placed externally in water in order to irradiate the UO_2/water interface (77). The corrosion rate via this method was found to increase with the alpha dose rate. For the second irradiation method, Lucchini *et al.* reported on the work carried out by Gray in 1988 which investigated the use of UO_2 pellets containing alpha emitters such as ^{238}Pu and ^{239}Pu (78) (77).

For comparison purposes, Lucchini *et al.* also investigated the effect of hydrogen peroxide on UO_2 dissolution out of irradiation (77). The uranium release rate was found smaller for leaching tests with H_2O_2 solution than for those performed under irradiation. These results show that other radiolytic

species such as the OH radical, can be involved in the oxidation/dissolution processes of UO_2 under irradiation.

First, Lucchini *et al.* investigated the effects of alpha emission on the release of uranium at the UO_2/H_2O interface and how this may alter the UO_2 surface (77). For this experiment, a high energy alpha beam (He^{2+}) from a cyclotron was used to pass through a UO_2 disk and then emerge through the water that the UO_2 disk was in contact with (77). The same experiment was also conducted using the same pH conditions H_2O_2 concentration which was created by the alpha beam, but without irradiation to assess the specific effect of radiolysis on UO_2 dissolution (77). It was found that as the alpha beam flux was increased, the release of uranium and the hydrogen peroxide concentrations also increased, whereas the pH decreased. A possible explanation for the decrease in pH is described below.

As the alpha radiolysis of water generates H_2O_2, an increase in alpha beam flux also increases hydrogen peroxide generation. Therefore, an increase in H_2O_2 was observed to subsequently lead to an increase in the uranyl alteration product metastudtite ($UO_4.2H_2O$). The reaction of metastudtite precipitation can be given by the following equation:

$$UO_2^{2+} + H_2O_2 \rightarrow UO_4 + 2H^+$$

Equation 1-24

The decrease of the solution pH occurs due to generation of the two H+ ions (77).

The above results concluded that the amount of uranium released into solution depended on the dose of radiation that was deposited on the solution by the alpha beam (77).

The second method used to study the impact of alpha-radiolysis on UO_2 dissolution which, as mentioned above, was carried out by Grey and reported on by Lucchini *et al.*, was, the use of UO_2 pellets containing alpha emitters such as Pu-238 and Pu-239 (77) (78).

The leaching of both Pu-doped and undoped UO_2 pellets were investigated by Grey in a salt brine at 90°C, so that the leachates could be compared to one another (78). The results from the pellets doped with Pu-239 gave a specific activity of 1.06 x 10^6 Bq.g^1, whilst the pellets doped with Pu-238 gave a specific activity of 1.72 x 10^8 Bq.g^1 (78). It was found that the total uranium mass loss rate from Pu-doped UO_2 pellets was about 10 times greater than from the undoped pellets. The mass loss rates for the two sets of Pu-doped UO_2 pellets were found to be approximately equal (78).

Rondinella *et al*. also investigated the uranium release from undoped and Pu-238 doped UO_2 pellets, it was however in demineralised water under an anoxic atmosphere and at room temperature (79). The specific alpha-activity of the first set of samples was 3.76 x 10^{10} Bq.g^1 and for the second set of samples it was 3.76 x 10^8 Bq.g^1 (79). The amounts of uranium that were released during the leaching process were 2 to 3 orders of magnitude higher for the doped UO_2 than for the undoped UO_2 (79). These results therefore indicate a clear effect that alpha-radiolysis has on the dissolution of UO_2. In spite of the 100-fold difference in the alpha-decay rates of the two types of investigated specimen, no significant difference was observed in the dissolution behaviour of uranium for the two doped materials.

As aforementioned, apart from comparing the leaching of doped UO_2 pellets to undoped pellets, Lucchini *et al.* also looked at the effects of alpha radiation on UO_2 dissolution out of irradiation. It was found that the rate of release of uranium in water was significantly higher for leaching experiments conducted under irradiation than for leaching experiments that were conducted out of irradiation and only with hydrogen peroxide solutions (77). Due to the fact that the concentration of uranium was found to be lower during leaching experiments in H_2O_2 and out of irradiation, it was concluded that not only hydrogen peroxide, but also other radiolytic species that are formed during the alpha radiolysis of water are involved in the oxidation and dissolution process of UO_2 (77).

Sattonnay *et al.* conducted similar experiments to Lucchini *et al.* in 2001 by using an external alpha beam. Sattonnay *et al*. used an alpha beam provided by a cyclotron and investigated the behaviour of the UO_2/water interface under irradiation in aerated deionised water. During these experiments they observed that an alteration product had formed on the UO_2 surface that was yellow in colour (80). As with Lucchini *et al.* it was also found here that as the alpha beam flux increased, that the concentrations of uranium and hydrogen peroxide also increased in solution, whilst the pH

decreased. The observation of a yellow coloured alteration product was found to be a hydrated uranium peroxide mineral (see Section 1.5 for transformation phases), which was identified by X-ray diffraction as metastudtite (UO_4 . $2H_2O$), (80). The production of metastudtite is a direct effect of water alpha radiolysis which is caused by the production of hydrogen peroxide (80).

The transformation phases that are formed on the UO_2 surface due to the presence and interaction with radiolytically formed hydrogen peroxide are further discussed in Section 1.5. Next, we will discuss the effects that one of the major species from the alpha radiolysis of water will have on the corrosion of UO_2 – hydrogen.

1.4.6 Dissolved hydrogen

As aforementioned, in case of canister failure in a deep geological repository, the release of radionuclides into groundwater will depend on the chemical environment near the fuel surface (81). We know that the corrosion of spent fuel is influenced by hydrogen peroxide, which is generated via the radiolysis of water. There is however, another factor that affects the corrosion of UO_2 (82) due to the presence of large amounts of iron in the fuel canister that the waste will be enclosed in, which results in the reaction of water with the steel clad, producing H_2 and Fe^{2+} via the following mechanisms (83):

$$Fe + 2H_2O \rightarrow Fe^{2+} + H_2 + 2OH^-$$

Equation 1-25

$$3Fe + 4H_2O \rightarrow Fe_3O_4 + 4H_2$$

Equation 1-26

Hydrogen gas can be produced inside a failed waste canister in either one of the following ways: it can either be generated by the corrosion of the steel canister due to its interaction with groundwater, as shown in the equations above, or, it can be produced radiolytically as shown in Figure 1-20, which outlines the species that are formed during the radiolysis of water – hydrogen being one of the predominant species (as seen in Figure 1-21).

To investigate whether the generation of hydrogen influences the corrosion of the spent nuclear fuel, i.e. the release of radionuclides from the fuel matrix, experiments were set up by Fors *et al.* in 2009 with an irradiated MOX fuel, a high burn-up UO_2 fuel and an α-doped UO_2 fuel which were studied under simulated repository conditions (81). During these studies it was found that the fuel surfaces became protected from oxidation by the presence of hydrogen and that the release of radionuclides was inhibited. It was further asserted that the amount of dissolved uranium in the leachate gradually decreased, and, regardless of the fuel type that had been used in this investigation, a value below the reported solubility limit for $UO_{2(amorphous)}$ had been reached (81). It was also found that neither strong α- radiation fields, nor intense mixed radiation fields, increased the concentration of uranium in solution (81). Furthermore, it was observed that hydrogen had a protecting effect on UO_2 in the case of pure 10% U233-doped UO_2 and also that the dissolved uranium concentration in contact with this particular fuel decreased to 9×10^{-12} mol dm^{-3} (81). The conclusion that the solubility limiting phase governing this uranium concentration was likely to be more crystalline than any other previously observed UO_2 precipitate formed in contact with water at near-neutral pH, was drawn (81). It was concluded that as a result, the hydrogen would completely protect the spent nuclear fuel from corrosion until its activity had reached an α-activity that was below the α-activity threshold, i.e. until the activity of the fuel is too low to sustain fuel oxidation (81).

In 2010, Broczkowski *et al.* looked at the combined influence of hydrogen peroxide (see next section for isolated effects of hydrogen peroxide) and dissolved H_2 on the oxidation of spent fuel using a simulated fuel (SIMFUEL) (83). They concluded that in a sealed repository, they would expect that the anoxic corrosion of steel would generate substantial amounts of hydrogen gas pressures which would lead to the dissolved hydrogen concentration of up to 10^{-1} mol l^{-1} (82). This suggests that the hydrogen gas produced by steel corrosion can scavenge the hydrogen peroxide that is generated through the radiolysis of water and thereby limit the corrosion of fuel, and hence, delay the release of radionuclides (82).

Broczkowski *et al.* also reported in 2007 that some studies have shown that in the presence of hydrogen gas, the corrosion rate is decreased by more than 4 orders of magnitude when compared to corrosion rates under oxidising conditions (84). There are two possible explanations for this:

I. a reductive influence on fuel corrosion brought about by $H^{\cdot}$ radicals, which are produced via a catalytic effect of the UO_2 surface upon the decomposition of H_2; and
II. the process of scavenging of radiolytic oxidants via reaction with H_2 (84)

The second process coincides with standard radiolytic models, which predict that a hydrogen concentration of less than 10^{-5} mol l^{-1} is sufficient to suppress the production of hydrogen peroxide (84).

All of the mechanisms that have been proposed to explain the suppression of radionuclide release by the presence of dissolved hydrogen involve the activation of molecular hydrogen to produce the strongly reducing radical $H^{\cdot}$ (85). The $H^{\cdot}$ radical works by scavenging radiolytic oxidants and thereby suppressing the oxidation of the fuel and also the process of dissolution (85). Gamma and alpha radiation can both produce the $H^{\cdot}$ radical surface species. In the case of alpha radiation, the decomposition of water to $OH^{\cdot}$ and $H^{\cdot}$ radicals leads to the reaction of the $OH^{\cdot}$ radical with hydrogen, to yield an additional $H^{\cdot}$ radical. It is this additional $H^{\cdot}$ radical that then suppresses the oxidation of the fuel and scavenges the radiolytic oxidants (85). It is also possible that in the absence of radiation fields, that the activation of oxidation can occur on the surface of epsilon particles. Epsilon particles are galvanically coupled to the fuel matrix and therefore behave as anodes for the process of hydrogen oxidation, which subsequently forces the uranium dioxide to adopt a low potential (85).

Shoesmith *et al.* also concluded that it would be possible to completely suppress the corrosion of spent fuel in the presence of dissolved hydrogen depending on the radiation fields and number density of epsilon particles present (85). This is said to be achievable in hydrogen pressures going as low as 0.1 – 1 bar. The corrosion of steel liners within a failed waste container could produce hydrogen gas pressures of up to 50 bar, meaning that according to this, fuel corrosion could be completely suppressed under the long-term conditions which are expected in a sealed repository (85).

The studies described above emphasise that the oxidative dissolution of spent nuclear fuel can be suppressed by the presence of hydrogen. Counter-intuitively, this only goes to emphasise how important it is to have an understanding of the oxidation processes that may occur oxically and

anoxically. In the case that dissolved H_2 does in fact inhibit the corrosion of spent fuel, it is imperative that it is understood which processes precisely will be inhibited, so it is not just the feasibility of application in a geological repository, but also academic curiosity that is the driving force of this work.

Several reviews and synthesis reports regarding the radiolytic decomposition of groundwater in deep geological repositories, and in particular, radiolytically generated UO_2 corrosion have been published in the past (70). However, to predict the long term behaviour of spent nuclear fuel in a deep geological repository, the mechanisms that are involved in the radiolytical processes must be understood. An understanding of this includes not only the processes in pure systems – such as deionised water or simple electrolyte solutions – but also the influence of possible contaminants and of long-lived radiolysis products on groundwater radiolysis (70).

We will therefore now look at the influence of hydrogen peroxide and the effects it has on the corrosion of spent nuclear fuel in a deep geological repository. It is vital to discuss the baseline corrosion behaviour in the presence of hydrogen peroxide as a radiolysis product simulant before the additional complexity of hydrogen is introduced, which is why this thesis will focus on the effects of deliberately added H_2O_2, and the effects of hydrogen are beyond the scope of this work.

1.4.7 Hydrogen peroxide

It is assumed that canister failure, which would result in the wetting of the spent fuel, will not occur until all beta/gamma fields have decayed to levels that would be insignificant (86). Should this be the case, then only the effects that the alpha radiolysis of water (see Section 1.1.4 for alpha radiolysis) will have on the spent fuel will be of significance and importance (86).

Although the effects of alpha radiolysis on the corrosion of UO_2 have previously been investigated, resulting in a number of models that are to predict its influence on the release of radionuclides, there is no strong understanding of the effect that hydrogen peroxide has on the corrosion of UO_2 (86). As hydrogen peroxide is the primary oxidising product of alpha radiolysis, its effects on UO_2 corrosion are of importance (86).

Hydrogen peroxide causes the electrochemical dissolution of UO_2; however the complication arises due to the coupling of two reactions (Equation 1- and Equation 1-).

$$UO_2 \rightarrow UO_2^{2+} + 2e^-$$

Equation 1-27

$$H_2O_2 + 2e^- \rightarrow 2OH^-$$

Equation 1-28

Hydrogen peroxide can also decompose to OH^- and O_2, which is a coupling of Equation 1- with an alternative anodic reaction:

$$H_2O_2 \rightarrow O_2 + 2H^+ + 2e^-$$

Equation 1-29

The O_2 that is produced in Equation 1- is also an oxidant for the corrosion of UO_2. This occurs via the coupling of Equation 1- and Equation 1-:

$$O_2 + 4e^- + 2H_2O \rightarrow 4OH^-$$

Equation 1-30

However the dissolution that would be driven by Equation 1- would be kinetically slower than if the dissolution was driven by Equation 1- (86).

In dissolution rate studies on CANDU (CANada Deuterium Uranium) SIMFUEL at pH 6 by Goldik *et al.*, it was found that the hydrogen peroxide consumption rate was greater than the UO_2 dissolution rate (60). This was due to the formation of uranyl oxides on the fuel surface, a possibility of which being shoepite $[(U(VI)O_2)_8O_2(OH)_{12}] \cdot 12H_2O$ (60). Shoepite is a rare alteration product of uranitite which can form in hydrothermal uranium deposits (87). It was suggested by Goldik *et al.* that these surface

oxides would be able to catalyse the hydrogen peroxide decomposition process, which would partially explain the differences in H_2O_2 consumption rates in comparison to UO_2 dissolution rates (60). Sunder *et al.* had also found that at low hydrogen peroxide concentrations (10^{-4} mol dm^{-3}), shoepite tended to be the more predominant surface deposit (86). However it was found that at higher hydrogen peroxide concentrations (≥ 1.5 x 10^{-2} mol dm^{-3} at near-neutral pH (80)), the formation of studtite occurs, which can limit the rate at which UO_2 reacts with H_2O_2 (86). Studtite is a secondary uranyl mineral which contains peroxide, the peroxide being formed via the alpha radiolysis of water (87). Studtite or metastudtite, which is a dehydrated form of studtite (87), may readily form on the surface of spent nuclear fuel under long-term storage, and have been reported to be found on the surface of spent nuclear fuel at the Hanford site (88). Studite has also been reported to have been observed on Chernobyl corium lavas (88). As there is considerable evidence that these uranyl peroxide alteration phases can be of importance when considering spent nuclear fuel, they will be looked at in more detail in Section 1.5.

We will now consider the mechanism that occurs between H_2O_2 and UO_2.

The mechanism that has been proposed for the reaction between hydrogen peroxide and UO_2 is a Fenton-like mechanism, shown by the following equations (60):

$$UO_2 + H_2O_2 \rightarrow UO_{2(surface)}^{+} + OH^{\cdot} + OH^{-}$$

Equation 1-31

which is followed by either:

$$2UO_{2(surface)}^{+} \rightarrow UO_2^{2+} + UO_2$$

Equation 1-32

Or

$$UO_{2(surface)}^{+} + OH^{\cdot} \rightarrow UO_2^{2+} + OH^{-}$$

Equation 1-33

The above mechanism confirms that the UO_2 dissolution process is dependent on the concentration of hydrogen peroxide (60) (86).

Lucchini *et al.* investigated the effect of hydrogen peroxide on UO_2 dissolution out of irradiation and compared this to the results obtained when performing the same experiments under irradiation (77). In order to achieve this they performed leaching tests without irradiation but in the presence of hydrogen peroxide with a concentration of 10^{-3} mol/L (this value was close to the concentration that was measured when the leaching experiments were carried out under irradiation). The results that were obtained showed that the amount of uranium that was released was two orders of magnitude smaller than the uranium concentration that was measured under irradiation (77). These results show that other radiolytic species, as OH radical, can be involved in the oxidation/dissolution processes of UO_2 under irradiation.

The focus of the work within this thesis will be on the effects that deliberately added hydrogen peroxide to different groundwater simulations will have on the corrosion behaviour of UK specific spent nuclear fuel.

It should be noted that during the establishment of oxidising conditions, the dissolution process would be a corrosion reaction that is fuelled by the hydrogen peroxide which is generated by radiolysis (72). The rate at which the fuel corrodes will decrease as the conditions become less oxidising, where the rate of corrosion will be determined by the types of corrosion products formed, which are controlled by the minerals which are contained in the groundwater (72). The effects of silicate, calcium, carbonate and bicarbonate are discussed in Sections 1.4.10-1.4.12.

As aforementioned, the type of radiation field that will be prevalent in a geological disposal facility once the thermal pulse has occurred is alpha radiation, which is what the next section will focus on.

1.4.8 Fuel pre-oxidation

It is possible for the 'dry' oxidation of UO_2 to occur as a consequence of package failure during the early stages of waste packaging (21). When spent fuel is exposed to high temperatures during the

thermal pulse, the extent to which oxidation of the fuel could occur is broad. If the fuel is oxidised to U_3O_8, it could lead to the breaking-up of the fuel grains and to an increase in volume by a factor of 1.35 (21). As this occurrence would put a significant amount of stress on the clad, the unzipping of the clad can be expected, which would subsequently lead to an area of the spent fuel being exposed to the groundwater in the repository (21).

Another likely scenario is one that will expose the spent fuel to a moist and aerated environment at post-cladding failure which would lead to the preoxidation caused by the reaction with aerated steam (oxidation by steam being a potential failure mechanism that has previously been investigated (89)) (21). Should this occur, it is expected that oxidation will take place in the grain boundaries on a preferential basis. This preferential oxidation could initiate the breaking up of fuel pellets. This scenario has been especially evident in experiments where the samples had been exposed to radiolytic effects, such as carried out by Wasywich *et al.* in 1993 (90).

1.4.9 Effect of pH

It was found that there were no significant effects on corrosion rates imposed onto the fuel clad by varying pH in the range of $5 \leq pH \leq 10$ (21), which is predominantly a result of passive layer formation at the steel surface. However, the same is not true of UO_2 where the production of a thin film of $UO_{2.33}$ on the UO_2 surface in the first instance has been observed (91) (92).

In 1991, Sunder *et al.* looked at the oxidative dissolution of uranium dioxide in different solutions as a function of pH (93). The solutions used were $NaClO_4$ and Na_2SO_4, over a pH range of 0.8 – 12. It was found that in solutions over a pH of 5 or more, that dissolution was followed by the growth of a thin film of $UO_{2.33}$ on the surface of UO_2 (see Section 1.4.2 for uranium dioxide hyperstoichiometry) (93). Although this film was observed to achieve a steady-state thickness between 5 – 10 h, the thickness was able to be increased with an increase in pH (93). Between 10 and 100 h, further oxidation occurs to form $UO_3 . xH_2O$. Upon the formation of $UO_3 . xH_2O$, a steady-state dissolution condition was achieved (93). The formation of this hydrated form of UO_3 is a precursor to dissolution and appears to only occur in the grain boundaries. It was also established that the film formation of $UO_{2.33}$ did not occur in acidic solutions and oxidation would proceed directly to the U(VI) state (93). The dissolution rate, which was measured by extrapolating the steady-state current to the corrosion potential, was found to be ca. 50 times greater at pH 2.5 than what it was at pH 9.7 (93). This observed

dependence of the steady-state corrosion potentials on pH indicates that the rate of the anodic dissolution at pH greater than 10 is rate controlled, whilst the corrosion potentials between pH 2 – 10 only vary slightly with pH (93).

1.4.10 Effect of Temperature

There is evidence to show the formation of secondary mineral deposits at higher temperatures from studies of fuel dissolution in Mg^{2+} containing groundwaters. The formation of such deposits explains the low activation energy that is obtained in neutral groundwaters that are not complexing (21). This low activation energy indicates the presence of a partial suppression of dissolution which is attained by the accumulation of corrosion product deposits (21). If the temperature is increased then the acceleration of dissolution is observed to be counterbalanced by an increasing amount of U(VI) phase deposits. This is especially apparent if the accumulation of U(VI) phase deposits are inversely dependent on the solubility with regards to temperature (21).

Studies conducted in the presence of carbonates have shown that the deposition of corrosion products is prevented by carbonate-containing solutions (21). It was, however observed that changes occurred in the underlying layers of these deposits as the temperature was increased (between 150 and 200 °C). As these thicknesses have not been measured under steady state conditions, it is expected that the thicknesses could be significantly larger to the ones that had been measured (between 100 – 500 nm, temperature and exposure dependant) (21).

The effects of temperature on the stability of secondary uranyl phases are discussed in Section 1.5.1

1.4.11 Carbonate Concentration in Groundwater

Carbonates and bicarbonates are known to affect the solubility of U(VI) corrosion products, it is therefore important to take carbonates and bicarbonates into consideration with regards to groundwater content as these are likely to affect the corrosion of nuclear fuel in a geological repository (94). Shoesmith *et al*. found that during single pass flow-through experiments using low concentrations of O_2, the carbonate concentrations did have an effect on corrosion rates (21). It was believed however that the dependency of carbonate concentration on the corrosion rates would change with varying redox conditions. This is due to the fact that carbonate is a strong complexing

agent for UO_2^{2+}, but not so much for U^{4+}, as U^{4+} is preferentially hydrolysed and therefore is unlikely to accelerate corrosion under conditions that are marginally oxidising (21). It is therefore expected that the rate at which oxidation occurs to generate UO_2^{2+} will become more rate-determining as the conditions become less oxidising. This means that as the concentration of carbonate decreases, the overall corrosion rate under marginally oxidising conditions will therefore also decrease (21).

Changes in carbonate dependency have been observed to occur with changes in temperature. During an increase in temperature from room temperature to 40 °C, the corrosion process had changed from O_2 reduction, i.e. a cathodic process, to UO_2^{2+} dissolution, which is an anodic process (21).

Experimental data from Steward *et al.* (95) has shown that corrosion rates increased with an increase in carbonate concentration in the following order (21):

$$r_{SF} \approx r_{UO_2} < r_{U_3O_8} << r_{UO_3 \,.\, H_2O}$$

Equation 1-34

where SF = spent fuel

The corrosion of the samples from the above mentioned experiments can be understood in terms of two sequential processes: the oxidation of uranium from an insoluble U(IV) state to a soluble U(VI); followed by the dissolution of the so-formed UO_2^{2+} via complexation with carbonate (95). The dependance of the overall corrosion rate on the carbonate concentration is then determined by the path of the rate determining step (95). In the case of UO_3, oxidation is already well advanced, and therefore the rate determining step here is the carbonate complexation during the UO_2^{2+} dissolution process (95). As such, the overall corrosion rate of UO_3 would be expected to exhibit a profound dependance on the carbonate concentration. In contrast, the rate determining step in the corrosion of UO_2 and the UO_2 spent fuel samples is the oxidation of U(IV) to U(VI)/UO_2^{2+} prior to the complexation of U(VI) (95). Consequently the concentration of carbonate has very little effect on the overall corrosion rate. U_3O_8 can be considered an intermediate case due to the

potential oxidation of U(IV) to U(VI) – although the uranium is not oxidised to the same extent as in UO_3.

One of the half reactions that occur during corrosion is the reaction of anodic dissolution, and so, in 2010, Keech *et al.* studied the anodic dissolution of SIMFUEL in carbonate and bicarbonate solutions using electrochemical techniques including voltammetric/potentiostatic methods and also impedance spectroscopy (94). The resulting cyclic voltammogram can be seen in Figure 1-22 below.

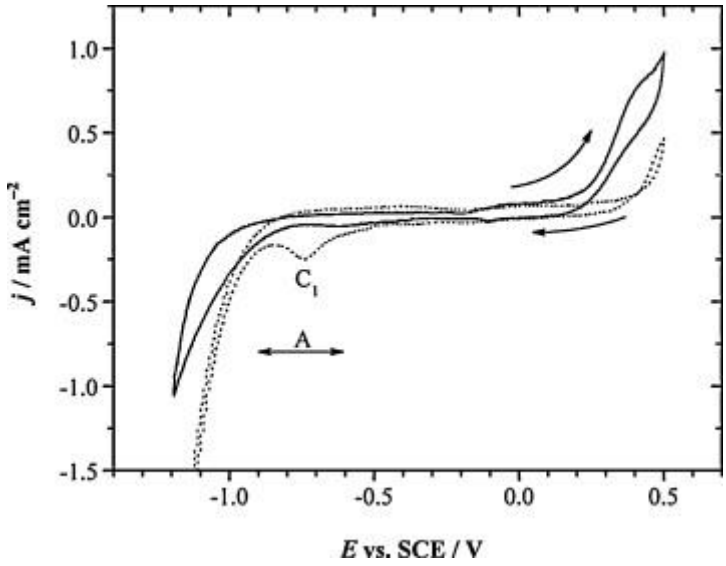

Figure 1-22 showing cyclic voltammograms recorded on 1.5 % at. SIMFUEL in a 0.1 mol dm^{-3} NaCl (represented by the dashed line), and a 0.1 mol dm^{-3} NaCl with 0.1 mol dm^{-3} $Na_2CO_3/NaHCO_3$ (represented by the solid line), at pH 9.7 and a scan rate of 10 mV/s (94)

The small anodic currents observed during the forward scan in the potential range of – 0.2 V to 0 V have been attributed to surface oxidation to a mixed U^{IV}/U^{V} (UO_{2+x}) oxide. At more positive potentials, larger anodic currents for the oxidative dissolution of the UO_{2+x} layer to the soluble $(UO_2)^{2+}$ are observed (94). As can be seen in the cyclic voltammogram above, this dissolution is accelerated in the carbonate containing solution. This result is indicative of the HCO_3^-/CO_3^{2-} ions to strongly complex the $(UO_2)^{2+}$. The current plateau that is seen during the forward going scan and also at the lower anodic currents during the reverse scan indicate the formation of surface intermediates. These surface intermediates partially inhibit the anodic dissolution reaction (94). In the absence of carbonates, the surface oxidation to UO_{2+x} in the potential region −0.2 V to 0 V produces a small reduction peak (denoted C_1) during the reverse scan in the potential range of −0.6

V to −0.9 V (labelled region A). This reduction peak however, is noticeably diminished in the carbonate solution. The large increase that is observed in the cathodic current for potentials negative to −1 V is due to H_2O reduction, a process believed to be catalysed by the metallic epsilon particles in the SIMFUEL (94).

From this study it was concluded that the observed reaction occurred via a single electron transfer, namely U(IV) → U(V), followed by another one electron transfer, U(V) → U(VI) (94). At potentials below or equal to 250 mV, the rate determining step was found to be the rate of the first reaction. This was not dependent on the concentration of carbonate and/or bicarbonate (94). It was however, found that at potentials above 250 mV, the dissolution rate was starting to be inhibited. This inhibition was caused by the formation of the $U(VI)O_2CO_3$ surface layer (94). At this point it was evident that the current became independent of potential, which means that the chemical dissolution of the layer is controlling the rate of the reaction (94).

In 2006 Goldik *et al.* found that dissolved carbonate and bicarbonate ions had an effect on the redox kinetics of UO_2 in hydrogen peroxide solutions (60). During electrochemical studies it was found that when carbonate was present in solution, there was no complexation taking place, hence the formation of a hydrated U^{VI} species, such as a uranyl peroxide mineral, does not occur (60). Subsequently, this meant that the reduction of H_2O_2 did take place. However, at more cathodic potentials, the carbonate ions were found to be adsorbed onto the active reduction sites, which meant that the reduction of H_2O_2 was inhibited (60). It was also found that the pH dependence of the H_2O_2 reduction reaction changed with the presence of carbonate ions. When carbonate ions were present in solution, the reduction reaction was found to be stronger, when compared to solutions where carbonate ions were not present (60).

1.4.12 Effects of Calcium and Silicate Ions on Corrosion Product Deposits

In order to determine to what extent calcium influences the formation of corrosion product deposits, Santos *et al.* investigated the influence of calcium ions on the anodic dissolution of SIMFUEL in 2006 (96).

Santos *et al.* found that calcium ions did not influence the conversion of $U(IV)O_2$ to $U(IV)_{1-2x}U(V)_{2x}O_{2+x}$. However, it was found that calcium ions could in fact suppress the reaction which produces a U(VI) surface species and subsequently follows on to produce $UO_3 . yH_2O$ (96). This suppression is brought about by calcium ions being adsorbed onto the UO_2 surface which in turn inhibits dissolution (96). Dissolution is inhibited by either blocking the transfer reaction of O^{2-} anions from the fuel surface, or by inhibiting the stabilisation of the precursor $(UO_2(OH)_2)_{ads}$ (96). The suppression however, is dependent on the concentration of calcium ions (96).

A similar behaviour was observed by Santos *et al.* in 2006 when they investigated the influence of silicate ions on the formation of secondary phase and corrosion product deposits (97). It was found that the presence of silicate ions did not have any significant influence on the oxidation process of UO_2 to produce the $U(IV)_{1-2x}U(V)_{2x}O_{2+x}$ layer (97).

However, for potentials below or equal to 250 mV and depending on the concentration of silicate ions, the conversion reaction $U(IV)_{1-2x}U(V)_{2x}O_{2+x} \rightarrow UO_3 . yH_2O$ is supressed (97). This is similar to the suppression that was observed by the calcium ions above. In the case of the silicate ions it also appears that the suppression is due to the adsorption of silicate ions on the fuel surface (97). A hydrated form of U(VI) silicate accumulates on the fuel surface after U(VI) is formed anodically at higher potentials (97). This results in the suppression of anodic dissolution. Through this work it has been established that the presence of silicate ions can supress the generation of acidity in localised sites on the fuel surface, however, the formation of acidity cannot be completely prevented (97). This is due to the fact that once the UO_2^{2+} that is dissolved in these acidified sites has been transported out of these sites, it is once again accumulated on the outer surface of the fuel as a hydrated U(VI) silicate (97).

1.4.13 Effect of chloride

It has been found in a study by Engelhardt *et al.* that when UO_2 is oxidised by oxygen in a saturated salt solution, i.e. containing chloride, that there is a build-up of an U_30_7 surface layer which is generated by the diffusion of oxygen ions into the crystal structure (98). This surface layer, which in fact is a semi-conductor, is always present. Once the build-up of the U_3O_7 layer has taken place, the

oxidation of a UO_2^{2+} ion which reacts with the salt solution takes place (98). At low pH values, the UO_2^{2+} dissolved directly, the corrosion rate being dominated by the solubility of uranylhydroxide (98). At higher pH values, from pH 5 to pH 8, the reaction of UO_2^{2+} with hydroxide produces $UO_2(OH)_2$ as a possible precipitate, which is an insulating phase and hinders the reduction of oxygen. At high pH values however, the direct reaction of the above formed U_3O_7 layer with oxygen and the hydroxide ion occurs as a simultaneous oxidation and complexation reaction (98). When the highest solubility of the uranium (VI) in a saturated NaCl solution is reached, a precipitation procedure starts, generating a secondary uranyl phase believed to be shoepite (98). Finally a protecting surface layer is also produced, meaning that the corrosion rates are not higher than what was observed at pH values between pH 5 and pH 8 (98). However, at no stage during any of the above does Engelhardt see any influence of chloride ions on the UO_2 corrosion reaction, confirming Shoesmith's observation of no effect due to chloride ions at low chloride concentrations of up to 0.1 mol dm^{-3} (91). These concentrations of chloride are applicable, as they are associated with brine (91).

1.5 Transformation phases – Corrosion products

Should the uranium dioxide of the spent fuel matrix undergo oxidative dissolution via a change in the oxidation state of U from (IV) to (VI) (99), then the mobilisation of uranium from UO_2 solid phases can take place (99). Uranium (IV) phases, are frequently found in geological media. Furthermore, U(VI) phases are known to be found in minor concentrations in several mineral phases (99). The phases which can be formed during hydrothermal processes are of particular interest, as temperatures inside a repository may rise above 100 ^oC during the first thousand years (before the thermal pulse, which is expected to take place between 1,000 and 10,000 years (100)) (99).

In a geological repository such as the one foreseen for the UK however, anoxic conditions are expected. In 2005, Amme *et al.* investigated the potential alteration mechanisms of UO_2 which had been in contact with groundwater ions under anoxic conditions (99). The samples that had been treated under ambient conditions showed no significant change in the surface structure. However, the samples that had been investigated under hydrothermal conditions had been significantly altered (99). In particular, the samples that had been treated with carbonate and silicate showed the formation of a secondary phase on the surface of the sample. The mineral phases that had

formed under these conditions were not able to be fully characterised or matched to any known uranyl mineral phases (99). However, in 2005, the Center for Nuclear Waste Regulatory Analyses carried out a series of co-precipitation experiments in which certain radionuclides were added to solutions from which uranyl minerals are typically synthesised (101), which were able to be characterised (101).

Below is a table of common uranium minerals which includes transformation phases that have been found in geological formations, as well as transformation phases that have been generated in experiments.

Uranium Mineral	**Chemical Formula**
Becquerelite	$Ca(UO_2)_6O_4(OH)_6{\cdot}8H_2O$
Curite	$Pb_2U_5O_{17}{\cdot}4H_2O$
Lanthinite	$UO_2{\cdot}5UO_3{\cdot}10H_2O$
Metaschoepite	$UO_3{\cdot}nH_2O$ (n<2)
Metastudtite	$UO_4{\cdot}2H_2O$
Na-compreignacite	$(Na,K)_2(UO_2)_6O_4(OH)_6{\cdot}8H_2O$
Schoepite	$UO_3{\cdot}2H_2O$
Sklodowskite	$(H_3O)_2Mg(UO_2)_2(SiO_4)_2{\cdot}2H_2O$
Soddyite	$(UO_2)_2SiO_4{\cdot}2H_2O$
Sodium Boltwoodite	$(H_3O)(Na,K)(UO_2)SiO_4{\cdot}H_2O$
Studtite	$UO_4{\cdot}4H_2O$
Uraninite	UO_2
Uranophane	$(H_3O)_2Ca(UO_2)_2(SiO_4)_2{\cdot}3H_2O$

Table 1-11 nominal uranium minerals and their formulae (101)

The focus of this work, however, is on the lesser studied studtite and metastudtite phases. Due to the fact that hydrogen peroxide is one of the oxidants which is formed during the alpha radiolysis of water, it contributes to the formation of secondary uranyl phases (102).

Secondary uranyl phases containing peroxide are limited to studtite $(UO_2)O_2(H_2O)_4$ and metastudtite $(UO_2)O_2(H_2O)_2$ (88). Metastudtite is a dehydration product of studtite (103). In nature, studtite is unstable in the absence of hydrogen peroxide (102). With respect to spent nuclear fuel surfaces, it has been observed that the radiolytic species hydrogen peroxide that is produced during the alpha radiolysis of water, is the main component in the generation of uranium peroxides studtite and metastudtite (102). The formation of these phases have also been observed on unirradiated UO_2 that have been exposed to hydrogen peroxide solutions (102).

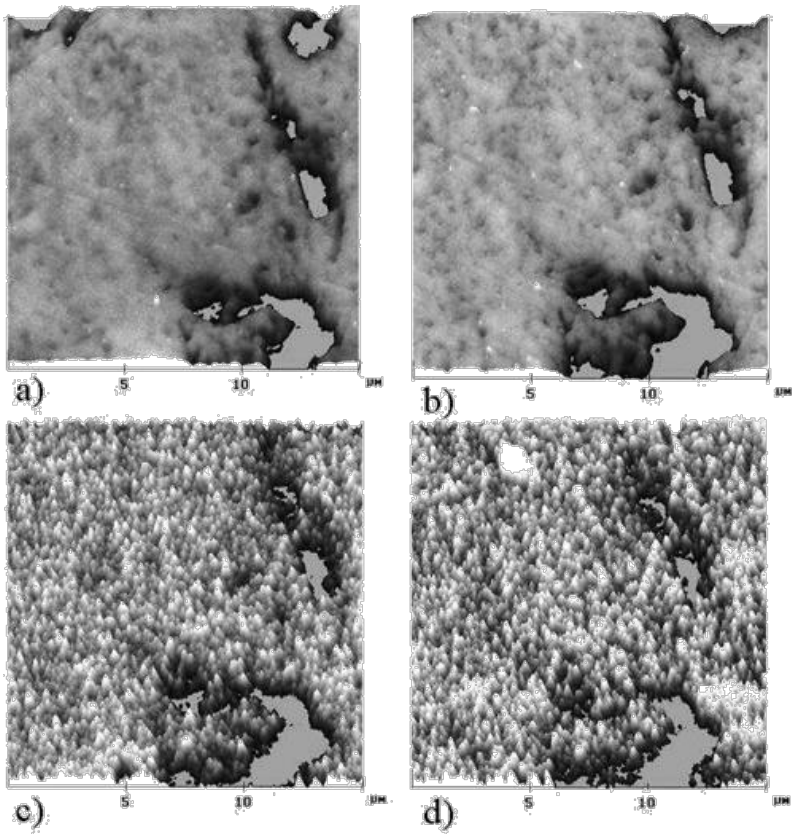

Figure 1-23 showing SFM images of UO_2 surface; a) initial surface, b) after 69.6 hr, c) after 141.6 hr and d) after 314.4 hr of contact with a hydrogen peroxide solution (5 x 10^{-4} mol dm^{-3}) (102)

In 2004, Clarens *et al.* studied the oxidative dissolution of UO_2 at varying hydrogen peroxide concentrations. This was carried out by measuring the amount of uranium left in solution by ICP-MS and thereby deducing the evolution of uranium (102). The observation made was that there was a decrease in uranium concentration following an initial increase which suggests the precipitation of a uranyl secondary phase.

1.5.1 Stability of Uranium Peroxides

Studtite and metastudtite can both be readily synthesised by the addition of hydrogen peroxide to a solution bearing uranium (88). Several studies have been conducted on uranyl peroxides by dissolution experiments, where uranyl peroxides have been formed in the presence of hydrogen peroxide and the absence of carbonates, as described by Rey *et al.* (104). As described above, it is known that studtite and metastudtite are the only peroxide minerals that are found in nature (102) and the alpha radiolysis of water is the only source that can provide enough hydrogen peroxide for the formation of studtite in nature (88).

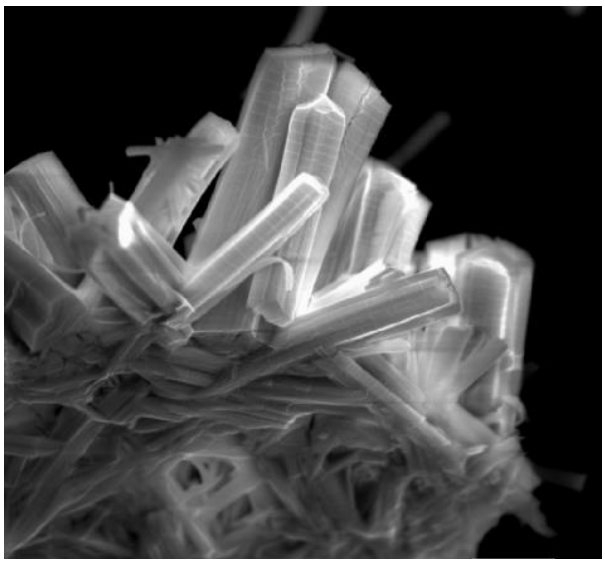

Figure 1-24 Showing metastudtite formation on interfacial suspensions of spent fuel (105)

Relevant studies on studtite formation with regards to commercial spent fuel have only been reported by McNamara *et al.* (105). During experimentation, McNamara *et al.* observed crystallites of shoepite and metashoepite (which is a hydrated form of a uranyl oxide (104)), at short contact times (with demineralised water) at temperatures of 60, 75 and 90 °C on hydrated fuel particles

(105). However, it was observed that at long contact times, studtite and metastudtite appeared instead.

During a two-year period, shoepite and metashoepite had completely disappeared in many samples, but appeared to be coated by new alteration phases, which by examination were found to be studtite and metastudtite (105).

Studtite has also been reported to have been identified on the zircaloy cladding of various fuel elements at the Hanford K-East Basin. It was however observed that on the insides of the cladding, metashoepite had formed (105). The precipitation of studtite that was found on the outside of the fuel clad indicates that a critical point in the concentration of hydrogen peroxide was reached in the mildly oxidising solution that the fuel elements are surrounded in (105). One explanation for the presence of metashoepite on the inside of the clad is that the concentrations of oxygen and hydrogen peroxide may have been lowered (due to restricted flow) which would result in metashoepite being the predominant alteration phase (105).

In order to assess the safety performance of spent fuel in a geological repository, the effect that secondary phases have on the dissolution of spent fuel must be taken into consideration (104). In order to do so, the stability of these secondary phases must be investigated. Various studies have shown that the precipitation of secondary phases on unirradiated UO_2 follow a paragenetic sequence in which the formation of hydrated uranyl oxides, oxides with alkaline/alkaline-earth elements, U(IV) silicates and uranyl sulphates, phosphates and carbonates were observed, the type of secondary phase formed depending on the composition of the groundwater used for experimentation (104).

During experimentation with spent fuel, a similar paragenetic sequence is evident as shoepite/metashoepite, as well as some U(IV) silicates are observed (104). The formation of studtite and metastudtite, as aforementioned, are limited to hydrogen peroxide bearing conditions (88).

In 2009, Rey *et al.* investigated the effect that temperature would have on the stability of studtites using thermogravimetric and differential scanning calorimetry techniques (104). They reported that in previous literature, metastudtite was formed when the precipitate was allowed to dry under specific controlled conditions, whilst studtite was found to be stable when dried at room temperature (104). Elsewhere it has been reported however, that studtite was successfully obtained at temperatures below 50 °C, meta-studtite was obtained at temperatures above 70 °C, and that a mixture of both bases was obtained at 60 °C (104). This particular study concluded that if the material is dried at a certain temperature (100°C), then this would influence the occurrence of the transition from studtite to metastudtite. It was also found that the transformation can occur at room temperature if the experiment is carried out under vacuum. (104).

When thermal decomposition experiments were carried out on synthetic uranium peroxides using various techniques, it was found that the thermal decomposition only took place via the formation of metastudtite, with the final products being U_3O_8 and UO_2 (104).

From the above observations and the observations summarised in Table 1-12 below, Rey *et al.* decided to investigate the synthesis of studtite in the temperature range of 25 - 150 °C in order to establish the final product, alongside determining the stability of the synthesised phases to investigate behaviour of such phases in the a geological repository (104).

Thermal transformation reported	Analysis
Synthetic studtite	
$UO_2O_2 \cdot 4H_2O \xrightarrow[100\ °C]{} UO_2O_2 \cdot 2H_2O \xrightarrow[220\ °C]{} UO_x \xrightarrow[485\ °C]{} \alpha - UO_3 \xrightarrow[580\ °C]{} U_3O_8 \quad 3<x<3.5$	TG XRD IR
$UO_2O_2 \cdot 4H_2O \xrightarrow[330\ °C]{} UO_2O_2 \cdot 2H_2O \xrightarrow[485\ °C]{} UO_3 \cdot 0.5H_2O \xrightarrow[520\ °C]{} UO_{3am} \xrightarrow[580\ °C]{} UO_{2.9} \rightarrow \gamma - UO_3 \rightarrow U_3O_8$	TG DTA
$UO_2O_2 \cdot 4H_2O \xrightarrow[110\text{-}150\ °C]{} UO_2O_2 \cdot 2H_2O \xrightarrow[150\text{-}300\ °C]{} UO_3 \cdot xH_2O \xrightarrow[450\ °C]{} UO_3 \xrightarrow[580\ °C]{} U_3O_8/UO_2$	TG DTA IR
$UO_2O_2 \cdot 4H_2O \xrightarrow[130\ °C]{} UO_2O_2 \cdot 2H_2O \xrightarrow[230\ °C]{} UO_3/UO_3 \cdot nH_2O \xrightarrow[567\ °C]{} U_3O_8$	TG XRD DSC
Natural studtite	
$UO_2O_2 \cdot 4H_2O \xrightarrow[60\ °C]{} UO_2O_2 \cdot 2H_2O$	XRD
$UO_2O_2 \cdot 4H_2O \xrightarrow[115\ °C]{} UO_2O_2 \cdot 2H_2O \xrightarrow[300\ °C]{} UO_x \cdot nH_2O \rightarrow UO_{3am} \rightarrow \alpha - UO_{2.89} \rightarrow UO_{2.67}$	XRD TG IR
$3<x<3.5$, $0<n<0.5$, am = amorphous	

Table 1-12 showing summary of studtite transformations at various temperatures where, TG = thermogravimetry; XRD = X-ray diffraction; IR = infrared spectroscopy; DTA = differential thermal analysis (104)

Rey *et al.* established that different solid phases were formed at different temperatures. The following solid phases were characterised according to the international central diffraction data (ICDD) database (104):

- a tetrahydrated uranyl peroxide – studtite ($UO_2O_2 \cdot 4H_2O$) at 25 °C
- a dehydrated uranyl peroxide – metastudtite ($UO_2O_2 \cdot 2H_2O$) at 100 °C
- a hydrated uranium oxide – metashoepite ($UO_3 \cdot nH_2O$) at 150 °C

From these studies it was concluded that studtite can be obtained in the temperature range $25 < T < 100$ °C, metastudtite is obtainable in the temperature range $100 \leq T \leq 150$ °C and metashoepite at $T = 150$ °C (104). By combining TG and DTA analyses, the transformation behaviour of studtite was investigated and a correlation between transformation temperatures and heats of transformations was found (104).

$$UO_2O_2 \cdot 4H_2O \xrightarrow[-42\ kj\ mol^{-1}]{130\ °C} UO_2O_2 \cdot 2H_2O \xrightarrow[-46.26\ kj\ mol^{-1}]{230\ °C} UO_3/UO_3 \cdot nH_2O \xrightarrow{567\ °C} U_3O_8$$

Equation 1-13

Rey *et al.* concluded that there was scope for further study to investigate whether the transformation from studtite into metastudtite involved one or several stages, which would vary the number of water molecules in the structure of these phases (104).

Whilst the formation and stability of secondary uranyl phases is important in the assessment of radionuclide release, this work will pay more attention to the behaviour of the fuel itself under repository conditions and the transformation phases/corrosion products that may be formed therein.

The study of real spent fuel is challenging from a radiological safety perspective. Thus the majority of the work reported in the literature relating to spent fuel behaviour has been conducted on simulant systems – either for the fuel matrix itself or the surface transformation products.

Thus the next section will summarise some of the methods used in the study of the behaviour of spent fuel and spent fuel simulants.

1.6 Spent Fuel Simulant Systems

In order to assess the performance of the disposal of spent nuclear fuel, a thorough understanding of the electrochemistry of uranium dioxide is necessary. The main driving force for the degradation of spent fuel that is incontact with groundwater is the oxidative dissolution, i.e. corrosion, which releases fission products and other actinides from its matrix (106). There are two principal ways in

which to conduct corrosion experiments in this context, either on pellets or on thin films. UO_2 SIMFUEL samples are most commonly fabricated in pellet form. A SIMFUEL is a simulated spent nuclear fuel, which aims to replicate the chemistry, as well as the microstructure of spent nuclear fuel (107). Due to the high activity of real spent fuel, it is generally not feasible for them to be used for experimental work, and hence simulated fuels, or SIMFUELs, are used instead.

AGR SIMFUELs, after development and characterisation, are the main focus of this thesis; they are therefore discussed in detail in the next chapter. Thus in this section, we shall restrict our discussion to a brief review of the literature relating to the other main SNF simulant system, thin films.

There are two main means for fabricating thin films, one is by electrodeposition, and the other by sputtering (108). These are discussed in the next sections.

1.6.1 Electrodeposition

Thin films of UO_2 can be readily deposited onto disc substrates and then used for a range of materials characterisation studies including corrosion experiments.

One route to a uranium dioxide layer is by electrodeposition via electrolysis of a UO_2^{2+} solution. However, this results in the precipitation of a mixed, ill characterised U(IV)/(VI) oxyhydrate, more akin to shoepite (see Table 1-11 for common secondary uranyl phases) than UO_2. It is therefore more appropriately used as a transformation simulant. The electrolysis can be described via the following equations (109):

At the cathode:

$$UO_2^{2+} + 4H^+ + 6e^- \rightarrow U^o + 2H_2O$$

Equation 1-14

$$2H_2O + 2e^- \rightarrow H_2 + 2OH^-$$

Equation 1-15

$$2H^+ + 2e^- \rightarrow H_2$$

Equation 1-16

At the anode:

$$2Cl^- \rightarrow Cl_2 + 2e^-$$

Equation 1-17

$$4OH^- \rightarrow O_2 + 2H_2O + 4e^-$$

Equation 1-18

As explained above, the resulting precipitate is not of a sufficient quality, mainly due to the fact that the starting solution has a low concentration of uranium. If a uranyl nitrate is used as the starting solution, there will then be a high concentration of NH_4^+ in the electrodeposited material, meaning that the NH_3 may replace the water molecules, and that the electrodeposited layers are likely to be a mixture of polymeric structure with monomeric formulae (109).

For the electrodeposition of thin films in an acidic environment, there is a reliable set of conditions that was established in 1972 by Talvitie (110), and has been adapted by dos Santos (111), Maya (112), and Seibert (113).

The electrodeposition cell is constructed from a 20 ml polyethylene liquid scintillation vial which has had the bottom removed. The cap is replaced with a cap that has a hole in it in order to establish contact with the electrode. A polished stainless steel planchet is inserted into the cap. The polished side faces the solution. The platinum wire forms the other electrode (the anode) (114).

Below is a representation of an electrodeposition cell.

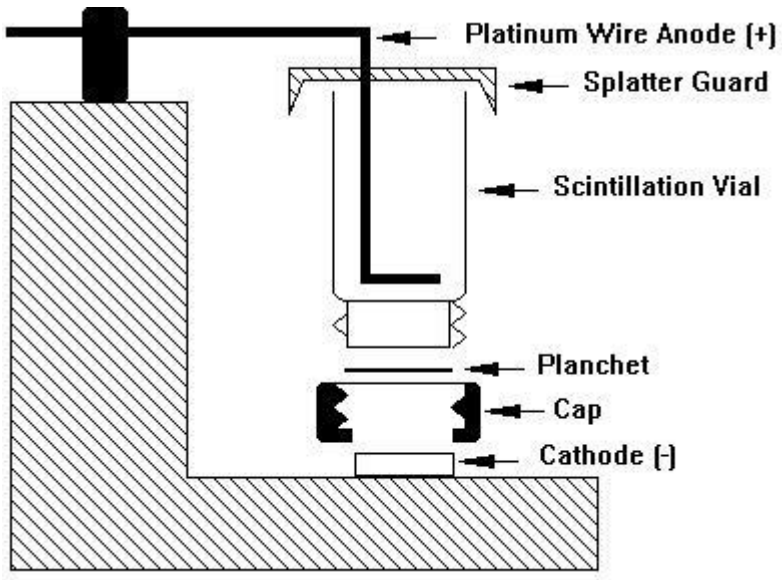

Figure 1-25 Showing set-up of electrodeposition cell (114)

The procedure is summarised below:

Electropolished planchets are evaporated to dryness using an ion-exchange eluate. The remaining residue on the planchet is then dissolved with concentrated nitric acid, and the solution is then evaporated until all the nitric acid has volatilised (110).

After this the anode is introduced into the electrodeposition cell along with the electrolyte. The anode is electrolysed and eventually ammonium hydroxide is added. The electrolysis is terminated by lifting the anode out of the cell, pouring out the electrolyte and flushing the cell with ammonium nitrate and ammonium hydroxide. Once the cell is taken apart, the planchet is rinsed immediately with ethyl alcohol after which the planchet is heated to 200 -250 °C on a hot plate (110).

We will now look at the other main method of fabricating thin films, specifically sputtering techniques.

1.6.2 Deposition by Sputtering

Pure UO_2 thin films can be deposited onto target substrates by reactive sputtering of a uranium metal target in an argon atmosphere (106) (115). The UO_2 thin films are prepared by reactive dc sputter deposition from a U metal target with ultrahigh argon/oxygen mixtures as sputter gas (106). Examples of substrates that can be used for the sputtering of uranium are: gold, yttrium, aluminium, silicon. The films can be deposited by varying the Ar/O_2 mixture to control the oxygen stoichiometry of the UO_2 film (115). The uranium metal target is a commercially available uranium metal disc that is mechanically polished and etched using nitric acid (115). Uranium metal and oxide thin films are commonly produced for fuel and storage research. One particular example for the use of thin films in spent fuel research is the study by Seibert *et al.* who had sputtered thin films of UO_2 onto quartz crystals and have used microgravimetric measurements on these films to support the assignment of redox reactions to the peaks that are seen in similar electrochemical studies (106). This work will be further discussed in Chapter 3. It should be noted however that such films have to be typically extensively characterised post-deposition due to the potential of U_4O_9, rather than UO_2, formation. Techniques that have been used for the characterisation of such films include X-Ray Photoelectron Spectroscopy (XPS), X-Ray Diffraction (XRD), Atomic Force Microscopy (AFM) and Scanning Electron Microscopy (SEM).

The composition of thin films of this type is usually determined by the availability of suitable target materials. Thus the composition is usually restricted to UO_2 only, with thin film SIMFUEL fabrication being difficult to achieve.

Hence, the chosen form of UO_2 and SIMFUELs that will be used for this work is that of pellets. The next chapter will focus on the experimental methods used to study the corrosion behaviour of spent UK nuclear fuel.

References

1. Britannica. https://www.britannica.com/science/nuclear-fission. [Online]

2. Stock photos. https://www.dreamstime.com/stock-photos-nuclear-fission-illustration-white-background-image35501453. [Online]

3. G.L. Squires. *Introduction to the theory of thermal neutron scattering.* s.l. : Cambridge University Press, 1978.

4. Radioactivity.eu.com. http://www.radioactivity.eu.com/site/pages/lesnoyauxfissiles.htm. [Online]

5. Editors of Encyclopedia. *Fissile material.* s.l. : Encyclopedia Britannica, 2015.

6. G. Baker. *Thorium in Australia.* s.l. : Parliament of Australia - Statistics and Mapping Section, 2007, Vol. 11.

7. R. Hargreaves, R. Moir. *Forum on physics and society - Liquid fuel nuclear reactors.* American physical society sites. http://www.aps.org/units/fps/newsletters/201101/hargraves.cfm. [Online]

8. A. Dyakov. Nuclear Fuel Cycle. *Nuclear Reset: Arms Reduction and Nonproliferation.* Moskow : Carnegie Moscow Center, 2012. Vol. Chapter 16.

9. World Nuclear Association. http://www.world-nuclear.org/ [Online]

10. R. Williamson. *Mechanisms of fixed contamination of commonly engineered surfaces.* s.l. : Lancaster University, 2017.

11. C. Squire. *Extraction, processing and fuel manufacture - Lecture notes.* s.l. : Lancaster University, 2017.

12. Nuclear Decommissioning Authority. *Draft Business Plan - 1 April 2022 to 31 March 2025.* s.l. : NDA, 2021

13. Nuclear Decommissioning Authority. *Strategy.* s.l. : NDA Report no. SG/2016/53, 2016.

14. M. Joyce. *Nuclear engineering lecture 14 reactor designs 2: CO_2-cooled reactors.* s.l. : Lancaster University, 2017.

15. E. Nonbol. *Description of the advanced gas cooled type reactor (AGR).* Roskilde : Riso National Laboratory, 1996.

16. R.N. Thomas, A. Paluszny, D. Hambley, F.M. Hawthorne, R.W. Zimmerman. *Permeability of observed three dimensional fracture networks in spent fuel pins.* s.l. : Journal of Nuclear Materials, 2018, Vol. 510. pp. 613 - 622.

17. D. Halabuk, J. Martinec. *Calculations of stress and deformation in fuel rod cladding during pellet-cladding interaction.* s.l. : Acta Polytechnica, 2015, Vol. 55. pp. 384 - 387.

18. N. Rauff-Nisthar, C. Boxall, D. Hambley, Z. Hiezl, C. Padovani, R. Wilbraham. *Corrosion behaviour of AGR SIMFUELs.* s.l. : ECS Trans, 2015, Vol. 66. pp. 85-94.

19. M.J. Bennett, J.A. Desport, P.A. Labun. *Analytical electron microscopy of a selective oxide scale formed on 20%Cr-25%Ni-Nb stainless steel.* s.l. : Oxidation of Metals, 1984, Vol. 22. pp. 291-306.

20. C.H. Phuah, M.P. Ryan, W.E. Lee. *Corrosion of spent AGR fuel cladding.* s.l. : DIAMOND Consortium, 2009.

21. D.W. Shoesmith. *Fuel corrosion processes under waste disposal conditions.* s.l. : Journal of Nuclear Materials, 2000, Vol. 282. pp. 1-31.

22. N. Rauff-Nisthar, C. Boxall, I. Farnan, Z. Hiezl, W. Lee, C. Perkins, R.J. Wilbraham. *Corrosion behaviour of AGR simulated fuels - evolution of the fuel surface.* s.l. : ECS Trans, 2013, Vol. 53. pp. 95-104.

23. T. Liang. *Something about nuclear graphite.* s.l. : IAEA Nuclear Power Meetings, 2012.

24. The Institution of Electrical Engineers. *Nuclear Reactor Types.* 2005.

25. Fuel burnup - definition, calculation & units. https://www.nuclear-power.com/nuclear-power/reactor-physics/reactor-operation/fuel-burnup/. [Online]

26. M.J. Dunn, I.R. Topliss. *The status of spent fuel storage in the UK.* British Nuclear Fuels plc : s.n.

27. IAEA. *Classification of radioactive waste.* s.l. : No. GSG-1.

28. D. Cui, J. Low, K. Spahiu. *Environmental behaviours of spent nuclear fuel and canister materials.* s.l. : Energy & Environmental Science, 2011, Vol. 4. pp. 2537.

29. A. Sneyers. *Understanding and physical and numerical modelling of the key processes in the near field and their coupling for different host rocks and repository strategies (NF-PRO).* s.l. : Euratom, 2008.

30. Nuclear Decommissioning Authority. *Geological Disposal - Site characterisation for a geological disposal facility.* s.l. : NDA Report no. NDA/RWMD/057, 2010.

31. Nuclear Decommissioning Authority. *Geological Disposal - Review of options for accelerating implementation for the geological disposal programme.* http://www.nda.gov.uk/documents/upload/Geological-Disposal-Review-of-options-for-accelerating-implementation-of-the-Geological-Disposal-programme-December-2011.pdf. [Online]

32. Nuclear Decommissioning Authority. *Geological Disposal - An overview of the generic disposal system safety case.* http://www.nda.gov.uk/documents/upload/Geological-Disposal-An-overview-of-the-generic-Disposal-System-Safety-Case-December-2010.pdf. [Online]

33. Nuclear Decommissioning Authority. *Geological Disposal - Generic disposal facility designs.* s.l. : NDA Report no. NDA/RWMD/048, 2010.

34. N. Rauff-Nisthar, C. Boxall, I. Farnan, Z. Hiezl, W. Lee, C. Perkins, R. Wilbraham. *Corrosion behaviour of AGR simluated fuels - evolution of the fuel surface.* s.l. : ECS Transactions, 2013, Vol. 53. pp. 95-104.

35. L.O. Werme, L.H. Johnson, V.M. Oversby, F. King, K. Spahiu, B. Grambow, D.W. Showesmith. *Spent fuel performance under repository conditions: a model for use in SR-Can.* Stockholm : SKB, 2004.

36. IAEA. *Final report of a co-ordinated research project on spent fuel performance assessment and research*. Vienna : SPAR, 2003.

37. Secretary of State for Business. *Meeting the energy challenge a white paper on nuclear power.* s.l. : Enterprise & Regulatory Reform, 2008.

38. SERCO. *Modelling pH evolution in the near field.* s.l. : SERCO, 2010.

39. R. Artinger, G. Buckau, S. Geyer, P. Fritz, J.I. Kim. *Characterization of groundwater humic substances: influence of sedimentry organic carbon.* s.l. : Applied Geochemistry, 2000, Vol. 15. pp. 97-116.

40. J.G. Moore, M.T. Morgan, E.W. McDaniel, H.L. Green, G.A. West. *Cement technology for plugging boreholes in radioactive waste repository sites: progress report for the period October 1, 1978, to September 30, 1979.* s.l. : Oak Ridge National Laboratory, 1981.

41. G.D. Sizgek, *Thermal considerations in a very deep borehole nuclear waste repository for synroc.* s.l. : Materials Research Society, 2001, Vol. 663.

42. NIRAS. *Development and Demonstration (RD&D) plan.* s.l. : ONDRAS/NIRAS Research, 2012.

43. H. Geckeis, T. Stumpf. *KIT Scientific Reports 7559.* s.l. : Institut fuer Nukleare Entsorgung, 2009.

44. M. Kelm, V. Metz, E. Bohnert, E. Janata, C. Bube. *Interaction of hydrogen with radiolysis products in NaCl solution - comparing pulse radiolysis experiments with simulations.* s.l. : Radiation Physics and Chemistry, 2011, Vol. 80. pp. 426-434.

45. Nuclear Decommissioning Authority. *Geological Disposal - Generic design assessment: Summary of disposability assessment for wastes and spent fuel arising from operation of the UK EPR.* s.l. : NDA Technical Note no. 11261814, 2009.

46. Amec Foster Wheeler. *Scoping studies of the matrix dissolution rate and instant release fraction of spent AGR fuel.* s.l. : Studsvik, 2016.

47. United Kingdom Nirex Limited. *Outline design for a reference repository concept for UK high level waste/spent fuel.* s.l. : Nirex technical note ref: 02644, 2005.

48. B. Kursten, F. Druyts. *Methodology to make a robust estimation of the carbon steel overpack lifetime with respect to the Belgian supercontainer design.* s.l. : Journal of Nuclear Materials, 2008, Vol. 379. pp. 91-96.

49. G. Rossiter, M. Mignanelli. *The characteristics of LWR fuel at high burnup and their relevance to AGR fuel.* s.l. : NDA, 2011.

50. D.O. Brasnarof, A.C. Marino, J.E. Bergallo, L.E. Juanico. *A new fuel design for two different HW Type reactors.* s.l. : Science and Technology of Nuclear Installations, 2011, Vol. 2011. pp. 1-15.

51. D.W. Shoesmith, S. Sunder, W.H. Hocking. *Electrochemistry of Novel Materials.* s.l. : VCH, 1994.

52. M. J. Nicol, C.R.S Needes, N.P. Finkelstein. *Leaching and reduction in hydrometallurgy.* s.l. : Institute of Mining and Metallurgy, 1975.

53 F. Cattant, D. Crusset, D. Feron. *Corrosion issues in nuclear industry today.* s.l. : Materials today, 2008, Vol. 11. pp. 32-37.

54. J.-M. Gras. *Life prediction for hlw containers - issues related to long-term extrapolation of corrosion resistance .* s.l. : Comptes Rendus Physique, 2002, Vol. 3. pp. 891-902.

55. R.C. Ecob, R.C. Lobb, V.L. Kohler. *The formation of G-phase in 20/25 Nb stainless AGR fuel cladding alloy and its effect on creep properties.* s.l. : Journal of Materials Science, 1987, Vol. 22. pp. 2867-2880.

56. ANDRA. *Andra reserach on the geological disposal of high-level long-lived radioactive waste; Results and perspectives.* s.l. : ANDRA, 2005.

57. D. Feron, D. Crusset, J-M. Gras. *Corrosion issues in nuclear waste disposal.* s.l. : Journal of Nuclear Materials, 2008, Vol. 379. pp. 16-23.

58. H. He, M. Broczkowski, K. O'Neil, D. Ofori, O. Semenikhim, D. W. Shoesmith. *Corrosion of nuclear fuel (UO_2) inside a failed nuclear waste container.* s.l. : TR-2012-09 NWMO and University of Western Ontario, 2012.

59. A.J. Bard, L.R. Faulkner. *Electrochemical Methods: Fundamentals and Applications.* s.l. : Wiley, 2001.

60. J. Goldik, J. Noel, D. Shoesmith. *Surface electrochemistry of UO_2 in dilute alkaline hydrogen peroxide solutions part II: effects of carbonate ions.* s.l. : Electrochimica Acta, 2006, Vol. 51. 3278-3286.

61. H. He, Z. Qin, D.W. Shoesmith. *Characterizing the relationship between hyperstoichiometry, defect structure and local corrosion kinetics of uranium dioxide.* s.l. : Electrochimica Acta, 2010, Vol. 56. pp. 53-60.

62. T.E. Eriksen, D.W. Shoesmith, M. Jonsson. *Radiation induced dissolution of UO_2 based nuclear fuel - a critical review of predictive modelling approaches.* s.l. : Journal of Nuclear Materials, 2012, Vol. 420. pp. 409-423.

63. K.N. Kudin, G.E. Scuseria, R.L. Martin. *Hybrid density-functional theory and the insulating gap of UO_2.* s.l. : Physical Review Letters, 2002, Vol. 89. pp. 266402/1-226402/4.

64. K.D. O'Neil, H. He, P. Keech, D.W. Shoesmith, O.a. Semenikhin. *Anisotropy of local electrical conductivity of hyper-stoichiometric uranium dioxide revelaed by current-sensing atomic force microscopy.* s.l. : Electrochemistry Communications, 2008, Vol. 10. pp. 1805-1808.

65. G.C. Allen, P.A. Tempest. *Ordered defects in the oxides of uranium.* s.l. : Proceedings of the Royal Society A, 1986, Vol. 406. pp. 325-344.

66. H.Y. Geng, Y. Chen, Y. Kaneta, M. Kinoshita. *Ab initio investigation on oxygen defect clusters in UO_{2+x}.* s.l. : Applied Physics Letters, 2008, Vol. 93. pp. 201903/1-201903/3.

67. J.M. Elorietta, L.J. Bonales, N. Rodriguez-Villagra, V.G. Baonza, J. Cobos. *A detailed Raman and X-ray study of UO_{2+x} oxides and related struture transitions.* s.l. : Physical Chemistry Chemical Physics, 2016, Vol. 18. pp. 28209 - 28216.

68. M. Razdan. *Electrochemical and surface compositional studies on uranium dioxide.* s.l. : The University of Western Ontario, 2013.

69. R.J. McEachern, P. Taylor. *A review of the oxidation of uranium dioxide at temperatures below 400 C.* s.l. : Journal of Nuclear Materials, 1998, Vol. 254. pp. 87 - 121.

70. V. Metz, H. Geckeis, E. Gonzales-Robles, A. Loida, C. Bube, B. Kienzler. *Radionuclide behaviour in the near-field of a geological repository for spent nuclear fuel.* s.l. : Radiochmica Acta, 2012, Vol. 100. pp. 699-713.

71. J.S. Goldik, H.W. Nesbitt, J.J. Noel, D.W. Shoesmith. *Surface electrochemistry of UO_2 in dilute alkaline hydrogen peroxide solutions.* s.l. : Electrochimica Acta, 2004, Vol. 49. pp. 1699-1709.

72. D.W. Shoesmith. *Used fuel and uranium dioxide dissolution studies - a review.* Ontario : NWMO, 2007.

73. S.L. Caer. *Water radiolysis: Influence of oxide surfaces on H_2 production under ionising radiation.* s.l. : Water, 2011, Vol. 3. pp. 235-253.

74. N.D.M. Evans. *Radiation Chemistry Reactions - Lecture Notes.* s.l. : Loughborough University, 2009.

75. Andor. *An Oxford instruments company.* http://www.andor.com/learning-academy/transient-spectroscopy-an-introduction-to-pump-probe-spectroscopy [Online].

76. E.C. Buck, R.S. Wittman, F.N. Skomurski, K.J. Cantrell, B.K. McNamara, C.Z. Soderquist. *Radiolysis process modelling results for scenarios.* s.l. : Pacific Northwest National Laboratory, 2012.

77. J.F. Lucchini, G. Sattonnay, C. Ardois, C. Jegou, C. Corbel. *Effects of water alpha radiolysis on the spent fuel matrix corrosion.* s.l. : CEA (France).

78. W.J. Gray. *Effect of surface oxidation, alpha radiolysis, and salt brine composition on spent fuel and uranium dioxide leaching performance: Salt Repository Project.* s.l. : Pacific Northwest Laboratory, 1988.

79. V.V. Rondinella, H.J. Matzke, J. Cobos, T. Wiss. *Alpha-radiolysis and alpha-radiation damage effects on UO_2 dissolution under spent fuel storage conditions.* s.l. : Materials Research Society, 1999, Vol. 556.

80. G. Sattonnay, C. Ardois, C. Corbel, J.F. Lucchini, M. Barthe, F. Garrido, D. Gosset. *Alpha-radiolysis effects on UO_2 alteration in water.* s.l. : Journal of Nuclear Materials, 2001, Vol. 288. pp. 11-19.

81. P. Fors. *The effect of dissolved hydrogen on spent nuclear fuel corrosion.* s.l. : Chalmers University of Technology, 2009.

82. M.E. Broczkowski, J. Noel, D. Shoesmith. *The inhibiting effects of hydrogen on the corrosion of uranium dioxide under nuclear waste disposal conditions.* s.l. : Journal of Nuclear Materials, 2005, Vol. 346. pp. 16-23.

83. M.E. Broczkowski, P.G. Keech, J.J. Noel, D.W. Shoesmith. *Corrosion of uranium dioxide containing simulated fission products in dilute hydrogen peroxide and dissolved hydrogen.* s.l. : Journal of the Electrochemical Society, 2010, Vol. 157. pp. C275.

84. M.E. Broczkowski, J.J. Noel, D.W. Shoesmith. *The influence of dissolved hydrogen on the surface composition of doped uranium dioxide under aqueous corrosion conditions.* s.l. : Journal of Electroanalytical Chemistry, 2007, Vol. 602. pp. 8-16.

85. D.W. Shoesmith. *The role of dissolved hydrogen on the corrosion/dissolution of spent nuclear fuel.* Ontario : NWMO, 2008.

86. S. Sunder, N.H. Miller, D.W. Shoesmith. *Corrosion of uranium dioxide in hydrogen peroxide solutions.* s.l. : Corrosion Science, 2004, Vol. 46. pp. 1095-1111.

87. Mineral Database. https://www.mindat.org/ [Online].

88. K.-A. H. Kubatko, K. B. Helean, A. Navrotsky, P.C Burns. *Stability of peroxide-containing uranyl minerals.* s.l. : Science, 2003, Vol. 302. pp. 1191-1193.

89. A.J. Rothman. *Potential corrosion and degradation mechanisms of zircalloy cladding on spent nuclear fuel in a tuff repository.* s.l. : Lawrence Livermore National Laboratory, 1984.

90. K.M. Wasywich, W.H. Hocking, D.W. Shoesmith, P. Taylor. *Differences in oxidation behaviour of used CANDU fuel during prolonged storage in moisture-saturated air and dry air at 150 C.* s.l. : Nuclear Technology, 1993, Vol. 104. pp. 309-329.

91. S. Sunder, D.W. Shoesmith. *Chemistry of UO_2 fuel dissolution in relation to the disosal of used nuclear fuel.* s.l. : Atomic Energy of Canada Limited, 1991.

92. D.W. Shoesmith, S. Sunder, M.G. Bailey, G.J. Wallace. *The corrosion of nuclear fuel (UO_2) in oxygenated solutions.* s.l. : Corrosion Science, 1989, Vol. 29. pp. 1115-1128.

93. S. Sunder, D.W Shoesmith, R.J. Lemire, M.G. Bailey, G.J. Wallace. *The effcte of pH on the corrosion of nuclear fuel (UO_2) in oxygenated solutions.* s.l. : Corrosion Science, 1991, Vol. 32. pp. 373-386.

94. P.G. Keech, J.S. Goldik, Z. Qin, D.W. Shoesmith. *The anodic dissolution of SIMFUEL (UO_2) in slightly alkaline sodium carbonate/bicarbonate solutions.* s.l. : Electrochimica Acta, 2011, Vol. 56. pp. 7923-7930.

95. S.A. Steward, W.J. Gray. *Comparison of uranium dissolution rates from spent fuel and uranium dioxide.* s.l. : American Society of Civil Engineers, 1994. pp. 2602 - 2608.

96. B.G. Santos, J.J. Noel, D.W Shoesmith. *The influence of calcium ions on the development of acidity in corrosion product deposits on SIMFUEL, UO_2.* s.l. : Journal of Nuclear Materials, 2006, Vol. 350. pp. 320-331.

97. B.G. Santos, J.J Noel, D.W. Shoesmith. *The influence of silicate on the development of acidity in corrosion product deposits on SIMFUEL (UO_2).* s.l. : Corrosion Science, 2006, Vol. 48. pp. 3852-3868.

98. J. Engelhardt, F. Feldmaier, M. Laske, G. Marx. *Impedance measurements on UO_{2+x} in saturated NaCl solutions.* s.l. : Journal of Nuclear Materials, 1996, Vol. 238. pp. 104-109.

99. M. Amme, T. Wiss, H. Thiele, P. Boulet, H. Lang. *Uranium secondary phase formation during anoxic hydrothermal leaching processes of UO_2 nuclear fuel.* s.l. : Journal of Nuclear Materials, 2005, Vol. 341.

100. J. Heierli. *A comparative study of engineering options for the disposal of high-level radioactive waste with regard to thermal effects and chemical degradation.* s.l. : Journal of Nuclear Science and Technology, 2016, Vol. 53.

101. D.A. Pickett. *Effect of spent nuclear fuel uranyl alteration phases on radionuclide dissolved concentration limits.* s.l. : Center for Nuclear Waste Regulatory Analyses, 2005.

102. F. Clarens, J. de Pablo, I. Diez-Perez, I. Casas, J. Gimenez, M. Rovira. *Formation of studtite during oxidative dissolution of UO_2 by hydrogen peroxide: a SFM study.* s.l. : Environmental Science & Technology, 2004, Vol. 38. pp. 6656-6661.

103. M. Deliens, P. Piret. *Metstudtite, $UO_4 . 2H_2O$, a new mineral from Shinkolobwe, Shaba, Zaire.* s.l. : American Minerologist, 1983, Vol. 68. pp. 456-458.

104. A. Rey, I. Casas, J. Gimenez, J. Quinones, J. de Pablo. *Effect of temperature on studtite stability: thermogravimetry and differential scanning calorimetry investigations.* s.l. : Journal of Nuclear Materials, 2009, Vol. 385. pp. 467-473.

105. B. McNamara, E. Buck, B. Hanson. *Observations of studtite and metastudtite on spent fuel.* s.l. : Materials Research Society, 2002.

106. A. Seibert, D.H. Wegen, T. Gouder, J. Romer, T. Wiss, J.-P. Glatz. *The use of the electrochemical quartz crystal (EQCM) in corrosion studies of UO_2 thin film models.* s.l. : Journal of Nuclear Materials, 2011, Vol. 419. pp. 112-121.

107. Z. Hiezl, *Processing and microstructural characterisation of UO_2-based simulated spent nuclear fuel ceramics for the UK's advanced gas-cooled reactors.* s.l. : Imperial College London, 2015.

108. A. Adamska, L. Havela, S. Danis, J. Pesicka, J. Macl, K. Uhlirova, T. Gouder, R. Eloirdi, F. Huber, N.-T. H. Kim-Ngan, A.G. Balogh. *Uranium compounds prepared by sputter deposition: UFe_{2+x}.* s.l. : Journal of Physics: Conference Series 200 , 2010.

109. R.J. Wilbraham. *Surface decontamination by photocatalysis.* **s.l. : Lancaster University, 2011.**

110. N.A. Talvitie. *Electrodeposition of actinides for alpha spectrometric determination.* s.l. : Analytical Chemistry, 1972, Vol. 44.

111. L.R. dos Santos, M.E. Sbampato, A.M. dos Santos. *Characterization of electrodeposited uranium films.* s.l. : Journal of RAdioanalytical and Nuclear Chemistry, 2004, Vol. 261. pp. 203-209.

112. L. Maya, B.D. Gonzalez, M.J. Lance, D.E. Holcomb. *Electrodeposition of uranium dioxide films.* s.l. : Journal of Radioanalytical and Nuclear Chemistry, 2008, Vol. 261. pp. 605-607.

113. A. Seibert, D.H. Wegen, T. Gouder, J. Romer, J.-P. Glatz. *Microgravimetric corrosion studies on UO_2 thin film models.* Budapest : Seventh International Conference on Nuclear and Radiochemistry, 2008.

114. Pheonix Scientific. http://www.owt.com/seltech/products/ep_alpha.htm [Online].

115. F. Miserque, T. Gouder, D.H. Wegen, P.D.W. Bottomley. *Use of UO_2 films for electrochemical studies.* s.l. : Journal of Nuclear Materials, 2001, Vol. 298. pp. 280-290.

116. A.O. Allen, C.J. Hochanadel, J.A. Ghormley, T.W. Davis *Decomposition of water and aqueous solutions under mixed fast neutron and gamma radiation.* s.l. : Decomposition of Water and Aqueous Solutions, 1952, Vol. 56. pp. 575-586.

Chapter 2 Experimental Procedures

2.1 Introduction

This chapter will serve as an introductory chapter to the various techniques that have been used for the experimental work throughout this thesis. It will also contain a detailed description of all the experimental work, the results of which are discussed in the following chapters.

2.2 Chemicals, Materials and Sample Preparation

General chemical reagents used in this work are described immediately below. As well, some non-general chemical reagents are described in the section of the thesis where the specific reagent is used.

Double deionised water was employed to make both solutions, groundwater simulants and to rinse all electrodes between use. This was purified using a Direct Q UV3 Millipore system to a resistivity of 18.2 MΩ cm (Millipore Ltd, UK). Where nitrogen sparging of solutions was employed, an N_2 stream (WS grade, BOC Ltd, UK) was utilised to purge those solutions for 15 minutes prior to use. All reagents used in this work were AnalaR grade or higher (99.99% purity), unless stated otherwise, purchased from Sigma Aldrich UK or VWR UK, and used as received. Unless stated differently, all the products employed are concentrated with 99.99% purity purchased from Sigma Aldrich, UK.

2.2.1 Fabrication of UO_2 and SIMFUEL pellets and slices

In order to conduct laboratory experiments simulating real life conditions, SIMFUEL pellets replicating the chemical state and the microstructure of UK specific spent nuclear fuel that has been discharged from an Advanced Gas-cooled Reactor (1), and simulating 25 GWd/tU and 43 GWd/tU burn-ups, were fabricated at the UK National Nuclear Laboratory (Springfields, Preston, UK) (2). The two different burn-ups represent an average case and a peak case, respectively. The average case, referred to as the 'mean' case, has been fabricated to be representative of the following reactor conditions (3): an enrichment of 2.65 wt% of ^{235}U, a constant power rate of 15 W/gU and an irradiation time of approximately 4.57 years, which gives the resulting end-of-life burn-up of 25 GWd/tU. The 'peak case', has been fabricated to the same conditions as the mean case, but to an enrichment of 3.2 wt % and an irradiation time of approximately 7.84 years, which results in an end-of-life burn-up of 43 GWd/tU (3).

SIMFUEL pellets, as well as UO_2 pellets as a means of control, were prepared by sintering powder precursors containing thirteen dopants (2), compositions of which are given in Table 2-1 below (3). The SIMFUEL compositions were calculated using the FISPIN nuclear inventory calculation code

(developed by the National Nuclear Laboratory UK and formerly distributed by AMEC (Jacobs being the current owner) (4)) and are representative of a fuel pellet that has aged for 100 years after removal from the reactor. Given the relatively small differences in radionuclide inventory expected over longer time periods, the SIMFUEL studied in this work is expected to be also representative of spent fuel after significantly longer periods (e.g. 1,000 years) (2).

SIMFUEL Composition	**100 years cooling time (at.%)**		**100 years cooling time (wt.%)**	
Oxides:	25 GWd/tU (Low-doped)	43 GWd/tU (High doped)	25 GWd/tU (Low-doped)	43 GWd/tU (High doped)
UO_2	95.705	92.748	97.588	95.869
Nd_2O_3	0.761	1.284	0.483	0.827
ZrO_2	0.793	1.276	0.369	0.602
MoO_3	0.614	1.027	0.334	0.566
RuO_2	0.512	0.892	0.257	0.455
$BaCO_3$	0.328	0.576	0.244	0.435
CeO_2	0.297	0.499	0.193	0.329
PdO	0.195	0.425	0.090	0.199
Rh_2O_3	0.080	0.115	0.038	0.056
La_2O_3	0.156	0.256	0.096	0.160
SrO	0.081	0.126	0.032	0.050
Y_2O_3	0.095	0.149	0.041	0.064
Cs_2CO_3	0.311	0.495	0.191	0.309
TeO_2	0.073	0.130	0.044	0.080

Table 2-1 Showing dopant compositions and their respective percentages in weight and atomic weight for a 25 and 43 GWd/tU SIMFUEL pellet that has 'aged' for 100 year (3)

As described by Hiezl et al. both the UO_2 and SIMFUEL pellets were prepared by first formulating a 60 g blend of each composition (3). A procedure, which is a non-standard ceramic powder processing route that is known as master-batching, was used for the production of the SIMFUEL and UO_2 pellets (3). During this process, the additives are mixed in first to create a concentrated mixture, to which the UO_2 is then added to, as it is the larger component (3). The aim of this technique is to prepare a powder that will consist of the matrix material and dopants, to shape it into the desired form using a uniaxial

or isostatic press, and to subsequently sinter it to the density that is required (3). Owing to the fact that LWR SIMFUELS have previously been fabricated using this process, the AGR SIMFUELs used in this work have also been fabricated following the above described process (3).

The 60 g blended powder compositions (as described above), were milled overnight with a ZrO_2 milling medium (5). In order to pre-compact the powder into granulates, a pressure of 75 MPa was applied. 0.2 wt. % zinc stearate was added as the binder and the material was slowly mixed for 5 minutes using a rotary mixer (5). The granulates were then pressed into green pellets by applying a pressure of 400 MPa using a uniaxial machine. All pellets were sintered at a heating rate of 5 °C/min to 300 °C, and then 15 °C/min to 1730 °C (5). The sintering time was 300 minutes which was followed by cooling, with a cooling rate of 15 °C/min until room temperature had been reached (5). The furnace (supplied by Cambridge Vacuum Engineering) atmosphere contained 99.5 vol % H_2 and 0.5 vol % CO_2. The finished pellets were cut into slices ranging from approximately 1–3 mm thick using a Struers Accutom-2 precision cut-off machine with a Struers MOD13 diamond cut-off wheel (5). The finished pellets can be seen in Figures 2-1 and 2-2 below.

Figure 2-1 Showing finished pellet with low burn-up (25 GWd/tU) (3)

Figure 2-2 Showing finished pellet with high burn-up (43 GWd/tU) (3)

Scanning Electrode Microscopy (SEM) and Scanning Electrode Microscopy Back Scattered (SEM-BS) images were taken of the UO_2 and SIMFUEL pellets in order to investigate the grain structures and sizes. These images can be seen in Figures 2-3 to 2-5 below. The SEM and SEM-BS techniques used here are discussed in section 2.6.

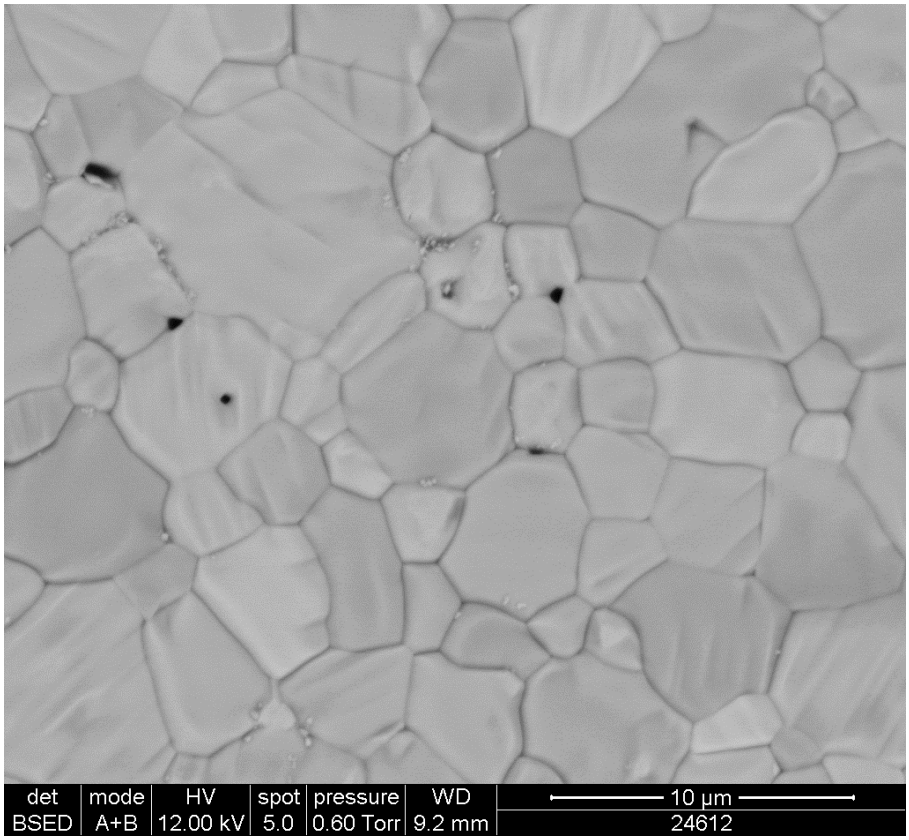

Figure 2-3 showing SEM image of microstructure of UO_2 pellet (3)

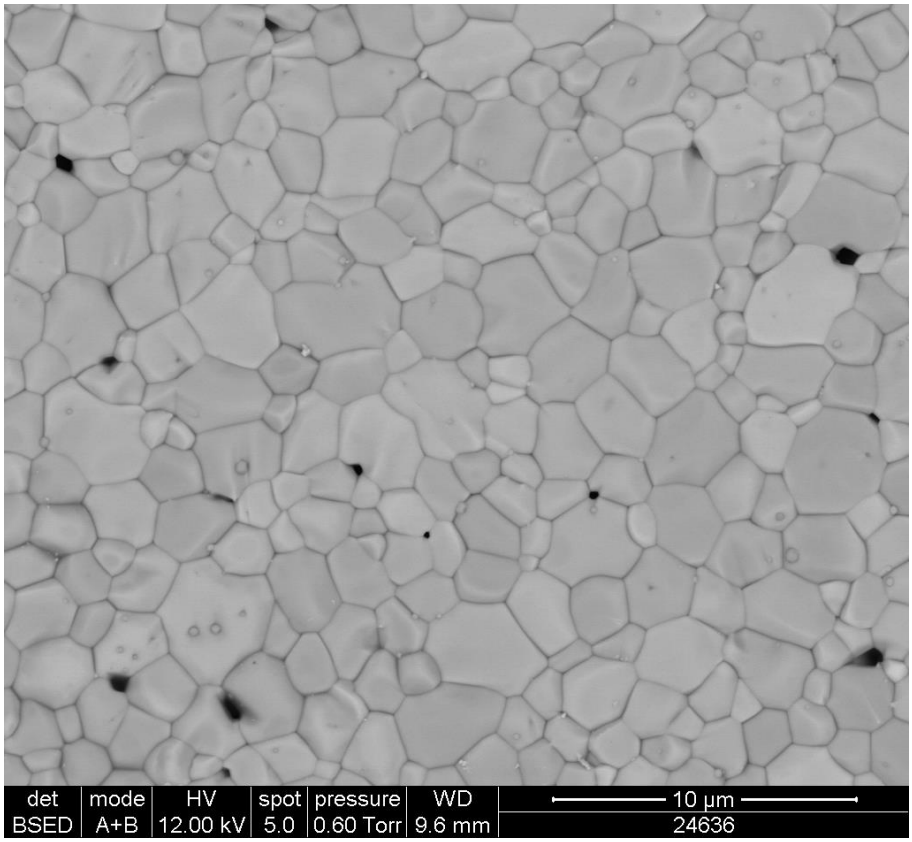

Figure 2-4 showing SEM image of microstructure of low-doped SIMFUEL (3)

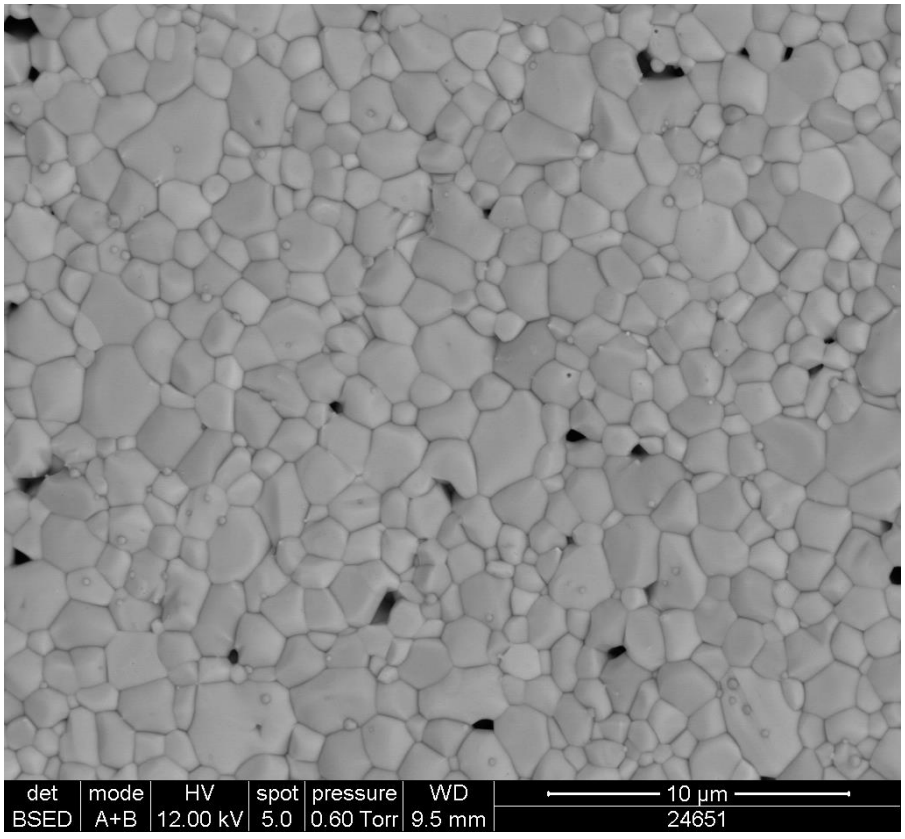

Figure 2-5 showing SEM image of microstructure of high-doped SIMFUEL with open pores (3)

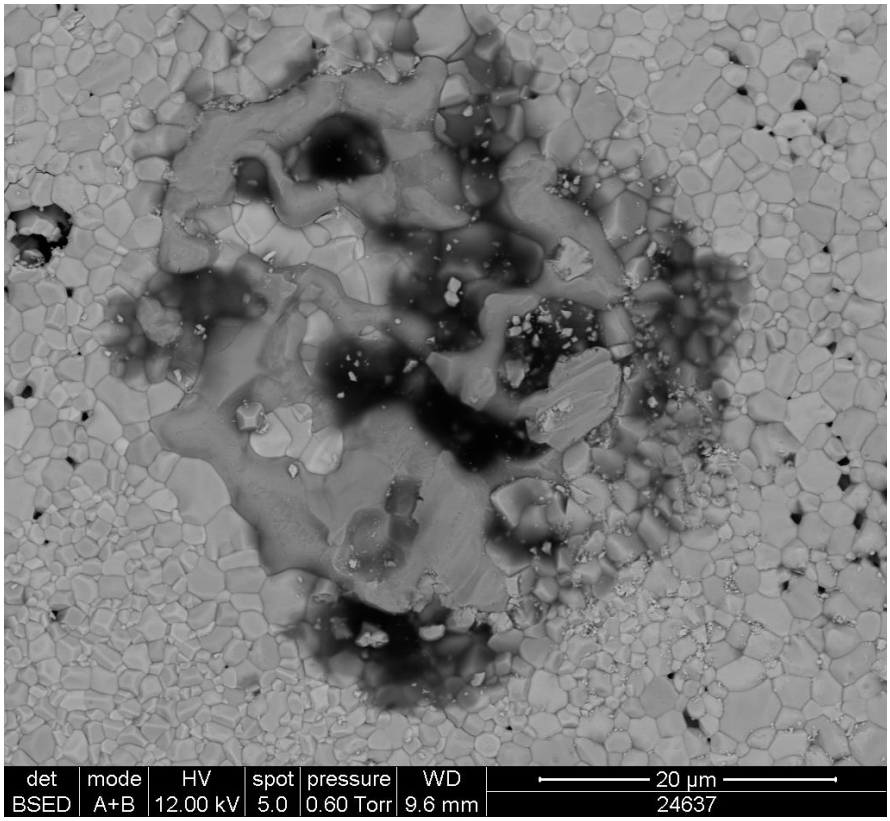

Figure 2-6 showing SEM image identified as metallic precipitate on surface of low-doped 25 GWd/tU SIMFUEL by Hiezl (3)

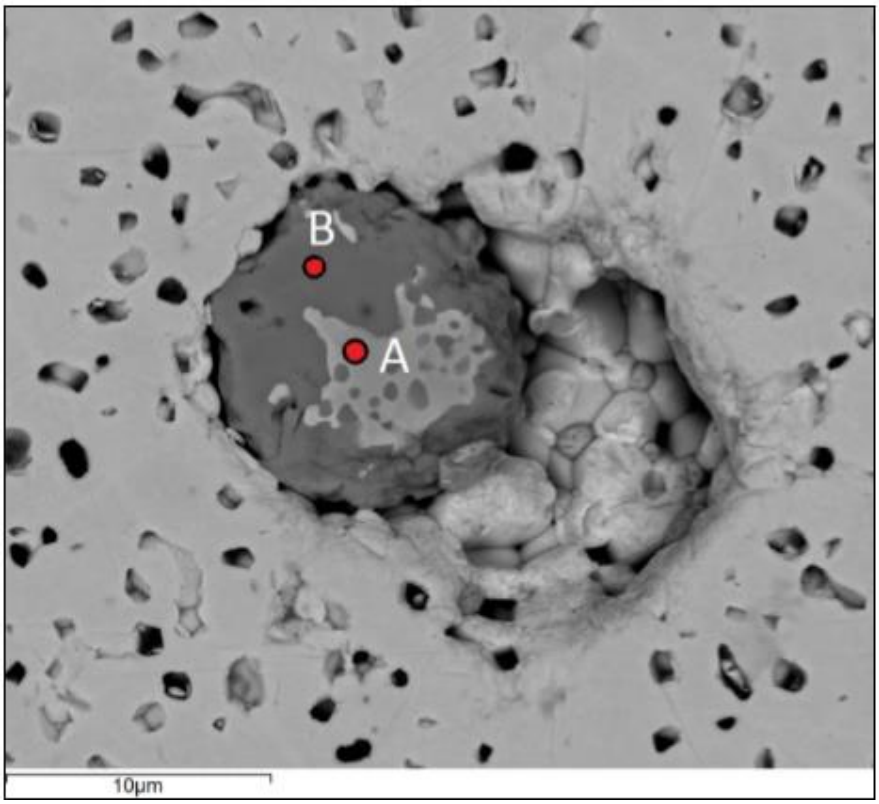

Figure 2-6a SEM-BS image of an oxide precipitate commonly found in the low-doped 25 GWd/tU SIMFUEL (3)

Regions A and B in Figure 2-6a above refer to higher and lower regions of uranium respectively. Region A also contains a lower barium content. The higher U content of region A indicates that uranium may have been in solid solution in the grey phase (oxide precipitate) at sintering temperature, but had separated out as it cooled. Region A also contains neodymium which is expected as neodymium is most likely to go into solution in the uranium matrix due to the higher oxygen potential of the mixed oxide **(3)**.

The fabricated SIMFUEL pellets are up to 92 % dense with grain sizes measured at approximately 3-30 μm, larger than that measured in real AGR SIMFUEL of approximately 2-5 μm (2). The mean grain size of the SIMFUELs decreases with increasing simulated burnup. The grains of the undoped UO_2 pellet have a grain size of 4.45 ± 0.41 μm, the low-doped SIMFUEL pellet grains have a grain size of 2.29 ± 0.63 μm, whereas the high-doped SIMFUEL pellet consists of grains with grain sizes of < 2-3 μm, which are surrounded by grains of grain sizes of > 3-4 μm (3).

It should be noted from Figures 2-3 – 2-5 that the pellet surfaces do not remain homogenous throughout. Doped SIMFUEL samples do exhibit compositional inhomogeneity and evidenced by the metallic and oxide precipitates observed in Figures 2-6 and 2-6a respectively. Both such precipitates are known to occur in real PWR and AGR spent fuel and are referred to as ε-particles and grey phases respectively. Here, both precipitates are formed during the sintering process in an H_2 atmosphere (3). These grey-phases are principally (Ba, Sr)(Zr, RE)O_3 oxide precipitates (where RE = rare earth elements). Apart from the grey-phases, metallic precipitates have also formed within the UO_2 matrix – commonly referred to as ε-particles. These ε-particle precipitates are made up of Mo, Ru, Rh and-Pd (2).

Of interest here is that metallic particles/Ɛ-particles in real spent fuel are generally spherical and have a submicron particle size of 0.8 ±0.7 μm (2). In our fabricated SIMFUELs however, they are about one order of magnitude larger. This is something that should be borne in mind in the interpretation of the electrochemical corrosion data for these samples later in this thesis.

Conversion of these pellets into UO_2/ SIMFUEL electrodes is described in the section below.

2.3 Electrode Fabrication Methods

2.3.1 UO_2 and SIMFUEL Electrode Fabrication

The UO_2 and SIMFUEL pellet slices fabricated as in section 2.2.1 were made into electrodes to be used in electrochemical experiments via the flowing method.

A cylindrical brass section was used as the core for the electrode. The pellet slice was then attached to the brass section using a silver loaded epoxy adhesive to ensure an electrical contact (Stock no. 186-3616, RS Components Ltd, Corby, Northhants, UK) (6). The entire electrode was then sealed in a resin layer (HY1300 and CY1300, Aeropia Ltd, Newton Road, Crawley, UK), and moulded into a cylindrical shape using a pre-made mould (6). The final electrode was ejected from the mould using a silicone spray. A thread was added to the bottom of the electrode so that a screw could be inserted for the experimental set-up of the electrochemical studies.

The tip of the electrode was then polished using a series of abrasives. 600 grit SiC paper was used in water to avoid uranium dust formation, followed by polishing using diamond abrasive compounds (Marcon, Codicote, Hitchin, Herts, UK) of 6, 3 and 1 microns. Below is a representation of the finished electrode (5) (6).

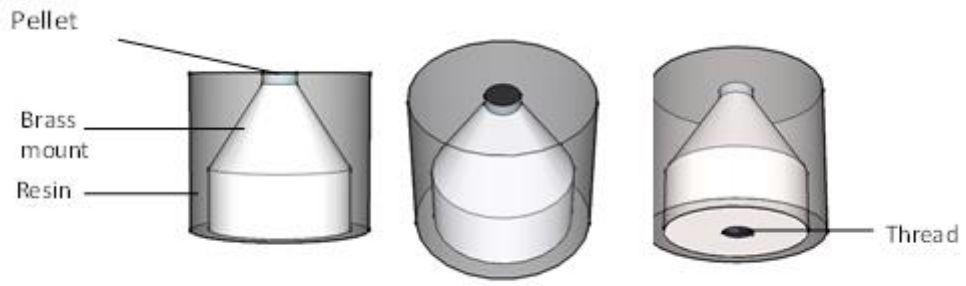

Figure 2-7 showing schematic of UO_2 and SIMFUEL pellet (6)

Now that we have looked into how the UO_2 and SIMFUELS pellets are produced, we will move onto the micro-electrode fabrication.

2.3.2 Electrode fabrication

Five different electrodes were fabricated to investigate the behaviour of minor actinides in waste streams (see section 8). The fabrication process of each electrode is detailed below.

Table 2-2 below summarises the electrodes that were used in experiments and their corresponding sizes.

Electrode material	Electrode size
Gold	10 µm
Gold	50 µm
Gold	100 µm
Gold	250 µm
Gold	500 µm
Platinum	100 µm
Graphene Ring Nanoelectrode (GRiN)	231 – 238.9 nm ring thickness
Glassy carbon	7.2 mm

Table 2-2 summarising the types of electrodes used, with their respective sizes

2.3.2.1 Gold electrode

All gold micro-disk electrodes were fabricated using the method described by Wilbraham *et al.* (7) which is described below.

Glass Pasteur pipettes made of borosilicate were used as the casing for the electrodes. Gold wire (99.99% purity) in various sizes (as given in the table above) were acquired from Advent Research Materials Ltd (7). The pipettes and gold wires were washed by sonication in successive washes of acetone, ethanol, 0.5 mol dm^{-3} HNO_3 and distilled deionised water. After the washings, the pipettes and gold wires were dried overnight in an oven at 60°C, to evaporate off any excess solvent or water (7). Following this, approximately 30 mm of each gold wire was sealed into a glass pipette by using a micro blowtorch (7). Electrical contact with the gold wire was established by inserting Woods metal (Bi 50%, Cd 12.5%, Pb 25%, Sn 12.5%) into the sealed glass tube and melting it by immersion in boiling water (7). Copper wire was then inserted into the molten Woods metal and allowed to set, creating an electrical contact between the copper and gold wires. The electrode was furthered strengthened by back filling the sealed glass tube with aircraft grade resin (Aeropia Ltd, Newton Road, Crawley, UK) (7). The excess glass that remained from the narrow end of the pipette was then removed, exposing a cross section of the gold wire. To finish the electrode, the gold micro-disk was polished using abrasive diamond polish (Marcon Diamond Products Ltd.) in descending granular size (6, 3 and 1 micron), using polishing microcloth® pads (product no. 40-7212, Buehler, Lake Bluff, Illinois, USA) and then sonicated

in deionised distilled water before use. A schematic of the fabricated gold micro-disk electrode is shown below.

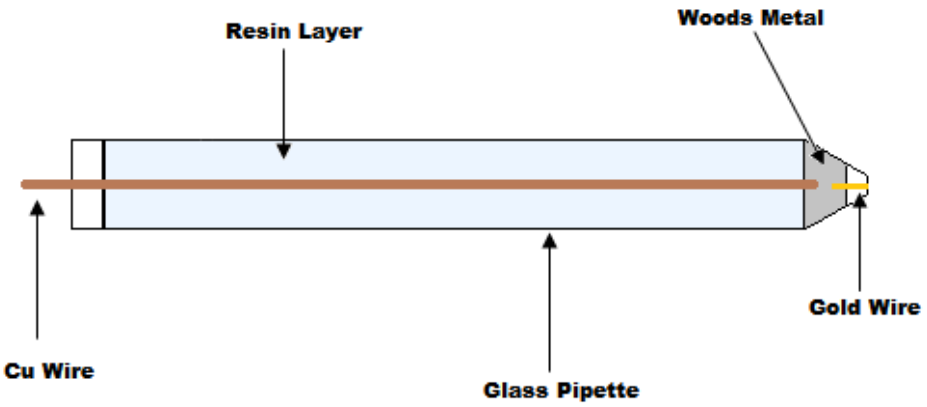

Figure 2-8 Schematic of a completed gold micro-disk electrode (7)

2.3.2.2 Platinum electrode

A platinum micro-disk electrode with a diameter of 100 µm was purchased from Alvatek UK (MF-2150 MPTE Platinum Microelectrode). The electrode is pictured below.

Figure 2-9 showing platinum microelectrode (8)

2.3.2.3 Graphene Ring Nanoelectrodes

A graphene ring nanoelectrode (GRiN) with a ring diameter of 220 µm and a ring thickness of approximately 231 – 238.9 nm was fabricated in the following way.

GRiNs were fabricated by coating fibre optics with graphene oxide (GO) using solutions of GO that were prepared in house (9). The GO coated fibre optic was then reduced to graphene by both chemical and thermal means, using hydrazine and a furnace in an inert atmosphere, respectively (9). The resulting graphene coated fibre optics were then wired, potted in insulating epoxy and cleaved to expose a nanoring graphene electrode (9). The fabrication procedure is outlined below.

GO solutions were prepared in accordance with the modified Hummers Method (10). This method involves the chemical delamination of graphite powder using oxidising solutions of permanganate in nitrate, in which the following reagents were used (9): flake graphite black powder (average particle diameter of <20 µm, synthetic, 99.95% purity, Sigma-Aldrich CAS 7782-42-5), sodium nitrate ($NaNO_3$) (ACS reagent Sigma Aldrich CAS 7631-99-4), sulfuric acid (H_2SO_4) (96.6% purity Sigma-Aldrich CAS 7664-93-9), potassium permanganate ($KMnO_4$) powder (99,5% AnalaR) and hydrogen peroxide (H_2O_2) (30% conc. Sigma-Aldrich CAS 7722-84-1) (9).

The subsequently-produced suspensions of GO are brown in colour and required purification before use by a process involving centrifugation, redispersion by sonication and filtration. Recovery of the dispersed GO was then achieved by centrifugal solid/liquid separation using a MSE Sanyo Mistral 3000i centrifuge (9). Redispersion of the decanted solid into deionised water with H_2SO_4/H_2O_2 (35 wt % in H_2O Acros Organic) or HCl (37% conc. ACS reagent Sigma-Aldrich CAS 7647-01-0) required sonication provided by a Fisherbrand FB11005 sonicator (9). The GO then underwent 19 cycles of redispersion by sonication and recovery by centrifugation, ultimately resulting in a purified dispersion of GO in distilled water. Filtration of the freshly delaminated GO was performed using a vacuum drying filter system, employing 2 paper filters (110 mm Ø num 1001 110, Whatman Schleicher & Schuell) obtaining a dried graphene oxide that was black in colour (9).

The final, purified dispersion of GO was then used to dip coat the fibre optics. These had previously been declad i.e. their plastic sleeving had been removed (9). The characteristics of the fibre optics were 0.12NA UV/VIS 220 µm x 10 m (Ref 59300) purchased from Edmund Optics Europe. Thermal annealing of the GO to form graphene coated fibre optics was achieved using a tube furnace (Elite Thermal Systems Ltd TSH15/50/180-2416CG) (9). The graphene coat was then contacted to copper flags using silver conducting epoxy resin paste (CW2400 Circuit Works, Chemtronics). The copper flags were fabricated from copper sheets of 1 mm thickness, and were polished with sand paper before being cut and folded (9). For each GRiN, a conventional soldering iron and soldering wire were then used to join the copper sheet with standard electrical wire. The entire assembly was then potted in

insulating epoxy resin (general-purpose epoxy lay-up resin comprised of a hardener and a resin (UN No 3082) purchased from ABL (Stevens) Resin & Glass (www.resin-supplies.co.uk)) and cleaved to expose a nanoring graphene electrode. The resin employed to encapsulate and isolate the GRiN ensemble was a general-purpose epoxy lay-up resin comprised of a hardener and a resin (UN No 3082) purchased from ABL (Stevens) Resin & Glass (www.resin-supplies.co.uk) (9).

The resultant GRiNs then needed to be polished. This involved a series of coarse followed by finer polishes. The coarse polishes were achieved using polishing paper of 240, 400, 800, 1200 and 1500 grain size (Halfords, UK). The finer polishes were achieved using polishing microcloth® pads (product no. 40-7212, Buehler, Lake Bluff, Illinois, USA) spread with Marcon diamond abrasive compound for fine lapping and polishing (1 micron, 3 micron and 6 micron) from Marcon Diamond Products Ltd (9).

2.3.2.4 Glassy carbon electrode

A glassy carbon electrode with a diameter of 7.2 mm (Metrohm, Switzerland) was fabricated in the same way as the SIMFUEL and UO_2 electrodes. See section 2.3. for more details.

2.4 Specialist solution preparation

2.4.1 Groundwater simulant preparation

Simulants were prepared for the two different groundwaters studied in this work. A granitic groundwater simulant, hereafter referred to as the modified simplified groundwater, and a high salt strength evaporite groundwater. As well, a simple 0.1 mol dm^{-3} sodium sulfate solution was used to provide an inert electrolyte system for the purposes of chloride-free control studies.

The modified simplified groundwater simulant was prepared according to the composition employed by the European FIRST Nuclides Consortium (11). The composition of the solution was as follows:

- 10 mmol/dm^{-3} sodium chloride
- 2 mmol/dm^{-3} sodium bicarbonate
- pH 8.2

The evaporite groundwater simulant was prepared according to the following table.

Required elements	Required molarity	Compounds used	g/L
Na	4.87	NaCl	278
K	2×10^{-2}	KCl	1.51
Mg	8.2×10^{-2}	$Cl_2Mg.6H_2O$	16.7
Ca	2.7×10^{-2}	$CaCl_2.2H_2O$	3.90
Cl	4.76	NaCl	X
SO_4^{2-}	5.3×10^{-2}	Na_2SO_4	7.53
HCO_3	2.1×10^{-3}	$NaHCO_3$	0.176

Table 2-3 showing components of Evaporite simulant groundwater (12)

The pHs of these solutions were found to be as follows:

- Na_2SO_4: pH = 5.43 @ 19.2 °C
- Modified simplified groundwater: pH = 8.20 @ 19.2 °C
- Evaporite simulant groundwater: pH = 7.10 @ 19.2 °C

2.4.2 Americium solution preparation

Below is a detailed description of the preparation of the americium stock solution, and the subsequent solutions made from the stock

2.4.2.1 Preparation of stock solution

A 150 ppm (6.2×10^{-4} mol dm^{-3}) solution of Am(III) - representative of the concentration of americium found in PUREX raffinates (see Chapter 1 Section 1.1.3.2 for the PUREX process) - was prepared to study the aqueous electrochemistry of Am(III) on inert noble metal and carbon-based microelectrodes.

2.4.2.2 Accurate calculation of concentration of Am in stock

For a target concentration of 150 ppm Am it is assumed that 1 µg/g ~ 1 µg/cm^3 as the density of 1 mol dm^{-3} nitric acid solution is approximately 1.03 g/dm^3 (the stock solution was made up in nitric acid to give a 1 mol dm^{-3} solution).

A stock solution was prepared containing enough Am to make 8 final solution samples, each with a volume of 15 cm^3. Each final solution contained 150 x 15 / 1000 = 2.25 mg Am. Hence a total of 8 x

2.25 mg Am was needed in total to make up the final solution, which equals 18 mg of americium. Americium oxide (in-house material, JRC Karlsruhe, Germany) exists as $Am(IV)O_2$ (273.06 g/mol) or as $Am_2(III)O_3$ (530.11 g/mol) depending on its preparation. In this case the sesquioxide, Am_2O_3 was used which is prepared from Am(IV) oxide by reductive treatment in hydrogen at 600 °C. The mass of the oxygen in the sesquioxide makes up approximately 10 % of the total weight, hence the exact amount of the oxide powder needed equals 19.73 mg.

As discussed below, a stock solution that can be divided into 8 final solutions was to be prepared. As each final solution should contain 1.5 cm^3 of the Am stock, the exact total volume of the stock should be 8 x 1.5 = 12 cm^3.

A total of 12.2 cm^3 was in the end prepared, the extra 0.2 cm^3 was a budget for small losses and to allow removal of an aliquot for sampling by gamma analysis. The stock was made up in a 20 ml liquid scintillation vial with a plastic lid. To make the stock solution, 21.7 mg +/- 0.2 mg (weighing uncertainty of the analytical balance, 1 σ) of Am_2O_3 powder was weighed into the 20 mL scintillation glass vial. The glass vial was placed on a hot plate, 1 mL of 8 mol dm^{-3} nitric acid added and the temperature slowly increased until close to boiling conditions was reached. The dissolution in 8 mol dm^{-3} nitric acid was not complete and the small amount of residues left were completely dissolved by three additions of 0.1 mL 3 mol dm^{-3} HCl. In the end a greenish Am solution was formed. This solution was slowly evaporated to dryness, taking care not to calcine the residue. Once evaporated to dryness, the residue was dissolved again, this time in 1 ml of 1 mol dm^{-3} nitric acid. The last step was repeated once more to ensure that all chloride ions had evaporated. The stock solution was prepared by a final dissolution in 12.2 ml (12.5897 g) of 1 mol dm^{-3} nitric acid.

The concentration from weight is then 1564.9 ppm +/- 28.8 ppm (2 σ, measured gravimetrically). The density of the solution was measured to be 1.034 g/mL. The contact dose rate of the scintillation vial was roughly 25 mSv/h and it was stored in a thin (2mm) lead shielding.

2.4.2.3 Gamma counting of stock

The calculated ^{241}Am gamma activity of a 1500 ppm Am nitric solution is 191 MBq/g solution. A sample of 100 mg was taken from the stock solution, which was then gravimetrically diluted 10^6 times in 1 mol dm^{-3} nitric acid. A 2 cm^3 sample of the final dilution was measured by gamma spectrometry and confirmed a ^{241}Am concentration of ~ 1500 ppm of the stock solution.

2.4.2.4 Preparation of subsequent solutions from stock solution to be used for electrochemical measurements

These solutions were prepared from the above described stock solution of 1500 ppm, 6.2 x 10^{-3} mol dm^{-3}, Am(III) in 8 mol dm^{-3} nitric acid:

- Simplified reprocessing stream simulants comprised of 1, 3 & 5 mol dm^{-3} HNO_3
- Background electrolyte of 0.1 mol dm^{-3} KNO_3 as a control system

The final solution of each solution sample had a volume of 15 ml. As the stock solution was made up to contain 1500 ppm Am, and the desired Am concentration is 150 ppm, 1.5 ml from the stock solution was required to make up each final solution to 15 ml, the final concentration of Am contained in each solution being 150 ppm or 6.22 x 10^{-4} mol dm^{-3}.

To make up the final solutions in acid media, 1.5 ml of the Am stock solution was transferred into 13.5 ml of nitric acid for each of the nitric acid concentrations (1 mol dm^{-3}, 3 mol dm^{-3} and 5 mol dm^{-3}). The acids were compensated for due to their concentrations being subject to being diluted by the stock. Hence the desired 3 mol dm^{-3} nitric acid solution was made up to 3.22 mol dm^{-3} nitric acid, and the desired 5 mol dm^{-3} nitric acid solution was made up to 5.44 mol dm^{-3} nitric acid before the stock was added to give 3 and 5 mol dm^{-3} solutions.

The remaining stock solution (7.6 ml) was used to make up the remaining final solutions in 0.1 mol dm^{-3} KNO_3. 1.5 ml of the stock solution was again used to make up each of the solutions. Once the 1.5 ml of the Am stock had been evaporated to dryness – taking care not to calcine, the remaining residue was then dissolved in 0.1 mol dm^{-3} KNO_3 solution and made up to a total volume of 15 mL.

2.5 Introduction to Raman Spectroscopy

Raman spectroscopy is an analysis technique commonly used to provide a 'fingerprint' by which a molecule can be identified. The technique involves shining a monochromatic laser onto the desired sample, and detecting the light that is scattered from the sample (13). The vast majority of this scattered light will be at the same frequency as that of the excitation source. This proportion is known as elastic scattering, or also Rayleigh scattering (13). The remaining fraction that is not scattered at

the same frequency as the excitation source, which amounts to approximately 1 in 10^7 photons, arises from inelastic scattering and is known as the Raman Effect (13). The process of inelastic scattering is caused by the inelastic collision between monochromatic light at the point of incidence and the molecules of the sample (13), more accurately, the electric dipole of the molecule (13). If the frequency / energy of the scattered photon is lower than that of the incident photon, stoke lines are apparent (13). In contrast, if the frequency / energy of the scattered light is more than that of the incident beam, anti-stokes are apparent. This phenomenon is explained in Figure 2-10 below.

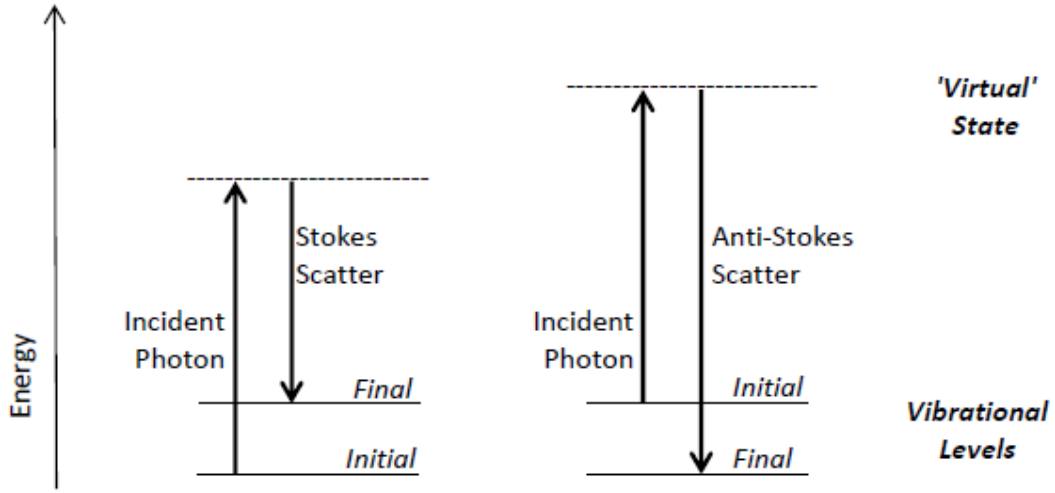

Figure 2-10 showing Stokes and anti-Stokes Raman scattering on an energy level diagram (13)

During Rayleigh scattering the incident photon causes the molecule to be excited into a higher, notionally virtual, energy state from which it then relaxes back to a lower level, at which point a scattered photon is emitted (13) The reason that Rayleigh scattering is referred to as elastic scattering is because the molecule relaxes back to the same energy level as it had started from (13) During the Raman effect however, a molecule that is excited during the scattering process subsequently relaxes back to a different energy level, typically vibrational, from which it had started, causing its scattering to be inelastic (13) The difference in energy that is observed between the two differing photons is indicated in Figure 2-10 above by the energy arrows having varying lengths.

Raman Spectroscopy is a vibrational spectroscopic technique, similar to Infrared (IR). Both Raman and IR spectroscopy work on the fact that each chemical bond has a unique vibrational energy (13). Owing

to this unique vibrational energy, every compound will subsequently have its own unique 'fingerprint', as aforementioned. The major difference between Raman and IR spectroscopy is the type of vibration and transmittance that is measured (13). Raman spectroscopic measurements depend on the fact that a change in the polarisability of a molecule can take place, whereas IR spectroscopy depends on a change in the dipole moment taking place (13).

2.5.1 Micro-Raman spectroscopy

Micro-Raman spectroscopy is a particularly useful technique for studying defect structures within the UO_2 sub-lattice, by exploiting the small size of the laser spot to obtain spatially specific compositional information. This involves measurement of Raman spectra from microscopic samples, or microscopic cross sections from macroscopic samples. In the case of the latter, the technique can be used to build up a Raman map of a surface, by rastering the laser spot over the surface of the sample. However, the construction of such a map should be supported by parallel morphological/topographical imaging of the surface – especially if the surface is non-homogeneous in terms of its physical structure. This is usually achieved through the use of a technique such as Scanning Electron Microscopy (SEM) or a scanning probe microscopy (SPM) technique such as atomic force microscopy (AFM).

2.5.2 Experimental set-up

Each pellet was attached to a stainless steel rod using PTFE tape to ensure that only one side of the slice would be exposed to solution during measurements following immersion. The slices were characterised before and after immersion by 785 nm, micro-Raman spectroscopy (Voyage System, B&W Tek, USA) using a laser power below 5 mW in order to avoid any thermal conversion of UO_2 to U_3O_8 (7).

As received sample slices were immersed in the following samples for various periods of time ranging from 1 to 4 hours with the exception of a single experiment that lasted 53 hours:

- deionised water;
- 0.1 mol dm^{-3} sodium sulfate electrolyte;
- Modified simplified groundwater; and
- Evaporite groundwater

The pellets were immersed in each of the solutions without the addition of hydrogen peroxide, as well as with the following concentrations of hydrogen peroxide:

- 10 µmol dm^{-3}
- 100 µmol dm^{-3}, and
- 1 mmol dm^{-3}

Unless otherwise noted, all solutions were sparged with a constant supply of air in order to provide a source of agitation. In each instance, Raman spectra were recorded from the surface of the pellet sample before and after immersion. After each set of immersions, the pellets were polished using the polishing technique outlined in section 2.3.1, before conducting further experiments

2.6 Introduction to Scanning Electron Microscopy (SEM)

Scanning Electron Microscopy (SEM) is a surface analysis technique used to characterise different materials by providing information about the morphology, crystalline structure and orientation, and also the composition of the sample (14).

When using an SEM to analyse the surface of a material, a beam of electrons is focused on a spot of the sample, resulting in a transfer of energy to the spot in question (15). The purpose of the electrons that are used to bombard the spot, which are known as primary electrons, is to dislodge electrons from the sample itself. These dislodged electrons are then known as secondary electrons. The secondary electrons are attracted to and subsequently collected by a positively charged detector, and translated into a signal (15).

In order to produce an SEM image, a beam of electrons is swept across the desired area, producing many such signals as mentioned above (15). The signals that are generated are then amplified, analysed and translated into images. These images show the topography of the sample being analysed (15).

The amount of secondary electrons that can be collected during the analysis is determined by the energy of the primary electrons. As the energy of the beam of the primary electrons is increased, the emission of secondary electrons from the sample also increases, until a limit has been reached (15).

Once this limit has been reached, any secondary electrons that are collected start to diminish. This is because the energy of the beam from the primary electrons is so high that is starts to activate electrons which are deep below the surface of the sample. Electrons which come from such depths typically recombine before they can reach the surface for emission (15).

It must be noted that the primary electron beam does not only result in the emission of secondary electrons, but also in the emission of backscattered (also known as reflected) electrons (15). Backscattered electrons (BSE) are generated when a significant fraction of the beam of primary electrons undergo sufficient scattering events to fully reverse their original direction of travel into the sample, which causes these electrons to return to the entrance (at the surface) and exit the sample (16). Backscattered electrons possess more energy than secondary electrons, and due to their definite direction, they are typically not able to be collected by a secondary electron detector (15). Backscattered electrons can only be collected by a secondary electron detector if the detector is directly in the path of the BSE. All emissions above 50 eV are considered to be BSE (15).

BSE imaging can prove useful in that is can distinguish one material from another. This is because the yield of the collected BSE increases monotonically with the sample's atomic number (15). BSE imaging is capable of distinguishing elements which have a difference of at least three in their atomic number, resulting in images with good contrast (15).

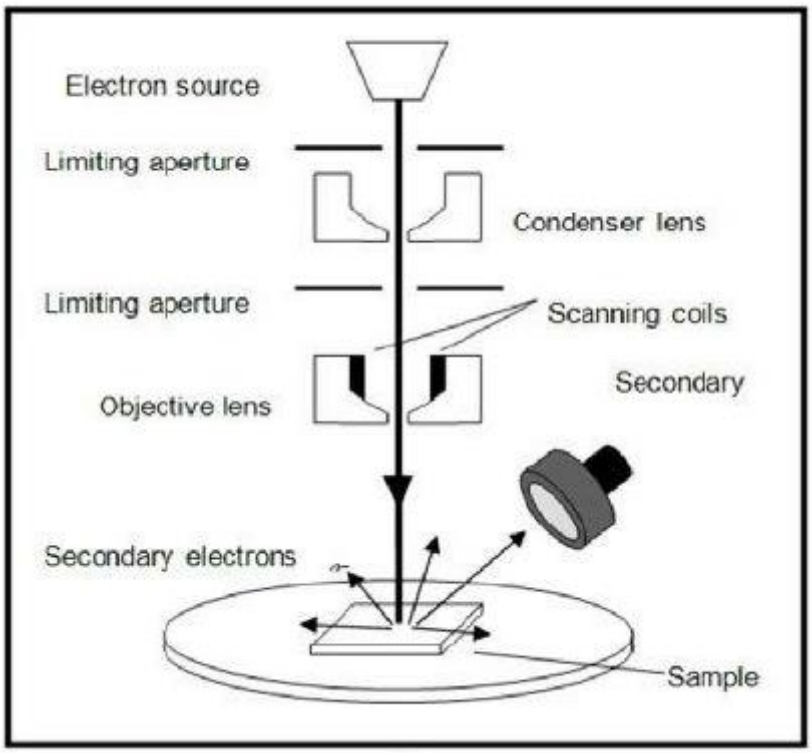

Figure 2-11 schematic showing set-up of an SEM (17)

A Scanning Electron Microscope may also be equipped with an Energy Dispersive X-Ray (EDX) analysis system, which enables the SEM to perform compositional analysis on the desired sample (15). The X-ray emission from the EDX is stimulated by the irradiation of the surface with a high energy beam of charged particles, or a focused X-ray beam (18). In an adequately equipped SEM, the atoms on the surface of the sample are excited by the electron beam, emitting specific wavelengths of X-rays, which are characteristic of the element's atomic structure (19). An energy dispersive detector can then analyse these X-ray emissions (19). Analysis using an EDX system can aid in identifying materials and contaminants, and can also estimate relative concentrations of said materials and contaminants on the surface of the sample in question (15).

2.6.1 Experimental set-up

There are three sets of SEM images that are presented in this thesis. These are namely the UO_2 and SIMFUEL pellets taken at point of synthesis by Hiezl using an FEI Quanta SEM at Springfields (FEI UK Limited, Cambridge, UK) (3). For the interested reader, further details can be found in reference (3). The second set of SEM images are those of steel samples taken prior to their use in electrochemical studies in americium containing solutions – the so-called inactive samples. And lastly those taken of

the same steel samples after they had been used in electrochemical experiments in americium containing solutions – the so-called active samples. Details of the instructions used to study the latter two classes of sample are as follows.

The polished steel samples were mounted onto SEM probes.

The inactive samples were analysed using a Vega Tescan TS5130LSH Scanning Electron Microscope, 200 V 200 V - 30 keV, tungsten filament, emission-current till 300 µA, SE –Detector + BSE-Detector, 3 nm resolution and a magnification of 3 – 1000000x. The SEM is equipped with an Oxford EDX system. The Oxford EDX system is made up of an EDX detector, 10 mm^2, Si(Li), polymer-based thin window, multi-channel Pulse Processor (110 eV – 80 keV X-ray energy range), with a resolution of $<$ 138 eV.

After the electrochemical investigation of the samples (see section 2.9.3), where the samples were exposed to solutions containing americium, the steel samples were once again analysed by SEM.

The active samples were analysed inside a glovebox using a FEI Philips XL 40, 200 V - 30 keV, tungsten filament, emission-current till 200 µA, SE –Detector + BSE-Detector, 3 nm resolution and a magnification of 10 – 400000 x. The SEM is equipped with a SAMx EDX detector.

The SAMx EDX system is made up of a Silicon Drift Detector (SDD), free of liquid nitrogen, 10 mm^2, Si(Li), polymer-based thin Window, multi-channel Pulse Processor (110 eV – 80 keV X-ray energy range), with a resolution of $<$ 138 eV.

2.7 Electrochemical Characterisation Techniques

A range of common electrochemical techniques were used to study the corrosion behaviour of both SIMFUEL pellets and cladding. These include cyclic voltammetry, potentiometry and electrochemical impedance spectroscopy. For the convenience of the reader, the salient features of each technique are described below.

2.7.1 Introduction to cyclic voltammetry

Cyclic voltammetry (CV), is an electrochemical measurement technique, commonly employed to investigate the reduction and oxidation processes of molecular species (20). A redox reaction is a type of chemical reaction in which the oxidation states of atoms are changed. Redox reactions are

characterised by the transfer of electrons between chemical species, most often with one species undergoing oxidation (oxidation being the loss of electrons during a reaction), while another species undergoes reduction (reduction being the gain of electrons during a reaction). Cyclic voltammetry is also a useful tool in studying electron transfer-initiated chemical reactions (20). It is a measurement technique, in which the current that is passed through a sample electrode, upon application of an external potential to that electrode in an electrochemical cell, is measured (21) (22).

Cyclic voltammetry uses a three electrode system; a working electrode, a reference electrode, and a counter electrode. A cyclic voltammogram is carried out by cycling the potential of the working electrode, and then measuring the current that is generated as a result of the cycling of the potential (21). The potential of the working electrode is measured against a reference electrode, which, as the name suggests, is used as a reference point and therefore remains at a constant potential (21) (22). The purpose of the counter electrode is to complete the circuit, i.e. to carry the current around the system.

During cyclic voltammetry, the measurement commences from a starting potential, which usually is in a region of the CV where no current is measured. In other words, it is the region where no electrochemistry occurs. The potential is then either scanned positively or negatively of said starting potential, depending upon whether the desired study is of the oxidation or reduction reaction. The direction of the initial scan is then arbitrarily defined as the forward direction. The voltage continues scanning until an instrumentally defined maximum value is reached. The potential maximum is called the switching potential. The switching potential is the point at which the voltage is high enough to have initiated the oxidation or reduction of the analyte (21). At this point, the forward going scan switches direction and doubles back on itself. The system is now said to be conducting a reverse scan. The potential continues to sweep in this reverse direction, passes the starting potential, and then, once an instrumentally defined switching potential is reached, changes direction once more, and re-enters the forward scanning direction. The voltage then continues to scan until it reaches the starting potential. At this point, the voltage scan is either stopped, or the above cycle repeated for an experimentally defined number of times (21).

Typically, a cyclic voltammogram is reported by displaying the current measured at the working electrode as a function of the applied potential for both the forward and reverse scans. Below is a

schematic showing a typical cyclic voltammogram that is obtained from a single electron oxidation and reduction (22):

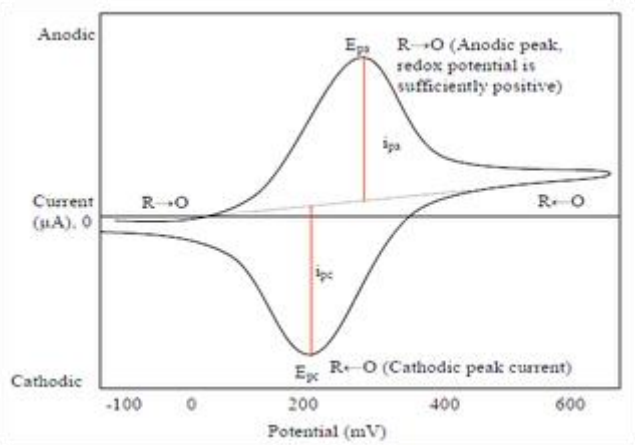

Figure 2-12 showing a typical cyclic voltammogram of the oxidation-reduction process of a single electron (21) (22)

Figure 2-12 above showing a typical cyclic voltammogram of the oxidation-reduction process of a single electron. From the figure above we can see that the oxidation process occurs during the forward going sweep. Here, the potential is being scanned positively, which causes the oxidation (22). The current that results from this is called the anodic current, denoted (i_{pa}). The corresponding peak potential is called the anodic peak potential, and is denoted (E_{pa}) (22) (21). The cathodic peak potential is reached once all of the substrate located on the surface of the electrode has been reduced. This corresponding peak potential to this, occurs in the region denoted (E_{pc}). Once the aforementioned switching potential has been reached, the potential will then scan negatively. This backward sweep results in reduction, for which the resulting current is called the cathodic current (i_{pc}) (21). The E_{pa} is reached, as was the case for the E_{pc}, when all of the substrate that is at the surface of the electrode has been oxidised (unlike for the E_{pc}, where all of the substrate had been reduced) (21).

2.7.2 Current interrupt (iR) method

The current interrupt method is a way to measure resistance in a fuel cell. It is achieved by interrupting the current for a very short interval, usually a few milliseconds, and recording the resulting voltage. The resistance of the cell is calculated by taking the difference between the cell voltage before and after the current interrupt, and dividing it by the current.

2.7.3 Experimental set-up

Undoped UO_2, 25 GWd/tU and 43 GWd/tU SIMFUEL electrodes were fabricated as outlined in section 2.3.1.

All electrochemical studies were carried out on a Metrohm Autolab potentiostat model PGSTAT 10 using GPES control and data acquisition software. Cyclic voltammetric (CV) studies on the UO_2, 25 GWd/tU and 43 GWd/tU SIMFUEL electrodes immersed in simple 0.1 mol dm^{-3} Na_2SO_4 aqueous electrolytes and groundwater simulants were conducted at a voltage scan rate of 100 mV s^{-1} over a potential range of -1.8 to 0.4 V. Unless stated otherwise, the starting potential was -1.8 V. A three electrode cell was employed using a platinum mesh counter with a saturated calomel electrode (SCE) as the reference electrode. Due to the resistive nature of the UO_2 and SIMFUEL electrodes, IR compensation was used during voltammetric measurements.

2.8 Introduction to Open Circuit Potential

The Open Circuit Potential (OCP) measurement is a passive experiment (23). It is a measurement technique that can be used to determine the thermodynamic tendency of a material to undergo oxidation in a corrosive medium (24). OPC is carried out by bypassing the counter electrode of a conventional 3-electrode system. By bypassing the counter electrode, no current is passed through the system. In this way only the resting potential between the working and reference electrode is measured (23).

After the working electrode is immersed in electrolyte, it will stabilise around a stationary value which will be its rest potential. This potential however, can vary with time, as the nature of the electrode surface can change due to oxidation, the formation of a passive layer, or due to immunity (24).

2.8.1 Experimental set-up

See sections 2.3.1 and 2.7.3 above for electrode fabrication and electrochemical set-up.

Open circuit potential (E_{OC}) measurements on UO_2, 25 GWd/tU and 43 GWd/tU SIMFUEL electrodes immersed in 0.1 mol dm^{-3} Na_2SO_4 aqueous electrolytes and ground-water simulants were conducted

over a period of 4 hours using a simple 2 electrode cell with SCE reference. Unless otherwise noted, all solutions were sparged with N_2 or Ar gas.

2.9 Introduction to Electrochemical Impedance Spectroscopy (EIS)

Electrical resistance is defined by the ability of a circuit element to resist the flow of an electrical current. Electrical resistance, is limited to only one circuit element, which is the ideal resistor (25). An ideal resistor follows Ohm's law at all current and voltage levels and its resistance values are not dependant on frequency. Moreover, in an ideal resistor, the AC current and voltage signals, through the resistor, are always in phase with one another (25).

Ohm's law is defined by the relationship between current (I) and voltage (V) in an ideal conductor (26). Thus, the relationship is described as:

'the potential difference across an ideal conductor being proportional to the current through it', where the potential difference is the voltage, and the constant of proportionality is the resistance (R) (26). Ohm's law can therefore be given by the following equation:

$$V = I R$$

Equation 2-1 (26)

where the resistance can be measured by:

$$R \equiv E / I$$

Equation 2-2 (25)

Impedance, in this sense, is similar to electrical resistance, in that it is also a measure of the ability of a circuit to resist the flow of an electric current. However, unlike electrical resistance, impedance is not limited by the above mentioned properties (25).

Electrochemical impedance is thus the response of an electrochemical cell or system, to an applied AC potential (25) (27).

Systems in general can be viewed as either linear systems or non-linear systems (28). The definition of a linear system is as follows:

'a linear system is a system that possesses the property of superposition. If the input consists of the weighted sum of a number of signals, the output is then simply the weighted sum, or in other words, the superposition, of the responses of the system to each of the signals' (29).

Relating this back to an electrochemical cell, the input is the potential, and the output is the current (28).

2.9.1 Pseudo-linearity of electrochemical systems

Electrochemical cells are in fact non-linear. If the input into an electrochemical cell, the voltage, were to be doubled, the output from the cell, the current, would not be double its input (28).

At an input of a small AC signal, for example 1 - 10 mV, an electrochemical cell will become pseudo-linear (28). Due to the fact that linear systems do not produce any harmonics of the excitation frequency, the presence and absence of any significant harmonic responses can be used to check the system for linearity (28).

In order to measure a system, the system must be at steady state, without which, problems will arise in standard Electrochemical Impedance Spectroscopy (EIS) measurements (28). Reasons as to why a system may not be at steady state are listed below:

- changes in temperature
- the degradation of coating – failed coating (25)
- the build-up of reaction products
- the growth of an oxide layer, or
- the adsorption of in-solution impurities (28)

These problems however, can be overcome by faster detection techniques such as fast Fourier-transform impedance spectroscopy (28), which is a technique that simultaneously applies 30 – 50

frequencies, and also simultaneously registers all the EIS spectra at these frequencies (30). Such techniques however are, beyond the scope of this work.

2.9.2 Representation of complex impedance

As aforementioned, electrochemical impedance is normally measured through the application of an AC potential to an electrochemical cell. A measurement is then taken of the current that is passing through the cell (25). Assuming that the potential that is applied is a sinusoidal potential, the resulting AC current signal can then be analysed as a sum of sinusoidal functions, or in other words, as a Fourier series (25).

In the case of small excitations (and electrochemical impedance is usually measured using small excitation signals (25)), a pseudo-linear response would result in a characteristic phase shift (28), although the current response to the sinusoidal potential will be a sinusoid which is at the same frequency (25). The excitation signal is expressed as a function of time (28). The phase shift can be seen in the figure below:

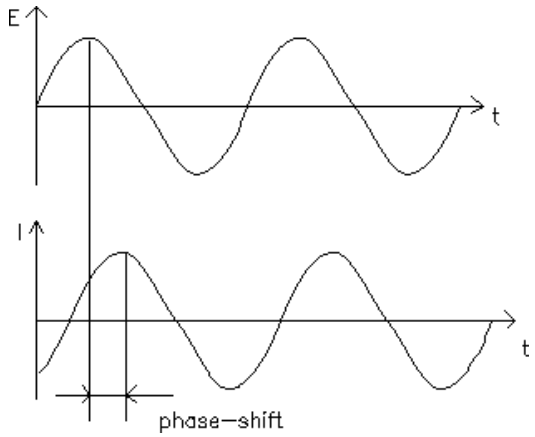

Figure 2-13 showing sinusoidal current response in a linear system (25)

The excitation signal that has been used to achieve the above shown current response can be expressed in the following form:

$$Et = E0\ sin\ (\omega\ t)\ (25)$$

Equation 2-3(24)

where E_t is the potential at time t,

E_0 is the amplitude of the signal, and

ω is the radial frequency

The relationship between the radial frequency ω, which is expressed in radians per second, and the frequency f, which is expressed in hertz, is given by the following equation:

$$\omega = 2\pi f$$

Equation 2-4 (25)

As aforementioned, in a linear or pseudo-linear system, the response signal I_t, is shifted in phase (ϕ), and will have a different amplitude than I_0 (25). The response signal is expressed in the following form:

$$It = I0\ sin\ (\omega\ t + \varphi)\ (25)$$

Equation 2-5

To subsequently calculate the impedance of the system, an expression analogous to Ohm's law and taking the above elements into consideration can be used, and is given in the equation below:

$$Z = Et/It = E0\ sin\ (\omega\ t) / I0\ sin\ (\omega\ t + \varphi) = Z0\ sin\ (\omega\ t) / sin\ (\omega\ t + \varphi)$$

Equation 2-6 (25) (28)

Thus, electrochemical impedance (Z) is expressed in terms of a magnitude that is Z_0, and a phase shift ϕ (25).

If the applied sinusoidal signal, which is E(t), is plotted on the x-axis of a graph, versus the sinusoidal response signal, I(t) on the y-axis, the resulting shape is an oval. This oval is known as the Lissajous Figure, and was the accepted method of impedance before modern electrochemical impedance spectroscopy instruments came into existence (25) (28). Below is a representation of the Lissajous Figure.

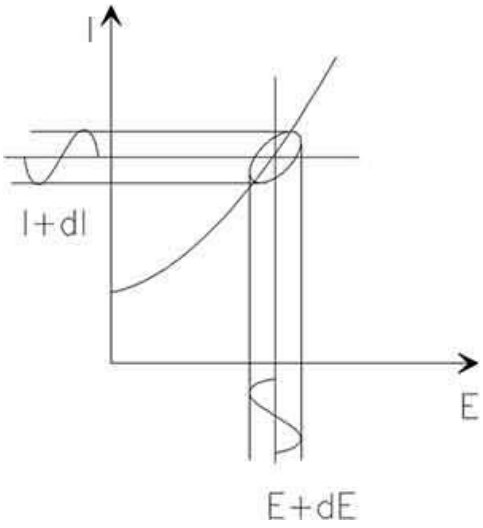

Figure 2-14 showing the origin of the Lissajous Figure (25)

With the use of Eulers relationship, it is possible to express the impedance as a complex function. Eulers relationship is given below:

$$exp\,(j\varphi) \;=\; cos\,\varphi \;+\; j\,sin\,\varphi$$

Equation 2-7

The impedance can now be expressed as a complex function, as shown in the figure below:

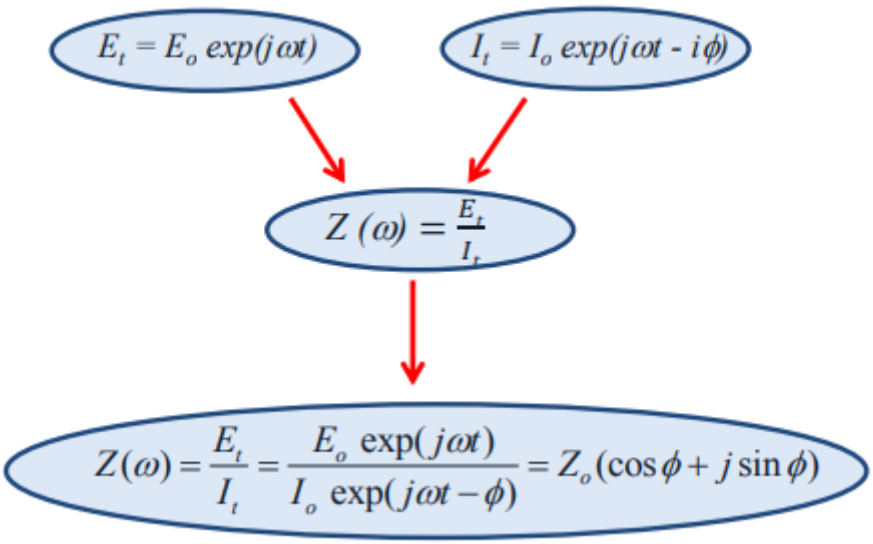

Figure 2-15 showing representation of impedance as a complex function (28)

From the above figure it can be seen that there is a real and an imaginary part to impedance being represented as a complex function, when expressed as Z (ω) (28). To plot Z (ω) on a graph, the real part is plotted on the *x*-axis and the imaginary part is plotted on the *y*-axis (28). The resulting graph is known as a Nyquist plot (25). A representation of a Nyquist plot can be seen below:

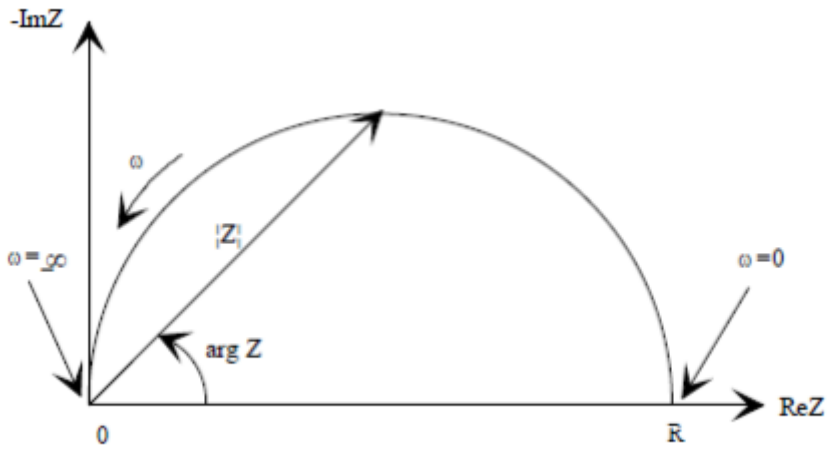

Figure 2-16 showing representation of a Nyquist plot (28)

Each point on the Nyquist plot represents the impedance at one frequency, and the *y*-axis is negative. It should also be noted that low frequency data is on the right hand side, and that high frequency data is on the left hand side (25). On the Nyquist plot, the impedance is represented as a vector of length |Z|. This can be seen on the figure above (25). The angle that is then between this vector and the *x*-axis is known as the phase angle. The phase angle is represented by ø, which is equal to arg Z (28).

Nyquist plots are based on equivalent circuits. The plot shown above is based on the circuit shown below:

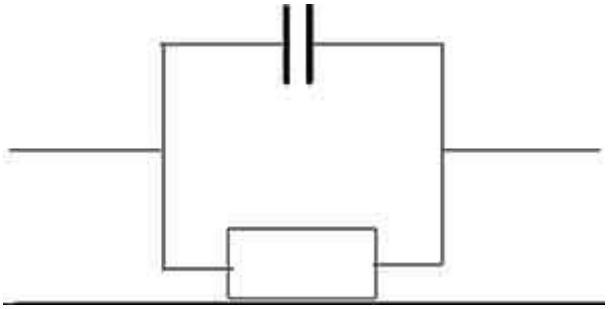

Figure 2-17 showing equivalent circuit that Nyquist plot is based on (25)

The semi-circle that is seen on the Nyquist plot is characteristic of a single time constant. The disadvantage of plotting impedance as a Nyquist plot is that the frequencies at which the impedance was recorded is unknown (25).

A Bode plot however shows information about the frequencies (28). A Bode plot is plotted with the impedance and its log frequencies on the *x*-axis, and the absolute values of the impedance, along with the phase shift on the *y*-axis, as seen in Figure 2-18 below (25) (28).

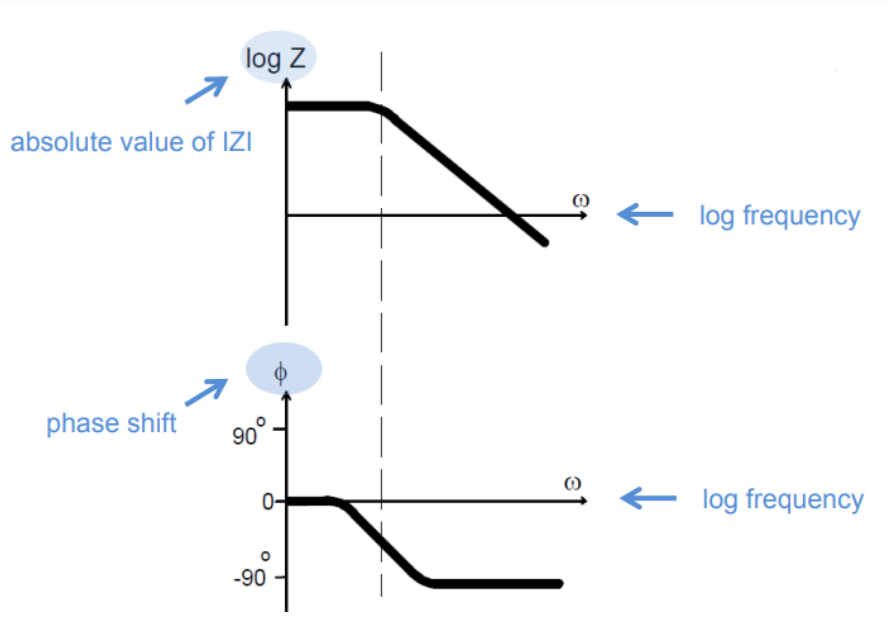

Figure 2-18 – showing representation of bode plot based on equivalent circuit shown in Figure 2-17 (28)

2.9.3 Experimental set-up – baseline corrosion study

Cyclic voltammetry experiments were set up using a conventional three-electrode cell that consisted of a working electrode (WE), a commercially available saturated calomel electrode (SCE) as the reference electrode (RE) and a platinum foil as the counter electrode (CE). All potentials given are versus the SCE.

All experiments were conducted in a nitrogen glovebox under negative pressure. The oxygen content of the glovebox is always at ≤ 3 %. All solutions were purged with Ar gas for 15 mins.

Nitric acid solutions were made by diluting concentrated 65 % Suprapur nitric acid (Merck) in MiliQ water.

All electrochemical measurements were carried out with a Zahner potentiostat.

2.9.4 Experimental set-up – Electrochemical Impedance Spectroscopy

Electrochemical impedance spectroscopy (EIS) experiments were set up using a three-electrode cell consisting of a working electrode (WE), a commercially available silver /silver chloride electrode via a Luggin capillary as the reference electrode (RE), and a platinum grid as the counter electrode (CE).

A small sinusoidal potential was applied to the working electrode and the resulting sinusoidal current response signal from the electrochemical cell measured and analysed in accordance with Ohm's law.

All EIS measurements were carried out with a Zahner potentiostat.

References

1. Z. Hiezl, D. Hambley, W. E. Lee. *Preparation and characterisation of UO_2-based AGR SIMFuel.* s.l. : MRS Online Proceeding Library Archive 1665, 2014.

2. Z. Hiezl, D. Hambley, C. Padovani, W.E. Lee. *Processing and microstructural characterisation of a UO_2-based ceramic for diposal studies on spent AGR fuel.* s.l. : Journal of Nuclear Materials, 2014, Vol. 456. pp. 74-84.

3. Z. Hiezl. *Processing and microstructural characterisation of UO_2-based simluated spent nuclear fuel ceramics for the UK's advanced gas-cooled reactors.* s.l. : Imperial College London, 2015.

4. R.F. Burstall. *UK Atomic Energy Authority Report ND-R-328 (R).* 1979.

5. N. Rauff-Nisthar, C. Boxall, D. Hambley, Z. Hiezl, C. Padovani, R. Wilbraham. *Corrosion behaviour of AGR SIMFUELs.* s.l. : ECS Transactions, 2015, Vol. 66. p.p. 85-94.

6. R.C. Williamson. *Mechanisms of fixed contamination of commonly engineered surfaces.* s.l. : Lancaster University, 2015.

7. R.J. Wilbraham. *Surface Decontamination by Photocatalysis.* s.l. : Lancaster University, 2011.

8. Alvatek. http://www.alvatek.co.uk/mf-2150/ [Online].

9. M.F. Huerta. *The Graphene Ring Nanoelectrodes (GRiNs) and its application as an electroanalytical sensor for environmental monitoring.* s.l. : Lancaster University, 2020.

10. H.A. Becerril, J. Mao, Z. Liu, R.M. Stoltenberg, Z. Bao, Y. Chen. *Evaluation of solution-processed reduced graphene oxide films as transparent conductors.* s.l. : American Chemical Society - Nano, 2008, Vol. 2. pp. 463 - 470.

11. B. Kienzler, V. Metz, L. Duro, A.Valls. *2nd annual workshop proceedings of the collaboratie project 'fast/instant release of safety relevant radionuclides from spent nuclear fuel'.* Antwerp : KIT Scientific Reports 7676, 2013.

12. C. Anwyl, C. Boxall, R. Wilbraham, D. Hambley, C. Padovani. *Corrosion of AGR fuel pin steel under conditions relevant to permanent disposal.* s.l. : Procedia Chemistry, 2016, Vol. 21. pp. 247 - 254.

13. Princeton Instruments. http://web.pdx.edu/~larosaa/Applied_Optics_464-564/Projects_Optics/Raman_Spectrocopy/Raman_Spectroscopy_Basics_PRINCETON-INSTRUMENTS.pdf [Online].

14. S. Wapp. *Scanning Electron Microscopy.* https://serc.carleton.edu/research_education/geochemsheets/techniques/SEM.html [Online].

15. B. Krishanu. *Scanning Electron Microscopy (SEM).* s.l. : Indian Institute of Technology Kanpur.

16. J.I. Goldstein, D.E. Newbury, J.R. Michael, N.W.M. Ritchie, J.H.J. Scott, D.C. Joy. *Scanning Electron Microscopy and X-ray microanalysis.* s.l. : Springer, 2018.

17. A. Mukhopadhyay. *Measurement of magnetic hysteresis loops in continuous and patterned ferromagnetic nanostrutures by static magneto-optical kerr effect magnetometer.* Guwahati : Indian Institute of Technology, 2015.

18. N. Mehrban, J. Bowen. *Monitoring and evaluation of biomaterials and their performance in vivo.* s.l. : Woodhead Publishing, 2017.

19. S. Ebnesajjad. *Surface treatment of materials for adhesive bonding.* s.l. : Elsevier, 2014.

20. N. Elgrishi, K.J. Rountree, B.D. McCarthy, E.S. Rountree, T.T. Eisenhart, J.L. Dempsey. *A practical beginner's guide to cyclic voltammetry.* s.l. : Journal of Chemical Education, 2018, Vol. 95. pp. 197 - 206.

21. A. Quigora. *Cyclic Voltammetry.* s.l. : LibreTexts, 2019.

22. M. Pandiarajan, S. Rajendran, J.S. Bama, R.J. Rathis, S.S. Prabha. *Applications of cyclic voltammetry in corrosion inhibition studies.* s.l. : International Journal of Nano Corrosion Science and Engineering, 2016.

23. T. Paschkewitz. *Open Circuit Potential (OCP).* https://pineresearch.com/shop/kb/software/methods-and-techniques/basic-methods/open-circuit-potential-ocp/ [Online].

24. Y.S. Jimenez, M.T. Gil, M.T. Guerra, L.S. Baltes, J.C.M. Rosca. *Interpretation of open circuit potential of two titanium alloys for a long time immersion in physiological fluid.* s.l. : Bulletin of the Transilvania University of Brasov, 2009, Vol. 2.

25. Gamry Instruments. *Basics of Electrochemical Impedance Spectroscopy.* https://www.gamry.com/application-notes/EIS/basics-of-electrochemical-impedance-spectroscopy/ [Online].

26. Guelph Physics. *Ohm's Law.* https://www.physics.uoguelph.ca/tutorials/ohm/Q.ohm.intro.html [Online].

27. C. Reece. *An introduction to electrochemical impedance spectroscopy (EIS).*

28. C. Breitkopf, *Impedance Spectroscopy - old technique - new applications.* s.l. : Technische Universitaet Dresden, 2012.

29. A. V. Oppenheim, A. S. Willsky. *Signals and Systems.* s.l. : Prentice Hall, 1996.

30. I. Morkvenaite-Vilkoniene, A. Valiuniene,J. Petroniene, A. Ramanavicius. *Hybrid system based in fast Fourier transform electrochemical impedance spectroscopy combined with scanning electrochemical microscopy.* s.l. : Electrochemistry Communications, 2017, Vol. 83, pp. 110 -112

Chapter 3 Characterisation of UO_2 & SIMFUEL Samples

3.1 Introduction

This chapter presents a study of the baseline corrosion behaviour UO_2 and the UO_2 SIMFUELs described in Chapter 2, in inert sodium sulfate electrolyte under near-neutral pH conditions. The two principal techniques used in this study are electrochemistry (voltammetry and chronopotentiometry) and spectroscopy. In the case of the latter, Raman spectroscopy is used. Thus, the next section is concerned with a description of the main features of Raman spectroscopy, before presenting and discussing the experimental results.

3.2 Features of Raman Spectroscopy of UO_2

The Raman spectroscopic behaviour of UO_2 has been well studied in the literature by the likes of Shoesmith (1), Guimbretiere (2) and He (3). Figure 3-1 below shows a typical Raman spectrum taken of a sintered UO_2 sample with a composition close to stoichiometric, recorded by He *et al.* (4). The principal features of this spectrum, as assigned by He *et al.* are as follows:

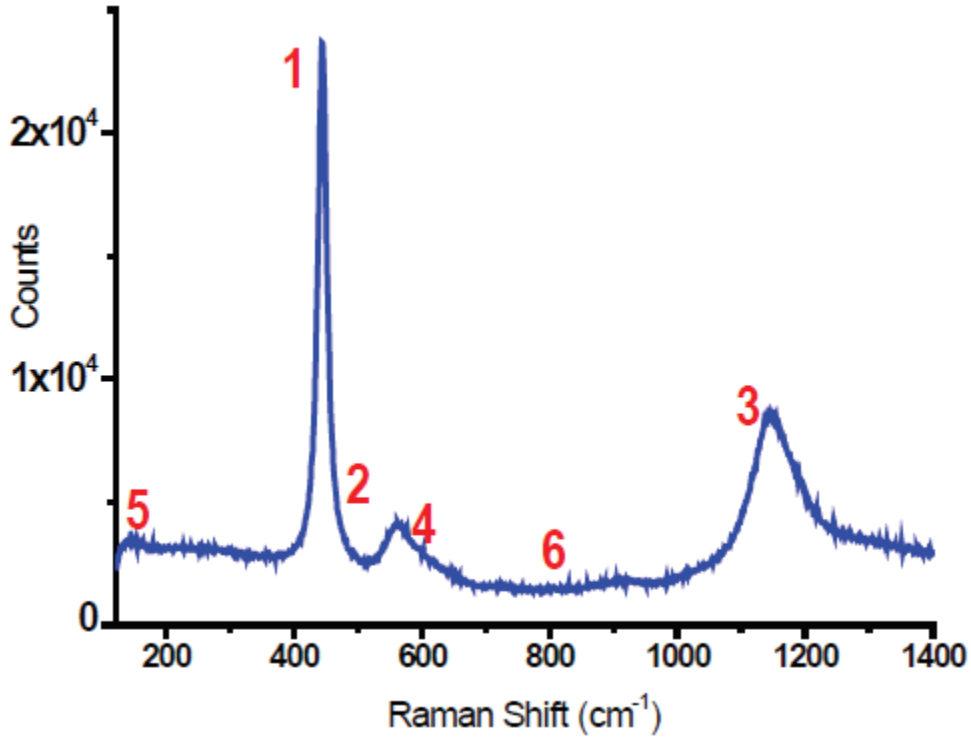

Figure 3-1 showing a typical Raman spectrum of near-stoichiometric UO_2 (4), recorded by He *et al*

(i) The dominant peak observed at 445 cm^{-1} (indicated as number 1 in Figure 3-1) is attributed to the fundamental O-U stretch in the cubic UO_2 lattice, which exhibits a perfect cubic fluorite structure. If a loss in intensity were to occur in this peak, it would indicate deviations from the perfect cubic fluorite structure (4).

(ii) The broader peak located at 1150 cm^{-1} (peak 3 in Figure 3-1) is the first overtone of a Longitudinal-Optical (L-O) phonon band at 575 cm^{-1}, the band at 575 cm^{-1} being IR active but selection rule forbidden in the Raman – and thus absent in table 3-1. As this peak has been attributed to vibrations of the lattice structure, it is sensitive to lattice distortions. Such distortions will impede propagation of the phonon through the lattice and thus the strength of this band can be considered to be indicative of the presence of the fluorite structure; the stronger the band, the lower the degree of lattice distortion. This peak can therefore be considered as a fingerprint for the fluorite structure (5). It should be noted here that even though the band at a Raman shift of 575 cm^{-1} whilst being IR active, is selection rule forbidden in the Raman, the selection rule may be relaxed with the introduction of lattice distortions. This would allow for the 575cm^{-1} peak to be observed in samples containing such lattice distortions. These said lattice distortions may be expected to arise as a result of simulated burnup, which in turn would result from the consequent introduction of Ln(III) dopants and oxygen interstitials/vacancies into the urania matrix. We shall return to this point below.

(iii) The broad multi-component band in the region 500 to 700 cm^{-1} (peak 4 in Figure 3-1) is indicative of lattice distortion due to the presence of defects which are dependent on the availability of interstitial oxygens in the lattice structure, the UO_2 grain size, and the level of dopants, and possible associated oxygen vacancies, introduced. A recent study by Elorrieta *et al.* (6) shows that a broad peak between 500 – 700 cm^{-1} can appear where $x \geq 0.03$ in UO_{2+x}. This broad peak has been attributed to being the result of two peaks that are located around 560 and 630 cm^{-1}.The former may be associated with the fundamental of the L-O phonon band discussed above. The latter band has been observed at 630 cm^{-1} by Elorrieta *et al.* (6) has been attributed to be caused by the distortion of anion sublattices, which are caused by the excess of oxygen. Furthermore, this peak has also been attributed to be caused by Willis clustering, which is a structural defect of the U_4O_9 i.e. cuboctahedral symmetry. We shall return to the nature of this peak later.

(iv) The regions labelled as 5 (155 cm^{-1}) and 6 (approx. 800 - 900 cm^{-1}) indicate phenomena which would be expected to develop to UO_{2+x} or higher stoichiometric oxides as a result of fuel oxidation. The former is due to a tetragonal structure induced by major distortions of both the O and U sublattices, arising from oxygen being incorporated into the UO_2 matrix. The latter is due to the presence of uranyl ion-containing phases such as studtite or metastudtite, appearing as surface entities (7).

(vi) Although not present in the spectrum of Figure 3-1, the appearance of a shoulder at ~470 cm^{-1} (peak 2 in Figure 3-1) would suggest the development of a tetragonal structure; i.e., a distortion of the cubic lattice along one axis.

3.3 Results & Discussion

Figure 3-2 below shows a 20-point averaged Raman spectrum of the UO_2 samples prepared at Springfields, Preston, as described in Chapter 2.

Confirmation that this sample is stoichiometric UO_2 is provided by the XRD of the same specimen, Figure 3-3 immediately below Figure 3-2. Keeping this, and the peak assignments of Figure 3-1 in mind, the key features of the Raman spectrum of our UO_2 sample shown in Figure 3-2 will be described further on.

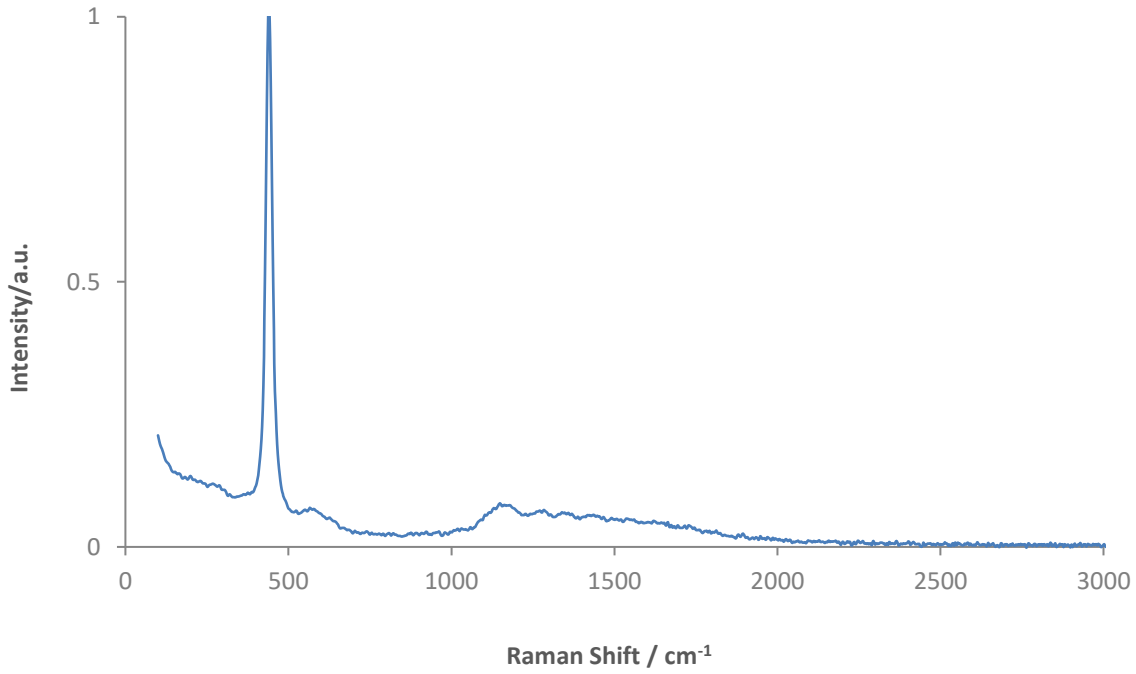

Figure 3-2 showing a 20-point averaged Raman spectrum of as-received undoped UO_2, normalised to the fundamental UO peak

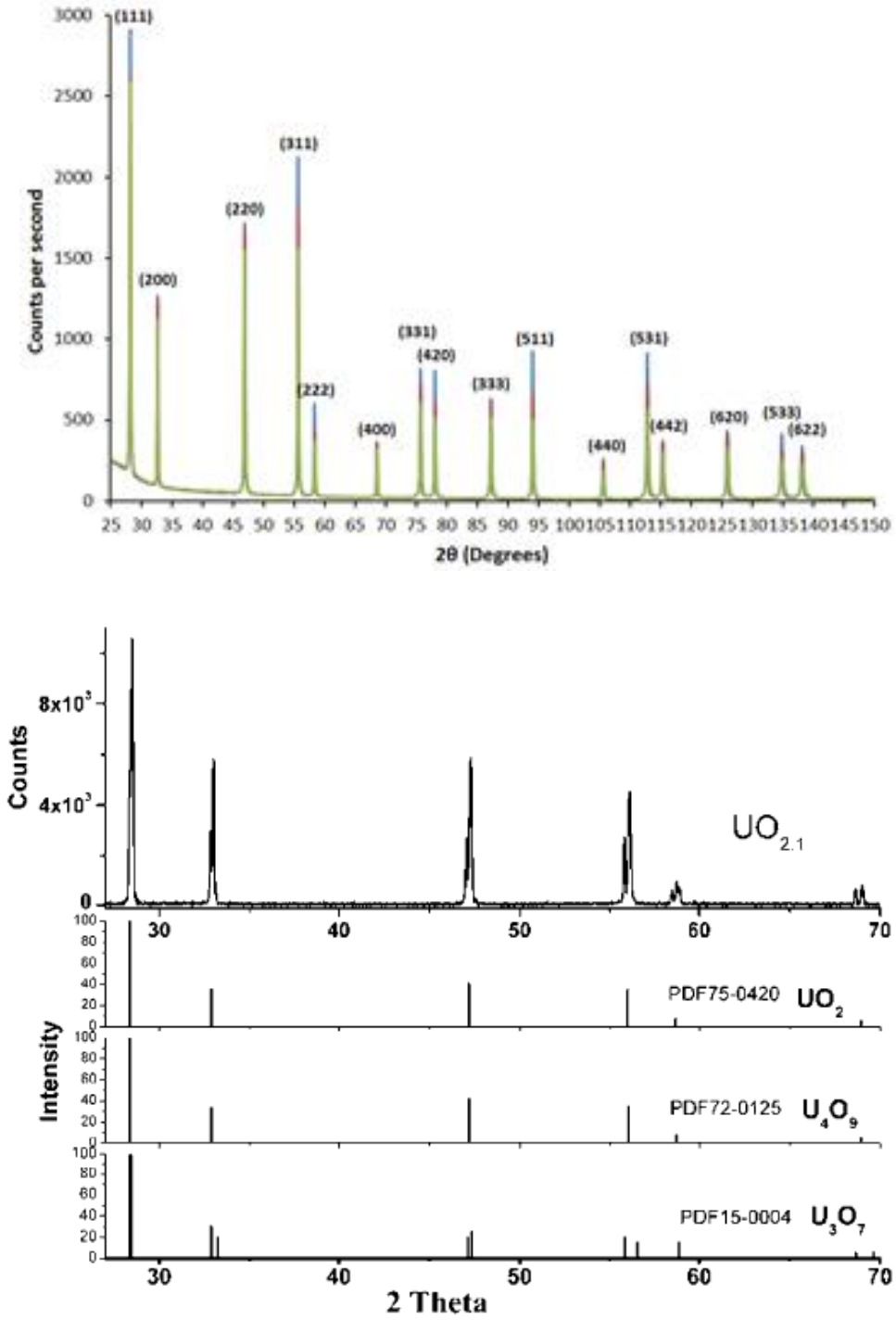

Figures 3-3a & 3-3b showing the XRD data of the undoped UO_2 sample taken by Wilbraham *et al*. (8), and an XRD from literature showing samples of U_3O_7, U_4O_8, stoichiometric UO_2 and hyperstoichiometric UO_2, respectively

In Figures 3-3a and 3-3b above, we can see the XRD patterns recorded from our undoped UO_2 and SIMFUEL pellets, along with the XRD spectral data of U_3O_7, U_4O_8, UO_2 and $UO_{2.1}$ from the literature for comparison reasons. The XRD measurements on the UO_2 and SIMFUEL pellets were carried out by Wilbraham *et al.* at Lancaster University (8). If we look at the UO_2 sample from the literature (Figure

3-3b), we can see that the same peaks appear in the XRD of our UO_2 and SIMFUEL pellets. These peaks occur at 2 theta values of 28° (corresponding to reflections from the (111) plane), 33° (200), 47° (220), 56° (311), 59° (222) and 69° (400). However, the peaks observed in literature data for the XRD of UO_2, are very similar in position to the peaks that have been observed for U_4O_7 (Figure 3-3b). In order to distinguish between UO_2 and U_4O_7 in our samples, Wilbraham *et al*. have carried out lattice parameter measurements.

In order to calculate the lattice parameter, a Rietveld refinement of the entire XRD pattern was carried out using the Rietveld software MAUD (Material Analysis Using Diffraction) (8) (9). The resultant calculated lattice parameter for our undoped UO_2 pellet was then found to be 547.12 pm. This is different to the lattice parameter of 544.1 pm reported in a review by Elorrieta *et al* (6) for U_4O_9 and is close to the lattice parameter value of 547 ± 0.02 pm reported by He *et al.* for CANDU (Canada Deuterium Uranium) SIMFUEL (8) (10), and that of 547.08 pm reported for undoped stoichiometric UO_2 pellets prepared by Lucuta *et al*. (11) The above mentioned lattice parameter for our undoped UO_2 sample is also close to the more recently reported 547.127 ± 0.008 by Leinders *et al.* (12), which strongly suggests that our undoped UO_2 sample described here is also highly stoichiometric.

It is worth noting one final observation here from the data of Figure 3-3a. The lattice parameters of the 25 and 43 GWd/tU SIMFUEL samples, again calculated by Rietveld refinement of the entire XRD pattern, are found to be 546.85 and 546.79 pm, respectively. The change in lattice parameter in going from the undoped UO_2 to the 25 GWd/tU SIMFUEL corresponds to 0.109 pm per 10 GWd/tU simulated burnup. However, the change in going from the 25 GWd/tU to the 43 GWd/tU SIMFUEL is substantially smaller at 0.03 pm per 10GWd/tU simulated burnup. We shall return to the difference in these two values – as well as the origin of the contraction itself – later on.

Having confirmed that the uranium oxide matrix of our UO_2 and SIMFUEL samples is comprised of near stoichiometric UO_2, let us now return to the Raman spectra recorded from these materials. From Figure 3-2 above we can see that our undoped UO_2 sample does indeed correspond to the aforementioned peak assignments from Figure 3-1. At a Raman shift of 445 cm^{-1} we observe the fundamental UO stretch, followed by the broader peak located at 1150 cm^{-1}, which is the first overtone of a L-O phonon band and, as described above, a characteristic spectral fingerprint for the cubic fluorite phase. The absence in Figure 3-2 of all other peaks highlighted in Figure 3-1 indicates that this

is a near defect-free sample (evidenced by the absence of peaks at 470 and 500-700 cm^{-1}) with a low degree of excess oxidation (evidenced by the absence of peaks at 155 and 800-900 cm^{-1}).

Having looked at the fundamental Raman features of an undoped UO_2 pellet, we will now consider the Raman spectra of the low and high doped 25 & 43 GWd/tU, in comparison to the undoped UO_2 pellet. For ease of comparison, Figure 3-4 shows the Raman spectra of all three samples taken over a 20-point average over an expanded Raman shift range of 350 – 750 cm^{-1}. Restricting the wavenumber values to this range allows for the compound peak at 500-700 cm^{-1} to be inspected in greater detail, but also means that the longitudinal overtone at 1150 cm^{-1} of the first order L-O phonon band located at 575 cm^{-1} (13), which is sensitive to lattice distortions (as described in Figure 3-1 above), is not shown in this figure, although it is seen in all three samples. As previously described, the band at 575 cm^{-1} is absent in undoped UO_2 but is observed with increased burnup due to the introduction into the urania matrix of lattice defects associated with e.g. the ingrowth/addition of rare earth lanthanides. However, as the band at 1150 cm^{-1} is an overtone of the band at 575cm^{-1}, it can be assumed that any changes in the spectra at 575 cm^{-1} as a result of increased simulated burnup in these samples would translate to the overtone at 1150 cm^{-1} too. Thus, the band at 1150 cm^{-1} need not be considered separately in the context of Figure 3-4.

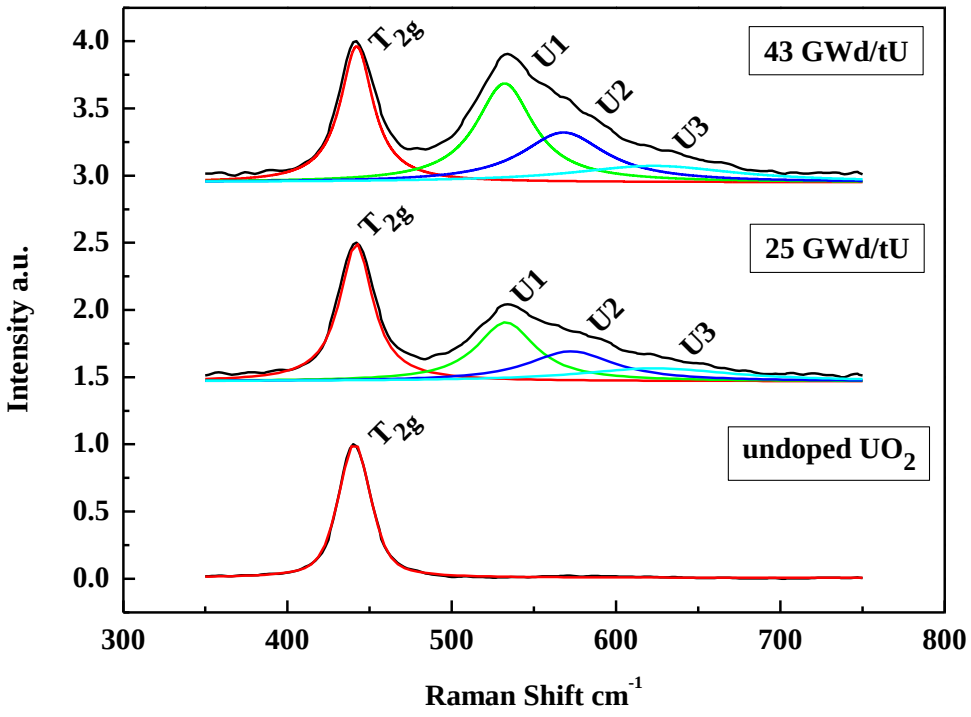

Figure 3-4 showing the Raman spectra of the UO_2 and 25 & 43 GWd/tU SIMFUEL pellets as received, represented as Lorentzian

Turning to the peaks that are shown in the spectral range studied in Figure 3-4, the spectrum for the undoped UO_2 sample is again typical of a Raman Spectroscopy measurement of UO_2, with a strong absorbance at 450 cm^{-1} due to the fundamental UO stretch of the cubic fluorite structure. Indeed, this feature is observed in the spectra of the 25 & 43 GWd/tU SIMFUEL pellets as well, confirming that the urania phases in all samples have the cubic fluorite structure.

The principal difference between the spectra of the SIMFUEL pellets and the unadulterated UO_2 pellet is the presence of a broad peak in the range 500-700 cm^{-1}. As described in section 3.1, this is a compound feature indicative of the presence of lattice defects; as such, it may be deconvoluted into a number of component peaks.

In order to deconvolute the various component peaks that comprise this band, a second derivative analysis was used to determine the peak wavenumber positions of the main spectral contributors in

the range 350-750 cm^{-1}, as per Elorrieta *et al*. (6). Having determined the main contributors, a multiple unconstrained Lorentzian fit was conducted using an iterative least-squares fit at the obtained wavenumber values. The fit analysis using this method for an area of the 25 GWd/tU SIMFUEL sample is shown in Figure 3-4 (middle spectrum), which reveals that three overlapping peaks can be identified with maxima at the following wavenumbers: ~530 cm^{-1}, ~575 cm^{-1} and ~630 cm^{-1}. Similar peaks, in terms of number, position and relative intensities, are observed in the deconvoluted spectrum for the 43 GWd/tU simulated burnup sample, also shown in Figure 3-4 (upper spectrum).

These peaks, labelled U1, U2 and U3 respectively, may be assigned as follows:

U1 – with an absorption maximum at 530 cm^{-1}: this peak is attributed to a local phonon mode related to oxygen-vacancy induced lattice distortion. These oxygen vacancies are generated to part-charge compensate for the presence of 3+ lanthanide dopants. As the simulated burn-up increases there is a marked increase in lanthanide concentration. Thus, this peak is larger for the 43 GWd/tU SIMFUEL pellet than for the 25 GWd/tU SIMFUEL pellet (14).

U2 – with an absorption maximum at 575 cm^{-1}: this peak is attributed to the fundamental of the longitudinal optical phonon overtone peak seen at ~1150 cm^{-1}, the fundamental being selection rule forbidden in pure UO_2. The structure of UO_2 matrix deviates from the perfect fluorite structure in the SIMFUEL samples due to the presence of oxygen-vacancy sites (see U1 above), defect clustering (see U3 below) and hyperstoichiometry – the latter caused by O^{2-} ion incorporation into the interstitial sites in the UO_2 fluorite matrix, forming UO_{2+x} (6) (see Chapter 1 Figure 1-14 showing schematic representation of the cubic fluorite structure of the UO_2 lattice (15)). This results in the break-down of selection rules and the observation of the fundamental absorption band at 575 cm^{-1}. As the structure becomes more hyperstoichiometric and transformation to a tetragonal structure begins, there is an associated decrease in this peak (14). However, there is a small increase in this peak with simulant burn-up of the SIMFUELs. Thus, this is attributed to the introduction of lanthanides resulting in increased oxygen-vacancy sites (16). Hyperstochiometry is unlikely to be the cause for reasons highlighted in the following point (14).

U3 – with an absorption maximum at 630 cm^{-1}: This peak is attributed to the presence of clusters of interstitial oxygen i.e. is due to the hyperstoichiometry of UO_2 as it transitions to form U_4O_9 with increasing x. In a study conducted by Elorrieta *et al*., it was also seen that the band observed at a Raman shift of approx. 630 cm^{-1} continues to increase in intensity as the amount of oxygen content increases (17). Curiously, for the SIMFUEL samples examined here, the 630 cm^{-1} peak decreases slightly with increased burn-up. A possible explanation for this is that at high dopant levels the number of sites that may accommodate oxygen interstitials is decreased (18) – or that additional oxygens that may otherwise reside interstitially are instead filling oxygen vacancies associated with Ln(III) dopants. However due to its weak intensity (indicative of a low level of hyperstoichiometry), interpretation of this peak should be considered with caution (14).

The U1 and U2 peaks are especially noteworthy. This is because, as discussed above, it is the fundamental L-O phonon band that is selection rule forbidden in pure (undoped) cubic fluorite UO_2. In Figure 3-4, we can clearly see that the bands U1 and U2, increase in intensity as we move from the low doped 25 GWd/tU SIMFUEL pellet to the high doped 43 GWd/tU SIMFUEL pellet. This has been attributed to UO_2 lattice damage, due to the defects that are formed caused by the introduction of dopants (10) and interstitial oxygens. As the effective burnup of the pellets increases, the amount of oxygen interstitials that are available in the lattice structure may also increase. This is possibly due to the fact that the UO_2 grain size decreases as effective burnup is increased as shown in Chapter 2 Figures 2-3 - 2-5. Hiezl *et al.* (19) have hypothesised that this variation in grain size may be due to a higher degree of liquid phase sintering obtaining during firing of the SIMFUEL samples compared to the pure UO_2 samples where a simple solid phase sintering mechanism may dominate. Contrary to the 575 cm^{-1} band, the broad L-O phonon band at 1150 cm^{-1}, which is an overtone of the longitudinal 575 cm^{-1} band, and which is not shown here, does not grow in intensity with increased burnup. In actual fact, the intensity of the 1150 cm^{-1} band decreases with increased simulated burnup, with an almost identical trend to that of the fundamental UO stretch at 445 cm^{-1}. For both these peaks (the 445 and 1150 cm^{-1}), the intensity of the peak decreases with increased burnup. As the simulated burnup is increased, there is also an increase in the defect population of the UO_2 crystal structure. This in turn will result in increased phonon scattering, hence reducing the intensity of the 2 L-O phonon band.

Having discussed the Raman features of our UO_2 and SIMFUEL samples in detail, we will now move on to discuss the main features of their respective electrochemistries before presentation of a discussion of coupled Raman-electrochemical experiments and what they can tell us about the equilibrium

corrosion behaviour of each sample. We begin by discussion of electrochemical measurements on UO_2 presented in the literature and their interpretation.

Figure 3-5 below shows a cyclic voltammogram of a UO_2 thin film electrode recorded by Seibert *et al.* (20) with their proposed assignments for the reactions occurring in each region of the voltammogram, the principal regions of interest here being labelled A, C, D, E and F. These may be summarised as follows (20).

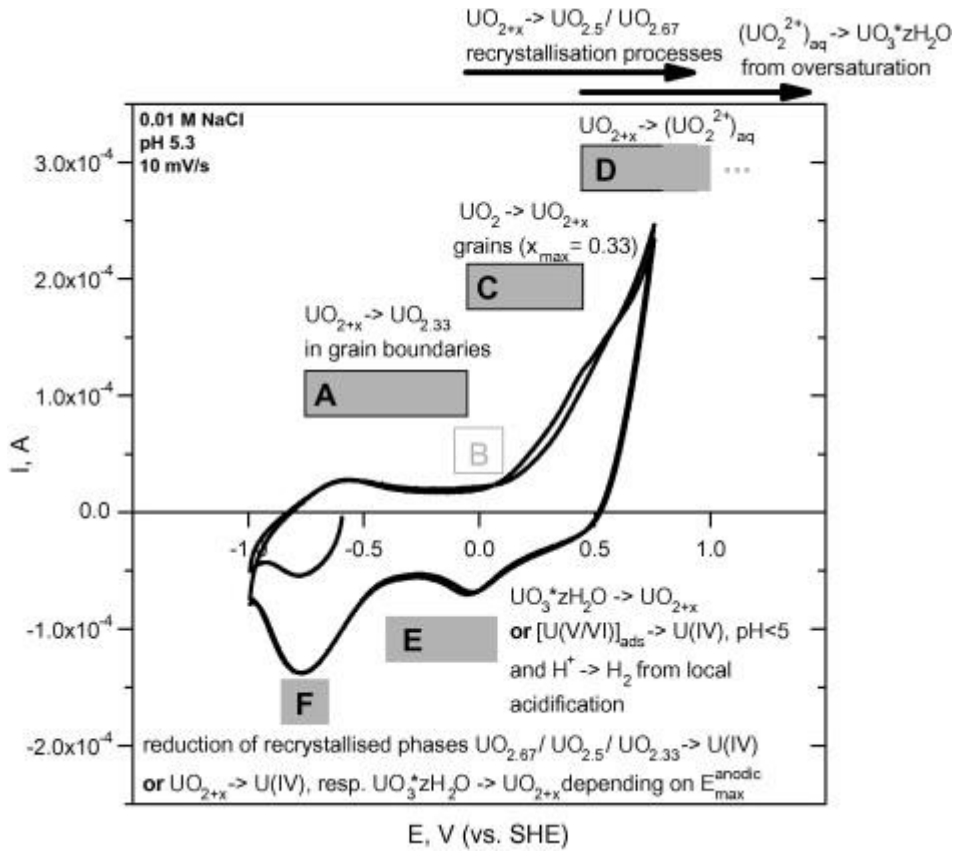

Figure 3-5 showing the cyclic voltammogram of a UO_2 thin film electrode, with proposed reactions (20)

1. Region A: The broad oxidation peak observed between approximately -1 and -0.5 V_{SHE} is attributed to the oxidation at the grain boundaries of UO_{2+x} sites with differing energies to a higher oxidation state $UO_{2.33}$ (this is in contrast to the bulk sites in the UO_2 grains) (20)

2. Region C: A distinct shoulder can often be observed in this region. The oxidation of UO_2 in grains up to a limiting stoichiometry of $UO_{2.33}$ is expected to occur between – 0.06 – 0.44 V_{SHE}. In basic pH solutions, a mixed U(IV)/U(V) surface layer can be found in the potential range up

to 0.24 V_{SHE}. It is also assumed here that the injection of O^{2-} into the interstitial sites of the fluorite lattice generates a film growth process, which is accompanied by the oxidation of U(IV) to U(V). An increase in potential brings about further oxidation to U(VI). Oxidation beyond $UO_{2.33}$ (which marks the end of the fluorite structure range) would involve the dissolution of U(V/VI), as well as a recrystalisation process via adsorbed UO_2^{2+} species up to $UO_{2.5}$ and $UO_{2.66}$ (20)

3. Region D: In this region, which is above 0.44 V_{SHE}, the current is observed to continue to increase, which indicates that further oxidation of the UO_{2+x} film to soluble UO_2^{2+} is taking place. Depending on the pH of the solution, UO_2^{2+} will have limited solubility and may re-precipitate as either schoepite ($UO_3.2H_20$) or metaschoepite ($UO_3.H_2O$). Even though these UO_3 phases are insulators, they are believed to be porous, meaning that they do not stop the corrosion reactions, and can in some cases even increase the UO_2^{2+} dissolution by local acidification. At pH levels below 5, there is a suppression of the growth of the $UO_{2.33}$ film (20)

4. Region E: This region (peak appearing at – 0.2 V_{SHE}) is observed during the cathodic scan, which is the reduction of the above mentioned oxidation layers. For pH values below 4, this peak is assumed to show the reduction of higher oxidised U atoms, or the reduction of H^+ ions to H_2 due to the acidification process. For solutions above pH 4, the uranium is believed to be U(VI) from the above-mentioned precipitated schoepite or metaschoepite. The thickness of this layer, which is predominantly dependent on the pH of the solution, determines the height of the observed peak (20)

5. Region F: In neutral to alkaline solutions, the peak appearing at approximately -0.76 V_{SHE} is attributed to the reduction of underlying $UO_{2.33}/UO_{2+x}$ oxide layers which were generated in Region C. The peak can also be attributed to the higher oxides, namely $UO_{2.5}$ or $UO_{2.67}$ building up in the recrystralisation and/or reduction reactions from the adsorbed U(VI). The height of this peak has been found to directly correlate with the maximum anodic potential that the sweep is driven to, as well as the time allowed for oxidation to take place (20)

Having looked at the regional assignments from the literature, we have adapted these assignments to the cyclic voltammetry of our undoped UO_2, 25 & 43 GWd/tU SIMFUEL samples. These can be found in Figure 3-6 below.

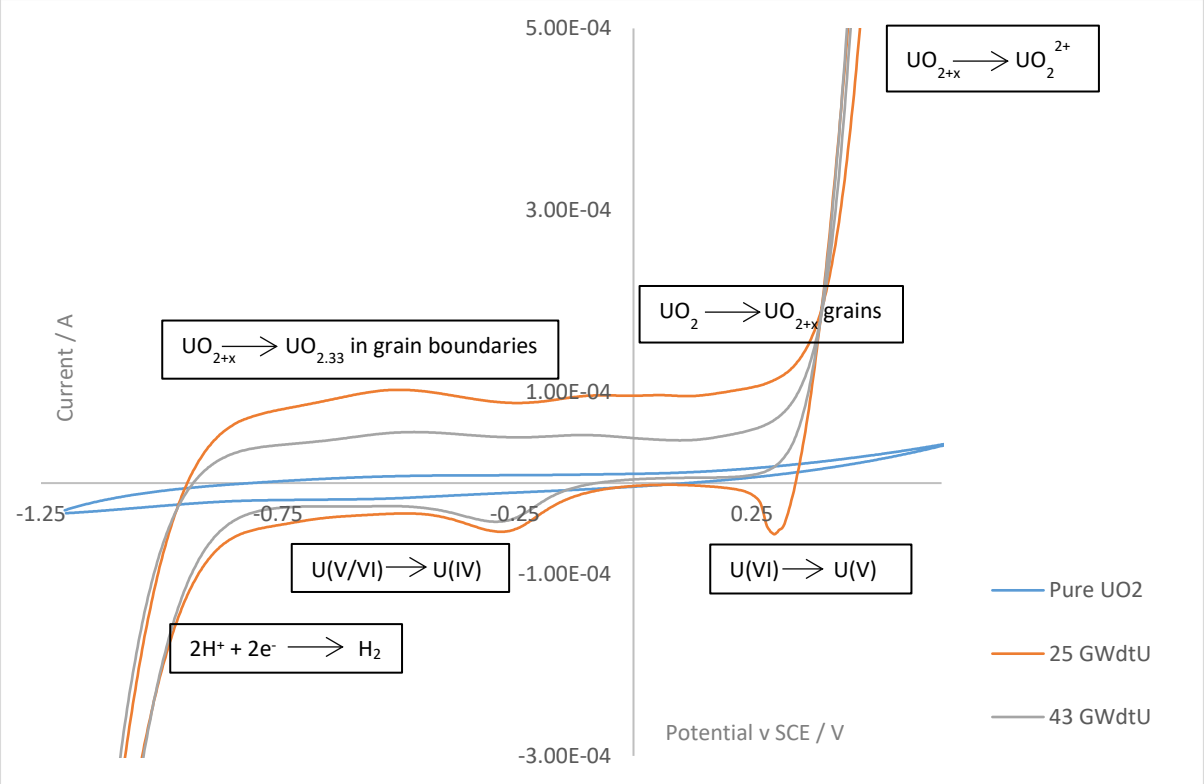

Figure 3-6 showing cyclic voltammograms of UO_2, 25 & 43 GWd/tU SIMFUEL pellets in a 0.1 mol dm^{-3} Na_2SO_4 background electrolyte, cycled at a potential range of (-) 1.2 to (+) 0.7, at a scan rate of 10 mV/s, adapted from Seibert *et al* 2011 (20)

Figure 3-6 above shows the cyclic voltammograms of the undoped UO_2, 25 & 43 GWd/tU SIMFUEL pellets in a 0.1 mol dm^{-3} Na_2SO_4 background electrolyte. The main difference in assignments between the cyclic voltammograms seen in Figure 3-6 and those of Figure 3-5 is that there is a large reduction current seen at approximately - 1 V_{SCE} on the SIMFUEL samples. Such a large reduction wave is not seen on the pure UO_2 sample of Figure 3-6 or Figure 3-5. This wave may be assigned to hydrogen evolution – a reaction promoted on the SIMFUEL samples by the presence of epsilon particles at the material surface. Such epsilon particles are predominantly comprised of noble metals which are typically good electrocatalysts for H^+ reduction / hydrogen generation.

We can see that the undoped UO_2 pellet has the lowest electrochemical activity out of the three samples. This is evident by the fact that the UO_2 pellet is not 'carrying' current during the scans. As the amount of dopants is increased from the undoped UO_2 pellet to the 25 GWd/tU SIMFUEL pellet, the electrochemical reactivity increases, due to the amount of dopants and metallic particles present in the SIMFUELs, meaning that the doped pellets are more efficient charge carriers.

Looking at the three samples of Figure 3-6 it can be seen that the difference in electrochemical reactivity between the three samples is not uniform. The difference between the undoped UO_2 and low doped 25 GWd/tU SIMFUEL samples is significantly larger than the electrochemical reactivity observed between the low and high doped 25 & 43 GWd/tU SIMFUEL samples.

The trend that we see here in electrochemical activity and conductivity, mentioned above, is similar to that seen for the lattice parameters for the undoped UO_2 and SIMFUELs samples as determined in Figure 3-3a. With regards to the lattice parameters, the trend we observe is that the lattice parameter is greatest for the 43 GWd/tU SIMFUEL, closely followed by the 25 GWd/tU SIMFUEL, with the undoped UO_2 exhibiting the smallest lattice parameter. In other words, the major change in each material property is seen going form the undoped UO_2 to the 25 GWd/tU SIMFUEL, with only marginal changes or even counter-intuitive decreases in going from the 25 to the 43 GWd/tU SIMFUEL samples. Both these trends may be explained by the fact that both these effects have a common origin – specifically the addition of lanthanide dopants in to the UO_2 lattice with increasing burnup.

In order to compensate for the resultant charge imbalance in the urania matrix resulting from the introduction of Ln(III) species, some of the U(IV) ions adopt a U(V) oxidation state. The presence of these U(V) sites has a profound effect on both the lattice parameter and the electrical properties of the UO_2 matrix. Let us consider the effects on the lattice parameter first.

In terms of the lattice parameter trend, this phenomenon can be explained by the fact that there is an observed contraction of the UO_2 lattice upon introduction of trivalent lanthanide dopants. The dependence of the UO_2 lattice parameter on lanthanide dopant concentration has been described by Ohmichi *et al* (21), with an additional analysis provided by Ho *et al* (22). Both studies concluded that the dependence of the lattice parameter on the type and level of trivalent lanthanide doping in UO_2 systems was a function of two opposing lattice expansion and contraction effects (8). These effects are described below:

(1) An expansion of the lattice arising from the incorporation of Ln^{3+} ions consisting of ionic radii larger than that of the native U^{4+} ions whilst at the same time creating an accompanying charge compensating oxygen vacancy

(2) A contraction of the lattice arising from the formation of U(V) ions that are created to charge compensate for the incorporation of 3+ Ln ions into the UO_2 matrix, the U(V) ionic radius being significantly smaller than that for U^{4+} (84 pm and 100 pm respectively) (23)

The change in lattice parameter that has previously been reported can be taken to be a combination of the two explanations above, with the latter having a greater effect on lattice parameter than the former. This explanation is consistent with two further experimentally observed phenomena (8):

(1) An increase in the magnitude of the lattice parameter contraction exhibited when the concentration in the UO_2 lattice of a Ln^{3+} dopant is increased (24) (21) – which is consistent with Vegard's Law (25)

(2) A decrease in the magnitude of the lattice parameter contraction exhibited when the atomic number of the dopant is decreased, and thus ionic radius is increased, along the lanthanide period at a constant dopant concentration (25) (22)

Looking at measured lattice parameter data of the high doped 43 GWd/tU SIMFUEL pellet, this sample showed a smaller lattice parameter than that measured for the low doped 25 GWd/tU SIMFUEL sample (8). In other words, the UO_2 crystal lattice is further contracting with higher simulated burnup. Comparing the measured lattice parameter data to the FISPIN calculations of dopant compositions (Chapter 2 Table 2-1), we can see that the concentration of dissolved lattice contracting elements (Nd^{3+}, $Ce^{3+/4+}$ and Zr^{4+}) in the UO_2 lattice approximately doubles with the doubling in burnup (8).
However, Wilbraham *et al.* (8). have highlighted the fact that the difference in the size of the contraction between the low doped 25 and high doped 43 GWd/tU SIMFUEL pellets, which is approximately 0.03 pm per 10 GWd/tU simulated burnup, is less than that observed between the undoped UO_2 reference sample and the 25 GWd/tU SIMFUEL pellet, which is 0.109 pm per 10 GWd/tU of simulated burnup (8) – a difference that we also highlighted in our discussion of Figure 3-3a above. One possible explanation for this by Wilbraham *et al.* is that at least one of the main lattice parameter contraction-inducing dopants (Nd^{3+}, $Ce^{3+/4+}$ or Zr^{4+}), is wholly or partially partitioning into segregated precipitate phases, such as the grey phase particulates, in the higher doped SIMFUEL samples (8). Such a partitioning of dopants would result in a reduced lattice contraction, especially if they were in the dissolved state (8). Looking at the SEM-EDX data by Hiezl (see Figure 2.6a, Chapter 2) (19), which was conducted within the scope of this works' consortium, we can see that there are grey phase precipitates in both low and high doped AGR SIMFUELs. The data also shows that there is some Ce, La

and Nd present in the grey phases of the high doped 43 GWd/tU SIMFUEL pellets only. In particular it can be seen that Ce is present in much higher amounts in the grey phase precipitates compared to its added concentration than either Nd or La in the 43 GWd/tU SIMFUEL sample.

Looking at the atomic modelling simulations that have been conducted by Cooper *et al.* (26) with respect to the partitioning of some of the tetravalent and trivalent ions into $BaZrO_3$ and $SrZrO_3$ phases, we can see that they predict, based on calculations of the partition energy of In^{3+}, Lu^{3+}, Er^{3+}, Y^{3+}, Dy^{3+}, Gd^{3+}, Sm^{3+}, Nd^{3+}, Pr^{3+}, La^{3+}, Am^{4+}, Pu^{4+} and Np^{4+} and Ce^{4+} into $BaZrO_3$ and $SrZrO_3$, that both medium ionic radii trivalent ions (radii < Sm^{3+}) and the tetravalent cations are unlikely to segregate into the grey phase. However, large ionic radii trivalent cations such as Nd^{3+}, La^{3+} and Ce^{3+} may partition from UO_2 into $BaZrO_3$. In light of these calculations and considering

(i) the increased prevalence of grey phase material in the 43 GWd/tU AGR SIMFUEL compared to our lower burnup samples, and
(ii) the increased concentration of Nd and Ce in the 43 GWd/tU samples, see Table 3-1;

segregation of at least some part of these elements to the grey phase at the higher 43 GWd/tU burnup seems likely and thus the cause of the decrease in the magnitude of the lattice parameter contraction with respect to expected values observed in our higher burnup samples.

Similar arguments that have been discussed above with respect to the lattice parameter also apply for the electrochemical activity and conductivity of the undoped UO_2 and 25 & 43 GWd/tU SIMFUEL samples. As can be seen from Figure 3-6, the 25 GWd/tU SIMFUEL sample carries significantly more current than the undoped UO_2 sample – this is again due to the presence of U(V) ions resulting from the introduction of Ln(III) ions into the urania matrix. As discussed in Chapter 1, the undefected and undoped UO_2 is a Mott-Hubbard insulator. The introduction of U(V) into the matrix however, results in the formation of electron vacancies or holes in the inter-band 5f level shown in Chapter 1 Figure 1-17 – resulting in the Ln(III) doped material subsequently exhibiting a p-type conductivity.

As in the case of the changes observed in the lattice parameter with simulated burnup, the change in electrochemical activity and conductivity can then also be understood in terms of the amount of added Ln (III) that partitions in to the solid solution matrix which induces the formation of U(V) species.

Initially, in going from UO_2 to the 25 GWd/tU SIMFUEL sample, a large increase in conductivity is observed as at least some of the Ln(III) ions added to the sample precursor blend enter the UO_2 matrix.

A smaller increase in conductivity would be expected in going from the 25 to the 43 GWd/tU SIMFUEL sample as some of the additional Ln(III) partitions in to the grey phase. Particularly as these grey phases are present at increased concentrations in the 43 GWd/tU SIMFUEL sample. The fact that however the conductivity actually appears to decrease, may be indicative of the fact that a proportionately greater amount of Ln(III) partitions in to the grey phase in the 43 GWd/tU SIMFUEL sample than in the 25 GWd/tU SIMFUEL sample. This effectively means that decreasing the concentration of U(V) sites in the 43 GWd/tU SIMFUEL sample compared to the 25 GWd/tU SIMFUEL sample, results in the apparent lower conductivity of the former with respect to the latter. Furthermore, a study conducted by He et *al*. suggests that doping at higher lanthanide levels may stabilise the fluorite lattice against anodic oxidation and dissolution by decreasing the amount of vacancy sites free for O_2^- - incorporation (10).

We will now look at open circuit potential (OCP) studies of the three samples and compare the data to the Raman spectra of the same samples recorded before and after OCP measurements. Figure 3-7b below shows the Raman spectra taken of the undoped UO_2, 25 & 43 GWd/tU burnup pellets taken after an OCP measurement, Figure 3-7a.

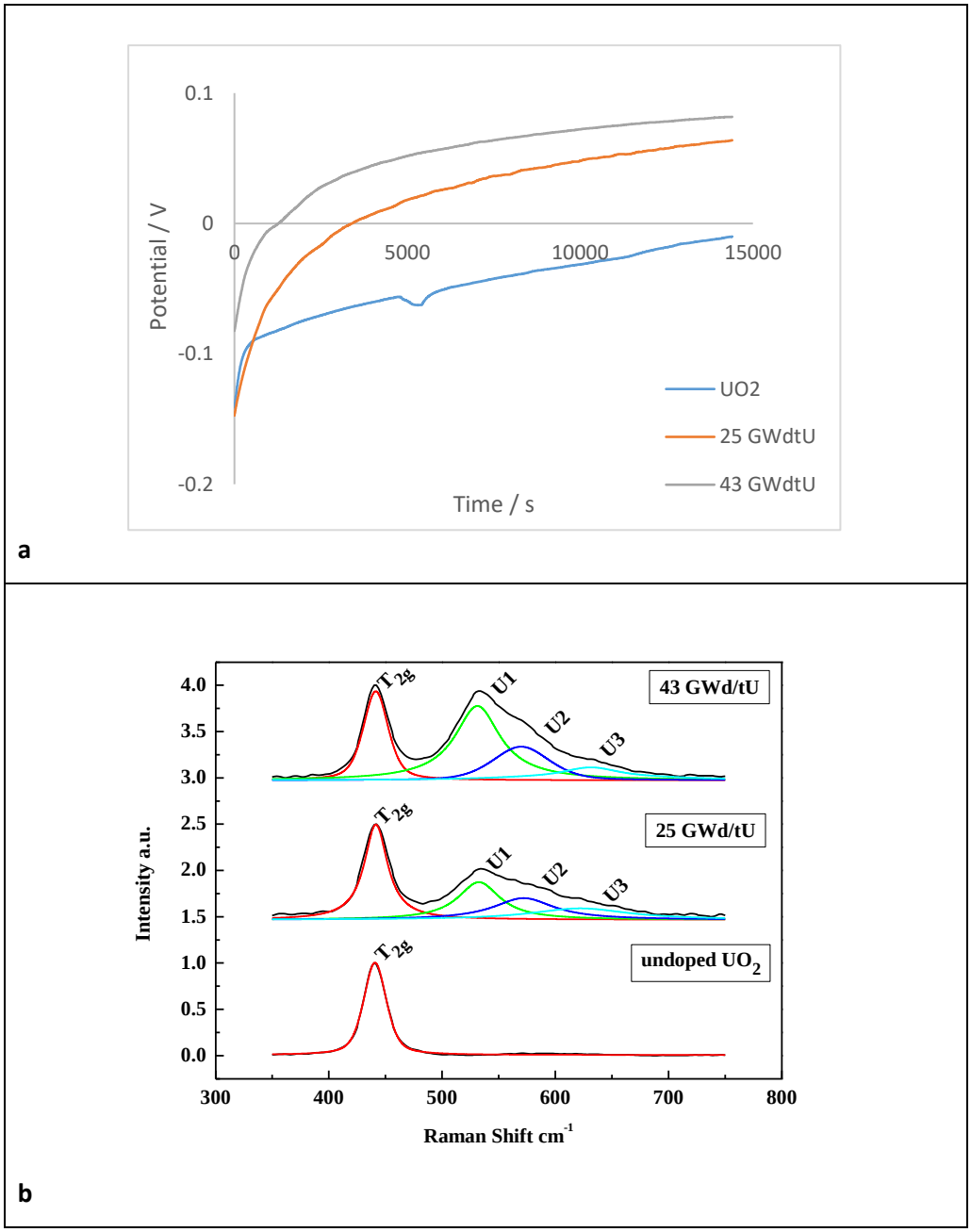

Figures 3-7a and 3-7b – (a) showing the open circuit potential of the UO_2 and 25 & 43 GWd/tU SIMFUEL pellets over a 4 hour period in a 0.1 mol dm^{-3} Na_2SO_4 background electrolyte, (b) the Raman spectra of the UO_2 and 25 & 43 GWd/tU SIMFUEL pellets after OCP measurements in Figure 3-7a

The OCP was taken in a 0.1 mol dm^{-3} sodium sulfate background electrolyte solution over a 4 hour period. As with the Raman spectra, there are differences between the OCP vs time trace recorded from the undoped UO_2 sample and those recorded from the SIMFUEL samples. Those differences may be summarised as follows.

1. The OCPs recorded from the SIMFUEL samples are more positive than those recorded from the undoped UO_2 sample, most likely due to the Fermi levels of the former having been shifted to more positive potentials by the introduction of lanthanide (III) ions into their respective urania matrices. This has also been observed by Howett et *al*. during OCP studies of UO_2 and SIMFUELs under similar conditions (27). As described above, this replacement of a fraction of the U(IV) ions in UO_2 with lower-valent Ln(III) ions requires further ionisation of the remaining uranium ions to maintain overall charge balance. This creates mobile holes in the U 5f band, rendering the samples p-type conductivity and shifting their Fermi levels to more positive potentials.

2. The SIMFUEL samples approach their equilibrium potentials at a faster rate than the undoped UO_2 sample, again as observed by Howett et *al.* (27). This is again most likely due to the higher concentration of charge carriers in the SIMFUEL samples derived from doping effects associated with the addition of fission product simulants to the SIMFUEL matrix. The higher charge carrier concentration will support higher exchange current densities at the surface of the SIMFUEL samples, with a consequent increase in charge transfer kinetics and thus also an increase in the rate of approach to equilibrium in the context of an OCP experiment.

The long-immersion time OCPs for the undoped UO_2, 25 GWd/tU and 43 GWd/tU SIMFUEL samples in 0.1 mol dm^{-3} Na_2SO_4 are observed to be -0.01 V, 0.05 V and 0.06 V respectively as shown in Figure 3-7a. If the long-immersion time OCP values are compared to their positions on their respective CV in Figure 3-6, it is seen that the OCPs of all samples sit on the anodic side of the current-voltage peak associated with the in-grain UO_2 to UO_{2+x} oxidation process. This indicates that under the near neutral conditions employed here, whilst all samples are gradually oxidising to form UO_{2+x}, formation of U(VI) is not as yet observed, again making grain dissolution highly unlikely. The conclusion that the in-grain UO_2 to UO_{2+x} oxidation process is slow is supported by the post-immersion Raman data of Figure 3-7b. Comparison of this with the corresponding pre-immersion data of Figure 3-6 indicates that both sets of spectra are near identical – suggesting that the immersion in the sodium sulfate electrolyte has not made any significant chemical and/or structural changes to the electrode surfaces in the timescale of the OCP experiments reported here.

It is worth noting that whilst the long-immersion time OCPs are consistent with potentials just positive of those associated with the onset of the in-grain UO_2 to UO_{2+x} oxidation process, suggesting that if

this process is occurring at all, it is occurring only slowly, they are significantly positive of the potential associated with the oxidation of UO_{2+x} to $UO_{2.33}$ at the grain boundaries. The rate at which this grain boundary corrosion process occurs is best studied by analysis of the potentiodynamic polarisation curves for these samples, shown in Figure 3-8 below.

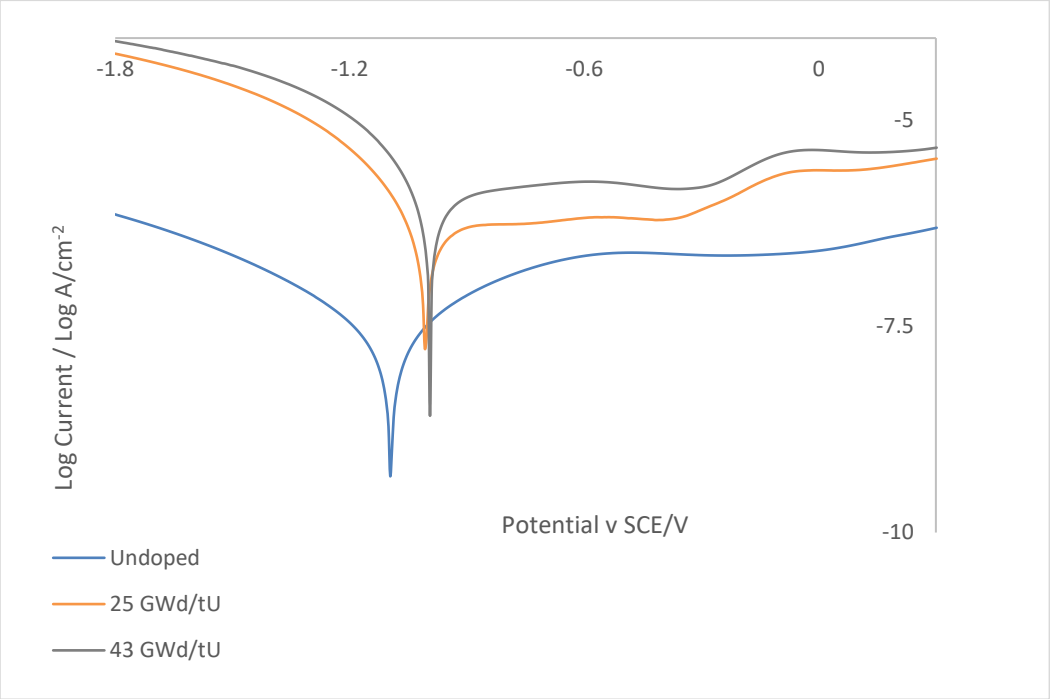

Figure 3-8 showing the potentiodynamic polarisation curve of an undoped UO_2, 25 & 43 GWd/tU SIMFUELs exposed to a 0.1 mol dm^{-3} Na_2SO_4 background electrolyte

From Figure 3-8 above, values of the corrosion potentials, E_{corr}, for the undoped UO_2, 25 and 43 GWd/tU SIMFUEL samples can be obtained, and are found to be -1.1, -1.01 and -1 respectively. The oxidation and reduction reactions controlling the corrosion potentials, E_{corr}, observed from these curves will correspond to the oxidation of UO_{2+x} at grain boundaries and the hydrogen evolution reaction respectively. The corrosion currents, i_{corr}, at the corrosion potential, calculated from the extrapolated crossing point of the anodic and cathodic arms of the polarisation curve either side of the E_{corr} are given in Table 3-1 below.

Sample	Undoped UO_2	25 GWd/tU	43 GWd/tU
i_{corr} / Amps cm^{-2}	3.15E-08	5.33E-07	1.14E-06

Table 3-1 showing corrosion current density of UO2, 25 & 43 GWd/tU SIMFUEL pellets

As expected, the corrosion current values are low, but can be seen to increase with increased doping. One explanation for this is that the higher concentration of metallic particles in the matrix of the SIMFUEL pellets allow a larger current to flow through, promoting hydrogen evolution, and allowing corrosion to occur at a faster rate. This can also be seen on the axis showing the log current, where we can see that a higher amount of current can pass through the 43 GWd/tU SIMFUEL pellet, than it can for the 25 GWd/tU SIMFUEL pellet. The undoped UO_2 pellet allows an even smaller amount of current to pass through its matrix. It is important to know where the onset of corrosion in the three samples in a background electrolyte is, before moving onto more complex systems. This will be the focus of the following chapters.

Finally, it is interesting to note that the i_{corr} for the 25 GWd/tU sample is 17 times that for the undoped UO_2 sample, whilst that for the 43 GWd/tU sample is only just over twice that for the 25 GWd/tU sample. Again, the smaller change observed in going from the 25 to the 43 GWd/tU SIMFUEL sample compared to that seen in going from the undoped UO_2 to the 25 GWd/tU SIMFUEL sample may potentially be due to Ln(III) ions partitioning into the grey phase to a greater extent in the higher burnup SIMFUEL compared to the lower burnup sample. This progression aside, it can still be seen that the SIMFUEL samples corrode at a faster rate than the UO_2 sample, albeit at a slow rate overall.

3.4 Conclusions

In conclusion, we were able to establish that our undoped UO_2 sample was stoichiometric UO_2 by comparing its XRD data to data from the literature (8). We were also able to eliminate the possibility that our sample could in fact be U_4O_7, by looking at the lattice parameter of our sample and comparing it to the literature values of UO_2 and U_4O_7 (6) (8) (11) (12).

Once we had confirmed that our sample was indeed stoichiometric UO_2, the peak assignments for a typical Raman spectrum of uranium dioxide were compared to our undoped UO_2 sample. We were able to confirm the fundamental UO stretch at a Raman shift of 445 cm^{-1}, as well as the multi-component peak at a Raman shift from 500-700 cm^{-1} in the 25 & 43 GWd/tU SIMFUEL pellets, indicating defects to the perfect cubic fluorite structure of UO_2 (14) (28). In order to deconvolute the multi-component peak, a 2nd derivate anaylsis was used to fix the peak maxima and represent the peaks as Lorentzian, as carried out by Elorietta *et al.* (6). Here we observed that the peak at a Raman shift of 530 cm^{-1} increases as the simulated burnup increases, as there is a marked increase in lanthanide concentration. Thus, this peak is larger for the 43 GWd/tU SIMFUEL pellet than for the 25 GWd/tU SIMFUEL pellet (14) (28).

The peak at a Raman shift of 575 cm^{-1} is due to a lattice phonon and is selection rule forbidden in undefected and undoped UO_2 (14) (28). As the hyperstoichiometry of UO_2 increases and its structure moves towards a tetragonal structure via a defected cubic fluorite structure, the selection rules start to relax, allowing for observation of this peak. There is an associated decrease in the intensity of this peak as the structure becomes more hyperstoichiometric (14), the associated defects acting as scattering centres for the lattice phonon. However, there is a small increase in this peak with simulant burn-up of the SIMFUELs (14) (28). The same has also been observed by Howett and Wilbraham *et al*, and has been attributed to the introduction of lanthanides resulting in increased oxygen-vacancy sites, allowing the selection rules to further relax (14) (28). The observed intensity of the band can thus be viewed as a convolution of an increase in intensity arising from defect induced relaxation of the selection rule, said increase mitigated against by a decrease in intensity arising from phonon scattering at the defect sites. At high defect loading, it can be expected that the peak will exhibit an overall decrease in intensity with increasing defect concentration – an expectation consistent with experimental observations of Elorrieta *et al*. (17).

The peak at a Raman shift of 630 cm^{-1} is attributed to the presence of clusters of interstitial oxygen and continues to increase in intensity as the amount of oxygen content increases, as observed by Howett & Wilbraham *et al.* (14) (28). However, the peak decreases slightly with increased burn-up (14) (28). As outlined by Howett, a possible explanation for this is that at high dopant levels the number of sites that may accommodate oxygen interstitials is decreased – or that additional oxygens that may otherwise reside interstitially are instead filling oxygen vacancies associated with Ln(III) dopants (14) (28).

The following trends were also observed in the cyclic voltammetry of the three samples after comparison to regional assignments as established by Seibert *et al*. (20). Initially, in going from UO_2 to the 25 GWd/tU SIMFUEL sample, a large increase in conductivity is observed as at least some of the Ln(III) ions added to the sample precursor blend enter the UO_2 matrix, and the U(IV) ions adopting a U(V) oxidation state to charge compensate (27). The same phenomenon has been reported by Howett *et al*. when comparing SIMFUELs to UO_2 samples. Whilst mobile holes are created in the U 5f band to maintain charge balance, an increase in conductivity is observed with the addition of trivalent rare earths (such as Ln (III) ions), especially in going from undoped UO_2 to SIMFUEL. This increase in conductivity is observed as the passage of higher electrochemical currents is allowed in the SIMFUELs as opposed to undoped UO_2, due to the increase in said mobile holes (27).

As we move from the 25 to the 43 GWd/tU SIMFUEL sample, the conductivity decreases. Two possible explanations exist for this observation.

1. The decrease in current upon increasing burnup from 25 to 43 GWd/tU may be due to a proportionately greater amount of Ln(III) partitioning in to the grey phase in the 43 GWd/tU SIMFUEL sample than in the 25 GWd/tU SIMFUEL sample. This effectively means that decreasing the concentration of U(V) sites in the 43 GWd/tU SIMFUEL sample compared to the 25 GWd/tU SIMFUEL sample, results in the lower conductivity of the 43 GWd/tU SIMFUEL sample when compared to the 25 GWd/tU SIMFUEL sample (10) (27).
2. An alternative explanation has been advanced by Howett *et al*. who also observe this current decrease with increasing burnup. Based on the work of He *et al*., they suggest that the suppression in current observed at higher burnup may be due to the fact that doping at higher lanthanide levels may stabilise the fluorite lattice against anodic oxidation and dissolution by decreasing the amount of vacancy sites free for O_2^- incorporation, and that it may be this

stabilisation that leads to the decrease in the currents observed for the 43 GWd/tU SIMFUEL sample when compared to the 25 GWd/tU SIMFUEL sample (27) (35). This attribution coincides with the above-mentioned decrease in the concentration of U(V) sites, resulting in the observed decrease in current.

However, recent work by Berhane *et al*. (36) indicates that, upon loading the 43 GWd/tU SIMFUEL with additional Ln(III) – but no extra grey phase – a net increase in current is observed, suggesting that the former of these two explanations is the most likely to describe the physical reality.

Having characterised the baseline Raman spectroscopic and electrochemical response of our SIMFUELs in sulfate background electrolyte, we now move on to consider the effects of the deliberate addition of hydrogen peroxide on the undoped UO_2 and 25 & 43 GWd/tU SIMFUEL pellets immersed in the same background electrolyte. This will be the subject of the next chapter.

References

1. D.W. Shoesmith, *Fuel corrosion processes under waste disposal conditions.* s.l. : Journal of Nuclear Materials, 2000, Vol. 282. pp. 1 - 31.

2. G. Guimbretiere, A. Canizares, N. Raimboux, J. Joseph, P. Desgardin, L. Desgranges, C. Jegou, P. Simon. *High temperature Raman study of UO_2: a possible tool for in situ estimation of irradiation-induced heating.* s.l. : Journal of Raman Spectroscopy, 2015, Vol. 46.

3. H. He, D.W. Shoesmith. *Raman spectroscopic studies of defect structures and phase transitions in hyper-stoichiometric UO_{2+x}.* s.l. : Physical Chemistry Chemical Physics, 2010, Vol. 12. pp. 8108 - 8117.

4. H. He, M. Broczkowski, K. O'Neil, D. Ofori, O. Semenikhin, D. Shoesmith. *Corrosion of a nuclear fuel (UO_2) inside a failed nuclear waste container.* s.l. : Nuclear Waste Management Organisation, 2012.

5. T. Livneh, E. Sterer. *Effect of pressure on the resonant multiphonon Raman scattering in UO_2.* s.l. : Physical Review B, 2006, Vol. 73.

6. J.M. Elorietta, L.J. Bonales, N. Rodriguez-Villagra, V.G. Baonza, J. Cobos. *A detailed Raman and X-ray study of UO_{2+x} oxides and related structure transitions.* s.l. : Physical Chemistry Chemical Physics, 2016, Vol. 18. pp. 28209 - 28216.

7. F. Clarensn J. de Pablo, I. Diez-Perez, I. Casas, J. Gimenez, M. Rovira. *Formation of studtite during the oxidative dissolution of UO_2 by hydrogen peroxide: a SFM study.* s.l. : Environmental Science & Technology, 2004, Vol. 38. pp. 6656 - 6661.

8. R.J. Wilbraham, E. Howett, C. Boxall, D. Hambley, J.K. Higgins. *Simulated advanced gas-cooled reactor spent nuclear fuels: determination of the U/O ratio - and XRD, XPS and Raman study.* s.l. : Journal of Nuclear Materials, 2020, Vol. 18. [in print].

9. L. Lutterotti, S. Matthies, H.-R. Wenk. *MAUD (Material Analysis Using Diffraction): a user friendly Java program for Rietveld texture analysis and more.* s.l. : NRC Reasearch Press Canada, 1999, Vol. Proceeding of the Twelth International Conference on Textures of Materials.

10. H. He, P.G. Keech, M.E. Broczkowski, J.J. Noel, D.W. Shoesmith. *Characterization of the influence of fission product doping on the anodic reactivity of uranium dioxide.* s.l. : Canadian Journal of Chemistry, 2007, Vol. 85. pp. 702 - 713.

11. P.G. Lucata, R.A. Verral, H.J. Matzke, I.J. Hastings. *Characterisation and thermal properties of hyperstoichiometric SIMFuel.* s.l. : Canadian Nuclear Society, 1992. pp. 61 - 73.

12. G. Leinders, T. Cardinaels, K. Binnemans, M. Verwerft. *Accurate lattice parameter measurements of stoichiometric uranium dioxide.* s.l. : Journal of Nuclear Materials, 2015, Vol. 459. pp. 135 - 142.

13. N. Liu, J. Kim, J. Lee, Y-S. Youn, J-G. Kim, J-Y. Kim, J.J. Noel, D.W.Shoesmith. *Influence of Gd doping on the structure and electrochemical behaviour of UO_2.* s.l. : Electrochimica Acta, 2017, Vol. 247. pp. 496 - 504.

14. E.A. Howett. *The behaviour of spent nuclear fuel in wet interim storage.* s.l. : Lancaster University, Lancaster University, 2019.

15. N. Rauff-Nisthar, C. Boxall, I. Farnan, Z. Hiezl, W. Lee, C. Perkins, R. Wilbraham. *Corrosion behaviour of AGR simluated fuels - evolution of the fuel surface.* s.l. : ECS Transactions, 2013, Vol. 53. pp. 95-104.

16. Z. Talip, T. Wiss, P.E. Raison, J. Paillier, D. Manara, J. Somers, R.J.M. Konings. *Raman and X-ray studies of uranium-lanthanum-mixed oxides before and after air oxidation.* s.l. : Journal of the American Ceramic Society, 2015, Vol. 98.

17. J.M. Elorrieta, L.J. Bonales, N. Rodriguez-Villagra, V.G. Baonza, J. Cobos. *A detailed Raman and X-ray study of UO_{2+x} oxides and related structure transitions.* s.l. : Physical Chemistry Chemical Physics, 2016, Vol. 18. pp. 28209 - 28216.

18. K. Park. *The oxygen potential of neodymia-doped urania based on a defect structure.* s.l. : Journal of Nuclear Materials, 1994, Vol. 209. pp. 259 - 262.

19. Z. Hiezl. *Processing and microstructural characterisation of UO_2-based simulated spent nuclear fuel ceramics for the UK's advanced gas-cooled reactors.* s.l. : Imperial College London, 2016.

20. A. Seibert, D.H. Wegen, T. Gouder, J. Roemer, T. Wiss, J-P. Glatz. *The use of electrochemical quartz crystal microbalance (EQCM) in corrosion studies of UO_2 thin film models.* s.l. : Journal of Nuclear Materials, 2011, Vol. 491. pp. 112 - 121.

21. T. Ohmichi, S. Fukushima, A. Maeda, H. Watanabe. *On the relation between lattice parameter and O/M ratio for uranium dioxide - trivalent rare earth oxide solid solution.* s.l. : Journal of Nuclear Materials, 1981, Vol. 102. pp. 40-46.

22. S.M. Ho, K.C. Radford. *Structural chemistry of solid solutions in the UO_2-Gd_2O_3 system.* s.l. : Nuclear Technology, 1986, Vol. 73. pp. 350 - 360.

23. R.D. Shannon. *Revised effective ionic radii and systematic studies of interatomic distances in halides and calcogenides.* s.l. : Acta Crystallographica, 1976, Vol. A32. pp. 751 - 767.

24. J. Lee, J. Kim,Y.-S. Youn, N. Liu, J.-G. Kim, Y.-K. Ha, D.W. Shoesmith, J.-Y. Kim. *Raman study on structure of U1-yGdyO_{2-x} (y=0.005,0.01, 0.03, 0.05 and 0.1) solid solutions.* s.l. : Journal of Nuclear Materials, 2017, Vol. 486. pp. 216-221.

25. U. Benedict, M. Coquerelle, J. De Bueger, C. Dufour. *A study of local composition variations in irradiated oxide fuel by X-ray difractometry.* s.l. : Journal of Nuclear Materials, 1972, Vol. 45. pp. 217 - 229.

26. M.W.D Cooper, S.C. Middleburgh and R.W. Grimes. *Partition of soluble fission products between the grey phase, ZrO_2 and uranium dioxide.* s.l. : Journal of Nuclear Materials, 2013, Vol. 438. pp. 238 - 245.

27. E.A. Howett, C. Boxall, R.J. Wilbraham, D.I. Hambley. *The behavior of advanced gas reactor simulated spent nuclear fuels in wet interim storage.* s.l. : Progress in Nuclear Science and Technology, 2018, Vol. 5. pp. 140 - 143.

28. R.J. Wilbraham, N. Rauff-Nisthar, C. Boxall, E.A. Howett, D.I. Hambley, Z. Hiezl, W.E. Lee, C. Padovani. *Raman studies of adanced gas-cooled reactor simulated spent nuclear fuels.* s.l. : Progress in Nuclear Science and Technology, 2018, Vol. 5. pp. 213 - 216.

29. Inphotonics. https://inphotonics.com/raman.html [Online].

30. Kosi. https://kosi.com/na_en/products/raman-spectroscopy/raman-technical-resources/raman_tutorial.php [Online].

31. G.S: Bumbrah, R.M. Sharma. *Raman spectroscopy - Basic principle, instrumentation and selected applications for the characterization of drugs of abuse.* s.l. : Egyptian Journal of Forensic Sciences, 2015, Vol. 6. pp. 209-215.

32. *Study.com.* https://study.com/academy/lesson/vibrational-spectroscopy-definition-types.html [Online].

33. Zhang, R. Ji, L. Wang, L. Yu, J. Wag, B. Geng, G. Wang. *Controllable synthesis of silver nanoendrites on copper rod and its application to hydrogen peroxide and glucose detection.* s.l. : Crystal Engineering Communication, 2013, Vol. 15. pp. 1173 - 1178.

34. J. O'M. Bockris, A.K.N. Reddy. *Modern Electrochemistry* s.l. : Springer, 2000.

35. H. He, P.G. Keech, M.E.Broczkowski, J.J. Noel, D.W. Shoesmith. *Characterization of the influence of fission product doping on the anodic reactivity of uranium dioxide.* s.l. : Canadian Journal of Chemistry, 2007, Vol. 85. p.p. 702 – 713

36. G. Berhane, C. Boxall, R. Wilbraham. *The corrosion behaviour of high density fuels under conditions relevant to wet storage & geologic disposal.* s.l. : National Nuclear Laboratory, 2021, Report no. 15705

Chapter 4 Effect of Hydrogen Peroxide on UO_2 & SIMFUEL Pellets

4.1 Introduction - deliberate addition of H_2O_2

In this chapter, we will look at the effects of the deliberate addition of hydrogen peroxide on undoped UO_2 as well as the 25 & 43 GWd/tU SIMFUEL samples. The effects of deliberately added hydrogen peroxide will be studied in a sodium sulfate background electrolyte, as was in Chapter 3. This is in order to establish baseline behaviour of our three samples before moving onto more complex systems. Sodium sulfate was the electrolyte of choice as it is a single component, widely used inert electrolyte. Studies have also shown that sulfate only reacts with uranium at low pH values (which are seen through Pourbaix diagrams produced using Medusa software) (1), as well as the fact that sodium sulfate does not cause stress corrosion cracking (2).

The effects of deliberately added H_2O_2 will be investigated in terms of the samples electrochemical and Raman behaviour. It is important to look at the effects of hydrogen peroxide as it is expected to be produced during the alpha radiolysis of water. This phenomenon would occur in case of the engineered barrier of the spent fuel failing, meaning that the groundwater would be able to ingress through to the spent fuel. This scenario would be expected to occur in an underground repository following the thermal pulse (see Chapter 1, section 1.1.6).

4.2 Results & Discussion

The approach adopted to investigate the behaviour of our SIMFUEL and undoped pellets in a background electrolyte that is spiked with hydrogen peroxide is as follows. The corrosion of the UO_2 and SIMFUEL pellets will be studied in a range of hydrogen peroxide concentrations, ranging from 10 µmol dm^{-3} to 1 mmol dm^{-3} for the following reasons. The lower limit to this range is the concentration of hydrogen peroxide that can be expected to be found in the groundwater after the alpha-radiolysis of water (see Chapter 1 Figure 1-21). The reason for choosing the upper limit of the range as 1 mmol dm^{-3} of H_2O_2 is due to the fact that studtite formation has been observed on UO_2 when exposed to 1 mmol dm^{-3} of hydrogen peroxide – and is currently the focus of some speculation as to whether it can form in repository (3). Regardless of whether the concentration of hydrogen peroxide in the groundwater would reach 1 mmol dm^{-3}, it is interesting to investigate the effects up to and including this concentration – and will allow for an investigation as to whether the lesser studied studtite is formed as one of the UO_2 transformation products in repository.

The above behaviours will primarily be studied by use of electrochemical and Raman techniques. The purpose of this comparative analysis is to correlate corrosion susceptibility of the fuel, as determined by measurement of the open circuit potential (OCP) and voltammetric characteristics of each sample, with its structural features as elucidated by Raman spectroscopy.

To begin with we measured the open circuit potential of an undoped UO_2 pellet along with a 25 and 43 GWd/tU SIMFUEL pellets in a 0.1 mol dm^{-3} background electrolyte of Na_2SO_4, spiked with 10 µmol dm^{-3} of H_2O_2, recorded over a period of 4 hours. The open circuit potential is compared to Raman spectra taken of all three samples. The Raman spectra were recorded on the same samples used for the OCP, after reaching their open circuit potentials. Both the OCP data and the Raman spectra for all three samples in the presence of 10 µmol dm^{-3} peroxide can be seen in Figure 4-1 below. These should be interpreted in comparison to the same measurements conducted in the absence of peroxide as shown in Figures 3-7a and 3-7b in Chapter 3. For the convenience of the reader, these figures are reproduced here as Figures 4-1(a) and 4-1(c).

The Raman spectra presented in this chapter are represented as Lorentzian peak fits where the peak centred at ~550 cm^{-1} in the Raman spectra of the 25 and 43 GWd/tU samples has been deconvoluted, in much the same way as analogous spectral data was treated in Chapter 3.

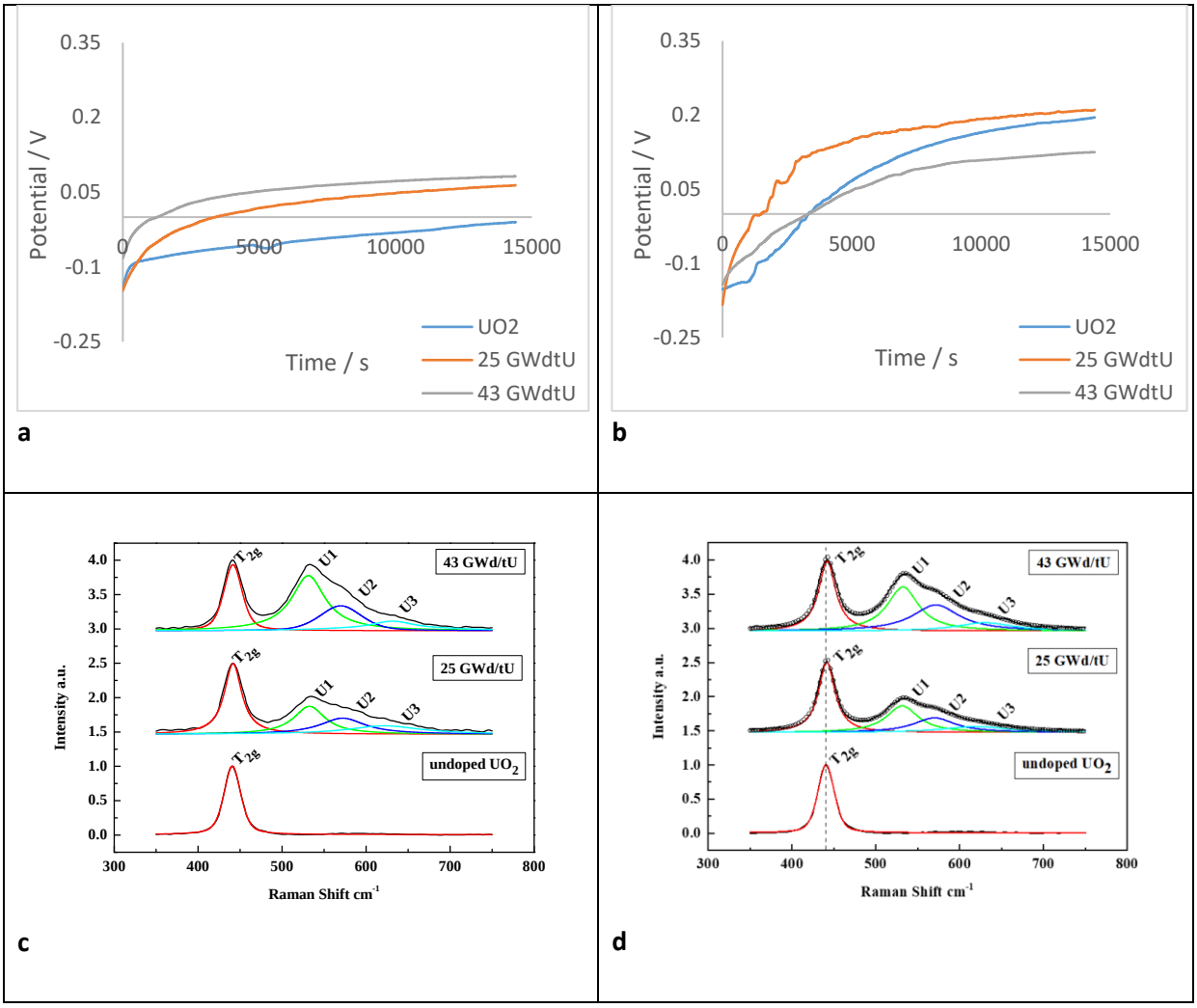

Figures 4-1a to 4-1d – (a) showing the open circuit potential of the UO_2 and 25 & 43 GWd/tU SIMFUEL pellets over a 4 hour period in a 0.1 mol dm^{-3} Na_2SO_4 background electrolyte; (b) the open circuit potential of the UO_2 and 25 & 43 GWd/tU SIMFUEL pellets over a 4 hour period in a 0.1 mol dm^{-3} Na_2SO_4 background electrolyte spiked with 10 µmol dm^{-3} H_2O_2; (c) the 20-point averaged Raman spectra of the UO_2 and 25 & 43 GWd/tU SIMFUEL pellets after OCP measurement shown in Figure 4-1a; (d) the 20-point averaged Raman spectra of the UO_2 and 25 & 43 GWd/tU SIMFUEL pellets after OCP measurement shown in Figure 4-1b,respectively

Looking at the open circuit potentials, it is apparent by comparing Figures 4-1a and 4-1b that introduction of peroxide has driven the equilibrium potential more positive – from ~0 - 50mV vs SCE (reference electrode) in the absence of peroxide to ~100-200 mV vs SCE in its presence. This may be expected as hydrogen peroxide will place an oxidative stress on the surface of all three pellet samples.

In the presence of peroxide, the UO_2 and 25 GWd/tU SIMFUEL pellets both approach the same equilibrium potential of ~200 mV vs SCE with the 25 GWd/tU SIMFUEL pellet approaching its equilibrium potential at a faster rate. As discussed in Chapter 3, this is most likely due to the higher

concentration of charge carriers in the 25 GWd/tU SIMFUEL sample derived from doping effects associated with the addition of fission product simulants to the SIMFUEL matrix. The higher charge carrier concentration will support higher exchange current densities at the surface of the 25 GWd/tU SIMFUEL sample, with a consequent increase in charge transfer kinetics and thus rate of approach to equilibrium in the context of an OCP experiment.

On the basis of the above we would expect the 43 GWd/tU SIMFUEL sample to also approach the same equilibrium potential at an even faster rate. However, the potential reached by the 43 GWd/tU SIMFUEL sample is ~100 mV vs SCE, almost 100 mV negative of that reached by the undoped UO_2 and the 25 GWd/tU SIMFUEL pellet sample after 4 hours of immersion. Furthermore, the 43 GWd/tU SIMFUEL sample approaches this equilibrium value at a substantially slower rate than both the 25 GWd/tU SIMFUEL sample and the undoped UO_2 pellet.

The reason for this is most likely the catalytic decomposition of hydrogen peroxide due to the ε-particles present on the SIMFUEL surface. As stated in Chapter 2, these ε-particles are predominantly comprised of Mo, Ru, Rh, Pd, and Tc. Platinum group metals such as these are known to catalytically decompose dilute peroxide solutions under neutral and basic conditions (4), leading us to expect this decomposition to occur at the SIMFUEL surfaces. This decomposition will suppress the effective concentration of peroxide at the SIMFUEL surface, resulting in both a less positive equilibrium potential than that observed on the UO_2 and 25 GWd/tU SIMFUEL pellets and a slower approach to that potential with respect to immersion time.

The fact that the above is seen to occur on the 43 GWd/tU SIMFUEL sample but not the 25 GWd/tU SIMFUEL sample is most likely due to the higher Mo, Ru, Pd and Tc loadings employed in the fabrication of the former and a higher incidence of epsilon particles at the surface of the 43 sample GWd/tU SIMFUEL sample, as seen in Chapter 2, Table 1 (note that Tc and Ru are both represented by RuO_2. ^{99}Ru is the daughter element of ^{99}Tc, which is the only Tc isotope present in spent nuclear fuel) (5).

At this point, it is useful to compare the equilibrium OCPs obtained for each SIMFUEL sample in the presence and absence of peroxide with the voltammogram recorded for each sample in the absence

of peroxide, Figure 3-6 in Chapter 3 and represented here as Figure 4-2 for the convenience of the reader. This will allow for ready identification of the redox / corrosion processes that may obtain at the surface of each sample at its observed equilibrium OCP. Accordingly, by comparing the OCP range of 0 – 50 mV vs SCE observed for all samples in the absence of peroxide to the cyclic voltammogram of Figure 4-2, we can see that this OCP range corresponds to the same region in the labelled CV in which a low level of UO_2 oxidation to UO_{2+x} may be seen to be occurring. However, if we compare the OCP in the presence of hydrogen peroxide to the same CV measured in the absence of peroxide, we can see that in the OCP region of 100 – 200 mV vs SCE there is an enhancement in the amount of UO_{2+x} generation. This means that the peroxide generates an increase in *x*, however, it must be noted that this increase is not high enough as to result in the generation of UO_2^{2+}, which would lead to subsequent dissolution.

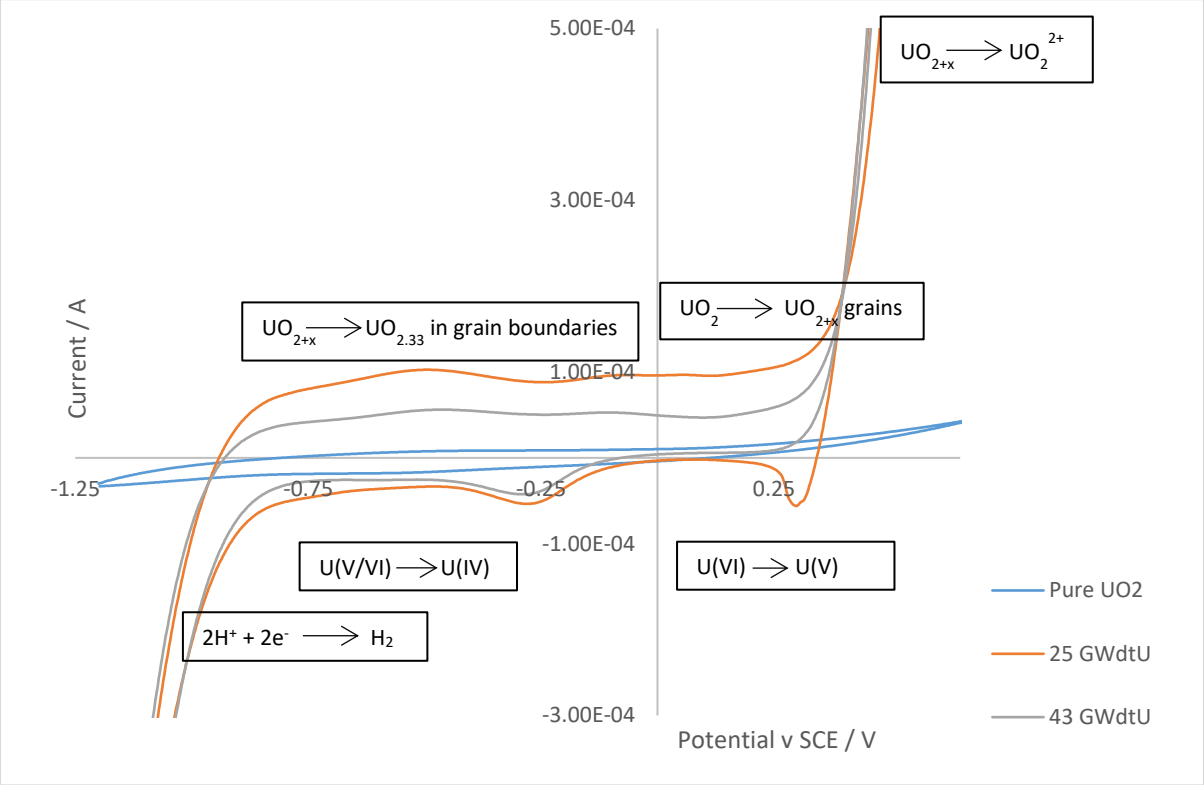

Figure 4-2 showing cyclic voltammograms of UO_2, 25 & 43 GWd/tU SIMFUEL pellets in a 0.1 mol dm^{-3} Na_2SO_4 background electrolyte, cycled at a potential range of (-) 1.2 to (+) 0.7 V, at a scan rate of 10 mV/s

Turning again to the Lorentzian peak fits of the Raman spectra in Figure 4-1d, we can see that all three samples exhibit the expected fundamental UO stretch at a Raman shift of approximately 445 cm^{-1}, denoted as the T_{2g} band. However we can also see bands for the low and high-doped 25 and 43

GWd/tU SIMFUEL pellets in the region of 500 – 700 cm^{-1}, denoted as U1, U2 and U3. As seen in Chapter 3, these bands are indicative of lattice damage and distortion of the perfect cubic fluorite structure to a more tetragonal structure.

Looking again at the Raman spectra in Figures 4-1c and 4-1d, it can be seen that both in the presence and absence of hydrogen peroxide, the 25 & 43 GWd/tU SIMFUEL samples exhibit an increase in the intensity of the broad compound peak seen at 575 cm^{-1} with increasing simulated burnup. This is again, simply due to the fact that the added dopants induce a range of lattice distortions. The behaviour of the component peaks of this have been discussed in detail in Chapter 3, however, for the convenience of the reader, the assignments and behaviour with increased simulated burnup may be summarised as follows:

U1 – with an absorption maximum at 530 cm^{-1}, primarily related to oxygen-vacancy induced lattice distortions, said vacancies generated to part-charge compensate for the presence of 3+ lanthanide dopants. As the simulated burn-up increases, there is a marked increase in lanthanide concentration, and therefore this peak is larger for the 43 GWd/tU SIMFUEL pellet than for the 25 GWd/tU SIMFUEL pellet (1).

U2 – with an absorption maximum at 575 cm^{-1}, attributed to the fundamental of the longitudinal optical phonon overtone peak seen at ~1150 cm^{-1}. As the sample becomes more hyperstoichiometric, we would expect a decrease in this peak due to increased phonon scattering by the resultant lattice defects (1). However, with our SIMFUEL samples, there is a small increase with simulant burnup. This is due to selection rule relaxation effects, explained in detail in Chapter 3.

U3 – with an absorption maximum at 630 cm^{-1}, attributed to the presence of clusters of interstitial oxygen i.e. is due to the hyperstoichiometry of UO_2 as it transitions to form U_4O_9 with increasing x. This peak continues to increase in intensity as the amount of oxygen content increases (6), however for our SIMFUEL samples, the 630 cm^{-1} peak decreases slightly with increased burn-up. This is again, explained in more detail in Chapter 3.

Broadly speaking, the spectra that are recorded after immersion in peroxide are similar to those recorded before, with one possible exception: there appears to be a small decrease in intensity for the U1 peak post-immersion in the 43 GWd/tU SIMFUEL sample compared to the pre-immersion of the 43 GWd/tU SIMFUEL sample. A possible explanation for the decrease in intensity of U1 upon immersion in peroxide is afforded by the OCP of the 43 GWd/tU SIMFUEL sample. As discussed above, the OCP measurements indicate that immersion in the presence of hydrogen peroxide, puts the sample into a potential range whereby conversion may occur of UO_{2+x} to $UO_{2.33}$ (U_3O_7) at grain boundaries and UO_2 to UO_{2+x} within the grains themselves. The value of *x* in the latter case is expected to be larger in the presence of hydrogen peroxide than in its absence, as discussed above. This introduction of O^{2-} ions into the lattice may be acting to reduce the intensity of the U1 peak. The fact that this is not seen in the 25 GWd/tU SIMFUEL sample post H_2O_2 immersion, is likely due to there being a lower number of oxygen vacancies in the low burn-up SIMFUEL to begin with.

Finally, it is now useful to return to the cyclic voltammetric data and look at the CVs of the three SIMFUEL samples in 0.1 mol dm^{-3} Na_2SO_4 background electrolyte that has been spiked with 10 µmol dm^{-3} of hydrogen peroxide.

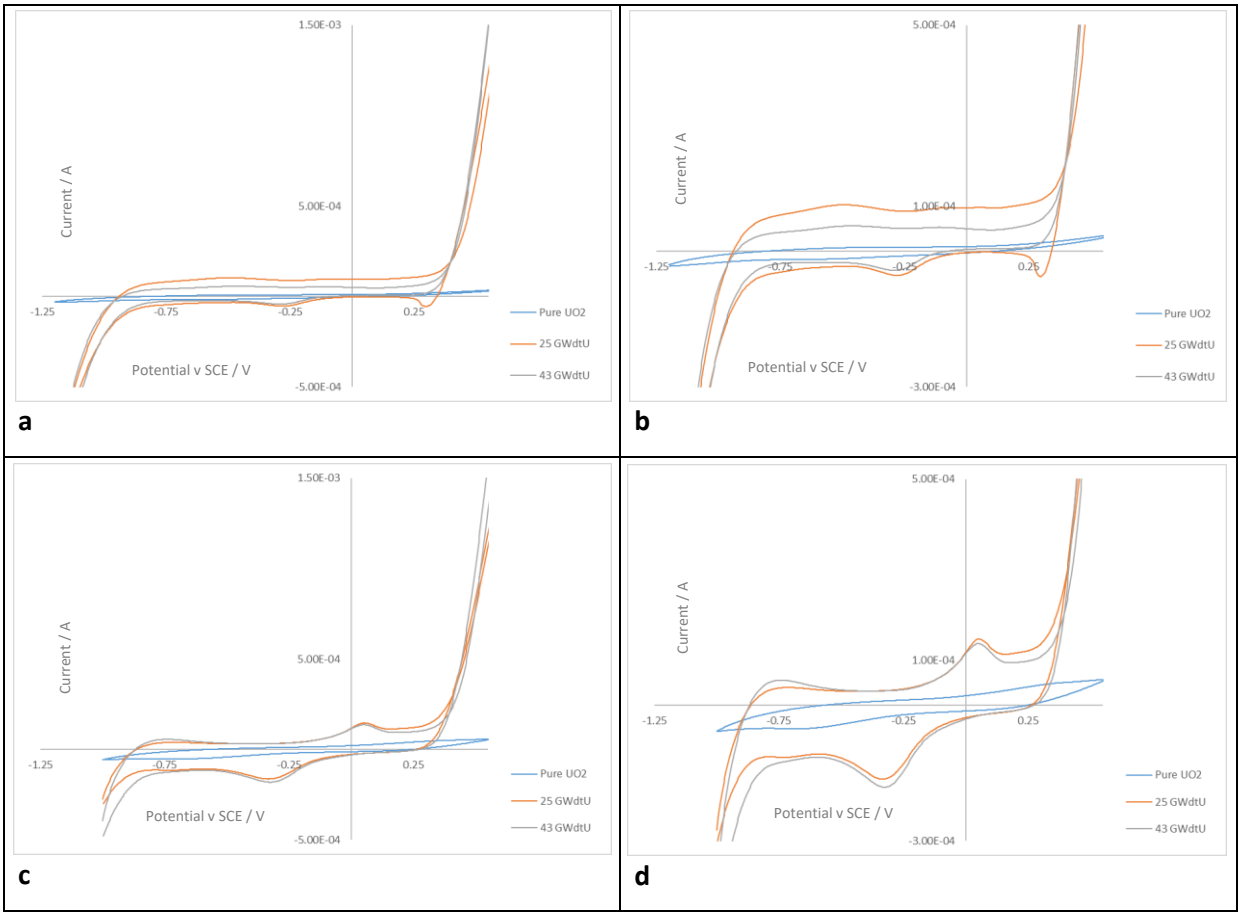

Figures 4-3a to 4-3d – (a) showing the cyclic voltammograms of UO_2, 25 & 43 GWd/tU SIMFUEL pellets in a 0.1 mol dm^{-3} Na_2SO_4 background electrolyte, cycled at a potential range of (-) 1.2 to (+) 0.7 V, at a scan rate of 20 mV/s; (b) a blown-up image of 4-3a; (c) the cyclic voltammograms of UO_2, 25 & 43 GWd/tU SIMFUEL pellets in a 0.1 mol dm^{-3} Na_2SO_4 background electrolyte spiked with 10 µmol dm^{-3} H_2O_2, cycled at a potential range of (-) 1.2 to (+) 0.7 V, at a scan rate of 10 mV/s; (d) a blown up image of 4-3c, respectively

Figures 4-3c and 4-3d above show cyclic voltammograms of the undoped UO_2 pellet as well as the low and high burnup SIMFUEL pellets (25 and 43 GWd/tU) in a 0.1 mol dm^{-3} sodium sulfate background electrolyte that has been spiked with 10 µmol dm^{-3} of hydrogen peroxide. Figures 4-3a and 4-3b show the same in a 0.1 mol dm^{-3} sodium sulfate background electrolyte in the absence of hydrogen peroxide. In both Figures 4-3b and 4-3d we can clearly see that the undoped UO_2 pellet, which is a Mott-Hubbard insulator (see Chapter 1), has the lowest electrochemical activity out of the three samples. This is evident by the fact that virtually no current is being carried by the UO_2 pellet during the scans. As the amount of dopants is increased from the undoped to the 25 GWd/tU and to the 43 GWd/tU pellets, the electrochemical reactivity also increases, due to the amount of dopants and metallic particles present in the SIMFUELs, meaning that the doped pellets are more efficient charge carriers.

As can be seen from the voltammograms recorded in the absence of peroxide, Figures 4-3a and 4-3b, the electrochemical reactivity of the low doped 25 GWd/tU SIMFUEL pellet is higher than that of the higher doped 43 GWd/tU SIMFUEL pellet. As discussed in Chapter 3, this is most likely due to increased partitioning of Ln(III) dopants into the higher grey phase loading of the 43 GWd/tU SIMFUEL sample.

When comparing Figures 4-3b and 4-3d we can see two new peaks appearing in the voltammetry – one in the forward sweep at approximately 0.05 V_{SCE}, and one in the reverse sweep at approximately -0.3 V_{SCE}. Comparison with electrochemical data for the redox behaviour of hydrogen peroxide recorded on metal electrodes at similar pHs as those used in Figures 4-3a to 4-3d (see Zhang *et al* 2013 (7)) suggests that these additional peaks are simply associated with the oxidation and reduction of H_2O_2 respectively (7), the former due to the two electron oxidation of peroxide to form oxygen. It is interesting to note that the position of this peak is negative of the OCP imposed on the SIMFUEL samples in the presence of peroxide, suggesting that it is not the H_2O_2/O_2 redox couple that is controlling the equilibrium OCPs observed in Figure 1b. Rather it is more likely that this is driven by the 1 electron transfer $H_2O_2/HO_2\bullet$ process which has a standard redox potential of + 1.27 V_{SCE} at pH 0.

As can be seen in Figures 4-3c and 4-3d, the electrochemical reactivity of the low doped 25 GWd/tU SIMFUEL pellet towards peroxide oxidation is higher than that of the higher doped 43 GWd/tU SIMFUEL pellet. This is most likely a convolution of the effect of Ln(III) dopant partitioning into the grey phases of the latter sample as discussed above and the aforementioned fact that the 43 GWd/tU SIMFUEL sample has a higher loading of epsilon particles. This subsequently leads to the decomposition of hydrogen peroxide. The suppression of the effective H_2O_2 concentration caused by this decomposition results in a lowering of the peroxide oxidation currents observed from the 43 GWd/tU SIMFUEL pellet.

We can now have a look at how increasing the amount of hydrogen peroxide in the background electrolyte from 10 µmol dm^{-3} to 100 µmol dm^{-3} affects reactivity and stability of the undoped UO_2 and SIMFUELs pellets. Consequently Figures 4-4a and 4-4b show the open circuit potential for the undoped UO_2, 25 and 43 GWd/tU SIMFUEL pellets recorded as a function of immersion time in a 0.1 mol dm^{-3} Na_2SO_4 background electrolyte, both in the absence and presence of 100 µmol dm^{-3} H_2O_2;

whilst Figures 4-4c and 4-4d show the Lorentzian peak fits of 20-point averaged Raman spectra recorded before and after 4 hours exposure to the 0.1 mol dm^{-3} Na_2SO_4 background electrolyte spiked with 100 µmol dm^{-3} hydrogen peroxide.

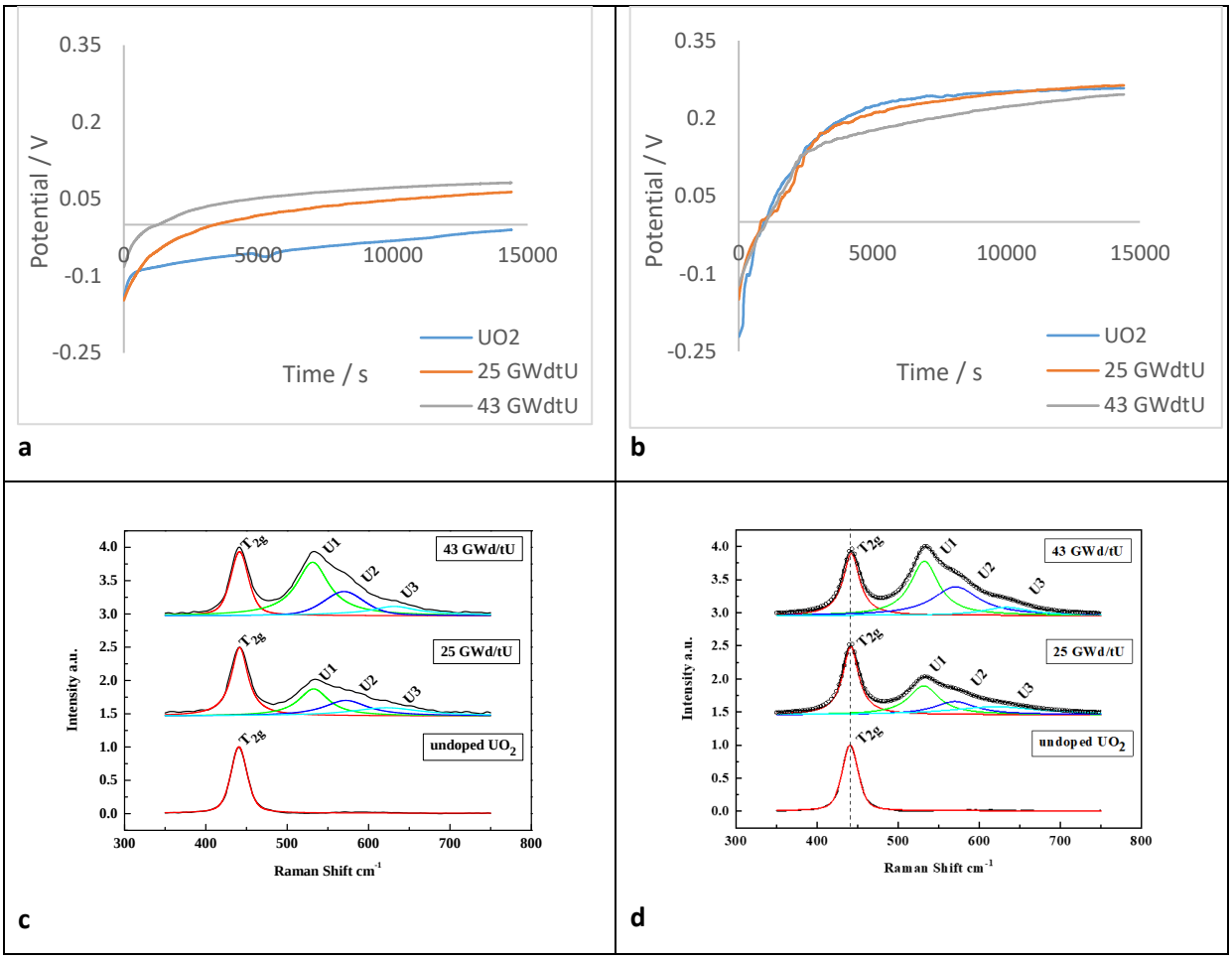

Figures 4-4a to 4-4d – (a) showing the open circuit potential of the UO_2 and 25 & 43 GWd/tU SIMFUEL pellets over a 4 hour period in a 0.1 mol dm^{-3} Na_2SO_4 background electrolyte; (b) the open circuit potential of the UO_2 and 25 & 43 GWd/tU SIMFUEL pellets over a 4 hour period in a 0.1 mol dm^{-3} Na_2SO_4 background electrolyte spiked with 100 µmol dm^{-3} H_2O_2; (c) the 20-point averaged Raman spectra of the $UO_2$and 25 & 43 GWd/tU SIMFUEL pellets after OCP measurement in Figure 4-4a; (d) the 20-point averaged Raman spectra of the UO_2 and 25 & 43 GWd/tU SIMFUEL pellets after OCP measurement in Figure 4-4b,respectively

From the open circuit potential in Figure 4-4b above, we can see that all three samples, the undoped UO_2 pellet, as well as the low and high burnup 25 & 43 GWd/tU SIMFUEL pellets, all come to rest at approximately 200 mV vs SCE after 4 hours immersion in the peroxide spiked solution. This is ~150 mV positive of the equilibrium OCP values recorded from the same samples in the same electrolyte system in the absence of peroxide, Figure 4-4a, and as discussed in reference to Figure 4-1 above, is simply a reflection of the oxidative stress imposed on the SIMFUELs by the presence of H_2O_2.

As aforementioned with respect to Figure 4-1, when the same samples were left to reach their open circuit potentials under the same conditions, but in a background electrolyte containing 10 µmol dm^{-3} as opposed to 100 µmol dm^{-3} hydrogen peroxide, we saw that the undoped UO_2 pellet and the low burnup 25 GWd/tU SIMFUEL pellet both came to rest at approximately the same OCP value of 200 mV vs SCE as all three samples in Figure 4-4b, as well as at the same rate.

Contrary to what we observed in the OPC with the 43 GWd/tU SIMFUEL pellet spiked with 10 µmol dm^{-3} hydrogen peroxide (Figure 4-1b), where we saw the 43 GWd/tU SIMFUEL pellet reach the equilibrium value at a substantially slower rate than the undoped and 25 GWd/tU SIMFUEL pellets, which was due to the catalytic decomposition of hydrogen peroxide. We here see what we initially expected to see, which was that the 43 GWd/tU SIMFUEL sample would also approach the same equilibrium potential (Figure 4-4b).

At a concentration of 100 µmol dm^{-3} hydrogen peroxide, the higher concentration of epsilon particles in the 43 GWd/tU SIMFUEL pellets still seem to somewhat have an effect on the decomposition of the hydrogen peroxide, but as the concentration is now higher than previously seen with the 10 µmol dm^{-3} concentration; it is not unreasonable to propose that the peroxide decomposition effect is proportionately less significant at the higher peroxide concentration, resulting in the 43 GWd/tU SIMFUEL pellet coming to rest at the same potential as the undoped UO_2 and the 25 GWd/tU SIMFUEL pellet, however, at a slightly slower rate.

As already seen in Figure 4-1d, the defect peaks U1, U2 and U3 seen at Raman shifts of approx. 530, 575 and 630 cm^{-1} respectively, are higher in intensity for the high burnup 43 GWd/tU SIMFUEL pellet than for the low burnup 25 GWd/tU SIMFUEL pellet. As aforementioned, this is attributed to the fact that through the addition of dopants, the concentration of defects in the lattice is increased (6). Hence, as the amount of dopants is increased from the 25 GWd/tU SIMFUEL pellet to the 43 GWd/tU SIMFUEL pellet, the intensities of the U1, U2 and U3 peaks are seen to increase respectively. Likewise, as mentioned previously, the undoped UO_2 pellet does not exhibit peaks U1, U2 and U3 as it contains no dopants and therefore maintains its perfect cubic fluorite structure.

As described in Figure 4-1d, the dotted lines represent the cumulative curve of all the peaks, and indicate that the Lorentzian peak fits show a realistic fitting of the experimental data observed through Raman spectra.

It must be noted however, that the U2 peak observed from the 43 GWd/tU SIMFUEL in the presence of peroxide in Figure 4-4d above has a slightly higher intensity than that observed from the corresponding sample in the absence of peroxide in Figure 4-4c and at the lower peroxide concentration of 10 μmol dm^{-3} in Figure 4-1d. This is because not only the amount of dopants in the samples is affecting the resulting Raman spectra, but also the increase in hydrogen peroxide concentration. As this band is associated with lattice defect-driven relaxation of the selection rule prohibiting it from being observed in the perfect fluorite lattice of our UO_2 sample, it is not unreasonable to conclude that the effect of hydrogen peroxide at this concentration is to increase the concentration of defects at the surface of the 43 GWd/tU sample. Given the value of the long immersion time OCP previously recorded from this sample, it is also not unreasonable to conclude that this is due to an increase in the value of x in UO_{2+x} i.e. the increase in defect concentration is associated with the introduction of additional interstitial oxygen anions.

Looking at the U3 peak, which has been observed by Elorrieta *et al.* (6) to increase in intensity due to the formation of defect clusters with increasing x, we see that there is not much change when comparing Figures 4-1d and 4-4d. This seems to contradict the above description of the behaviour of U2 but may simply reflect that the change in interstitial oxygen ion concentration promoted by the action of peroxide on the surface is not high enough to change the population of defect clusters associated with U3. In contrast, U2 seems sensitive to the interstitial oxygen ion concentration, clustered or not.

Now that we have looked at the open circuit potential and the Raman spectra of all three samples at an increased concentration of 100 μmol dm^{-3}, we can have a look at the cyclic voltammetry of the three samples in the 0.1 mol dm^{-3} Na_2SO_4 background electrolyte spiked with 100 μmol dm^{-3}.

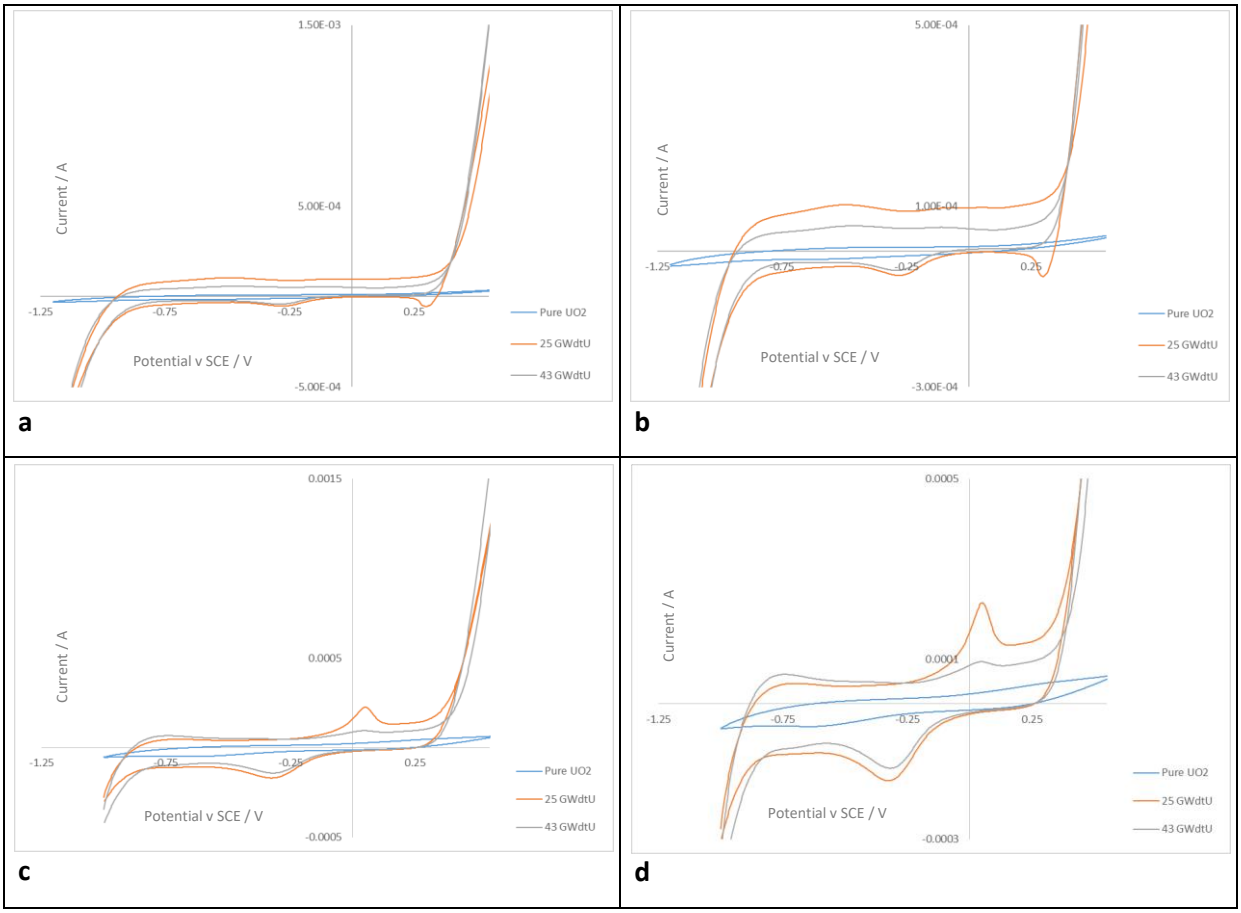

Figures 4-5a to 4-5d – (a) showing the cyclic voltammograms of UO_2, 25 & 43 GWd/tU SIMFUEL pellets in a 0.1 mol dm^{-3} Na_2SO_4 background electrolyte, cycled at a potential range of (-) 1.2 to (+) 0.7 V, at a scan rate of 20 mV/s; (b) a blown-up image of 4-5a; (c) the cyclic voltammograms of UO_2, 25 & 43 GWd/tU SIMFUEL pellets in a 0.1 mol dm^{-3} Na_2SO_4 background electrolyte spiked with 100 µmol dm^{-3} H_2O_2, cycled at a potential range of (-) 1.2 to (+) 0.7 V, (d) at a scan rate of 10 mV/s; a blown up image of 4-5c, respectively

Above, in Figures 4-5c and 4-5d are the cyclic voltammetries of the undoped UO_2 as well as the low and high burnup 25 & 43 GWd/tU SIMFUEL pellets in a 0.1 mol dm^{-3} Na_2SO_4 background electrolyte spiked with 100 µmol dm^{-3}, at a potential window of -1 V to +1.8 V, at a scan rate of 20 mV/s. For ease of comparison, Figures 4-5a and 4-5b again show the same in the absence of hydrogen peroxide.

Here we can see that the high burnup 43 GWd/tU SIMFUEL pellet is again electrochemically less reactive than the low burnup 25 GWd/tU SIMFUEL pellet. The undoped UO_2 pellet, remains, as expected, electrochemically unreactive due to it being a Mott-Hubbard insulator and containing no dopants or metallic particles which could carry the current through. In Figure 4-5d we again see two new peaks appearing when compared with Figure 4-5b. As aforementioned, it is believed that these

peaks are associated with the oxidation and reduction of H_2O_2. Comparing Figure 4-5d (100 µmol dm^{-3} spike) to Figure 4-3d (10 µmol dm^{-3} spike), we can clearly see that the peaks have substantially increased in size. This is due to the higher concentration of hydrogen peroxide present in Figure 4-5d, controlling the oxidation and reduction processes.

Having looked at the effect of a hydrogen peroxide concentration of 10 and 100 µmol dm^{-3} on the three samples, we will now look at the electrochemical and Raman effect that a hydrogen peroxide concentration of 1 mmol dm^{-3} will have on the three samples.

Owing to what has been observed in Figure 4-4b above, we expect the 43 GWd/tU SIMFUEL sample in a background electrolyte spiked with 1 mmol dm^{-3} hydrogen peroxide to reach the same equilibrium potential as the undoped and 25 GWd/tU SIMFUEL samples, and at an even faster rate than seen with a 100 µmol dm^{-3} spike, in Figure 4-4b above.

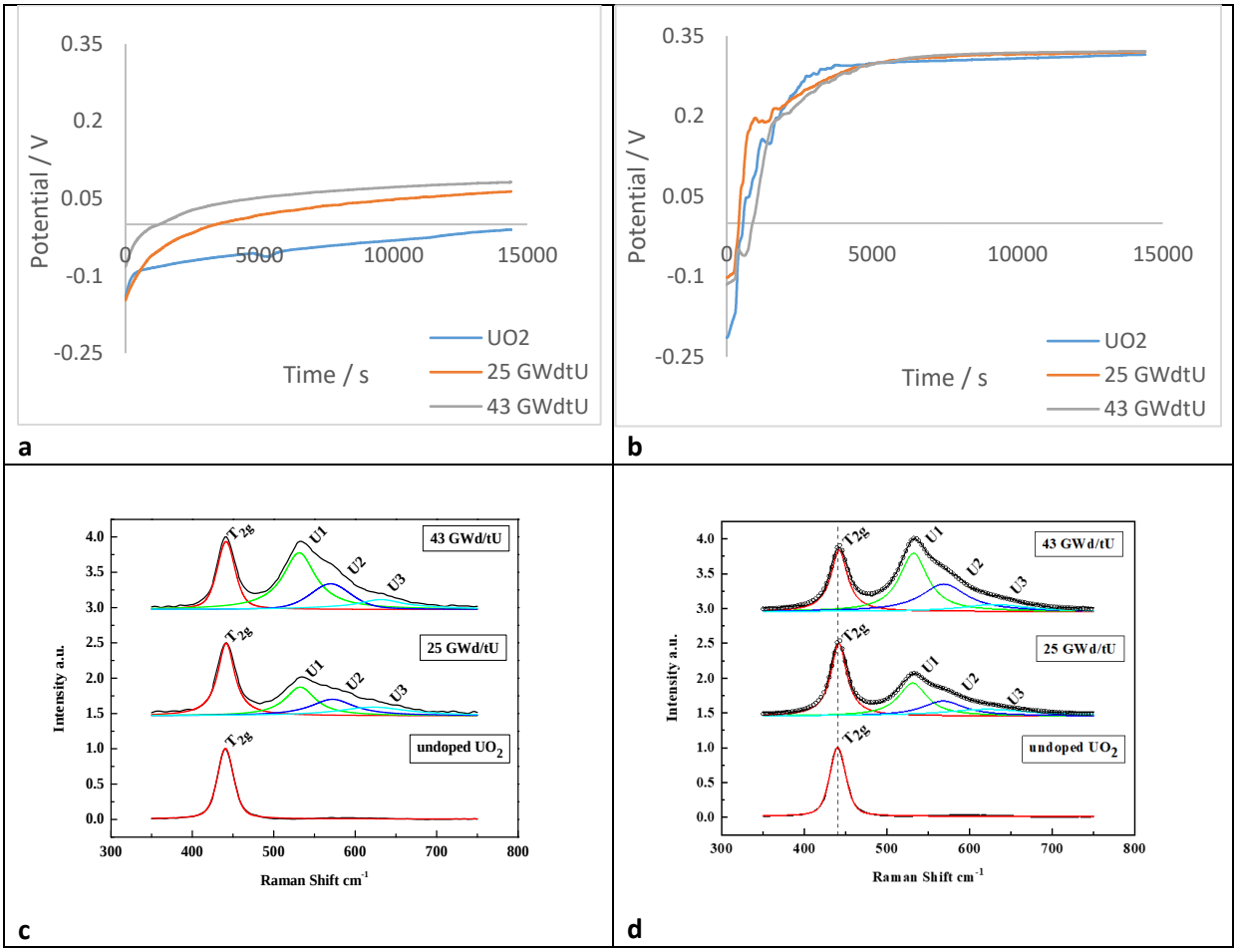

Figures 4-6a to 4-6d – (a) showing the open circuit potential of the UO_2 and 25 & 43 GWd/tU SIMFUEL pellets over a 4 hour period in a 0.1 mol dm^{-3} Na_2SO_4 background electrolyte; (b) the open circuit potential of the UO_2 and 25 & 43 GWd/tU SIMFUEL pellets over a 4 hour period in a 0.1 mol dm^{-3} Na_2SO_4 background electrolyte spiked with 1 mmol dm^{-3} H_2O_2; (c) the 20-point averaged Raman spectra of the UO_2 and 25 & 43 GWd/tU SIMFUEL pellets after OCP measurement in Figure 4-6a; (d) the 20-point averaged Raman spectra of the UO_2 and 25 & 43 GWd/tU SIMFUEL pellets after OCP measurement in Figure 4-6b,respectively

Above in Figure 4-6d is a 20-point averaged Raman spectra of an undoped UO_2 pellet, a low burnup 25 GWd/tU SIMFUEL pellet and a high burnup 43 GWd/tU SIMFUEL pellet, taken after four hours of an open circuit potential in a 0.1 mol dm^{-3} Na_2SO_4 background electrolyte spiked with 1 mmol dm^{-3} of hydrogen peroxide, represented as Lorentzian.

Looking at the open circuit potentials, we saw that for the two previous concentrations of hydrogen peroxide (10 µmol dm^{-3} and 100 µmol dm^{-3}), the undoped UO_2 pellet and the low burnup 25 GWd/tU SIMFUEL pellets both came to rest at approximately 200 mV after 4 hours of open circuit potential. For the high burnup 43 GWd/tU SIMFUEL pellet however, we saw that it came to rest at approximately 100 mV after four hours of open circuit potential in a background electrolyte spiked

with 10 µmol dm^{-3} hydrogen peroxide, and furthermore, after exposure to 100 µmol dm^{-3} for four hours, we saw that the high burnup 43 GWd/tU SIMFUEL came to rest at a potential of 200 mV, as did the undoped UO_2 and the low burnup 25 GWd/tU SIMFUEL pellets.

When all three samples are exposed to the background electrolyte that is spiked with 1 mmol dm^{-3} hydrogen peroxide for four hours however, we see that all three samples come to rest at approximately 300 mV after open circuit potential. This is ~100 mV positive of the equilibrium OCP values recorded from the same samples in the same electrolyte system in the presence of 100 µmol dm^{-3} peroxide and, as discussed above, is simply a reflection of the increased oxidative stress imposed on the SIMFUELs by the increased concentration of H_2O_2.

As aforementioned in Figure 4-4b, the previously seen effect of the high concentration of epsilon particles in the 43 GWd/tU SIMFUEL pellet which decomposed the hydrogen peroxide at lower concentrations is no longer seen here. This is because the concentration of hydrogen peroxide is so high now (1 mmol dm^{-3}) that the decomposition no longer takes place. This is confirmed by the fact that the 43 GWd/tU SIMFUEL pellet comes to rest at the same resting potential and also at the same rate as the undoped UO_2 and 25 GWd/tU SIMFUEL pellets in a 1 mmol dm^{-3} spike.

Looking at the above Raman spectra in Figure 4-6d and comparing it to the Raman spectra where all three samples were exposed to lower concentrations of hydrogen peroxide, namely 10 µmol dm^{-3} in Figure 4-1d and 100 µmol dm^{-3} in Figure 4-4d, we can see that the absolute intensity of the defect peaks U1 and U2 observed at Raman shifts of 530 and 575 cm^{-1} show the highest intensity for the high burnup 43 GWd/tU SIMFUEL pellet. This is once again due to its increased dopant and metallic particle content.

It should be noted here that the intensity of the U1 peak does not only increase in going from the low burnup pellet to the high burnup pellet with increased hydrogen peroxide concentration, but the intensity also increases for each individual SIMFUEL as the hydrogen peroxide concentration is increased. This is demonstrated in Figures 4-7 and 4-8 below.

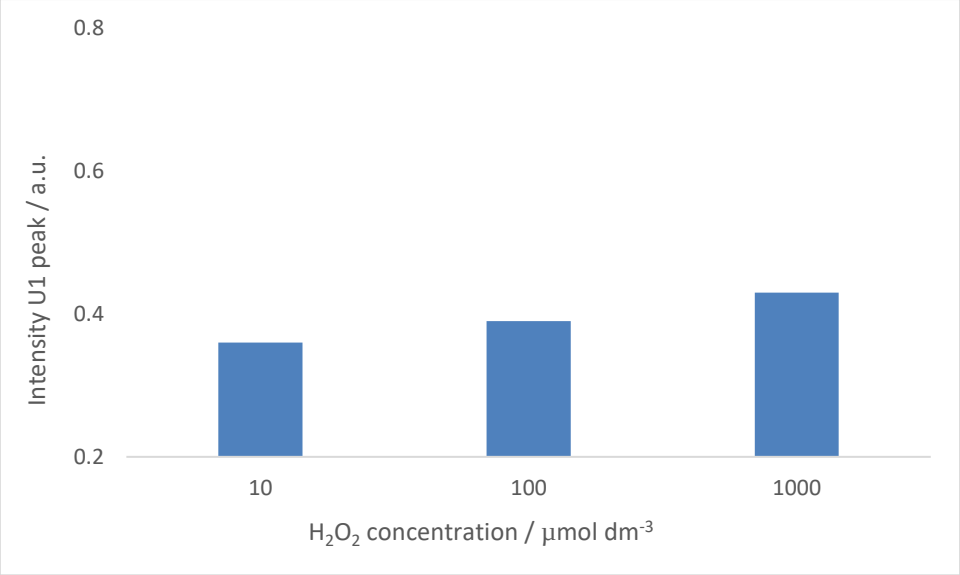

Figure 4-7 showing the increasing intensity of the U1 peak of the 25 GWd/tU SIMFUEL pellet taken after an OCP measurement in a 0.1 mol dm^{-3} Na_2SO_4 background electrolyte spiked with increasing concentrations of H_2O_2, taken over a 4 hour period

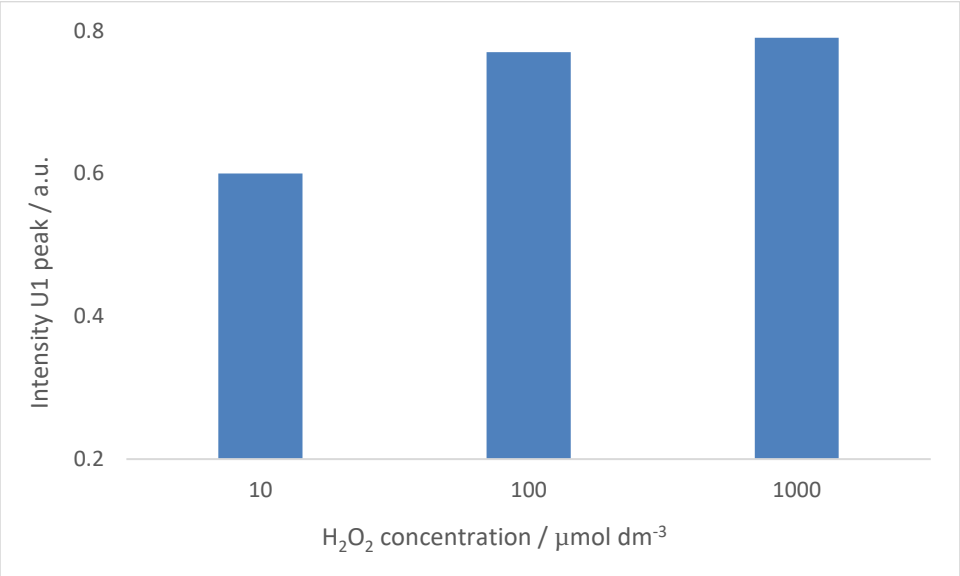

Figure 4-8 showing the increasing intensity of the U1 peak of the 43 GWd/tU SIMFUEL pellet taken after an OCP measurement in a 0.1 mol dm^{-3} Na_2SO_4 background electrolyte spiked with increasing concentrations of H_2O_2, taken over a 4 hour period

In Figure 4-7 we can see the intensity of the U1 peak of the low doped 25 GWd/tU SIMFUEL pellet measured after exposure to increasing concentrations of hydrogen peroxide. It can be seen here that the intensity of the U1 peak increases slightly with increased hydrogen peroxide concentration. Looking at Figure 4-8 above however, we can clearly see that the intensity of the U1 peak increases for the high burnup 43 GWd/tU SIMFUEL pellet as the concentration of hydrogen peroxide is

increased from 10 µmol dm^{-3} to 1 mmol dm^{-3}. This increase in the intensity of U1 with increasing peroxide concentration is surprising as U1 is associated with the presence of trivalent dopants and it is not expected that this will be affected by the addition of peroxide.

However, this increase in intensity of U1 with increasing peroxide concentration can be explained by consideration of the possible existence of a fourth defect peak that may make a minority contribution to the overall profile of the compound defect peak observed in the range 500 to 700 cm^{-1}. Maslova *et al* (8) report the existence of a weak band at 550 cm^{-1} on undoped UO_2; this they refer to as the U* band and have associated it with an unspecified feature of the grain boundaries (6) (8). Due to the weak nature of this band, it is not expected to contribute significantly to the overall intensity of the compound peak and will be difficult to deconvolute from same; thus, it has not featured in our analysis of this compound feature so far. However, the U* band may be playing a role at the elevated concentrations of peroxide employed here. Given that it occurs at 550 cm^{-1}, it may make a small contribution to the overall intensity of the U1 peak centred at 530 cm^{-1} and may be responsible for the small increase in U1 observed with increasing hydrogen peroxide concentration. If this were the case, it would suggest that the U* peak is actually associated with hyperstoichiometry at grain boundaries – a hypothesis that is supported by two pieces of evidence:

1. The increase in the intensity of U1 with peroxide concentration is strongest on the 43 GWd/tU SIMFUEL sample; it is not seen on the undoped UO_2 pellet and only slightly in the 25 GWd/tU SIMFUEL pellet. As stated above, the U* band is associated with an unspecified feature at grain boundaries. As the high doped 43 GWd/tU SIMFUEL pellet contains a higher concentration of grain boundaries (see Figures 2-3 to 2-5 in Chapter 2), compared to the undoped and low doped pellets, it will be easiest to see any effects due to changes in U* on the high doped 43 GWd/tU SIMFUEL pellet
2. As seen from the cyclic voltammogram of Figure 4-2 and the OCP data of Figures 4-1, 4-4 and 4-6, the equilibrium OCPs for all three sample systems studied in Figures 4-7 and 4-8 are well positive of Region A where the oxidation of UO_{2+x} to $UO_{2.33}$ occurs at grain boundaries - . meaning that the added hydrogen peroxide is contributing to said grain boundary oxidation. This grain boundary alteration process may then affect the U* band, its increase in intensity with peroxide concentration suggesting that it is associated with increased grain boundary hyperstoichiometry

For reasons discussed in Chapter 3, the wavenumber range shown in Figures 4-1, 4-4 and 4-6 does not extend past 750 cm^{-1}. However, during the Raman studies of pellets exposed to the higher hydrogen peroxide concentration of 1 mmol dm^{-3} for four hours, an additional peak was seen to develop with a maximum at 819 cm^{-1} on the undoped UO_2 pellet. This peak, denoted v1 (9), can be seen in Figure 4-9 below.

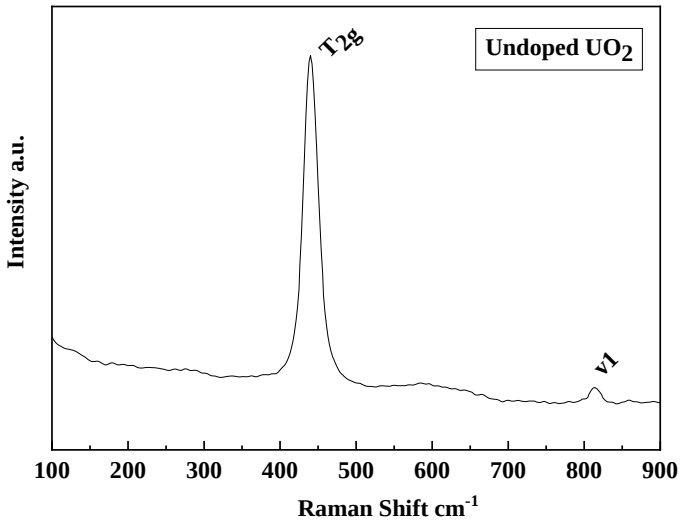

Figure 4-9 showing the Raman spectra of an undoped UO_2 pellet exposed to a 0.1 mol dm^{-3} Na_2SO_4 background electrolyte spiked with 1 mmol dm^{-3} H_2O_2

Generally, bands in the range of 800 - 820 cm^{-1} are assigned to the symmetric (O=U=O) stretch, indicating the presence of surface adsorbed uranyl (10). Given that this peak is only seen in the presence of the highest concentration of peroxide used in this study, it is not unreasonable to conclude that the uranyl is adsorbed in the form of the uranyl peroxide phases of studtite and metastudtite – arising from the hydrogen peroxide reacting with uranyl ions released from oxidising uranium dioxide surfaces. Supporting this conclusion is the fact that studtite is known to exhibit a peak in the region 800-850 cm^{-1} (10), with pristine studtite being recorded at a Raman shift of 819 cm^{-1} by Fairley *et al*. (10). The formation of studtite at the surface of the samples under study here is further investigated below.

We will now return to the electrochemical behaviour of the undoped UO_2, the low burnup 25 GWd/tU and the high burnup 43 GWd/tU SIMFUEL pellets. Below are the cyclic voltammograms of our samples in a background electrolyte containing 1 mmol dm^{-3} hydrogen peroxide.

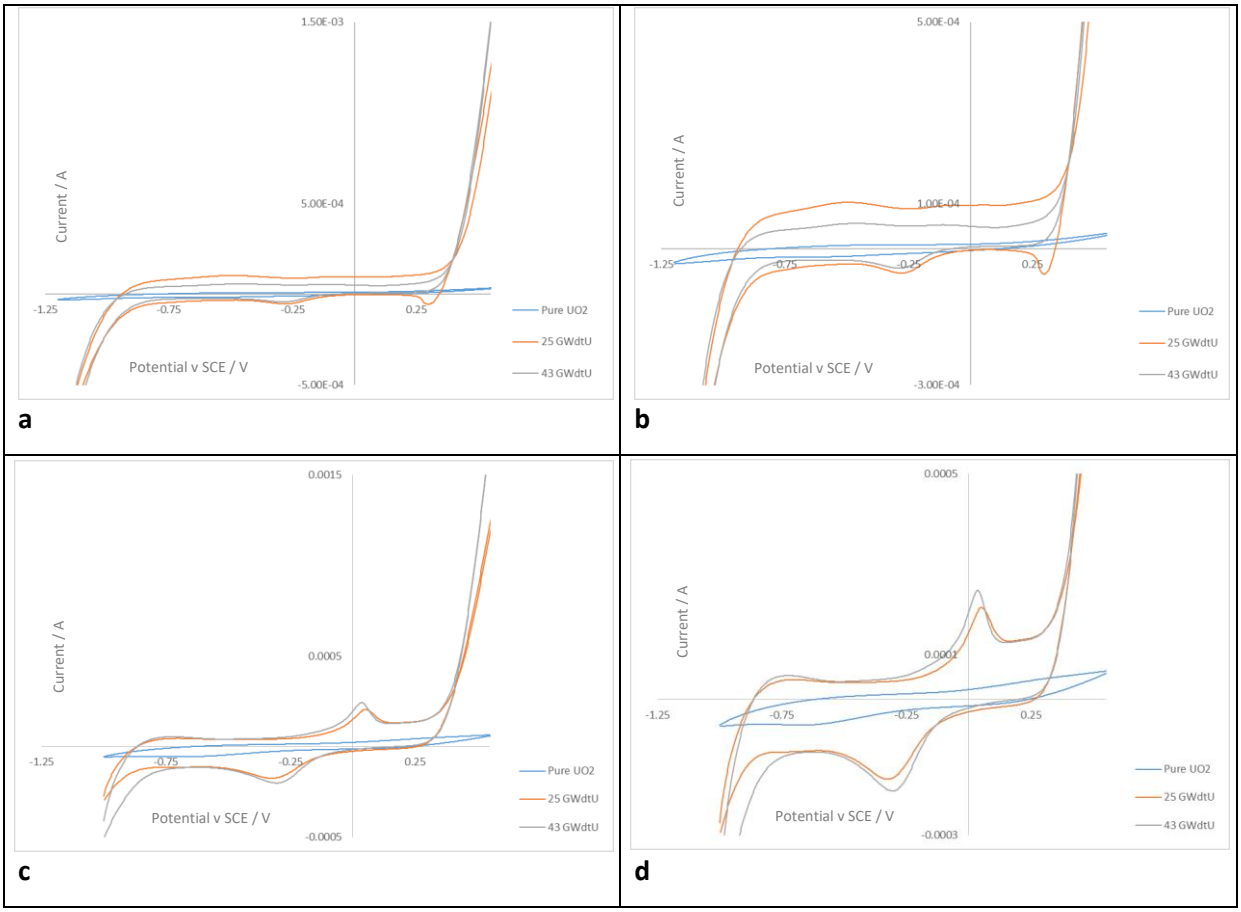

Figures 4-10a to 4-10d – (a) showing the cyclic voltammograms of UO_2, 25 & 43 GWd/tU SIMFUEL pellets in a 0.1 mol dm^{-3} Na_2SO_4 background electrolyte, cycled at a potential range of (-) 1.2 to (+) 0.7 V, at a scan rate of 20 mV/s; (b) a blown-up image of 4-10a; (c) the cyclic voltammograms of UO_2, 25 & 43 GWd/tU SIMFUEL pellets in a 0.1 mol dm^{-3} Na_2SO_4 background electrolyte spiked with 1 mmol dm^{-3} H_2O_2, cycled at a potential range of (-) 1.2 to (+) 0.7 V, at a scan rate of 10 mV/s; (d) a blown up image of 4-10c, respectively

Above in Figures 4-10c and 4-10d are the cyclic voltammetries of an undoped UO_2 pellet, a low burnup 25 GWd/tU SIMFUEL pellet and a high burnup 43 GWd/tU SIMFUEL pellet in a 0.1 mol dm^{-3} Na_2SO_4 background eletrolyte spiked with 1 mmol dm^{-3} hydrogen peroxide, at a potential window of - 1 V to + 1.8 V, taken at a scan rate of 20 mV/s.

Here once again we can see that the undoped UO_2 pellet remains electrochemically unreactive, due to the absence of dopants and metallic particles to increase matrix conductivity and catalyse

hydrogen evolution respectively, and that the presence of hydrogen peroxide has an insignificant effect on the undoped UO_2 sample. As before, the low doped 25 GWd/tU and the high burnup 43 GWd/tU SIMFUEL pellets are both electrochemically more reactive than the undoped UO_2, the 43 GWd/tU having a slightly higher electrochemical reactivity in this case. This is again due to the fact that they both contain concentrations of dopants and metallic particles to increase matrix conductivity and catalyse hydrogen evolution respectively. At a hydrogen peroxide concentration of 1 mmol dm^{-3}, we see that the low doped 25 GWd/tU and the high doped 43 GWd/tU SIMFUEL pellets both have similar reactivities in this case. This is due to the fact that the suppression of the effective H_2O_2 concentration caused by the catalytic decomposition of H_2O_2 resulting from the epsilon particle concentration in the 43 GWd/tU SIMFUEL pellet seen at peroxide concentrations lower than 100 µmol dm^{-3} is proprotionally less important at this higher peroxide concentration of 1 mmol dm^{-3} and so is effectively not observed. We can also see that the 43 GWd/tU SIMFUEL pellet displays a higher electrochemical reactivity when compared to the low doped 25 GWd/tU SIMFUEL pellet at this concentration of hydrogen peroxide. This is potentially due to this elevated H_2O_2 concentration acting cooperatively to increase the defect concentration at the surface of the 43 GWd/tU SIMFUEL sample, leading to its increase in the electrochemical reactivity observed here – a phenomenon discussed in reference to Figure 1-15 in Chapter 1. We will return to this point below. Comparing Figure 4-9d above to Figure 4-5d, we can see that the oxidation and reduction peaks that appeared in the presence of H_2O_2 have further increased in size with increased H_2O_2 concentration, as expected.

Returning to the discussion of observed uranyl phases, as discussed above, we saw the formation of a peak in the Raman spectrum of undoped UO_2 at a Raman shift of 819 cm^{-1} after 4 hr exposure to a 0.1 mol dm^{-3} sodium sulfate background electrolyte in the presence of 1 mmol dm^{-3} hydrogen peroxide, see Figure 4-9, a peak that we took as evidence of the formation of studtite / metastudtite at the UO_2 surface. This formation of studtite / metastudtite in accordance with Equations 4-1 and 4-2 below respectively, is only expected to be observed in high peroxide concentration containing background electrolyte and not peroxide containing simulated groundwaters due to the presence of carbonates in the latter that may form complexes with the uranyl species in accordance with Equation 4-3, so interrupting studtite / metastudtite formation:

$$UO_2^{2+} + H_2O_2 + 4H_2O \leftrightarrow UO_4 \cdot 4H_2O + 2H^+$$

Equation 4-1 (11)

$$UO_2^{2+} + H_2O_2 + 2H_2O \leftrightarrow UO_4 \cdot 2H_2O + 2H^+$$

Equation 4-2 (12)

$$UO_2^{2+} + H_2O_2 + 2CO_3^{2-} \leftrightarrow UO_4 \cdot 2CO_3^{4-} + 2H^+$$

Equation 4-3 (13)

Interestingly, the formation of studtites after a relatively short 4 hour exposure to 1 mmol dm^{-3} H_2O_2 in sodium sulfate has only been observed on the undoped UO_2 pellet, and not on the 25 or 43 GWdt/U SIMFUELs. Formation of studtites on the 25 GWd/tU SIMFUEL pellet is only observed after longer exposure to a Na_2SO_4 background electrolyte spiked with 1 mmol dm^{-3} H_2O_2. This is shown in the associated Raman spectrum of a so-exposed 25 GWd/tU SIMFUEL sample. in Figure 4-11 below; a peak due to the characteristic symmetric (O=U=O) stretch is plainly seen at a Raman shift of 819 cm^{-1}.

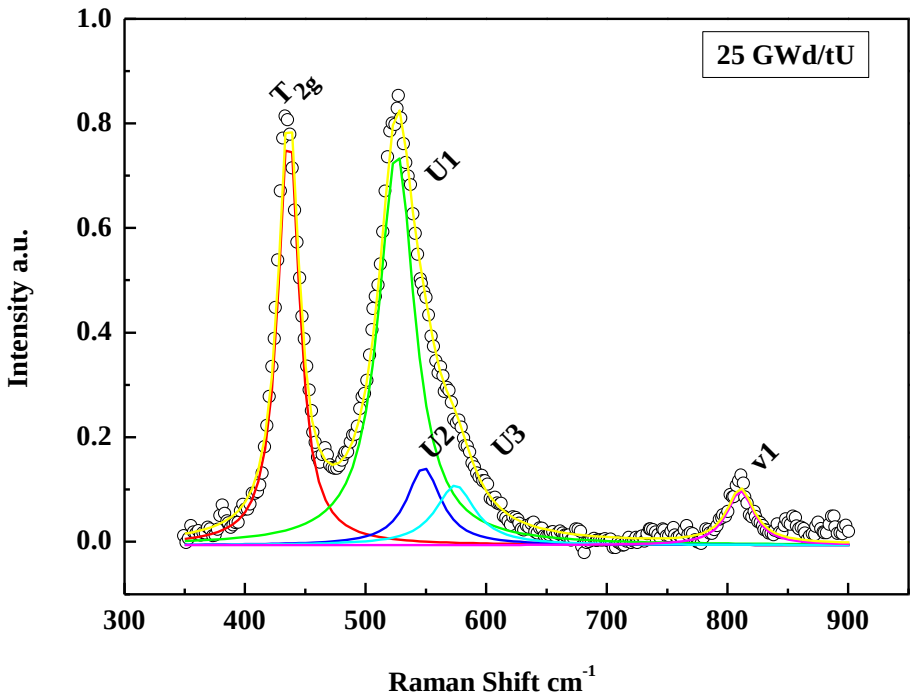

Figure 4-11 showing the Raman spectra of a 25 GWd/tU SIMFUEL pellet exposed to a 0.1 mol dm^{-3} Na_2SO_4 background electrolyte spiked with 1 mmol dm^{-3} H_2O_2 for 53 hours

This peak, denoted v1 (9) in Figure 4-11, only appears after 5 h exposure to 1 mmol dm^{-3} H_2O_2. This grows in intensity up to 50 h exposure and, as described above, is seen a result of the reaction between H_2O_2 and UO_2^{2+} to form studtite / metastudtite as given by Equations 4-1 and 4-2 – the uranyl generated as a result of H_2O_2–driven corrosion of the AGR SIMFUEL UO_2 matrix.

As discussed in Chapter 1, the process of fuel corrosion in the presence of H_2O_2 is complicated by the hyperstoichiometric behaviour of UO_2. As UO_2 moves towards hyperstoichiometry through the peroxide-driven oxidation of U(IV) sites, U(V)/U(IV) donor-acceptor sites may be generated, which in turn catalyse the reduction of H_2O_2 (14). The balance of electrons in this process is provided by the coupled chemical/electrochemical oxidation of U(IV) to U(V), catalytically further accelerating the rate of peroxide reduction, and (similarly coupled) U(IV) oxidation to U(VI) with its release to solution as UO_2^{2+}. The increase in lattice disorder with the increased burn-up in our samples will also yield an increase in the concentration of $U^{IV/V}$. This in turn increases the corrosion rate as the burnup is increased.

Figure 4-12 below shows a schematic representing the mechanism of UO_2 dissolution in the presence of H_2O_2. As pointed out above, such oxidative generation of UO_2^{2+} in the presence of H_2O_2 as oxidant may result in the formation of studtite/metastudtite (14), again in accordance with Equations 4-1 and 4-2.

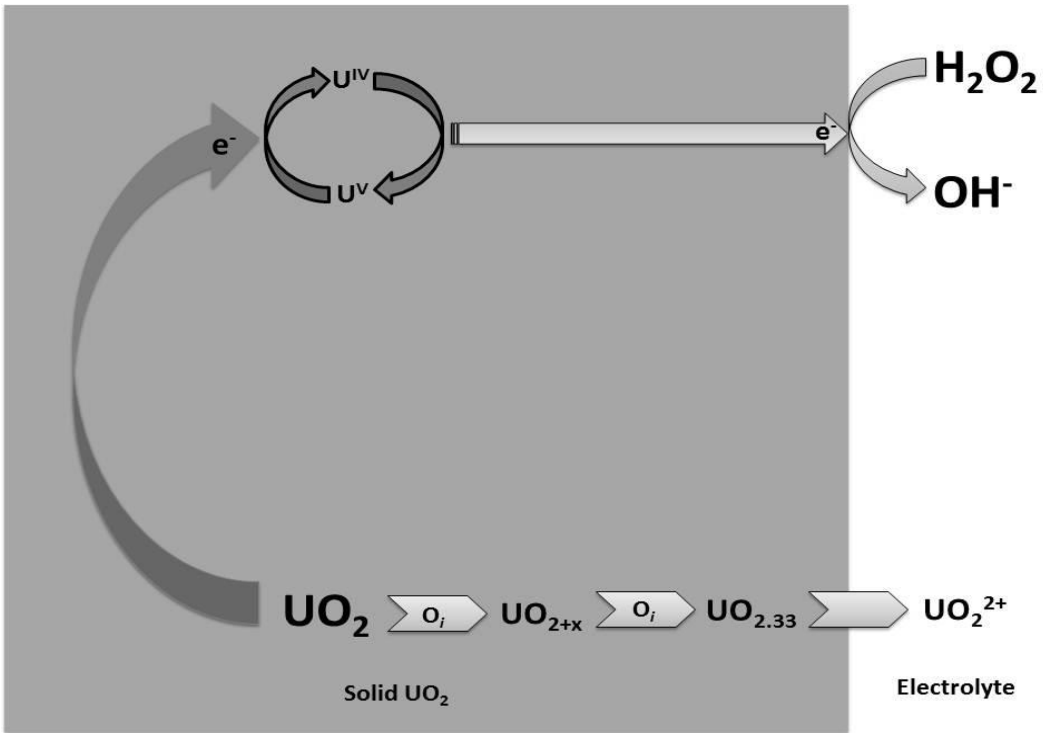

Figure 4-12 showing schematic representation of the mechanisms of UO_2 dissolution in the presence of hydrogen peroxide

Given the mechanism of Figure 4-12 above, it should also be possible for a high burnup 43 GWd/tU SIMFUEL pellet to form studtite or metastudtite in the presence of hydrogen peroxide, as the generation of UO_2^{2+} would be expected to occur faster on the high burnup SIMFUEL pellet as opposed to the low burnup SIMFUEL pellet – an expectation that arises from the fact that the high burnup 43 GWd/tU SIMFUEL pellet is more prone to corrosion (as seen from the electrochemical data), and thus the dissolution of the fuel surface and the release to solution of the generated UO_2^{2+} to solution will occur sooner. This greater susceptibility to corrosion is most plainly evidenced by Figure 4-2 and Table 4-1 below which presents i_{corr} data obtained for each sample (see Chapter 3 for more details). The latter in particular reveals that the i_{corr} for the undoped pellets is at least an order of magnitude smaller than that for the doped pellets meaning that less current is being able to be carried through the undoped samples due to the absence of both dopants in the solid solution matrix and the catalytic effect of metallic particles at the SIMFUEL surface.

Sample	Undoped UO_2	25 GWd/tU	43 GWd/tU
i_{corr} / Amps cm^{-2} (A)	3.15E-08	5.33E-07	1.14E-06

Table 4-1 showing the corrosion current densities of the undoped UO_2, the 25 & 43 GWd/tU SIMFUEL pellets

Thus, based on this simple analysis of corrosion currents, we expect the rate of uranyl release from the 43 GWd/tU sample to be similar to that observed from the 25 GWd/tU sample, both being faster than that observed on the undoped UO_2 sample. The interaction of this uranyl with hydrogen peroxide to form studtite / metastudtite would therefore also be expected to follow a similar hierarchy. Unfortunately, due to time constraints and restrictions on instrument availability, this experiment was however not carried out for the 43 GWd/tU SIMFUEL. The unavailability of the data for the 43 GWd/tU sample notwithstanding, this analysis may be overly simple in light of the fact that it actually takes longer for the 25 GWd/tU than the undoped UO_2 sample to exhibit formation of a peak associated with studtite / metastudtite.

One possible explanation for the prolonged formation time of studtite/metastudtite on a low doped 25 GWd/tU SIMFUEL pellet may be that a hydrogen peroxide sink is formed upon exposure to said SIMFUEL pellet. The presence of this sink may lead to a decrease in the peroxide concentration at the SIMFUEL surface, hence suppressing and/or not driving the formation of studtite upon release of uranyl in to solution. This may offer an explanation as to why prolonged exposure times are required for the formation of studtite/metastudtite to take place. As evidenced by the i_{corr} data above, the undoped UO_2 pellet has a lower electrochemical activity when compared to the 25 GWd/tU SIMFUEL pellet. This lower electrochemical activity of the UO_2 is what is causing the matrix oxidation to occur less aggressively and/or more slowly, with a lower degree of peroxide consumption. The surface concentration is thus maintained at a level that may precipitate studtite at the UO_2 surface when UO_2^{2+} is released. The onset of studtite formation on undoped UO_2 corresponds to that seen by Wilbraham *et al* (15). Owing to the above explanation it could be speculated that the formation of studtite/metastudtite would also be possible on a high-doped 43 GWd/tU SIMFUEL pellet with prolonged exposure times to hydrogen peroxide, however with the unavailability of experimental data it is not possible to make this prediction.

Finally, it is worthwhile briefly revisiting the open circuit potential data for all three pellets, the undoped UO_2, the low as well as the high burnup 25 and 43 GWd/tU SIMFUEL pellets, as they are exposed to different concentrations of hydrogen peroxide. Figure 4-13 is a summary of the OCP measurements presented within this chapter and has been reproduced here for ease of comparison with the following figures below.

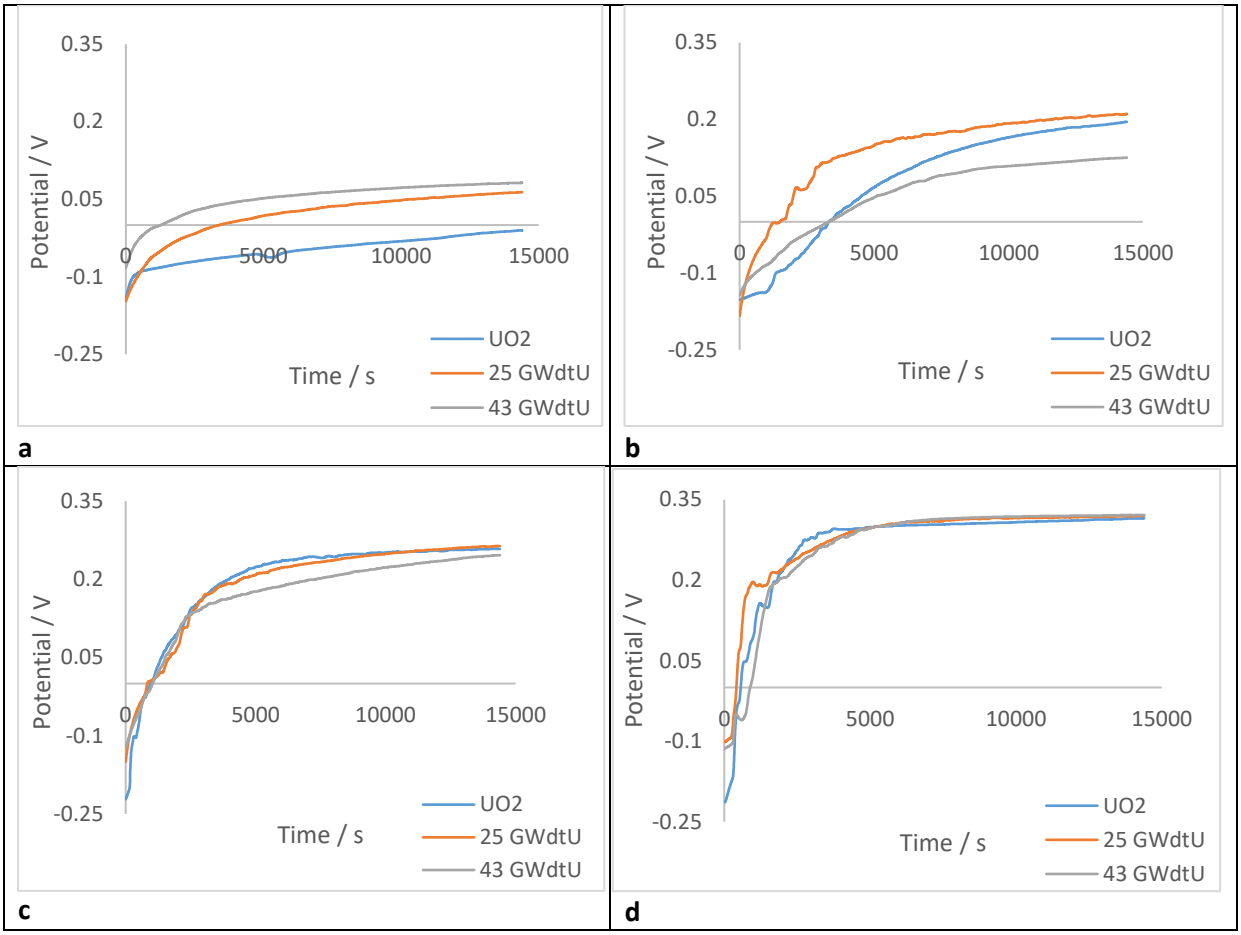

Figures 4-13a to 4-13d showing- (a) Open circuit potentials of the UO_2 and 25 & 43 GWd/tU SIMFUEL pellets over a 4 hour period in a 0.1 mol dm^{-3} Na_2SO_4 background electrolyte; (b) the open circuit potential of the UO_2 and 25 & 43 GWd/tU SIMFUEL pellets over a 4 hour period in a 0.1 mol dm^{-3} Na_2SO_4 background electrolyte spiked with 10 µmol dm^{-3} H_2O_2; (c) the open circuit potential of the UO_2 and 25 & 43 GWd/tU SIMFUEL pellets over a 4 hour period in a 0.1 mol dm^{-3} Na_2SO_4 background electrolyte spiked with 100 µmol dm^{-3} H_2O_2; (d) the open circuit potential of the UO_2 and 25 & 43 GWd/tU SIMFUEL pellets over a 4 hour period in a 0.1 mol dm^{-3} Na_2SO_4 background electrolyte spiked with 1 mmol dm^{-3} H_2O_2

Figure 4-13 (a) shows the undoped UO_2 and 25 & 43 GWd/tU SIMFUEL pellets exposed to a background electrolyte of 0.1 mol dm^{-3} soldium sulfate, without any hydrogen peroxide spike. In the absence of hydrogen peroxide we can see that the undoped UO_2 pellet exhibits the slowest change in potential as a function of immersion time and, at any one immersion time, has the lowest measured potential of all three samples studied. The faster rate of approach to equilibrium exhibited by the 25 and 43 GWd/tU burnup samples compared to the UO_2 sample is reflective of the higher, dopant-derived charge carrier density and thus conductivity of the former. This is also the underlying cause of the different equilibrium potentials exhibited as the introduction of lanthanide ions into the solid solution matrix of the 25 and 43 GWd/tU samples increases the p-type character of the SIMFUELs, shifting the Fermi level to more positive potentials (see Chapter 3 for details).

In Figure 4-13 (b), which is a solution containing 10 µmol dm^{-3} H_2O_2, we immediately see that all three samples have responded strongly to the presence of hydrogen peroxide. The rate of change of potential is faster for all three samples and the extrapolated equilibrium potentials for all three samples are well positive of those seen in the absence of peroxide in Figure 4-13 (a). Whilst the high burnup 43 GWd/tU SIMFUEL pellet had the highest resting potential in the absence of hydrogen peroxide as seen in Figure 4-13 (a), we can see that in Figure 4-13 (b), the same pellet has the lowest resting potential in the presence of 10 µmol dm^{-3} peroxide when compared to the undoped UO_2 and 25 GWd/tU SIMFUEL pellets. As discussed above, we attribute this to effect that the higher population of epsilon particles at the surface of the 43 GWd/tU SIMFUEL surface has on promoting the decomposition of peroxide at that surface. At the low bulk concentration of 10 µmol dm^{-3} peroxide used in Figure 4-13 (b), this decomposition significantly suppresses the concentration of peroxide at the pellet surface, so suppressing the measured potential. The 25 GWd/tU SIMFUEL has a lower epsilon particle loading and so this effect is not seen, or at least is not seen so strongly, on this lower simulated burnup sample.

As discussed before, we can see in Figures 4-13 (c), which shows an OCP measurement of our samples immersed in a solution containing 100 µmol dm^{-3} H_2O_2, and (d), which is an OCP measurement of the same samples exposed to a solution containing 1 mmol dm^{-3} H_2O_2, that the rate at which all three samples reach their resting potentials increases as the concentration of hydrogen peroxide that the samples are exposed to increases. Moreover, the suppression of the measured potential seen on the 43 GWd/tU SIMFUEL sample in Figure 4-13 (b) is not seen here as, presumably, the epsilon particle promoted decomposition, and thus the local concentration suppression of peroxide at the pellet surface is not as significant at the higher peroxide concentrations used in Figures 4-13 (c) and 4-13 (d).

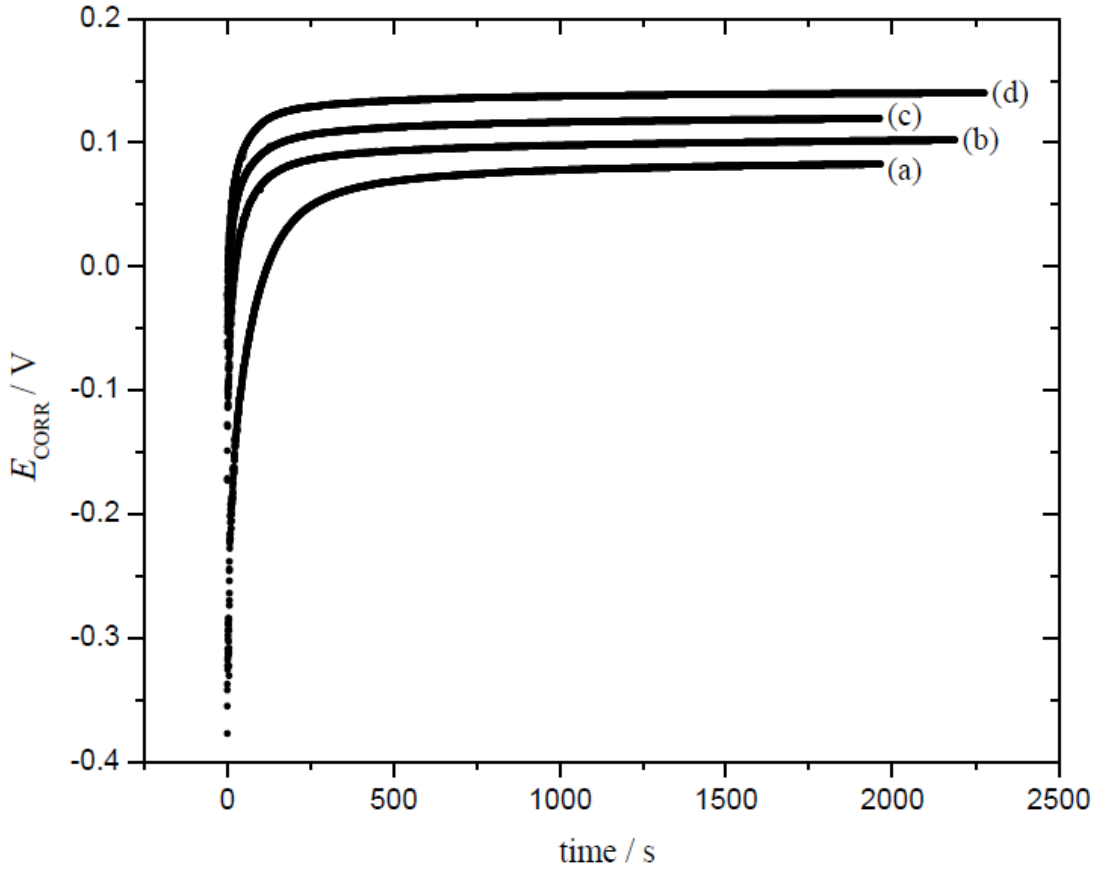

Figure 4-14 showing the OCP of CANDU SIMFUEL after exposure to (a) 480 µmol dm^{-3}, (b) 2.4 mmol dm^{-3}, (c) 8 mmol dm^{-3} and (d) 17 mmol dm^{-3} hydrogen peroxide (16)

Figure 4-14 shows the open circuit potentials of a 1.5 at. % CANada Deuterium Uranium (CANDU) SIMFUEL after exposure in an alkaline solution spiked with the following concentrations of hydrogen peroxide respectively: (a) 480 µmol dm^{-3}, (b) 2.4 mmol dm^{-3}, (c) 8 mmol dm^{-3} and (d) 17 mmol dm^{-3} (16), for 37.5 minutes.

From this, we can see that there is also a dependence of the equilibrium open circuit potentials on the concentration of hydrogen peroxide for CANDU SIMFUEL – in broad agreement with our results. However, care must be taken in a direct comparison of our results with those of Figure 4-14 as the hydrogen peroxide concentrations used in obtaining the data of Figure 4-14 are considerably higher than those used in our analogous experiments on undoped UO_2 and low and high burnup 25 and 43 GWd/tU AGR SIMFUELs.

Regardless of the high hydrogen peroxide concentrations, the CANDU SIMFUELs come to rest at a lower potential than the AGR SIMFUELs when exposed to H_2O_2. From this we can deduce that the AGR SIMFUELs are electrochemically more susceptible to oxidation and so potentially oxidative dissolution than the CANDU SIMFUELs. This is almost certainly a reflection of the fact that the CANDU SIMFUELs were prepared at a considerably lower burnup of 1.5 at. % compared to our 25 and 43 GWd/tU samples which are compositionally equivalent to 3 and 6 at. % burnup CANDU fuels respectively (5). The higher dopant density in, and thus p-type character of, the latter will render them more electrochemically active than the former.

4.3 Conclusions

In this chapter, we have investigated the corrosion effects of deliberately added hydrogen peroxide on our undoped UO_2, as well as our 25 & 43 GWd/tU SIMFUEL pellets in a background electrolyte. In order to do this we employed open circuit potential measurements, cyclic voltammetry and Raman spectroscopy.

With regards to the open circuit potential measurements, we observed that when our samples were exposed to increasing concentrations of hydrogen peroxide, their rates of approach to their rest potentials also increased. At the same time, we observed that the rest potentials reached also increased with increasing concentrations of hydrogen peroxide for all three of our samples.

When comparing our SIMFUEL pellets to that of CANDU SIMFUELs, which had been subjected to similar conditions under OCP in a study carried out by Goldik *et al*. (16), it was observed that our AGR SIMFUELs exhibited the same general trends explained above. It was also observed that our AGR SIMFUELs were more electrochemically susceptible to oxidation and potentially oxidative dissolution than the CANDU SIMFUELs (16). This was attributed to the fact that the CANDU SIMFUELs had been prepared at a lower burnup of 1.5 at. % (16), as opposed to compositions equivalent to 3 and 6 at. % burnup CANDU fuels for our low doped 25 GWd/tU and high doped 43 GWd/tU SIMFUEL pellets respectively.

The measured Raman spectra revealed that hydrogen peroxide had no significant effect on the undoped UO_2 pellet. For the 25 GWd/tU SIMFUEL pellet and the 43 GWd/tU SIMFUEL pellet we saw that, whether in the absence or presence of H_2O_2, the broad compound peak at 575 cm^{-1} exhibited an increase with increased burn-up. As illustrated by Howett *et al*., this feature is attributed to the fact that the increase in dopants induces a range of lattice distortions (1). It was observed however, that the 43 GWd/tU SIMFUEL sample, after exposure to a solution containing 10 µmol dm^{-3} H_2O_2, showed a small decrease in intensity of its U1 peak. This may be explained by the fact that the H_2O_2 puts the SIMFUEL pellet into a potential range whereby the conversion of UO_{2+x} to $UO_{2.33}$ (U_3O_7) at grain boundaries and UO_2 to UO_{2+x} within the grains themselves may occur, as shown by the regional assignments of the cyclic voltammogram established by Seibert *et al*. (30). This introduction of O^{2-}

ions into the lattice may be reducing the intensity of U1. We do not see this effect with the 25 GWd/tU SIMFUEL pellet, likely due to there being less oxygen vacancies to begin with.

Contrary to the observed decrease in the intensity of the U1 peak with the addition of hydrogen peroxide in the 43 GWd/tU SIMFUEL pellet, there was a marked increase in its intensity upon the addition of 1 mmol dm^{-3} hydrogen peroxide to the background electrolyte. This observation can be explained by the possible existence of a fourth defect peak, referred to as the U* band (8). As this peak is associated with the hyperstoichiometry at grain boundaries (8), it may be contributing to the overall intensity of the U1 peak. As the concentration of grain boundaries is lower in the low doped 25 GWd/tU SIMFUEL pellet as opposed to the high doped 43 GWd/tU SIMFUEL pellet, due to the larger grain sizes in the former (5), the observed increase in the intensity of the U1 peak is smaller than it is for the 43 GWd/tU SIMFUEL pellet. Given that U1 for the 43 GWd/tU SIMFUEL is seen to decrease in intensity in 10 μmol dm^{-3} peroxide dosed electrolyte compared to undosed electrolyte, it would seem that apparent increase in U1 intensity associated with U* is only observed at high peroxide concentrations – an observation consistent with U* being an intrinsically weak feature as reported by Maslova *et al.* (8).

Furthermore, we observed that exposure to a background electrolyte containing a 1 mmol dm^{-3} H_2O_2 spike drove the formation of the uranyl phase studtite/metastudtite in the undoped UO_2 sample after 4 hrs, which is consistent with findings by Wilbraham et *al*. (3), and in the 25 GWd/tU SIMFUEL pellet after prolonged exposure times. The formation of studtites on SIMFUELs in the presence of H_2O_2 has been well documented in the literature by the likes of Shoesmith, Li, Wu, Corbel and Hansen et *al*. (17) (18) (19) (20). Due to unavailability of instruments, this experiment was not performed on the 43 GWd/tU SIMFUEL pellet.

Finally, we were able to confirm through calculated i_{corr} data that the current densities of SIMFUEL samples increased when compared to our undoped UO_2 sample, meaning that with the addition of dopants, the sample becomes more susceptible to corrosion, which is in accordance with our electrochemical and Raman spectral data.

In the next chapter we will proceed to the study of corrosion behaviour of our undoped UO_2, 25 & 43 GWd/tU SIMFUEL pellets in simulated groundwaters.

References

1. E.A. Howett. *The behaviour of spent nuclear fuel in wet interim storage.* s.l. : Lancaster University, 2019.

2. D. Shoesmith, S. Ramamurthy. *Mechanical and chemical indicators for SCC in alloy 800 steam generator tubing.* s.l. : Western University, 2014.

3. R.J. Wilbraham, C. Boxall, D.T. Goddard, R.J. Taylor, S.E. Woodbury. *The effect of hydrogen peroxide on uranium oxide films on 316L stainless steel.* s.l. : Journal of Nuclear Materials, 2015, Vol. 464. pp. 86-96.

4. D.W. McKee, *Catalytic decomposition of hydrogen peroxide by metals and alloys of the platinum group.* s.l. : Journal of Catalysis, 1969, Vol. 14. pp. 355-364.

5. Z. Hiezl. *Processing and microstructural characterisation of UO_2-based simluated spent nuclear fuel ceramics for the UK's advanced gas-cooled reactors.* s.l. : Imperial College London, 2015.

6. J.M. Elorrieta, L.J. Bonales, N. Rodriguez-Villagra, V.G. Baonza, J. Cobos. *A detailed Raman and X-ray study of UO_{2+x} oxides and related structure transitions***.** s.l. : Physical Chemistry Chemical Physics, 2016, Vol. 18. pp. 28209 - 28216.

7. X. Zhang, R. Ji, L. Wang, L. Yu, J. Wag, B. Geng, G. Wang. *Controllable synthesis of silver nanoendrites on copper rod and its application to hydrogen peroxide and glucose detection.* s.l. : Crystal Engineering Communication, 2013, Vol. 15. pp. 1173 - 1178.

8. O.A. Maslova, G. Giumbretiere, M.R. Ammar, L. Desgranges, C. Jegou, A. Canizares, P. Simon. *Raman imaging and principal component analysis-based data processing on uranium oxide ceramics.* s.l. : Materials Characterization, 2017, Vol. 129. pp. 260 - 269.

9. R. Mohun, L. Desgranges, A. Canizares, N. Raimboux, F. Duval. *Investigating the role of irradiation defects during UO_2 oxidative dissolution.* s.l. : Journal of Nuclear Materials, 2018, Vol. 509. pp. 305 - 312.

10. M. Fairley, N.M. Myers, J.E.S Szymanowski, G.E. Sigmon, P.C. Burns, J.A. LaVerne. *Stability of solid uranly peroxides under irradiation.* s.l. : Inorganic Chemistry, 2019, Vol. 58. pp. 14112 - 14119.

11. J. Li. *Stability of studtite under spent nuclear fuel repository conditions.* s.l. : KTH Royal Institute of Technology in Stockholm, 2019.

12. X. Guo, S.V. Ushakov, S. Labs, H. Curtis, D. Bosbach, A. Navrotsky. *Energetics of metastudtite and implications for nuclear waste alteration.* s.l. : Proceedings of the National Academy of Sciences, 2014, Vol. 111.

13. T. Watanabe, Y. Ikeda. *A study on identification of uranyl complexes in aqueous solutions containing carbonate ion and hydrogen peroxide.* s.l. : Energy Procedia, 2012, Vol. 39. pp. 81 - 95.

14. H. He, M. Broczkowski, K. O'Neil, D. Ofori, O. Semenikhim, D. Shoesmith. *Corrosion of Nuclear Fuel (UO_2) Inside a Failed Nuclear Waste Container.* s.l. : Western University Report, 2012, Vol. NWMO TR-2012-09.

15. R.J. Wilbraham. *Surface contamination by photocatalysis.* s.l. : Lancaster University, 2011.

16. J.S. Goldik, H.W. Nesbitt, J.J. Noel, D.W. Shoesmith. *Surface electrochemistry of UO_2 in dilute alkaline hydrogen peroxide solutions.* s.l. : Electrochimica Acta, 2004, Vol. 49. pp. 1699-1709

17. J. Li, A.C. Maier, M. Jonsson. *Stability of studtite in aqueous suspension: impact of HCO_3- and ionizing radiation on the dynamics of dissolution.* s.l. : ACS Applied Energy Materials, 2020, Vol. 3. pp. 352 - 357.

18. L. Wu. *The Electrochemistry of hydrogen peroxide on uranium dioxide and the modelling of used nuclear fuel corrosion under permanent disposal conditions.* s.l. : Western University, 2014.

19. C. Corbel, G. Sattonnay, S. Guilbert, F. Garrido, M.F. Barthe, C. Jegou. *Addition versus radiolytic production effects of hydrogen peroxide on aqueous corrosion of UO_2.* s.l. : Journal of Nuclear Materials, 2006, Vol. 348. pp. 1 - 17.

20. B.D. Hanson, B. McNamara, E.C. Buck, J.I. Friese, E. Jenson, K. Krupka, B.W. Arey. *Corrosion of commercial spent nuclear fuel. 1. Formation of studtite and metastudtite.* s.l. : Radiochimica Acta, 2009, Vol. 93.

21. G. Hinds. *The electrochemistry of corrosion.* s.l. : Corrosion Doctors Publications, 1996, pp. 4-5.

22. D.R. Rittman, S. Park, C.L. Tracy, L. Zhang, R.I. Palomares, M.Lang, A. Navrotsky, W.L. Mao, R.C. Ewing. *Structure and bulk modulus of Ln-doped UO_2 (Ln = La, Nd) at high pressure.* s.l. : Journal of Nuclear Materials, 2017, Vol. 490. pp. 28 - 33

23. Quigora, A. *Cyclic Voltammetry.* s.l. : LibreTexts, 2019.

24. M. Pandiarajan, S. Rajendran, J.S. Bama, R.J. Rathis, S.S. Prabha. *Applications of cyclic voltammetry in corrosion inhibition studies.* s.l. : International Journal of Nano Corrosion Science and Engineering, 2016.

25. Y.S. Jimenez, M.T. Gil, M.T. Guerra, L.S. Baltes, J.C.M. Rosca. *Interpretation of open circuit potential of two titanium alloys for a long time immersion in physiological fluid.* s.l. : Bulletin of the Transilvania University of Brasov, 2009, Vol. 2.

26. N. Liu, J. Kim, J. Lee, Y-S. Youn, J-G. Kim, J-Y. Kim, J.J. Noel, D.W.Shoesmith. *Influence of Gd doping on the structure and electrochemical behaviour of UO_2.* s.l. : Electrochimica Acta, 2017, Vol. 247. pp. 496 - 504.

27. H. He, P.G. Keech, M.E. Broczkowski, J.J. Noel, D.W. Shoesmith. *Characterization of the influence of fission product doping on the anodic reactivity of uranium dioxide.* s.l. : Canadian Journal of Chemistry, 2007, Vol. 85. pp. 702 - 713.

28. Z. Talip, T. Wiss, P.E. Raison, J. Paillier, D. Manara, J. Somers, R.J.M. Konings. *Raman and X-ray studies of uranium-lanthanum-mixed oxides before and after air oxidation.* s.l. : Journal of the American Ceramic Society, 2015, Vol. 98.

29. K. Park. *The oxygen potential of neodymia-doped urania based on a defect structure.* s.l. : Journal of Nuclear Materials, 1994, Vol. 209. pp. 259 - 262.

30. A. Seibert, D.H. Wegen, T. Gouder, J. Roemer, T. Wiss, J.-P. Glatz. *The use of the electrochemical quartz crystal microbalance (EQCM) in corrosion studies of UO_2 thin film models.* s.l. : Journal of Nuclear Materials, 2011, Vol. 491. pp. 112 - 121.

Chapter 5 Behaviour of UO_2 & SIMFUELs in Simulated Groundwaters

5.1 Introduction

In the previous Chapter, we have investigated the Raman spectral, electrochemical and open circuit potential measurements of the undoped UO_2, as well as the low and high burnup 25 & 43 GWd/tU SIMFUEL pellets in a background electrolyte in the presence of varying concentrations of hydrogen peroxide. In order to assess how real spent nuclear fuel may behave in an underground repository after the cladding has been compromised and groundwater has ingressed to the fuel matrix, we must also investigate the behaviour of our undoped UO_2 and SIMFUEL pellets in simulated groundwaters. In order to do so we have selected two different simulated groundwaters to investigate: a modified simplified groundwater, and an evaporate groundwater. The modified simplified groundwater has been made up to the same chemical composition as that suggested by Studsvik (see Chapter 2) (1). The evaporite groundwater has been chosen as one of the groundwaters to be investigated as an underground repository in the UK may potentially be built on a site where evaporite rock is prevalent (see Chapter 1 for rock formations and Chapter 2 for simulated groundwater compositions) (2). This chapter will focus on the corrosion behaviour of our three samples in simulated groundwaters in the absence of hydrogen peroxide, whilst the following chapter (Chapter 6) will investigate the effects of deliberately added hydrogen peroxide on the corrosion behaviour of our samples in simulated groundwaters.

5.2 Results & Discussion

First, we will look into the open circuit potential measurement along with the Raman spectral data of the undoped UO_2 as well as the low and high burnup 25 and 43 GWd/tU SIMFUEL pellets in the modified simplified groundwater simulant.

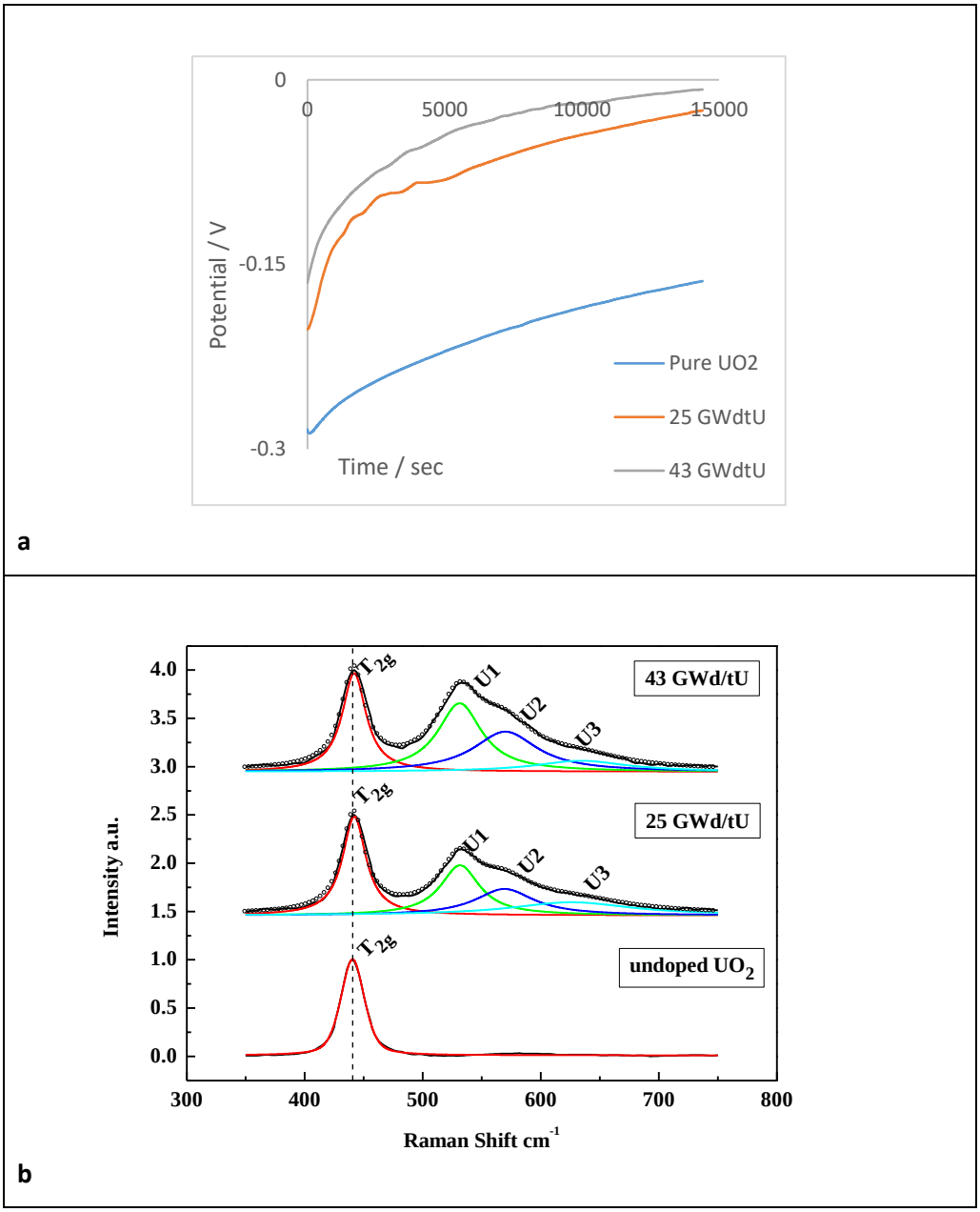

Figures 5-1a and 5-1b - (a) showing the open circuit potential of the UO_2 and 25 & 43 GWd/tU SIMFUEL pellets over a 4 hour period in a modified simplified groundwater simulant pH 8.2; (b) the 20-point averaged Raman spectra of the UO_2 and 25 & 43 GWd/tU SIMFUEL pellets after OCP measurement in Figure 5-1a, represented as Lorenztian

Figure 5-1b above shows the 20 point Raman average spectra represented as Lorentzian of the undoped UO_2 as well as the low and high burnup 25 & 43 GWd/tU SIMFUEL pellets taken after an open circuit potential measurement of four hours in modified simplified groundwater.

Looking at the Raman spectra of Figure 5-1b, we can see that all three samples exhibit a strong absorbance at a Raman shift of 450 cm^{-1} due to the fundamental UO stretch of the cubic fluorite structure (3), as expected.

As seen in previous chapters, we again observe a broad peak in the region of 500 – 700 cm^{-1} for the 25 & 43 GWd/tU SIMFUEL pellets, indicating the presence of lattice defects, deconvoluted as the U1, U2 and U3 peaks (4). When comparing the low doped 25 GWd/tU SIMFUEL pellet to the high doped 43 GWd/tU SIMFUEL we can see that there is a marked increase in the intensity of the U1 peak with increased burn-up. As discussed in Chapters 3 and 4 before, this is due to the increase in lanthanide concentration from going to the low doped to the high doped SIMFUEL pellet (5). We also observe a small increase in the intensity of the U2 peak in going from the 25 to the 43 GWd/tU SIMFUEL sample. Again, as per Chapters 3 and 4, we are able to observe this peak due to the break-down of selection rules which are caused by the structure of the UO_2 matrix deviating from the perfect fluorite structure in the SIMFUEL samples due to the presence of oxygen-vacancy sites, defect clustering and hyperstoichiometry – the latter caused by O^{2-} ion incorporation into the interstitial sites in the UO_2 fluorite matrix, forming UO_{2+x} (4) The small increase that we observe in the intensity of the U2 peak is attributed to the introduction of lanthanides, which increases the number of oxygen-vacancy sites (5) (6).

As previously discussed in Chapter 3, the peak observed as U3 is expected to increase in intensity with increasing hyperstoichiometry. With our SIMFUEL samples however, we observe a small decrease in the intensity of the U3 peak in background electrolyte as shown in Chapter 3, a decrease that is also seen here in Figure 5-1b in a modified simplified groundwater simulant. A possible explanation for this is that at high dopant levels the number of sites that may accommodate oxygen interstitials is decreased (7) – or that additional oxygens that may otherwise reside interstitially are instead filling oxygen vacancies associated with Ln(III) dopants. However as aforementioned, due to its weak intensity (indicative of a low level of hyperstoichiometry), interpretation of this peak should be considered with caution (5).

Returning to the OCP measurement in Figure 5-1a, we can see that the potentials measured from the SIMFUEL samples are more positive than those recorded for the undoped UO_2 sample. This is again most likely due to the Fermi levels of the SIMFUEL samples having been shifted to more

positive potentials by the introduction of lanthanide (III) ions into their respective urania matrices. This replacement of a fraction of the U(IV) ions in UO_2 with lower-valent Ln(III) ions requires further ionisation of the remaining uranium ions to form U(V) sites in order to maintain the overall charge balance. This in turn creates mobile holes in the U 5f band, rendering the samples p-type conductivity and shifting their Fermi levels to more positive potentials. The rest potentials measured in this OCP experiment are consistent with the findings of Jung et *al* (8), who under the same conditions, measured rest potentials for a 3 at.% SIMFUEL sample at 0.12 V_{SCE} after 72 hrs of exposure. Extrapolation of the results observed above in Figure 5-1a would yield similar results, however due to time constraints and availability of instruments, our experiments have been limited to four hours. Furthermore, studies conducted by Shoesmith and Sunder (9), and Shoesmith et *al*. (10) showed that corrosion potentials of SIMFUEL electrodes reached 0.0 V_{SCE} in aerated neutral containing chloride and carbonate ions. This is again consistent with the effect that pH has on the rest potentials that are reached during an OCP experiment. We shall return to this point in Figure 5-2 below.

In Figure 5-1a we also see that the SIMFUEL samples approach their equilibrium potentials at a slightly faster rate than the undoped UO_2 sample, as we saw in Chapter 3 in the background electrolyte. This is most probably due to the higher concentration of charge carriers in the SIMFUEL samples derived from doping effects associated with the addition of fission product simulants to the SIMFUEL matrix. The higher charge carrier concentration will support higher exchange current densities at the surface of the SIMFUEL samples, with a consequent increase in charge transfer kinetics and thus also an increase in the rate of approach to equilibrium in the context of an OCP experiment.

Interestingly in Figure 5-1a we also observe that exposure to the modified simplified groundwater has shifted all three samples to more negative potentials when compared to the OCPs measured in a background electrolyte (see Chapter 3). For the convenience of the reader, said OCP measurement taken in a 0.1 mol dm^{-3} Na_2SO_4 background electrolyte has been reproduced in Figure 5-2 below.

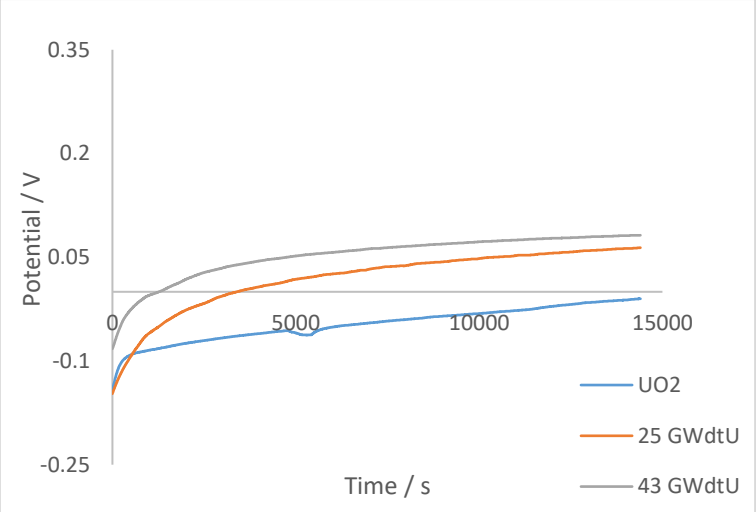

Figure 5-2 showing open circuit potential of the UO_2 and 25 & 43 GWd/tU SIMFUEL pellets over a 4 hour period in a 0.1 mol dm^{-3} Na_2SO_4 background electrolyte at pH 5.43

As mentioned above, we can clearly see that the potentials measured for our three samples are more positive than those measured in the modified simplified groundwater simulant. A reason for this change in measured potential between the two solutions which both contain no hydrogen peroxide may be explained by the change in pH from one solution to the other.

The pH of the 0.1 mol dm^{-3} Na_2SO_4 background electrolyte was measured at 5.43, whilst the pH of the modified simplified groundwater was measured at 8.2, indicating that the equilibrium OCP shifts towards more positive potentials with increasing acidity / decreasing pH. This observation is further supported by the data of Figure 5-3 that shows the results of OCP measurements, conducted over four hours, on our UO_2 and SIMFUEL samples immersed in a 0.1 mol dm^{-3} Na_2SO_4 background electrolyte adjusted to pH 3, with hydrochloric acid.

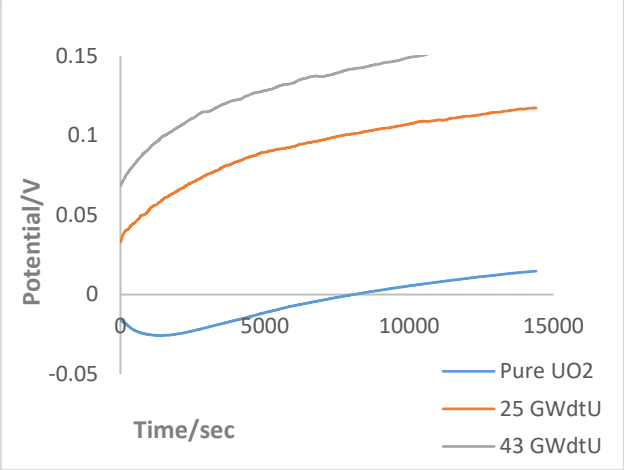

Figure 5-3 showing open circuit potential of the UO_2 and 25 & 43 GWd/tU SIMFUEL pellets over a 4 hour period in a 0.1 mol dm^{-3} Na_2SO_4 background electrolyte adjusted to pH 3

The more acidic pH has resulted in a further movement of the equilibrium OCPs to more positive potentials compared to those observed in Figure 5-2 and 5-1a.

An explanation for this positive movement in equilibrium OCP with decreasing pH may be afforded by the fact that the measured OCP is a mixed potential whose value is determined by the balance between two redox processes - one an oxidation, one a reduction - taking place at the surface of our electrodes. The nature of these reactions can be elucidated by inspection of the Pourbaix diagram of UO_2 shown in Figure 5-4 below.

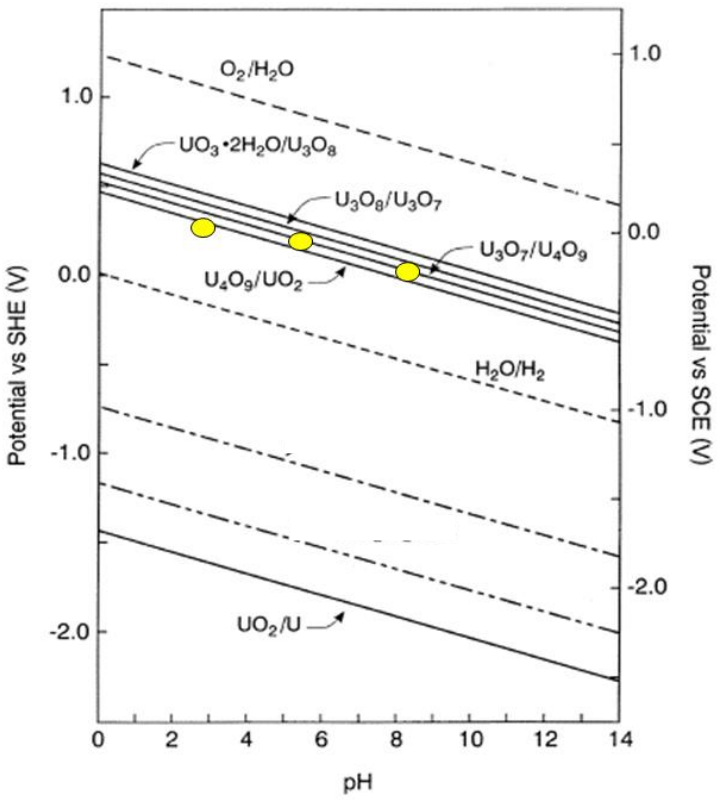

Figure 5-4 showing Pourbaix diagram of UO_2 in water. Indictaed by circular yellow markers are also the OCP equilibrium values for UO_2 from Figures 5-1a, 5-2 and 5-3, representing the OCP equilibrium values in pH 3 pH, 5.43 and pH 8.2 solutions, respectively (11).

Above in Figure 5-4 we can also see the measured rest/equilibrium open circuit potentials of the undoped UO_2 sample in the three different solutions – 0.012 V at pH 3 (taken from Figure 5-3), - 0.01 V at the background electrolyte pH of 5.43 (taken from Figure 5-2), and - 0.16 V at the modified simplified groundwater simulant pH of 8.2 (taken from Figure 5-1a).

We can clearly see here that the measured rest potentials of UO_2 lie on the boundary of UO_2 and its higher oxides. This gives a strong indication of the redox processes that are dominant in determining the measured value of the mixed potential.

Based on the positioning of the OCP rest potentials for undoped UO_2 shown in Figure 5-4, the anodic process that is most likely controlling the mixed potential is the solid state oxidation of U(IV) to U(V) in UO_2 to form a higher oxide, in the first instance via UO_{2+x}. This oxidation will introduce additional holes in the U 5f band, moving the material Fermi level to lower electron energies / more positive

potentials. As the bands are pinned at the surface by the protonation/deprotonation of surface oxide/hydroxide sites (i.e. H^+ is the potential determining ion) the bands will bend upwards in energy as the material surface is approached from within the urania bulk (see Chapter 1 Figure 1-17). This in turn results in migration of the holes to the surface rendering it quasi-metallic and so facilitating further redox processes.

The associated cathodic process of our mixed potential, which grows in dominance with increased immersion time, is most likely the reduction of the above-mentioned higher oxide. As no electrochemical cleaning of the electrode surface prior to the OCP measurements had taken place, it is not unreasonable to assume that there may be a thin oxidation layer on the surface of the UO_2 electrode. Therefore, the reduction of surface UO_{2+x} / U_4O_9 may be expected to play a role in determining the potentials measured during the OCP experiments from the very beginning of the immersion period. This role grows in dominance as more of the higher oxide layer is formed at the electrode surface. The equilibrium, or the measured rest potential is then obtained when the UO_2 oxidation reaction and higher oxide reduction reaction come into a mass action influenced balance.

The above explanation would mean that the measured potentials of an OCP trace with our three samples exposed to the pH 7.1 evaporite groundwater simulant would be similar to that measured in the pH 8.2 modified simplified groundwater simulant, as there is not a significant change of pH between the two groundwater simulants. The measured potentials of the OCP trace in evaporite groundwater should however be more negative than those recorded in the pH 5.43 background electrolyte. We shall return to this point later on in Figure 5.6.

Having discussed the open circuit measurements and Raman spectral data of the undoped UO_2, low and high burnup 25 & 43 GWd/tU SIMFUEL samples in a modified simplified groundwater, as well as the comparison of the OCP measurements with those made at other pHs, we will now move on to consider the electrochemical behaviour of the three samples in modified simplified groundwater.

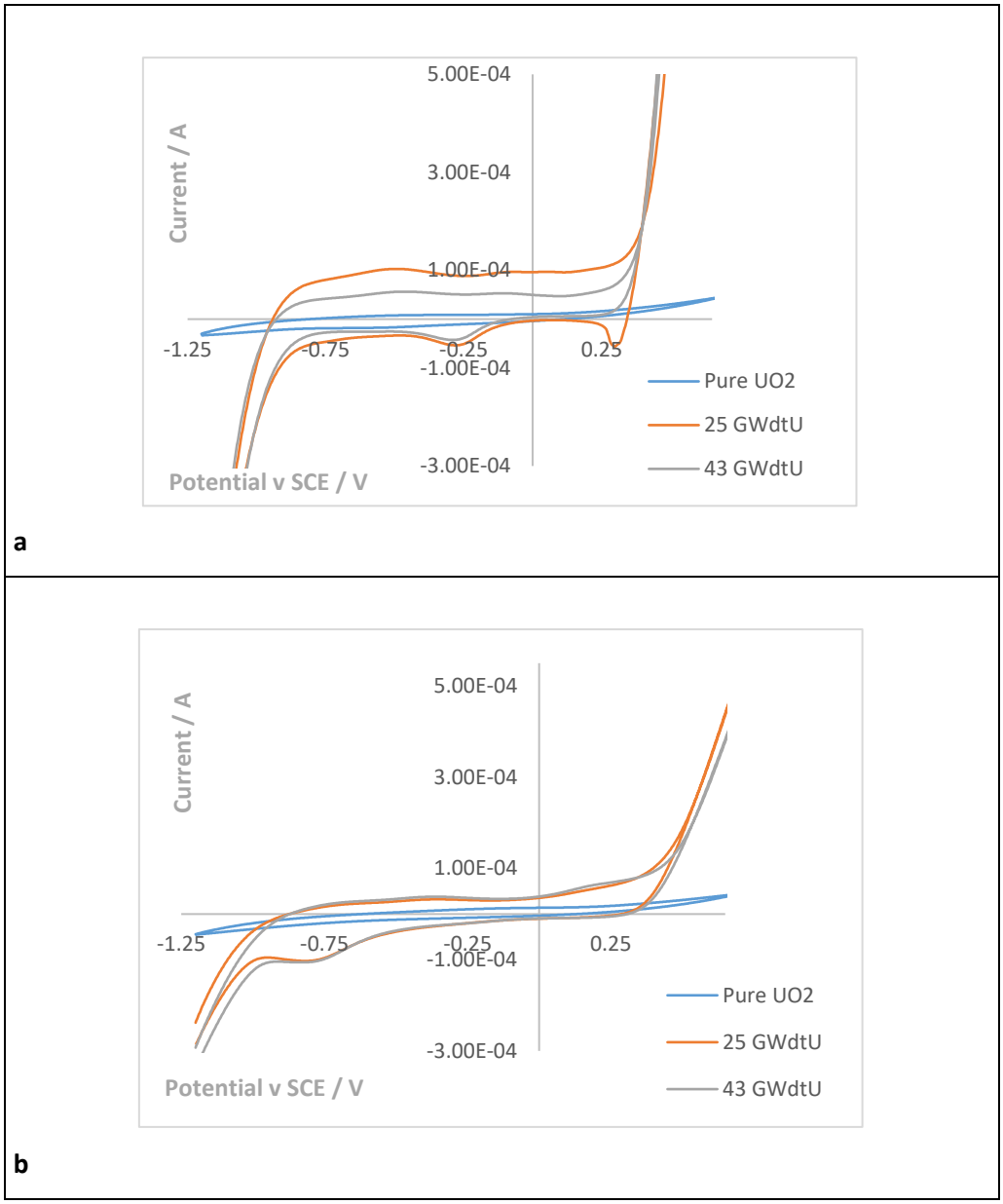

Figure 5-5a and 5-5b – (a) showing the cyclic voltammograms of UO_2, 25 & 43 GWd/tU SIMFUEL pellets in a 0.1 mol dm^{-3} Na_2SO_4 background electrolyte, cycled at a potential range of (-) 1.2 to (+) 0.7 V, at a scan rate of 20 mV/s; (b) showing the cyclic voltammograms of UO_2, 25 & 43 GWd/tU SIMFUEL pellets in a modified simplified groundwater simulant, cycled at a potential range of (-) 1.2 to (+) 0.7 V, at a scan rate of 10 mV/s

Above in Figure 5-5b is the cyclic voltammogram of undoped UO_2, 25 & 43 GWd/tU in modified simplified groundwater, scanned between a potential range of -1.2 to +0.7 V, at a scan rate of 10 mV/s. The cyclic voltammogram of all three samples in a 0.1 mol dm^{-3} Na_2SO_4 background electrolyte has been reproduced in Figure 5-5a for ease-of-comparison. As seen in Chapters 3 and 4, we can again see here that the undoped UO_2 pellet is the least electrochemically active of the samples in comparison to the low and high burnup 25 & 43 SIMFUEL pellets.

As seen in previous chapters, we again observe here that the difference in electrochemical reactivity between the three samples is not uniform. The difference between the undoped UO_2 and low doped 25 GWd/tU SIMFUEL samples is significantly larger than the electrochemical reactivity observed between the low and high doped 25 & 43 GWd/tU SIMFUEL samples. This former can be attributed to the fact that the 25 GWd/tU SIMFUEL pellet has more U(V) ions resulting from the introduction of Ln(III) ions into the urania matrix. As previously discussed in Chapter 1 and Chapter 3, the undefected and undoped UO_2 is a Mott-Hubbard insulator. The introduction of Ln(III) dopants into the matrix of the 25 GWd/tU samples results in the formation of U(V) sites and thus electron vacancies or holes in the inter-band 5f level shown in Chapter 1 Figure 1-17 – resulting in the doped material subsequently exhibiting a p-type conductivity.

Thus, in going from UO_2 to the 25 GWd/tU SIMFUEL sample, a large increase in conductivity is observed as at least some of the Ln(III) ions added to the sample precursor blend enter the UO_2 matrix. However, a similar increase in conductivity is not seen in going from the 25 to 43 GWd/tU sample. As discussed in Chapter 3, even though there is a higher concentration of added Ln (III) ions in the 43 GWd/tU matrix, there is actually a larger part of ions partitioning in the grey phase rather than into the solution matrix – explaining why we do not see an increase in electrochemical activity in going from the low doped to the high doped 43 GWd/tU SIMFUEL sample.

By comparing Figure 5-5b above with the cyclic voltammograms of Chapter 3, namely Figures 3-5 and 3-6, we can make the following assignments for the forward going sweeps of the 25 and 43 GWd/tU SIMFUEL pellets. At an onset of approximately -0.75 V_{SCE} we observe the oxidation of UO_{2+x} sites at grain boundaries to $UO_{2.33}$. (12) At approximately 0.2 V_{SCE} the oxidation of UO_2 grains to UO_{2+x} (up to a limiting stoichiometry of $UO_{2.33}$) takes place (12). At potentials above 0.25 V_{SCE} we observe the oxidation of UO_{2+x} to U(VI) species (12). At the higher pH of our modified simplified groundwater simulant, we might expect to see the passivation of the latter process due to the formation of insoluble U(VI) (hydr-) oxides at the surface. The fact that this is not observed here is most likely due to the fact that carbonate complexation with U(VI) in the form of uranyl is taking place, preventing its precipitation at the surface of the SIMFUELs.

On the reverse sweep in Figure 5-5b, we observe a reduction peak for the low doped 25 GWd/tU and the high doped 43 GWd/tU SIMFUEL pellets with an onset at approximately -0.5 V_{SCE}, plateauing

at -0.75 V_{SCE} This can be speculated to be the reduction of the carbonate complexed uranyl. The onset of the reduction wave observed for the carbonate complexed uranyl is consistent with the data recorded by Butorin *et al* (13). Furthermore, the onset of the carbonate complexed uranyl reduction wave in the vicinity of – 0.6 V_{SCE} is also observed by Morris and Wander *et al* (14) (15), confirming that the wave we observe, is in fact the reduction of the carbonate complexed uranyl. The wave we observe at -1 V_{SCE} is due to hydrogen evolution. This is more prominent on the SIMFUEL samples than on the pure UO_2 sample due to the presence of epsilon particles on the surface of the former; as discussed in Chapter 3, epsilon particles are primarily comprised of noble metals which are good electrocatalysts for hydrogen evolution reactions.

Having looked at the Raman spectra, open circuit potential measurements and electrochemical data of the three samples in modified simplified groundwater, we will now examine the undoped UO_2, 25 & 43 GWd/tU SIMFUEL pellets under similar conditions in a high chloride content evaporite groundwater simulant.

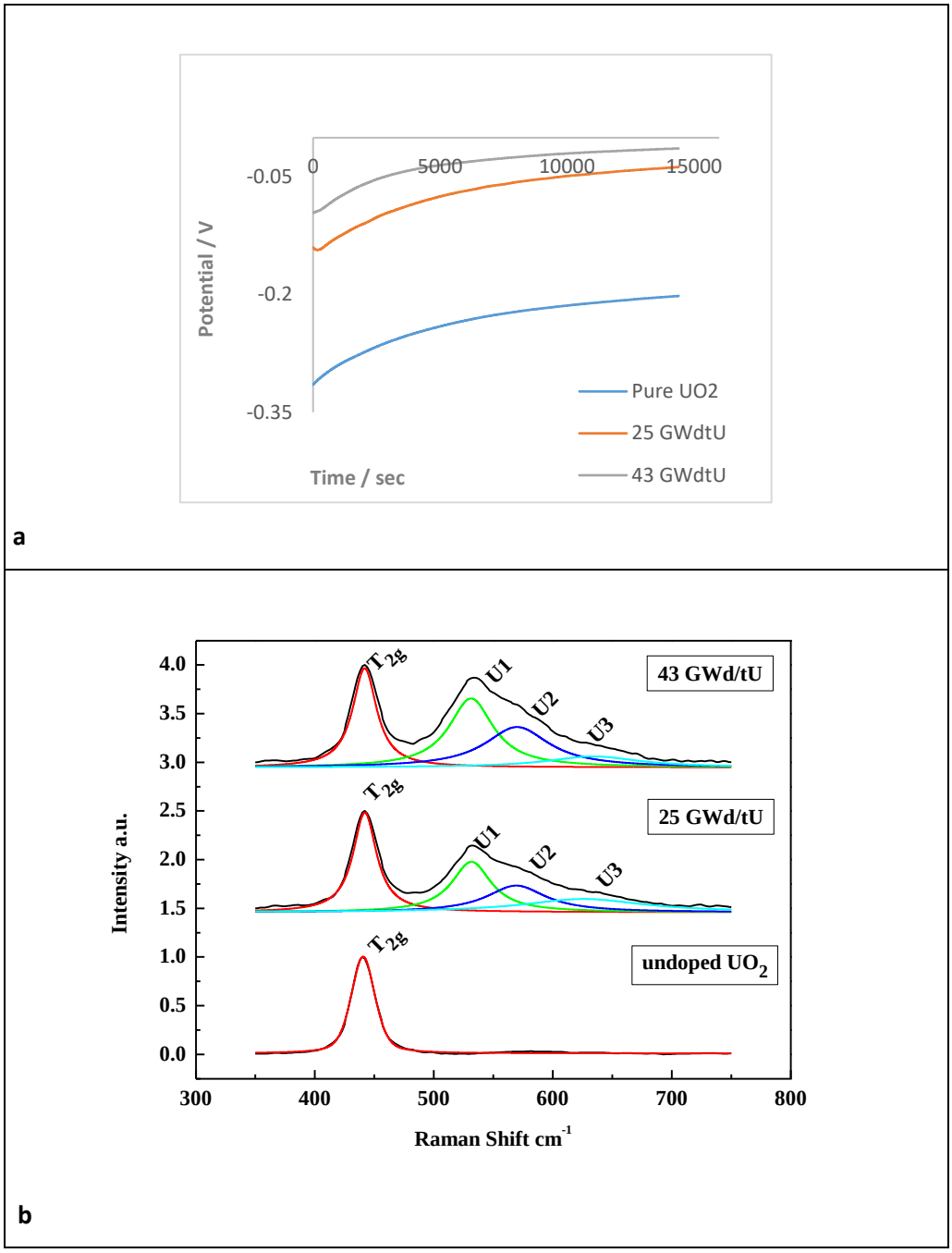

Figure 5-6a and 5-6b – (a) showing the open circuit potential of the UO_2 and 25 & 43 GWd/tU SIMFUEL pellets over a 4 hour period in an evaporite groundwater simulant at pH 7.1; (b) the 20-point averaged Raman spectra of the UO_2 and 25 & 43 GWd/tU SIMFUEL pellets after OCP measurement in Figure 5-6a, represented as Lorenztian

Figure 5-6b above shows the 20 point average Raman spectra represented as Lorentzian, of the undoped UO_2, low and high burnup 25 & 43 GWD/tU SIMFUEL pellets in an evaporite groundwater simulant, as well as the open circuit potential of all three samples taken over a 4 hour period in Figure 5-6a.

As aforementioned, the measured rest potentials of our samples from the OCP measurements are indeed more negative when compared to the pH 3 solution and the background electrolyte at pH 5.43. As the pH of the evaporite groundwater simulant, pH 7.2, is similar to that of the modified simplified groundwater simulant (pH 8.1), the measured rest potentials of both OCPs are also similar.

In Figure 5-6b we can once more see that the undoped UO_2 pellet only shows a peak at a Raman shift of 450 cm^{-1}, indicating that it has retained its perfect cubic fluorite structure in the evaporite groundwater simulant medium. The low and high burnup 25 & 43 GWd/tU SIMFUEL pellets behave in a similar way as they have done in background electrolyte as well as in modified simplified groundwater. The intensity of the U1 peak increases with increased burn-up. There is a small increase in intensity of the U2 peak in going from the 25 GWd/tU to the 43 GWd/tU SIMFUEL pellet. Likewise there is a small decrease in intensity of the U3 peak with increased burn-up in the evaporite groundwater simulant. Given that this is behaviour exactly similar to that exhibited by these samples in the modified simplified groundwater, a similar explanation for this behaviour to that described for the samples in modified simplified groundwaters will also apply here.

We will now have a look at the electrochemical behaviour of the three pellets in an evaporite simulant groundwater.

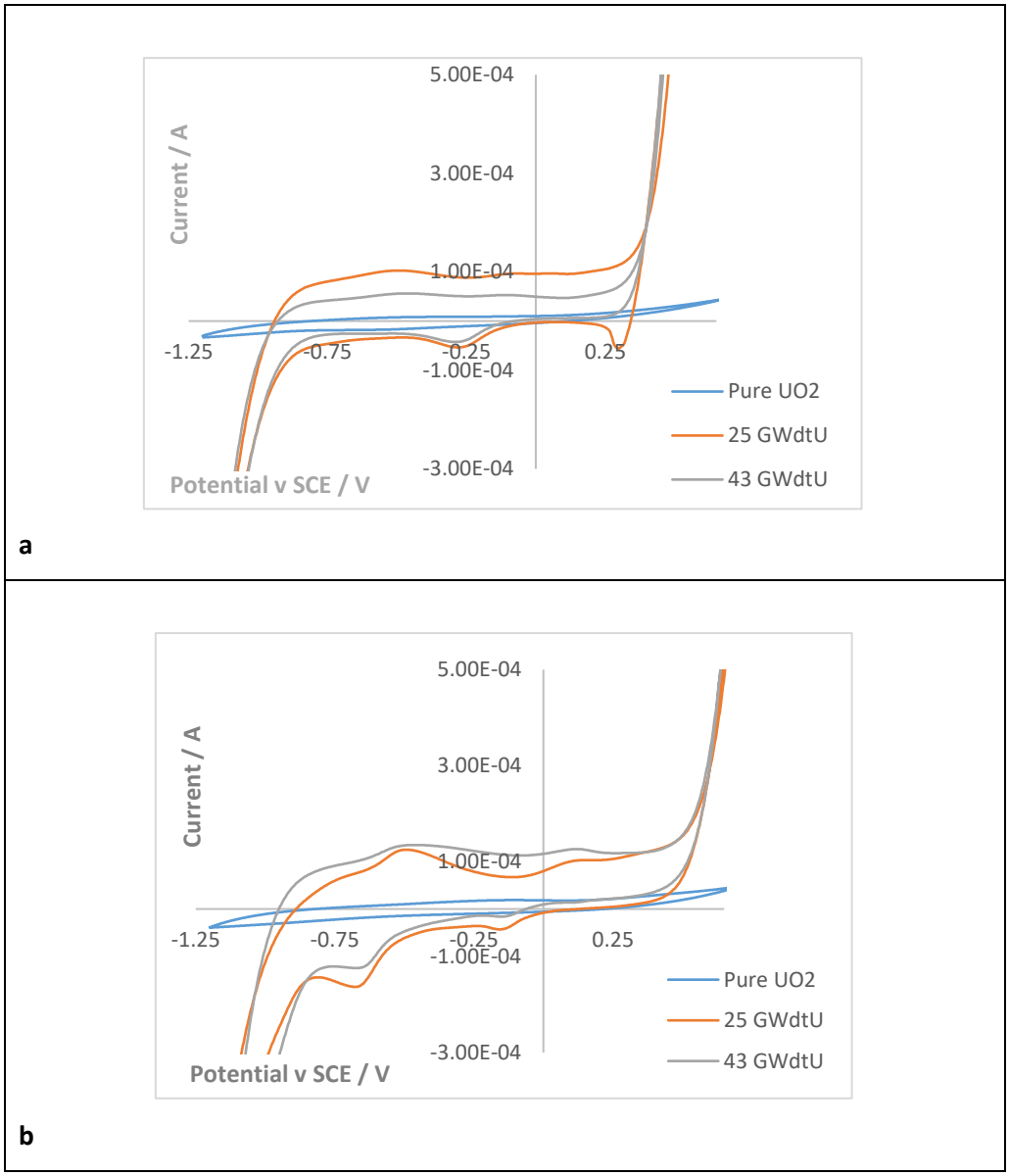

Figure 5-7a and 5-7b – (a) showing the cyclic voltammograms of UO_2, 25 & 43 GWd/tU SIMFUEL pellets in a 0.1 mol dm^{-3} Na_2SO_4 background electrolyte, cycled at a potential range of (-) 1.2 to (+) 0.7 V, at a scan rate of 20 mV/s; (b) showing the cyclic voltammograms of UO_2, 25 & 43 GWd/tU SIMFUEL pellets in an evaporite groundwater simulant, cycled at a potential range of (-) 1.2 to (+) 0.7 V, at a scan rate of 10 mV/s

In Figure 5-7b above we can see the cyclic voltammetry of the undoped UO_2, the low and high burnup 25 & 43 GWd/tU SIMFUEL pellets in an evaporite groundwater simulant, taken at a potential window of -1.2 to +0.7 V, at a scan rate of 10 mV/s. Here we can once again see that the undoped UO_2 pellet is significantly less electrochemically inactive than the SIMFUEL sample, with the UO_2 pellet exhibiting virtually no prominent current peaks in the evaporite groundwater simulant.

On the forward going sweep of the 25 GWd/tU SIMFUEL sample there is a peak around - 0.50 V_{SCE}. This peak, denoted as Region C in Figure 3-5 of Chapter 3, can be attributed to the UO_{2+x} in grain boundaries oxidising to $UO_{2.33}$ as described by Seibert *et al.* (12).

Further along the forward going sweep of the 25 GWd/tU SIMFUEL sample, we observe another peak appearing at approximately 0.15 V_{SCE}. Here, the oxidation of in-grain UO_2 to UO_{2+x} takes place, with the maximum of *x* being 0.33. As discussed in Chapter 3, at a potential above 0.25 V_{SCE} we would enter Region D. An increase in potential brings about further oxidation to U(VI). Oxidation beyond $UO_{2.33}$ (which marks the end of the fluorite structure range) would involve the dissolution of U(V/VI), as well as a recrystalisation process via adsorbed UO_2^{2+} species up to $UO_{2.5}$ and $UO_{2.66}$ (12). As aforementioned in Figure 5-5b, we also do not see passivation of the surface layer here, due to carbonate complexation; the evaporite groundwater, like the modified simplified groundwater discussed above, also contains 10 mmol dm^{-3} total carbonate.

The high doped 43 GWd/tU SIMFUEL sample has a similar electrochemical reactivity to that of the low doped 25 GWd/tU SIMFUEL sample. As seen in previous cyclic voltammograms, the difference in electrochemical reactivity between the undoped UO_2 and the SIMFUELs is much larger than that between the two SIMFUELs. As discussed before, the former is due to some of the Ln(III) ions that have been added to the SIMFUEL sample precursor blend enter the UO_2 matrix, which induces the formation of U(V) species. The electrochemical reactivity and conductivity between the 25 GWd/tU and the 43 GWd/tU SIMFUEL sample stay similar due to the fact that the additional Ln(III) ions added to the 43 GWd/tU SIMFUEL pellet matrix partition into the grey phase, the grey phases being more abundant in the 43 GWd/tU SIMFUEL sample.

On the reverse sweeps of the low and high doped 25 & 43 GWd/tU SIMFUEL samples, we observe two reduction peaks with onsets of approximately - 0.1 and - 0.5 V_{SCE}. The second feature, with a peak at approximately – 0.75 V_{SCE}, can be speculated to be due to the reduction of carbonate complexed uranyl as above, see discussion of Figure 5-5b.

The first peak appearing at approximately - 0.1 V_{SCE} can be attributed to either the reduction of the recrystalised phases from $UO_{2.67}$/$UO_{2.5}$/$UO_{2.33}$ to U(IV), or the conversion of UO_{2+x} to U(IV) (12). This

peak arises due to the build-up of higher oxides, namely $UO_{2.5}$ or $UO_{2.67}$ caused by the recrystallisation/reduction reactions from adsorbed U(VI) species (12). That this peak is seen in evaporite groundwater and not in the modified simplified groundwater is most likely due to the difference in pH between the two groundwaters affecting the efficacy of carbonate complexation with uranyl. The pH of evaporite and modified simplified groundwater simulants are 7.1 and 8.2 respectively, whilst the pK_a of the H_2CO_3/HCO_3^- equilibrium is 6.4. Thus, even though the concentration of total carbonate is the same in both groundwaters, there will be a higher concentration of free HCO_3^- in the modified simplified simulant than the evaporite – with a consequently higher efficacy for soluble uranyl-carbonate complex formation. From this it may be inferred that, whilst uranyl-carbonate complex formation may still be expected in the evaporite system, it will occur to a lesser extent than in the modified simplified simulant. This opens the possibility of the formation / precipitation of some insoluble U(VI) (hydr-) oxide at the electrode surface upon oxidation of UO_{2+x} to U(VI) species in forward going voltammetric scans recorded in evaporite simulants – which may then be reduced in the reverse scan. This precipitation may be further facilitated by the solubility of U(VI) (as schoepite) being at its minimum in the pH range 7-8.

Finally, the wave observed at approximately -1 V_{SCE} is, as aforementioned, due to hydrogen evolution, and is not as prominent on the undoped UO_2 sample as it is on the SIMFUEL samples, due to the absence of epsilon particles in the undoped UO_2.

5.3 Conclusions

In this chapter we have investigated the effect that various groundwater simulants, namely a modified simplified groundwater simulant, and an evaporate groundwater simulant, have on the electrochemical and corrosion behaviour of our undoped UO_2 and 25 & 43 GWd/tU SIMFUEL samples.

In order to evaluate these effects, we have studied the open circuit potentials, the Raman spectral data and the cyclic voltammograms measured for our samples in the above named groundwater simulants. Whilst investigating and comparing the open circuit potential measurements of our samples, it was observed that immersion of the samples in solutions of a higher pH than that of the 0.1 mol dm^{-3} Na_2SO_4 background electrolyte led to the rest potentials of the samples being measured at much more negative potentials than those previously measured. Upon further investigation, it was discovered that immersion in a solution of a lower pH, namely that of pH 3, the rest potentials measured for the three samples during open circuit potential measurements, yielded much more positive results when compared to the immersion in higher pH solutions. This is consistent with findings by Shoesmith and Sunder (9), and Shoesmith *et al.* (10), whose measured rest potentials in solutions of varying pHs correlate with our findings.

An explanation for this positive movement in equilibrium OCP with decreasing pH may be afforded by the fact that the measured OCP is a mixed potential, whose value is determined by the balance between two redox processes - an oxidation process and a reduction process – both taking place at the surface of our electrodes.

The anodic process that is most likely controlling the mixed potential is the solid state oxidation of U(IV) to U(V) in UO_2 to form a higher oxide, in the first instance via UO_{2+x}. This oxidation will introduce additional holes in the U 5f band, moving the material Fermi level to lower electron energies / more positive potentials. As the bands are pinned at the surface by the protonation/deprotonation of surface oxide/hydroxide sites (i.e. H^+ is the potential determining ion) the bands will bend upwards in energy as the material surface is approached from within the urania bulk. This in turn results in migration of the holes to the surface, resulting in the formation of an

accumulation layer and rendering it quasi-metallic and so facilitating further redox processes. It must be noted here that a decrease in pH will make this anodic reaction easier. In other words, generating more U(V) and additional holes in the U 5f band will in turn generate positive movement in the OCP.

The associated cathodic process of our mixed potential, is most likely the reduction of the above-mentioned higher oxide. As we assume that there may be a thin oxidation layer on the surface of the UO_2 electrode, the reduction of surface UO_{2+x} / U_4O_9 may be expected to play a role in determining the potentials measured during the OCP experiments from the very beginning of the immersion period. This role grows in dominance as more of the higher oxide layer is formed at the electrode surface. The equilibrium, or the measured rest potential is then obtained when the UO_2 oxidation reaction and higher oxide reduction reaction come into a mass action influenced balance. As mentioned above, this again supports positive movement in the OCP as the U_4O_9 reduction becomes more difficult with decreasing pH. This means there is less 'loss' of U(V) and therefore less 'loss' of holes in the U 5f band with decreasing pH. This complements and enhances the effect of the anodic reaction above.

The Raman measurements of our three samples taken after immersion in the two groundwater simulants are consistent with those observed in neutral background electrolyte (Chapter 3) and in peroxide loaded background electrolyte (Chapter 4). As already discussed in Chapter 3, the intensity of the U1 peak increases with simulated burnup, which is due to the increase in lanthanide concentration from going to the low doped to the high doped SIMFUEL pellet, as observed by Howett (5). We also observe a small increase in the intensity of the U2 peak in going from the 25 to the 43 GWd/tU SIMFUEL sample. This small increase in the intensity of the U2 peak (which is visible in the SIMFUELs due to the relaxation of selection rules) has been attributed to the introduction of lanthanides, which increases the number of oxygen-vacancy sites, by Elorietta *et al*., who also observe a small increase in intensity (4). When analysing the intensity of the U3 peak, we observe a small decrease in the intensity when going from the 25 GWd/tU SIMFUEL pellet to the 43 GWd/tU SIMFUEL pellet. A possible explanation for this is that at high dopant levels the number of sites that may accommodate oxygen interstitials is decreased (7) – or that additional oxygens that may otherwise reside interstitially are instead filling oxygen vacancies associated with Ln(III) dopants. The former has also been observed by Park, where it was found that the site number of the dopant-interstitial cluster is reduced with the addition of dopants (7). It must be noted here that this peak

should be interpreted with caution due to its weak intensity, which is indicative of a low level of hyperstoichiometry, as also outlined by Howett (5).

Analysis of the cyclic voltammogram in modified simplified groundwater showed that the electrochemical behaviour of the three samples was similar to that seen in the 0.1 mol dm^{-3} Na_2SO_4 background electrolyte, with the following exceptions:

Based on the higher pH of the modified simplified groundwater, we expect to see passivation on the surface of the electrodes at potentials above 0.25 V_{SCE} on the forward going sweep due to the formation of insoluble U(VI) (hydr-) oxides, as per the regional assignments of Seibert *et al.* (12). We however, do not observe this passivation, most likely due to carbonate complexation, as documented by Morris and Wander *et al.* (14) (15). We see the electro-reduction of this carbonate complex on the reverse sweep between – 0.5 and – 0.75 V_{SCE}.

With regards to the cyclic voltammograms measured in evaporite groundwater simulant, the scans were again similar to those measured in 0.1 mol dm^{-3} Na_2SO_4, with the exceptions of:

On the reverse sweeps we observe two reduction peaks. The peak observed between 0.5 -0.75 V_{SCE} can be attributed to the reduction of the carbonate complexed uranyl mentioned above (14) (15). The peak observed at approximately 0.1 V_{SCE} can be attributed to either the reduction of the recrystalised phases from $UO_{2.67}$/$UO_{2.5}$/$UO_{2.33}$ to U(IV), or the conversion of UO_{2+x} to U(IV), according to Seibert *et al.* (12). This peak arises due to the build-up of higher oxides ($UO_{2.5}$ or $UO_{2.67}$) caused by the recrystallisation/reduction reactions from adsorbed U(VI) species (12).

We observe this peak only in the evaporite groundwater simulant, and not in the modified simplified groundwater simulant, most likely due to the difference in pH between the two groundwaters affecting the efficacy of carbonate complexation with uranyl, as aforementioned in the Results & Discussion section above.

Having looked at the behaviour of the three samples in simulant groundwaters in the absence of hydrogen peroxide, we will now investigate the effects of hydrogen peroxide on the undoped UO_2, the low and high burnup 25 & 43 GWd/tU SIMFUEL pellets in simulant groundwaters. This will be the subject of the next chapter.

References

1. N. Rauff-Nisthar, C. Boxall, I. Farnan, Z. Hiezl, W. Lee, C. Perkins, R.J. Wilbraham. *Corrosion behaviour of AGR simulated fuels - evolution of the fuel surface.* s.l. : ECS Trans, 2013, Vol. 53. pp. 95-104.

2. Nuclear Decommissioning Authority *Geological Disposal - Generic disposal facility designs.* s.l. : NDA Report no. NDA/RWMD/048, 2010.

3. H. He, M. Broczkowski, K. O'Neil, D. Ofori, O. Semenikhim, D. W. Shoesmith. *Corrosion of nuclear fuel (UO_2) inside a failed nuclear waste container.* s.l. : NWMO and University of Western Ontario Report no. TR-2012-09, 2012.

4. J.M. Elorietta, L.J. Bonales, N. Rodriguez-Villagra, V.G. Baonza, J. Cobos. *A detailed Raman and X-ray study of UO_{2+x} oxides and related struture transitions.* s.l. : Physical Chemistry Chemical Physics, 2016, Vol. 18. pp. 28209 - 28216.

5. E.A. Howett. *The behaviour of spent nuclear fuel in wet interim storage.* s.l. : Lancaster University, 2019.

6. Z. Talip, T. Wiss, P.E. Raison, J. Paillier, D. Manara, J. Somers, R.J.M Konings. *Raman and X-ray studies of uranium-lathanum-mixed oxides before and after air oxidation.* s.l. : Journal of the American Ceramic Society, 2015, Vol. 98.

7. K. Park. *The oxygen potential of neodymia-doped urania based on a defect structure.* s.l. : Journal of Nuclear Materials, 1994, Vol. 209. p.p. 259 - 262.

8. H. Jung, T. Ahn, K. Axler, R. Pabalan, D. Pickett. *Corrosion of SIMFUEL in aerated carbonate solution containing calcium and silicate.* s.l. : U.S. Nuclear Regulatory Commission, 2011.

9. D.W. Shoesmith, S. Sunder. *Validation of an electrochemical model for the oxidative dissolution of used CANDU fuel.* s.l. : Journal of Nuclear Materials, 1998, Vol. 257. pp. 89 - 98.

10. D.W. Shoesmith, S. Sunder, M.G. Bailey, N.H. Miller. *Corrosion of used nuclear fuel in aqueous perchlorate and carbonate solutions.* s.l. : Journal of Nuclear Materials, 1996, Vol. 227. pp. 287 - 299.

11. D.W. Shoesmith. *Fuel corrosion processes under waste disposal conditions.* s.l. : Journal of Nuclear Materials, 2000, Vol. 282.

12. A. Seibert, D.H. Wegen, T. Gouder, J. Roemer, T. Wiss, J.-P. Glatz. *The use of the electrochemical quartz crystal microbalance (EQCM) in corrosion studies of UO_2 thin film models.* s.l. : Journal of Nuclear Materials, 2011, Vol. 491. pp. 112 - 121.

13. S. Butorin, K. Ollila, Y. Albinsson, J. Norgren, L. Werme. *Reduction of uranyl carbonate and hydroxyl complexes and neptunyl carbonate complexes studied with chemical-electrochemical methods and rixs spectroscopy.* s.l. : Swedish Nuclear Fuel and Waste Management Co, 2003.

14. D.E. Morris. *Redox energetics and kinetics of uranyl coordination complexes in aqeuous solution.* s.l. : Inorganic Chemistry, 2002, Vol. 41. pp. 3542 - 3547.

15. M.C.F. Wander, S. Kerisit, K.M. Rosso, M.A.A. Schoonen. *Kinetics of Triscarbonato uranyl reduction by aqeuous ferrous iron: a theoretical study.* s.l. : Journal of Physical Chemistry, 2006, Vol. 110.

16. G. Krishnan. *Cyclic Voltammetry.* s.l. : Ohio University, 2011.

17. K.C. Sole, P.M. Cole, A.M. Feather, M. Kotze. *Solvent extraction and ion exchange applications in Africa's resurging uranium industry: a review.* s.l. : Solvent Extraction and Ion Exchange, 2011, Vol. 29. pp. 868 - 899.

Chapter 6 Effect of Hydrogen Peroxide on UO_2 & SIMFUELs in Simulated Groundwater

6.1 Introduction

In the previous chapter, we investigated the effects that different simlulant groundwaters, namely a modified simplified groundwater, and an evaporite simulant groundwater had on the electrochemical and Raman spectral measurements of undoped UO_2, low burn-up 25 GWd/tU, and high burn-up 43 GWd/tU SIMFUEL pellets. In this next chapter, we will investigate the effects that added hydrogen peroxide has on our undoped UO_2 and SIMFUEL pellets in the above mentioned groundwater simulants. In order to do so, we will once again look at the various Raman spectra, open circuit potentials and, where available, cyclic voltammetric data recorded under the above mentioned new conditions.

6.2 Results & Discussion

As in the previous chapters, the main measurement techniques that will be employed in this work are Raman spectra and open circuit potentials. The solutions that will be investigated are modified simplified groundwater and evaporite simulant groundwater, the compositions of which can be found in Chapter 2. The hydrogen peroxide concentrations that the groundwater solutions have been spiked with are as follows (as in Chapter 4):

- 10 µmol dm^{-3} H_2O_2
- 100 µmol dm^{-3} H_2O_2 and
- 1 mmol dm^{-3} H_2O_2

We will firstly look at the Raman spectra, along with the open circuit potential measurements for the undoped UO_2, and the low and high burnup 25 & 43 GWd/tU SIMFUEL pellets in the modified simplified groundwater that has been spiked with 10 µmol dm^{-3} of hydrogen peroxide as shwon in Figure 6-1 below. For comparison reasons and the convenience of the reader the OCP measurements as well as the Raman spectra recorded in the absence of hydrogen peroxide (Chapter 5) are also represented in Figure 6-1:

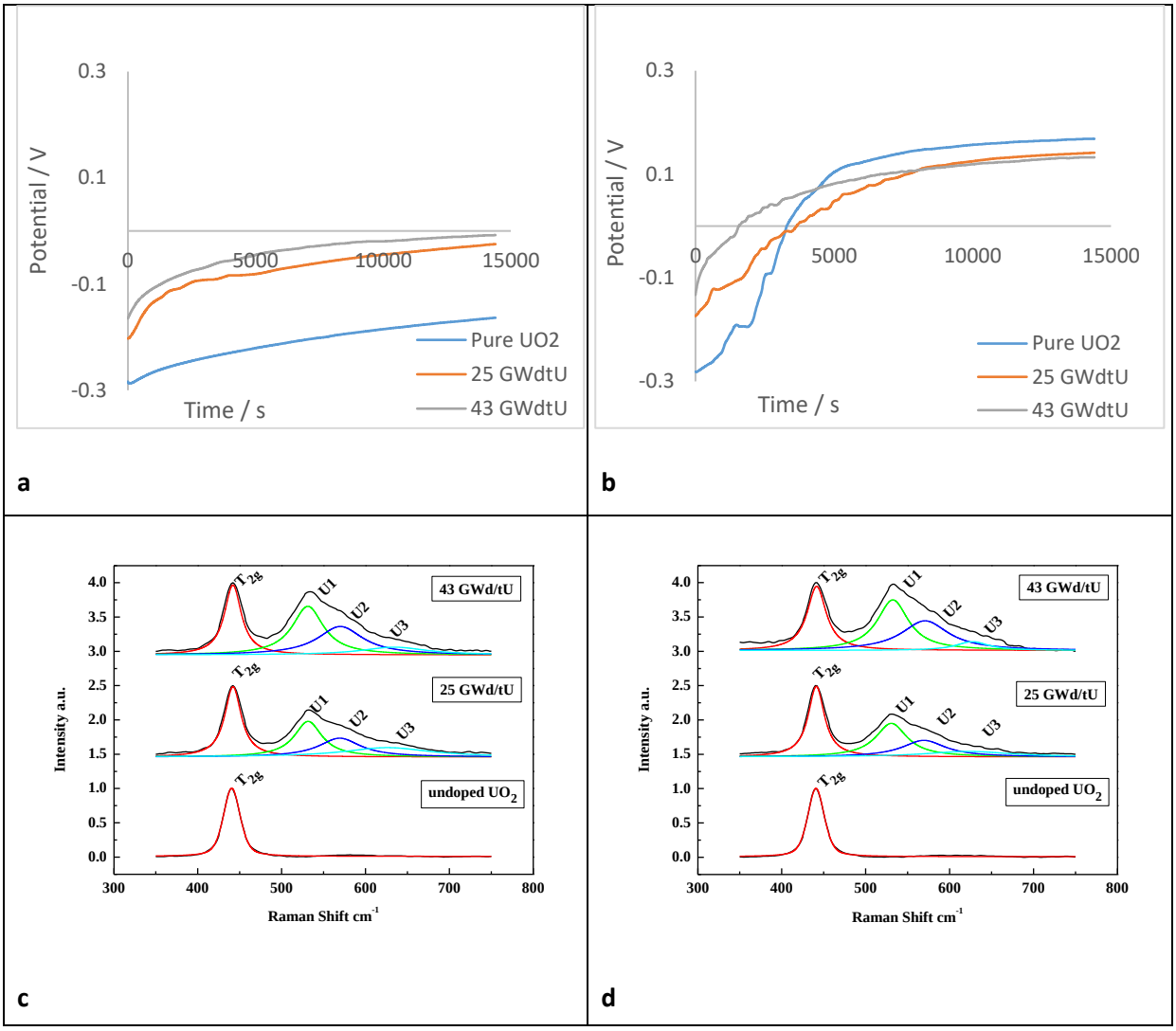

Figure 6-1a to 6-1d - (a) showing the open circuit potential of the UO_2 and 25 & 43 GWd/tU SIMFUEL pellets over a 4 hour period in a modified simplified groundwater simulant pH 8.2; (b) the open circuit potential of the UO_2 and 25 & 43 GWd/tU SIMFUEL pellets over a 4 hour period in a modified simplified groundwater simulant spiked with 10 µmol dm^{-3} H_2O_2; (c) the 20-point averaged Raman spectra of the UO_2 and 25 & 43 GWd/tU SIMFUEL pellets after OCP measurement shown in Figure 6-1a; (d) the 20-point averaged Raman spectra of the UO_2 and 25 & 43 GWd/tU SIMFUEL pellets after OCP measurement shown in Figure 6-1b,respectively

By comparing the OCP measurements from Figure 6-1a (absence of H_2O_2) and Figure 6-1b (presence of H_2O_2), we can immediately see that the addition of a 10 µmol dm^{-3} H_2O_2 spike to the pH 8.2 modified simplified groundwater simulant has shifted the rest potentials of the three samples to more positive potentials. More specifically, the rest potential of the undoped UO_2 has shifted from approximately – 0.16 V_{SCE} in the groundwater simulant with no H_2O_2 present, to + 0.17 V_{SCE} in the presence of H_2O_2. The resting potentials of the two SIMFUEL samples have shifted from approximately – 7 mV_{SCE} to 130 mV_{SCE}. As already discussed in Chapter 4, this can be attributed to

the fact that the hydrogen peroxide is placing an oxidative stress on the surface of all three pellet samples.

In the presence of hydrogen peroxide, we observe that all three samples reach almost the same rest potential, with the two SIMFUEL samples reaching rest potentials slightly below that of the pure UO_2 sample. The two SIMFUEL samples also reach their rest potentials at a slightly faster rate than the undoped UO_2 samples. As discussed in Chapters 3 &4, this is most probably due to the fact that the two SIMFUEL samples contain a higher concentration of charge carriers derived from the doping effects associated with the addition of fission product simulants to the SIMFUEL matrix. Subsequently, the higher charge carrier concentration will support higher exchange current densities at the surface of the SIMFUEL samples, with a consequent increase in charge transfer kinetics and thus rate of approach to equilibrium in the context of an OCP measurement.

That the two SIMFUEL samples reach rest potentials slightly below that of the pure UO_2 sample may be understood as follows. In Chapter 4, where the same experiments were carried out in a 0.1 mol dm^{-3} Na_2SO_4 background electrolyte, we observed that in the presence of H_2O_2, the 43 GWd/tU SIMFUEL sample reached a lower rest potential than both the UO_2 and 25 GWd/tU SIMFUEL, a result that we attributed to catalytic decomposition of hydrogen peroxide due to the epsilon particles present on the SIMFUEL surface. There is a higher concentration of epsilon particles on the 43 GWd/tU SIMFUEL than on the 25, so leading to a higher level of peroxide decomposition and thus less of an oxidative stress being placed on the 43 GWd/tU sample than the 25 in simple sodium sulfate at pH 5.43. However, the modified simplified groundwater simulant has a pH of 8.2 and hydrogen peroxide is known to decompose faster in alkaline media than in acidic media (1). This, combined with the presence of epsilon particles on both the 25 and 43 GWd/tU SIMFUEL sample surfaces may be the reason why the rest potentials for both the 25 and 43 GWd/tU samples are below that for the undoped UO_2 sample in the slightly alkaline groundwater simulant, but only the rest potential for the 43 GWd/tU is below that for the pure UO_2 sample in the slightly acidic sodium sulfate electrolyte.

When looking at the Raman spectra in Figure 6-1 above, we can see that in both the Raman spectra in the absence of H_2O_2 (Figure 6-1c) and the Raman spectra in the presence of H_2O_2 (Figure 6-1d) that all three peaks of the broad compound peak seen at 575 cm^{-1} – namely U1, U2 and U3, increase

in intensity with increased burn-up. This is as aforementioned, simply due to the fact that the added dopants induce a range of lattice distortions. It should be noted here that - contrary to the observations made in Chapters 3 & 4 regarding the intensity of the U3 peak, where a slight decrease was observed with increased burn-up - in Figure 6-1d, recorded in the presence of H_2O_2, we observe a slight increase with increased burn-up. The U3 peak is attributed to the presence of clusters of interstitial oxygen i.e. it is due to the hyperstoichiometry of UO_2 as it transitions to form U_4O_9 with increasing x. Therefore, this peak continues to increase in intensity as the amount of oxygen is increased (2). As described in Chapter 3 however, the interpretation of this peak should be considered with caution, due to its weak intensity which is indicative of a low level of hyperstoichiometry (3).

In comparing the intensities of the U1 and U2 peaks for the low and high burn-up 25 & 43 GWd/tU SIMFUEL samples in the absence (Figure 6-1c) and the presence (Figure 6-1d) of H_2O_2, we can see that the addition of hydrogen peroxide has no effect on the respective peak intensities. Slight changes in the U3 peak can be observed with the addition of H_2O_2 – the intensity of the U3 peak decreases slightly for the 25 GWd/tU SIMFUEL sample, whereas the intensity of the U3 peak increases slightly for the 43 GWd/tU SIMFUEL sample with the addition of H_2O_2. As aforementioned, the interpretation of this peak should be carried out with caution (3), and will therefore not be analysed further.

We will now turn our attention to investigating the effects the addition of a 10 µmol dm^{-3} H_2O_2 spike has on the cyclic voltammograms of the undoped UO_2, 25 GWd/tU & 43 GWd/tU SIMFUEL samples.

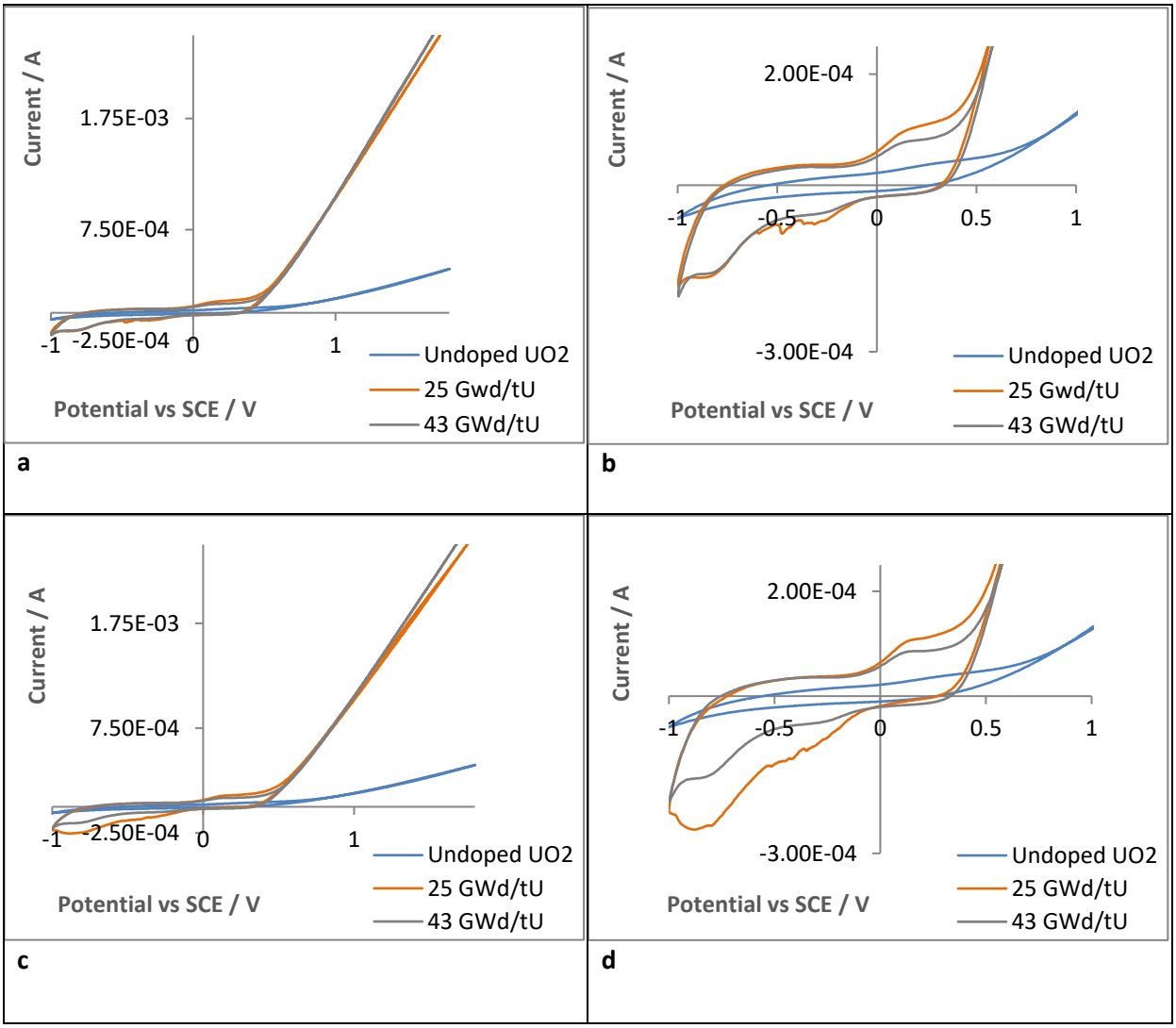

Figure 6-2a to 6-2d – (a) showing the cyclic voltammograms of UO_2, 25 & 43 GWd/tU SIMFUEL pellets in a modified simplified groundwater simulant, cycled at a potential range of (-) 1.0 to (+) 1.8 V, at a scan rate of 10 mV/s; (b) a blown-up image of 6-2a; (c) the cyclic voltammograms of UO_2, 25 & 43 GWd/tU SIMFUEL pellets in a modified simplified groundwater simulant spiked with 10 µmol dm^{-3} H_2O_2, cycled at a potential range of (-) 1.0 to (+) 1.8 V, at a scan rate of 10 mV/s; (d) a blown up image of 6-2c, respectively

Figure 6-2b above is similar to the cyclic voltammogram shown in Figure 5-5b in Chapter 5, with the exception that the voltammogram in Figure 6-2b above has been recorded over a potential window of – 1.0 to 1.8 V_{SCE}, as opposed to – 1.2 to 0.7 V_{SCE} (in Chapter 5). This simply means that we will see a bigger oxidation wave in the cyclic voltammograms of this chapter.

When looking at the forward going sweep of Figure 6-2b (absence of H_2O_2), we observe at an onset of approximately – 0.5 V_{SCE} for both the 25 GWd/tU SIMFUEL and the 43 GWd/tU SIMFUEL sample, the oxidation of UO_{2+x} sites at grain boundaries to $UO_{2.33}$ (4). From 0.15 V_{SCE} onwards, we observe the

oxidation of UO_2 grains to UO_{2+x}. for both SIMFUEL samples. The oxidation of UO_{2+x} to U(VI) species (4) takes place from approximately 0.45 V_{SCE}, again for both SIMFUEL samples. However, there seems to be virtually no additional current signal associated with the oxidation of H_2O_2, such a signal being plainly seen in our studies of peroxide-loaded sulfate electrolytes in Chapter 4 (see Figures 4-3d, 4-5d and 4-10d). We shall return to this point below.

On the reverse sweep, we observe a reduction peak for both the low and high doped 25 & 43 GWd/tU SIMFUEL pellets. The first one appearing at approximately – 0.2 V_{SCE}, and the second one appearing with an onset at approximately – 0.6 V_{SCE} and plateauing at approximately – 0.8 V_{SCE}. As aforementioned in Chapter 5, these can be speculated to be the reduction of the carbonate complexed uranyl (5) (6) (7).

On the reverse sweep in Figure 6-2d, we can see a general increase in the currents associated with the features seen at -0.2 and -0.8 V in Figure 6-2b for the low doped 25 GWd/tU SIMFUEL sample. We attribute this to the presence of an H_2O_2 reduction wave with an onset at approximately – 0.3 V_{SCE}. We speculate that the reason that we only observe the H_2O_2 reduction wave for the low doped 25 GWd/tU SIMUFUEL sample and not the high doped 43 GWd/tU SIMFUEL sample is that there is a higher concentration of epsilon particles present on the surface of the 43 GWd/tU SIMFUEL sample, causing the decomposition of hydrogen peroxide, and thus effectively lowering its local concentration at the pellet/electrode surface. This effective lower concentration of hydrogen peroxide therefore yields no H_2O_2 reduction wave in the case of the 43 GWd/tU SIMFUEL sample. The fact that hydrogen peroxide is less stable in solutions of a higher pH (1), as is the case for our modified simplified groundwater simulant, also means that the hydrogen peroxide is more prone to decomposing.

In a recent paper on the anodic behaviour of UO_2 SIMFUELs in the presence of H_2O_2 and carbonate, Noel *et al.* (8) have reported that the electrochemical oxidation of peroxide and UO_2 occur in parallel – with little in the way of solid U-based oxidation product being formed at the electrode surface at high carbonate. Such is almost certainly happening at E > 0 V in the forward going sweep of Figure 6-2b. However, this would suggest that, compared to the analogous experiment conducted in the simple carbonate-free electrolyte in Chapter 4, Figure 4-2 the electrode surface will be less occluded by solid oxidation products; this would lead us to expect larger currents in Figure 6-2 than in Figure

4-2 for any reduction process on the reverse sweep – including the reduction of hydrogen peroxide. However, comparison of these two results sets indicates that the hydrogen peroxide reduction peak seen for the 25 GWd/tU SIMFUEL pellet observed in Figure 6-2d is less prominent than the H_2O_2 reduction peak we observed in background electrolyte in Chapter 4. This is counter to expectation based on the paper of Noel *et al* (5) and may be due to the change in solution pH from 5.43 (background electrolyte) to pH 8.2 (modified simplified groundwater simulant). The change in solution pH means that the hydrogen peroxide is now less stable at a higher pH (1), meaning that the reduction peaks we observe in modified simplified groundwater will be less prominent, as evidenced by Figure 6-2d above. This pH and ε-particle promoted decomposition of H_2O_2 may also be the reason for the above-discussed absence of any clear current features in Figure 6-2d that may be attributed to the oxidation of H_2O_2.

Having looked at the Raman spectral data, open circuit potential and cyclic voltammetric behaviour of the three samples in a modified simplified groundwater simulant containing 10 µmol dm^{-3} H_2O_2, we will now have a look at the effects of increasing the hydrogen peroxide concentration to 100 µmol dm^{-3}.

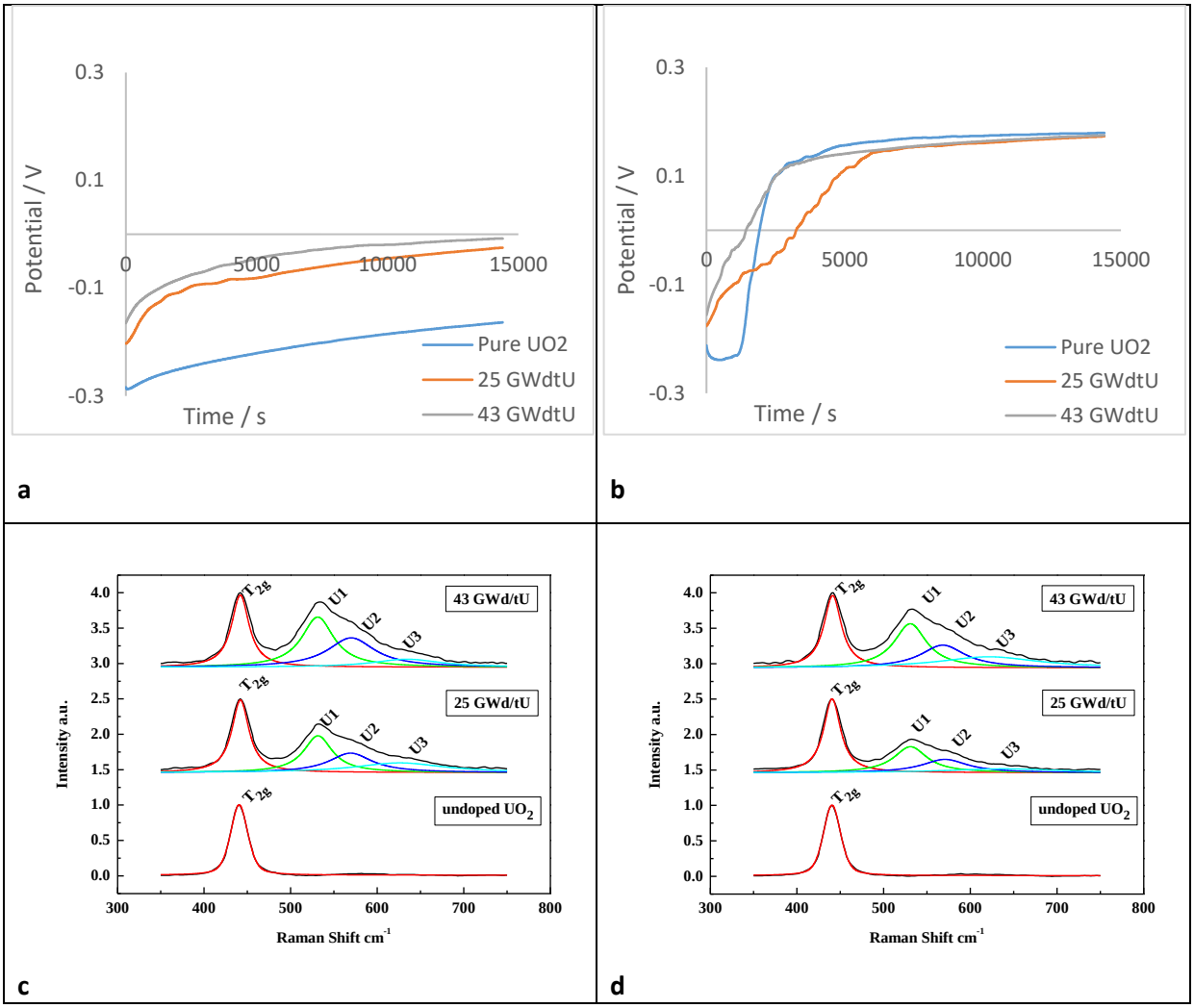

Figure 6-3a to 6-3d - (a) showing the open circuit potential of the UO_2 and 25 & 43 GWd/tU SIMFUEL pellets over a 4 hour period in a modified simplified groundwater simulant pH 8.2; (b) the open circuit potential of the UO_2 and 25 & 43 GWd/tU SIMFUEL pellets over a 4 hour period in a modified simplified groundwater simulant spiked with 100 µmol dm^{-3} H_2O_2; (c) the 20-point averaged Raman spectra of the UO_2 and 25 & 43 GWd/tU SIMFUEL pellets after OCP measurement shown in Figure 6-3a; (d) the 20-point averaged Raman spectra of the UO_2 and 25 & 43 GWd/tU SIMFUEL pellets after OCP measurement shown in Figure 6-3b,respectively

In Figure 6-3 above we can see that for the open circuit potential measurements, the resting potential of the undoped UO_2 has shifted positive in the presence of hydrogen peroxide, from approximately – 0.16 V_{SCE} (Figure 6-3a) to + 0.17 V_{SCE} (Figure 6-3b), as seen in Figure 6-1b with the addition of 10 µmol dm^{-3} to the groundwater simulant. Likewise both SIMFUEL samples have also shifted positive with regards to their rest potentials, from approximately – 7 mV_{SCE} (Figure 6-3a) in the absence of H_2O_2, to 170 mV_{SCE} (Figure 6-3b) in the presence of H_2O_2. As aforementioned, this can be attributed to the fact that the increased hydrogen peroxide concentration is placing an increased oxidative stress on the surface of all three pellet samples.

When looking at the open circuit potential measurement of Figure 6-3b, we can see that the addition of a 100 µmol dm^{-3} H_2O_2 spike has shifted the rest potentials of all three samples more positive when compared to the OCP measurement taken in the absence of hydrogen peroxide. This is due to the oxidative stress that is placed on the samples by the hydrogen peroxide. We also observe that all three samples come to the same rest potential at the end of the measurement. This is due to the fact that the epsilon-driven decomposition of hydrogen peroxide from the two SIMFUELs is less effective at this higher concentration of H_2O_2. Hence why the undoped UO_2 sample comes to rest at the same rest potential as the two SIMFUEL samples.

Looking at the Raman spectra of Figures 6-3c and 6-3d, we again observe that in the absence of hydrogen peroxide, as well as the presence of hydrogen peroxide, the intensities of the U1 and U2 peaks increase with increased intensity. As aforementioned, this is attributed to the fact that through the addition of dopants, the concentration of defects in the lattice is increased (2). Hence, as the amount of dopants is increased from the 25 GWd/tU SIMFUEL pellet to the 43 GWd/tU SIMFUEL pellet, the intensities of the U1 and U2 peaks are seen to increase respectively.

The effect of the addition of the hydrogen peroxide spike on the intensities of the defect peaks in Figure 6-3 is contrary to that which we observed for the analogous experiment conducted in simple sodium sulfate electrolytes in Chapter 4. There, the addition of a 100 µmol dm^{-3} hydrogen peroxide spike caused the intensity of the U1 peak of the 25 & 43 GWd/tU SIMFUEL samples to increase whilst the intensity of the U2 peak was seen to increase slightly for the high doped 43 GWd/tU SIMFUEL. These changes were attributed to the following causes:

For U1 - we attribute the increase in intensity of the U1 peak in both SIMFUEL samples in the presence of hydrogen peroxide in simple background electrolyte solutions to the presence of a very weak so-called U* band which we attribute to arising from hyperstoichiometry at grain boundaries. As hydrogen peroxide is introduced, this hyperstoichiometry should increase, leading to an increase in U* intensity – albeit a very small increase given the inherent weakness of this band.

For U2 - the slight increase in intensity for the high doped 43 GWd/tU SIMFUEL sample upon addition of hydrogen peroxide was attributed to a marginal increase in x. Given the long immersion

time over which the OCP was recorded from this sample, it is also not unreasonable to conclude that the value of *x* in UO_{2+x} increases, if only slightly i.e. there is a small increase in defect concentration associated with the introduction of additional interstitial oxygen anions. This increase in defect concentration may affect the U2 peak as such defects have been shown to lead to a relaxation of the selection rule associated with this band. Assigned to a 1LO mode, the selection rule in question prohibits the observation of this band in the Raman spectrum recorded from the pristine cubic fluorite structure of pure, undefected UO_2. However, this selection rule is relaxed in the presence of defects such as the interstitial oxygens present in UO_{2+x} – hence there is a slight increase in the intensity of the U2 peak observed from the 43 GWd/tU sample when it was exposed to a hydrogen peroxide spike in a simple background electrolyte solution, as described in Chapter 4.

Contrary to what we have observed in Chapter 4, we observed no increase in either the U1 or U2 peaks upon introduction of hydrogen peroxide in Figure 6-3. Indeed, it may be the case that there is a slight decrease in the intensity of the U1 peak for both SIMFUEL samples in going from the absence of H_2O_2 (Figure 6-3c) to the presence of 100 μmol dm^{-3} H_2O_2 (Figure 6-3d). However, it is difficult to say this with certainty.

The reason that these increases in the U1 and U2 peak intensities seen in Chapter 4 are not seen here in Figure 6-3 is most probably due to the fact that at the higher solution pH of our modified simplified groundwater simulant, the hydrogen peroxide is less stable, inevitably leading to its decomposition and thus preventing an increase in *x* which would have caused the increase in the intensity of the U2 peak observed from the 43 GWd/tU SIMFUEL pellet and, if occurring at grain boundaries, the increase in intensity of the U1 peak observed from both the 25 and 43 GWd/tU samples.

We will now look at the effects that a 100 μmol dm^{-3} H_2O_2 spike has on the cyclic voltammograms of our three samples.

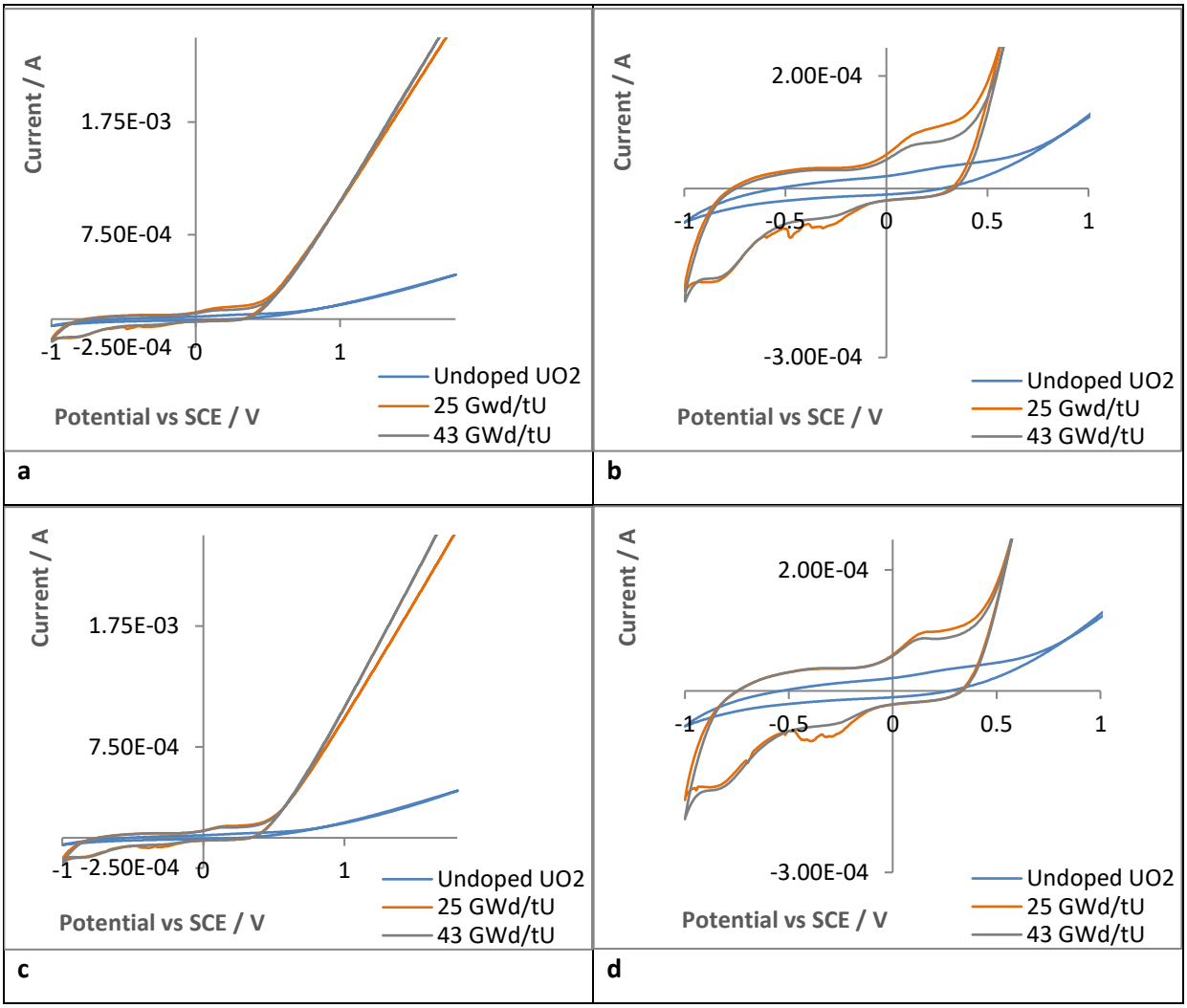

Figure 6-4a to 6-4d - (a) showing the cyclic voltammograms of UO_2, 25 & 43 GWd/tU SIMFUEL pellets in a modified simplified groundwater simulant, cycled at a potential range of (-) 1.0 to (+) 1.8 V, at a scan rate of 10 mV/s; (b) a blown-up image of 6-4a; (c) the cyclic voltammograms of UO_2, 25 & 43 GWd/tU SIMFUEL pellets in a modified simplified groundwater simulant spiked with 100 µmol dm^{-3} H_2O_2, cycled at a potential range of (-) 1.0 to (+) 1.8 V, at a scan rate of 10 mV/s; (d) a blown up image of 6-4c, respectively

In Figure 6-4d above, which is the cyclic voltammogram of our three samples measured in a modified simplified groundwater simulant spiked with 100 µmol dm^{-3} H_2O_2, we once again observe the region in which UO_{2+x} is oxidised to $UO_{2.33}$ at the grain boundaries in the forward going sweep. The onset of this takes place at approximately – 0.5 V_{SCE} for both SIMFUEL samples. Referring back to Figure 6-2d (presence of 10 µmol dm^{-3} H_2O_2), we observed the same taking place at also – 0.5 V_{SCE} for both the low doped 25 GWd/tU and the high doped 43 GWd/tU SIMFUEL samples.

Moving along the anodic sweep, the oxidation of UO_2 grains to UO_{2+x} takes place at approximately -0.15 V_{SCE} for both the SIMFUEL samples, almost in the same region as it did for the solution

containing 10 µmol dm^{-3} H_2O_2. However, again as per Figure 6-2d, there seems to be virtually no additional current signal associated with the oxidation of H_2O_2.

Looking at the reverse sweep, we again see features at -0.2 and -0.8 V_{SCE} for both the 25 GWd/tU & the 43 GWd/tU SIMFUEL samples that we attribute to the reduction of carbonate-complexed uranyl generated during the forward going sweep. Unlike in Figure 6-2, here we see no cathodic wave associated with the reduction of peroxide superimposed over these features. The reason for this is unclear and will be the subject of further investigations in the future. However, it may be that this is again due to the decomposition of hydrogen peroxide caused by the combined effect of the relatively high pH of the electrolyte and the presence of epsilon particles on the surface of both SIMFUELs. As for Figure 6-2d, this pH and ε-particle promoted decomposition of H_2O_2 may also be the reason for the above-discussed absence of any clear current features in Figure 6-4d that may be attributed to the oxidation of H_2O_2. The fact that we are not observing any significant changes in the voltammetry with the addition of a 100 µmol dm^{-3} H_2O_2 spike may simply be a reflection of the difficulty that is associated with carrying out hydrogen peroxide studies in simulated groundwaters under these conditions.

Now that we have looked at all three samples in a modified simplified groundwater solution with a spike of 10 and 100 µmol dm^{-3} hydrogen peroxide, we will have a look at the effects of the addition of a 1 mmol dm^{-3} spike of hydrogen peroxide.

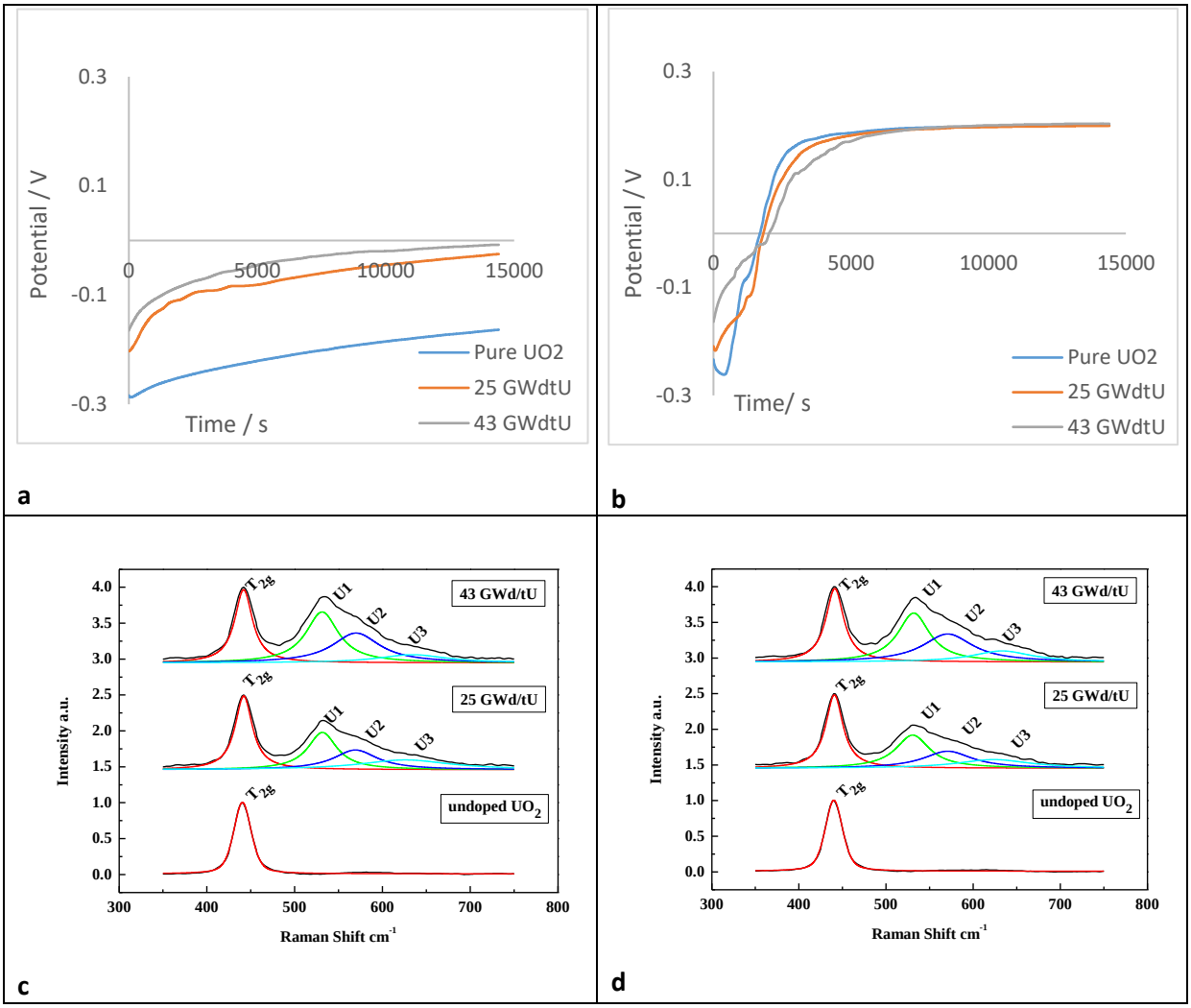

Figure 6-5a to 6-5d - (a) showing the open circuit potential of the UO_2 and 25 & 43 GWd/tU SIMFUEL pellets over a 4 hour period in a modified simplified groundwater simulant pH 8.2; (b) the open circuit potential of the UO_2 and 25 & 43 GWd/tU SIMFUEL pellets over a 4 hour period in a modified simplified groundwater simulant spiked with 1 mmol dm^{-3} H_2O_2; (c) the 20-point averaged Raman spectra of the UO_2 and 25 & 43 GWd/tU SIMFUEL pellets after OCP measurement shown in Figure 6-5a; (d) the 20-point averaged Raman spectra of the UO_2 and 25 & 43 GWd/tU SIMFUEL pellets after OCP measurement shown in Figure 6-5b,respectively

In Figures 6-5a and 6-5b we can see that as observed before, the addition of a 1 mmol dm^{-3} spike has shifted the rest potentials of all three samples more positive. More specifically, the rest potential of the undoped UO_2 sample has shifted from - 0.16 V_{SCE} in the absence of peroxide (Figure 6-5c) to + 0.2 V_{SCE} in the presence of H_2O_2 (Figure 6-5d). Likewise, the rest potentials of the two SIMFUEL samples have shifted from a rest potential of approximately – 7 mV_{SCE} in the absence of H_2O_2 (Figure 6-3c) to 200 mV_{SCE} in the presence of H_2O_2 (Figure 6-5d). This is again due to the oxidative stress that has been imposed onto the three samples by hydrogen peroxide. In Figure 6-5b we also see that the addition of the 1 mmol dm^{-3} spike of H_2O_2 has resulted in all three samples coming to rest at the same rest potential, and at the same rate. This is again simply a reflection of the increased oxidative

stress imposed by the increased concentration of hydrogen peroxide. Even though the concentration of charge carriers is higher in the SIMFUELs in comparison to the undoped UO_2 sample, meaning that the undoped UO_2 samples should reach its rest potential at a slower rate, all three samples come to rest at the same rate, due to the concentration of H_2O_2 being high enough to place the same oxidative stress on all three samples.

Looking at the Raman spectra above, we can see that once again, the intensities of the U1 and U2 peaks increase with increased burn-up, regardless of whether H_2O_2 is present or not. The addition of the 1 mmol dm^{-3} H_2O_2 spike however, has no effect on the intensities of the U1 and U2 peaks in either of the SIMFUEL pellets. This is consistent with what we have observed in Figure 6-3 with the addition of a 100 µmol dm^{-3} H_2O_2 spike. As aforementioned, the decomposition of hydrogen peroxide prevents the generation of x, with which the increase in intensity of the U2 peak is associated. We therefore do not observe an increase in intensity of the U2 peak for the 43 GWd/tU SIMFUEL sample with the addition of 1 mmol dm^{-3} H_2O_2. We also do not observe the previously observed increase in the intensity of the U1 peak for the two SIMFUEL samples (see Chapter 4). This is due to the fact that the U* band is not present due to the failed generation of hyper stoichiometric sites at grain boundaries related to the U* band. As aforementioned, this generation does not take place due to the decomposition of hydrogen peroxide at this higher solution pH, when compared to the sodium sulfate background electrolyte of Chapter 4.

We will now turn our attention to the cyclic voltammograms measured in the presence of a 1 mmol dm^{-3} H_2O_2 spike.

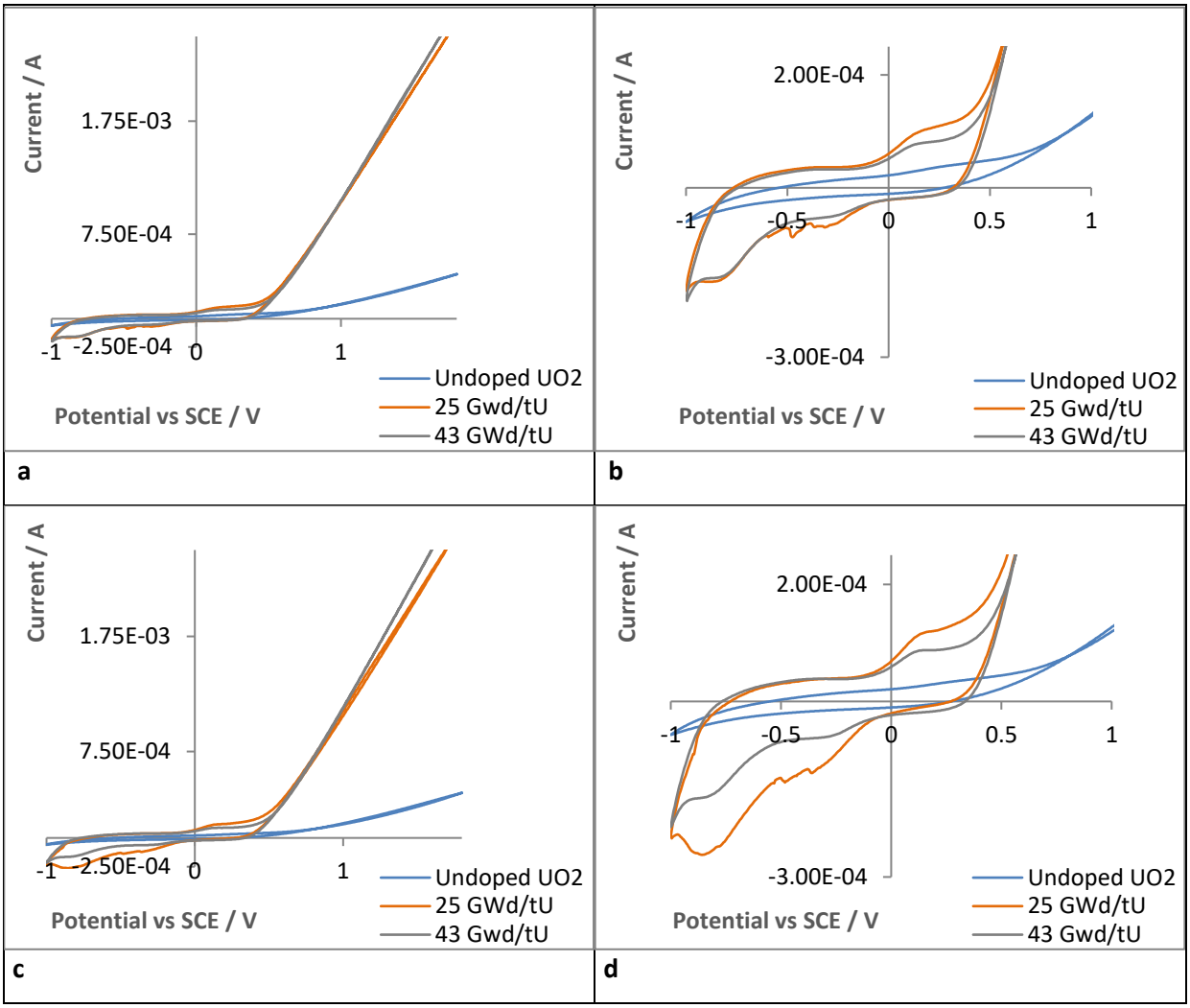

Figure 6-6a to 6-6d - (a) showing the cyclic voltammograms of UO_2, 25 & 43 GWd/tU SIMFUEL pellets in a modified simplified groundwater simulant, cycled at a potential range of (-) 1.0 to (+) 1.8 V, at a scan rate of 10 mV/s; (b) a blown-up image of 6-6a; (c) the cyclic voltammograms of UO_2, 25 & 43 GWd/tU SIMFUEL pellets in a modified simplified groundwater simulant spiked with 1 mmol dm^{-3} H_2O_2, cycled at a potential range of (-) 1.0 to (+) 1.8 V, at a scan rate of 10 mV/s; (d) a blown up image of 6-6c, respectively

Above in Figure 6-6d we can see that the oxidation of UO_{2+x} to $UO_{2.33}$ at the grain boundaries takes place at approximately – 0.6 V_{SCE} for both SIMFUEL samples during the anodic scan. This is consistent with what we observed in Figure 6-4d (addition of 100 µmol dm^{-3} H_2O_2 spike). At a potential of – 0.13 V_{SCE}, we see the onset of the oxidation of UO_2 grains to UO_{2+x} for both SIMFUEL samples. The oxidation of UO_{2+x} to U(VI) species (4) takes place from approximately 0.45 V_{SCE}, again for both SIMFUEL samples – although the current seen from the 25 GWd/tU SIMFUEL in this region is slightly larger in the presence of H_2O_2 than in its absence, an observation that may possibly be attributable to the oxidation of hydrogen peroxide. Oxidation of hydrogen peroxide was not seen in either of the lower peroxide concentration studies described in Figures 6-2d and 6-4d – and this was attributed to pH and ε-particle promoted decomposition of H_2O_2 suppressing the concentration of hydrogen

peroxide. The additional oxidation current seen for the 25 GWd/tU sample may indicate that the hydrogen peroxide concentration is now high enough to overcome these insults to its stability – at least on the 25 GWd/tU sample with its lower ε-particle loading.

Looking at the cathodic sweep, we once again observe the H_2O_2 reduction wave for the low doped SIMFUEL sample. This occurs at approximately – 0.35 V_{SCE}, which is again consistent with what we have observed in the solutions containing 10 µmol dm^{-3} H_2O_2. The reduction of the carbonate-complexed uranyl takes place at approximately – 0.78 V_{SCE} for both the low doped 25 GWd/tU SIMFUEL sample and the 43 GWd/tU SIMFUEL sample. These values are also consistent with what we observed at the lower concentrations of H_2O_2. As aforementioned, we again do not observe the reduction of hydrogen peroxide during the cathodic sweep of the cyclic voltammogram for the 43 GWd/tU SIMFUEL sample above, due to the fact that the increased concentration of epsilon particles is readily decomposing the hydrogen peroxide.

Now that we have looked at all the electrochemical data in the modified simplified groundwater simulant, it is useful to correlate the rest potentials of our undoped UO_2 and 25 & 43 GWd/tU SIMFUEL samples with the corresponding voltammetries in order to attempt to assess whether our samples would freely corrode on exposure to the modified simplified groundwater. Looking at the open circuit potential measurement with the addition of a 10 µmol dm^{-3} hydrogen peroxide spike(Figure 6-1b), we observed all three samples to reach almost the same rest potential, with the two SIMFUEL samples reaching their rest potentials at 0.13 V_{SCE}, slightly below that of the undoped UO_2 sample at 0.17 V_{SCE}. Looking at the corresponding cyclic voltammogram containing 10 µmol dm^{-3} H_2O_2 (Figure 6-2d), we can see that the rest potentials measured in the OCPs correspond to the potential region immediately preceding the onset of the oxidation of UO_{2+x} to U(VI) species. This means that whilst oxidation of UO_{2+x} to $UO_{2.33}$ at the grain boundaries takes place, with possible implications for the instant release fraction, there will be no substantial oxidation of the UO_2 grains to UO_{2+x} for the SIMFUEL samples at a hydrogen peroxide concentration of 10 µmol dm^{-3} taking place, with the consequent expectation of little release via matrix dissolution. Whilst the measured rest potential of 0.17 V_{SCE} for the undoped UO_2 sample would theoretically be high enough for oxidation of the UO_2 grains to take place, undoped UO_2 is electrochemically inactive for reasons discussed in Chapters 1, 3 and 4. The corresponding cyclic voltammogram of the UO_2 sample in Figure 6-2d concurs with this, being broadly featureless and thus suggesting that there is little or no

corrosion of this near-stoichiometric undoped UO_2 sample under the potential conditions studied. The reason for the elevated rest potential is simply due to the oxidative stress placed on the sample by the hydrogen peroxide.

Looking at the open circuit potential measurements in the presence of a 100 µmol dm^{-3} H_2O_2 spike (Figure 6-3b), we can see that all three samples reach their potential of 0.17 V_{SCE} at the same rate. The rest potential observed in the presence of a 100 µmol dm^{-3} H_2O_2 spike is the same as that observed for the undoped UO_2 sample in the presence of a 10 µmol dm^{-3} H_2O_2 spike. This means that at the elevated concentration of 100 µmol dm^{-3} H_2O_2, our samples would still not freely corrode, as only some oxidation of UO_{2+x} to $UO_{2.33}$ at the grain boundaries would take place for the two SIMFUEL samples.

Turning our attention to the open circuit potential containing the highest concentration of hydrogen peroxide, namely 1 mmol dm^{-3} (Figure 6-5b), we can see that all three samples reach the same rest potential of 0.2 V_{SCE} at the same rate. Comparing this value to the corresponding cyclic voltammetry in Figure 6-6d, we can see that our two SIMFUEL samples would indeed start to oxidise, with UO_2 being oxidised to UO_{2+x} on the grains. The rest potential is not, however, high enough for any further oxidation to take place at this concentration of H_2O_2.

Whilst the expected concentration of hydrogen peroxide to be found in the groundwater after the thermal pulse is only 10 µmol dm^{-3}, this study strongly suggests that even at the elevated concentration of 1 mmol dm^{-3} H_2O_2, the SIMFUELs (or spent fuel) would not corrode freely, leading us to conclude that matrix dissolution will not be an issue in granitic groundwater at the temperature of the experiments reported here. However, the rest potentials in all cases are significantly anodic of the potential region at which grain boundaries oxidise / corrode, and this may have implications for the instant release fraction. It is therefore recommended that the corrosion of the SIMFUELs in this potential region is the focus of future work.

Having looked at the Raman, open circuit potential and cyclic voltammetry measurements of the three samples in a modified simplified groundwater, we will now have a look at the three samples in an evaporite simulant groundwater with the addition of various hydrogen peroxide spikes.

Before we investigate the data obtained from the measurements taken in the evaporite groundwater simulant, we will briefly look into the effects that Cl^- has on the decomposition of hydrogen peroxide. The evaporite groundwater simulant contains a high saline concentration, and thus it is important to investigate how this may affect the decomposition of H_2O_2. Specifically, and as shown in Table 2-3 in Chapter 2, the evaporite groundwater simulant is made up of 278 g/L of NaCl and 1.51 g/L of KCl.

In a kinetic study conducted by De Laat & Le, it was found that the rates of decomposition of H_2O_2 in the presence of chloride decreased (9). Another study by Luna *et al*. which investigated the photodecomposition of hydrogen peroxide in a highly saline aqueous medium of 60 g/L NaCl, it was found that the influence of the chloride ions on the photodecomposition of H_2O_2 were negligible (10). Moreover, in a study conducted by Sun *et al*. on the decomposition of hydrogen peroxide using a micro-reactor, it was found that the presence of Cl^- ions in fact significantly supressed the decomposition of H_2O_2 (11). In light of the above, we can assume that the concentration of Cl^- in our evaporite groundwater simulant is most likely to supress the decomposition of H_2O_2, as demonstrated by the above-mentioned studies.

We will now look at the open circuit potential and Raman spectral data of our three samples in an evaporite groundwater simulant in the presence of a 10 µmol dm^{-3} H_2O_2 spike.

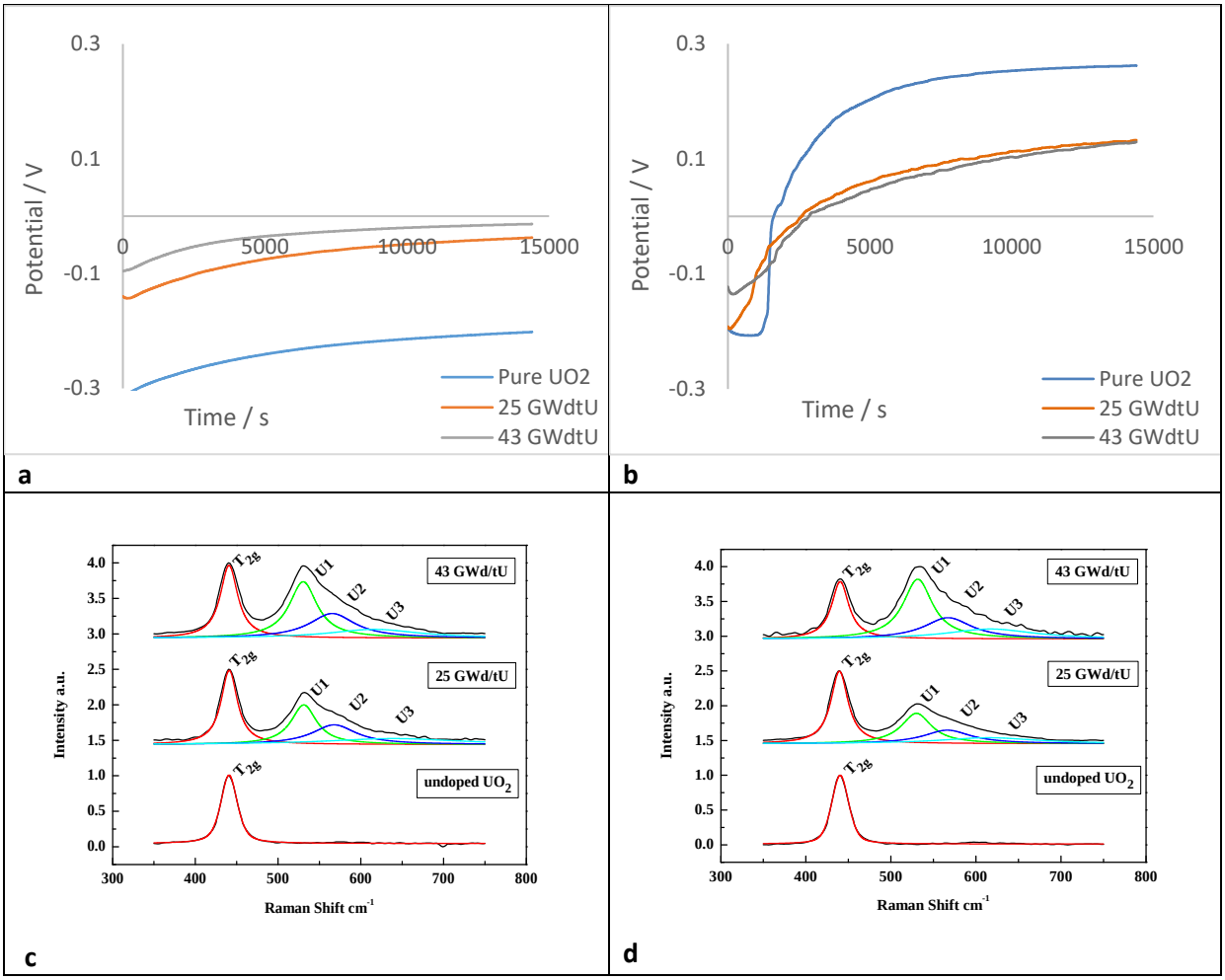

Figure 6-7a to 6-7d - (a) showing the open circuit potential of the UO_2 and 25 & 43 GWd/tU SIMFUEL pellets over a 4 hour period in an evaporite groundwater simulant pH 7.1; (b) the open circuit potential of the UO_2 and 25 & 43 GWd/tU SIMFUEL pellets over a 4 hour period in an evaporite groundwater simulant spiked with 10 µmol dm^{-3} H_2O_2; (c) the 20-point averaged Raman spectra of the UO_2 and 25 & 43 GWd/tU SIMFUEL pellets after OCP measurement shown in Figure 6-7a; (d) the 20-point averaged Raman spectra of the UO_2 and 25 & 43 GWd/tU SIMFUEL pellets after OCP measurement shown in Figure 6-7b,respectively

Above in Figure 6-7d we can see the Raman spectra of the undoped UO_2, the low burnup 25 GWd/tU and the high burnup 43 GWd/tU SIMFUEL pellets, taken after a four hour open circuit potential measurement in an Evaporite groundwater simulant electrolyte that has been spiked with 10 µmol dm^{-3} hydrogen peroxide. Here we once again observe the fundamental UO stretch denoted T_{2g} for all three samples. We also observe the U1, U2 and U3 defect peaks for the two SIMFUEL samples. As seen before, we also see here that the intensities of the U1 and U2 peaks increase with increased burn-up. The addition of H_2O_2 has not had an effect on the intensities of the U1 and U2 peaks for the either of the SIMFUEL samples. As described in Chapter 4, we would expect the intensity of the U1 peak to increase for both the SIMFUEL samples with the addition of hydrogen peroxide due to species associated with the U* band being generated. Due to the high pH of the evaporite

groundwater simulant (pH 7.1), we are again faced with the decomposition of hydrogen peroxide which prevents the phenomena observed in Chapter 4 to take place. Likewise, the increase in the peak intensity of U2 which would be evident in the 43 GWd/tU SIMFUEL sample due to the increase in x afforded by the presence of hydrogen peroxide is also not seen here due to the decomposition of hydrogen peroxide by the high solution pH.

Turning our attention to the open circuit potential measurements of Figure 6-7a (absence of H_2O_2) and Figure 6-7b (presence of H_2O_2), we immediately see that the resting potentials of all three samples have shifted positive with the addition of hydrogen peroxide. This again is due to the fact that the hydrogen peroxide is imposing an oxidative stress on the samples.

Looking at Figure 6-7b, we can see that the addition of 10 µmol dm^{-3} H_2O_2 causes the undoped UO_2 pellet sample to come to rest at a potential of 260 mV vs SCE. The low doped and the high doped 25 & 43 GWd/tU SIMFUEL samples both come to rest at a potential of 130 mV vs SCE. A possible explanation for this could be the catalytic decomposition of hydrogen peroxide due to the epsilon particles present on the 25 & 43 GWd/tU SIMFUEL sample's surfaces (12), despite the presence of the above-mentioned Cl^- ions in the evaporite groundwater simulant. Whilst the presence of the Cl^- ions inhibit the decomposition of H_2O_2 (10) (11) (9), it appears that in the presence of a 10 µmol dm^{-3} H_2O_2 spike however, this has not had a significant effect and the presence of the epsilon particles and subsequently the decomposition of H_2O_2 has taken precedence in this case.

We will now have a look at how this behaviour will change with the addition of a 100 µmol dm^{-3} spike.

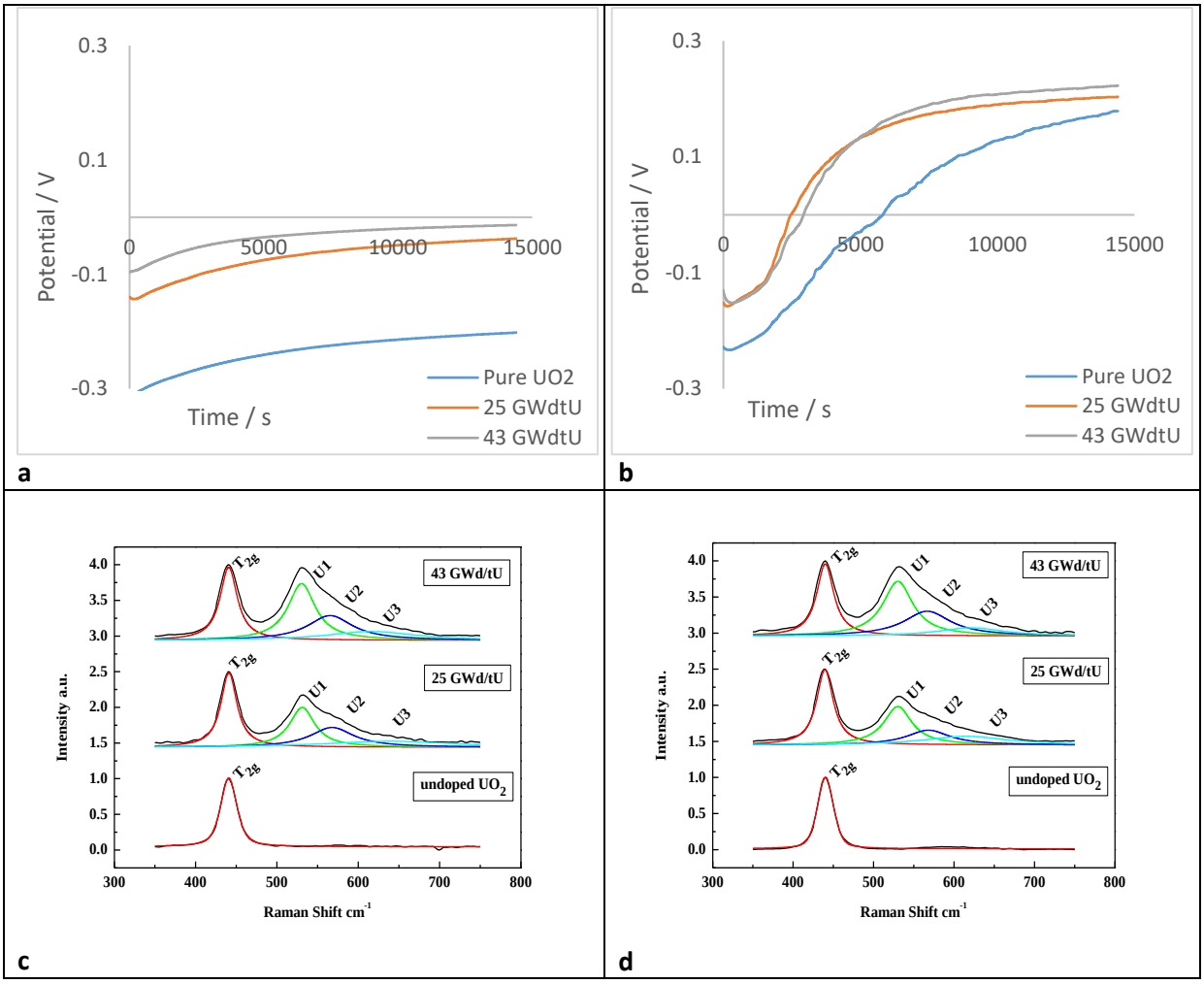

Figure 6-8a to 6-8d - (a) showing the open circuit potential of the UO_2 and 25 & 43 GWd/tU SIMFUEL pellets over a 4 hour period in an evaporite groundwater simulant pH 7.1; (b) the open circuit potential of the UO_2 and 25 & 43 GWd/tU SIMFUEL pellets over a 4 hour period in an evaporite groundwater simulant spiked with 100 µmol dm^{-3} H_2O_2; (c) the 20-point averaged Raman spectra of the UO_2 and 25 & 43 GWd/tU SIMFUEL pellets after OCP measurement shown in Figure 6-8a; (d) the 20-point averaged Raman spectra of the UO_2 and 25 & 43 GWd/tU SIMFUEL pellets after OCP measurement shown in Figure 6-8b,respectively

In Figure 6-8d above, we can see the Raman spectra of an undoped UO_2, a low burnup 25 and a high burnup 43 GWd/tU SIMFUEL pellets, taken after a four hour open circuit potential measurement in an evaporite groundwater simulant spiked with 100 µmol dm^{-3} hydrogen peroxide. Here we once again observe the typical peaks apparent in the previous Raman spectra. Whilst the increase in burn-up has increased the intensities of the U1 and U2 peaks, the addition of hydrogen peroxide has had no effect on the intensities of the defect peaks, as also seen in Figure 6-7 above with the addition of 10 µmol dm^{-3} H_2O_2.

Looking at the open circuit potential measurements of 6-8a (absence of H_2O_2) and 6-8b (presence of H_2O_2), we can immediately see again that the addition of hydrogen peroxide has shifted the rest potentials of all three samples more positive. More specifically, the addition of a 100 µmol dm^{-3} H_2O_2 spike has caused the rest potential of the undoped UO_2 to move from – 200 mV vs SCE to + 200 mV vs SCE. As we observed with the addition of a 10 µmol dm^{-3} H_2O_2 spike, we here also observe that the two SIMFUEL samples come to rest at the same rest potential, which in this case is approximately 220 mV vs SCE, at similar rates. The reason that the two SIMFUELs reach their rest potentials at a faster rate than the undoped UO_2 sample is because they both contain dopants and thus a higher concentration of charge carriers. The concentration of hydrogen peroxide is now high enough that the catalytic decomposition by the epsilon particles in the surface of the SIMFUELs samples no longer dominates (12). This, along with the fact that the presence of Cl^- ions supress the decomposition of hydrogen peroxide, means that even at the lower pH of 7.1, compared to that of the modified simplified groundwater simulant of 8.2, the two SIMUELs still reach a higher rest potential in the evaporite groundwater simulant, 0.22 V_{SCE} compared to 0.17 V_{SCE} in the modified simplified groundwater simulant with the addition of 100 µmol dm^{-3} H_2O_2 spike.

We will now have a look at the effect of the addition of a 1 mmol dm^{-3} H_2O_2 spike.

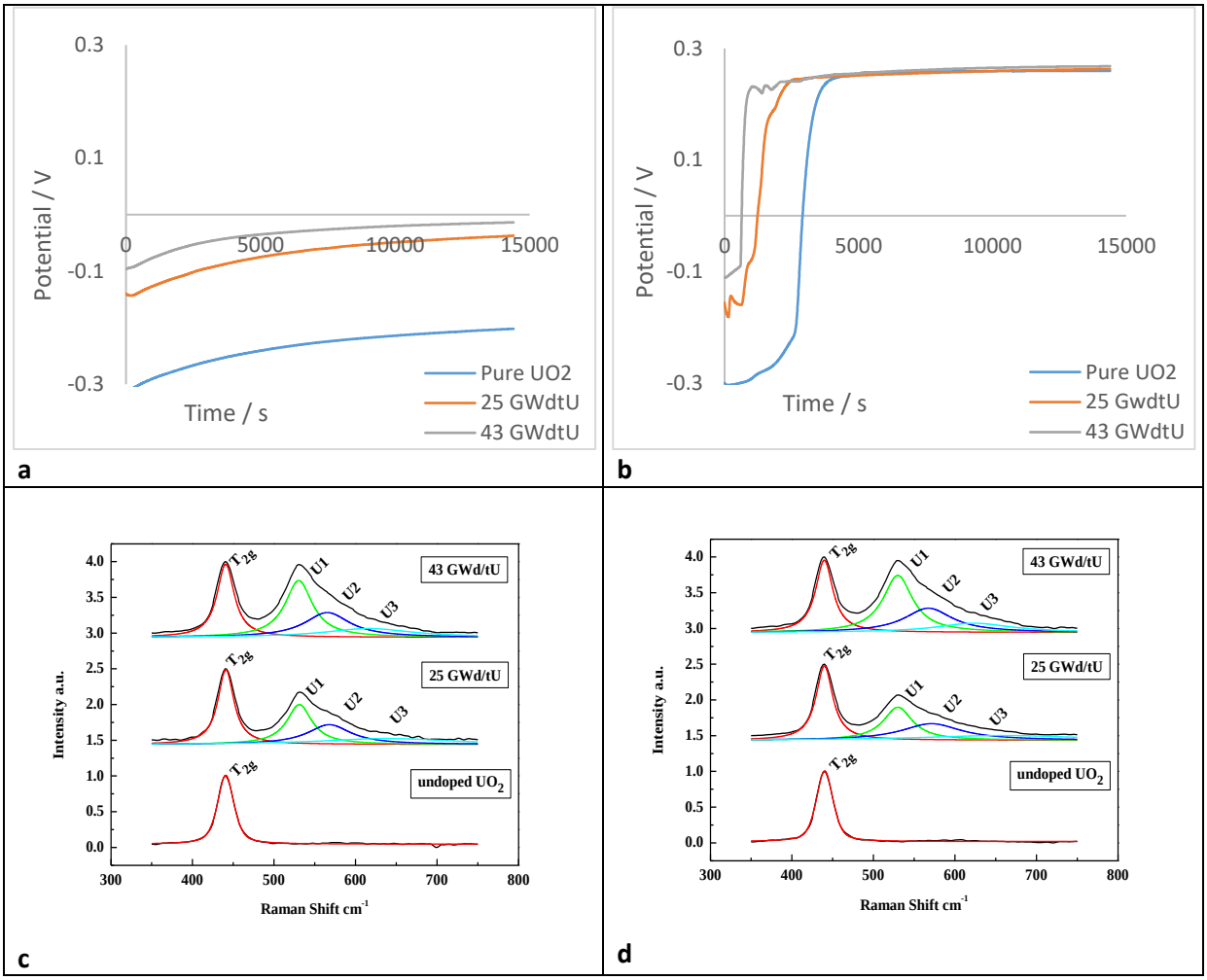

Figure 6-9a to 6-9d - (a) showing the open circuit potential of the UO_2 and 25 & 43 GWd/tU SIMFUEL pellets over a 4 hour period in an evaporite groundwater simulant pH 7.1; (b) the open circuit potential of the UO_2 and 25 & 43 GWd/tU SIMFUEL pellets over a 4 hour period in an evaporite groundwater simulant spiked with 1 mmol dm^{-3} H_2O_2; (c) the 20-point averaged Raman spectra of the UO_2 and 25 & 43 GWd/tU SIMFUEL pellets after OCP measurement shown in Figure 6-9a; (d) the 20-point averaged Raman spectra of the UO_2 and 25 & 43 GWd/tU SIMFUEL pellets after OCP measurement shown in Figure 6-9b,respectively

Above in Figure 6-9d we can see the Raman spectra of the undoped UO_2, the low burnup 25 GWd/tU and the high burnup 43 GWd/tU SIMFUEL pellets taken after a four hour open circuit potential measurement in an evaporite groundwater simulant electrolyte, spiked with 1 mmol dm^{-3} hydrogen peroxide. Here we can once again see that the increase in burn-up increases the intensities of the U1 and U2 peaks. The addition of a 1 mmol dm^{-3} H_2O_2 spike however, has had no effect on the intensities of the U1 and U2 peaks, which is consistent with what we have observed in Figures 6-7 and 6-8 above with the additions of 10 and 100 µmol dm^{-3} H_2O_2. This once again illustrates the difficulties that are encountered when carrying out studies of hydrogen peroxide in high pH solutions.

Looking at the open circuit potential measurements of Figure 6-9a (absence of H_2O_2) and Figure 6-9b (presence of H_2O_2), we can again immediately see that the addition of 1 mmol dm^{-3} H_2O_2 has caused the rest potentials of all three samples to shift positive. We can also see that the addition of H_2O_2 has imposed an oxidative stress great enough on all three samples that they all come to rest at the same rest potential of 270 mV vs SCE, all at the same rate. At this high concentration of hydrogen peroxide, the oxidative stresses that these samples are under override the catalytic decomposition of H_2O_2 by the epsilon particles present on the surface of the SIMFUEL samples. Even though the undoped UO_2 has a lower concentration of charge carriers in comparison, the concentration of H_2O_2 is high enough to cause enough oxidative stress for the undoped UO_2 sample to reach its rest potential at the same rate as the SIMFUEL samples with a higher concentration of charge carriers. As mentioned above, this along with the fact that the presence of the Cl^- ions is inhibiting the decomposition of hydrogen peroxide, we again observe a higher rest potential for the three samples in the evaporite groundwater simulant when compared with the modified simplified groundwater simulant with the addition of a 1 mmol dm^{-3} H_2O_2 spike, 0.27 V_{SCE} and 0.20 V_{SCE}, respectively.

Below is a table to summarise the rest potentials observed during OCP in the two groundwater simulants, as well as the 0.1 mol dm^{-3} Na_2SO_4 background electrolyte, with the addition of each H_2O_2 spike.

Solution / pH	**10 µmol dm^{-3} H_2O_2**	**100 µmol dm^{-3} H_2O_2**	**1 mmol dm^{-3} H_2O_2**
Na_2SO_4 (pH 5.4)	0.21 V_{SCE} (25 GWd/tU) 0.12 V_{SCE} (43 GWd/tU)	0.25 V_{SCE}	0.25 V_{SCE}
Evaporite groundwater (pH 7.1)	0.13 V_{SCE}	0.22 V_{SCE}	0.27 V_{SCE}
Modified simplified groundwater (pH 8.2)	0.13 V_{SCE}	0.17 V_{SCE}	0.20 V_{SCE}

Table 6-1 showing rest potentials of the undoped UO_2, 25 & 43 GWd/tU SIMFUEL samples in various media

Due to time constraints, we have been unable to carry out cyclic voltammetry experiments in the evaporite groundwater simulant with the various hydrogen peroxide spikes, we can however, using the cyclic voltammogram measured in the absence of hydrogen peroxide (Figure 5-7b), draw

conclusions on the corrosion potentials of our undoped UO_2 and SIMFUEL samples in evaporite groundwater by correlating the open circuit potentials to the cyclic voltammogram. Said cyclic voltammogram is reproduced below for the convenience of the reader.

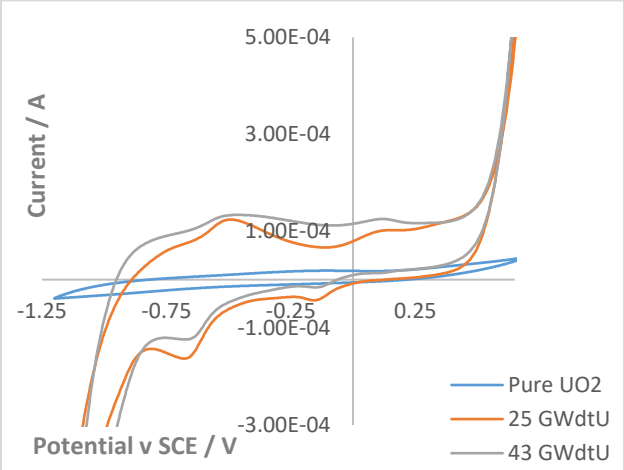

Figure 6-10 showing the cyclic voltammograms of UO_2, 25 & 43 GWd/tU SIMFUEL pellets in an evaporite groundwater simulant, cycled at a potential range of (-) 1.2 to (+) 0.7 V, at a scan rate of 10 mV/s

Referring back to the open circuit potentials measured in Figure 6-7b, we observed that the undoped UO_2 sample came to rest at a potential of 0.26 V_{SCE}, whilst the two SIMFUELs came to rest at 0.13 V_{SCE} with the addition of a 10 µmol dm^{-3} H_2O_2 spike. Correlating these figures to our cyclic voltammogram in Figure 6-10 above, we can see that the rest potential of the two SIMFUELs corresponds to the region just before the onset of oxidation of in-grain UO_2 to UO_{2+x} takes place at 0.15 V_{SCE}. This means that whilst some oxidation of UO_2 to UO_{2+x} may still occur due to the proximity of the two measured potentials, there is no indication however that the SIMFUELs would freely corrode at this hydrogen peroxide concentration. As aforementioned, even though the rest potential of the undoped UO_2 is measured at 0.26 V_{SCE}, we can see from the cyclic voltammogram that the UO_2 remains chemically inactive, and will therefore not corrode.

Looking at the measured open circuit potentials of our three samples in the presence of a 100 µmol dm^{-3} H_2O_2 spike in Figure 6-8b, we can see that all three samples come to rest at approximately the same potential of 0.22 V_{SCE}. Correlating this back to our cyclic voltamogramm, we are still in the region of oxidation of in-grain UO_2 to UO_{2+x}, which occurs between 0.15 – 0.25 V_{SCE}. From this we can

again conclude that whilst some oxidation of in-grain UO_2 to UO_{2+x} will occur, the SIMFUELs are still not able to freely corrode at this H_2O_2 concentration.

Turning our attention to the open circuit potential measurements in the presence of a 1 mmol dm^{-3} H_2O_2 spike in Figure 6-9b, we can see that all three samples come to rest at a potential of 0.27 V_{SCE}. In this region we would expect to see passivation of the surface layer, which does not occur due to carbonate complexation. At a potential below 0.44 V_{SCE} we are still in a region where our samples cannot freely corrode, and hence we again do not expect the SIMFUELs to corrode freely at this H_2O_2 concentration.

As aforementioned with the modified simplified groundwater, whilst the expected concentration of hydrogen peroxide to be found in the groundwater after the thermal pulse is only 10 µmol dm^{-3}, this study strongly suggests that even at the elevated concentration of 1 mmol dm^{-3} H_2O_2, the SIMFUELs (or spent fuel) would not corrode freely. These findings are in accordance with Razdan and Shoesmith (13), who observed that by varying the corrosion potential with time, redox conditions and the concentrations of HCO_3^-/CO_3^{2-}, as well as convective conditions, that the surface oxidation induced by hydrogen peroxide could be reversed by reaction with H_2, the latter reaction occurring dominantly on the noble metal particles in the SIMFUEL. For sufficiently large hydrogen peroxide concentrations, it was found that the influence of H_2 was overwhelmed, resulting in the irreversible oxidation of the surface to U^{VI}. Subsequently, corrosion was found to be controlled by the chemical dissolution rate of this U^{VI} layer (13). Furthermore, Zhu et *al*. (14) found that hydrogen peroxide would decompose to oxygen and water both homogeneously and heterogeneously, which resulted in the minimal amount of corrosion of UO_2 (14). In another hydrogen peroxide study, Zhu et *al*. (8) found that the corrosion of the SIMFUEL surface was limited by the slow dissolution of UVI species from a UVI surface layer (8).

The rest potentials in all cases however are significantly anodic of the potential region at which grain boundaries oxidise / corrode, and this may have implications for the instant release fraction. This will be explored in subsequent work.

6.3 Conclusions

In this chapter, we have looked at the Raman spectral and open circuit potential data for the undoped UO_2 pellet, the low burnup 25 GWd/tU SIMFUEL pellet, and the high burnup 43 GWd/tU SIMFUEL pellet in two different electrolytes. A modified simplified groundwater and an evaporite groundwater simulant were chosen for this study, as they are two likely candidates of the type of groundwater that could ingress through the fuel cladding and come into contact with the fuel matrix. In this chapter in particular we have looked at the effects on the corrosion behaviour of the three samples of adding increasing concentrations of hydrogen peroxide to the two simulant groundwaters. As explained in Chapters 1 and 4, hydrogen peroxide is a product that is generated by the alpha radiolysis of water (13) (14). This is why it is important to look at the effects brought about by the presence of hydrogen peroxide in the various groundwater simulants.

In addition to the Raman spectra and open circuit potential studies, we have also looked at the cyclic voltammograms measured for our three samples in the modified simplified groundwater with increasing concentrations of hydrogen peroxide. We have been able to link the data from the cyclic voltammograms to the open circuit potential data, in order to evaluate whether the SIMFUELs would corrode freely in groundwater of a similar composition to our modified simplified groundwater simulant, as well as our evaporite groundwater simulant. It was found that the SIMFUELs would not in fact corrode freely in either of the groundwater simulants, even in the presence of concentrations of hydrogen peroxide as high as 1 mmol dm^{-3}. As aforementioned in the Results & Discussion section, these findings are in accordance with analogous data recorded from CANDU SIMFUEL by Razdan and Shoesmith (13).

With regards to the Raman spectral measurements, we have observed that for the modified simplified groundwater simulant, as well as the evaporite groundwater simulant, the observed intensities of the U1 and U2 peaks remain unchanged for both SIMFUEL samples with increasing additions of H_2O_2, as opposed to the addition of hydrogen peroxide. The lack of increase in the intensities of the U1 and U2 peaks with increasing peroxide concentration in the groundwaters studied here is most probably due to the fact that at the higher solution pH of both our groundwater simulants; the hydrogen peroxide is less stable, leading to its decomposition and thus preventing an increase in *x*. An increase in *x* would have caused the increase in the intensity of the U2 peak

previously observed for the 43 GWd/tU SIMFUEL pellet in the sodium sulfate electrolyte, and also, if occurring at grain boundaries, the increase in intensity of the U1 peak previously observed for both the 25 and 43 GWd/tU SIMFUEL samples, also in the background electrolyte. The latter is due to the fact that the U* band is not present as the hyperstoichiometric sites at the grain boundaries related to the U* band have failed to generate (17). As aforementioned, this generation does not take place due to the decomposition of hydrogen peroxide at this higher solution pH (1), when compared to the sodium sulfate background electrolyte observed in Chapter 4.

With regards to the open circuit potential measurements, we have observed that in both simulant groundwaters, the addition of a hydrogen peroxide spike, immediately shifted the rest potentials of all three samples more positive when compared to the rest potentials measured in the absence of H_2O_2. This simply occurred due to the hydrogen peroxide placing an oxidative stress on the samples.

We also observed that the rest potentials measured for the open circuit potentials of our two SIMUEL samples in the evaporite groundwater simulant were higher with the addition of 100 μmol dm^{-3} and 1 mmol dm^{-3} H_2O_2 spikes when compared to the same measurements recorded in the modified simplified groundwater simulant. As the solution pH of the modified simplified groundwater is higher than that of the evaporite groundwater simulant (8.2 compared to 7.1), we would expect the hydrogen peroxide in the modified simplified groundwater to decompose more readily (1), and thus result in resting potentials more negative than those observed for the evaporite groundwater simulant. This is, in fact, what is observed. The rest potentials that we observe in the modified simplified groundwater are lower than those observed in the evaporite groundwater.

Based on this trend, we would expect the rest potentials recorded for the SIMFUELs in the evaporite groundwater to be negative of those recorded in pH 5.4. However, the presence of Cl^- ions in the evaporite groundwater simulant supresses the decomposition of hydrogen peroxide (11), and thus the rest potentials recorded for the two SIMFUELs in evaporite groundwater are either only slightly lower or similar to those recorded in background electrolyte of pH 5.4. These are summarised in Table 6-1.

Turning our attention to the cyclic voltammograms recorded in the modified simplified groundwater simulant, during the anodic scan we observe the oxidation of UO_{2+x} to $UO_{2.33}$ at the grain boundaries, as well as the oxidation of UO_2 grains to UO_{2+x}, both occurring at similar potentials for both the SIMFUEL samples, namely at – 0.6 V_{SCE} and – 0.13V_{SCE}, respectively. This was true for all three H_2O_2 spikes. These peaks have been assigned according to the regional assignments of Seibert *et al*. (18), and are in accordance with the peaks observed by Zhu *et al*. (8) during their electrochemical study of SIMFUELs in electrolyte containing H_2O_2 and various concentrations of HCO_3^-/CO_3^{2-}, whereby they used two different SIMFUELs – one being a rare earth-doped lattice containing noble metal (Ɛ) particles (8), representative of our high doped 43 GWd/tU SIMFUEL sample, and a second one not containing the noble metal elements and hence free of Ɛ (8), representative of our low doped 25 GWd/tU SIMFUEL sample.

For the cathodic sweep, we observe the reduction of the carbonate-complexed uranyl taking place at approximately – 0.8 V_{SCE} for both the 25 GWd/tU SIMFUEL and the 43 GWd/tU SIMFUEL sample. We also observe the H_2O_2 reduction wave for the low doped SIMFUEL sample at approximately – 0.2 V_{SCE}. We however do not observe the reduction of hydrogen peroxide during the cathodic sweep of the 43 GWd/tU SIMFUEL sample, due to the fact that the increased concentration of epsilon particles is readily decomposing the hydrogen peroxide (12). The same was observed on the SIMFUEL containing noble metal (Ɛ) particles during the above mentioned study by Zhu *et al.* (8).

References

1. E.Y. Yazici, H. Deveci. *Factors affecting decomposition of hydrogen peroxide.* s.l. : Proceedings of the XIIth International Mineral Processing Symposium, 2010.

2. J.M. Elorietta, L.J. Bonales, N. Rodriguez-Villagra, V.G. Baonza, J. Cobos. *A detailed Raman and X-ray study of the UO_{2+x} oxides and related structure transitions.* s.l. : Physical Chemistry Chemical Physics, 2016, Vol. 18. pp. 28209 - 28216.

3. E.A. Howett. *The behaviour of spent nuclear fuel in wet interim storage.* s.l. : Lancaster University, 2019.

4. G. Krishnan. *Cyclic Voltammetry.* s.l. : Ohio University, 2011.

5. **S. Butorin, K. Ollila, Y. Albinsson, J. Nordgren, L. Werme.** *Reduction of uranyl carbonate and hydroxyl complexes and neptunyl carbonate complexes studied with chemical-electrochemical methods and rixs spectroscopy.* s.l. : Swedish Nuclear Fuel and Waste Management Co, 2003.

6. D.E. Morris. *Redox energetics and kinetics of uranyl coordination complexes aqueous solution.* s.l. : Inorganic Chemistry, 2002, Vol. 41. pp. 3542 - 3547.

7. M.C.F. Wander, S. Kerisit, K.M. Rosso, M.A.A. Schoonen. *Kinetics of triscarbanato uranyl reduction by aqueous ferrous iron: a theoretical study.* s.l. : Journal of Physical Chemistry, 2006, Vol. 110.

8. Z. Zhu, L. Wu, J.J. Noel, D.W. Shoesmith. *Anodic reactions occuring on simulated spent nuclear fuel (SIMFUEL) in hydrogen peroxide solutions containing bicarbonate/carbonate - the effect of fission products.* s.l. : Electrochimica Acta, 2019, Vol. 320.

9. J. De Laat, T.G. Le. *Effects of chloride ions on the iron(III)-catalyzed decomposition of hydrogen peroxide and on the efficiency of the Fenton-like oxidation process.* s.l. : Applied Catalysis B: Environmental, 2006, Vol. 66. pp. 137 - 146

10. A.J. Luna, C.A.O. Nascimento, O. Chiavone-Filho. *Photodecomposition of hydrogen peroxide in highly saline aqueous medium.* s.l. : Brazilian Journal of Chemical Engineering, 2006, Vol. 23.

11. B. Sun, H. Zhu, Y. Jin, K. Qiao, W. Xu, J. Jiang. *Rapid hydrogen peroxide decomposition using a microreactor.* s.l. : Chemical Engineering & Technology, 2019, Vol. 42. pp. 252 - 256.

12. D.W. Mckee. *Catalytic decomposition of hydrogen peroxide by metals and alloys of the platinum group.* s.l. : Journal of Catalysis, 1969, Vol. 14. pp. 355 - 364.

13. M. Razdan, D.W. Shoesmith. *The influence of hydrogen peroxide and hydrogen on the corrosion of simulated spent nuclear fuel.* s.l. : Faraday Discussions, 2015, Vol. 180.

14. Z. Zhu, J.J. Noel, D.W. Shoesmith. *Hydrogen peroxide decomposition on simulated nuclear fuel.* s.l. : Electrochimica Acta, 2020, Vol. 340.

15. Nuclear Decommissioning Authority. *Geological Disposal - Generic disposal facility designs.* s.l. : NDA Report no. NDA/RWMD/048, 2010.

16. H.H.B. Lee, A.-H. Park, C. Oloman. *Stability of hydrogen peroxide in sodium carbonate solutions.* s.l. : Tappi Journal, 2000, Vol. 83.

17. O.A. Maslova, G. Giumbretiere, M.R. Ammar, L. Desgranges, C. Jegou, A. Canizares, P. Simon. *Raman imaging and principal component analysis-based data processing on uranium oxide ceramics.* s.l. : Materials Characterization, 2017, Vol. 129. pp. 260 - 269.

18. A. Seibert, D.H. Wegen, T. Gouder, J. Roemer, T. Wiss, J.-P. Glatz. *The use of the electrochemical quartz crystal microbalance (EQCM) in corrosion studies of UO_2 thin film models.* s.l. : Journal of Nuclear Materials, 2011, Vol. 491. pp. 112 - 121.

Chapter 7 Corrosion of UO_2 & SIMFUELs coupled with 20/25/Nb Stainless Steel Cladding

7.1 Introduction

In this final chapter of observing the behaviour of our SIMFUEL pellets, we will investigate how the undoped UO_2, 25 & 43 GWd/ tU SIMFUEL pellets behave when coupled with the 20/25/Nb stainless steel cladding that is typical of AGR fuel. The reason for investigating the coupled behaviour of the undoped UO_2 and SIMFUEL samples in conjunction with the steel cladding is due to the fact that once the fuel pins have been compromised in a GDF following the thermal pulse, and been subject to the ingress of groundwater, the spent fuel pellets will not then corrode in isolation. They will in fact, corrode in the presence of, and in contact with the stainless steel cladding. The stainless steel cladding will have its own corrosion behaviour in response to the invading groundwater. Furthermore, the individual corrosion behaviours of the pellets and the cladding may couple – the focus of this chapter being the investigation of said cladding.

The stainless steel cladding termed 20/25 Nb comprises of a niobium stabilised 20 wt. % Cr and 25 wt. % Ni fuel cladding alloy (1). It was supplied in the form of cladding tubes (internal diameter ~14.25 mm, external diameter ~15 mm) from Westinghouse's Springfields Fuel Ltd production line at Preston, UK. Process history involved a cold reduction / strain hardening of 20% followed by an hour's heat treatment at 930 ºC. This is designed to produce a fine dislocation structure during the cold reduction, followed by the precipitation of NbC inclusions within the grains of the steel, the latter stabilising the material against undesirable chromium carbide formation at elevated temperatures [6]. The exact composition of the steel is detailed below.

Component	*% wt.*
Cr	20.12
Ni	24.75
Nb	0.70
Mn	0.62
Si	0.57
C	0.049
N	0.016
S	0.0004
P	0.006
Co	0.0025
Ta	<0.001
Al, Zr, Ti	<0.05
Fe	balance

Table 7-1 showing composition of 20/25/ Nb stainless steel cladding in % wt. (2)

By use of simple open circuit potential measurements, we will investigate the corrosion behaviour of our undoped UO_2 and SIMFUEL samples when coupled with the 20/25/Nb stainless steel cladding. These coupled electrodes were fabricated as per Section 2.3 (Chapter 2), except that in this case a ring of the cladding material was also embedded around the pellet; the pellet diameter being 11.5 mm (3) and the cladding diameter being 15 mm (3). In conditions representative of a repository, these would be at even closer contact, with an AGR fuel pellet having a diameter of 14.5 mm (3) and the cladding one of 15 mm (4). The OCPs will be measured in a range of media, including those of relevance to geologic disposal, both in the absence and the presence of 10 µmol dm^{-3} H_2O_2. The reason for choosing this concentration of hydrogen peroxide is because modelling studies conducted by researchers at Pacific Northwest National Laboratory (PNNL) indicate that it is the concentration that is most likely to be found in groundwater as a result of alpha-radiolysis of water in the near field / at the fuel pin surface (5) (see Chapter 1). In this instance, we are only considering alpha radiolysis as, at the point when it is expected that groundwater may penetrate any compromised fuel pins, >10,000 years in the future, the beta/gamma field will have subsided (6) (7) (8).

7.2 Summary of Corrosion Behaviour of 20/25/Nb under Conditions relevant to Geological Disposal

Simple linear sweep voltammetry (LSV) can provide a range of mechanistic insights into the corrosion behaviour of steels in solution phase environments. In a typical linear sweep voltammagram of an electroactive metal such as a steel in aqueous solution, as the current density increases in response to varying the potential, so too does the corrosion rate. Plotting the logarithm of the current density versus the applied potential is a typical way of presenting this data. These are known as polarisation curves or Tafel plots, an example of which is shown in Figure 7.1 below.

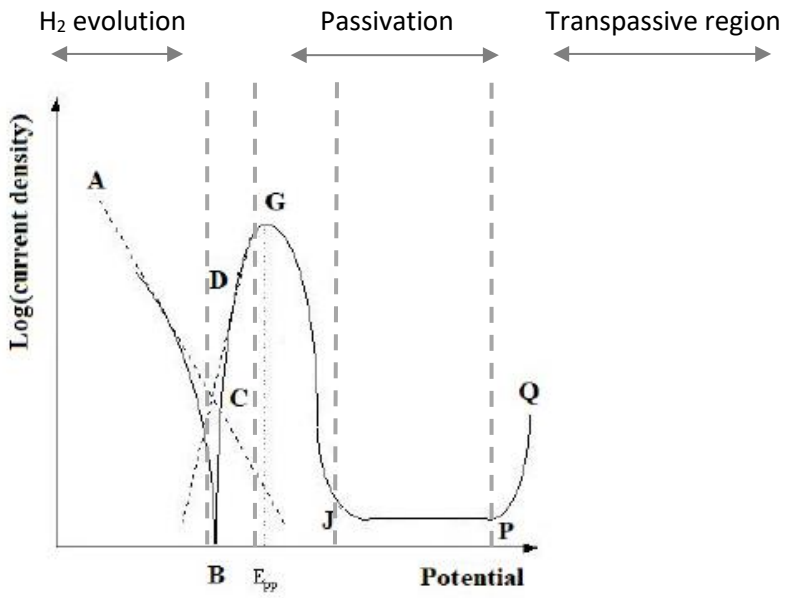

Figure 7-1 showing schematic of a typical polarisation curve for a passivating metal (9)

The curve of Figure 7-1 above can be broken down into a number of characteristic regions such as AB, BC and so forth. These can be described as follows. AB is a cathodic reaction, most commonly attributed to hydrogen evolution. At potential B, the metal corrodes freely. This potential is called the corrosion potential. Oxidative corrosion of the metal occurs from B to G, which is the so-called active region. As the potential increases from G to J, a protective oxide begins to grow on the surface of the electrode, so reducing the current density. The potential at G is referred to as the passivation potential, E_{pp}. Between J and P, the current density remains at this passivation limited reduced current density. The associated corrosion rate is low so the surface is protected. This region is referred to as the passive region. In stainless steels such as 20/25/Nb, the passive layer consists mainly of iron/chromium oxides and hydroxides. At P, the oxide layer begins to break-down intermittently and pitting is likely to occur. This potential is known as the critical pitting or break-down potential (E_{pit}). As the potential increases further from P to Q, dissolution of the passive layer takes place. This is called the transpassive region.

As in the cases of the undoped UO_2 and SIMFUEL electrodes studied in Chapter 4 through to Chapter 6, inspection of the measured OCP values and the corresponding linear sweep voltammograms recorded using the same steel/SIMFUEL couple in the same aqueous medium system, can provide insight into the equilibrium corrosion behaviour of the steel coupled with the SIMFUELs under the solution conditions in question. For example, the OCP may fall in a region of passivity on the LSV, so allowing us to conclude that the steel/SIMFUEL couple may not be corroding under the solution

conditions employed. Alternatively, the OCP may lie in the region of transpassivity in the LSV, so allowing us to conclude that the steel/SIMFUEL couple may be freely corroding.

Thus, in the sections that follow, we will first present the OCPs of the undoped UO_2 and SIMFUEL samples separately, followed by OCP measurements repeated in the same range of electrolytes, this time on the undoped UO_2 and SIMFUEL pellets coupled with cladding material. Measurements will be conducted in simple sulfate electrolyte, modified simplified and evaporite groundwater simulants. The OCPs will then be compared with the corresponding LSVs for each electrode/steel couple in order to identify the dominant corrosion processes that obtain on each couple in the electrolyte under study.

7.3 Results & Discussion

We will first study the open circuit potential behaviour of our three samples in the 0.1 mol dm^{-3} Na_2SO_4 background electrolyte. All open circuit potential measurements are represented without and with steel coupling in the various solutions, for ease of comparison of trends. As there are no corrosion inhibitors present in the background electrolyte, we can expect the stainless steel cladding to corrode to a certain extent which may, potentially, then subsequently sacrificially protect the undoped UO_2 and SIMFUEL samples.

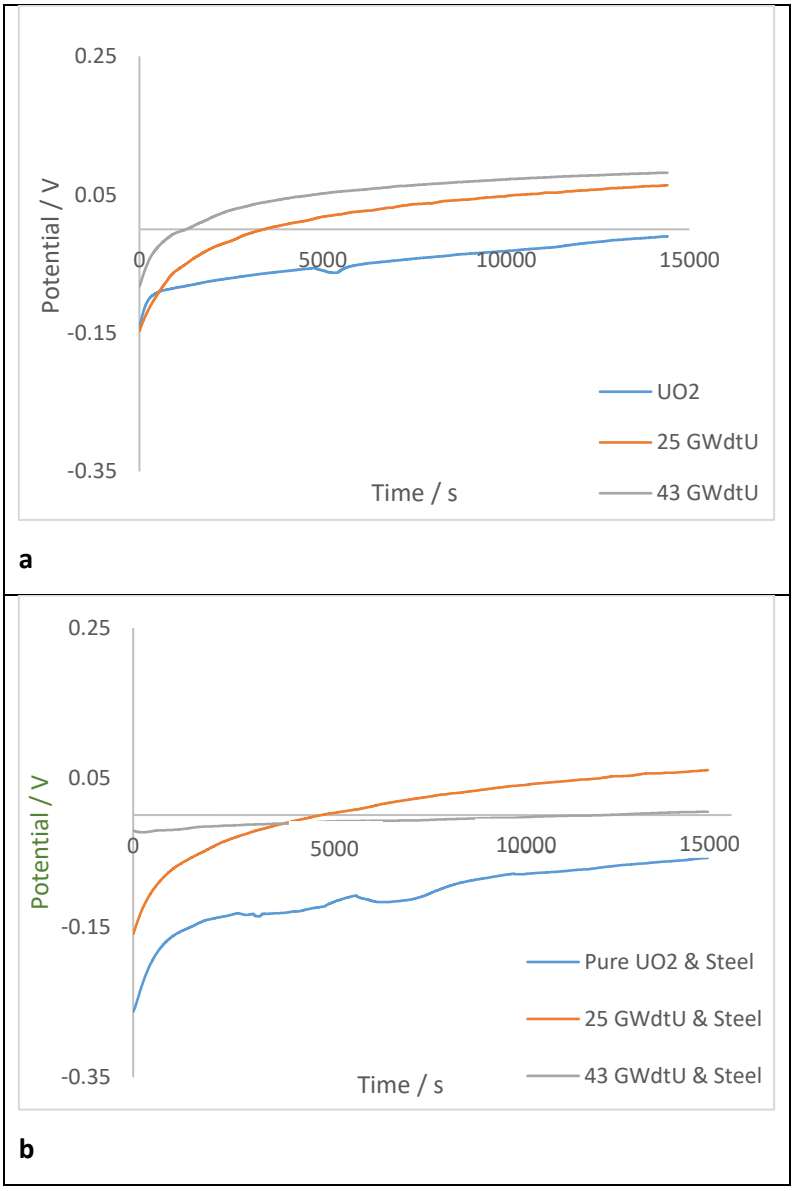

Figure 7-2a and 7-2b – (a) showing the open circuit potential of the UO_2 and 25 & 43 GWd/tU SIMFUEL pellets over a 4 hour period in a 0.1 mol dm^{-3} Na_2SO_4 background electrolyte; (b) showing the open circuit potential of the UO_2 and 25 & 43 GWd/tU SIMFUEL pellets coupled with 20/25/Nb steel over a 4 hour period in a 0.1 mol dm^{-3} Na_2SO_4 background electrolyte, both at pH 5.43

Looking at the open circuit potential measurement in Figure 7-2a, we can see that the undoped UO_2 pellet reaches its resting potential slower than the two SIMFUEL samples. The undoped UO_2 pellet also comes to rest at a lower potential than the two SIMFUEL pellets. As explained in Chapter 3, this is due to the higher concentration of charge carriers in the two SIMFUEL samples derived from doping effects associated with the addition of fission product simulants to the SIMFUEL matrix. The higher charge carrier concentration will support higher exchange current densities at the surface of the two SIMFUEL samples, with a consequent increase in charge transfer kinetics and thus rate of approach to equilibrium. The higher the burn-up of the SIMFUEL, the higher its resting potential, due to the fact that the metallic particle loaded SIMFUELs are more prone to corrosion than the Mott-Hubbard insulator that is the undoped UO_2 sample.

Comparing this to the open circuit potential measurement of Figure 7-2b, which shows the results of coupling each of the three samples with the 20/25/Nb stainless steel cladding, we can see that the rest potential of the undoped UO_2 sample has been lowered by coupling with the stainless steel cladding from – 10 mV_{SCE} to – 60 mV_{SCE}. Likewise, the low doped 25 GWd/tU SIMFUEL sample also reaches a lower rest potential when coupled with the stainless steel cladding, from the uncoupled rest potential of 80 mV_{SCE} to 60 mV_{SCE}. With regards to the high doped 43 GWd/tU SIMFUEL, an even greater effect was seen when the SIMFUEL was coupled with the stainless steel cladding, as the rest potential was lowered from 80 mV_{SCE} in the uncoupled scenario, to 5 mV_{SCE} in the coupled scenario. This indicates that the stainless steel cladding is in fact protecting the undoped UO_2 and SIMFUEL samples against oxidation under open circuit conditions, which is especially true for the 43 GWd/tU SIMFUEL sample. This point will be explored further in Figure 7-4.

We will now look at the effect that the addition of 10 µmol dm^{-3} H_2O_2 will have on the open circuit potential measurements of our three samples coupled with the stainless steel cladding

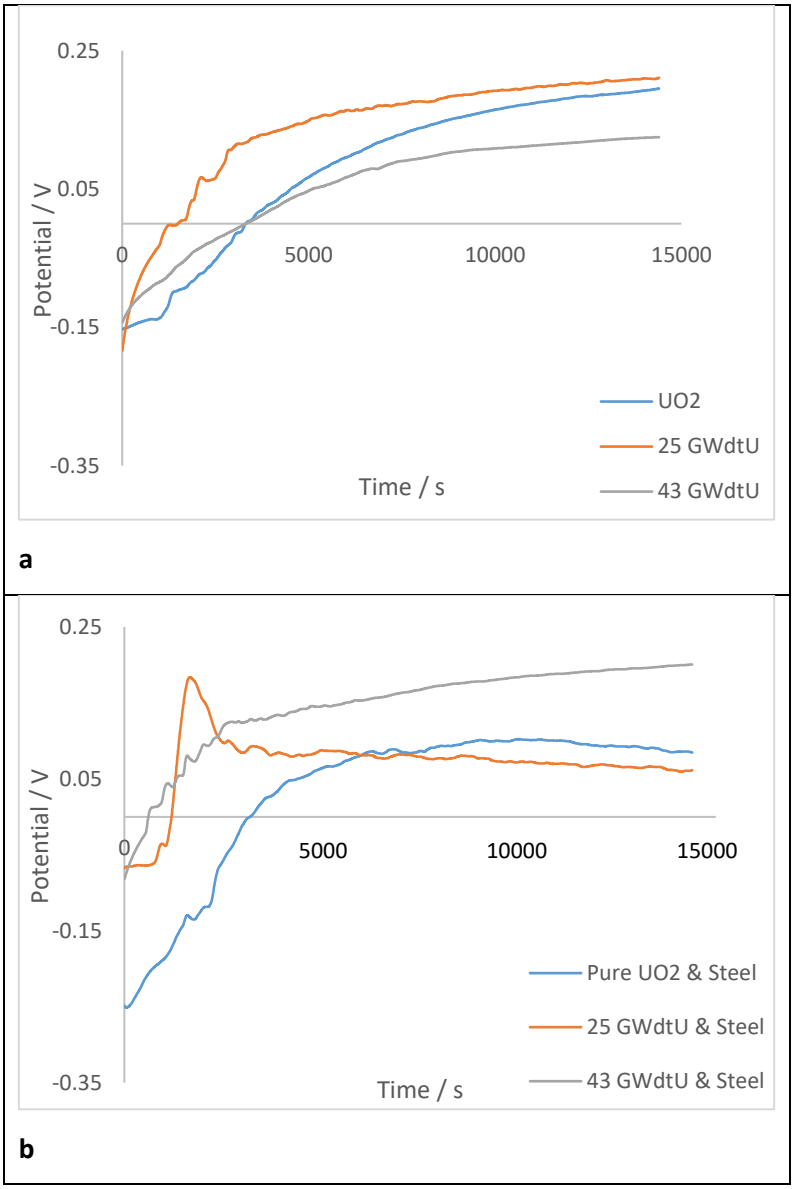

Figure 7-3a and 7-3b – (a) showing the open circuit potential of the UO_2 and 25 & 43 GWd/tU SIMFUEL pellets over a 4 hour period in a 0.1 mol dm^{-3} Na_2SO_4 background electrolyte spiked with 10 µmol dm^{-3} H_2O_2; (b) showing the open circuit potential of the UO_2 and 25 & 43 GWd/tU SIMFUEL pellets coupled with 20/25/Nb steel over a 4 hour period in a 0.1 mol dm^{-3} Na_2SO_4 background electrolyte spiked with 10 µmol dm^{-3} H_2O_2

Looking at Figure 7-3a above we can see that the addition of hydrogen peroxide has shifted the rest potentials of all three samples positive. This is due to the fact that the hydrogen peroxide is placing an oxidative stress on the samples. The coupling with the stainless steel cladding, the results of which are shown in Figure7-3b, shows that with the addition of hydrogen peroxide, similar trends are observed as in Figure 7-2b with the exception of the 43 GWd/tU SIMFUEL. Here we observe the rest potentials of both the undoped UO_2 and the low doped 25 GWd/tU SIMFUEL samples again being lowered upon coupling, from 210 mV to 90 and 60 mV_{SCE}, respectively. The rest potential of the high doped 43 GWd/tU SIMFUEL pellet appears to have been slightly *raised* as a result of coupling; however, the

interpretation of this shift should be considered with caution given that the increase on coupling is small, from 120 to 200 mV_{SCE}. The uncertainty associated with the results from the 43 GWd/tU SIMFUEL sample aside, it appears that, even in the presence of peroxide, the undoped UO_2 and 25 GWd/tU SIMFUEL pellet samples are again being protected by the cladding. This may be due to the fact that the cladding is removing some of the oxidative stress that was imposed on the undoped UO_2 and low doped 25 GWd/tU SIMFUEL samples by the hydrogen peroxide, in effect stabilising the two samples, as would be expected if it were a sacrificial corrosion inhibition effect by the stainless steel cladding. The effect observed with the high doped 43 GWd/tU SIMFUEL sample is too weak to draw any definite conclusions.

To obtain a better understanding of the corrosion behaviour of the 20/25/Nb steel cladding, we will have a look at the linear sweep voltammetry recorded of the cladding in a 0.5 mol dm^{-3} Na_2SO_4 background electrolyte.

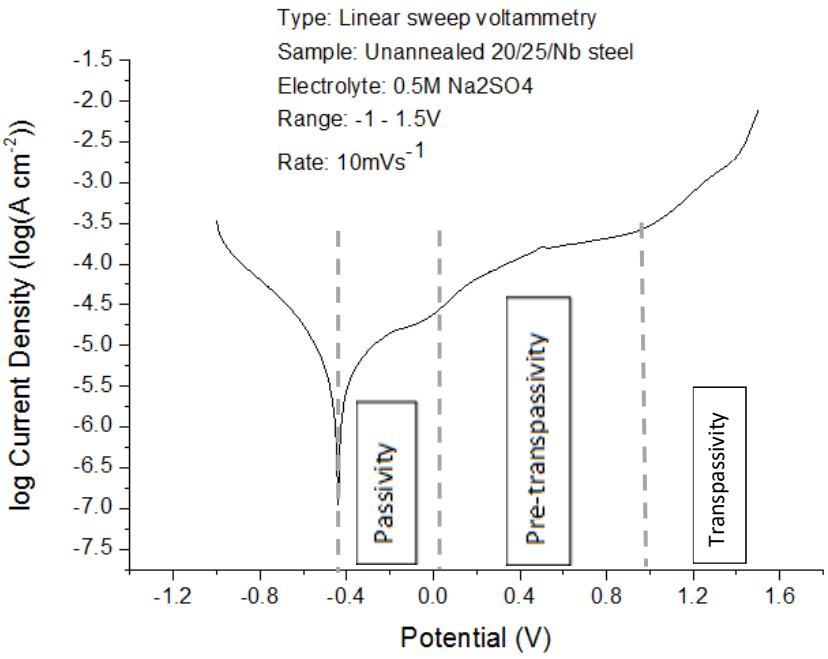

Figure 7-4 showing the linear sweep voltammetry of 20/25/Nb stainless steel cladding in 0.5 mol dm^{-3} Na_2SO_4 background electrolyte, in the absence of H_2O_2 (10)

Looking at Figure 7-4 above, we can see that the region of passivity starts at approximately – 40 mV_{SCE}. This region runs up to a potential of approximately 0 V_{SCE}, at which point the pre-transpassive region starts. This is the point at which the oxide layer begins to break-down as a result of slow oxidation of Cr(III) and its subsequent release as Cr(VI). Concomitantly, intermittent pitting corrosion may occur.

As the potential increases further to approximately 1 V_{SCE}, dissolution of the passive layer takes place and we move into the transpassive region.

As evidenced by Figure 7-4, which shows that from 0 V_{SCE} onwards, the break-down of the oxide layer occurs, with pitting also likely to occur, we can conclude that the cladding is in fact sacrificially protecting the SIMFUEL and the undoped UO_2 pellets.

In order to further assess the oxidative dissolution of our samples, we will compare the measured rest potentials from the OCPs of our samples, with the corresponding cyclic voltammograms measured in sodium sulfate background electrolyte.

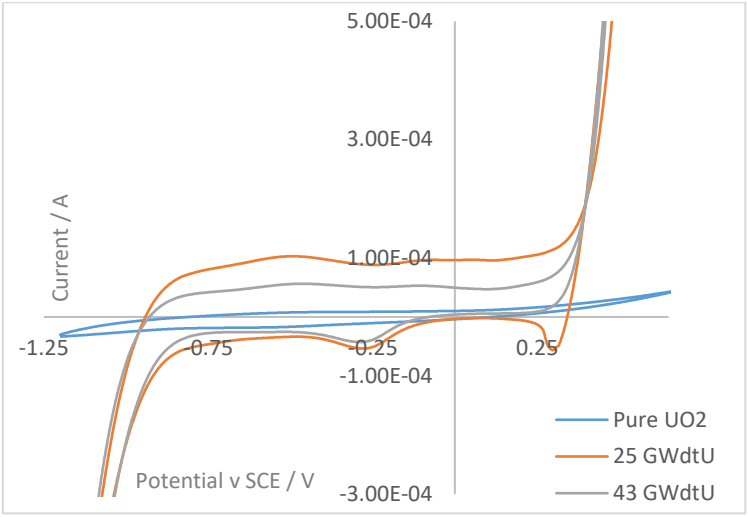

Figure 7-5 showing the cyclic voltammograms of UO_2, 25 & 43 GWd/tU SIMFUEL pellets in a 0.1 mol dm^{-3} Na_2SO_4 background electrolyte, cycled at a potential range of (-) 1.2 to (+) 0.7 V, at a scan rate of 10 mV/s

Looking at the rest potentials measured for the undoped UO_2 with and without the stainless steel cladding, we observed that the rest potential was lowered from – 10 mV_{SCE} in the absence of cladding to - 60 mV_{SCE} in its presence. From this we can conclude that the UO_2 is being cathodically protected by the cladding. Referring to the cyclic voltammogram above in Figure 7-5 however, we can see that the undoped UO_2 pellet, being a Mott-Hubbard insulator (11), is electrochemically unreactive and so, no corrosion is expected to take place in either the absence or presence of cladding in any case.

In the cyclic voltammogram above (Figure 7-5), we can see that the region where the low doped 25 GWd/tU SIMFUEL sample coupled with the stainless steel cladding came to rest in the OCP measurement (Figure 7-2b), namely 60 mV_{SCE}, is where oxidation of UO_2 to UO_{2+x} in grains occurs. A

low level of oxidation is expected to take place here in accordance with the rest potential we have measured during the OCP experiment. Referring back to the uncoupled OCP measurement in Figure 7-2a, the measured rest potential was 80 mV_{SCE}, which also lies in the region where the above mentioned oxidation will take place. The coupling however is inhibiting oxidation, meaning that a lower level of in-grain oxidation will take place in the case of coupling.

Turning our attention to the OCP measurement of our high doped 43 GWd/tU SIMFUEL sample coupled with the stainless steel cladding, we observed in going from Figure 7-2a (absence of cladding) to Figure 7-2b (presence of cladding), that the rest potential had been lowered significantly, to 5 mV_{SCE}. Referring back to our cyclic voltammogram above in Figure 7-5, at 5 mV_{SCE} we are still in the region where oxidation of UO_2 to UO_{2+x} in grains takes place. At this low potential however, an even lower degree of oxidation in comparison with the 25 GWd/tU SIMFUEL/cladding couple is expected to take place, again confirming that the 43 GWd/tU SIMFUEL sample is sacrificially being protected by the stainless steel cladding at a higher degree than the 25 GWd/tU SIMFUEL sample. This is also confirmed by the fact that the rest potential measured for the uncoupled 43 GWd/tU SIMFUEL sample in Figure 7-2a, which was 80 mV_{SCE}. Here, whilst we can see that this is still in the region where in-grain oxidation of UO_2 to UO_{2+x} would occur, the coupling has greatly supressed this oxidation, so much so that only a low level in-grain oxidation is expected to take place.

Focussing on the open circuit potentials measured in the presence of hydrogen peroxide, we observed in Figure 7-3b, that the rest potential measured for the undoped UO_2 sample spiked with H_2O_2, was lowered from 210 mV_{SCE} to 90 mV_{SCE} when coupled with the stainless steel cladding. Correlating this to our cyclic volatmmogram of Figure 7-5, we can see that the undoped UO_2 pellet remains electrochemically inactive. So even though the cladding is protecting the undoped UO_2 by lowering its rest potential in the presence of H_2O_2, there is no corrosion expected to take place on the pellet in either the absence or presence of the cladding.

Moving back to the open circuit potential of our low doped 25 GWd/tU SIMFUEL sample measured in the presence of H_2O_2 (Figure 7-3a & b), we observed once again that the rest potential measured in the absence of the cladding, namely 210 mV_{SCE}, was lowered to 60 mV_{SCE} in the presence of the cladding. Correlating these figures back to the cyclic voltammogram of Figure 7-5, we can see that the uncoupled rest potential of 210 mV_{SCE} lies in the region where UO_2 to UO_{2+x} oxidation in the grains takes place. Looking at the rest potential of the coupled SIMFUEL sample, we can see that it has been lowered to be in a region where only a low level of UO_2 to UO_{2+x} oxidation in the grains is expected to

take place, and therefore the cladding is protecting the SIMFUEL from a higher degree of in-grain oxidation taking place – as would be the case in the uncoupled scenario.

Finally, looking at the open circuit potential measured for the high doped 43 GWd/tU SIMFUEL sample in the presence of hydrogen peroxide in Figures 7-3a & b, we observed that the rest potential of the SIMFUEL sample was not lowered when coupled with the stainless steel cladding, as we had observed for the undoped UO_2 and low doped 25 GWd/tU SIMFUEL samples. As aforementioned, the slight increase in the rest potential is too small to be considered with certainty. However, referring the measured rest potentials back to our cyclic voltammogram in Figure 7-5, we can see that both uncoupled and coupled rest potentials, 120 and 200 mV_{SCE} respectively, lie in the region where oxidation of UO_2 to UO_{2+x} in grains would take place i.e. even in the presence of peroxide, the rest potentials observed in both the uncoupled and coupled scenarios are not high enough as to result in the generation of UO_2^{2+}, which would lead to subsequent dissolution.

Turning our attention back to the LSV of the cladding steel itself of Figure 7-4, we can conclude the following:

- In the case of the undoped UO_2 coupled with the stainless steel cladding, the measured rest potential from the open circuit potential (- 60 mV_{SCE}) lies in the passive region. This is the region where passive film growth will occur on the surface of the stainless steel cladding, which means that the cladding is protecting the undoped UO_2 from oxidation at the expense of a general, uniform corrosion/passive film growth across the steel surface. In the case of the undoped UO_2 coupled with the stainless steel cladding where the measured rest potential in the presence of H_2O_2 was 90 mV_{SCE}, we can see that this potential lies where pre-transpassivity begins. This is the point at which the oxide layer begins to break-down as a result of slow oxidation of Cr(III) and its subsequent release as Cr(VI), and where intermittent pitting corrosion may also occur. The undoped UO_2 sample is still being protected by the cladding.
- In the case of the low doped 25 GWdt/tU SIMFUEL sample coupled with the stainless steel cladding, the measured rest potential from the open circuit potential (60 mV_{SCE}) lies at the start of the pre-transpassive region. Here, break-down of the oxide film with some pitting will occur, and the SIMFUEL is sacrificially being protected by the cladding. In the case of the 25 GWd/tU SIMFUEL pellet coupled with the stainless steel cladding where the measured rest potential in the presence of H_2O_2 was also 60 mV_{SCE}, we can expect the same to occur.
- In the case of the high doped 43 GWdt/tU SIMFUEL sample coupled with the stainless steel cladding, the measured rest potential from the open circuit potential (5 mV_{SCE}) lies also at the

start of the pre-transpassive region where the break-down of the oxide film with some pitting will occur, and the SIMFUEL is sacrificially being protected by the cladding. In the case of the 43 GWd/tU SIMFUEL pellet coupled with the stainless steel cladding where the measured rest potential in the presence of H_2O_2 was 200 mV_{SCE}, we can expect the same to occur, possibly to a higher extent.

Now that we have investigated the effects of coupling in standard electrolyte in the absence of a corrosion inhibitor, we will proceed to look at the same set of experiments carried out in the modified simplified groundwater simulant. As this has a corrosion inhibiting pH of 8.2, this then also allows us to study the effect of the presence of a corrosion inhibitor on the dissolution behaviour of the SIMFUELs.

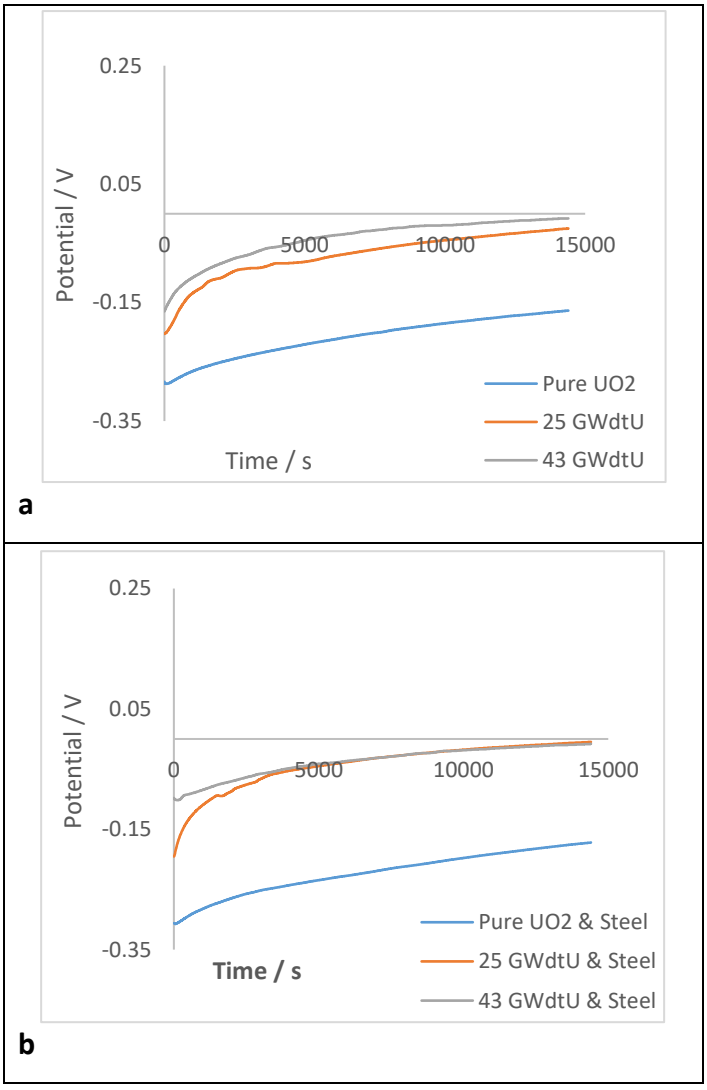

Figure 7-6a and 7-6b – (a) showing the open circuit potential of the UO_2 and 25 & 43 GWd/tU SIMFUEL pellets over a 4 hour period in a modified simplified groundwater simulant; (b) showing the open circuit potential of the UO_2 and 25 & 43 GWd/tU SIMFUEL pellets coupled with 20/25/Nb steel over a 4 hour period in a modified simplified groundwater simulant, both at pH 8.2

Figure 7-6a shows that the open circuit potential measurements taken of the three samples are shifted more negative in a modified simplified groundwater simulant, when compared to the background electrolyte in Figure 7-2a. This is due to the higher solution pH of the modified simplified groundwater simulant, as described in Chapter 5.

When comparing the measured rest potentials of the OCPs from Figure 7-6a in the absence of cladding, to Figure 7-6b in the presence of cladding, we can see that for the undoped UO_2 sample, the cladding has slightly lowered the undoped UO_2 sample's rest potential from – 160 mV_{SCE} to – 170 mV_{SCE}. It is tempting to say that this indicates that the cladding is protecting the undoped UO_2. Likewise for the low and high doped SIMFUELs samples, we can also see that the rest potentials measured in the absence of cladding have again be slightly lowered by the presence of the cladding, namely from – 7.9 mV_{SCE} to – 8.5 mV_{SCE} in the absence and presence of the stainless steel cladding, respectively. Again, it is tempting to say that that this would again indicate that our SIMFUEL samples are also being protected by the coupling of said samples with the cladding. However, all of the potential shifts observed here are too small to draw such a conclusion with certainty. What may be stated with certainty though is

(i) that the rest potentials recorded in the modified simplified groundwater are lower for all samples than those recorded in the sulfate electrolyte, confirming the corrosion inhibiting effect of the pH of the former compared to that of the latter; and

(ii) that the coupling with the cladding produces a significantly smaller corrosion inhibition effect in the presence of an extant corrosion inhibitor (as in the modified simplified groundwater) than in its absence (as in the sodium sulfate electrolyte).

These two observations then suggest that, in the modified simplified groundwater, the corrosion inhibiting effect of the base dominates over the corrosion inhibiting effect of coupling to cladding. We shall return to this point below.

We will now have a look at the effect that the addition of hydrogen peroxide has on the coupled system in terms of an open circuit potential measurement.

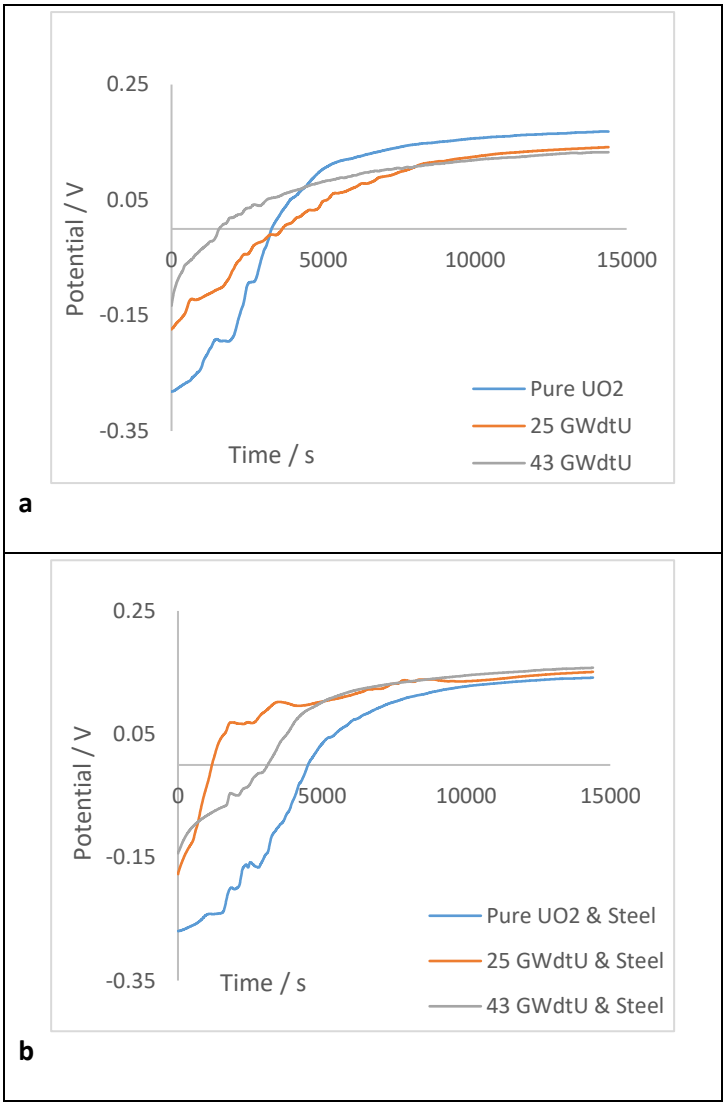

Figure 7-7a and 7-7b – (a) showing the open circuit potential of the UO_2 and 25 & 43 GWd/tU SIMFUEL pellets over a 4 hour period in a modified simplified groundwater simulant, spiked with 10 µmol dm^{-3} H_2O_2; (b) showing the open circuit potential of the UO_2 and 25 & 43 GWd/tU SIMFUEL pellets coupled with 20/25/Nb steel over a 4 hour period in a modified simplified groundwater simulant, spiked with 10 µmol dm^{-3} H_2O_2

By looking at Figure 7-7a above, we can immediately see that the addition of a 10 µmol dm^{-3} H_2O_2 spike has shifted the rest potentials of all of our three samples more positive, when compared with the rest potentials observed in Figure 7-6a in the absence of hydrogen peroxide. This is once again due to the oxidative stress placed on the three samples by the added H_2O_2. By comparing the rest potentials measured for our three samples in the presence of H_2O_2, with and without cladding, we can see that the rest potential measured for the undoped UO_2 sample was slightly lowered with the cladding, measuring 170 mV_{SCE} in the absence of the cladding in Figure 7-7a, to measuring 16 mV_{SCE} in the presence of cladding in Figure 7-7b. For the low and high doped 25 & 43 GWd/tU SIMFUEL samples, we observed that the measured rest potentials exhibited a small rise from 13 mV_{SCE} in the

absence of cladding (Figure 7-7a), to 160 mV_{SCE} in the presence of cladding (Figure 7-7b). However, as in the case of the UO_2 sample immediately above, these changes are too small to draw any definite conclusions and are tiny compared to the differences in rest potential observed from like-for-like samples in the absence and presence of a solution phase corrosion inhibitor i.e. in the sodium sulfate electrolyte and the modified simplified groundwater, respectively. This again suggests that, even in the presence of peroxide, the corrosion inhibiting effect of the base dominates over the corrosion inhibiting effect of coupling to cladding in the modified simplified groundwater.

We well now look at the linear sweep voltammetry of the 20/25/ Nb stainless steel cladding in a modified simplified groundwater simulant to determine where the onset of corrosion is.

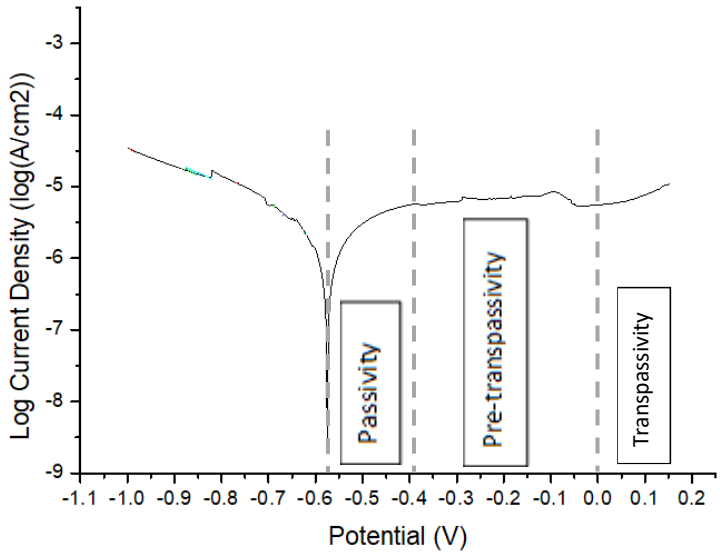

Figure 7-8 showing the linear sweep voltammetry of 20/25/Nb stainless steel cladding in modified simplified groundwater simulant, in the absence of H_2O_2 (10)

Looking at Figure 7-8 above, we can see that the region of passivity starts at approximately – 575 mV_{SCE}. This region runs up to a potential of approximately – 400 mV_{SCE}, at which point the pre-transpassive region starts. This is the point, as aforementioned, at which the oxide layer begins to break-down as a result of slow oxidation of Cr(III) and its subsequent release as Cr(VI). Simultaneously, intermittent pitting corrosion may also occur. As the potential increases further to approximately 0 V_{SCE}, dissolution of the passive layer takes place and we move into the transpassive region.

By comparing the LSV recorded in a modified simplified groundwater simulant (Figure 7-8), to the LSV recorded in sodium sulfate background electrolyte (Figure 7-4), we can see that the corrosion potentials are more negative than what we observed in the sodium sulfate background electrolyte. This is to be expected due to the aforementioned elevated solution pH of the modified simplified groundwater simulant.

In order to further assess the oxidative dissolution of our samples, we will once again compare the measured rest potentials from the OCPs of our samples, with the corresponding cyclic voltammograms measured in modified simplified groundwater simulant.

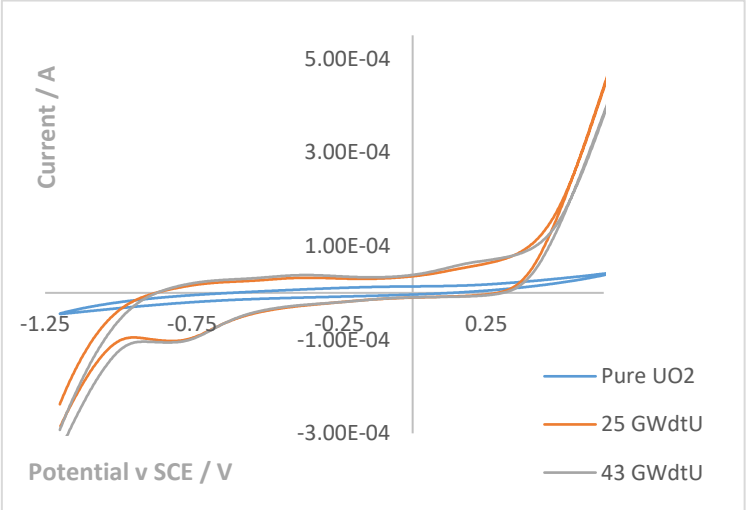

Figure 7-9 showing the cyclic voltammograms of UO_2, 25 & 43 GWd/tU SIMFUEL pellets in a modified simplified groundwater simulant, cycled at a potential range of (-) 1.2 to (+) 0.7 V, at a scan rate of 10 mV/s

Looking at the rest potentials measured for the undoped UO_2 with and without the stainless steel cladding in the absence of peroxide, we observed that the rest potential had been slightly lowered, from – 160 mV_{SCE} in the absence of cladding, to - 170 mV_{SCE} in its presence - although in practice these are nearly the same due to the corrosion inhibiting effect of the basicity of this groundwater dominating over corrosion inhibiting effect of coupling to cladding. Referring to the cyclic voltammogram above in Figure 7-9 however, we can see that the undoped UO_2 pellet, being a Mott-Hubbard insulator (11), is electrochemically unreactive and so, no corrosion is expected to take place in either the absence or presence of cladding in any case.

For the low and high doped 25 and 43 GWd/tU SIMFUEL pellets in the absence of peroxide, we observed that the rest potential measured in the absence of the cladding were only slightly changed

in the presence of the cladding, shifting from – 7.9 mV_{SCE} to – 8.5 mV_{SCE} and from – 7.9 mV_{SCE} to – 8.5 mV_{SCE} respectively – although, again, in practice are nearly the same due to the corrosion inhibiting effect of the basicity of this groundwater dominating over corrosion inhibiting effect of coupling to cladding. Referring to the cyclic voltammogram in Figure 7-9 above, we can see that all of these potentials lie in the region where the oxidation of UO_{2+x} sites at grain boundaries takes place i.e. the rest potentials observed in both the uncoupled and coupled scenarios are not high enough as to result in the generation of U(VI), which would lead to subsequent dissolution. Comparing this to the rest potentials we had observed recorded in the sodium sulfate background electrolyte, we can see that the modified simplified groundwater simulant has shifted the rest potentials more negative, meaning that only some oxidation at grain boundaries takes place in this scenario, as opposed to the in-grain oxidation we has observed in the sodium sulfate background electrolyte. As mentioned above, this is most likely due to the higher solution pH of the modified simplified groundwater simulant having a corrosion inhibiting effect.

Turning our attention to the open circuit potentials measured in the presence of hydrogen peroxide, we observed that the measured rest potential of the undoped UO_2 was again only slightly lowered from 170 mV_{SCE} in the absence of the clad (Figure 7-7a), to 160 mV_{SCE} in the presence of the cladding material (Figure 7-7b). Referring back to our cyclic voltammogram in Figure 7-9 however, we can see that the undoped UO_2 pellet remains electrochemically inactive, so no corrosion is expected to take place.

Moving on to the rest potentials measured for the low and high doped 25 and 43 GWd/tU SIMFUEL sample in the presence of H_2O_2, we observed from both that rest potential increases from 130 mV_{SCE} in the absence of the cladding (Figure 7-7a) to 160 mV_{SCE} in the presence of the cladding (Figure 7-7b). However, as in the case of the UO_2 sample immediately above, these changes are too small to draw any definite conclusions and, as in the absence of peroxide, they are in practice nearly the same due to the corrosion inhibiting effect of the basicity of this groundwater dominating over corrosion inhibiting effect of coupling to cladding.

Referring back to our cyclic voltammograms in Figure 7-9, we can see that for both SIMFUEL samples, both rest potentials lie in the region where the oxidation of UO_{2+x} at the grain boundaries takes place, with the coupled rest potential of 160 mV_{SCE} undergoing a slightly higher level of oxidation of UO_{2+x}. Whilst in this scenario the coupled rest potentials of the two SIMFUELs have indeed been raised, only

oxidation of UO_{2+x} at the grain boundaries, and no oxidation of UO_2 to UO_{2+x} in the grains, will take place.

Turning our attention back to the LSV of the cladding steel itself of Figure 7-8, we can conclude the following:

- In the case of the undoped UO_2 coupled with the stainless steel cladding, the measured rest potential from the open circuit potential (- 170 mV_{SCE}) lies in the pre-transpassive region. This is the point at which the oxide layer begins to break-down as a result of slow oxidation of Cr(III) and its subsequent release as Cr(VI), and where intermittent pitting corrosion may also occur. In the case of the undoped UO_2 coupled with the stainless steel cladding where the measured rest potential in the presence of H_2O_2 was 160 mV_{SCE}, we can see that this potential lies where transpassivity begins. This is where dissolution of the passive layer begins.
- In the case of the low doped 25 GWdt/tU SIMFUEL sample coupled with the stainless steel cladding, the measured rest potential from the open circuit potential (- 8.5 mV_{SCE}) lies also in the pre-transpassive region. This, as aforementioned, is the point at which the oxide layer begins to break-down as a result of slow oxidation of Cr(III) and its subsequent release as Cr(VI), and where intermittent pitting corrosion may also occur. In the case of the 25 GWd/tU SIMFUEL pellet coupled with the stainless steel cladding where the measured rest potential in the presence of H_2O_2 was 160 mV_{SCE}, we are in the region of transpassivity where the dissolution of the passive layer begins.
- In the case of the high doped 43 GWdt/tU SIMFUEL sample coupled with the stainless steel cladding, the measured rest potential from the open circuit potential (- 8.5 mV_{SCE}) lies also in the pre-transpassive region where the oxide layer begins to break-down. In the case of the 43 GWd/tU SIMFUEL pellet coupled with the stainless steel cladding where the measured rest potential in the presence of H_2O_2 was 160 mV_{SCE}, we are in the region of transpassivity where the dissolution of the passive layer begins.

Comparing the above observations to those seen in the sodium sulfate background electrolyte, we can see that the onset of the passive regime observed measured in the LSVs for the cladding is more negative in the modified simplified groundwater simulant than in the sodium sulfate background electrolyte. Likewise, the onset of the transpassive region observed in the modified simplified groundwater is also more negative when compared to the background electrolyte. This indicates that, despite the low level of chloride present in the modified simplified groundwater simulant, the presence of the base therein is still having the net effect of inhibiting the corrosion of the clad (9).

Now that we have investigated the behaviour of our three samples coupled with the 20/25/Nb stainless steel cladding in a 0.1 mol dm^{-3} Na_2SO_4 background electrolyte and a modified simplified groundwater simulant in the presence and absence of 10 µmol dm^{-3} H_2O_2, let us investigate how the coupled samples will behave in the presence of the evaporite groundwater simulant. As this has a corrosion inhibiting pH of 7.1, this then also allows us to again study the effect of the presence of a corrosion inhibitor on the dissolution behaviour of the SIMFUELs. However, evaporite also contains a very high concentration of chloride, 4.76 mol dm^{-3}. Chloride is a known corrosion accelerator on steels, and at this concentration would be expected to dominate over any corrosion inhibiting effect associated with the groundwater's weak basicity. Thus, study of the behaviour of the SIMFUELs in evaporite groundwater also allows us to study their behaviour in the presence of a steel corrosion accelerator.

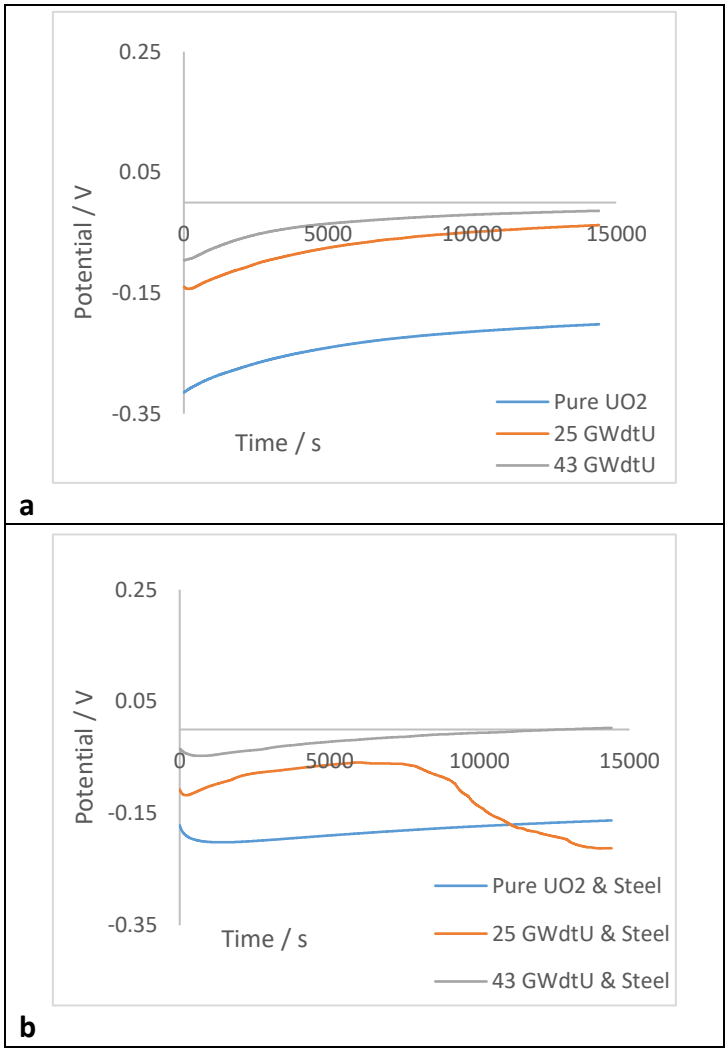

Figure 7-10a and 7-10b – (a) showing the open circuit potential of the UO_2 and 25 & 43 GWd/tU SIMFUEL pellets over a 4 hour period in an evaporite groundwater simulant; (b) showing the open circuit potential of the UO_2 and 25 & 43 GWd/tU SIMFUEL pellets coupled with 20/25/Nb steel over a 4 hour period in an evaporite groundwater simulant, both at pH 7.1

Looking at Figures 7-10a &b above, we can see that in the case of the undoped UO_2, the coupling has slightly raised its measured rest potential from – 200 mV_{SCE} to – 160 mV_{SCE}. The low doped 25 GWd/tU SIMFUEL sample has had its rest potential lowered in the presence of the stainless steel cladding, namely from – 14 mV_{SCE} to – 210 mV_{SCE}. The high doped 43 GWd/tU SIMFUEL sample however, is having its rest potential slightly raised in going from the absence of cladding to the presence of cladding, - 14 mV_{SCE} to 3 mV_{SCE}, respectively. Interestingly for the low doped 25 GWd/tU SIMFUEL, we can see in Figure 7-10b, that the potential trace behaves in the same way that it does in the absence of the clad in Figure 7-10a, up to a potential of – 70 mV_{SCE}, at which point the potential suddenly drops, and continues to decrease until it reaches its rest potential of – 210 mV_{SCE}. We shall return to this point later on.

However, at this point we can conclude:

(i) that the rest potentials recorded in the evaporite groundwater simulant are lower for all samples than those recorded in the sulfate electrolyte (as was the case of the modified simplified groundwater simulant), confirming the corrosion inhibiting effect of the pH of the former compared to that of the latter, and

(ii) that the coupling with the cladding produces a significantly smaller, or no, corrosion inhibition effect in the presence of an extant corrosion inhibitor, as in the evaporite groundwater simulant (and also as we observed in the modified simplified groundwater simulant), than in its absence – as in the sodium sulfate electrolyte.

As seen in the modified simplified groundwater simulant, these two observations suggest that also in the evaporite groundwater simulant, the corrosion inhibiting effect of the base dominates over the Corrosion inhibiting effect of coupling to cladding.

Having seen the effect that coupling with stainless steel has on our three samples with respect to their corrosion potential in an evaporite groundwater simulant, let us turn our attention to the effect that added hydrogen peroxide will have on the corrosion potentials.

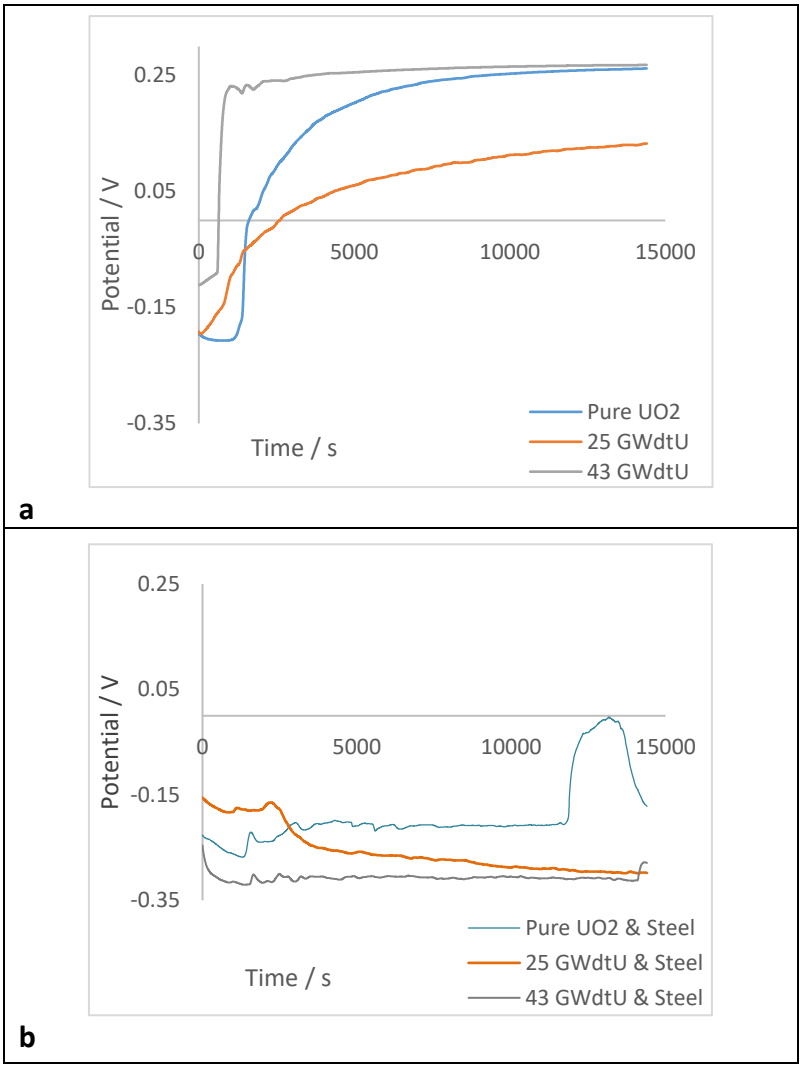

Figure 7-11a and 7-11b – (a) showing the open circuit potential of the UO_2 and 25 & 43 GWd/tU SIMFUEL pellets over a 4 hour period in an evaporite groundwater simulant, spiked with 10 µmol dm^{-3} H_2O_2; (b) showing the open circuit potential of the UO_2 and 25 & 43 GWd/tU SIMFUEL pellets coupled with 20/25/Nb steel over a 4 hour period in an evaporite groundwater simulant, spiked with 10 µmol dm^{-3} H_2O_2

Above in Figure 7-11a we can see that the addition of a 10 µmol dm^{-3} H_2O_2 spike has shifted the rest potentials of all our three samples more positive, when compared to Figure 7-10a in the absence of hydrogen peroxide. This is again, as before mentioned, due to the oxidative stress placed on our samples by H_2O_2 (12). However, the coupling of the undoped UO_2 and the 25 & 43 GWd/tU SIMFUEL samples with the 20/25 Nb stainless steel cladding has significantly lowered the rest potentials of all three samples during the open circuit potential measurements. This means that the stainless steel cladding is protecting all three samples by lowering their corrosion potentials in the presence of H_2O_2.

More precisely, the undoped UO_2 has its rest potential lowered from 270 mV_{SCE} to – 170 mV_{SCE} in the absence and presence of the stainless steel cladding, respectively. In the case of the low doped 25

GWd/tU SIMFUEL sample, we can see that the measured rest potential has been shifted negative from 130 mV_{SCE} to – 310 mV_{SCE} in the absence and presence of the clad, respectively. Finally, in the case of the high doped 43 GWd/tU SIMFUEL sample, the biggest effect is seen, where the rest potential has been lowered from 270 mV_{SCE} in the absence of the cladding, to – 280 mV_{SCE} in the presence of the cladding.

These observations indicate that in the presence of hydrogen peroxide, any corrosion inhibition afforded by the base is overcome, and that the stainless steel cladding is able to corrode freely, offering maximum protection through sacrificial corrosion to the three UO_2/SIMFUEL samples.

We will now look at the linear sweep voltammetry of the 20/25/ Nb stainless steel cladding in an evaporite groundwater simulant to determine where the onset of corrosion for the cladding is.

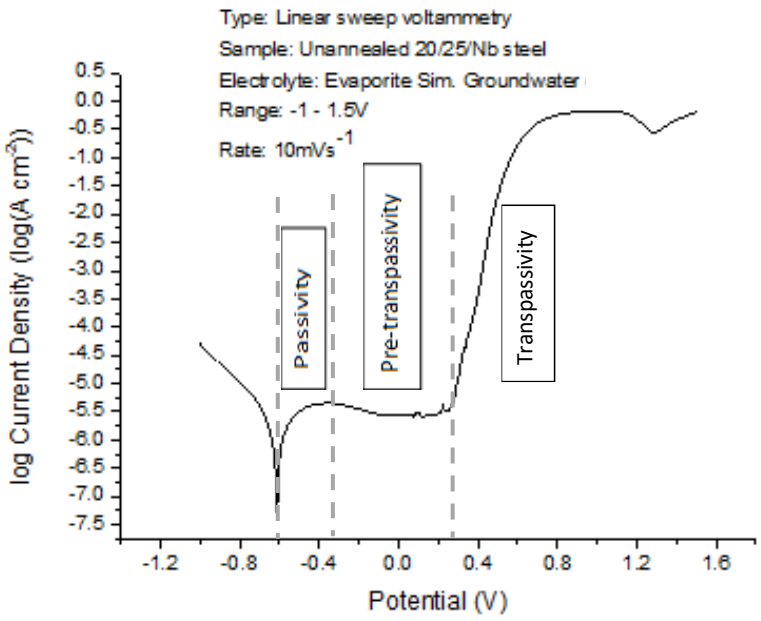

Figure 7-12 showing the linear sweep voltamogram of 20/25/Nb stainless steel cladding in evaporite groundwater simulant, in the presence and absence of 10 µmol dm^{-3} H_2O_2 (2)

Looking at Figure 7-12 above, we can see that the region of passivity starts at approximately – 600 mV_{SCE}. This region runs up to a potential of approximately - 350 mV_{SCE}, at which point the pre-transpassive region starts. This is the point, as described above, at which the oxide layer begins to break-down as a result of slow oxidation of Cr(III) and its subsequent release as Cr(VI). At the same time, intermittent pitting corrosion may also occur. As the potential increases further to

approximately 250 mV_{SCE}, dissolution of the passive layer takes place and we move into the transpassive region.

In order to further assess the oxidative dissolution of our samples, we will once again compare the measured rest potentials from the OCPs of our samples, with the corresponding cyclic voltammograms measured in evaporite groundwater simulant.

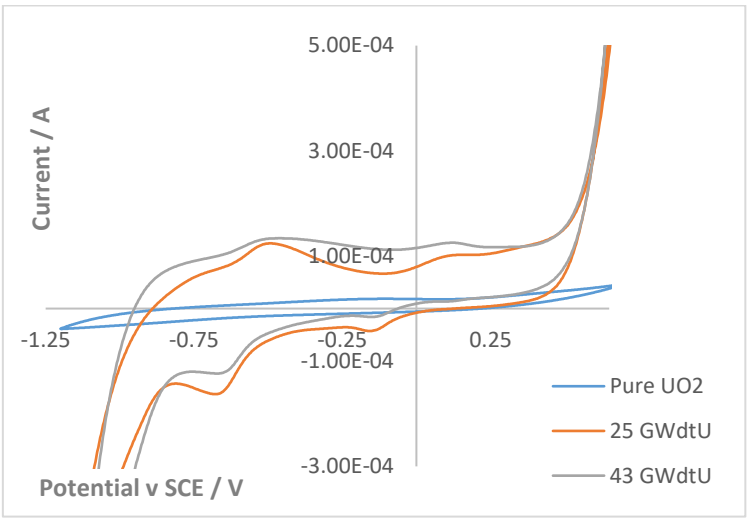

Figure 7-13 showing the cyclic voltammograms of UO_2, 25 & 43 GWd/tU SIMFUEL pellets in an evaporite groundwater simulant, cycled at a potential range of (-) 1.2 to (+) 0.7 V, at a scan rate of 10 mV/s

Referring back to the rest potentials measured for the undoped UO_2 with and without the stainless steel cladding, we observed that the rest potential had been raised, from – 200 mV_{SCE} in the absence of cladding, to - 160 mV_{SCE} in its presence. From this it would appear that the undoped UO_2 was not being protected by the stainless steel cladding Referring to the cyclic voltammogram above in Figure 7-13 however, we can see that the undoped UO_2 pellet, being a Mott-Hubbard insulator (11), is electrochemically unreactive and so, no corrosion is expected to take place in either the absence or presence of cladding.

Looking back at the rest potentials measured for the low doped 25 GWd/tU SIMFUEL sample in the absence and presence of the cladding, we observed that the rest potentials were lowered from – 14 mV_{SCE} to – 210 mV_{SCE} in the presence of the cladding. Referring back to the cyclic voltammogram in Figure 7-13 above, we can see that both these rest potentials lie in the region where the oxidation of UO_{2+x} at the grain boundaries takes place. The lowering of the rest potential achieved by the coupling with the cladding lowers the degree of UO_{2+x} oxidation at the grain boundaries taking place.

Turning our attention to the high doped 43 GWd/tU SIMFUEL sample, we observed that the measured rest potential in the absence of the cladding, namely – 14 mV_{SCE}, had been raised to 3 mV_{SCE} in the presence of the cladding. Referring to the cyclic voltammogram in Figure 7-13 above, we can see that the rest potential measured in the absence of the cladding lies in the region where the oxidation of UO_{2+x} at the grain boundaries would take place. Likewise, the rest potential measured in the presence of the cladding also lies in the region where the oxidation of UO_{2+x} at the grain boundaries takes place. From this we can conclude that, whilst the rest potential for the 43GWd/tU SIMFUEL coupled with cladding is being raised, only the oxidation at the boundaries is expected to take place, with no oxidation of the grains taking place.

Turning our attention to the open circuit potentials measured in the presence of hydrogen peroxide, we observed that the measured rest potential of the undoped UO_2 was lowered from 270 mV_{SCE} in the absence of the clad (Figure 7-11a), to - 170 mV_{SCE} in the presence of the cladding material (Figure 7-11b). Referring back to our cyclic voltammogram in Figure 7-13 however, we can see that the undoped UO_2 pellet remains electrochemically inactive, so no corrosion is expected to take place.

Moving on to the rest potentials of the low doped 25 GWd/tU SIMFUEL sample measured in the presence of H_2O_2, we observed that in the absence of the cladding the measured rest potential of 130 mV_{SCE} was lowered to – 310 mV_{SCE}. Correlating these figures back to our cyclic voltammogram above in Figure 7-13, we can see that both rest potentials lie in the region where the oxidation of UO_{2+x} at grain boundaries takes place. The uncoupled rest potential however, lies closer to the region where the oxidation of UO_2 to UO_{2+x} in the grains takes place, so the coupling of the SIMFUEL lower its rest potential in to a region where a lower level of grain boundary oxidation of UO_{2+x} takes place.

Looking at the rest potentials measured for the high doped 43 GWd/tU SIMFUEL sample in the presence of hydrogen peroxide, we observed that the uncoupled rest potential of 270 mV_{SCE} had been lowered to the coupled rest potential of – 280 mV_{SCE}. Looking at the cyclic voltammogram of Figure 7-13, we can see that the region where the uncoupled rest potential was measured lies in the region where oxidation in the grains from UO_2 to UO_{2+x} takes places. By the process of coupling, we are lowering the measured rest potential to a region where the only the oxidation of UO_{2+x} at the boundaries takes place.

Turning our attention back to the LSV of the cladding steel itself of Figure 7-12, we can conclude the following:

- In the case of the undoped UO_2 coupled with the stainless steel cladding, the measured rest potential from the open circuit potential (- 160 mV_{SCE}) lies in the pre-transpassive region. This is where the oxide layer begins to break-down intermittently and pitting is likely to occur. In the case of the undoped UO_2 coupled with the stainless steel cladding where the measured rest potential in the presence of H_2O_2 was - 170 mV_{SCE}, we can see that this potential also lies in the pre-transpassive region. The same as above is expected to happen here.
- In the case of the low doped 25 GWdt/tU SIMFUEL sample coupled with the stainless steel cladding, the measured rest potential from the open circuit potential (- 210 mV_{SCE}) lies in the-pre-transpassive region. Here, as aforementioned, is the region where the oxide layer begins to break-down intermittently and pitting is likely to occur. We also observe the potential increasing until - 70 mV_{SCE}, at which point it starts to drop until the rest potential of – 210 mV_{SCE} is reached. This shows evidence of the fact that the potential was headed towards the transpassive region, meaning that it likely underwent pitting, before the cladding started protecting the fuel, which is why the coupled potential comes to rest a lower potential after the pitting starts to occur. In the case of the 25 GWd/tU SIMFUEL pellet coupled with the stainless steel cladding where the measured rest potential in the presence of H_2O_2 was - 310 mV_{SCE}, we are in the region where passivity starts. This is where a protective oxide layer begins to grow on the surface of the electrode, which means that the cladding is protecting the SIMFUEL from oxidation at the expense of a general, uniform corrosion/passive film growth across the steel surface.
- In the case of the high doped 43 GWdt/tU SIMFUEL sample coupled with the stainless steel cladding, the measured rest potential from the open circuit potential (3 mV_{SCE}) lies also in the pre-transpassive region where breakdown of the oxide film begins. In the case of the 43 GWd/tU SIMFUEL pellet coupled with the stainless steel cladding where the measured rest potential in the presence of H_2O_2 was - 280 mV_{SCE}, we are again in the pre-transpassive region, although the breakdown of the oxide film will take place to a lesser extent when compared to the coupled rest potential in the absence of the hydrogen peroxide, meaning that greater protection of the SIMFUEL is achieved.

From these observations we can see that in the absence of H_2O_2 all three samples are being somewhat protected by the presence of the base, this protection however is only slight when compared to the modified simplified groundwater simulant due to the lower basicity of the evaporite groundwater simluant. In the case of the low doped 25 GWd/tU SIMFUEL sample, we observe the measured potential rising and then suddenly dropping. This is due to the fact that pitting has occurred on the

surface of the stainless steel cladding coupled with the 25 GWd/tU SIMFUEL sample, the initiation of which is presumably facilitated by the high Cl^- concentration present in the evaporite groundwater simulant. The cladding can only protect the sample when it corrodes, which it does sacrificially once pitting occurs. When H_2O_2 is added to the evaporite groundwater simulant, the cladding is able to corrode freely in combination with the presence of the Cl^- ions, meaning that all three samples are sacrificially protected by the cladding.

7.4 Conclusions

In this final chapter of investigating the corrosion behaviour of our undoped UO_2 and low and high doped 25 & 43 GWd/tU SIMFUEL samples, we have also investigated the baseline corrosion behaviour of the 20/25/Nb stainless steel cladding. More specifically, we have investigated the effect that the coupling of the stainless steel cladding with the undoped UO_2 and SIMFUEL samples has in basic background electrolyte, as well as in the modified simplified and evaporite groundwater simulants, in the absence and presence of hydrogen peroxide.

In the case of the undoped UO_2 sample, we found that in simple background electrolyte, coupling did lower the rest potential measured during OCP. The same was true in background electrolyte, where the presence of 10 µmol dm^{-3} hydrogen peroxide and coupling dragged the OCP in a negative direction. In the case of the two simulated groundwaters, we found that coupling had little effect on the rest potential of the undoped UO_2 in the absence of H_2O_2. In contrast, in the presence of H_2O_2, coupling moved the rest potential of the undoped UO_2 in a negative direction in both simulated groundwaters, even more so in the evaporite groundwater simulant.

Looking at the low doped 25 GWd/tU SIMFUEL sample, we observed that in simple background electrolyte in the absence and presence of H_2O_2, coupling with the stainless steel cladding moved the rest potentials measured during OCP in a negative direction. In the case of the simulated groundwaters, we found that for both the modified simplified and evaporite groundwaters, the measured rest potential moved in a negative direction when the SIMFUEL was coupled with the cladding in the absence of H_2O_2. In the presence of H_2O_2, we only found the measured rest potential to be lowered when coupled with the stainless steel cladding in the evaporite groundwater simulant. In the case of the modified simplified groundwater simulant, the measured rest potential was found to be slightly raised when coupled with the cladding, in the presence of H_2O_2.

In the case of the high doped 43 GWd/tU SIMFUEL pellet, coupling in the absence of hydrogen peroxide lowered the measured rest potential in the simple background electrolyte, as well as both simulated groundwaters. In the case of added H_2O_2, we observed that coupling raised the measured rest potential of the coupled SIMFUEL in the background electrolyte, as well as the modified simplified groundwater, however in the evaporite groundwater simulant, we observed that the measured rest potential was lowered in the presence of H_2O_2.

In the sodium background electrolyte, where there are no corrosion inhibitors present, we expect the steel to corrode and sacrificially protect the pellet. This is indeed what we observe for all three samples in the absence of H_2O_2. In the presence of H_2O_2, the same is also observed, except for the high doped 43 GWd/tU SIMFUEL sample. This result is curious and will be the subject of further work.

In the case of the modified simplified groundwater, where there is a corrosion inhibitor present, namely the base due to the elevated solution pH, we expect there to be additional protection for the UO_2 and SIMFUEL samples. This expectation is based on the fact that observations have been made by Whillock *et al.* that the presence of a base acts as corrosion inhibitor in the case of AGR fuel cladding (13). In our study of the modified simplified groundwater we observe that coupling with the cladding does not have much effect on the equilibrium OCPs of the samples, and that they are better protected by the base. This is due to the fact that the stainless steel cladding cannot freely corrode in the presence of the base, as also observed by Howett et al. in their study of 20/25/Nb stainless steel corosion in alkaline media (9). As the steel cannot corrode, it cannot offer any sacrificial protection to the UO_2 and SIMFUELs. It is due to this reason that the rest potentials measured in the presence of the cladding are only slightly lower than those measured in the absence of the clad.

In the presence of hydrogen peroxide, we observe the measured rest potential for the coupled UO_2 in the modified simplified groundwater to only slightly decrease, whilst the measured rest potentials of the two SIMFUELs are slightly raised. This is most probably due to the fact that after the measured rest potentials have been initially raised due to the oxidative stress imposed by the H_2O_2 on the samples, since no corrosion of the steel takes place (due to a corrosion inhibitor being present), there is no protection afforded by the cladding. The protection offered by the base to the UO_2 matrix and the SIMFUELs is not strong, and therefore the already raised rest potentials stay high after coupling too.

In the case of the evaporite groundwater simulant, we have a corrosion inhibitor (the base) and a corrosion accelerator (Cl^- ions) present. Thus we see some protection afforded by the base, but not as much as we observed in the modified simplified groundwater simulant, due to the evaporite groundwater simulant having a lower solution pH. This is in accordance with studies by Whillok *et al.* and Howett, who both observe protection offered to the cladding in highly alkaline media of ~ pH 11 (9) (13). In the absence of H_2O_2, we observe that all three samples are being somewhat protected by the presence of the base. This protection, however, is not especially strong given that the solution pH is only just above 7, which is why the measured rest potentials are slightly raised for the undoped UO_2

and high doped 43 GWd/tU SIMFUEL samples. In the case of the low doped 25 GWd/tU SIMFUEL sample, we observe the measured potential is also raised initially, until it suddenly drops and comes to rest at a lower potential than the one it initially started at. This is due to the fact that a pitting event occurs on the surface of the stainless steel cladding coupled with the 25 GWd/tU SIMFUEL sample. As the cladding can only protect the sample when it can corrode, then, once pitting occurs, the cladding can and does sacrificially protect the SIMFUEL sample. When H_2O_2 is added to the evaporite groundwater simulant, the cladding is able to corrode freely as the H_2O_2 acts in combination with the presence of the Cl^- ions, meaning that all three samples are sacrificially protected by the cladding. Even though there is a low level of Cl^- ions present in the modified simplified groundwater simulant too, the protection afforded by the stainless steel cladding has been switched off by the higher solution pH of the modified simplified groundwater which acts as a corrosion inhibitor. This is why the protection that we see is not as great as with the sodium sulfate background electrolyte or evaporite groundwater simulant.

The greatest protection afforded by the stainless steel cladding however is seen in the above described scenario where the cladding is allowed to freely corrode in the presence of the H_2O_2 and Cl^- ions in the evaporite simulant groundwater. From this we can conclude that the uranium is only protected when cladding can corrode freely.

The findings above are supported by a study conducted by Wodall *et al*. where spent AGR fuel from Windscale was analysed after having spent over 40 years in cans in pond storage (14). It was found that all the cans had been flooded, whereby cans containing cut pins also contained sludge, whilst cans with intact or uncut pins where found to contain no sludge (14). Analysis of the sludge indicated that the sludge was rich in U and Fe, whilst further analysis indicated that the uranium in the sludge only existed as UO_2. This would suggest the presence of uncorroded fuel. The further analysis also revealed that the Fe found in the sludge existed in the form of α/γ-FeOOH – suggesting the presence of corrosion products (14). From these findings, Wodall *et al*. concluded that that UO_2, even when irradiated, appears to resist corrosion with no evidence of U in any other form in the sludge particulates. This means that the fuel is protected either by the solution pH of the pond water, or by sacrificial cladding corrosion (14). These observations are consistent with the findings of our voltammetry studies of SIMFUELs coupled with the fuel cladding and the conclusions drawn from said findings.

References

1. R.C. Ecob, R.C. Lobb, V.L. Kohler. *The formation of G-phase in 20/25 Nb stainless steel AGR fuel cladding alloy and its effect on creep properties.* s.l. : Journal of Materials Science, 1987, Vol. 22. pp. 2867 - 2880.

2. C. Anwyl, C. Boxall, R. Wilbraham, D. Hambley, C. Padovani. *Corrosion of AGR fuel pin steel under conditions relevant to permanent disposal.* s.l. : Procedia Chemistry, 2016, Vol. 21. pp. 247 - 254.

3. Z. Hiezl. *Processing and microstructural characterisation of UO_2-based simulated spent nuclear fuel ceramics for the UK's advanced gas-cooled reactors.* s.l. : Imperial College London, 2015.

4. S. Jiang. *Thermally induced sensitisation of austenistic stainless steel for AGR fuel cladding.* s.l. : University of Birmingham, 2018.

5. E.C. Buck, R.S. Wittman, F.N. Skomurski, K.J. Cantrell, B.K. McNamara, C.Z. Soderquist. *Radiolysis process modelling results for scenarios.* s.l. : Pacific Northwest National Laboratory Report no. PNNL-21554, 2012.

6. ONDRAS/NIRAS Research. *Development and Demonstration (RD&D) plan.* s.l. : NIRAS, 2012.

7. H. Geckeis, T. Stumpf. *KIT Scientific Reports 7559.* s.l. : Institut fuer Nukleare Entsorgung, 2009.

8. M. Kelm, V. Metz, E. Bohnert, E. Janata, C. Bube. *Interaction of hydrogen with radiolysis products in NaCl solution - comparing pulse radiolysis experiments with simulations.* s.l. : Radiation Physics and Chemistry, 2011, Vol. 80. pp. 426-434.

9. E.A. Howett. *The behaviour of spent nuclear fuel in wet interim storage.* s.l. : Lancaster University, Lancaster University, 2019.

10. C. Anwyl, C. Boxall, R. Wilbraham. *Corrosion of AGR fuel pin steel under conditions relevant to permanent disposal.* s.l. : 227th ECS Meeting, 2015.

11. K.N. Kudin, G.E. Scuseria, R.L. Martin. *Hybrid density-functional theory and the insulating gap of UO_2.* s.l. : Physical Review Letters, 2002, Vol. 89. pp. 23 - 26.

12. D.W. McKee. *Catalytic decomposition of hydrogen peroxide by metals and alloys of the platinum group.* s.l. : Journal of Catalysis, 1969, Vol. 14. pp. 335 - 364.

13. G.O.H Whillock, B.J Hands, and T Carey. *Assessed efficacy of sodium hydroxide as a corrosion inhibitor for AGR fuel at elevated temperatures.* s.l. : National Nuclear Laboratory, 2014.

14. S.D. Woodall, M. Hambley, J. Rawcliffe, D. Willey, D. Hambley. *Characterisation of corrosion products from degraded uranium dioxide fuel.* s.l. : Journal of Nuclear Materials, 2021, Vol. 552.

Chapter 8 Surface Alteration Influenced by Actinides

8.1 Introduction

In the previous chapter, our focus shifted from the corrosion behaviour of our fabricated SIMFUELs to the effect that the presence of the 20/25/Nb stainless steel cladding would have on the corrosion behaviour of our SIMFUELs. Steels however, are ubiquitous across the fuel cycle with one major application being their use as the fabric of process pipework and vessels in reprocessing plants. This chapter therefore focuses on the behaviour of the commonly used process steels in reprocessing scenarios. In this, rather than using non-radioactive simulants as in previous chapters, we will study the corrosion behaviour of the steels in question in the presence of a real alpha emitting transuranic – specifically, americium.

As stated above, steels are ubiquitous across the nuclear fuel cycle with experimental studies of actinide/steel interactions usually focussing on the interactions of non-active actinide analogues with steels or real actinides with FeOOH surfaces as steel surrogates. There are comparatively few fundamental experimental studies of the interaction of actinide species with real process steels (1).

An exception is a recent study by Kadar *et al* on Pu and Cm adsorption onto the passivating oxide layer formed on stainless steel surfaces, highlighting the importance of the nature of the studied nuclide and the structure/composition of the oxide layer in the mechanism of sorption (2). Studies of the sorption behaviour of americium on steel surfaces or their components are rarer still. A recent review by the Savannah River Site highlights only two papers in this area, reporting the adsorption of Am(III) at hematite and ferrihydrite surfaces as corroding carbon steel substitutes (3).

Thus, there is a paucity of experimental data relating to the interaction of Am with steels and particularly Cr/Ni containing stainless steels. This lack of data extends to Am interaction with (and potential generation of) corrosion products formed on real steel surfaces and the passivating layer formed on stainless steels. The latter is especially relevant given the potential for largely unstudied actinide uptake by the chromite constituent.

Knowledge of the interfacial electrochemistry of radiotoxic Am on steels, particularly in the ubiquitous Am(III) state, is vital to underpin our understanding of its behaviour as a contaminant and/or a corrosion promoter in a number of safety related scenarios across the fuel cycle including waste separation processes, storage & treatment, geological repository (post ground water incursion) and plant decontamination. However, study of the behaviour of Am(III) on reactive (i.e. prone to corrosion) electrode materials such as steels requires an understanding of the baseline

behaviour of Am(III) on non-reactive (i.e. inert) electrode materials (the noble metals, glassy carbon etc).

Thus, before examining the effect of Am(III) on the corrosion behaviour of common process steels, the next section will focus on the electrochemical behaviour of Am (III) on a range of assumed- inert electrode materials in varying concentrations of nitric acid representative of a range of reprocessing streams.

Once the electrochemical behaviour of americium has been investigated in the next section, the subsequent section will focus on the following points:

- to determine whether and in what form Am incorporates into passivating layers on Cr/Ni rich low carbon steels in acid media (relevant to nuclear fuel reprocessing)
- to determine whether and in what form Am incorporates into corrosion products formed on low carbon steels under acid conditions (of relevance to HAL evaporators)
- to determine whether Am affects steel corrosion, either as a corrosion accelerator or by changing the corrosion product (as per U uptake in iron oxyhydroxides)

Electrochemically controlled growth of passivating oxides on low carbon steels can be directly monitored using Electrical Impedance Spectroscopy (EIS) (4). Using this method, the incorporation of americium into the passive oxide formed on steels will be attempted, and the incorporation will be assessed by monitoring changes to the EIS response against non-Am baseline behaviour. The effect of americium inclusion on layer morphology will be assessed using SEM and EDX. The effect of this incorporation on the corrosion vulnerability of the steel will then be assessed by electrochemical means.

The improved understanding of the incorporation of Am into steel surfaces will aid in the identification of a potential source of surface contamination and therefore radiological hazards. It will also give way to underpinning the formulation of more efficient Am decontamination strategies with potentially lower secondary waste arising and faster decontamination rates, reducing cost, hazard and operator exposure time.

In the following section, the electrochemical behaviour of Am(III) using various electrodes and media simulating reprocessing will be described.

8.2 Results & Discussion – Part 1

Preparation of the americium stock solution used in the experiments featured in this chapter is described in section 2.4.2. As per section 2.4.2.3, one sample of 100 mg was taken from the stock solution, which was then diluted 10^{-6} times to be used in gamma spectroscopy for activity measurements.

UV–VIS–NIR absorption spectroscopy has been widely used to characterise americium solution species (5). The major absorbance that has been measured to speciate Am(III) corresponds to the transition $^{7}F_{0} \rightarrow {}^{5}L_{6}$ with its maximum at 503.2 nm ($\varepsilon \sim 410$ L mol cm^{-1}) for $Am^{3+}(aq)$ (5). Therefore, a UV-Vis spectrum was taken of the prepared Am (III) solution (see Figure 8-1a). This was compared to a spectrum from the literature (see Figure 8-1b).

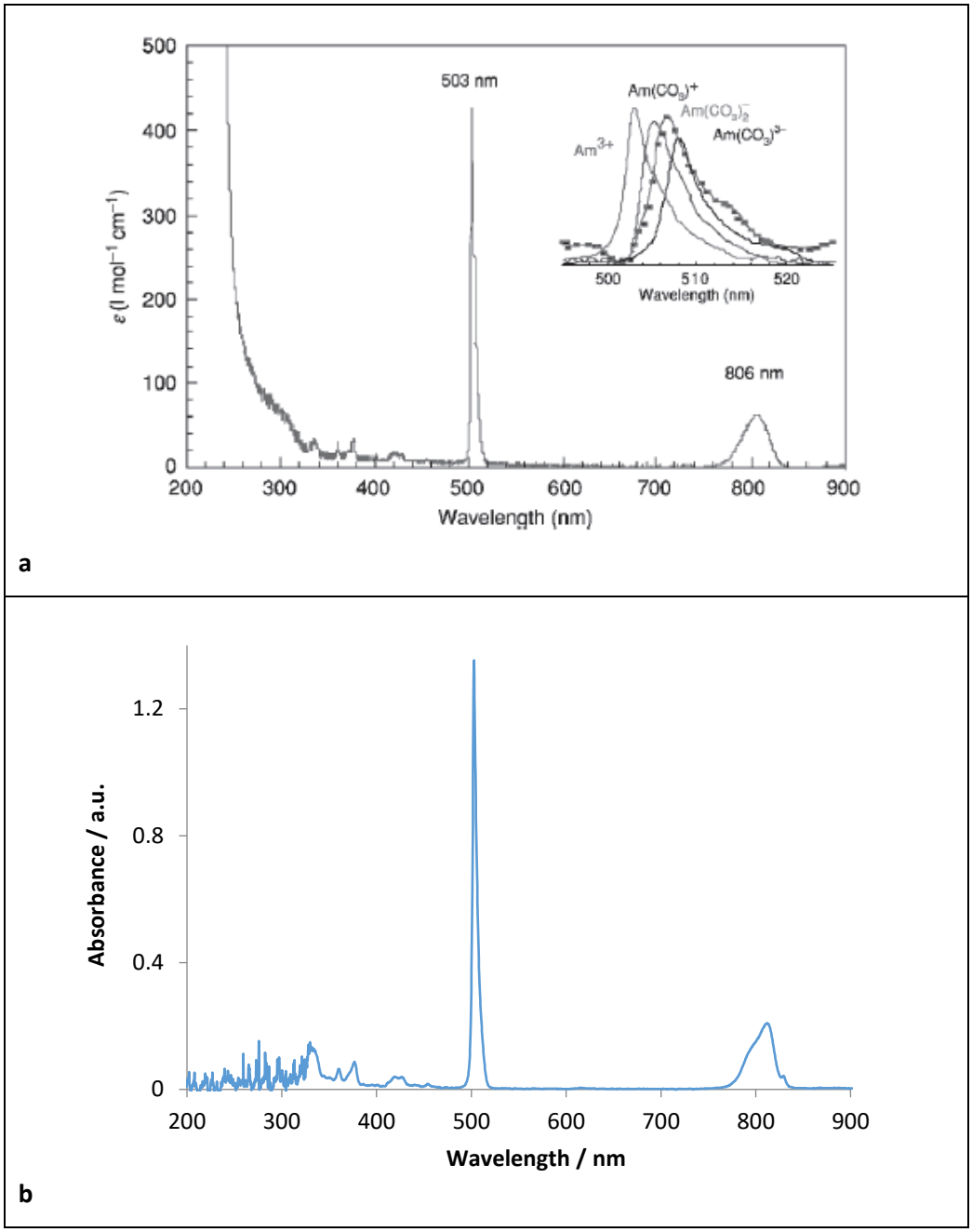

Figures 8-1a and 8-1b – (a) showing the electronic absorption spectra of Am^{3+} in 1 mol dm^{-3} $HClO_4$ and of the predominant Am(III) species in carbonate-containing solutions; (b) the UV-Vis spectrum of the Am(III) stock solution in 1 mol dm^{-3} HNO_3 (5)

In Figure 8-1 above we can see that the americium stock solution we have prepared contains Am(III) by comparing its UV-Vis spectrum (Figure 8-1b) with the electronic absorption spectra of Am^{3+} (Figure 8-1a) from the literature.

We will now investigate the electrochemical behaviour of americium (III).

8.2.1 Electrochemical behaviour of americium (III)

The first part of this work is to establish the baseline electrochemical behaviour of americium on a range of commonly used electrode materials. A particular aim of this baseline study is to determine whether it is possible to determine the as-yet-unreported standard electrochemical rate constant, k^0 for the Am(III) oxidation reaction. One method by which this may be achieved is that of Myland, Oldham, Zoski and Bond (6) (7), involving the analysis of steady state voltammograms recorded on microelectrodes of a range of radii. This requires the measurement of quarter, half and three quarter wave potentials from those voltammograms and analysis of their dependence on microelectrode radius. These dependences may then be used to obtain k^0 values from a series of look-up tables provided by Myland *et al*. (6) (7) in their paper.

Small-sized electrodes such as microelectrodes, especially those which possess convergent spherical diffusion fields, are valuable tools in electrochemistry due to their unique electrochemical properties - high current densities that result from enhanced mass transport, reduced solution resistance, and high signal-to-noise ratios, being some of them. This makes microelectrodes versatile tools in the measurement of electron transfer kinetics (8).

Gold, being chemically inert and resistant to oxide formation within the stability potential window of water (9), is commonly used as a material of choice. Thus, gold microelectrodes of varying sizes were used as the working electrode in a three-electrode electrochemical cell in solutions of 1 (Figures 8-2 to 8-7) and 3 mol dm^{-3} nitric acid (Figures 8-8 to 8-16) containing 6.22 x 10^{-4} mol dm^{-3} Am. Experiments under the same conditions were also set-up not containing americium as comparisons, in order to investigate the electrochemical behaviour of americium.

Below is a series of cyclic voltammetry experiments, carried out with gold microelectrodes at a potential window of 0.8 – 1.9 – 0.3 V, with increasing scan rates. All solutions have been purged with argon gas for 15 mins, and all electrodes have been polished with abrasive paper and diamond polish at 6, 3 and 1 microns (see section 2.3.1 for details). In the first instance, we have examined the voltammatric behaviour of the smallest of the gold microelectrodes available to us, a microdisc of 10 μm diameter, in nitric acid solutions in the absence and presence of the Am spike. Results recorded at scan rates of 10, 100 and 1000 mV / s are shown in Figures 8.2 – 8.4 respectively.

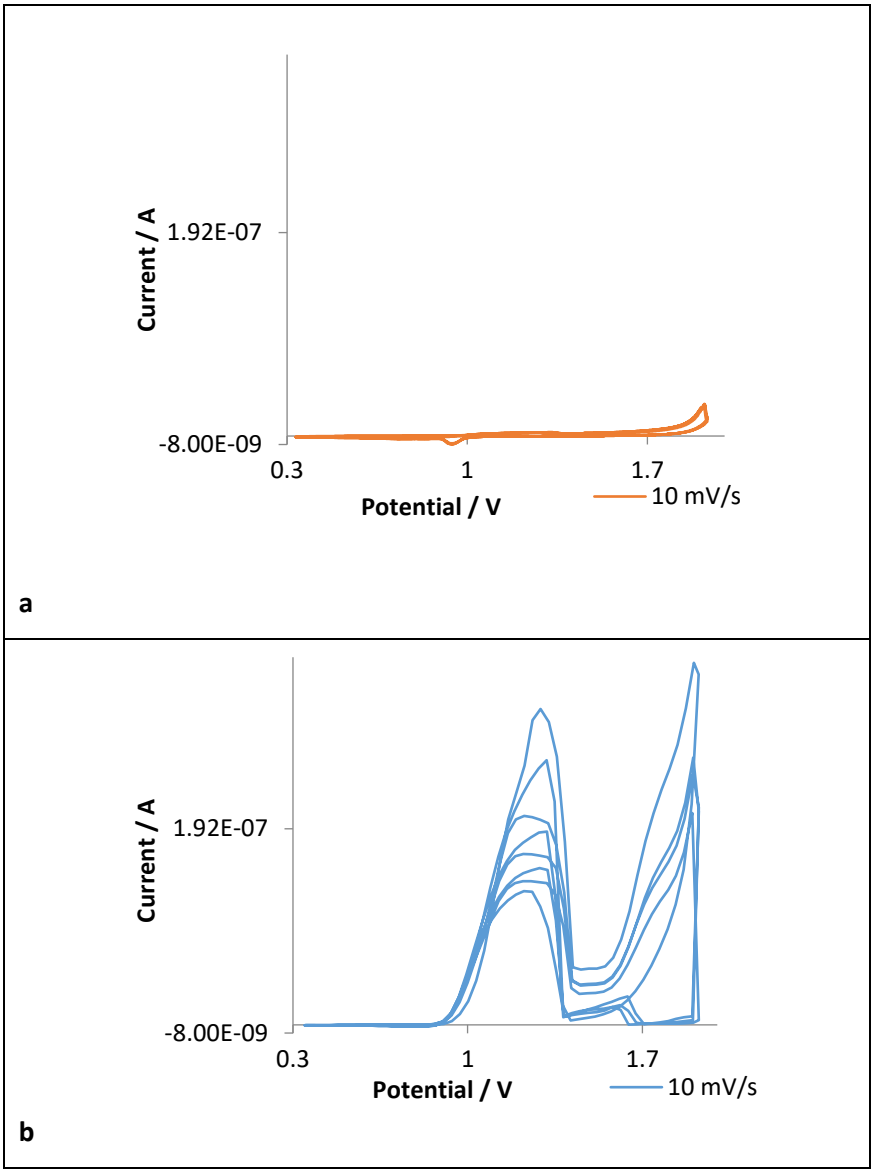

Figure 8-2a and 8-2b – (a) showing the cyclic voltammogram of a 10 µm gold electrode in 1 mol dm^{-3} nitric acid scanned at a potential window of 0.8 – 1.9 – 0.3 V at a scan rate of 10 mV/s; (b) showing the cyclic voltammogram of a 10 µm gold electrode in 1 mol dm^{-3} nitric acid scanned at a potential window of 0.8 – 1.9 – 0.3 V_{SCE} at a scan rate of 10 mV/s containing a 0.62 mmol dm^{-3} Am spike

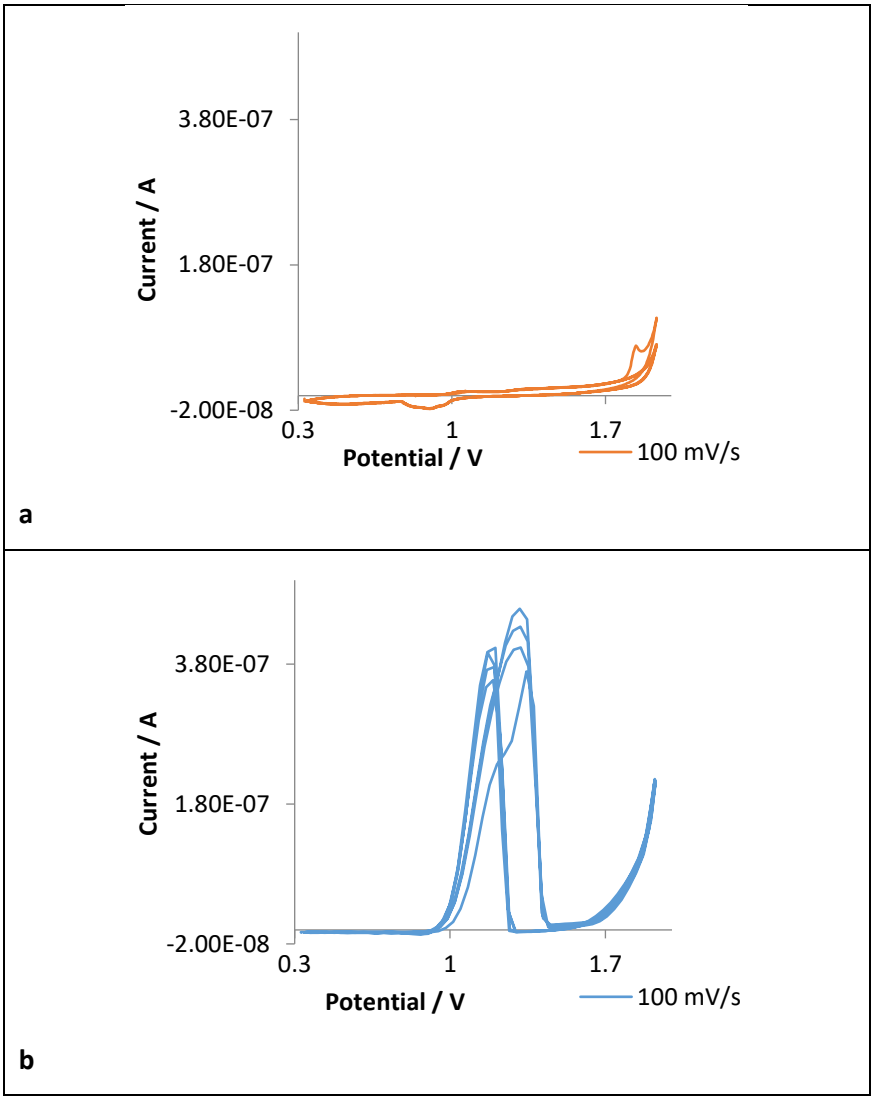

Figure 8-3a and 8-3b – (a) showing the cyclic voltammogram of a 10 µm gold electrode in 1 mol dm^{-3} nitric acid scanned at a potential window of 0.8 – 1.9 – 0.3 V at a scan rate of 100 mV/s; (b) showing the cyclic voltammogram of a 10 µm gold electrode in 1 mol dm^{-3} nitric acid scanned at a potential window of 0.8 – 1.9 – 0.3 V_{SCE} at a scan rate of 100 mV/s containing a 0.62 mmol dm^{-3} Am spike

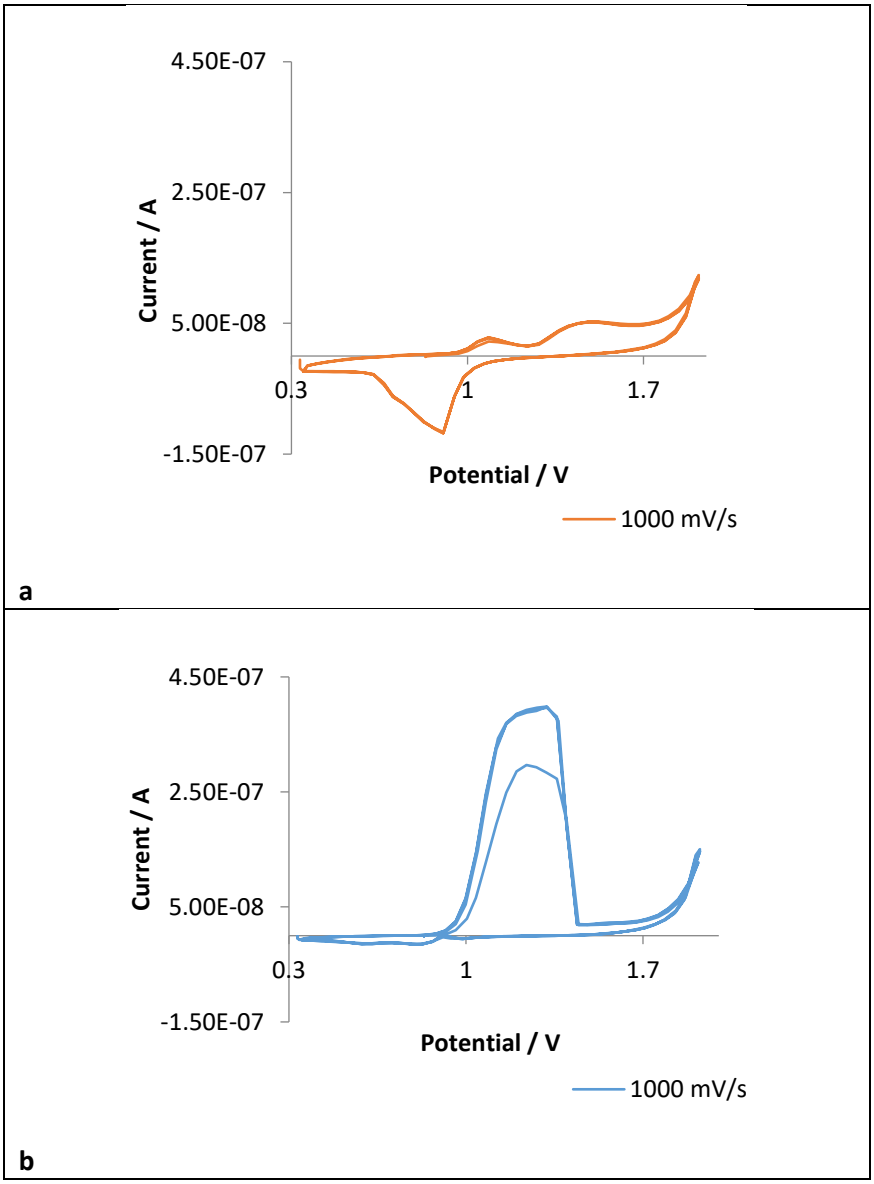

Figure 8-4a and 8-4b – (a) showing the cyclic voltammogram of a 10 µm gold electrode in 1 mol dm^{-3} nitric acid scanned at a potential window of 0.8 – 1.9 – 0.3 V at a scan rate of 1000 mV/s; (b) showing the cyclic voltammogram of a 10 µm gold electrode in 1 mol dm^{-3} nitric acid scanned at a potential window of 0.8 – 1.9 – 0.3 V_{SCE} at a scan rate of 1000 mV/s containing a 0.62 mmol dm^{-3} Am spike

The data of Figures 8.2 – 8.4 both answers and raises key questions about the electrochemistry of Am(III) on gold electrodes. On first inspection, comparison of Figure 8-2a with 8-2b, Figure 8-3a with 8-3b and Figure 8-4a with 8-4b suggests that the presence of Am(III) results in the observation of two anodic current waves with onsets of approximately 0.9 V and approximately 1.7 V that are not observed in the absence of Am(III). A preliminary analysis would therefore attribute both of these waves to the oxidation of americium.

However,

(i) The shape of the first wave is not consistent with it being due to a wholly solution-based oxidation as current quickly rises to a peak with increasing voltage and then even more abruptly drops back to near zero before the onset of the second wave

(ii) Neither wave rises to a convincing diffusive mass transfer limited current plateau. This makes the extraction of quarter, half and three quarter waves impossible and thus use of the above-described method of Myland *et al*. for obtaining k^0 equally difficult

(iii) The steady state, diffusive mass transfer limiting current at a disc microelectrode, i_L, is given by the following expression (10):

$$i_L = 4nFDCr$$

Equation 8-1

where,

n = stoichiometric electron number for the redox couple under study (assuming 3 for the Am(III)/Am(VI) couple, see Equation 8-1a below for Am(III) to Am(VI) oxidation),

F = Faraday's constant (96484.6 C mol^{-1}),

D = diffusion coefficient (in this case, for the species being oxidised, Am(III), assuming a value of 5 x 10^{-10} m^2 s^{-1}),

C = bulk concentration of the reactant in question (in this case [Am(III)] = 0.62 mol m^{-3}) and,

r = radius of the microdisc (for the data of Figures 8-5 to 8-7, this is 5 μm)

$$Am(III) \xrightarrow{-e^-} Am(VI)$$
$$Am(VI) \xrightarrow{-e^-} Am(V)$$
$$Am(V) \xrightarrow{+2H_2O - 4H^+} [Am^{V}O_2]^+$$
$$[Am^{V}O_2]^+ \xrightarrow{-e^-} [Am^{VI}O_2]^{2+}$$

Equation 8-1a

Insertion of the values given in parentheses into Equation 8-1 for i_L above gives a value for i_L of ~2 nA. This is almost two orders of magnitude smaller than the peak current observed at approximately 1.1 V in the experiment recorded under nearest to steady state conditions, shown in Figure 8-2b, suggesting that the electro-oxidation of Am(III) in Figures 8-2 to 8-4 is not described by a simple electrochemical reaction. Rather, it would appear to be coupled with a following reaction that significantly enhances the current observed. Current enhancements of this type are seen in the case of coupled electrochemical-chemical processes such as the so-called EC' process (11). In an EC' process, the product of the electrochemical step, E, reacts in a chemical step to regenerate the reactant in the electrochemical step, so locally increasing the concentration of the electrochemical reactant and thus increasing the current observed. In the case of Figures 8-2 to 8-4, this would mean that Am(III) is being oxidised at the electrode surface presumably to Am(VI), only to quickly be reduced back to Am(III), most likely by the reaction of the Am(VI) with water. The regenerated Am(III) may then be re-oxidised at the electrode surface only for the cycle to repeat itself, thus resulting in the larger-than-expected currents seen in the Am-spiked experiments of Figure 8-2 to 8-4.

However, complexities associated with the first anodic peak are not simply limited to the possible involvement of an EC' mechanism for Am(III) electro-oxidation. As well, the shape of the first wave as described in point (i) is actually closer in form to that of an electrode where the fabric of the electrode itself first undergoes active oxidative dissolution and then passivates i.e. it has the same form as region BCGJ of Figure 7-1 in Chapter 7. This would suggest that the waves observed in Figures 8-2b, 8-3b and 8-4b are influenced by the electrochemistry of the gold microelectrodes themselves; however, this conclusion is contradicted by the absence of such waves in Figures 8-2a, 8-3a and 8-4a.

Thus, given point (ii) above, the approach of Myland *et al*. was abandoned at this nitric acid concentration. Nicholson and Shain have derived models for the analysis of EC' processes (12) that allow for the extraction of a value for the kinetic rate parameter associated with the chemical step – assumed in this case to be the reduction of electrogenerated Am(VI) to Am(III). However, as in the case of the approach of Myland *et al*. this requires the availability of voltammetric data that are attributable solely to the redox couple under study (again, in this case Am(III)/Am(VI)) and not convoluted with any other electrochemical response (in this case the possible involvement of the underlying electrochemistry of the gold electrode). Thus EC'-based analysis of the data of Figures 8-2 to 8-4 was not attempted in light of (iii) above. Rather, given the complications associated with the

possible presence of gold electrochemistry in those data, experiments were conducted to elucidate whether gold electrochemistry was indeed influencing the waves seen in Figures 8-2b, 8-3b and 8-4b. In the first instance, this involved repeating the experiments of Figures 8-2 to 8-4 on the largest of the gold microelectrodes available to use, a microdisc with a diameter of 500 μm, for the following reasons. In accordance with extant models of EC' processes on mircrodisc electrodes (13) (14), the currents observed from solution phase processes such as the putative oxidation of Am(III) considered here have a mixed dependence on both electrode area and radius i.e. it will scale with area or radius depending on the ration of the diffusion coefficient for the electroactive species and the value of the rate parameter for the chemical reaction describing regeneration of the electroactive species. However, currents associated with surface processes, such as the putative oxidation of gold also under consideration in Figures 8-2 to 8-4, will only increase with increasing electrode area i.e. will scale with the square of the electrode radius. Thus, and dependent upon the ratio of rate parameter to diffusion coefficient described above, increasing the electrode diameter from 10 to 500 μm may potentially maximise the possibility of seeing the latter, gold oxidation electrochemistry - if it is present as speculated above. Results of using the largest available microdisc electrode to us are shown in Figures 8-5 to 8-7 below.

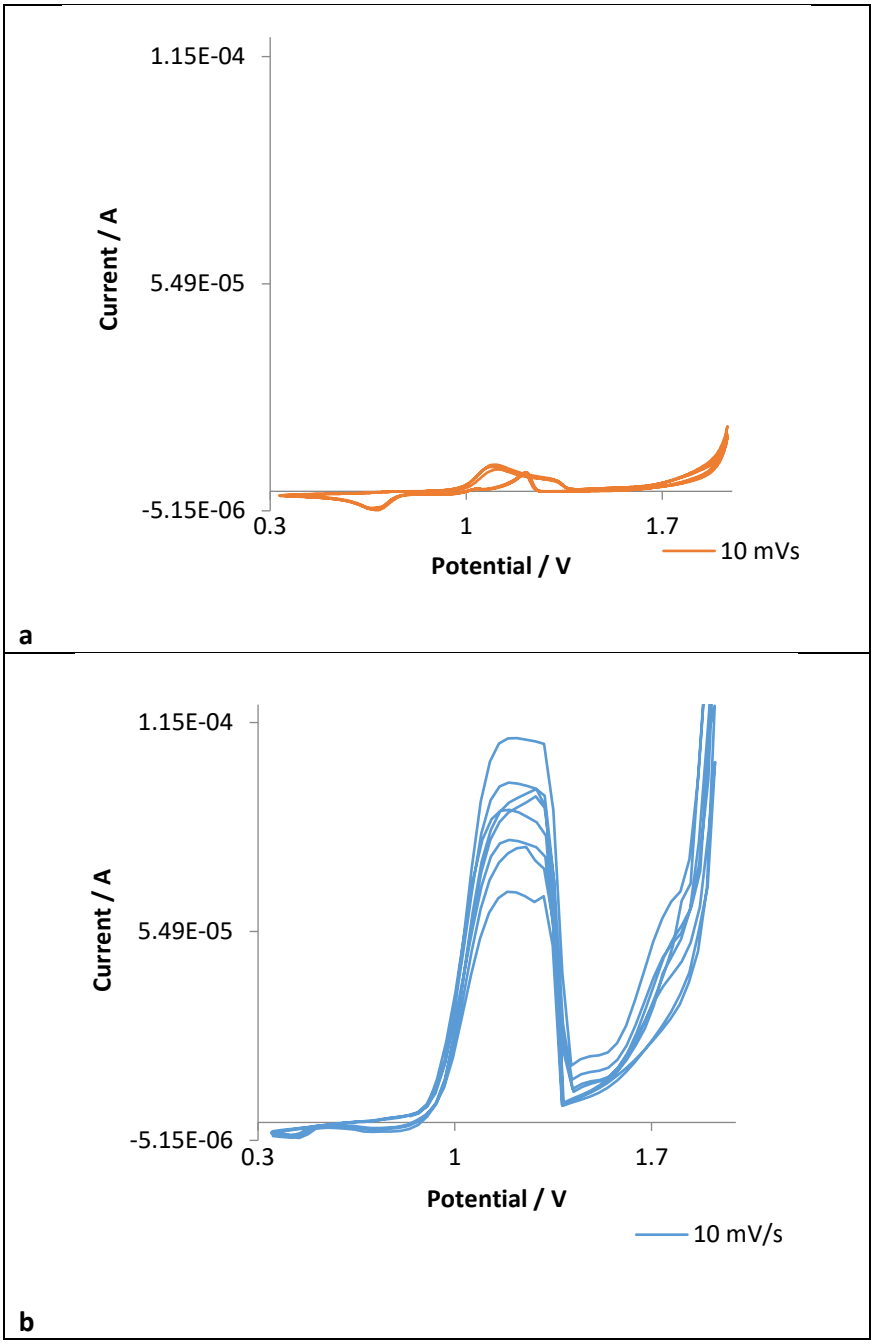

Figure 8-5a and 8-5b – (a) showing the cyclic voltammogram of a 500 µm gold electrode in 1 mol dm^{-3} nitric acid scanned at a potential window of 0.8 – 1.9 – 0.3 V at a scan rate of 10 mV/s; (b) showing the cyclic voltammogram of a 500 µm gold electrode in 1 mol dm^{-3} nitric acid scanned at a potential window of 0.8 – 1.9 – 0.3 V_{SCE} at a scan rate of 10 mV/s containing a 0.62 mmol dm^{-3} Am spike

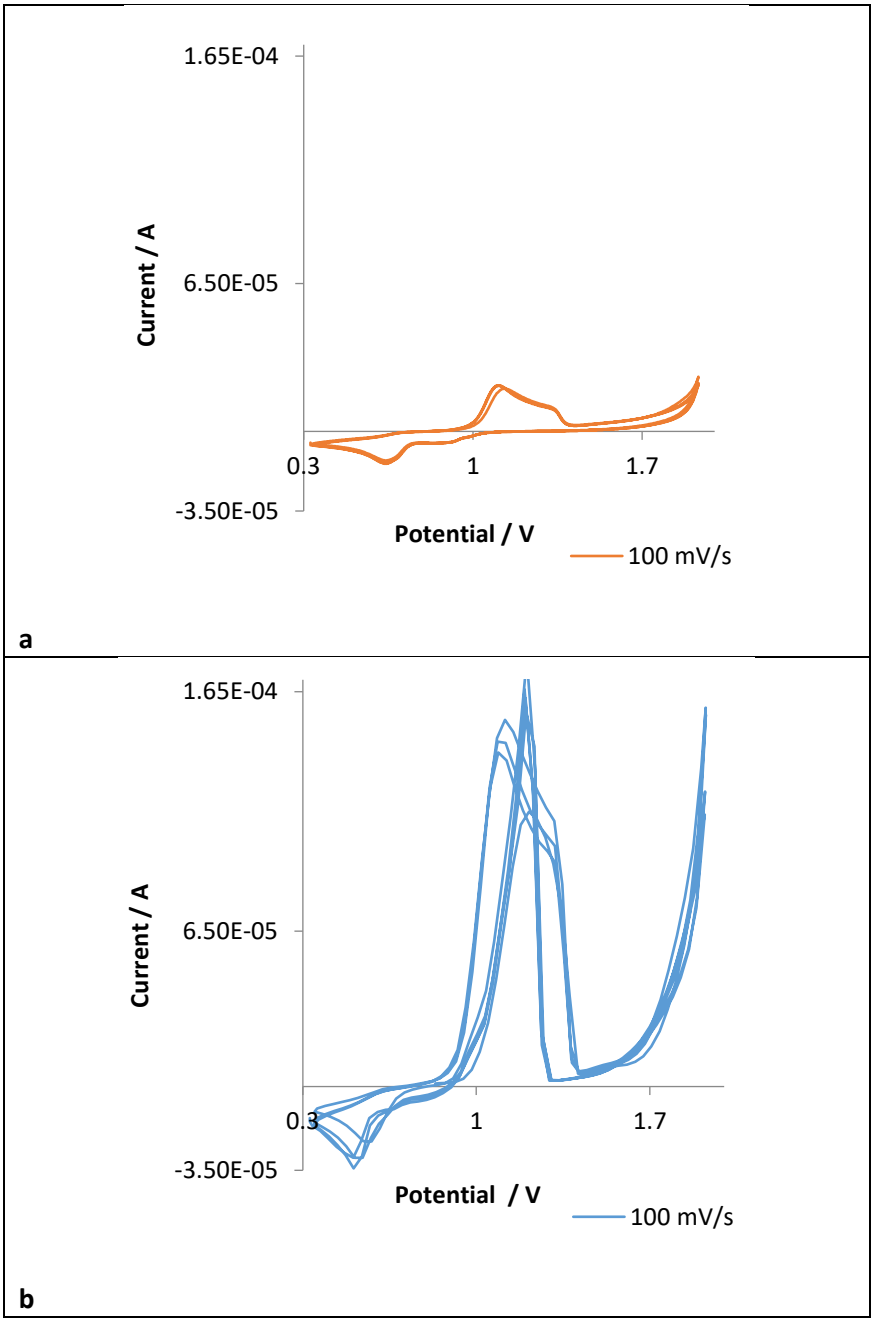

Figure 8-6a and 8-6b – (a) showing the cyclic voltammogram of a 500 µm gold electrode in 1 mol dm^{-3} nitric acid scanned at a potential window of 0.8 – 1.9 – 0.3 V at a scan rate of 100 mV/s; (b) showing the cyclic voltammogram of a 500 µm gold electrode in 1 mol dm^{-3} nitric acid scanned at a potential window of 0.8 – 1.9 – 0.3 V_{SCE} at a scan rate of 100 mV/s containing a 0.62 mmol dm^{-3} Am spike

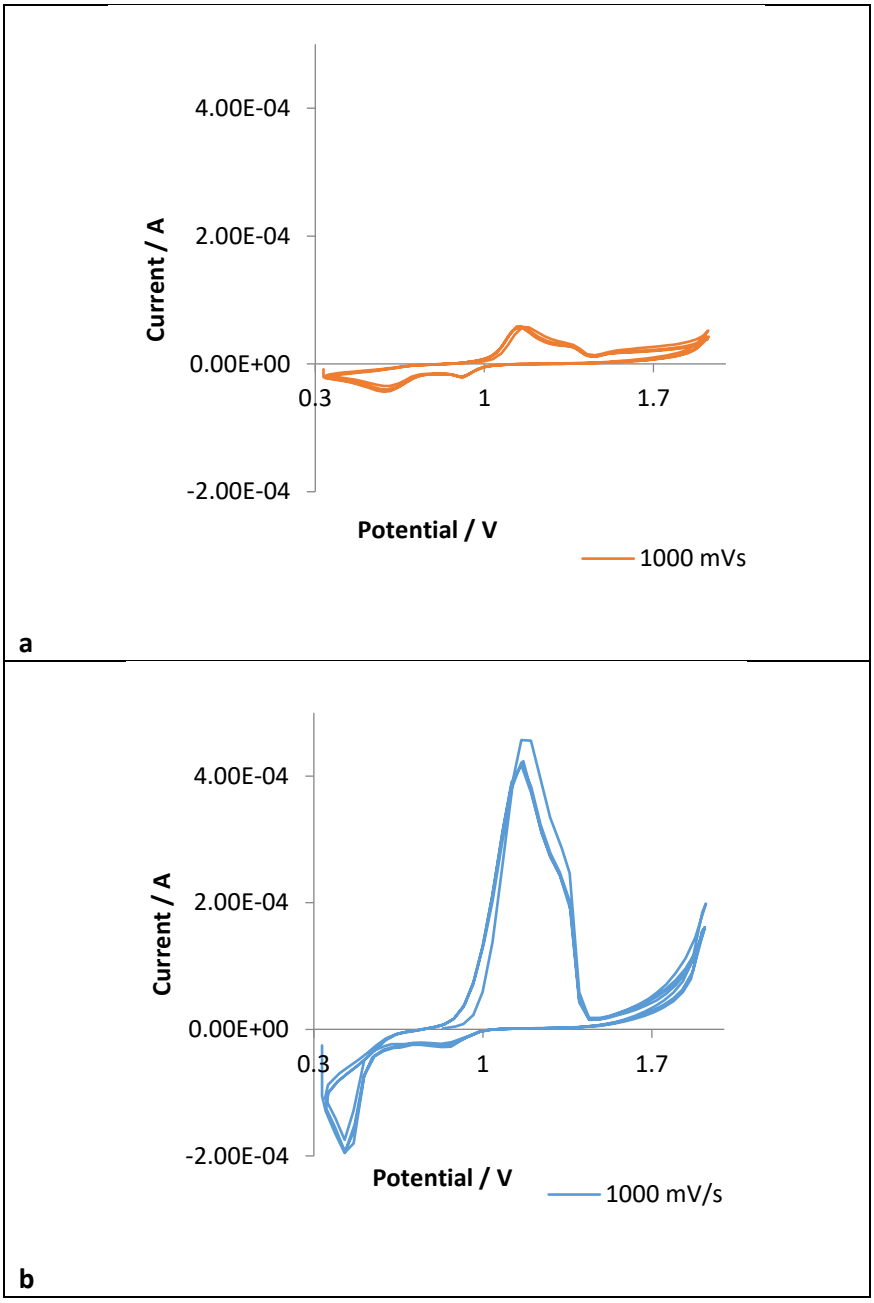

Figure 8-7a and 8-7b – (a) showing the cyclic voltammogram of a 500 µm gold electrode in 1 mol dm^{-3} nitric acid scanned at a potential window of 0.8 – 1.9 – 0.3 V at a scan rate of 1000 mV/s; (b) showing the cyclic voltammogram of a 500 µm gold electrode in 1 mol dm^{-3} nitric acid scanned at a potential window of 0.8 – 1.9 – 0.3 V_{SCE} at a scan rate of 1000 mV/s containing a 0.62 mmol dm^{-3} Am spike

From the cyclic voltammograms recorded in the absence of americium, it can be seen that the gold electrode surface is indeed electro-oxidising at approximately 1 V whilst, from the cyclic voltammograms measured in the presence of americium, it can be seen that the americium electrochemistry occurs near-coincident with this gold oxidation and so is heavily convoluted with it. This convolution means that it is not possible to clearly extract the dependence of the Am(III) oxidation process on electrode radii (or in our case circumferences) from the cyclic voltammograms

presented from Figures 8-2 to 8-7. Neither is it possible to conduct an analysis of the recorded voltammograms in accordance with the kinetic models of the EC' process described by Nicholson and Shain (12); the latter being a particular inconvenience as this would allow for the derivation of a value of the kinetic rate parameter for the chemical reduction of Am(VI) to Am(III) in the nitric acid solutions under study here.

Some understanding of the underlying Au electrochemistry, however, is possible. This has previously been described by Shackleford *et* a (15)l. in an EQCM-based study of the behaviour of Au-coated quartz piezoelectrodes in concentrated nitric acids (15). Here it was found that at a solution pH of 1, the Au readily dissolved through a three-electron oxidation, Equation 8-2, at a potential of 1 V_{SCE} at scan rates lower or equal to 10 mV/s. This process however, was seen to be hindered at scan rates greater than 10 mV/s by the underpotential deposition of OH surface sublattices, as well as the subsequent formation of 2-D-phase oxides (15). This hindrance is thought to arise from the presence of a close packed surface layer of NO_3^- ions, which are eventually disrupted and removed by the dissolution of and the subsequent re-precipitation of Au, resulting from the above-mentioned processes that occurred at scan rates lower than 10 mV/s (15).

$$Au \longleftrightarrow Au^{3+} + 3^{e-}$$

Equation 8-2

Noteworthy from the CVs recorded at slower scan rates, Figures 8-5 and 8-6, are the oxidation currents seen in the potential range 1 - 1.4 V during the return sweep – where we would usually expect to see reduction currents. Such current reversals are usually indicative of a layer of oxide having been formed on the forward going sweep that is then stripped on the reverse sweep, allowing for the oxidation of any oxidisable solution species present (in this case Am(III)) to then be observed. Consulting the Pourbaix diagram for americium in Figure 8-17a below, we can see that this peak lies in the region where an Am(V)oxide layer may be formed – suggesting that the possible, irreversible formation of Am oxide may be in part occluding the microelectrode surface. As described above, two factors are preventing the implementation of either the theory of Myland *et al*. in determining k^0 for the electro-oxidation of Am(III) on our gold microdisc electrodes, or that of Nicholson and Shain in determining the rate parameter for the solution phase chemical re-reduction of the presumed Am(VI) electrochemical product:

(i) the convolution of the electrochemistry of the gold electrode material itself with the electrochemistry of the Am(III); and

(ii) the lack of a clear observation of a diffusive mass transfer limited current plateau (in Figures 8-5 & 8-6)

Referring to point (ii) above, it appears that the lack of a clear mass transfer-limited current plateau is due to the possible formation of a passivating americium oxide layer at the electrode surface. However, Figures 8-5 to 8-7 also indicate that the possible EC'-enhanced current signal associated with the oxidation of Am(III) is substantially larger than that associated with the oxidation of gold. This indicates the possibility of simple deconvolution of the Au and Am electrochemistries and thus the implementation of the method of Nicholson and Shain – as long as the assumed formation of passivating americium oxide can be suppressed and a mass transfer limited current plateau observed. Inspection again of the Am Pourbaix of Figure 8-17a suggests that this may be possible at pH < 0 where the product of Am(III) oxidation may be expected to be the AmO_2^{2+} ion rather than americium oxide. Thus, we repeated the experiments of Figures 8-2 through to 8-7, in 3-mol dm^{-3} nitric acid. Figures 8-8 to 8-16 show the resultant CVs recorded at electrode diameters of 50, 250 and 500 μm and scan rates of 10, 100 and 1000 mV/s.

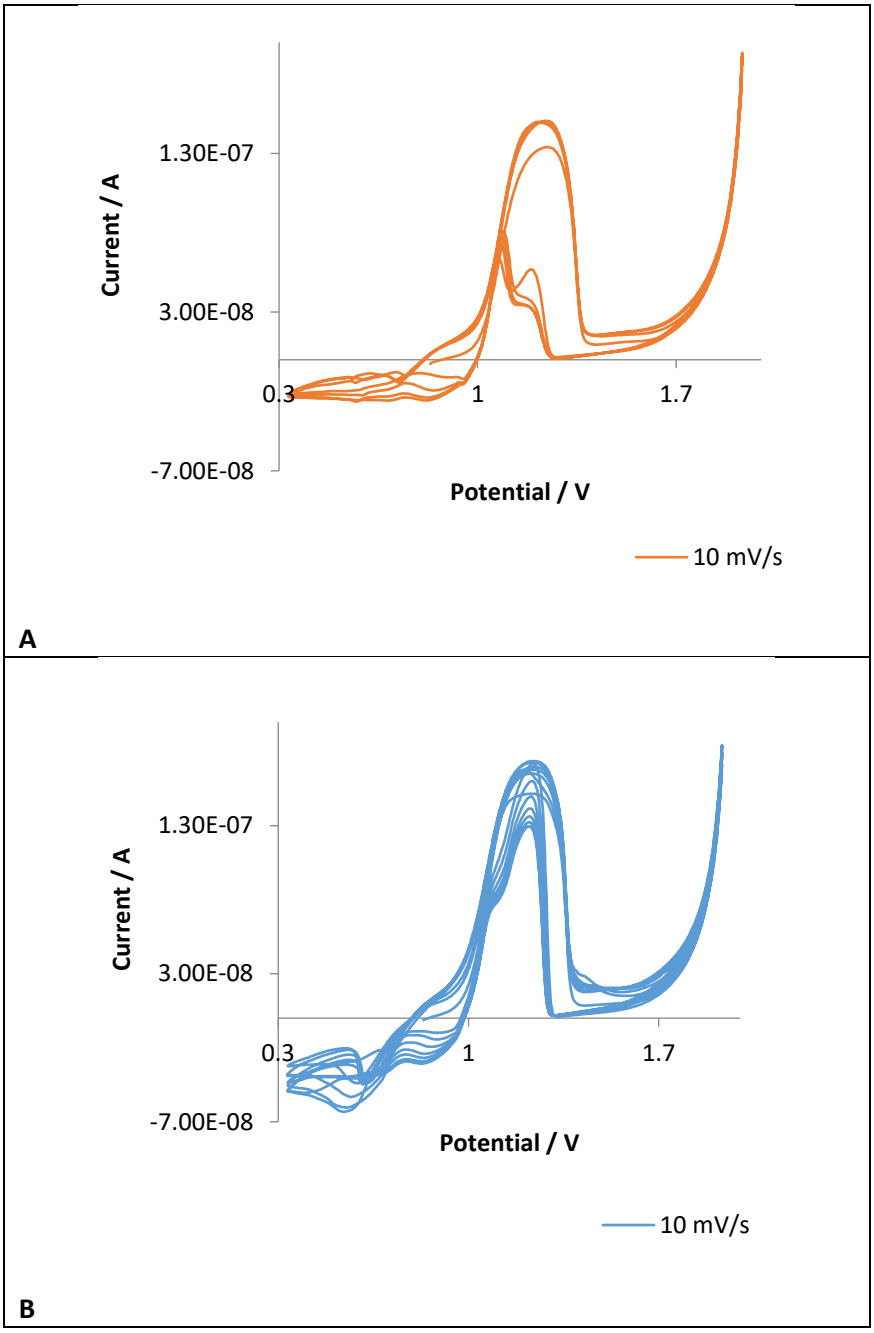

Figure 8-8a and 8-8b – (a) showing the cyclic voltammogram of a 50 µm gold electrode in 3 mol dm^{-3} nitric acid scanned at a potential window of 0.8 – 1.9 – 0.3 V at a scan rate of 10 mV/s; (b) showing the cyclic voltammogram of a 50 µm gold electrode in 3 mol dm^{-3} nitric acid scanned at a potential window of 0.8 – 1.9 – 0.3 V_{SCE} at a scan rate of 10 mV/s containing a 0.62 mmol dm^{-3} Am spike

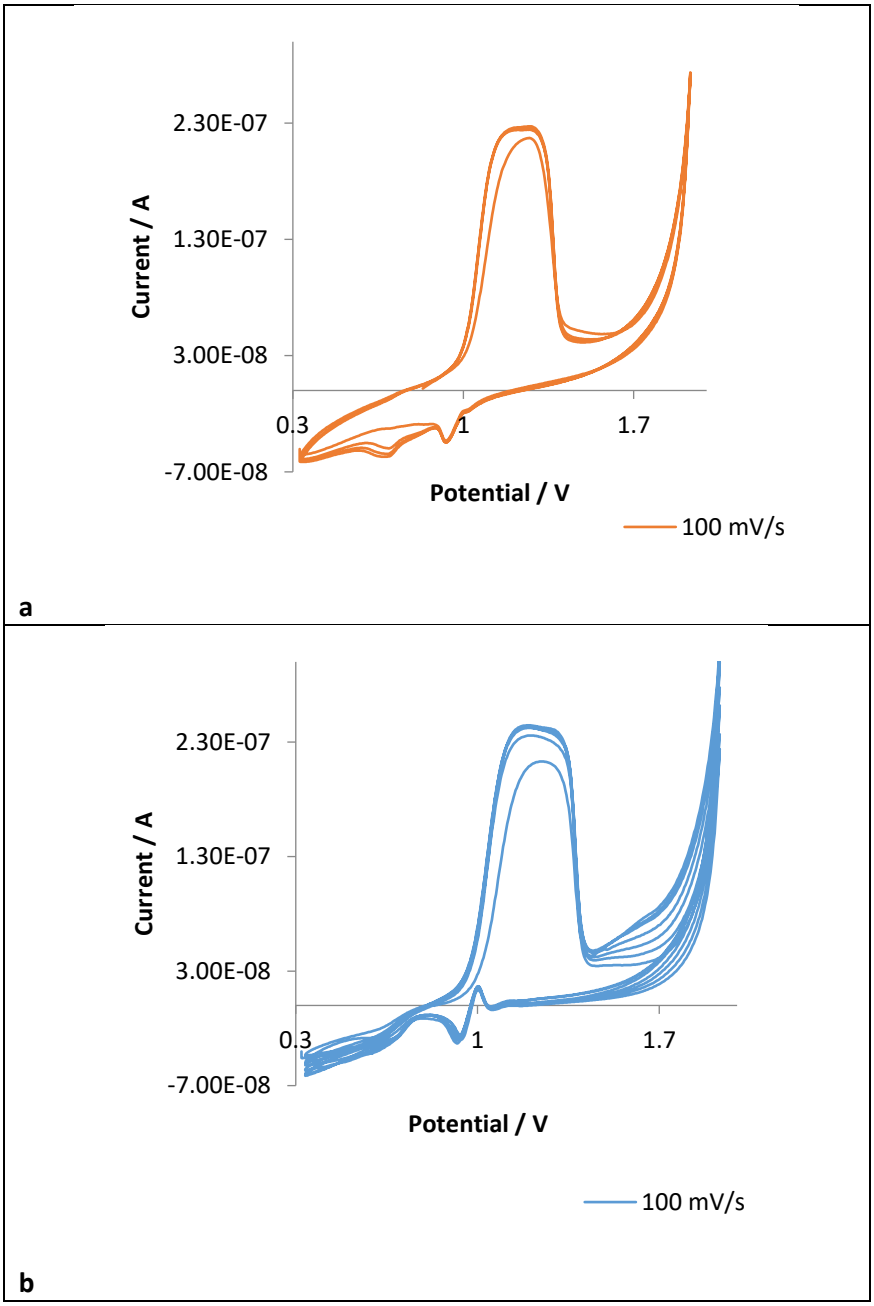

Figure 8-9a and 8-9b – (a) showing the cyclic voltammogram of a 50 µm gold electrode in 3 mol dm^{-3} nitric acid scanned at a potential window of 0.8 – 1.9 – 0.3 V at a scan rate of 100 mV/s; (b) showing the cyclic voltammogram of a 50 µm gold electrode in 3 mol dm^{-3} nitric acid scanned at a potential window of 0.8 – 1.9 – 0.3 V_{SCE} at a scan rate of 100 mV/s containing a 0.62 mmol dm^{-3} Am spike

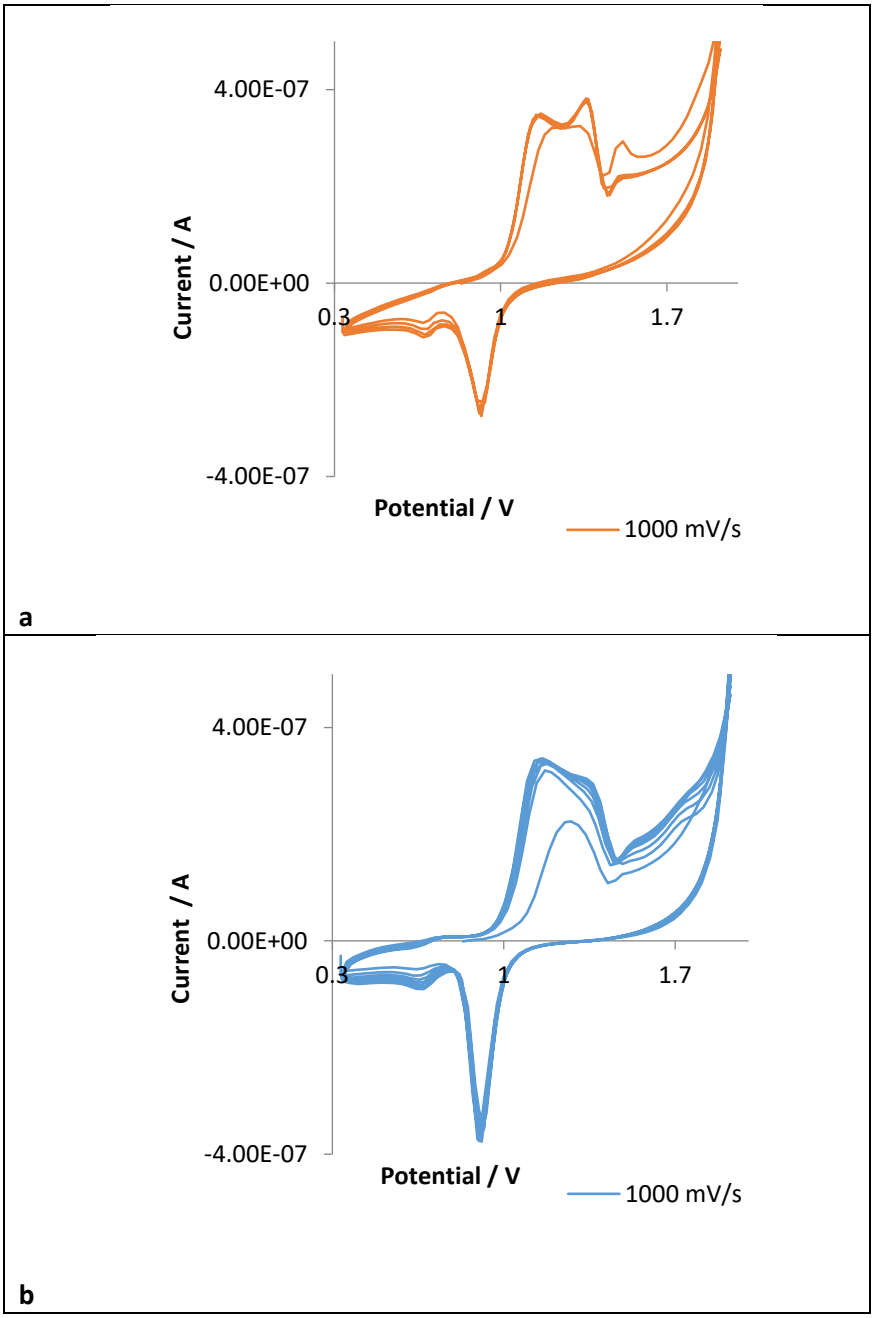

Figure 8-10a and 8-10b – (a) showing the cyclic voltammogram of a 50 µm gold electrode in 3 mol dm^{-3} nitric acid scanned at a potential window of 0.8 – 1.9 – 0.3 V at a scan rate of 1000 mV/s; (b) showing the cyclic voltammogram of a 50 µm gold electrode in 3 mol dm^{-3} nitric acid scanned at a potential window of 0.8 – 1.9 – 0.3 V_{SCE} at a scan rate of 1000 mV/s containing a 0.62 mmol dm^{-3} Am spike

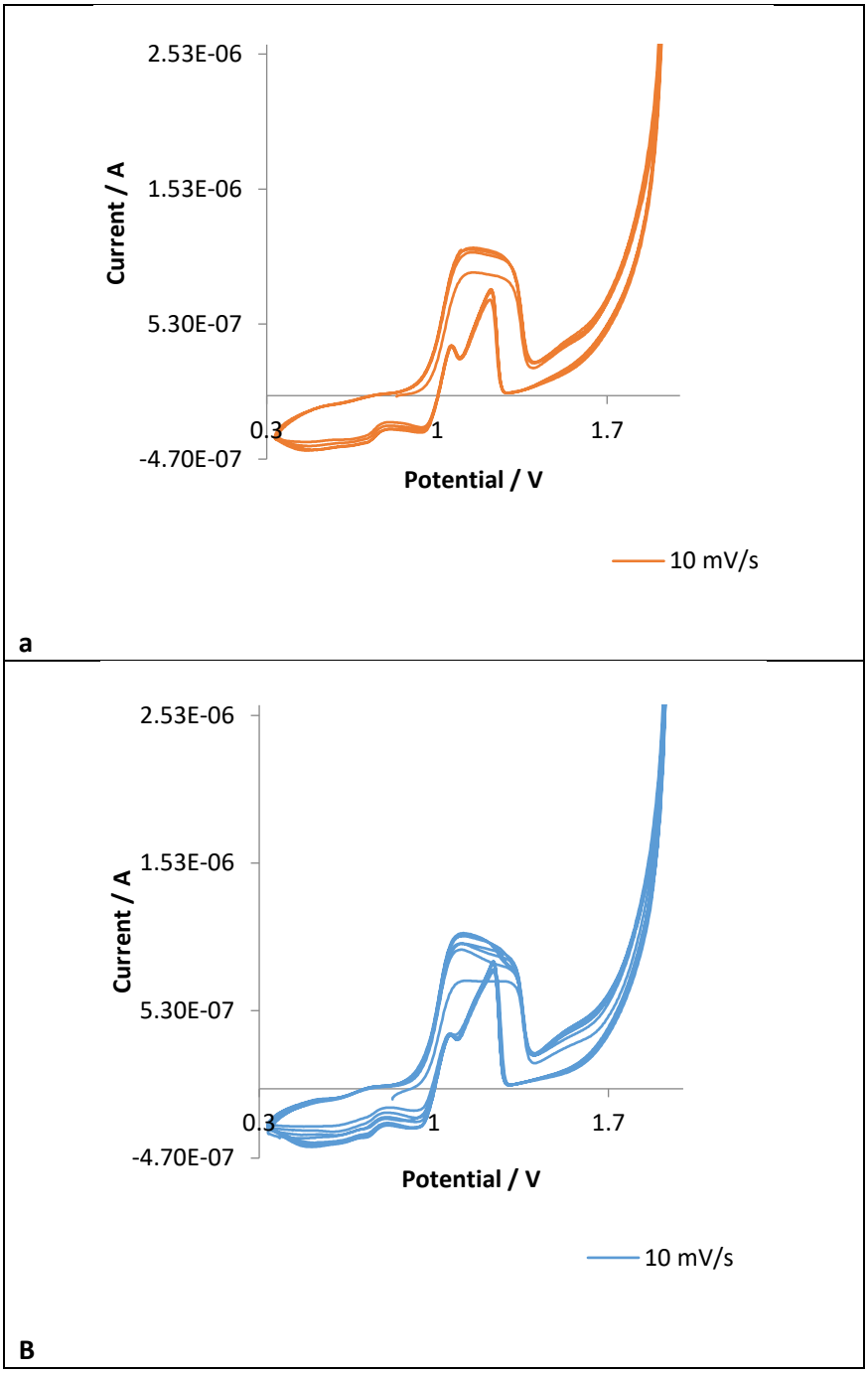

Figure 8-11a and 8-11b – (a) showing the cyclic voltammogram of a 250 µm gold electrode in 3 mol dm^{-3} nitric acid scanned at a potential window of 0.8 – 1.9 – 0.3 V at a scan rate of 10 mV/s; (b) showing the cyclic voltammogram of a 250 µm gold electrode in 3 mol dm^{-3} nitric acid scanned at a potential window of 0.8 – 1.9 – 0.3 V_{SCE} at a scan rate of 10 mV/s containing a 0.62 mmol dm^{-3} Am spike

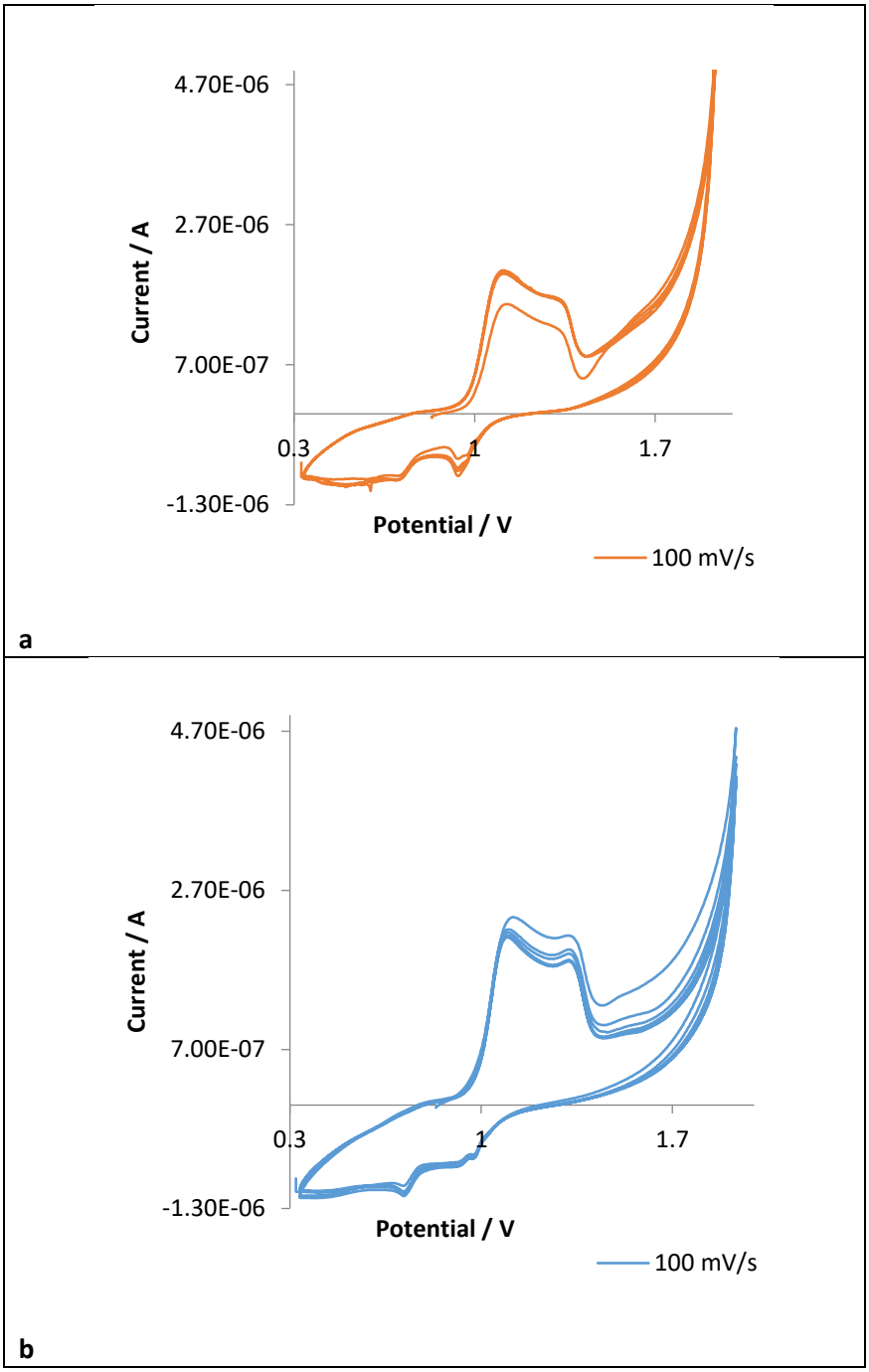

Figure 8-12a and 8-12b – (a) showing the cyclic voltammogram of a 250 µm gold electrode in 3 mol dm^{-3} nitric acid scanned at a potential window of 0.8 – 1.9 – 0.3 V at a scan rate of 100 mV/s; (b) showing the cyclic voltammogram of a 250 µm gold electrode in 3 mol dm^{-3} nitric acid scanned at a potential window of 0.8 – 1.9 – 0.3 V_{SCE} at a scan rate of 100 mV/s containing a 0.62 mmol dm^{-3} Am spike

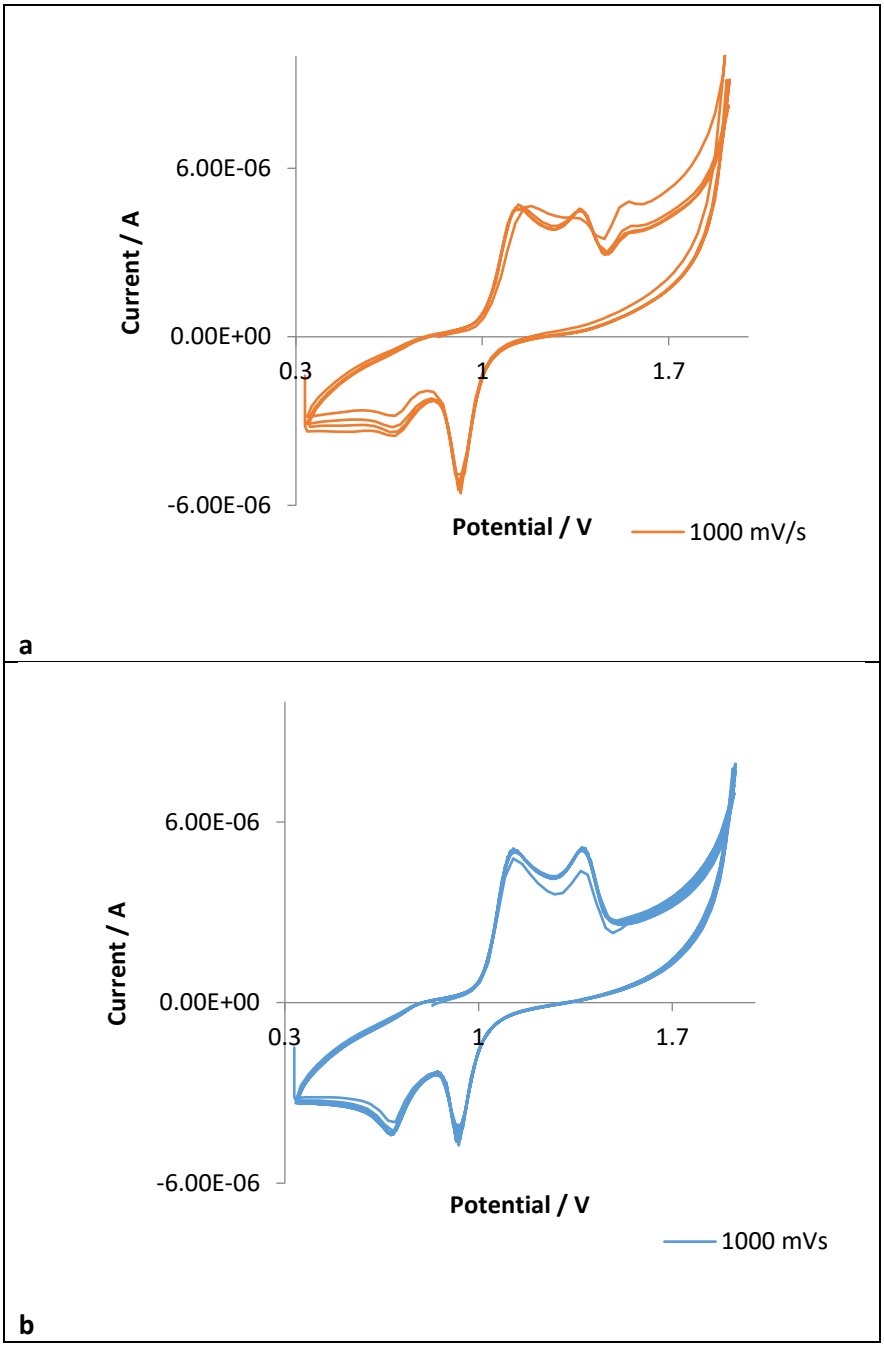

Figure 8-13a and 8-13b – (a) showing the cyclic voltammogram of a 250 µm gold electrode in 3 mol dm^{-3} nitric acid scanned at a potential window of 0.8 – 1.9 – 0.3 V at a scan rate of 1000 mV/s; (b) showing the cyclic voltammogram of a 250 µm gold electrode in 3 mol dm^{-3} nitric acid scanned at a potential window of 0.8 – 1.9 – 0.3 V_{SCE} at a scan rate of 1000 mV/s containing a 0.62 mmol dm^{-3} Am spike

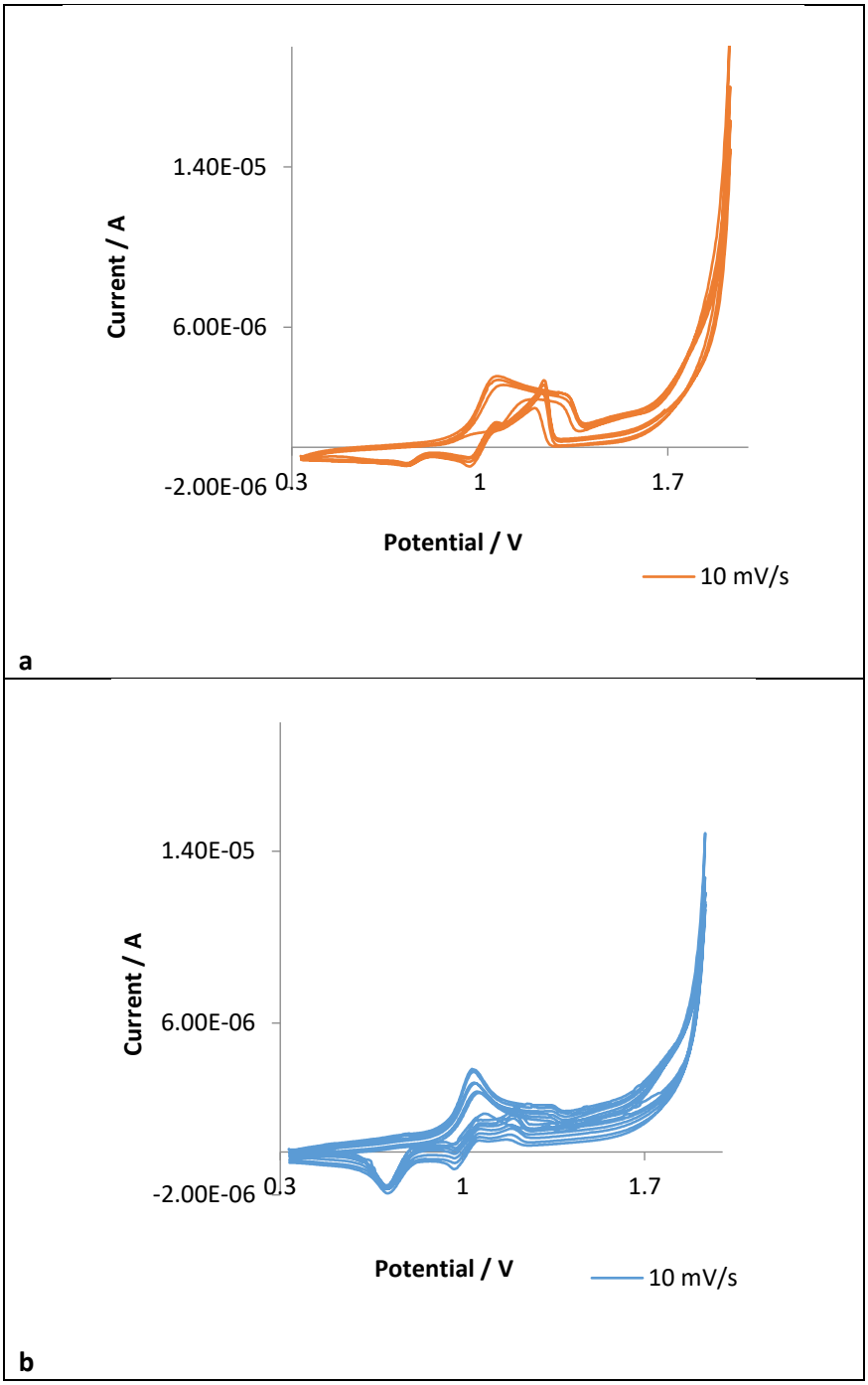

Figure 8-14a and 8-14b – (a) showing the cyclic voltammogram of a 500 µm gold electrode in 3 mol dm^{-3} nitric acid scanned at a potential window of 0.8 – 1.9 – 0.3 V at a scan rate of 10 mV/s; (b) showing the cyclic voltammogram of a 500 µm gold electrode in 3 mol dm^{-3} nitric acid scanned at a potential window of 0.8 – 1.9 – 0.3 V_{SCE} at a scan rate of 10 mV/s containing a 0.62 mmol dm^{-3} Am spike

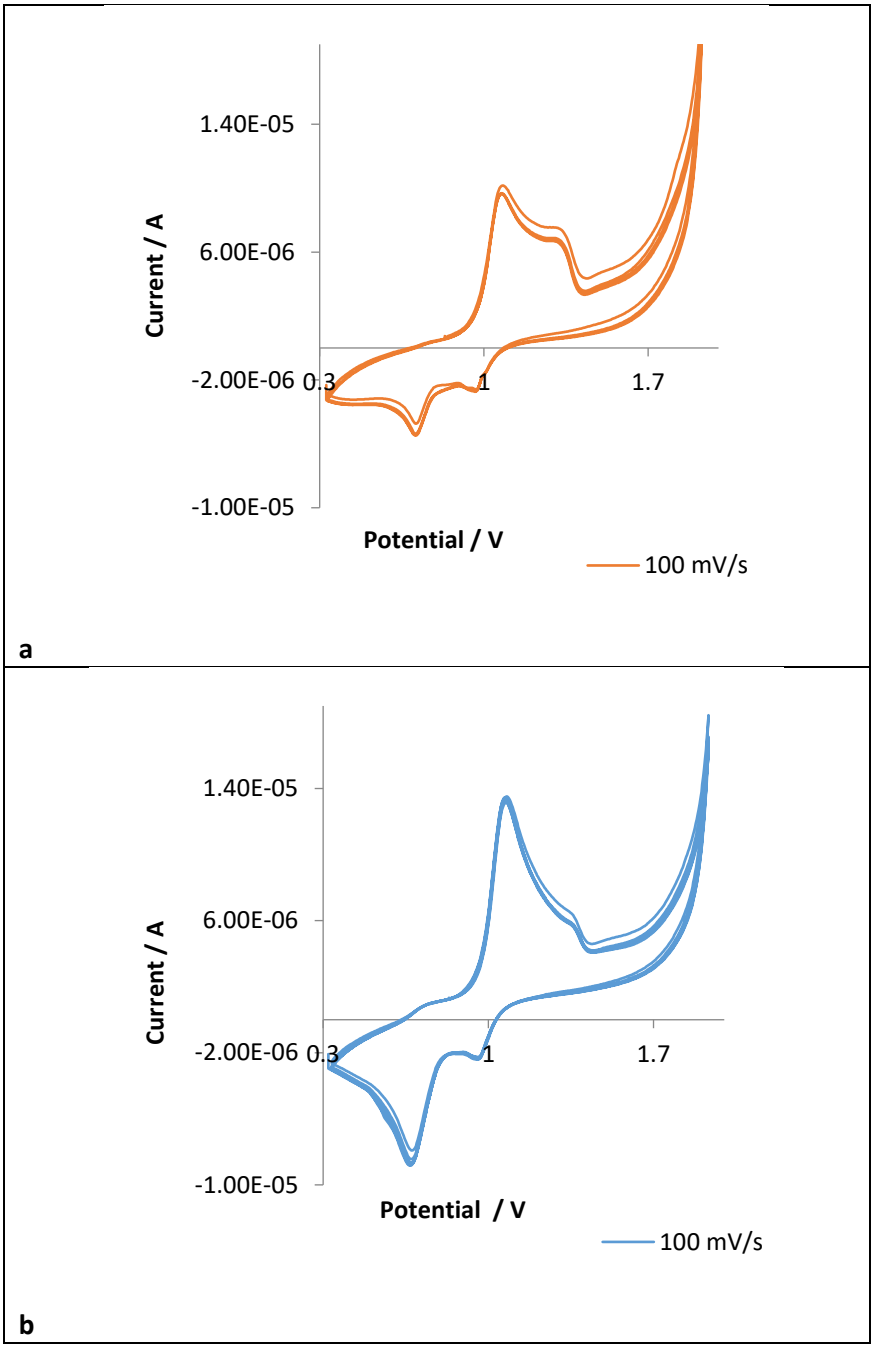

Figure 8-15a and 8-15b – (a) showing the cyclic voltammogram of a 500 µm gold electrode in 3 mol dm^{-3} nitric acid scanned at a potential window of 0.8 – 1.9 – 0.3 V at a scan rate of 100 mV/s; (b) showing the cyclic voltammogram of a 500 µm gold electrode in 3 mol dm^{-3} nitric acid scanned at a potential window of 0.8 – 1.9 – 0.3 V_{SCE} at a scan rate of 100 mV/s containing a 0.62 mmol dm^{-3} Am spike

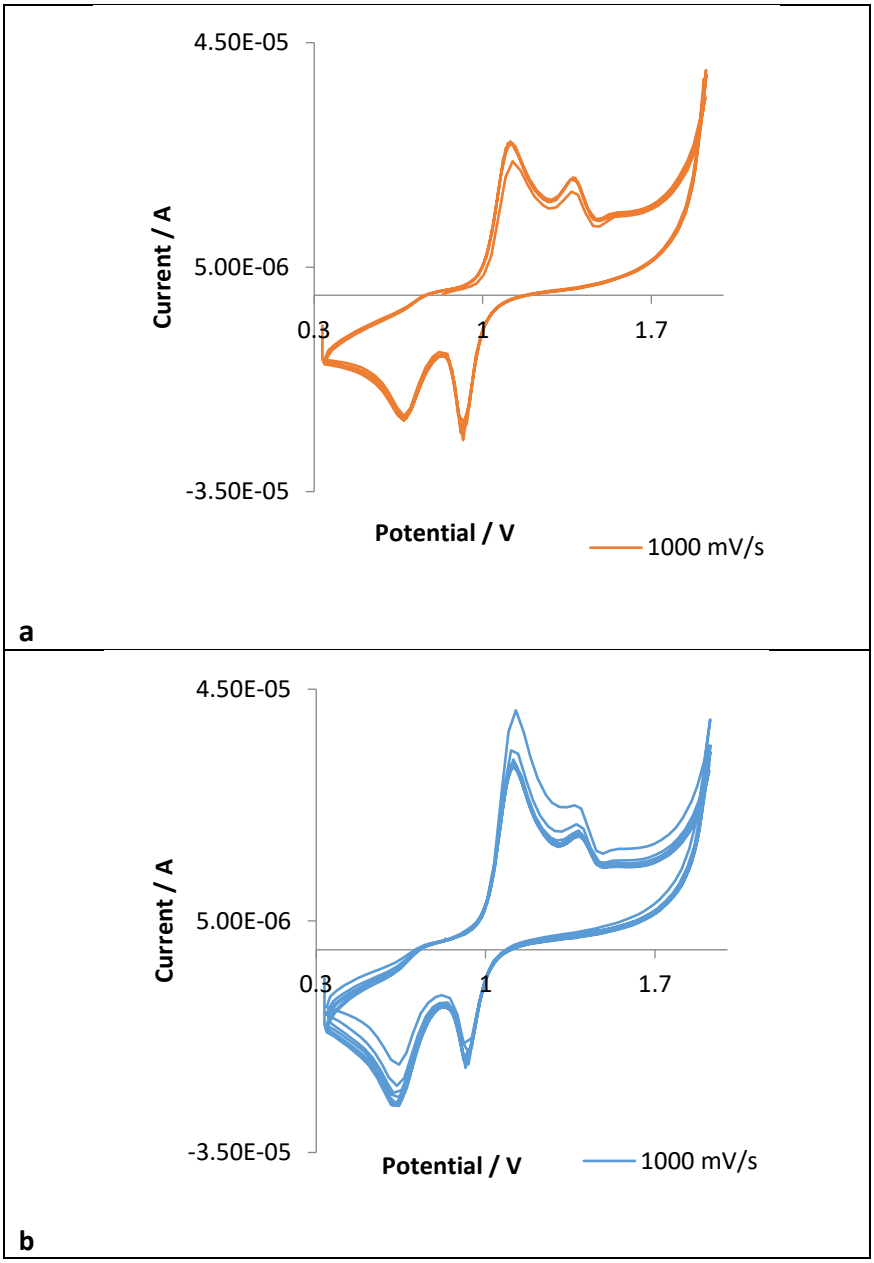

Figure 8-16a and 8-16b – (a) showing the cyclic voltammogram of a 500 µm gold electrode in 3 mol dm^{-3} nitric acid scanned at a potential window of 0.8 – 1.9 – 0.3 V at a scan rate of 1000 mV/s; (b) showing the cyclic voltammogram of a 500 µm gold electrode in 3 mol dm^{-3} nitric acid scanned at a potential window of 0.8 – 1.9 – 0.3 V_{SCE} at a scan rate of 1000 mV/s containing a 0.62 mmol dm^{-3} Am spike

In Figures 8-2 to 8-7, we looked at both the smallest and largest gold microelectrodes available to us in terms of its diameter. We first inspected the smallest available, namely a 10 µm electrode, as described above, followed by the largest available, the reason for choosing this was to maximise our chances of seeing gold oxidation electrochemistry if present – which has been under consideration as well as the Am(III) oxidations.

Following on from this, when inspecting the electrochemistry taking place in 3 mol dm^{-3} HNO_3, we also investigated the largest microdisc electrode available to us, as well as a 250 µm and 50 µm microdisc electrode, the results of which are presented in the cyclic voltammograms above.

From Figures 8-8 through to Figure 8-16, it can be seen that, at any one electrode diameter and scan rate, the CVs recorded in the presence of Am(III) are similar to those recorded in its absence. We attribute this result to increased susceptibility of Au to undergo oxidative dissolution at the higher nitric acid concentrations employed for this latter batch of experiments – a conclusion consistent with the work of Shackleford *et al*. as discussed above (15). The gold electrochemistry in this pH range then still prevents us from consulting the look-up tables provided by Myland, Oldham, Zoski and Bond. However, the similarity of the voltammograms recorded in the absence and presence of Am(III) no longer allow us to definitively propose that Am(III) electro-oxidation proceeds via an EC' process. That an EC' process may be occurring was originally proposed on the basis of the oxidation currents observed in Figures 8-2 to 8-4 being much larger than those predicted upon application of equation 8-1 to straightforward electro-oxidation of Am(III) by a three-electron transfer. On the basis of Figures 8-8 to 8-16, we can now see that this enhancement is almost certainly dominated by gold electrochemistry, making our conclusion that an EC' process is occurring much less certain.

Thus, in order to study the Am(III) oxidation in the removal of gold-related interferences, it is necessary to eliminate the electro-oxidative gold dissolution process that dominates the voltammagrams presented to this point. One means to do this would be to conduct the voltammetry under alkaline conditions where gold dissolution of the type described by Shackleford et al. may be expected to be suppressed (12). However, inspection of the Am-H_2O E_h-pH (Pourbaix) diagram shown in the figure below indicates that it will not be straightforward to conduct electrochemical studies of the Am(III)/Am(VI) couple in alkaline media, due to the Am(III) precipitating out of solution under such conditions. Experiments must therefore be restricted to acid media.

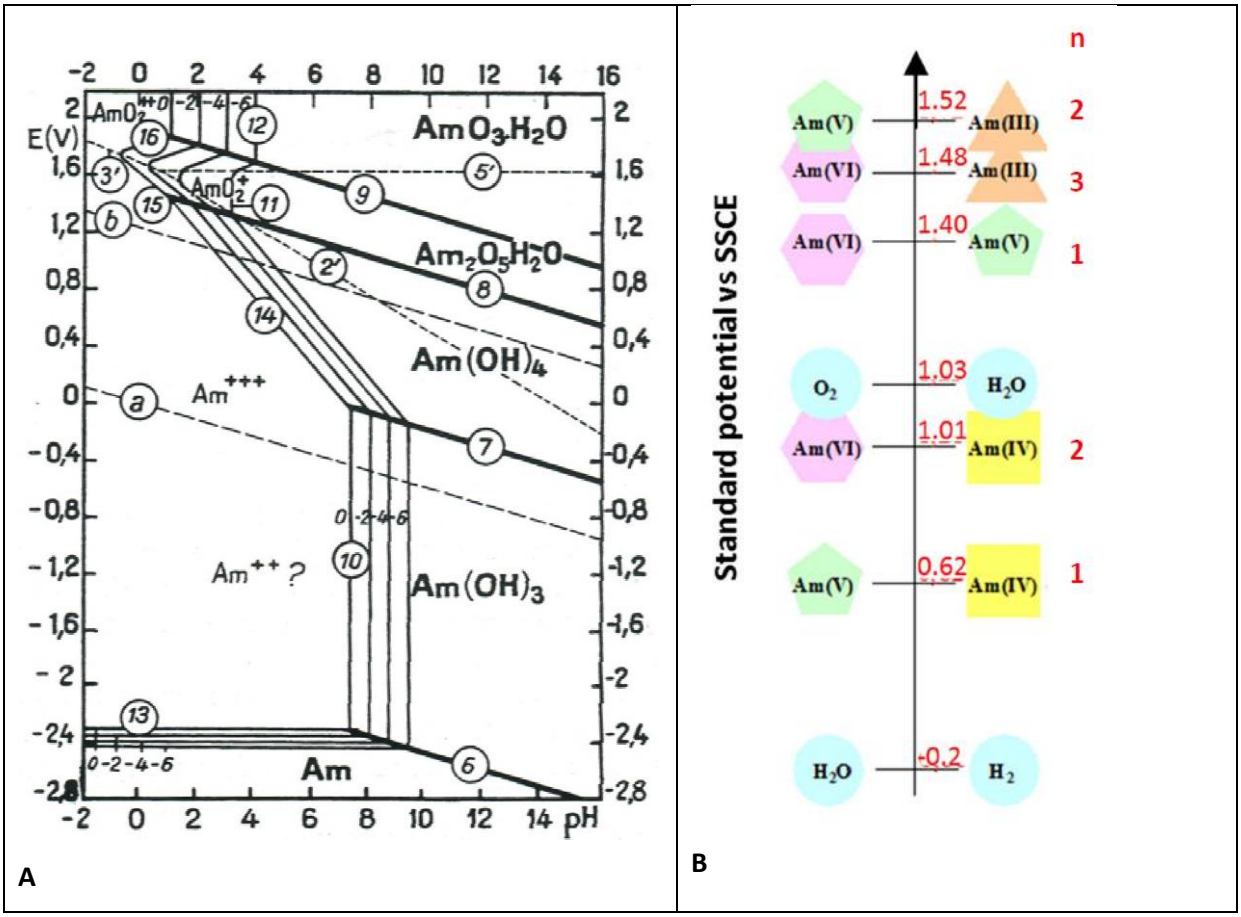

Figure 8-17a and 8-17b – (a) showing the Eh-pH (Pourbaix) diagram for the Am-H_2O system at 298 K (16); (b) showing the key redox potentials for the Am-H_2O system at pH 0, 298 K (17)

Further inspection of the key redox processes of Am(III) and (VI) as shown in Figure 8-17b also reveals an additional problem associated with using gold. The reactions of interest, Am(III)/(V) and Am(III)/(VI), occur between the potential range 1.4 to 1.6 V vs the saturated silver chloride reference electrode (SSCE) at pH 0. Thermodynamically, this potential range is collocated with that associated with oxygen evolution from the oxidation of water at pH 0. Thus, in order to assess potential interferences from this reaction, and to eliminate gold electrochemistry from our studies, a series of baseline voltammograms were recorded in acid media in the absence of Am(III) using alternative electrode materials as listed in Chapter 2. These are shown in Figures 8-18 to 8-20 below.

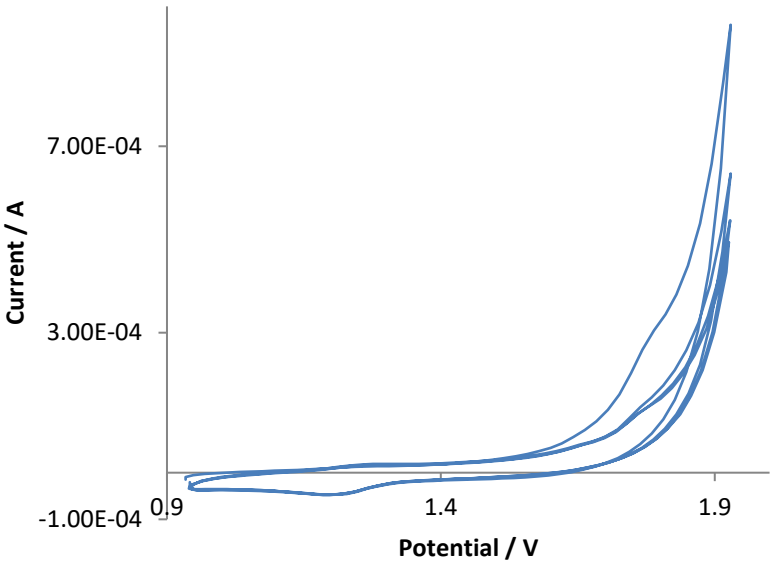

Figure 8-18 showing the cyclic voltammetry of a glassy carbon electrode in 1 mol dm^{-3} HNO_3, sparged with argon, potential range 0.9 – 1.9 V, scanned at 100 mV/s

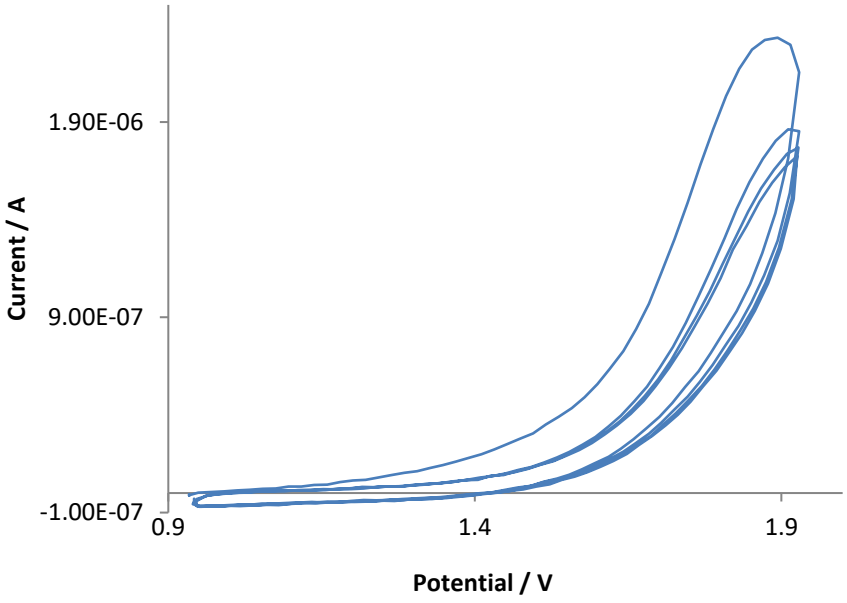

Figure 8-19 showing the cyclic voltammetry of a graphene ring nanoelectrode (GRiN) in 1 mol dm^{-3} HNO_3, sparged with argon, potential range 0.9 – 1.9 V, scanned at 100 mV/s

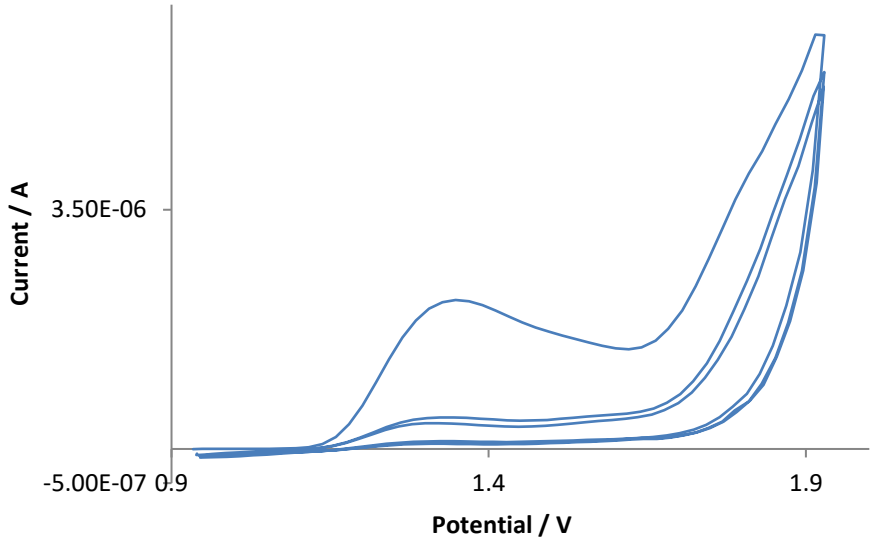

Figure 8-20 showing the cyclic voltammetry of a 100 µm Pt electrode in 1 mol dm^{-3} HNO_3, sparged with argon, potential range 0.9 – 1.9 V, scanned at 100 mV/s

Based on Figure 8-20, platinum was immediately discounted as a potential electrode material for the study of the Am(III)/Am(VI) and the Am(III)/Am(V) couple due to the presence of a large oxidative peak associated with platinum oxide generation at an applied potential of approximately 1.3 V_{SSCE}. The oxygen evolution wave was displaced to potentials greater than 1.6 V_{SSCE} on the glassy carbon and graphene electrodes. Thus, these electrodes were deemed worthy of preliminary investigation using Am(III) spiked solutions, the preparations of which are described in Chapter 2.

In the case of graphene, the voltammogram recorded in the presence of Am(III) was found to be identical to that recorded in its absence with very little, if any, current associated with Am(III) oxidation being resolvable out of the water oxidation wave (not shown). This is most likely due to the graphene electrode being a nano-ring electrode with a thickness in the sub-100 nm range – leading to faradaic currents from electroactive solutes in the electrolyte (as opposed to electrolyte decomposition) being of the order of no more than nanoamps, especially at the low Am(III) concentrations of 0.62 mmol dm^{-3} used here.

Thus, glassy carbon emerged as the electrode material of choice. Figure 8-21 shows a typical cyclic voltammogram recorded from a pH 0 nitric acid solution containing 0.62 mmol dm^{-3} Am(II) using the glassy carbon electrode of Figure 8-18. Here, we are able to electrochemically detect the Am(VI) state.

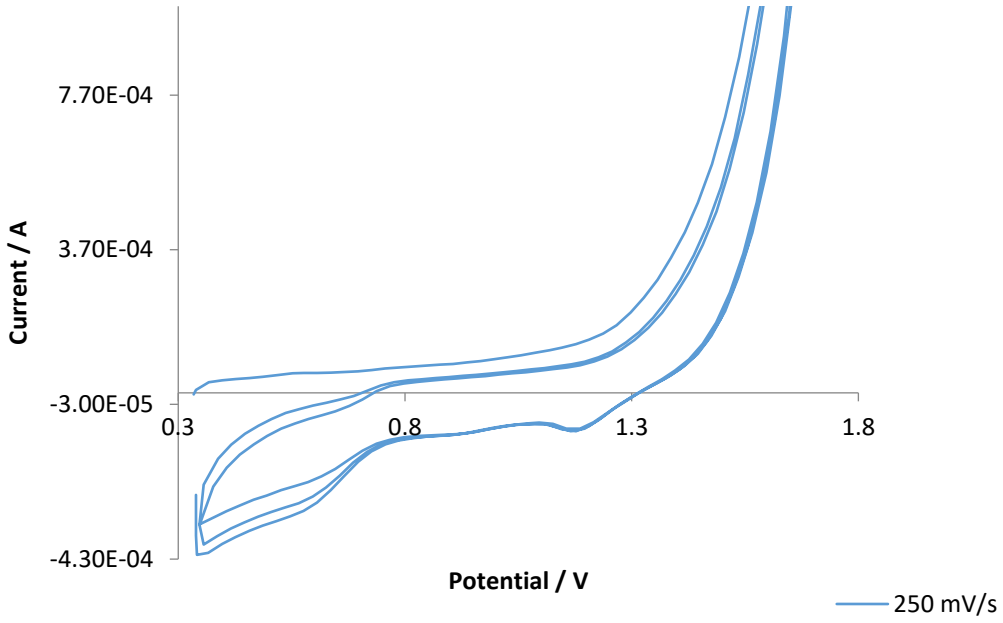

Figure 8-21 showing the cyclic voltammetry of a glassy carbon electrode in 1 mol dm^{-3} HNO_3 spiked with Am, sparged with argon, potential range 0.3 – 1.7 V, scan rate 250 mV/s

As in Figure 8-18, it can be seen here that the oxygen evolution wave has been displaced from an expected onset of approximately 1.1 V to 1.4 V. It therefore still masks a current associated with Am(III) oxidation, either to Am(V) or Am(VI), expected at + 1.52 and + 1.48 V_{SSCE} respectively, according to Figure 8-17b. Inspection of the voltammograms recorded in the presence of Am(III) shown in Figure 8-21 reveal the presence of reduction peaks on the return sweep that are not present on the corresponding part of the voltammograms recorded in the absence of Am(III) in Figure 8-18. It must be noted here that the absence of a clear oxidation peak with an onset at 0.9 V as seen in Figures 8-2b, 8-3b and 8-4b indicates that the peaks in those earlier figures are almost certainly due to gold. This suggests that the actual Am(III) oxidation wave is 'hidden' in the oxygen evolution wave. This, and the fact that this carbon electrode is not a microdisc electrode means that it is not possible to carry out an analysis in accordance with the theory of Myland *et al*. to determine k^0 for the electro-oxidation of Am(III).

However, it is possible to gain some insights into the fundamental electrochemistry of Am on carbon electrodes by analysis of the reduction peaks observed during the reverse sweep. For the peak seen at approximately + 1.2 V_{SSCE} in the reverse sweep, the peak current is found to be linearly proportional to potential sweep rate (not shown). This indicates that the reduction associated with

this peak is a surface controlled process. Comparison with Figure 8-19 suggests that this feature is then associated with some intrinsic surface electrochemistry of carbon in this electrolyte.

A substantial reduction wave is also seen at approximately + 0.65 V_{SSCE} in Figure 8-21. Comparison with Figure 8-18 suggests that this is due to the reduction of Am(V) to form Am(IV). Randles-Sevick analysis on this peak (not shown) indicates that the peak current value is linearly proportional to the square root of the scan rate, suggesting that this is derived from the reduction of a solution based species i.e. AmO_2^+.

Further analysis of the peak height as a function of potential sweep rate using models developed by Nicholson and Shain for non-chemically coupled electrochemical processes i.e. processes that do not involve an EC' process (12) reveals the size of the feature at + 0.65 V_{SSCE} is consistent with a local concentration of Am(V) that reflects stoichiometric oxidation of Am(III) during the forward going sweep. These observations are then consistent with the following sequence of electrochemical reactions:

In the forward going sweep we observe the oxidation of Am(III)/Am^{3+} to Am(VI) / AmO_2^{2+} at + 1.48 V_{SSCE}, in part masked by the O_2 evolution wave.

During the reverse sweep, stoichiometric reduction of Am(VI) / AmO_2^{2+} generated in the forward going sweep to Am(V) / AmO_2^+ occurs at + 1.4 V, a process that is expected to be kinetically facile due to the comparatively low charge density on both cations and the lack of any requirement for metal-oxygen bond formation or fracture. This reduction process can be observed as a slight inflection in the current during the reverse sweep immediately before the peak at + 1.2 V, said peak associated with carbon's intrinsic surface electrochemistry.

Also in the reverse sweep, we observe that the Am(V) / AmO_2^+ generated as a result of the Am(VI) / AmO_2^{2+} reduction detailed above, is further reduced to Am(IV) at ~+0.65V.

From this sequence of reactions, it can be concluded that it is straightforward to oxidise Am(III) through to Am(VI) on carbon electrodes, an observation that has important ramifications for the control of the Am(VI) valence state during advanced separations schemes for Am. Work conducted by Mincher *et al*.(18) suggests that Am(VI) generated by sodium bismuthate is stable in aqueous media in the absence of any readily oxidisable organic species or corrodable steel surfaces. Our work

similarly indicates that the higher oxidation states of Am may have a useful lifetime when generated electrochemically using carbon electrodes. Taken together, these observations suggest that reagentless, electrochemical generation of Am(VI) may be feasible as a pre-cursor to high separation factor Am(VI) extraction from reprocessing raffinates using e.g. diamyl amylphosphonate (DAAP) / dodecane as the extractant system.

The original purpose of this work however, was to assess the potential for Am to affect the corrosion behaviour of process steels, either as a potential accelerator or inhibitor of corrosion. This question originally arose based on some work by Kato *et al.* (19), who have shown that the facile and reversible oxidation of Np(V) to Np(VI) cyclically / catalytically promotes the corrosion of 310Nb steel. This is due to the fact that the potential for Np(V) to Np(VI) oxidation lies at 0.95 V_{SSCE}, providing a means by which the corrosion potential of the steel can be driven into the near-transpassive region via varied potential control. Previously, we have conducted non-active electrochemical studies of 316 stainless steels at nitric acid concentrations typical of reprocessing streams and found that the corrosion potential varies with varying concentrations of nitric acid, up to 0.75 V_{SSCE} at a 35 % nitric acid concentration (equivalent to 8 mol dm^{-3} nitric acid) (20). Transpassivity in this system occurs at approximately 1 V. The oxidation of Am(III) to Am(VI) occurs at + 1.4 V_{SSCE} (Figures 8-17b and 8-21), indicating that Am(VI), if accessed, could potentially drive the corrosion potential into the transpassive region by an Am(V)/Am(VI) catalytic cycle of the type observed with Np. The question to be addressed here is therefore at which point the presence of Am(III) can be driven to Am(VI) in concentrated nitric acid and so trigger the expected oxidation of Am(III) to Am(VI), and, subsequently promote the corrosion of the steel. This will be further explored in Section 8.3 below.

8.3 Results & Discussion – Part 2

As aforementioned, the original purpose of this work was to assess the potential for Am to affect the corrosion behaviour of process steels, either as a potential accelerator or inhibitor of corrosion. In this section we will investigate whether the detected Am from Section 8.2 influences the corrosion behaviour of commonly used steels in the same way that Np promotes the corrosion of steel in 3 mol dm^{-3} HNO_3, as observed by Kato *et al.*(19).

From the results of Figure 8-21, it is possible to conclude that, while it is possible to oxidise Am(III) to Am(VI) using a carbon electrode, this oxidation is not without the O_2 evolution wave. This result would therefore confirm that Am(VI) will not be accessed from Am(III) under the redox conditions that obtain during conventional solvent extraction based reprocessing schemes e.g. in PUREX, even during maloperation (for example, nitric acid concentration excursions up to 8 mol dm^{-3}), as the aqueous matrix will be attacked first. Am(III) may therefore be discounted as a corrosion accelerator on steels.

However, Am(III) may affect the growth of the passive layers formed on the steels commonly used in reprocessing plants, potentially incorporating into those layers and influencing their corrosion behaviour e.g. by the provision of pitting sites. In order to do determine if this is the case, we will first inspect the linear sweep voltammetry recorded in the presence and absence of Am (the concentration of Am being 6.22 x 10^{-4} mol dm^{-3}, see Section 8.2.1), to establish whether we observe any differences in the corrosion behaviour. Below we present a series of LSVs recorded in the absence and presence of Am, in 1 mol dm^{-3} HNO_3 using various steels commonly used throughout the nuclear fuel cycle. The steels used for this study are shown in Table 8-1 below.

Steel
304L Stainless steel
316L Stainless steel
347L Stainless steel

Table 8-1 Showing types of steels used

The reasons that we have chosen the above steels for this study are as follows:

304L stainless steel is predominantly used in the fabrication vessels, equipment as well as tank piping at THORP Sellafield, at HNO_3 concentrations lower than or equal to 8 mol dm^{-3} (4). 316L stainless steel is mainly used for the construction of various process vessels and pipe work containing concentrations of less than 3 mol dm^{-3} HNO_3. 316L stainless steel is also used in liquor storage cans as well as some outdoor plants areas at the THORP facility that may be affected by the saline spray from the Cumbrian coastline. The added Mo in the 316 stainless steel is known to be resistant to pitting corrosion from Cl^-, which is prevalent in the saline spray and surrounding environment (4). 347L stainless steel is used in areas of high HNO_3 concentrations at THORP, such as Evaporator C. Evaporator C concentrates Highly Active Aqueous Raffinate (HAAR) from a concentration of approximately 3 mol dm^{-3} to approximately 8 mol dm^{-3} HNO_3 (4).

Although not many studies exist in the literature on the solution potential that obtains in aqueous reprocessing streams, it would appear that the solution potential may be up to 1.15 V, depending on certain variables such as which actinide species are present, as well as acidity and temperature (4) (19) (21).

Studies conducted by Williamson however, indicate that at HNO_3 concentrations lower than 1 mol dm^{-3}, the above mentioned potentials reside in the transpassive region on the 316L stainless steel, the onset of transpassivity being substantially lower, at approximately 0.8 V (4). Potentials that are positive of this value may therefore constitute maloperation conditions. As the aim of this study is, in the first instance, to investigate the behaviour of these steels under conventional safe operational conditions, our switching potentials in the following experiments have been restricted to values negative of the onset of transpassivity, switching at 0.5 V.

Below is a series of LSVs of the various steels listed above, recorded in 1 mol dm^{-3} in the absence of presence of americium.

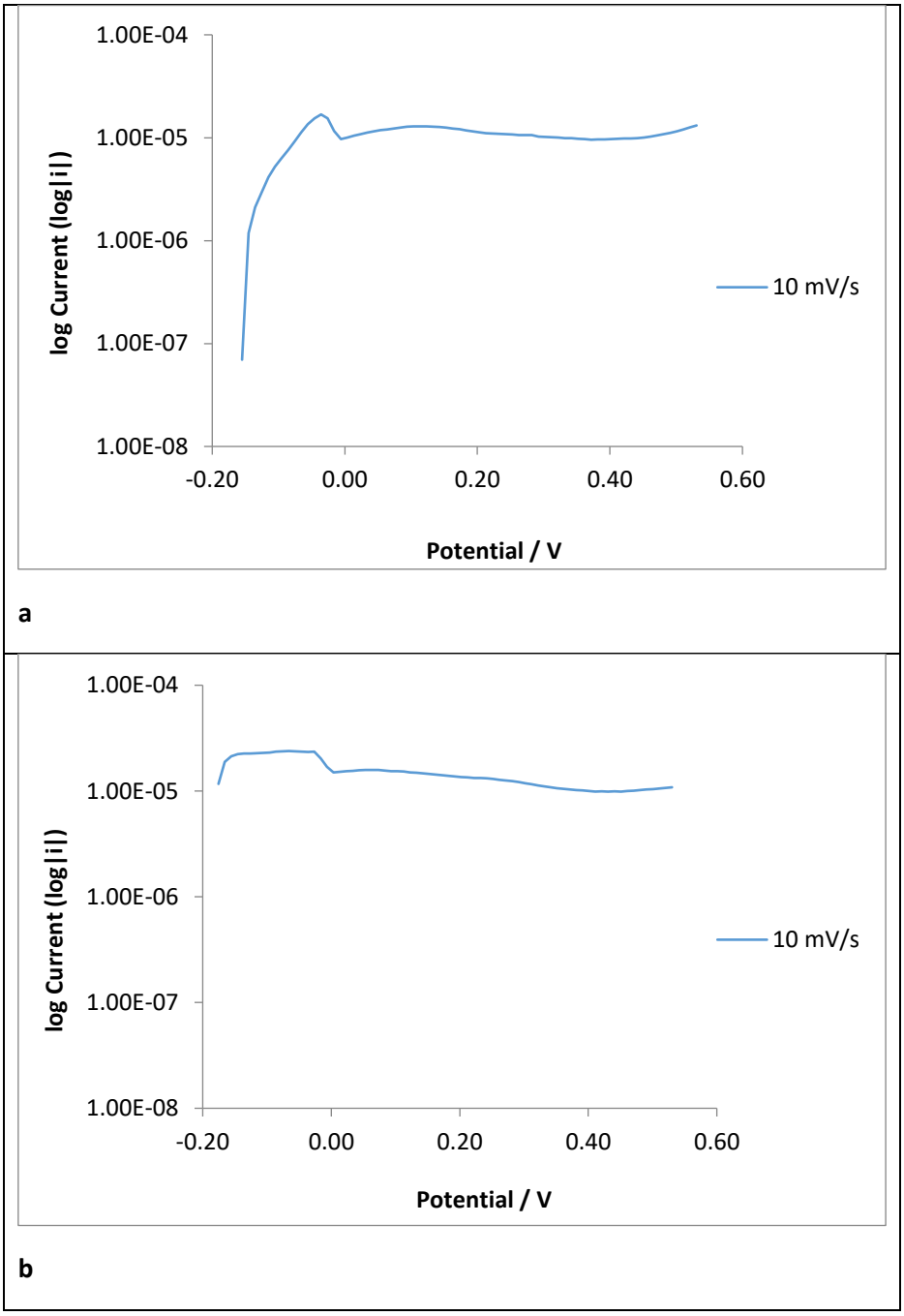

Figure 8-22 a & b – (a) showing the linear sweep voltammetry of 304L steel in 1 mol dm^{-3} HNO_3 at a scan rate of 10 mV/s; (b) showing the linear sweep voltammetry of 304L steel in 1 mol dm^{-3} HNO_3 at a scan rate of 10 mV/s containing a 0.62 mmol dm^{-3} Am spike

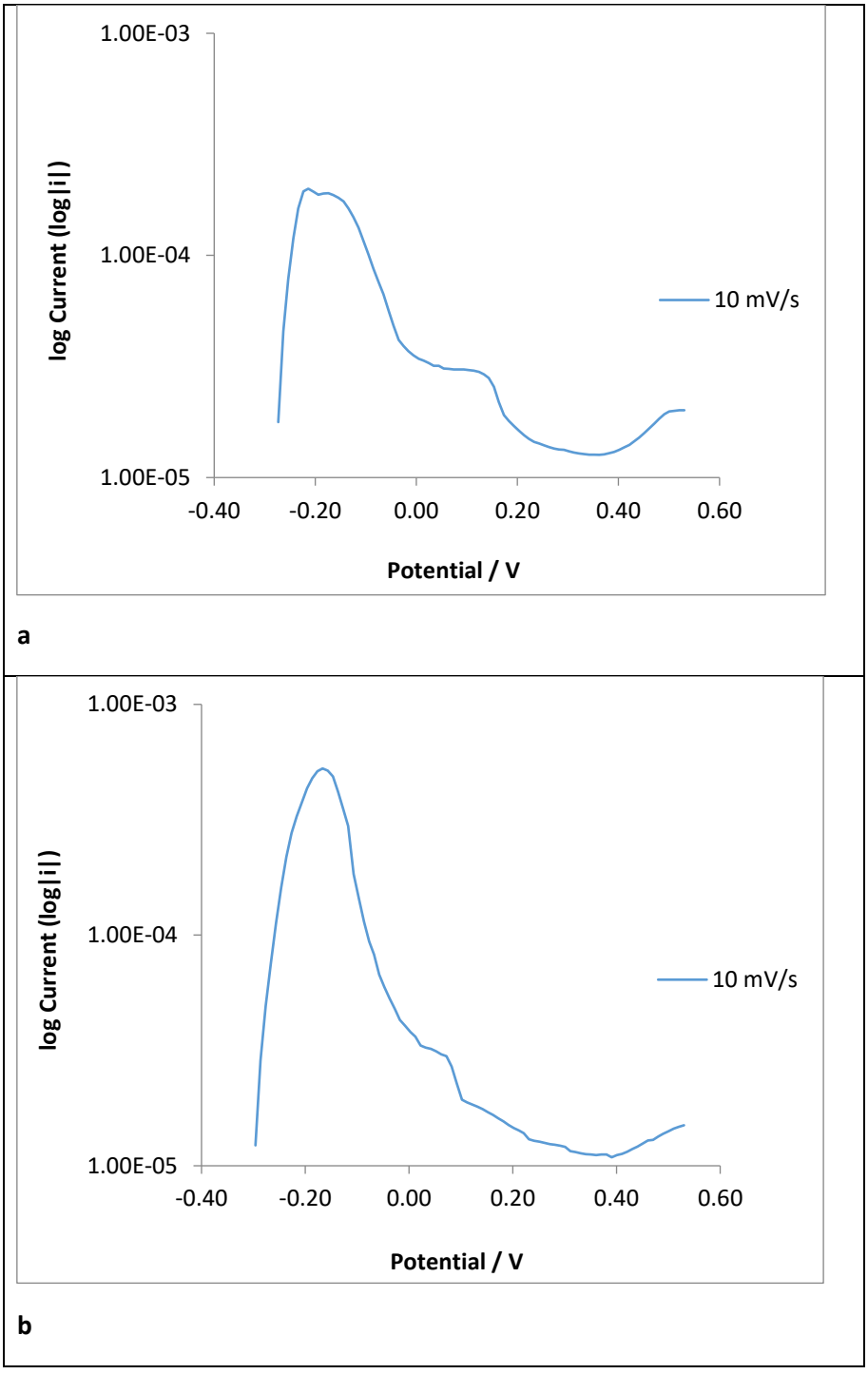

Figure 8-23 a & b – (a) showing the linear sweep voltammetry of 316L steel in 1 mol dm^{-3} HNO_3 at a scan rate of 10 mV/s; (b) showing the linear sweep voltammetry of 316L steel in 1 mol dm^{-3} HNO_3 at a scan rate of 10 mV/s containing a 0.62 mmol dm^{-3} Am spike

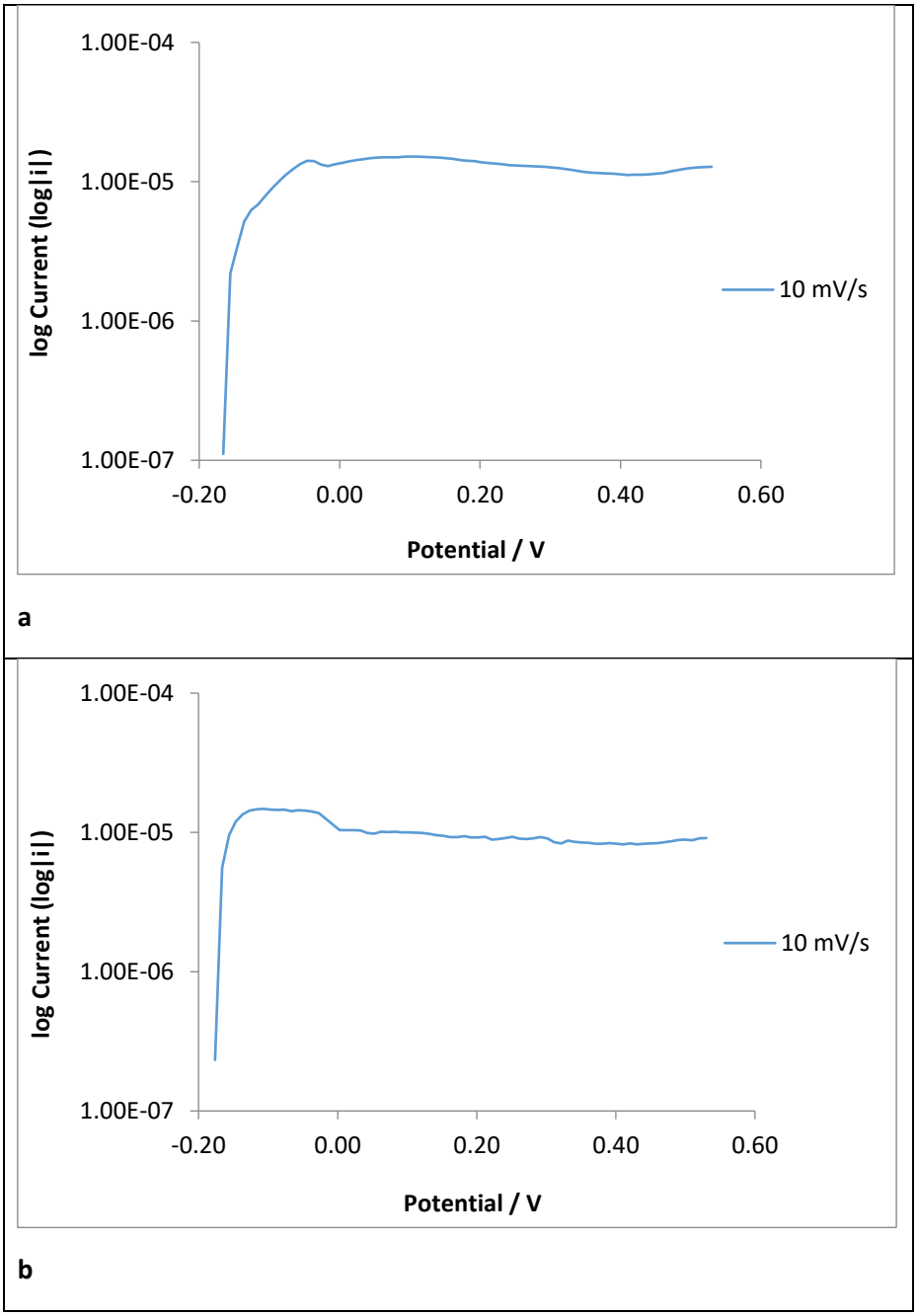

Figure 8-24 a & b – (a) showing the linear sweep voltammetry of 347L steel in 1 mol dm^{-3} HNO_3 at a scan rate of 10 mV/s; (b) showing the linear sweep voltammetry of 347L steel in 1 mol dm^{-3} HNO_3 at a scan rate of 10 mV/s containing a 0.62 mmol dm^{-3} Am spike

The above presented series of LSVs, which focus on the passive region of the steels, and thus the growth of the passive oxide layer, show little or no change upon the introduction of americium. This would suggest that americium may not have an effect on the passive film composition. Due to radiochemical laboratory access time constraints, we were unable to study the effects of carrying out the same experiments in 3 mol dm^{-3} HNO_3. We were however, able to measure EIS data for the three steel samples in the absence and presence of americium in 1 mol dm^{-3} HNO_3, the resulting Nyquist plots of which, should provide more detailed insight into the results of Figures 8-22 to 8-24 through provision of resistance and capacitance data related to the steel's passive layer. Using the Nyquist plots we can qualitatively evaluate whether any Am(III) is incorporated into the oxide layers whose growth is promoted in the passive and pre-transpassive regions of the LSVs. Incorporation of americium would present itself in the Nyquists by either changing the R or C of the so-formed oxide layers.

If we are able to observe americium incorporation, this would then mean that, Am(III), whilst electrochemically inactive under the conditions studied, may incorporate into the passive layers, potentially leading to a decontamination problem during the decommissioning of reprocessing plant, pipework and tanks. We shall return to this point later on.

The equivalent circuit used to fit the impedance data is shown in Figure 8-25, the associated total impedance being given by equation 8-3. Here, we have used a simple model to characterise the interface between the steel electrode and the solution during a faradaic process – which is known as a Randles cell (4).

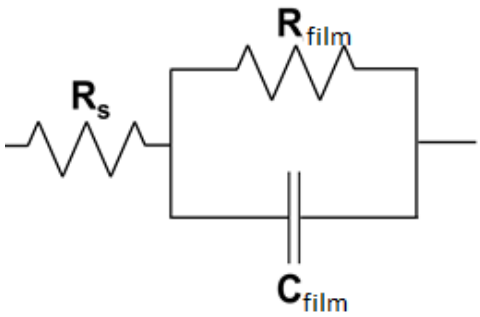

Figure 8-25 showing the equivalent circuit used to fit measured impedance data where R_S is the solution resistance, R_{film} is the passive film resistance, and C_{film} is the passive film capacitance

Components at the electrode-electrolyte interface are modelled in parallel due to the total current being the sum of the individual contributions of the components C_{film} and R_{film} as shown above (4).

Due to the fact that all current must pass through the solution resistance, $R_{solution}$ is inserted into the equivalent circuit in series to represent this effect (4).

$$Z_{eq} = R_s + \frac{1}{i\omega C_{film} + \frac{1}{R_{film}}}$$

Equation 8-3

When the resistor and capacitor (R_{film} and C_{film}) are connected in parallel as shown in the Randels cell in Figure 8-25, the current that is applied chooses the path of the lowest impedance (22). Due to the impedance of the capacitor being frequency-dependant, the path that the current chooses will change. This means that at high frequencies, the impedance of the capacitor will be low - the majority of the current flowing through the capacitor (22). As we decrease the frequency, the impedance of the capacitor will increase, meaning that a higher concentration of current will flow through the resistor. When this happens and the majority of the current is flowing through the resistor, the total imaginary impedance will decrease, as the real impedance increases. Under these conditions, an ideal capacitor in parallel with a resistor leads to a semi-circle in the Nyquist plot (22). At the highest point of the semi-circle, the capacitance of the film can be calculated using the frequency at the arc of the semi-circle (f_{max}) inserted in to the following equation (22):

$$C_{film} = 1/R_{film}2\pi f_{max}$$

Equation 8-4

The resulting Nyquist plots – the impedance of which have been recorded at a potential of 0.5 V_{SSCE} (representative of the passive region of the steels under investigation (20)), are presented below.

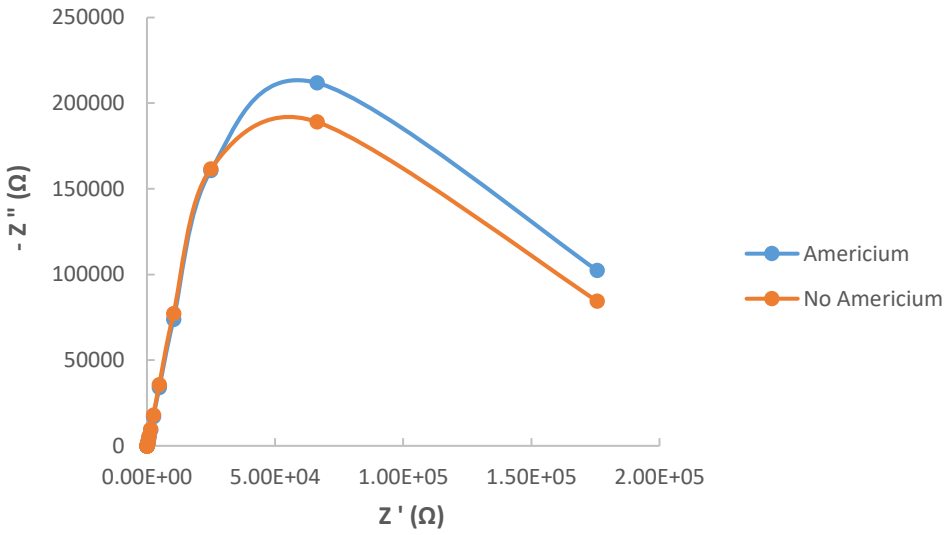

Figure 8-26 showing Nyquist plots of 304L stainless steel in 1 mol dm^{-3} HNO_3 in the absence and presence of Am, both recorded at a potential of 0.5 V_{SSCE}

In the Nyquist plots above, we can see that both plots measured in the absence and presence of americium are characterised by the presence of single incomplete semi-circles which indicate that similar corrosion mechanisms are occurring in both systems (23). We can see however, that for the 304L steel, americium does indeed influence the impedance behaviour of the film, most likely by incorporation in to the passive oxide layer. The fact that the height of the arc and the extrapolated point at which it intercepts the Z' axis at low frequency increase in the presence of americium indicate that the passive layer resistance has increased, most likely by americium incorporation into the passive oxide layer. Referring to Table 8-2 below, which shows the values for the equivalent circuit elements used to fit the data of Figure 8-26 to 8-28, we can see that as R_{film} has indeed increased in the presence of americium, so does C_{film}. An increase in the film resistance would indicate the thickening of the passive oxide layer, which would be evidenced by a decrease in the capacitance of the film (24). The increased film capacitance in the presence of americium observed here however is indicative of the fact that the thickness of the film is not increasing; rather, it is apparently decreasing (4). This apparent contradiction based upon simple consideration of layer thickness alone then indicates that the electrical properties of the films are different i.e. the Am(III) has, in some manner, been incorporated into the film generated in the presence of Am(III) ions.

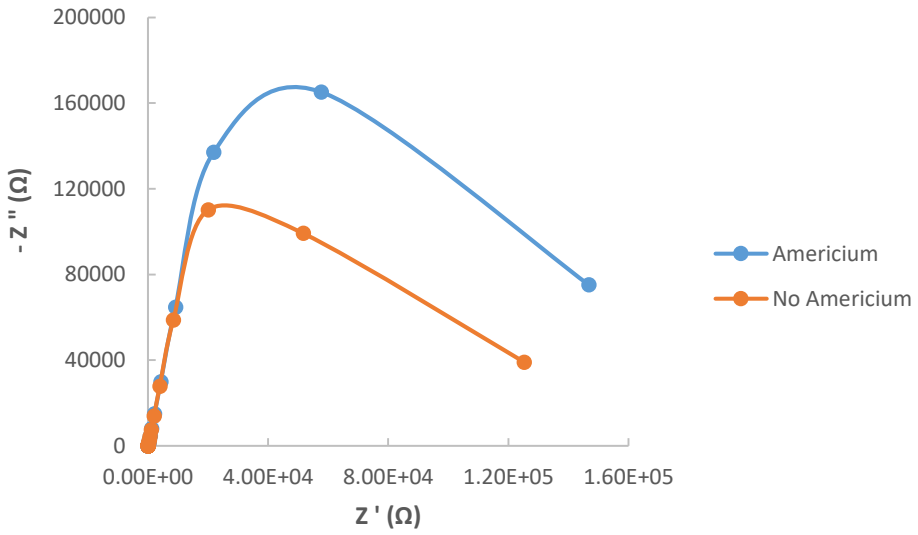

Figure 8-27 showing Nyquist plots of 316L stainless steel in 1 mol dm^{-3} HNO_3 in the absence and presence of Am, both recorded at a potential of 0.5 V_{SSCE}

Looking at the impedance for the 316L stainless steel, we can once again see the presence of unfinished semi-circles in both the presence and absence of americium, indicating that similar corrosion mechanisms are taking place (23). It should be noted here that an increase in the semi-circle arc is indicative of an increase in passive film stability, whilst a decrease in semi-circle radius is indicative of a decrease in the resistance of the passive film (23). Thus it can be seen that the presence of americium has increased the resistance of the passive layer, which is especially evident at medium and low frequencies. The incorporation of americium is more evident in the 316L steel when compared to the 304L stainless steel. The increase in film resistance is evidenced by the R_{film} and C_{film} values given in Table 8-2 below. In the presence of americium, we observe an increase in the resistance of the film, whilst simultaneously observing a decrease in the film capacitance. In contrast to the results seen with 304L above, the behaviour of the film resistance and capacitance for 316L is in more straightforward accordance with the thickening of the passive film, indicating that americium is in fact incorporating in to the passive oxide layer (24) – although on the basis of the results recorded from the 304L sample, some modification to the electrical properties of the film cannot be completely excluded.

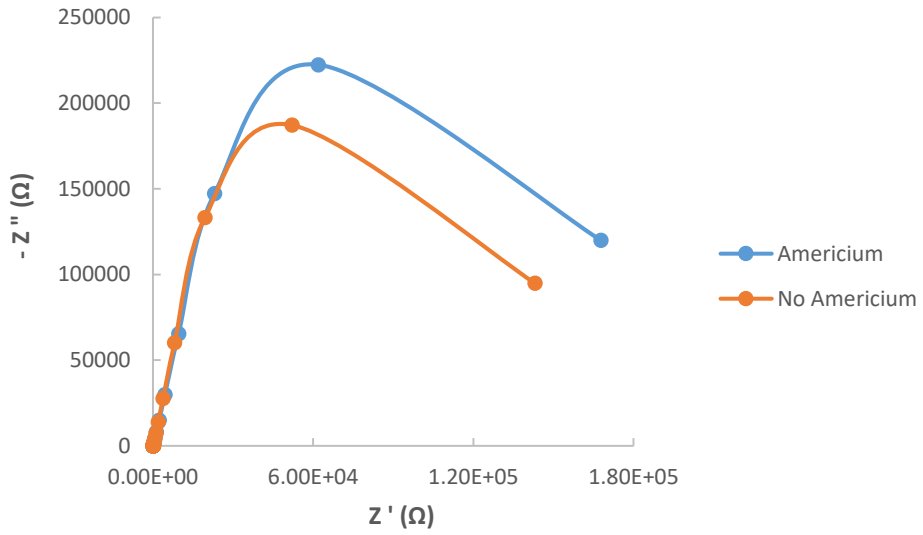

Figure 8-28 showing Nyquist plots of 347L stainless steel in 1 mol dm^{-3} HNO_3 in the absence and presence of Am, both recorded at a potential of 0.5 V_{SSCE}

When looking at the impedance of the 347L stainless steel, we can see here again the presence of unfinished semi-circles in both the presence and absence of americium, indicating that similar corrosion mechanisms are taking place (23). As described above, an increase in the semi-circle arc is indicative of an increase in passive film stability, whilst a decrease in semi-circle radius is indicative of a decrease in the resistance of the passive film (23). Thus it can once again be seen that the presence of americium has increased the resistance of the passive layer, which is especially evident at medium and low frequencies. As seen in Figure 8-27 above for the 316L steel, the incorporation of americium is more evident here when compared to the 304L stainless steel. The increase in film resistance is evidenced by the R_{film} and C_{film} values given in Table 8-2 below. As for the 316L steel, in the presence of americium, we observe an increase in the resistance of the film, whilst simultaneously observing a decrease in the film capacitance. This is in accordance with the thickening of the passive film, indicating that americium is in fact incorporating in to the passive oxide layer (24).

Below is a table summarising the EIS fitted values used for the various components outlined in the equivalent circuit of Figure 8-25 for our steel samples.

Sample	$R_{Solution}$ (Ω)	R_{Film} (kΩ)	C_{Film} (µF)
304	6.6	403.5	5.44
304 americium	14.38	435.4	5.74
316	5.03	240	6.97
316 americium	10.35	348.8	6.50
347	17.66	379.4	7.07
347 americium	1.98	446.2	6.54

Table 8-2 showing EIS fitted values for 304L, 316L and 347L stainless steel in the absence and presence of americium measured in a 1 mol dm^{-3} HNO_3 solution

From the EIS fitted data presented in Table 8-2 above we can see that as expected, as the passive film resistance increases in the presence of americium for both the 316L and 347L steels, the film capacitance decreases. This is in accordance with the thickening of the passive film, indicating that americium is in fact incorporating in to the passive oxide layer (24). Curiously however, for the 304L steel, as the passive film resistance increases in the presence of americium, so does the passive film capacitance. As described above, this apparent contradiction based upon simple consideration of layer thickness alone then indicates that the electrical properties of the films are different - the Am(III) has, in some manner, been incorporated into the film generated in the presence of Am(III) ions. As described above, it must be noted that based on the results recorded for the 304L sample, some modification to the electrical properties of the films for the 316L and 347L steels cannot be completely excluded.

Turning our attention back to the three LSVs presented herein (Figures 8-22 to 8-24) we can see that americium does in fact incorporate in to the passive layer for all three steel samples. This may have important ramifications for decommissioning in the future. Whilst it may be advantageous to have the Am incorporate in to the passive layer, obtaining to a higher layer resistance and thus affording a higher level of protection for the steel, the embedding of americium into the steel structure would pose a greater disadvantage, meaning that an attritive decontamination technique may be needed to subsequently remove the americium.

We shall now turn our attention to SEM images taken of the steel samples in order to spectroscopically analyse the effect that the americium has had on the steel surfaces.

Below are SEM images of as-received polished steel samples taken before exposure to americium containing solutions, along with the SEM images of the steel samples after exposure to americium containing solutions. The steel samples were exposed to americium containing nitric acid solutions during impedance experiments presented in Figures 8-26 to 8-28, after which SEM images of the exposed steel samples were taken. The images are presented in Figures 8-29 to 8-31 below.

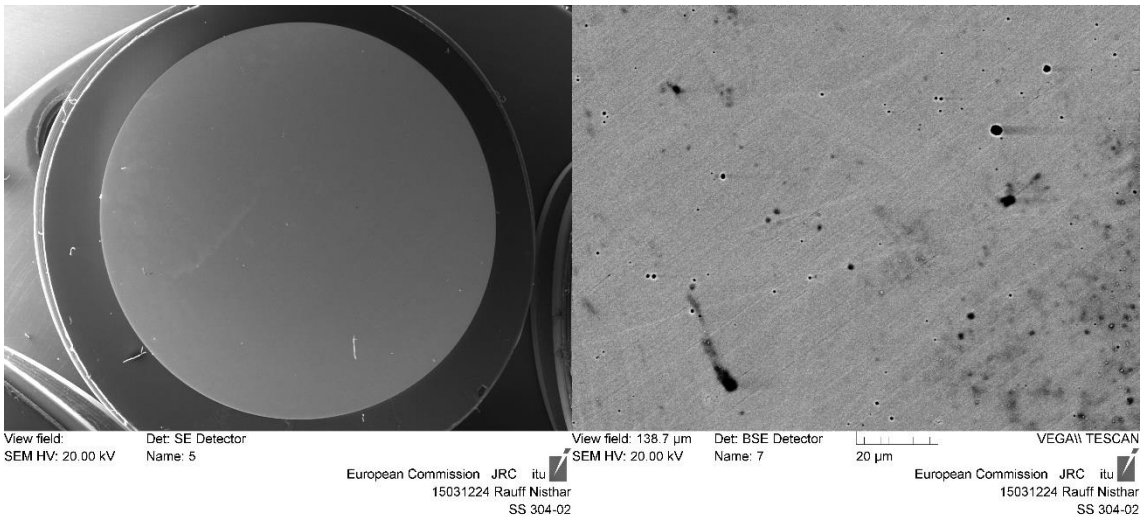

Figure 8-29a showing as-received SEM images of 304L stainless steel at 'fish eye view' and x 2000 magnification with an SE and BSE detector, respectively

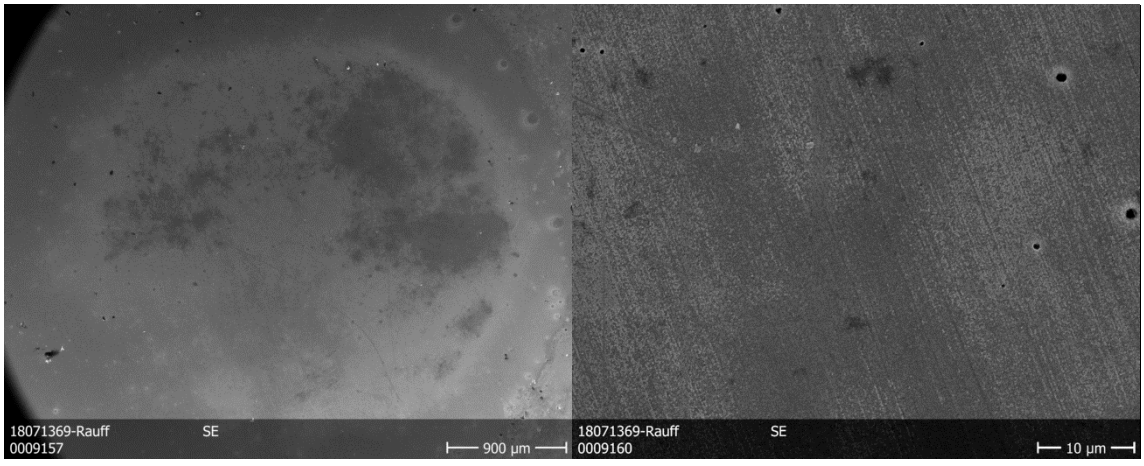

Figure 8-29b showing SEM images of 304L stainless steel after exposure to a 150 ppm Am containing solution at x 30 and x 2000 magnifications with an SE detector, respectively

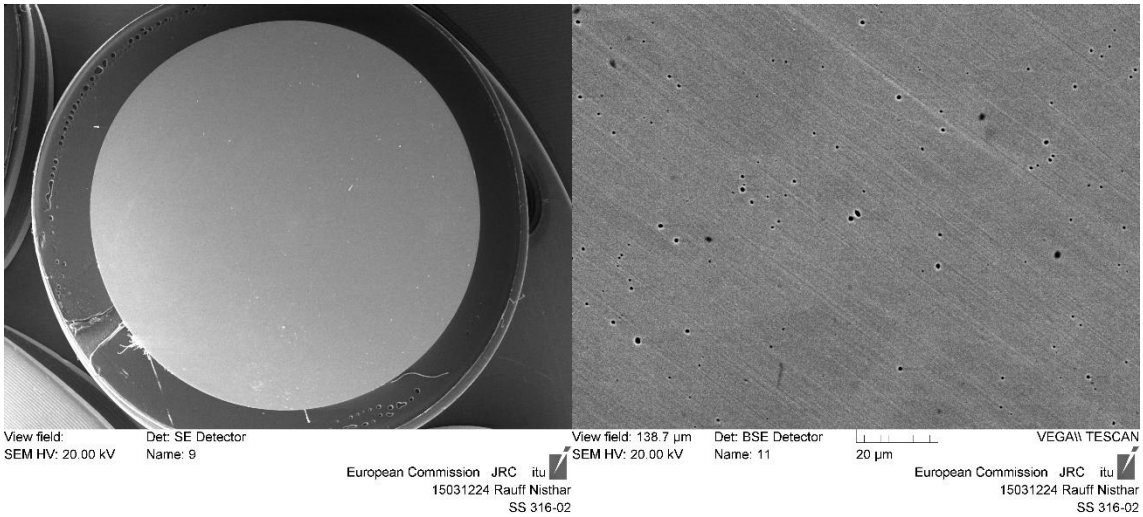

Figure 8-30a showing as-received SEM images of 316L stainless steel at 'fish eye view' and x 2000 magnifications with an SE and BSE detector, respectively

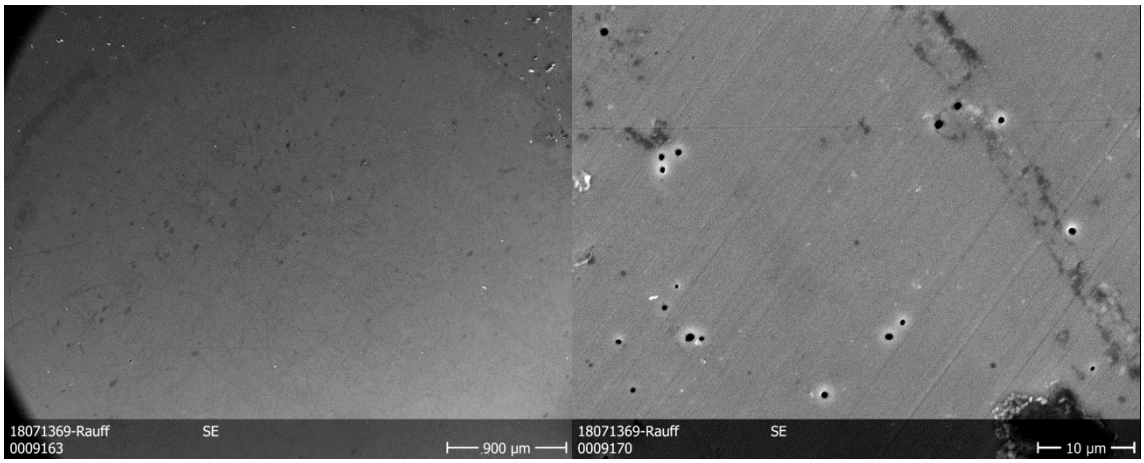

Figure 8-30b showing SEM images of 316L stainless steel after exposure to a 150 ppm Am containing solution at x 30 and x 2000 magnifications with an SE detector, respectively

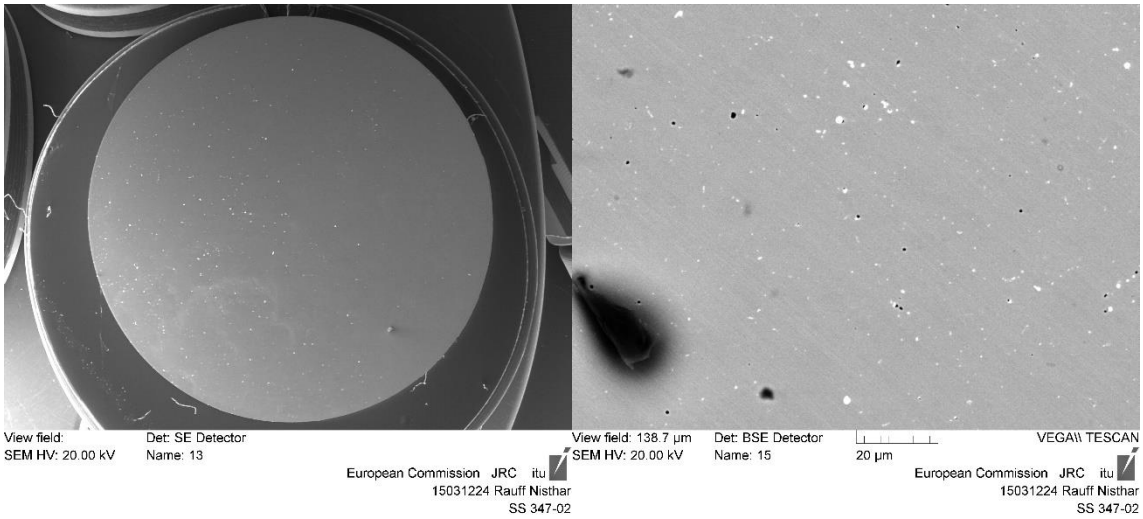

Figure 8-31a showing as-received SEM images of 347L stainless steel at 'fish eye view' and x 2000 magnifications with an SE and BSE detector, respectively

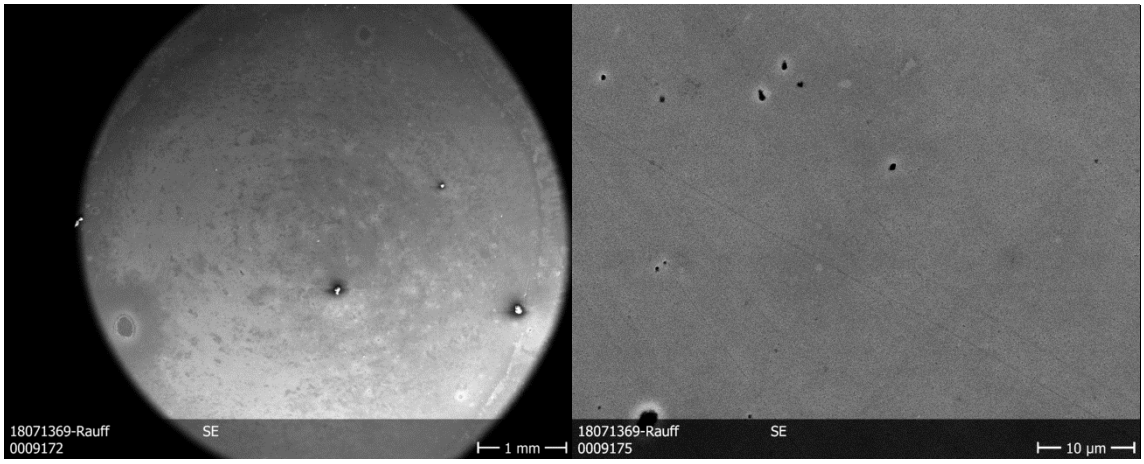

Figure 8-31b showing SEM images of 347L stainless steel after exposure to a 150 ppm Am containing solution at x 30 and x 2000 magnifications with an SE detector, respectively

In Figures 8-29 through to 8-31, SEM images taken with a BSE detector as well as an SE detector are presented. The advantage of using a BSE detector over an SE detector is that the topography of the surface can be analysed (25). For example, pores that appear on the surface are more prominently seen with a BSE detector. However, some images taken with an SE detector are presented here due to the fact that an SE detector is better at showing compositional contrast (25).

From the SEM and EDX data (EDX data not shown), it appears as though no americium has incorporated into the passive oxide layers of the three steel samples. This is contrary to the LSV and impedance data shown, which both strongly suggest that americium has in fact incorporated into the passive oxide layers of the steel surfaces. One reason that the incorporation of americium does not show in the EDX data may be due to the fact that an EDX only has a penetration depth of

approximately 2 µm (26), meaning that any signal received is obscured by the presence of the elements in higher concentrations.

8.4 Conclusions

The first section of this chapter had the aim of establishing the standard electrochemical rate constant k^0 for the Am(III) oxidation reaction by using the method of Myland, Oldham, Zoski and Bond (6) (7). This involved the analysis of steady state voltammograms recorded on microelectrodes on a range of radii. From this experimental work, we have made the following observations:

At a concentration of 1 mol dm^{-3} HNO_3, cyclic voltammetry with a gold microdisc electrode at various sizes revealed that the measurements were heavily convoluted with gold oxidation. This convolution meant that it was not possible to clearly extract the dependence of the Am(III) oxidation process on electrode radii from the cyclic voltammograms measured in 1 mol dm^{-3} HNO_3. Neither was it possible to conduct an analysis of the recorded voltammograms in accordance with the kinetic models of the EC' process described by Nicholson and Shain (12).

At a concentration of 3 mol dm^{-3} HNO_3, cyclic voltammetry with a gold microdisc electrode at various sizes revealed that at any one electrode diameter and scan rate, the CVs recorded in the presence of Am(III) are similar to those recorded in the absence. We attribute this result to increased susceptibility of Au to undergo oxidative dissolution at the higher nitric acid concentrations, which is in accordance with studies conducted by Shackleford *et al.* on polycrystalline gold electrodes in nitric acid solution (15). The gold electrochemistry in this pH range then still prevents us from consulting the look-up tables provided by Myland, Oldham, Zoski and Bond. However, the similarity of the voltammograms recorded in the absence and presence of Am(III) no longer allow us to definitively propose that Am(III) electro-oxidation proceeds via an EC' process. Due to these reasons, analysis with a gold electrode was abandoned and instead carried out with a glassy carbon electrode.

Investigation with a glassy carbon electrode revealed that although the measurements preliminarily showed promising results, the method of Myland, Oldham, Zoski and Bond was not able to be employed due to the fact that the carbon electrode was in fact not a microdisc electrode, along with the fact that the Am(III) oxidation wave was hidden in oxygen evolution. However, as discussed in the Results & Discussion section of Part 1, by consulting the redox potentials for the Am-H_2O system at pH 0 of Figure 8-17b (17), and by correlating these to our experimental results, we can conclude that it is straightforward to oxidise Am(III) through to Am(VI) on carbon electrodes. This is an observation that has important ramifications for the control of the Am(VI) valence state during advanced separations schemes for Am.

As the original purpose of this work was to assess the potential for Am to affect the corrosion behaviour of process steels, either as a potential accelerator or inhibitor of corrosion, we have studied the linear sweep voltammetries and electrochemical impedance spectroscopies of three process steels commonly found throughout the nuclear fuel cycle, our experimental work being based on the works of Williamson on the mechanisms of fixed contamination of commonly engineered surfaces (4). Our findings show that americium does in fact appear to be incorporating in to the passive oxide layer of the 304L, 316L and 347L stainless steels. This may have important ramifications for decommissioning in the future. Whilst it may initially appear to be advantageous to have Am incorporate in to the passive layer, as it results in a higher passive layer resistance, thus affording a higher level of protection for the steel, the embedding of americium into the steel structure would pose a greater disadvantage from a decontamination perspective. This would mean that an aggressive chemical or attritive decontamination technique may be needed to subsequently remove the americium, with subsequent significant secondary waste arising.

References

1. N. Rauff-Nisthar, C. Boxall. *A fundamental study of the interactions of americium with steel surfaces.* s.l. : European Commission - TALISMAN, 2015.

2. P. Kadar, K. Varga, B. Baja, Z. Nemeth, N. Vajda, Zs. Stefanka, L. Kover, I. Cserny, J. Toth, T. Pinter, J. Schunk. *Accumulation of uranium, transuranium and fission products on stainless steel surfaces II. Sorption studies in a laboratory model system.* s.l. : Journal of Radioanalytical and Nuclear Chemistry, 2011, Vol. 288.

3. D. Li, D.I. Kaplan. *Literature review on the sorption of plutonium, uranium, neptunium, americium and technetium to corrosion products on waste tank liners.* s.l. : Department of Energy, 2012.

4. B. Williamson. *Mechanisms of fixed contamination of commonly engineered surfaces.* s.l. : Lancaster University, 2018.

5. L.R. Morss, N.M. Edelstein, J. Fuger. *The chemistry of the actinide and transactinide elements.* s.l. : Springer, 2010.

6. A.M. Bond, K.B. Oldham, C.G. Zoski. *Steady-state voltammetry.* s.l. : Analytica Chimica Acta, 1989, Vol. 216. pp. 177 - 230.

7. K.B. Oldham, J.C. Myland, C.G. Zoski, A.M. Bond. *Kinetic parameters from steady-state voltammograms at microdisc electrodes.* s.l. : Journal of Electroanalytical Chemistry and Interfacial Electrochemistry, 1989, Vol. 270. pp. 79 - 101.

8. A. Sekretareva, M. Vagin, A. Volkov, I. Zozoulenko, M. Eriksson. *Evaluation of the electrochemically active surface area of microelectrodes by capacitive and faradaic currents.* s.l. : Chemistry Europe, 2019, Vol. 6. pp. 4411 - 4417.

9. S. Cherevko, A.A. Topalov, A. R. Zeradjanin, I. Katsounaros, K.J.J. Mayrhofer. *Gold dissolution: towards understanding of noble metal corrosion.* s.l. : RSC Advances, 2013, Vol. 3. pp. 16516 - 16527.

10. J.B. Sheppard, B. Hambly, B. Pendley, E. Lindner. *Voltammetric determination of diffusion coefficients in polymer membranes.* s.l. : Analyst, 2017, Vol. 142. pp. 930 - 937.

11. P. Song, A.C. Fisher, J.D. Wadhawan, J.J. Cooper, H.J. Ward, N.S. Lawrence. *A mechanistic study of the EC' mechanism – the split wave in cyclic voltammetry and square wave voltammetry.* s.l. : RSC Advances, 2016, Vol. 6. pp. 70237 - 70242.

12. R.S. Nicholson, I. Shain. *Theory of stationary electrode polarography. Single scan and cyclic methods applied to reversible, irreversible, and kinetic systems.* s.l. : Analytical Chemistry, 1964, Vol. 36. pp. 706 - 723.

13. A. Molina, E. Laborda, J. Gonzalez, R.G. Compton. *Effects of convergent diffusion and charge transfer kinetics on the diffusion layer thickness of spherical micro- and nanoelectrodes.* s.l. : Physical Chemistry Chemical Physics, 2013, Vol. 15. pp. 7106 - 7113.

14. K.B. Oldham. *Steady-state microelectrode voltammetry as a route to homogeneous kinetics.* s.l. : Journal of Electroanalytical Chemistry, 1991, Vol. 313. pp. 3-16.

15. S.G.D. Shackleford, C. Boxall, S.N. Port, R.J. Taylor. *An in situ electrochemical quartz crystal microbalance study of polycrystalline gold electrodes in nitric acid solution.* s.l. : Journal of Electroanalytical Chemistry, 2002, Vol. 538 - 539. pp. 109 - 119.

16. M. Pourbaix. *Atlas of electrochemical equilibria in aqueous solutions.* Oxford : Pergamon Press, 1966.

17. J.M. Adnet. *Separation of oxidised americium.* s.l. : SACSESS Conference, 2013.

18. B.J. Mincher. *Progress in high valent americium partitioning by solvent extraction.* Warsaw : SACSESS Annual Meeting and Workshop, 2015.

19. C. Kato, F. Ueno, M. Yamamoto, Y. Ban, G. Uchiyama, Y. Nojima, S. Fujine. *Effects of oxidation states of Np on polarization curve of stainless steel in boiling 3M-HNO_3.* s.l. : ECS Transactions, 2013, Vol. 53. pp. 45-55.

20. R. Woodhouse, C. Boxall, R.J. Wilbraham. *Nitric acid reduction on 316L stainless steel under conditions representative of reprocessing.* s.l. : ECS Transactions, 2013, Vol. 53. pp. 33-44.

21. B. Gwinner, M. Auroy, D. Mas, A. Saint-Jevin, S. Pasquier-Tilliette. *Impact of the use of the ferritic/martensitic ODS steels cladding on the fuel reprocessing PUREX process.* s.l. : Journal of Nuclear Materials, 2012, Vol. 428. pp. 110 - 116.

22. PalmSens. *Compact Electrochemical Interfaces. Bode and Nyquist Plot.* https://www.palmsens.com/knowledgebase-article/bode-and-nyquist-plot/ [Online].

23. S. Ningshen, U.K. Mudali, S. Ramya, B. Raj. *Corrosion behaviour of AISI type 304L stainless steel in nitric acid media containing oxidizing species.* s.l. : Corrosion Science, 2011, Vol. 53. pp. 64 - 70.

24. E.A. Howett. *The behaviour of spent nuclear fuel in wet interim storage.* s.l. : Lancaster University, 2019.

25. M. Schmid, A. Liebel, R. Lackner, D. Steigenhöfer, A. Niculae, H. Soltau. *A dedicated backscattered electron detector for high speed imaging and defect inspection.* s.l. : Microscopy Society of America, 2017, Vol. 23.

26. D. Titus, E. J. J. Samuel, S. M. Roopan. *Green synthesis, characterization and applications of nanoparticles - chapter 12 nanoparticle characterization techniques.* s.l. : Micro and Nano Technologies, 2019. pp. 303 - 319**.**

Chapter 9 Conclusions & Further Work

9.1 Aims & Objectives

The aims and objectives of this work were to investigate the corrosion behaviour of UK specific spent nuclear fuel in an underground repository. As it is not possible to handle real nuclear spent fuel without specialist equipment in a laboratory due to its high radioactivity, simulated fuels (SIMFUELs) have been fabricated to study their corrosion behaviours. These SIMFUELs have been fabricated at the National Nuclear Laboratory (Springfields, Preston, UK). In order to assess the corrosion behaviour of our SIMFUELs, we have also employed undoped UO_2, a means of control, in our experiments.

In this work we have followed a stepwise approach in investigating the corrosion behaviour of our SIMFUELs. To begin with, we have characterised our SIMFUEL and undoped UO_2 samples using XRD, Raman Spectroscopy and cyclic voltammetry. We have analysed our samples as-received, and, in a simple background electrolyte, to better analyse the baseline corrosion behaviour before moving on to more complex systems. Following this, we have repeated the same measurements, as well as open circuit potential measurements, in the presence of varying concentrations of hydrogen peroxide. The reason for doing so is due to the fact that α-radiation is expected to prevail once the thermal pulse has taken place. After the thermal pulse, if and when the engineered barrier fails, groundwater will ingress in to the fuel matrix, generating the α-radiolysis of water, subsequently producing H_2O_2. Once we had studied the effects of H_2O_2 in simple background electrolyte, we investigated using the same analytical tools, the corrosion behaviour of our samples in two simulated groundwaters, one of which is likely to be present where a geological disposal facility may be built in future in the UK. Here we approached the analysis in the same way, first investigating the corrosion behaviour in the simulated groundwaters in the absence of H_2O_2, followed by its presence. As above mentioned, when the engineered barrier fails and groundwater ingress takes place, the groundwater, before coming in contact with the fuel matrix itself, will first react with the stainless steel cladding that the spent fuel is encased in. In order to assess the effect that this stainless steel cladding may have on the corrosion behaviour of our samples, we have conducted the same experiments in all three media, in the absence and presence of H_2O_2, with the undoped UO_2 and SIMFUEL samples coupled to the cladding. This will provide insights to the corrosion behaviour of spent fuel in real-life scenarios.

As the stainless steel cladding, as well as other commonly used process steels are ubiquitous throughout the nuclear fuel cycle, we have also investigated the effect that the minor actinide americium, commonly found in process streams, has on the corrosion behaviour of these steels.

The results of our findings are summarised in the following sections below.

9.2 Characterisation of UO_2 & SIMFUELs

In characterising our undoped UO_2 and SIMFUEL samples, we were able to establish that our undoped UO_2 sample was stoichiometric UO_2 by comparing its XRD data to data from the literature. We were also able to eliminate the possibility that our sample could in fact be U_4O_7, by looking at the lattice parameter of our sample and comparing it to the literature values of UO_2 and U_4O_7.

Comparing the peak assignments of a typical Raman spectrum of uranium dioxide to our undoped UO_2 sample, we were able to confirm the fundamental UO stretch at a Raman shift of 445 cm^{-1}, as well as the multi-component peak at a Raman shift from 500-700 cm^{-1} in the 25 & 43 GWd/tU SIMFUEL pellets, indicating defects to the perfect cubic fluorite structure of UO_2. In order to deconvolute the multi-component peak, a 2nd derivate anaylsis was used to fix the peak maxima and represent the peaks as Lorentzian. Here we observed that the peak at a Raman shift of 530 cm^{-1} increases as the simulated burnup increases, as there is a marked increase in lanthanide concentration. Thus, this peak is larger for the 43 GWd/tU SIMFUEL pellet than for the 25 GWd/tU SIMFUEL pellet.

The peak at a Raman shift of 575 cm^{-1} is selection rule forbidden in undefected and undoped UO_2. As the hyperstoichiometry of UO_2 increases and its structure moves towards a tetragonal structure, the selection rules start to relax, allowing for observation of this peak. There is an associated decrease in the intensity of this peak as the structure becomes more hyperstoichiometric. However, there is a small increase in this peak with simulant burn-up of the SIMFUELs. This is attributed to the introduction of lanthanides resulting in increased oxygen-vacancy sites, allowing the selection rules to further relax.

The peak at a Raman shift of 630 cm^{-1} is attributed to the presence of clusters of interstitial oxygen and continues to increase in intensity as the amount of oxygen content increases. However, the peak decreases slightly with increased burn-up. A possible explanation for this is that at high dopant levels the number of sites that may accommodate oxygen interstitials is decreased – or that additional oxygens that may otherwise reside interstitially are instead filling oxygen vacancies associated with Ln(III) dopants.

The following trends were also observed in the cyclic voltammetry of the three samples after comparison to regional assignments from the literature. Initially, in going from UO_2 to the 25 GWd/tU SIMFUEL sample, a large increase in conductivity is observed as at least some of the Ln(III) ions added to the sample precursor blend enter the UO_2 matrix, and the U(IV) ions adopting a U(V) oxidation state to charge compensate.

As we move from the 25 to the 43 GWd/tU SIMFUEL sample, the conductivity decreases, which may be due to a proportionately greater amount of Ln(III) partitioning in to the grey phase in the 43 GWd/tU SIMFUEL sample than in the 25 GWd/tU SIMFUEL sample. This effectively means that decreasing the concentration of U(V) sites in the 43 GWd/tU SIMFUEL sample compared to the 25 GWd/tU SIMFUEL sample, results in the lower conductivity of the 43 GWd/tU SIMFUEL sample when compared to the 25 GWd/tU SIMFUEL sample.

9.3 Effect of H_2O_2 on UO_2 & SIMFUELs

Whilst investigating the corrosion effects of deliberately added hydrogen peroxide on our three samples in background electrolyte using open circuit potential measurements, cyclic voltammetry and Raman spectroscopy, we have observed the following:

With regards to the open circuit potential measurements, we observed that when our samples were exposed to increasing concentrations of hydrogen peroxide, their rates of approach to their rest potentials also increased. At the same time we observed that the rest potentials reached also increased with increasing concentrations of hydrogen peroxide for all three of our samples.

When comparing our SIMFUEL pellets to that of CANDU SIMFUELs, it was observed that our AGR SIMFUELs were more electrochemically susceptible to oxidation and potentially oxidative dissolution than the CANDU SIMFUELs. This was attributed to the fact that the CANDU SIMFUELs had been prepared at a lower burnup of 1.5 at. %, as opposed to compositions equivalent to 3 and 6 at. % burnup CANDU fuels for our low doped 25 GWd/tU and high doped 43 GWd/tU SIMFUEL pellets respectively.

The measured Raman spectra revealed that hydrogen peroxide had no significant effect on the undoped UO_2 pellet. For the 25 GWd/tU SIMFUEL pellet and the 43 GWd/tU SIMFUEL pellet we saw that, whether in the absence or presence of H_2O_2, the broad compound peak at 575 cm^{-1} exhibited an increase with increased burn-up. This is attributed to the fact that the increase in dopants induces a range of lattice distortions. It was observed however, that the 43 GWd/tU SIMFUEL sample, after exposure to a solution containing 10 μmol dm^{-3} H_2O_2, showed a small decrease in intensity of its U1 peak. This may be explained by the fact that the H_2O_2 puts the SIMFUEL pellet into a potential range whereby the conversion of UO_{2+x} to $UO_{2.33}$ (U_3O_7) at grain boundaries and UO_2 to UO_{2+x} within the grains themselves may occur. This introduction of O^{2-} ions into the lattice may be reducing the intensity of U1. We do not see this effect with the 25 GWd/tU SIMFUEL pellet, likely due to there being less oxygen vacancies to begin with.

Contrary to the observed decrease in the intensity of U1 peak with the addition of hydrogen peroxide in the 43 GWd/tU SIMFUEL pellet, there was a marked increase in its intensity upon the addition of 1 mmol dm^{-3} hydrogen peroxide to the background electrolyte. This observation can be explained by the possible existence of a fourth defect peak, referred to as the U* band. As this peak is associated with the hyperstoichiometry at grain boundaries, it may be contributing to the overall intensity of the U1 peak. As the concentration of grain boundaries is lower in the low doped 25 GWd/tU SIMFUEL pellet as opposed to the high doped 43 GWd/tU SIMFUEL pellet, the observed increase in the intensity of the U1 in smaller than it is for the 43 GWd/tU SIMFUEL pellet. Given that U1 for the 43 GWd/tU SIMFUEL is seen to decrease in intensity in 10 μmol dm^{-3} peroxide dosed electrolyte compared to undosed electrolyte, it would seem that apparent increase in U1 intensity associated with U* is only observed at high peroxide concentrations – an observation consistent with U* being an intrinsically weak feature.

Furthermore, we observed that exposure to a background electrolyte containing a 1 mmol dm^{-3} H_2O_2 spike drove the formation of the uranyl phase studtite/metastudtite in the undoped UO_2 sample after 4 hrs, and in the 25 GWd/tU SIMFUEL pellet after prolonged exposure times.

Finally, we were able to confirm through calculated i_{corr} data that the current densities of SIMFUEL samples increased when compared to our undoped UO_2 sample, meaning that with the addition of dopants, the sample becomes more susceptible to corrosion, which is in accordance with our electrochemical and Raman spectral data.

9.4 Behaviour of UO_2 & SIMFUELs in Simulated Groundwaters

Whilst investigating the effect that various groundwater simulants, namely a modified simplified and an evaporate groundwater simulant have on the corrosion behaviour of our undoped UO_2 and 25 & 43 GWd/tU SIMFUEL samples, we found that immersion of the samples in solutions of a higher pH than that of the 0.1 mol dm^{-3} Na_2SO_4 background electrolyte led to the rest potentials during an OCP measurement of the samples being at much more negative potentials than those previously measured. Upon further investigation, it was discovered that immersion in a solution of a lower pH, namely that of pH 3, the rest potentials measured for the three samples during open circuit potential measurements, yielded much more positive results when compared to the immersion in higher pH solutions.

An explanation for this positive movement in equilibrium OCP with decreasing pH may be afforded by the fact that the measured OCP is a mixed potential, whose value is determined by the balance between two redox processes - an oxidation process and a reduction process – both taking place at the surface of our electrodes.

The anodic process that is most likely controlling the mixed potential is the solid state oxidation of U(IV) to U(V) in UO_2 to form a higher oxide, in the first instance via UO_{2+x}. This oxidation introduces additional holes in the U 5f band, moving the material Fermi level to lower electron energies / more positive potentials. As the bands are pinned at the surface by the protonation/deprotonation of surface oxide/hydroxide sites (i.e. H^+ is the potential determining ion) the bands will bend upwards

in energy as the material surface is approached from within the urania bulk. This in turn results in migration of the holes to the surface, resulting in the formation of an accumulation layer and rendering it quasi-metallic and so facilitating further redox processes.

The associated cathodic process of our mixed potential, is most likely the reduction of the above-mentioned higher oxide. As we assume that there may be a thin oxidation layer on the surface of the UO_2 electrode, the reduction of surface UO_{2+x} / U_4O_9 may be expected to play a role in determining the potentials measured during the OCP experiments from the very beginning of the immersion period. This role grows in dominance as more of the higher oxide layer is formed at the electrode surface. The equilibrium, or the measured rest potential is then obtained when the UO_2 oxidation reaction and higher oxide reduction reaction come into a mass action influenced balance.

The Raman measurements of our three samples taken after immersion in the two groundwater simulants are consistent with those observed in neutral background electrolyte (see Section 9.2) and in peroxide loaded background electrolyte (see Section 9.3).

Analysis of the cyclic voltammogram in modified simplified groundwater showed that the electrochemical behaviour of the three samples was similar to that seen in the 0.1 mol dm^{-3} Na_2SO_4 background electrolyte, with the following exceptions:

Based on the higher pH of the modified simplified groundwater, we expect to see passivation on the surface of the electrodes at potentials above 0.25 V_{SCE} on the forward going sweep due to the formation of insoluble U(VI) (hydr-) oxides. We however, do not observe this passivation, most likely due to carbonate complexation. We see the reduction of this carbonate complex on the reverse sweep between – 0.5 and – 0.75 V_{SCE}.

With regards to the cyclic voltammograms measured in evaporite groundwater simulant, the scans were again similar to those measured in 0.1 mol dm^{-3} Na_2SO_4, with the exceptions of:

On the reverse sweeps we observe two reduction peaks. The peak observed between 0.5 -0.75 V_{SCE} can be attributed to the reduction of the carbonate complexed uranyl mentioned above. The peak observed at approximately 0.1 V_{SCE} can be attributed to either the reduction of the recrystalised phases from $UO_{2.67}$/$UO_{2.5}$/$UO_{2.33}$ to U(IV), or the conversion of UO_{2+x} to U(IV) (9). This peak arises due to the build-up of higher oxides ($UO_{2.5}$ or $UO_{2.67}$) caused by the recrystallisation/reduction reactions from adsorbed U(VI) species (9).

We observe this peak only in the evaporite groundwater simulant, and not in the modified simplified groundwater simulant, most likely due to the difference in pH between the two groundwaters affecting the efficacy of carbonate complexation with uranyl, as above-mentioned.

9.5 Effect of H_2O_2 on UO_2 & SIMFUELs in Simulated Groundwaters

Whilst studying the Raman spectral, open circuit potentials and cyclic voltammograms measured for our three samples with increasing concentrations of hydrogen peroxide, we have been able to link the data from the cyclic voltammograms to the open circuit potential data, in order to evaluate whether the SIMFUELs would corrode freely in groundwater of a similar composition to our modified simplified groundwater simulant, as well as our evaporite groundwater simulant. It was found that the SIMFUELs would not in fact corrode freely in either of the groundwater simulants, even in the presence of a high concentration of hydrogen peroxide (1 mmol dm^{-3}).

With regards to the Raman spectral measurements, we have observed that for both groundwater simulants, the observed intensities of the U1 and U2 peaks remain unchanged for both SIMFUEL samples with increasing additions of H_2O_2. This is most probably due to the fact that at the higher solution pH of both our groundwater simulants, the hydrogen peroxide is less stable, inevitably leading to its decomposition and thus preventing an increase in *x* which should have caused the increase in the intensity of the U2 peak observed for the 43 GWd/tU SIMFUEL pellet and, if occurring at grain boundaries, the increase in intensity of the U1 peak observed for both the 25 and 43 GWd/tU SIMFUEL samples. This is due to the fact that the U* band is not present due to the failed generation of hyper stoichiometric sites at grain boundaries related to the U* band. As aforementioned, this generation does not take place due to the decomposition of hydrogen

peroxide at this higher solution pH, when compared to the sodium sulfate background electrolyte observed in Chapter 4.

With regards to the open circuit potential measurements, we have observed that in both simulant groundwaters, the addition of a hydrogen peroxide spike, immediately shifted the rest potentials of all three samples more positive when compared to the rest potentials measured in the absence of H_2O_2. This simply occurred due to the hydrogen peroxide placing an oxidative stress onto the samples. We observed that the rest potentials measured for the open circuit potentials of our two SIMUEL samples in the evaporite groundwater simulant were higher with the addition of 100 μmol dm^{-3} and 1 mmol dm^{-3} H_2O_2 spikes when compared to the same measurements recorded in the modified simplified groundwater simulant. As the solution pH of the modified simplified groundwater is higher than that of the evaporite groundwater simulant (8.2 compared to 7.1), we would expect the hydrogen peroxide in the modified simplified groundwater to decompose more readily, and thus result in resting potentials more negative than those observed for the evaporite groundwater simulant. This is in fact what we do observe. The presence of Cl^- ions in the evaporite groundwater simulant however supress the decomposition of hydrogen peroxide, and the rest potentials recorded for the two SIMFUELs in evaporite groundwater are either lower or similar to those recorded in background electrolyte of pH 5.4.

Investigation of the cyclic voltammograms recorded in the modified simplified groundwater simulant we observed that the oxidation of UO_{2+x} to $UO_{2.33}$ at the grain boundaries takes place at approximately – 0.6 V_{SCE} for both SIMFUEL samples during the anodic scan and at a potential of – 0.13 V_{SCE}, we see the onset of the oxidation of UO_2 grains to UO_{2+x} for both SIMFUEL samples, with the various H_2O_2 spikes.

For the cathodic sweep, we observed the H_2O_2 reduction wave for the low doped SIMFUEL sample at approximately – 0.2 V_{SCE}, with the reduction of the carbonate-complexed uranyl taking place at approximately – 0.8 V_{SCE} for both the low doped 25 GWd/tU SIMFUEL sample and the 43 GWd/tU SIMFUEL sample. We do not observe the reduction of hydrogen peroxide during the cathodic sweep of the cyclic voltammogram for the 43 GWd/tU SIMFUEL sample, due to the fact that the increased concentration of epsilon particles is readily decomposing the hydrogen peroxide.

9.6 Corrosion of UO_2 & SIMFUELS coupled with 20/25/Nb Stainless Steel Cladding

Whilst investigating the effect that the coupling of the stainless steel cladding with the undoped UO_2 and SIMFUEL samples has in basic background electrolyte, as well as the two groundwater simulants in the absence and presence of hydrogen peroxide, we have found that in the case of the undoped UO_2 sample, coupling did lower the rest potential measured during OCP. The same was true in the presence of hydrogen peroxide. In the case of the two simulated groundwaters, we found that coupling raised the rest potential of the undoped UO_2 in both simulated groundwaters in the absence of H_2O_2, whilst the addition of H_2O_2 lowered the coupled rest potentials of the undoped UO_2 in both simulated groundwaters, even more so in the evaporite groundwater simulant.

For the low doped 25 GWd/tU SIMFUEL sample, we observed that in simple background electrolyte in the absence and presence of H_2O_2, the stainless steel cladding lowered the rest potentials measured during OCP when coupled with the SIMFUEL. In the case of the simulated groundwaters, we found that the measured rest potential was lowered when the SIMFUEL was coupled with the cladding in the absence of H_2O_2. In the presence of H_2O_2, we only found the measured rest potential to be lowered when coupled with the stainless steel cladding in the evaporite groundwater simulant. In the case of the modified simplified groundwater simulant, the measured rest potential was found to be raised when coupled with the cladding, in the presence of H_2O_2.

In the case of the high doped 43 GWd/tU SIMFUEL pellet, coupling in the absence of hydrogen peroxide lowered the measured rest potential in the simple background electrolyte, as well as both simulated groundwaters. In the case of added H_2O_2, we observed that coupling raised the measured rest potential of the coupled SIMFUEL in the background electrolyte, as well as the modified simplified groundwater, however in the evaporite groundwater simulant, we observed that the measured rest potential was lowered in the presence of H_2O_2.

In the sodium background electrolyte, where there are no corrosion inhibitors present, we expect the steel to corrode and sacrificially protect the pellet. This is indeed what we observe for all three samples in the absence of H_2O_2. In the presence of H_2O_2, the same is also observed, except for the high doped 43 GWd/tU SIMFUEL sample. This result is curious and subject to further work.

In the case of the modified simplified groundwater, where there is a corrosion inhibitor present, namely the base due to the elevated solution pH, we expect there to be additional protection for the UO_2 and SIMFUEL samples. We observe here that the cladding does not have much effect on the samples, and that they are better protected by the base. This is due to the fact that the stainless steel cladding cannot freely corrode in the presence of the base, and therefore cannot offer any sacrificial protection to the UO_2 and SIMFUELs. It is due to this reason that the rest potentials measured in the presence of the cladding are only slightly lower than those measured in the absence of the clad. In the presence of hydrogen peroxide, we observe the measured rest potential for the coupled UO_2 to only slightly decrease, whilst the measured rest potentials of the two SIMFUELs are slightly raised. This is most probably due to the fact that after the measured rest potentials have been initially raised due to the oxidative stress imposed by the H_2O_2 on the samples, since no corrosion takes place (due to a corrosion inhibitor being present), there is no protection afforded by the cladding. The protection offered by the base is not strong, and therefore the already raised rest potentials stay high after coupling too.

In the case of the evaporite groundwater simulant, where we have a corrosion inhibitor (the base) and a corrosion accelerator (Cl^- ions) present, we see some protection afforded by the base, but not as much as we observed in the modified simplified groundwater simulant, due to the evaporite groundwater simulant having a lower solution pH. In the absence of H_2O_2, we observe that all three samples are being somewhat protected by the presence of the base. This protection however, is not great enough, which is why the measured rest potentials are slightly raised for the undoped UO_2 and high doped 43 GWd/tU SIMFUEL samples. In the case of the low doped 25 GWd/tU SIMFUEL sample, we observe the measured potential also rising, until it suddenly drops and comes to rest at a lower potential than the one it initially started at. This is due to the fact that a pitting event occurs on the surface of the stainless steel cladding coupled with the 25 GWd/tU SIMFUEL sample. As the cladding can only protect the sample when it can corrode, once pitting occurs, the cladding can and does sacrificially protect the SIMFUEL sample. When H_2O_2 is added to the evaporite groundwater simulant, the cladding is able to corrode freely in combination with the presence of the Cl^- ions, meaning that all three samples are sacrificially protected by the cladding. Even though there is a low level of Cl^- ions present in the modified simplified groundwater simulant too, the protection afforded by the stainless steel cladding has been switched off by the solution pH which acts as a corrosion inhibitor. This is why the protection that we see is not as great as with the sodium sulfate background electrolyte or evaporite groundwater simulant.

The greatest protection afforded by the stainless steel cladding however is seen in the above described scenario where the cladding is allowed to freely corrode in the presence of the H_2O_2 and Cl^- ions in the evaporite simulant groundwater. From this we can conclude that the uranium is only protected when cladding can corrode freely.

9.7 Surface Alteration Influenced by Actinides

Whilst studying the electrochemical behaviour of the minor actinide americium in order to establish the standard electrochemical rate constant k^0 for the Am(III) oxidation reaction by using the method of Myland, Oldham, Zoski and Bond, which involved the analysis of steady state voltammograms recorded on microelectrodes of a range of radii, we have made the following observations:

At a concentration of 1 mol dm^{-3} HNO_3, cyclic voltammetry with a gold microdisc electrode at various sizes revealed that the measurements were heavily convoluted with gold oxidation This convolution meant that it was not possible to clearly extract the dependence of the Am(III) oxidation process on electrode radii from the cyclic voltammograms measured in 1 mol dm^{-3} HNO_3. Neither was it possible to conduct an analysis of the recorded voltammograms in accordance with the kinetic models of the EC' process described by Nicholson and Shain.

At a concentration of 3 mol dm^{-3} HNO_3, cyclic voltammetry with a gold microdisc electrode at various sizes revealed that at any one electrode diameter and scan rate, the CVs recorded in the presence of Am(III) are similar to those recorded in the absence. We attribute this result to increased susceptibility of Au to undergo oxidative dissolution at the higher nitric acid concentrations. The gold electrochemistry in this pH range then still prevents us from consulting the look-up tables provided by Myland, Oldham, Zoski and Bond. However, the similarity of the voltammograms recorded in the absence and presence of Am(III) no longer allow us to definitively propose that Am(III) electro-oxidation proceeds via an EC' process. Due to these reasons, analysis with a gold electrode was abandoned and instead carried out with a glassy carbon electrode.

Investigation with a glassy carbon electrode revealed that although the measurements preliminarily showed promising results, the method of Myland, Oldham, Zoski and Bond was not able to be

employed due to the fact that the carbon electrode was in fact not a microdisc electrode, along with the fact that the Am(III) oxidation wave was hidden in oxygen evolution. It can however be concluded that it is straightforward to oxidise Am(III) through to Am(VI) on carbon electrodes, an observation that has important ramifications for the control of the Am(VI) valence state during advanced separations schemes for Am.

Further investigation in to whether Am would affect the corrosion behaviour of process steels, either as a potential accelerator or inhibitor of corrosion, we have studied the linear sweep voltammetries and electrochemical impedance spectroscopies of three process steels commonly found throughout the nuclear fuel cycle. Our findings show that americium does in fact appear to be incorporating in to the passive oxide layer of the 304L, 316L and 347L stainless steels. This may have important ramifications for decommissioning in the future. Whilst it may be advantageous to have the Am incorporate in to the passive layer, obtaining to a higher layer resistance and thus affording a higher level of protection for the steel, the embedding of americium into the steel structure would pose a greater disadvantage, meaning that an attritive decontamination technique may be needed to subsequently remove the americium.

9.8 Further Work

(i) This work has been carried out on SIMFUELs to mimic the behaviour of real spent nuclear fuel. In order to assess the reliability of these results, electrochemical studies should be carried out on real spent fuel, the results of which should be compared to SIMFUELs in order to assess the likeness of the corrosion behaviour to one another.

(ii) We have studied the effects of coupling the 20/25/Nb stainless steel cladding to the SIMFUEL samples. In order to deconvolute the various mechanisms that are taking place, the corrosion behaviour of the stainless steel cladding should first be studied by itself, before investigating the coupling effects.

(iii) Further to point (ii), to better understand the coupling effect and its consequences on the corrosion behaviour of the SIMFUEL, further electrochemical methods such cyclic voltammetry should be conducted to complement the open circuit potential studies.

(iv) Further to point (iii), the stainless steel cladding used in these experiments has not been heat treated, irradiated or aged to mimic real life conditions such as the occurrence of a thermal pulse. For a more realistic analysis, treated stainless steel cladding should be used.

(v) We have studied the electrochemical behaviour of americium in 1 and 3 mol dm^{-3} HNO_3 using gold microelectrodes. In order to investigate whether it would be possible to deconvolute the gold electrochemistry from the americium electrochemistry, experiments should be carried out in higher concentrations of nitric acid.

(vi) Linear sweep voltammetry of our three steel samples have been carried out at a switching potential of 0.5 V_{SSCE}. In order to assess the growth and subsequent break-down of the passive oxide film, LSVs should be carried out a wider potential window to include the pre-transpassive and transpassive regions.

(vii) In order to further assess americium incorporation in to the passive oxide layer of the steels, EIS measurements should be carried out at several nitric acid concentrations.